

HIGH TEMPERATURE CORROSION STUDIES ON WELDED DISSIMILAR METALS

A THESIS

*Submitted in partial fulfilment of the
requirements for the award of the degree*

of

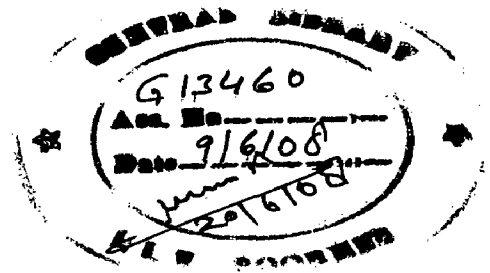
DOCTOR OF PHILOSOPHY

in

METALLURGICAL AND MATERIALS ENGINEERING

by

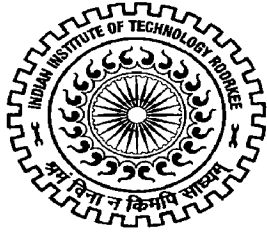
ARIVAZHAGAN. N



DEPARTMENT OF METALLURGICAL AND MATERIALS ENGINEERING
INDIAN INSTITUTE OF TECHNOLOGY ROORKEE
ROORKEE-247 667 (INDIA)

APRIL, 2007

**© INDIAN INSTITUTE OF TECHNOLOGY ROORKEE, ROORKEE, 2007
ALL RIGHTS RESERVED**



INDIAN INSTITUTE OF TECHNOLOGY ROORKEE

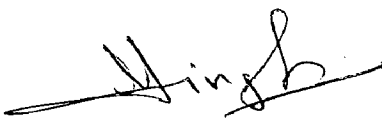
CANDIDATE'S DECLARATION


I hereby certify that the work which is being presented in the thesis, entitled **HIGH TEMPERATURE CORROSION STUDIES ON WELDED DISSIMILAR METALS** in partial fulfilment of the requirements for the award of the Degree of Doctor of Philosophy and submitted in the Department of Metallurgical and Materials Engineering of the Indian Institute of Technology Roorkee, Roorkee is an authentic record of my own work carried out during a period from January, 2003 to April, 2007 under the supervision of Dr. Satya Prakash, Professor and Dr. Surendra Singh, Associate Professor, Department of Metallurgical and Materials Engineering, Indian Institute of Technology Roorkee, Roorkee.

The matter presented in this thesis has not been submitted by me for the award of any other degree of this or any other Institute.


(ARIVAZHAGAN. N)

This is to certify that the above statement made by the candidate is correct to the best of our knowledge.

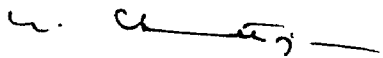

(Dr. SURENDRA SINGH)
Associate Professor


(Dr. SATYA PRAKASH)
Professor

Date:

The Ph.D. Viva-Voice Examination of Mr.Arivazhagan. N, Research Scholar, has been held on 5 Nov 2017.


Signature of Supervisor(s)


Signature of External Examiner

ABSTRACT

Dissimilar-metal joints are used widely in various industrial applications due to both technical and economic reasons. The adoption of dissimilar-metal combinations provides possibilities for the flexible design of the product by using each material efficiently, i.e., benefiting from the specific properties of each material in a functional way. Fusion welding is far the most important process used in the fabrication of modern boilers. Components are joined by the formation of a molten pool of metal between them. The production of high quality welds with a high degree of consistency is readily achievable. However, defects are more likely to occur in welds than in wrought material. In all arc welding processes, the intense heat source produced by the arc and the associated local heating and cooling results in a number of consequences in material corrosion behaviour and several metallurgical phase changes occur in different zones of a weldment. Because the occurrence of corrosion is due to electrochemical potential gradient developed in the adjacent site of a weld metal.

The materials used for high temperature applications are subjected to hot corrosion and high temperature wear. Hot corrosion can be defined as deposit modified, gas induced degradation of materials at high temperatures. For example, during the combustion stage in heat engines, particularly in gas turbines, sodium and sulphur impurities present either in fuel or in combustion air, react to form sodium sulphate (Na_2SO_4). If the concentration of the sulphate exceeds the saturation vapor pressure at the operating metal temperature for turbine blades and vanes ($700\text{-}1100^\circ\text{C}$), then deposition of the Na_2SO_4 will occur on the surface of these components. At higher temperatures the deposits of Na_2SO_4 are molten (m. p. = 884°C) and can cause accelerated attack. This type of attack is commonly called "Hot Corrosion". The accelerated corrosion can also be caused by the other salts, viz. vanadates or sulphates-vanadate mixtures as in oil ash corrosion and in the presence of solid or gaseous salts such as chlorides.

Low alloy steel and austenitic stainless steel possess a good combination of mechanical properties, formability, weldability, and resistance to stress corrosion cracking and other forms of corrosion. Owing to these attributes at moderately high temperatures, Cr-Mo steels are an extensively used family of engineering materials for applications such as steam generation/handling, petroleum processing/refining, thermal reforming/polymerization/cracking. However, the strength of the weldments of Cr-Mo steels is generally inferior, and most of the in-service failures are reported to take place

in the weld region ASME (1986). Given that the weldments are an indispensable part of most component fabrication, the frequent occurrence of weld failures has ensured ongoing research interest in the past few decades. However, most of the research effort has been directed to the correlation of the in-service failure of these steels to the microstructural degradation caused during welding. In recent years, first-ever systematic investigations have been initiated to study the influence of variation in alloy microstructure on gaseous corrosion of Cr-Mo steel weldments, with a view to developing a rather complete understanding of the complex interplay of the mechanical stress, microstructure, and environment which result in weld failure.

The present study is an attempt to evaluate the hot corrosion behaviour of dissimilar weldment of AISI 4140 and AISI 304 made by FRW, TIG and EBW in the temperature range from 500 to 900 °C with and without salt mixture of Na₂SO₄+ V₂O₅ (60%); Na₂SO₄ + NaCl (50%), K₂SO₄ + NaCl (60%) and Na₂SO₄ (40%) + K₂SO₄ (40%) + NaCl (10%) + KCl (10%) under cyclic conditions.

The welding work was carried out at Defence Metallurgical Research Laboratory (DMRL-Hyderabad) on the AISI 4140 and AISI 304 by FRW, EBW and TIG welding processes. The dissimilar alloy weldments in as welded condition were characterised by metallography, micro hardness across the weldment, tensile strength, impact toughness. XRD and EPMA analysis have also been carried out.

The behaviour of dissimilar alloy weldment has been studied in the air and molten salt. Air and molten salt studies performed in the laboratory furnace for 50 cycles each cycle consisting of 1 hour heating at different temperatures of exposure followed by 20 minutes cooling. At the end of each cycle the samples were critically examined and the change in weight was recorded. In case of studies under the molten salt, a uniform layer (3-5 mg/cm²) of the mixture of varying composition of Na₂SO₄, V₂O₅, NaCl, K₂SO₄ and KCl was coated on the samples with the help of camel hair brush by preheating the sample at 200°C.

At the end of each hot corrosion cycle the samples were critically examined regarding the colour, lustre, tendency to spall and adherence of scale and then subjected to weight change measurements. XRD and SEM/EDAX techniques were used to identify the phases obtained and the elemental analysis of the surface scale. These corroded samples were then cut across the cross-sections and mounted to study the cross-sectional details by EPMA.

The peak hardness on the weld zone made by FRW is less as compared to TIG and EBW. This can be attributed to more formation of carbides and intermetallic

compound in the weld zone when made by TIG and EBW which is also supported by XRD analysis.

The yield strength of dissimilar weldment made by EBW is higher as compared to the one made by TIG and FRW. Tensile testing of FRW weldment shows that the failure took on 4140 side, whereas in the case of weldment made by EBW and TIG, the failure occurred on the HAZ of AISI 4140. From the investigation in the friction welded dissimilar metals it was observed that nature of fracture become more brittle with increase in the burn off length. Whereas the SEM fractography of Impact tested dissimilar weldment made by EBW and TIG shows cleavage fracture.

In case of friction welded specimens the increase of burn off length led to more brittle fracture, which may be due to formation of more carbides and intermetallics. In case of EBW and TIG weldments the fractured surface indicates ductile nature.

The scale on the weldment was observed to be fragile and had tendency for spalling perhaps due to differences in the thermal-expansion coefficients of weld zone, and the two base metals and their oxides. From the X-ray mapping and elemental analysis on hot corroded sample, enrichment of Fe, Cr, Ni and C was observed in the weld region.

From the bar charts, it can be inferred that the friction welded dissimilar metals have shown low corrosion resistance against the given molten salt environments as compared to that against the air under cyclic conditions. The maximum weight gain in $\text{Na}_2\text{SO}_4 + \text{V}_2\text{O}_5$ (60%) environment at 600 °C is 50 times higher than that of one exposed under air under cyclic condition. Whereas it is 190 times in the environment of $\text{K}_2\text{SO}_4 + \text{NaCl}$ (60%). In the case of Na_2SO_4 (40%) + K_2SO_4 (40%) + NaCl (10%) + KCl (10%) the weight gain is around 100 times as compared to the weldment exposed to air. Whereas it is around 50 times in the environment of $\text{Na}_2\text{SO}_4 + \text{NaCl}$ (50%). XRD diffractograms and EDAX analysis have indicated the phases formed identical to those formed during oxidation in molten salt in almost all the corroded samples. At 700 and 900 °C higher corrosion rates were observed due to rapid reaction of molten salt when the friction welded dissimilar metals exposed to $\text{Na}_2\text{SO}_4 + \text{V}_2\text{O}_5$ (60%) environment.

The sequence for the overall resistance to hot corrosion behaviour of dissimilar weldment with variation of burn off length in all the molten salt environments used in this study has been observed as given below:

$$B5 > B7 > B9 > B12$$

The weight gain after 50 cycles of hot corrosion studies in all the environments could be arranged in the following order:

$K_2SO_4 + NaCl (60\%) > Na_2SO_4 (40\%) + K_2SO_4 (40\%) + NaCl (10\%) + KCl (10\%) > Na_2SO_4 + V_2O_5 (60\%) > Na_2SO_4 + NaCl (50\%) > Air$

The weight gain of weldment made by EBW and TIG exposed to $Na_2SO_4 + V_2O_5 (60\%)$ is around 1.5 times higher than that of the weight gain of weldment made by FRW. The weight gain of weldment made by FRW exposed to $K_2SO_4 + NaCl (60\%)$ is around 1.2 times higher than that of the weight gain of the weldment made by EBW and TIG. It shows that the environment of $K_2SO_4 + NaCl (60\%)$ is more aggressive for the weldment made by FRW as compared to one made by EBW and TIG. From the investigation it was observed that the weight gain for the weldment made by EBW and TIG, exposed to $K_2SO_4 + NaCl (60\%)$ is around 2 times higher than that of the weldment exposed to $Na_2SO_4 + V_2O_5 (60\%)$. The sequence for the overall resistant to hot corrosion behaviour of dissimilar weldment in molten salt environment has been observed as given below:

At 600 C exposed to $Na_2SO_4 + V_2O_5 (60\%)$:

FRW-B5 > FRW-B7 > FRW-B9 > FRW-B12 > EBW > TIG

At 600 C exposed to $K_2SO_4 + NaCl (60\%)$:

EBW > TIG > FRW-B5 > FRW-B7 > FRW-B9 > FRW-B12

Overall analysis of exposed samples in the three environments of study, formation of oxides of iron, chromium on the scale of the weldment has been identified by X-ray diffractograms and confirmed by the EDAX analysis. From the EDAX data, the scale on the weld zone of EBW and TIG weldment contains higher amount of Cr_2O_3 and NiO , which is also higher as compared to Friction weldment when exposed under $K_2SO_4 + NaCl (60\%)$ at 600 °C. It can be inferred from this that EBW and TIG weldment have provided maximum resistance to corrosion as compared to friction welded weldment in the above said environment. This may be attributed to the fast formation of a continuous chromia scale on the weld zone due to the easy diffusion of Cr, and Ni towards the weld zone from alloy 304 sides. The EPMA elemental analysis for most of the cases indicated the higher content of $Fe_2 O_3$ and $Cr_2 O_3$ on scale over weldment which may be due to enrichment of this zone with Fe and Cr.

PREFACE

The entire work carried out for this investigation has been presented into eight chapters.

Chapter-1 contains the introductory remarks about hot corrosion problem faced by the various industries and especially in coal fired boilers. The ways to counteract this problem are also briefly discussed.

Chapter-2 begins with exhaustive survey of literature regarding various aspects and mechanism of hot corrosion in different degrading environments. The various aspects for the problems of dissimilar alloy weldment and their degradations have also been reviewed. After reviewing the available literature the problem has been formulated.

Chapter-3 deals the experimental procedure to obtain the dissimilar alloy weldment, their characterisation, the hot corrosion studies and the analysis of final corrosion products in systematic way.

Chapter-4 presents the characterisation of dissimilar alloy weldment made by FRW, EBW and TIG welding process.

Chapter-5 contains the data regarding the cyclic oxidation studies performed on friction welded dissimilar metals in air at 500 and 600 °C also isothermal oxidation at 500, 700 and 900°C for 50 hours.

Chapter-6 includes the findings regarding the behaviour of friction welded dissimilar metals in cyclic hot corrosion in different molten salt environment of (i) $\text{Na}_2\text{SO}_4 + \text{V}_2\text{O}_5$ (60%); (ii) $\text{K}_2\text{SO}_4 + \text{NaCl}$ (60%); (iii) Na_2SO_4 (40%)+ K_2SO_4 (40%)+ NaCl (10%) + KCl (10%); (iv) $\text{Na}_2\text{SO}_4 + \text{NaCl}$ (50%) at 500 550 and 600 °C along with discussion of results.

Chapter-7 deals with the results and their discussion for the hot corrosion studies performed on the weldments made by EBW and TIG exposed at the temperature of 600 °C under the $\text{Na}_2\text{SO}_4 + \text{V}_2\text{O}_5$ (60%) and $\text{K}_2\text{SO}_4 + \text{NaCl}$ (60%) mixture of molten salt for 50 cycles.

Chapter-8 presents the comprehensive discussions on the results of mechanical properties of dissimilar welded metals. The results obtained in air and molten salt environment have been discussed incorporating the existing literature.

Chapter-9 compiles the results of the study are concluded in which begins with the key results of characterisation of dissimilar alloy weldment. Major conclusions of the study on the effect of various welding process on their behaviour in the corrosive environments under cyclic studies have been presented.

ACKNOWLEDGEMENTS

The author has great privilege and pride to express his immense sense of gratitude to **Dr. Satya Prakash**, Professor, Department of Metallurgical and Materials Engineering (MMED), Indian Institute of Technology, Roorkee for his valuable and intellectual guidance throughout the tenure of this work. He has been a motivating and driving force where targets appeared to be arduous during the course of work. Without his timely help, constructive criticism, positive attitude and painstaking efforts, it would have been impossible to complete this thesis in the present form.

The author is highly grateful to **Dr. Surendra Singh**, for his continuous encouragement and support as a co-supervisor. His constant motivation, valuable guidance, thought provoking discussions and his inspiring presence helped me to ride over the problems and complete this work successfully.

Author is highly indebted to Dr. S. K. Nath, Head, MMED for his co-operation in extending the necessary facilities and supports during the concluding phase of this work. Author is grateful to Dr. D. B. Goel for their valuable suggestions and timely help during the course of this work. Author wishes to record his deep sense of gratitude to Head, Institute Instrumentation Centre (IIC), Indian Institute of Technology Roorkee for extending necessary facilities during the experimental and analysis work.

Author is highly obliged and wishes to owe his sincere thanks to the technical and administrative staff of the MMED, especially to Mr. Rajinder S. Sharma, Mr. N. K. Seth, Mr. Vidya Prakash, Mr. T. K. Sharma, Mr. R. K. Sharma, who helped him in all possible ways during the experimental work.

Author would like to express his sincere thanks to Mr. S. K. Saini and Ms. Solan, Mrs. Rekha Sharma, and Mr. T. K. Ghosh of IIC, IIT, Roorkee for carrying out XRD, SEM and EPMA work respectively. Thanks are also acknowledged to Mr. Puran Sharma for preparing high quality micrographs and Mr. N. K. Varshney for tracing of the drawings.

Author is highly obliged to Dr. G. Madhusudhan Reddy, Scientist 'F' and Dr. T. Mohandas Scientist 'G' Defense Metallurgical Research Laboratory (DMRL), Hyderabad, Dr. M. Chakraborty, Professor, Metallurgical and Materials Engineering Department, IIT, Kharagpur,

Author owes his sincere thanks to Dr. Rabindranath Maiti of CRF IIT Khargpur for performing EDAX analysis.

Author would like to record his sense of gratitude for the library staff of IIT Roorkee, IIT Kharagpur, DMRL, Hyderabad and for their kind co-operation to carry out the literature survey. Thanks are also due to Mr. Sunil Sharma, Librarian of MMED for providing all the necessary help.

Author wishes to thank his friends and colleagues for their moral support, camaraderie help to keep things in perspective and for their loving support during my stay and lifting the moods whenever they arrived.

Author would like to express his reverence and great admiration for his parents, who have always been the guiding and encouraging force for him. Above all, author is highly indebted to almighty God who blessed him with spiritual support and fortitude at each and every stage of this work.


(ARIVAZHAGAN. N)

3.1.6 Scanning Electron Probe Micro Analysis (EPMA)	130
3.1.7 Hardness Test	130
3.1.8 Impact Test	130
3.1.9 Tensile Test	130
3.1.10 Scanning Electron Microscopy (SEM)	130
3.2 HIGH TEMPERATURE OXIDATION AND HOT CORROSION STUDIES	139
3.2.1 Experimental Setup	139
3.2.2 Oxidation Studies in Air	139
3.2.3 Hot Corrosion Studies in Molten Salt	140
<i>3.2.3.1 Molten Salt coating</i>	140
<i>3.2.3.2 Hot Corrosion Studies</i>	140
3.3 ANALYSIS OF CORROSION PRODUCTS OF OXIDATION IN AIR, MOLTEN SALT ENVIRONMENT	140
3.3.1 Visual Observation	141
3.3.2 Thermogravimetric Studies	141
3.3.3 Measurement of Scale Thickness	141
3.3.4 X-Ray Diffraction (XRD) Analysis	141
3.3.5 SEM/EDAX Analysis	142
<i>3.3.5.1 Surface morphology</i>	142
<i>3.3.5.2 Cross-section morphology</i>	142
3.3.6 Electron Probe Micro Analyser (EPMA)	142
CHAPTER 4 CHARACTERISATION OF WELDMENT	145
4.1 FRICTION WELDING	145
4.1.1 Visual Examination	145
4.1.2 Macro structure	145
4.1.3 Microstructure	149

2.10	BEHAVIOUR OF METALS AND ALLOYS IN VARIOUS OXIDISING ENVIRONMENTS	80
2.10.1	Air	80
2.10.2	Pure Na ₂ SO ₄	82
2.10.3	Vanadium Pentoxide (V ₂ O ₅)	85
2.10.4	Molten Salt (Na ₂ SO ₄ -V ₂ O ₅) Environment	87
2.10.5	Molten Salt Environment (40 wt% K ₂ SO ₄ , 60 wt% NaCl)	92
2.10.6	Molten Salt Environment (40 wt% K ₂ SO ₄ , 40 wt% Na ₂ SO ₄ , 10 wt% KCl, and 10 wt% NaCl)	96
2.10.7	Hot corrosion by NaCl/Na ₂ SO ₄ mixtures	104
2.10.8	Hot corrosion with 100% NaCl	109
2.11	HOT CORROSION ON THE WELDMENT	111
2.11.1	Weldment corrosion of Cr-Mo Steel	113
2.11.2	Internal Oxidation of Low alloy steel	114
2.11.3	Internal Oxidation in Weldment	114
2.11.4	High temperature corrosion on dissimilar Weldment	115
2.12	FORMULATION OF PROBLEM	118
CHAPTER 3	EXPERIMENTAL PROCEDURE	125
3.1	WELDMENT CHARACTERISATION	125
3.1.1	Selection of Base Metals	125
3.1.2	Friction Welding (FRW)	126
3.1.3	Electron Beam Welding (EBW)	126
3.1.4	Tungsten Inert Gas Welding (TIG)	129
3.1.5	Optical microscopy	129

CONTENTS

	Page No.
<i>Abstract</i>	i
<i>Preface</i>	v
<i>Acknowledgements</i>	vii
<i>Contents</i>	ix
<i>List of Figures</i>	xvii
<i>List of Tables</i>	xxxiii
<i>Research Papers Presented/Published</i>	xxxv
<i>Abbreviations</i>	xxxvii
CHAPTER 1 INTRODUCTION	1
CHAPTER 2 LITERATURE REVIEW	11
2.1 WELDABILITY ASPECTS OF AUSTENITIC SATINLESS STEELS	11
2.2 WELDABILITY ASPECTS OF LOW ALLOY STEELS	12
2.3 FRICTION WELDING	15
2.3.1 Friction Welding Process	15
2.3.2 Theoretical Considerations	21
2.3.3 Welding Characteristics of Continuous Drive Friction welding	25
<i>2.3.3.1 Rotational speed</i>	<i>29</i>
<i>2.3.3.2 Frictional Heating Time</i>	<i>29</i>
<i>2.3.3.3 Forging Pressure</i>	<i>29</i>
2.3.4 Dissimilar-metal joints with Friction welding	29
2.3.5 Advantages of friction welding	34

2.3.6	Limitations of friction welding	34
2.4	ELECTRON BEAM WELDING	35
2.4.1	Electron Beam Welding Process	35
2.4.2	Dissimilar-metal joints with EBW	36
2.4.3	Weldability of austenitic/ferritic stainless steel with EBW	42
2.4.4	Advantages	44
2.4.5	Limitations	44
2.5	TUNGSTEN INERT GAS WELDING (TIG)	47
2.6	HIGH TEMPERATURE OXIDATION	50
2.6.1	Mechanism of Oxidation	50
2.7	HOT CORROSION	51
2.7.1	Mechanisms of Hot Corrosion	52
2.7.2	Hot Corrosion Degradation Sequence	55
2.7.3	Salt Fluxing	57
2.8	SALT CHEMISTRY	63
2.8.1	Sulphate Solution Chemistry	63
2.8.2	Vanadate Solution Chemistry	63
2.9	HOT CORROSION IN ENERGY GENERATION AND COAL GASIFICATION SYSTEMS	69
2.9.1	Characterization of Gasification Environments	77
2.9.2	Chemistry of Salts in Combustion of Coal/Fuel Oils	78

4.1.4	XRD ANALYSIS	149
4.1.5	Electron Probe Micro Analysis	159
4.1.6	Micro Hardness	159
4.1.7	Impact Toughness	167
4.1.8	Tensile Testing	168
4.1.9	Discussions	183
4.2	ELECTRON BEAM WELDING	184
4.2.1	Visual Examination	184
4.2.2	Macro structure	184
4.2.3	Microstructure	184
4.2.4	XRD ANALYSIS	189
4.2.5	Electron Probe Micro Analysis	189
4.2.6	Micro Hardness	193
4.2.7	Impact Toughness	193
4.2.8	Tensile Testing	193
4.2.9	Discussions	194
4.3	TUNGSTEN INERT GAS WELDING	209
4.2.1	Visual Examination	209
4.2.2	Macro structure	209
4.2.3	Microstructure	209
4.2.4	XRD ANALYSIS	210
4.2.5	Electron Probe Micro Analysis	210
4.2.6	Micro Hardness	210
4.2.7	Impact Toughness	210
4.2.8	Tensile Testing	225
4.2.9	Discussions	225

CHAPTER 5	OXIDATION STUDIES OF FRICTION WELDED DISSIMILAR WELDMENT IN AIR	233
5.1	AIR OXIDATION TEST	233
5.2	RESULTS	233
5.2.1	Visual Examination	234
5.2.2	Thermogravimetric Data	234
5.2.3	X-ray Diffraction Analysis	234
5.2.4	Scale Thickness Measurement	243
5.2.5	SEM/EDAX Analysis	243
5.2.6	EPMA Analysis	243
5.2.7	Discussion	244
CHAPTER 6	HOT CORROSION STUDIES OF FRICTION WELDED DISSIMILAR METALS IN MOLTEN SALT ENVIRONMENT	273
6.1	RESULTS	273
6.1.1	Friction Welded Dissimilar Metals Exposed to $\text{Na}_2\text{SO}_4 + \text{V}_2\text{O}_5$ (60%)	274
6.1.1.1	<i>Visual Examination</i>	274
6.1.1.2	<i>Thermogravimetric Data</i>	274
6.1.1.3	<i>X-ray Diffraction Analysis</i>	281
6.1.1.4	<i>Scale Thickness Measurement</i>	282
6.1.1.5	<i>SEM/EDAX Analysis</i>	282
6.1.1.6	<i>EPMA / EDAX Analysis</i>	319
6.1.2	Friction Welded Dissimilar Metals Exposed to $\text{K}_2\text{SO}_4 + \text{NaCl}$ (60%)	320
6.1.2.1	<i>Visual Examination</i>	320
6.1.2.2	<i>Thermogravimetric Data</i>	320

6.1.2.3	<i>X-ray Diffraction Analysis</i>	359
6.1.2.4	<i>Scale Thickness Measurement</i>	359
6.1.2.5	<i>SEM/EDAX Analysis</i>	360
6.1.2.6	<i>EPMA Analysis</i>	360
6.1.3	Friction Welded Dissimilar Metals Exposed to Na₂SO₄ (40%) + K₂SO₄ (40%) + NaCl (10%) + KCl (10%)	405
6.1.3.1	<i>Visual Examination</i>	405
6.1.3.2	<i>Thermogravimetric Data</i>	405
6.1.3.3	<i>X-ray Diffraction Analysis</i>	406
6.1.3.4	<i>Scale Thickness Measurement</i>	406
6.1.3.5	<i>SEM/EDAX Analysis</i>	407
6.1.3.6	<i>EPMA Analysis</i>	407
6.1.4	Friction Welded Dissimilar Metals Exposed to Na₂SO₄ (50%) + NaCl (50%)	408
6.1.4.1	<i>Visual Examination</i>	408
6.1.4.2	<i>Thermogravimetric Data</i>	408
6.1.4.3	<i>X-ray Diffraction Analysis</i>	409
6.1.4.4	<i>Scale Thickness Measurement</i>	409
6.1.4.5	<i>SEM/EDAX Analysis</i>	409
6.1.4.6	<i>EPMA Analysis</i>	410
6.2	DISCUSSION	503
6.2.1	Friction Welded Dissimilar Metals Exposed to Na₂SO₄ + V₂O₅ (60%)	503
6.2.2	Friction Welded Dissimilar Metals Exposed to K₂SO₄ + NaCl (60%)	505
6.2.3	Friction Welded Dissimilar Metals Exposed to Na₂SO₄ (40%) + K₂SO₄ (40%) + NaCl (10%) + KCl (10%)	508
6.2.4	Friction Welded Dissimilar Metals Exposed to Na₂SO₄ (50%) + NaCl (50%)	511

CHAPTER 7	HOT CORROSION STUDIES OF EBW & TIG WELDED DISSIMILAR METALS IN MOLTEN SALT ENVIRONMENT	515
7.1	RESULTS	516
7.1.1	Electron Beam Weldment exposed to Na₂SO₄ + V₂O₅ (60%) & K₂SO₄ + NaCl (60%) environment at 600 °C	516
	<i>7.1.1.1 Visual Examination</i>	516
	<i>7.1.1.2 Thermogravimetric Data</i>	517
	<i>7.1.1.3 X-ray Diffraction Analysis</i>	517
	<i>7.1.1.4 Scale Thickness Measurement</i>	517
	<i>7.1.4.5 SEM/EDAX Analysis</i>	518
	<i>7.1.4.6 EPMA Analysis</i>	518
7.1.2	TIG Weldment exposed to Na₂SO₄+60%V₂O₅ and K₂SO₄ + NaCl (60%) environment at 600 °C	519
	<i>7.1.2.1 Visual Examination</i>	519
	<i>7.1.2.2 Thermogravimetric Data</i>	519
	<i>7.1.2.3 X-ray Diffraction Analysis</i>	520
	<i>7.1.2.4 Scale Thickness Measurement</i>	520
	<i>7.1.2.5 SEM/EDAX Analysis</i>	520
	<i>7.1.2.6 EPMA Analysis</i>	521
7.2	DISCUSSION	521
	7.2.1 Electron Beam Welding	521
	7.2.2 Tungsten Inert Gas welding	523
CHAPTER 8	COMPARATIVE DISCUSSION	561
CHAPTER 9	CONCLUSIONS	591
	SUGGESTIONS FOR FUTURE WORK	597
	REFERENCES	599

LIST OF FIGURES

Figure No.	Particulars	Page No.
2.1	Time-Temperature relationship for intergranular precipitation of carbides in AISI 304 austenitic stainless steel and weld metal as a function of carbon content	13
2.2	Relationship between carbon content and maximum hardness of steel with microstructures of 50 and 100% martensite.	17
2.3	5 CCT diagram of HTLA (AISI 4340) steel	17
2.4	Sequence of friction welding process	19
2.5	Time torque relationship for continuous drive friction welding process	23
2.6	Effect of rotational speed on duration of welding	23
2.7	Variations of process parameters with time for continuous drive friction welding	27
2.8(A)	Typical microstructure of friction welded AISI 304 and 4340.	31
2.8(B)	Microhardness traverse along the bond line of a typical friction weldment.	31
2.9 (A)	The macro SEM photo taken from welding interface of friction welded sample and representation of interface reactions.	31
2.9 (B)	The typical TIG welding process.	45
2.10	Schematic illustration of the growth of chromia scales in (i) the absence of oxygen active elements and with predominant outward transport of chromia through the scale, and (ii) the presence of oxygen active elements and with predominant inward transport of oxygen.	53
2.11	Schematic diagram showing a Na_2SO_4 deposit upon an alloy separating the alloy from the gas phase.	56
2.12	(a) Schematic diagram for fluxing showing dissolution of metal oxide at the oxide/salt interface (Shores, 1983) and (b) Precipitation of a porous MO oxide supported by the solubility gradient in a fused salt film.	61
2.13	Na-Cr-S-O phase stability diagram for 1200 °C.	65
2.14	Phase stability diagram for Na-V-S-O system at 900 °C.	67
2.15	Schematic of hot corrosion mechanisms.	73
2.16	Corrosion rate of Type 304 stainless steel in different mixtures of Na_2SO_4 - V_2O_5 .	75
2.17	Phase Diagram for K_2SO_4 -NaCl System.	89
2.18	Superimposed stability diagram of the (Fe, Cr, Ni)-O-Cl system at 550 °C.	93
2.19	Superimposed stability diagram of the (Fe, Cr, Ni)-O-Cl system at 550 C. calculated with HSC Chemistry.	101
2.20	phase Diagram for NaCl and Na_2SO_4 system	105
3.1	Microstructure of parent metals	127
3.2	Friction welding equipment	127
3.3	Hardness measurement along the weld	131
3.4	Charpy 'V' notch impact test sample	131
3.5	Tensile specimen preparation by EDM wire cut	133
3.6	Tensile specimen for friction weldment,	135

	Burn off length 'B' 5, 7, 9 and 12 mm	
3.7	Tensile specimen for EBW and TIG welded sample	137
4.1	Friction welded specimen (Burn-off length B5, B7, B9 and B12)	147
4.2	Effect of burn – off length on flash formation (Material on left side in the macrographs is AISI 304 stainless steel.) burn-off length: B5, B7, B9 and B12.	147
4.3	Microstructure at centre and periphery of the friction weld joint for B5, B7, B9 and B12. (B-Burn off length in mm)	151
4.4	Microstructures in different regions of AISI 304 in burn-off length 12	153
4.5(a)	X-Ray diffraction patterns for friction weldment as welded condition burn-off length B5 and B7	155
4.5(b)	X-Ray diffraction patterns for friction weldment as welded condition Burn-off length B9 and B12	157
4.6	Elemental distribution across the weld centre in 4140-304 weld joint (B5 and B12)	161
4.7(a)	Effect of burn-off length (B5 and B7) on hardness distribution across the weldment.	163
4.7(b)	Effect of burn-off length (B9 and B12) on hardness distribution across the weldment.	165
4.8	Fractographs of AISI 304 and AISI 4140 parent metal at the center	169
4.9(a)	Fractographs of 304 - 4140 weld, B5, B7 at the center (Burn-off length 5, 7 mm)	171
4.9(b)	Fractographs of 304 - 4140 weld, B9, B12 at the center (Burn-off length 9, 12 mm)	173
4.10	Photograph for fractured tensile specimen of friction welded specimen	175
4.11	Tensile Fractographs of friction welded AISI 304 and AISI 4140 by keeping burn off length 5 mm.	175
4.12	Tensile Fractographs of friction welded AISI 304 and AISI 4140 by keeping burn off length 7 mm.	177
4.13	Tensile Fractographs of friction welded AISI 304 and AISI 4140 by keeping burn off length 9 mm.	177
4.14	Tensile Fractographs of friction welded AISI 304 and AISI 4140 by keeping burn off length 12 mm.	179
4.15	Stress Vs Strain curve for tensile specimen for friction welded AISI 4140 and AISI 304	181
4.16	photograph of Electron Beam Welded specimen	185
4.17	Macro structure of electron beam welded AISI 4140 and AISI 304 dissimilar metals.	185
4.18	Microstructure of electron beam welded dissimilar AISI 4140 and AISI 304 metals	187
4.19	X-Ray diffraction patterns for Electron Beam weldment as welded condition.	191
4.20	Elemental distribution across the weld centre in 4140-304 of Electron Beam Weld joint	191
4.21	Hardness distribution across the EBW weldment of AISI 4140 and AISI 304	195
4.22	Photograph of Charpy 'V' notch tested sample for Electron Beam Welded Sample	197
4.23(i)	Fractographs of Electron beam welded AISI 304 – AISI 4140 metals	199
4.23(ii)	SEM Fractographs of Electron beam welded AISI 304 – AISI 4140	201

	metals	
4.23(iii)	Fractographs of Electron beam welded AISI 304 – AISI 4140 metals	203
4.24	Photograph for tensile fractured weldment made by EBW	205
4.25	SEM fractographs for tensile specimen for EBW welded AISI 4140 and AISI 304	205
4.26	SEM fractograph for tensile specimen for EBW welded AISI 4140 and AISI 304	207
4.27	Stress Vs Strain curve for EBW welded AISI 4140 and AISI 304 weldment	207
4.28	TIG Welded specimen	211
4.29	Macro structure of TIG welded AISI 4140 and AISI 304 dissimilar metals	211
4.30	Microstructure of TIG welded AISI 4140 and AISI 304 dissimilar metals	213
4.31	X-Ray diffraction patterns for TIG weldment as welded condition	215
4.32	Elemental distribution across the weld centre in 4140-304 TIG weld joint	217
4.33	Hardness distribution across the TIG weldment of AISI 4140 and AISI 304	219
4.34(i)	SEM Fractography of V notch Impact tested TIG weldment of AISI 4140 and AISI 304	221
4.34(ii)	SEM Fractography of V notch Impact tested TIG weldment of AISI 4140 and AISI 304	223
4.35	Photograph for tensile fractured TIG welded AISI 4140 and AISI 304	227
4.36	SEM fractograph for TIG welded AISI 4140 and AISI 304 tensile specimen	229
4.37	Stress Vs Strain curve for TIG welded tensile specimen	231
5.1	Photograph after complete the high temperature corrosion of friction welded AISI 4140 and AISI 304, exposed under air. (A) Cyclic oxidation at 500 °C, (B) Cyclic oxidation at 600 °C, (C) Isothermal Oxidation at 500 °C, (D) Isothermal Oxidation at 700 °C, (E) Isothermal Oxidation at 900 °C.	235
5.2	Plots of cumulative weight gain (mg/cm^2) as a function of time (number of cycles) for 500 and 600 °C after 50 cycles	237
5.3(A)	X-Ray diffraction patterns for dissimilar friction weldment made by AISI 4140 and AISI 304, exposed under cyclic air oxidation at 500 and 600 °C	239
5.3(B)	X-Ray diffraction patterns for dissimilar friction weldment made by AISI 4140 and AISI 304, exposed under cyclic air oxidation at 500 700 and 900 °C	241
5.4	Back Scattered Image after complete the high temperature corrosion of friction welded AISI 4140 and AISI 304, exposed under air. (i) Cyclic oxidation at 500 °C, (ii) Cyclic oxidation at 600 °C, (iii) Isothermal Oxidation at 500 °C, (iv) Isothermal Oxidation at 700 °C, (v) Isothermal Oxidation at 900 °C.	245
5.5(a)	EDAX on the weldment of 4140-304. Note: 500 °C cyclic oxidation, A- 4140, B- HAZ (4140), C-Weld, D- HAZ (304), E- 304.	247
5.5(b)	EDAX on the weldment of 4140-304. Note: cyclic oxidation at 600 °C, A- 4140, B- HAZ (4140), C-Weld, D- HAZ (304), E- 304.	247
5.5(c)	EDAX on the weldment of 4140-304. Note: 50 hours Isothermal	249

	oxidation at 500 °C. A- 4140, B- HAZ (4140), C-Weld, D- HAZ (304), E- 304.	
5.5(d)	EDAX on the weldment of 4140-304. Note: 50 hours Isothermal oxidation at 700 °C. A- 4140, B- HAZ (4140), C-Weld, D- HAZ (304), E- 304.	249
5.5(e)	EDAX on the weldment of 4140-304. Note: 50 hours Isothermal oxidation at 900 °C. A- 4140, B- HAZ (4140), C-Weld, D- HAZ (304), E- 304.	251
5.6	BSEI and X-ray mappings of the cross-section of dissimilar friction welded AISI 4140 and AISI 304 subjected to cyclic oxidation at 500°C in air after 50 cycles.	253
5.7	BSEI and X-ray mappings of the cross-section of dissimilar friction welded AISI 4140 and AISI 304 subjected to cyclic oxidation at 600°C in air after 50 cycles.	255
5.8	BSEI and X-ray mappings of the cross-section of dissimilar friction welded AISI 4140 and AISI 304 subjected to isothermal oxidation at 500°C in air after 50 cycles.	257
5.9	BSEI and X-ray mappings of the cross-section of dissimilar friction welded AISI 4140 and AISI 304 subjected to isothermal oxidation at 700°C in air after 50 cycles.	259
5.10	BSEI and X-ray mappings of the cross-section of dissimilar friction welded AISI 304 and AISI 4140 subjected to isothermal oxidation at 900°C in air after 50 cycles.	261
5.11	BSEI and X-ray mappings of the cross-section of dissimilar friction welded AISI 304 and AISI 4140 subjected to isothermal oxidation at 700°C in air.	263
5.12	BSEI and Elemental Distribution curve on the cross-section of dissimilar friction welded AISI 304 and AISI 4140 subjected to isothermal oxidation at 700°C in air.	265
5.13	BSEI and X-ray mappings of the cross-section of dissimilar friction welded AISI 304 and AISI 4140 subjected to isothermal oxidation at 900°C in air	267
5.14	BSEI and Elemental Distribution curve on the cross-section of dissimilar friction welded AISI 304 and AISI 4140 subjected to isothermal oxidation at 900°C in air.	269
6.1	Macrographs dissimilar friction welded AISI 4140 and AISI 304 subjected to cyclic hot corrosion exposed under Na ₂ SO ₄ (40%) + V ₂ O ₅ (60%) at 500, 550, 600, 700 and 900 °C after 50 cycles.	275
6.2	Plots of cumulative weight gain (mg/cm ²) as a function of time (number of cycles)	277
6.3	Plots of cumulative weight gain (mg/cm ²) as a function of time (number of cycles)	279
6.4	X-ray diffraction patterns for the hot corroded surfaces of friction welded samples by keeping four different burn-off length (B5, B7, B9 and B12 mm) exposed to the Na ₂ SO ₄ - 60% V ₂ O ₅ environment at exposure temperature of 500 after 50 cycles.	283
6.5	X-ray diffraction patterns for the hot corroded surfaces of friction welded samples by keeping four different burn-off length (B5, B7,	285

	B9 and B12 mm) exposed to the Na ₂ SO ₄ - 60% V ₂ O ₅ environment at exposure temperature of 550 after 50 cycles.	
6.6	X-ray diffraction patterns for the hot corroded surfaces of friction welded samples by keeping four different burn-off length (B5, B7, B9 and B12 mm) exposed to the Na ₂ SO ₄ - 60% V ₂ O ₅ environment at exposure temperature of 600 after 50 cycles.	287
6.7	X-ray diffraction patterns for the hot corroded surfaces of friction welded samples by keeping four different burn-off length (B5 mm) exposed to the Na ₂ SO ₄ - 60% V ₂ O ₅ environment at exposure temperature of 700 and 900 °C after 50 cycles.	289
6.8	BSEI for hot corroded friction weldment exposed temperature of 500, 550, 600, (i), (ii) and (iii): Exposed temperature 500, 550 and 600 °C respectively for weldment made by keeping 5 mm Burn off length. (iv), (v) and (vi): Exposed temperature 500, 550 and 600 °C respectively for weldment made by keeping 12 mm Burn off length.	291
6.9	BSEI for hot corroded friction weldment exposed temperature of 700 and 900 °C (vii) and (viii) Exposed temperature 700 and 900 °C respectively for weldment made by keeping 5 mm Burn off length.	293
6.10(A)	SEM/EDAX graph shows the friction weldment by keeping 5 mm burn off length, exposed at 500 °C under Na ₂ SO ₄ - 60% V ₂ O ₅ after 50 cycles	295
6.10(B)	SEM/EDAX graph shows the friction weldment by keeping 7 mm burn off length, exposed at 500 °C under Na ₂ SO ₄ - 60% V ₂ O ₅ after 50 cycles	297
6.10(C)	SEM/EDAX graph shows the friction weldment by keeping 9 mm burn off length, exposed at 500 °C under Na ₂ SO ₄ - 60% V ₂ O ₅ after 50 cycles.	299
6.10(D)	SEM/EDAX graph shows the friction weldment by keeping 12 mm burn off length, exposed at 500 °C under Na ₂ SO ₄ - 60% V ₂ O ₅ after 50 cycles	301
6.10(E)	SEM/EDAX graph shows the friction weldment by keeping 5 mm burn off length, exposed at 550 °C under Na ₂ SO ₄ - 60% V ₂ O ₅ after 50 cycles	303
6.10(F)	SEM/EDAX graph shows the friction weldment by keeping 7 mm burn off length, exposed at 550 °C under Na ₂ SO ₄ - 60% V ₂ O ₅ after 50 cycles	305
6.10(G)	SEM/EDAX graph shows the friction weldment by keeping 9mm burn off length, exposed at 550 °C under Na ₂ SO ₄ - 60% V ₂ O ₅ after 50 cycles	307
6.10(H)	SEM/EDAX graph shows the friction weldment by keeping 12 mm burn off length, exposed at 550 °C under Na ₂ SO ₄ - 60% V ₂ O ₅ after 50 cycles	309
6.10(I)	SEM/EDAX graph shows the friction weldment by keeping 5 mm burn off length, exposed at 600 °C under Na ₂ SO ₄ - 60% V ₂ O ₅ after 50 cycles	311
6.10(J)	SEM/EDAX graph shows the friction weldment by keeping 7mm burn off length, exposed at 600 °C under Na ₂ SO ₄ - 60% V ₂ O ₅ after 50	313

	cycles	
6.10(K)	SEM/EDAX graph shows the friction weldment by keeping 9 mm burn off length, exposed at 600 °C under Na ₂ SO ₄ - 60% V ₂ O ₅ after 50 cycles	315
6.10(L)	SEM/EDAX graph shows the friction weldment by keeping 12 mm burn off length, exposed at 600 °C under Na ₂ SO ₄ - 60% V ₂ O ₅ after 50 cycles.	317
6.11(A)	SEM/EDAX graph shows the friction weldment by keeping 5 mm burn off length, exposed at 700 °C under Na ₂ SO ₄ - 60% V ₂ O ₅ after 50 cycles.	321
6.11(B)	SEM/EDAX graph shows the friction weldment by keeping 5 mm burn off length, exposed at 700 °C under Na ₂ SO ₄ - 60% V ₂ O ₅ after 50 cycles.	323
6.11(C)	EDAX data shows the effect of burn off length and temperature on formation of Cr ₂ O ₃ on the friction weldment under molten salt environment of Na ₂ SO ₄ -60% V ₂ O ₅ .	325
6.11(D)	EDAX data shows the effect of burn off length and temperature on formation of Fe ₂ O ₃ on the friction weldment under molten salt environment of Na ₂ SO ₄ -60% V ₂ O ₅ .	325
6.11(E)	EDAX data shows the effect of burn off length and temperature on formation of NiO on the friction weldment under molten salt environment of Na ₂ SO ₄ -60% V ₂ O ₅ .	327
6.11(F)	EDAX data shows the effect of burn off length and temperature on formation of MoO ₃ on the friction weldment under molten salt environment of Na ₂ SO ₄ -60% V ₂ O ₅ .	327
6.11(G)	EDAX data shows the effect of burn off length and temperature on formation of SiO ₂ on the friction weldment under molten salt environment of Na ₂ SO ₄ -60% V ₂ O ₅ .	329
6.11(H)	EDAX data shows the effect of burn off length and temperature on formation of MnO on the friction weldment under molten salt environment of Na ₂ SO ₄ -60% V ₂ O ₅ .	329
6.12(A)	BSEI and elemental X-ray mapping of the cross-section of dissimilar weldment made by AISI 4140 and AISI 304 by keeping burn off length 5 mm, subjected to cyclic oxidation in Na ₂ SO ₄ -60%V ₂ O ₅ at 500 ⁰ C for 50 cycles, 800 X.	331
6.12(B)	BSEI and elemental X-ray mapping of the cross-section of dissimilar weldment made by AISI 4140 and AISI 304 by keeping burn off length 5 mm, subjected to cyclic oxidation in Na ₂ SO ₄ -60%V ₂ O ₅ at 550 ⁰ C for 50 cycles, 700 X	333
6.12(C)	BSEI and elemental X-ray mapping of the cross-section of dissimilar weldment made by AISI 4140 and AISI 304 by keeping burn off length 5 mm, subjected to cyclic oxidation in Na ₂ SO ₄ -60%V ₂ O ₅ at 600 ⁰ C for 50 cycles, 500 X.	335
6.12(D)	BSEI and elemental X-ray mapping of the cross-section of dissimilar weldment made by AISI 4140 and AISI 304 by keeping burn off length 12 mm, subjected to cyclic oxidation in Na ₂ SO ₄ -60%V ₂ O ₅ at 600 ⁰ C for 50 cycles, 500 X.	337
6.12(E)	BSEI and elemental X-ray mapping of the cross-section of dissimilar weldment made by AISI 4140 and AISI 304 by keeping burn off length 5 mm, subjected to cyclic oxidation in Na ₂ SO ₄ -60%V ₂ O ₅ at	339

	900 ^o C for 50 cycles, 500 X.	
6.12(F)	BSEI and X-ray mappings of the cross-section of dissimilar friction welded AISI 304 and AISI 4140 by keeping burn-off length 5mm exposed to Na ₂ SO ₄ -60%V ₂ O ₅ at 600 °C for 50 cycles	341
6.12(G)	BSEI and X-ray mappings of the cross-section of dissimilar friction welded AISI 304 and AISI 4140 by keeping burn-off length 7mm exposed to Na ₂ SO ₄ -60%V ₂ O ₅ at 600 °C for 50 cycles.	343
6.12(H)	BSEI and EDAX of the cross-section of dissimilar friction welded AISI 304 and AISI 4140 by keeping burn-off length 7mm exposed to Na ₂ SO ₄ -60%V ₂ O ₅ at 600 °C for 50 cycles.	345
6.12(I)	BSEI and X-ray mappings of the cross-section of dissimilar friction welded AISI 304 and AISI 4140 by keeping burn-off length 5mm exposed to Na ₂ SO ₄ -60%V ₂ O ₅ at 700 °C for 50 cycles.	347
6.12(J)	BSEI and EDAX of the cross-section of dissimilar friction welded AISI 304 and AISI 4140 by keeping burn-off length 5mm exposed to Na ₂ SO ₄ -60%V ₂ O ₅ at 700 °C for 50 cycles.	349
6.12(K)	BSEI and X-ray mappings of the cross-section of dissimilar friction welded AISI 304 and AISI 4140 by keeping burn-off length 5mm exposed to Na ₂ SO ₄ -60%V ₂ O ₅ at 900 °C for 50 cycles.	351
6.12(L)	BSEI and EDAX of the cross-section of dissimilar friction welded AISI 304 and AISI 4140 by keeping burn-off length 5mm exposed to Na ₂ SO ₄ -60%V ₂ O ₅ at 900 °C for 50 cycles.	353
6.13	Macrographs dissimilar friction welded AISI 4140 and AISI 304 subjected to cyclic hot corrosion exposed under K ₂ SO ₄ + NaCl (60%) after 50 cycles. (i-iii) Weldment made by keeping 5 mm burn off length and exposed temperature of 500, 550, 600 °C respectively.	355
6.14	Plots of cumulative weight gain (mg/cm ²) as a function of time (number of cycles).	357
6.15	X-ray diffraction patterns for the hot corroded surfaces of friction welded samples by keeping four different burn-off length (B5, B7, B9 and B12 mm) exposed to the K ₂ SO ₄ (40%) and NaCl (60 %) environment at exposure temperature of 500 °C after 50 cycles.	361
6.16	X-ray diffraction patterns for the hot corroded surfaces of friction welded samples by keeping four different burn-off length (B5, B7, B9 and B12 mm) exposed to the K ₂ SO ₄ (40%) and NaCl (60 %) environment at exposure temperature of 550 °C after 50 cycles.	363
6.17	X-ray diffraction patterns for the hot corroded surfaces of friction welded samples by keeping four different burn-off length (B5, B7, B9 and B12 mm) exposed to the K ₂ SO ₄ (40%) and NaCl (60 %) environment at exposure temperature of 600 °C after 50 cycles.	365
6.18	BSEI for hot corroded friction weldment under K ₂ SO ₄ + NaCl (60%), exposed temperature of 500, 550, 600. (i) and (ii): Exposed temperature 500 and 600 °C respectively for weldment made by keeping 5 mm Burn off length. (iii) and (iv): Exposed temperature 550 and 600 °C respectively for weldment made by keeping 12 mm Burn off length.	367
6.19(A)	SEM/EDAX graph shows the friction weldment made by keeping 5 mm burn off length, exposed at 500 °C under K ₂ SO ₄ (40%) and NaCl (60 %) after 50 cycles	369
6.19(B)	SEM/EDAX graph shows the friction weldment made by keeping 7	371

	mm burn off length, exposed at 500 °C under K ₂ SO ₄ (40%) and NaCl (60 %) after 50 cycles	
6.19(C)	SEM/EDAX graph shows the friction weldment made by keeping 9 mm burn off length, exposed at 500 °C under K ₂ SO ₄ (40%) and NaCl (60 %) after 50 cycles	373
6.19(D)	SEM/EDAX graph shows the friction weldment made by keeping 5 mm burn off length, exposed at 550 °C under K ₂ SO ₄ (40%) and NaCl (60 %) after 50 cycles	375
6.19(E)	SEM/EDAX graph shows the friction weldment made by keeping 7 mm burn off length, exposed at 550 °C under K ₂ SO ₄ (40%) and NaCl (60 %) after 50 cycles.	377
6.19(F)	SEM/EDAX graph shows the friction weldment made by keeping 12 mm burn off length, exposed at 550 °C under K ₂ SO ₄ (40%) and NaCl (60 %) after 50 cycles	379
6.19(G)	SEM/EDAX graph shows the friction weldment made by keeping 5 mm burn off length, exposed at 600 °C under K ₂ SO ₄ (40%) and NaCl (60 %) after 50 cycles	381
6.19(H)	SEM/EDAX graph shows the friction weldment made by keeping 7 mm burn off length, exposed at 600 °C under K ₂ SO ₄ (40%) and NaCl (60 %) after 50 cycles	383
6.19(I)	SEM/EDAX graph shows the friction weldment made by keeping 9 mm burn off length, exposed at 600 °C under K ₂ SO ₄ (40%) and NaCl (60 %) after 50 cycles	385
6.19(J)	SEM/EDAX graph shows the friction weldment made by keeping 12 mm burn off length, exposed at 600 °C under K ₂ SO ₄ (40%) and NaCl (60 %) after 50 cycles.	387
6.19(K)	EDAX data shows the effect of burn off length and temperature on formation of Fe ₂ O ₃ on the friction weldment under molten salt environment of K ₂ SO ₄ –60% NaCl.	389
6.19(L)	EDAX data shows the effect of burn off length and temperature on formation of Cr ₂ O ₃ on the friction weldment under molten salt environment of K ₂ SO ₄ –60% NaCl.	389
6.19(M)	EDAX data shows the effect of burn off length and temperature on formation of MnO on the friction weldment under molten salt environment of K ₂ SO ₄ –60% NaCl.	391
6.19(N)	EDAX data shows the effect of burn off length and temperature on formation of NiO on the friction weldment under molten salt environment of K ₂ SO ₄ –60% NaCl	391
6.20(A)	BSEI and elemental X-ray mapping of the cross-section of dissimilar weldment made by AISI 4140 and AISI 304 by keeping burn off length 5 mm, subjected to cyclic oxidation in K ₂ SO ₄ (40%) and NaCl (60 %) at 500 ⁰ C for 50 cycles, 500 X.	393
6.20(B)	BSEI and elemental X-ray mapping of the cross-section of dissimilar weldment made by AISI 4140 and AISI 304 by keeping burn off length 5 mm, subjected to cyclic oxidation in K ₂ SO ₄ (40%) and NaCl (60 %) at 600 ⁰ C for 50 cycles, 150 X.	395
6.20(C)	BSEI and elemental X-ray mapping of the cross-section of dissimilar weldment made by AISI 4140 and AISI 304 by keeping burn off length 12 mm, subjected to cyclic oxidation in K ₂ SO ₄ (40%) and NaCl (60 %) at 600 ⁰ C for 50 cycles, 150 X.	397

6.21(A)	BSEI and X-ray mappings of the cross-section of dissimilar friction welded AISI 304 and AISI 4140 by keeping burn-off length 5mm exposed to $K_2SO_4 + NaCl$ (60%) at 500 °C for 50 cycles.	399
6.21(B)	BSEI and X-ray mappings of the cross-section of dissimilar friction welded AISI 304 and AISI 4140 by keeping burn-off length 12mm exposed to $K_2SO_4 + NaCl$ (60%) at 600 °C for 50 cycles.	401
6.21(C)	BSEI and EDAX of the cross-section of dissimilar friction welded AISI 304 and AISI 4140 by keeping burn-off length 12mm exposed to $K_2SO_4 + NaCl$ (60%) at 600 °C for 50 cycles.	403
6.22	Macrographs dissimilar friction welded AISI 4140 and AISI 304 subjected to cyclic hot corrosion exposed under $K_2SO_4 + NaCl$ (60%) after 50 cycles. (i-iii) Weldment made by keeping 5 mm burn off length and exposed temperature of 500, 550, 600 °C respectively. (iv) Weldment made by keeping 12 mm burn off length and exposed temperature at 600 °C.	411
6.23	Plots of cumulative weight gain (mg/cm^2) as a function of time (number of cycles) for 500, 550 and 600 °C.	413
6.24(A)	The XRD patterns for the hot corroded surfaces of welded samples by keeping four different burn-off length (B5, B7, B9 and B12 mm) exposed to the Na_2SO_4 (40%) + K_2SO_4 (40%) + $NaCl$ (10%) + KCl (10%) environment at exposure temperature of 500, 550 and 600 °C after 50 cycles	415
6.24(B)	The XRD patterns for the hot corroded surfaces of welded samples by keeping four different burn-off length (B5, B7, B9 and B12 mm) exposed to the Na_2SO_4 (40%) + K_2SO_4 (40%) + $NaCl$ (10%) + KCl (10%) environment at exposure temperature of 500 and 550 °C after 50 cycles.	417
6.25	BSEI for hot corroded friction weldment under Na_2SO_4 (40%) + K_2SO_4 (40%) + $NaCl$ (10%) + KCl (10%) exposed temperature of 500, 550, 600. (i): Exposed temperature 500 °C for weldment made by keeping 5 mm Burn off length. (ii) and (iv): Exposed temperature 550 °C for weldment made by keeping 5, 7 and 12 mm Burn off length respectively. (v) and (vi): Exposed temperature of 600 °C for weldment made by keeping 5, and 12 mm Burn off length respectively.	419
6.26(A)	SEM/EDAX graph shows the friction weldment made by keeping 5 mm burn off length, exposed at 500 °C under Na_2SO_4 (40%) + K_2SO_4 (40%) + $NaCl$ (10%) + KCl (10%) after 50 cycles.	421
6.26(B)	SEM/EDAX graph shows the friction weldment made by keeping 5 mm burn off length, exposed at 550 °C under Na_2SO_4 (40%) + K_2SO_4 (40%) + $NaCl$ (10%) + KCl (10%) after 50 cycles	423
6.26(C)	SEM/EDAX graph shows the friction weldment made by keeping 9 mm burn off length, exposed at 550 °C under Na_2SO_4 (40%) + K_2SO_4 (40%) + $NaCl$ (10%) + KCl (10%) after 50 cycles	425
6.26(D)	SEM/EDAX graph shows the friction weldment made by keeping 12 mm burn off length, exposed at 550 °C under Na_2SO_4 (40%) + K_2SO_4 (40%) + $NaCl$ (10%) + KCl (10%) after 50 cycles	427
6.26(E)	SEM/EDAX graph shows the friction weldment made by keeping 5 mm burn off length, exposed at 600 °C under Na_2SO_4 (40%) + K_2SO_4 (40%) + $NaCl$ (10%) + KCl (10%) after 50 cycles	429

6.26(F)	SEM/EDAX graph shows the friction weldment made by keeping 12 mm burn off length, exposed at 600 °C under Na ₂ SO ₄ (40%) + K ₂ SO ₄ (40%) + NaCl (10%) + KCl (10%) after 50 cycles	431
6.26(G)	EDAX data shows the effect of burn off length and temperature on formation of Fe ₂ O ₃ on the friction weldment under molten salt environment of 40 wt% K ₂ SO ₄ , 40 wt% Na ₂ SO ₄ , 10 wt% KCl, and 10 wt% NaCl.	433
6.26(H)	EDAX data shows the effect of burn off length and temperature on formation of Cr ₂ O ₃ on the friction weldment under molten salt environment of 40 wt% K ₂ SO ₄ , 40 wt% Na ₂ SO ₄ , 10 wt% KCl, and 10 wt% NaCl.	433
6.26(I)	EDAX data shows the effect of burn off length and temperature on formation of MnO on the friction weldment under molten salt environment of 40 wt% K ₂ SO ₄ , 40 wt% Na ₂ SO ₄ , 10 wt% KCl, and 10 wt% NaCl.	435
6.26(J)	EDAX data shows the effect of burn off length and temperature on formation of NiO on the friction weldment under molten salt environment of 40 wt% K ₂ SO ₄ , 40 wt% Na ₂ SO ₄ , 10 wt% KCl, and 10 wt% NaCl.	435
6.26(K)	EDAX data shows the effect of burn off length and temperature on formation of MoO ₃ on the friction weldment under molten salt environment of 40 wt% K ₂ SO ₄ , 40 wt% Na ₂ SO ₄ , 10 wt% KCl, and 10 wt% NaCl.	437
6.26(L)	EDAX data shows the effect of burn off length and temperature on formation of Na ₂ O on the friction weldment under molten salt environment of 40 wt% K ₂ SO ₄ , 40 wt% Na ₂ SO ₄ , 10 wt% KCl, and 10 wt% NaCl.	437
6.26(M)	EDAX data shows the effect of burn off length and temperature on formation of SO ₃ on the friction weldment under molten salt environment of 40 wt% K ₂ SO ₄ , 40 wt% Na ₂ SO ₄ , 10 wt% KCl, and 10 wt% NaCl.	439
6.26(N)	EDAX data shows the effect of burn off length and temperature on formation of K ₂ O on the friction weldment under molten salt environment of 40 wt% K ₂ SO ₄ , 40 wt% Na ₂ SO ₄ , 10 wt% KCl, and 10 wt% NaCl.	439
6.26(A)	BSEI and elemental X-ray mapping of the cross-section of dissimilar weldment made by AISI 4140 and AISI 304 by keeping burn off length 5 mm, subjected to cyclic oxidation in Na ₂ SO ₄ (40%) + K ₂ SO ₄ (40%) + NaCl (10%) + KCl (10%) at 500 ⁰ C for 50 cycles, 500 X.	441
6.27(B)	BSEI and elemental X-ray mapping of the cross-section of dissimilar weldment made by AISI 4140 and AISI 304 by keeping burn off length 5 mm, subjected to cyclic oxidation in Na ₂ SO ₄ (40%) + K ₂ SO ₄ (40%) + NaCl (10%) + KCl (10%) at 550 ⁰ C for 50 cycles, 400 X.	443
6.27(C)	BSEI and elemental X-ray mapping of the cross-section of dissimilar weldment made by AISI 4140 and AISI 304 by keeping burn off length 7 mm, subjected to cyclic oxidation in Na ₂ SO ₄ (40%) + K ₂ SO ₄ (40%) + NaCl (10%) + KCl (10%) at 550 ⁰ C for 50 cycles, 700 X.	445
6.27(D)	BSEI and elemental X-ray mapping of the cross-section of dissimilar weldment made by AISI 4140 and AISI 304 by keeping burn off length 12mm, subjected to cyclic oxidation in Na ₂ SO ₄ (40%) + K ₂ SO ₄	447

	(40%) + NaCl (10%) + KCl (10%) at 550 ⁰ C for 50 cycles, 600 X.	
6.27(E)	BSEI and elemental X-ray mapping of the cross-section of dissimilar weldment made by AISI 4140 and AISI 304 by keeping burn off length 5mm, subjected to cyclic oxidation in Na ₂ SO ₄ (40%) + K ₂ SO ₄ (40%) + NaCl (10%) + KCl (10%) at 600 ⁰ C for 50 cycles, 500 X.	449
6.27(F)	BSEI and elemental X-ray mapping of the cross-section of dissimilar weldment made by AISI 4140 and AISI 304 by keeping burn off length 12mm, subjected to cyclic oxidation in Na ₂ SO ₄ (40%) + K ₂ SO ₄ (40%) + NaCl (10%) + KCl (10%) at 600 ⁰ C for 50 cycles, 500 X.	451
6.28(A)	BSEI and X-ray mappings of the cross-section of dissimilar friction welded AISI 304 and AISI 4140 by keeping burn-off length 7mm exposed to Na ₂ SO ₄ (40%) + K ₂ SO ₄ (40%) + NaCl (10%) + KCl (10%) at 550 ⁰ C for 50 cycles.	453
6.26(B)	BSEI and X-ray mappings of the cross-section of dissimilar friction welded AISI 304 and AISI 4140 by keeping burn-off length 12 mm exposed to Na ₂ SO ₄ (40%) + K ₂ SO ₄ (40%) + NaCl (10%) + KCl (10%) at 600 ⁰ C for 50 cycles.	455
6.28(C)	BSEI and EDAX of the cross-section of dissimilar friction welded AISI 304 and AISI 4140 by keeping burn-off length 12 mm exposed to Na ₂ SO ₄ (40%) + K ₂ SO ₄ (40%) + NaCl (10%) + KCl (10%) at 600 ⁰ C for 50 cycles.	457
6.29	Macrographs dissimilar friction welded AISI 4140 and AISI 304 subjected to cyclic hot corrosion exposed under Na ₂ SO ₄ + NaCl (50%) after 50 cycles. (i) and (ii) Weldment made by keeping 5 mm burn off length and exposed temperature of 500 and 550 °C respectively.	459
6.30	Plots of cumulative weight gain (mg/cm ²) as a function of time (number of cycles) for the friction weldment in the molten salt environment.	461
6.31(A)	X-Ray diffraction patterns for hot corroded dissimilar friction weldment at 500 °C. Burn-off length: B5, B7 and B9, Environment: Na ₂ SO ₄ + NaCl (50%)	463
6.31(B)	X-Ray diffraction patterns for hot corroded dissimilar friction weldment at 550 °C. Burn-off length: B5, B7, B9 and B12, Environment: Na ₂ SO ₄ + NaCl (50%)	465
6.32	BSEI for hot corroded friction weldment under Na ₂ SO ₄ + NaCl (50%) exposed temperature of 500, 550, 600 °C. (i) and (ii): Exposed temperature 500 °C for weldment made by keeping 5 and 7 mm Burn off length respectively. (iii) – (vi): Exposed temperature 550 °C for weldment made by keeping 5, 7, 9 and 12 mm Burn off length respectively.	467
6.33(A)	SEM/EDAX graph shows the friction weldment by keeping 5 mm burn off length, exposed at 500 °C under Na ₂ SO ₄ – NaCl (50%) after 50 cycles.	469
6.33(B)	SEM/EDAX graph shows the friction weldment by keeping 7 mm burn off length, exposed at 500 °C under Na ₂ SO ₄ – NaCl (50%) after 50 cycles.	471
6.33(C)	SEM/EDAX graph shows the friction weldment by keeping 9 mm burn off length, exposed at 500 °C under Na ₂ SO ₄ – NaCl (50%) after 50 cycles.	473
6.33(D)	SEM/EDAX graph shows the friction weldment by keeping 5 mm	475

	burn off length, exposed at 550 °C under Na ₂ SO ₄ – NaCl (50%) after 50 cycles.	
6.33(E)	SEM/EDAX graph shows the friction weldment by keeping 7 mm burn off length, exposed at 550 °C under Na ₂ SO ₄ – NaCl (50%) after 50 cycles.	477
6.33(F)	SEM/EDAX graph shows the friction weldment by keeping 9 mm burn off length, exposed at 550 °C under Na ₂ SO ₄ – NaCl (50%) after 50 cycles.	479
6.33(G)	SEM/EDAX graph shows the friction weldment by keeping 12 mm burn off length, exposed at 550 °C under Na ₂ SO ₄ – NaCl (50%) after 50 cycles.	481
6.33(H)	EDS analysis on the weld zone of hot corroded dissimilar weldment. Environment: Na ₂ SO ₄ + NaCl (50%), Exposure temp: 550 °C (50 cycles).	483
6.33(I)	EDS analysis on the weld zone of hot corroded dissimilar weldment. Environment: Air Oxidation, Exposure temp: 600 °C (50 cycles).	483
6.33(J)	EDAX data shows the effect of burn off length and temperature on formation of Fe ₂ O ₃ on the friction weldment under molten salt environment of Na ₂ SO ₄ –50% NaCl.	485
6.33(K)	EDAX data shows the effect of burn off length and temperature on formation of Cr ₂ O ₃ on the friction weldment under molten salt environment of Na ₂ SO ₄ –50% NaCl.	485
6.33(L)	EDAX data shows the effect of burn off length and temperature on formation of NiO on the friction weldment under molten salt environment of Na ₂ SO ₄ –50% NaCl.	487
6.33(M)	EDAX data shows the effect of burn off length and temperature on formation of MnO on the friction weldment under molten salt environment of Na ₂ SO ₄ –50% NaCl.	487
6.33(N)	EDAX data shows the effect of burn off length and temperature on formation of SiO ₂ on the friction weldment under molten salt environment of Na ₂ SO ₄ –50% NaCl.	489
6.34(A)	BSEI and elemental X-ray mapping of the cross-section of dissimilar weldment made by AISI 4140 and AISI 304 by keeping burn off length 7mm, subjected to cyclic oxidation in Na ₂ SO ₄ (50%) and NaCl (50 %) at 500 ⁰ C for 50 cycles, 500 X.	491
6.34(B)	BSEI and elemental X-ray mapping of the cross-section of dissimilar weldment made by AISI 4140 and AISI 304 by keeping burn off length 5mm, subjected to cyclic oxidation in Na ₂ SO ₄ (50%) and NaCl (50 %) at 550 ⁰ C for 50 cycles, 600 X.	493
6.34(C)	BSEI and elemental X-ray mapping of the cross-section of dissimilar weldment made by AISI 4140 and AISI 304 by keeping burn off length 7mm, subjected to cyclic oxidation in Na ₂ SO ₄ (50%) and NaCl (50 %) at 550 ⁰ C for 50 cycles, 250 X.	495
6.34(D)	BSEI and elemental X-ray mapping of the cross-section of dissimilar weldment made by AISI 4140 and AISI 304 by keeping burn off length 9mm, subjected to cyclic oxidation in Na ₂ SO ₄ (50%) and NaCl (50 %) at 550 ⁰ C for 50 cycles, 700 X.	497
6.34(E)	BSEI and elemental X-ray mapping of the cross-section of dissimilar weldment made by AISI 4140 and AISI 304 by keeping burn off length 12mm, subjected to cyclic oxidation in Na ₂ SO ₄ (50%) and NaCl	499

	(50 %) at 550 ⁰ C for 50 cycles, 500 X.	
6.35	BSEI and X-ray mappings of the cross-section of dissimilar friction welded AISI 304 and AISI 4140 by keeping burn-off length 5mm exposed to Na ₂ SO ₄ -NaCl (50%) at 550 °C for 50 cycles.	501
7.1	Macrographs dissimilar Electron Beam Welded AISI 4140 and AISI 304 subjected to cyclic hot corrosion exposed at temperature of 600 °C under Na ₂ SO ₄ + V ₂ O ₅ (60%) after 50 cycles.	525
7.2	Plots of cumulative weight gain (mg/cm ²) as a function of time (number of cycles) for the EBW weldment under cyclic hot corrosion at 600 °C, in the molten salt Na ₂ SO ₄ + V ₂ O ₅ (60%) and K ₂ SO ₄ + NaCl (60%).	527
7.3	X-Ray diffraction patterns for hot corroded dissimilar EBW weldment of AISI 4140 and AISI 304 exposed at 600 °C in Na ₂ SO ₄ + V ₂ O ₅ (60%) and K ₂ SO ₄ + NaCl (60%) for 50 cycles.	529
7.4	BSEI for hot corroded Electron Beam weldment at exposed temperature of 600 °C. (i) EBW exposed under Na ₂ SO ₄ + V ₂ O ₅ (60%) at 600 °C. (ii) EBW exposed under K ₂ SO ₄ + NaCl (60%) at 600 °C.	531
7.5	SEM/EDAX graph shows the EBW weldment of AISI 4140 and AISI 304 exposed at 600 °C under Na ₂ SO ₄ + V ₂ O ₅ (60%) after 50 cycles.	533
7.6	SEM/EDAX graph shows the EBW weldment of AISI 4140 and AISI 304 exposed at 600 °C under K ₂ SO ₄ + NaCl (60%) after 50 cycles.	535
7.7	BSEI and elemental X-ray mapping of the cross-section of dissimilar EBW weldment of AISI 4140 and AISI 304, subjected to cyclic hot corrosion in K ₂ SO ₄ + NaCl (60%) at 600 ⁰ C for 50 cycles, 100 X.	537
7.8	BSEI and EDAX of the cross-section of EBW dissimilar metals of AISI 304 and AISI 4140 exposed to K ₂ SO ₄ -60%NaCl at 600 °C for 50 cycles.	539
7.9(A)	Macrographs dissimilar TIG Welded AISI 4140 and AISI 304 subjected to cyclic hot corrosion exposed at temperature of 600 °C under Na ₂ SO ₄ + V ₂ O ₅ (60%) after 50 cycles.	541
7.9(B)	Macrographs dissimilar TIG Welded AISI 4140 and AISI 304 subjected to cyclic hot corrosion exposed at temperature of 600 °C under K ₂ SO ₄ + NaCl (60%) after 50 cycles.	541
7.10	Plots of cumulative weight gain (mg/cm ²) as a function of time (number of cycles) for the TIG weldment under cyclic hot corrosion, at 600 °C in the molten salt Na ₂ SO ₄ + V ₂ O ₅ (60%) and K ₂ SO ₄ + NaCl (60%).	543
7.11	X-Ray diffraction patterns for hot corroded dissimilar TIG weldment of AISI 4140 and AISI 304 exposed at 600 °C in Na ₂ SO ₄ + V ₂ O ₅ (60%) and K ₂ SO ₄ + NaCl (60%) for 50 cycles.	545
7.12	BSEI for hot corroded TIG weldment at exposed temperature of 600 °C. (i) TIG exposed under Na ₂ SO ₄ + V ₂ O ₅ (60%) at 600 °C. (ii) TIG exposed under K ₂ SO ₄ + NaCl (60%) at 600 °C.	547
7.13	SEM/EDAX graph shows the TIG weldment of AISI 4140 and AISI 304 exposed at 600 °C under Na ₂ SO ₄ + V ₂ O ₅ (60%) after 50 cycles.	549
7.14	SEM/EDAX graph shows the TIG weldment of AISI 4140 and AISI 304 exposed at 600 °C under K ₂ SO ₄ + NaCl (60%) after 50 cycles.	551
7.15(A)	BSEI and elemental X-ray mapping of the cross-section of dissimilar	553

	TIG weldment of AISI 304 and weld zone, subjected to cyclic hot corrosion in K ₂ SO ₄ - 60%NaCl at 600 ⁰ C for 50 cycles, 120 X.	
7.15(B)	BSEI and EDAX form cross section of dissimilar TIG weldment of AISI 304 and weld zone, subjected to cyclic hot corrosion in K ₂ SO ₄ - 60%NaCl at 600 ⁰ C for 50 cycles, 120 X.	555
7.16(A)	BSEI and elemental X-ray mapping of the cross-section of dissimilar TIG weldment of weld zone and AISI 4140, subjected to cyclic hot corrosion in K ₂ SO ₄ - 60%NaCl at 600 ⁰ C for 50 cycles.	557
7.16(B)	BSEI and EDAX form cross section of dissimilar TIG weldment of weld zone and AISI 4140, subjected to cyclic hot corrosion in K ₂ SO ₄ - 60%NaCl at 600 ⁰ C for 50 cycles.	559
8.1	Bar charts showing cumulative mechanical properties of AISI 4140 and AISI 304 dissimilar metals made by FRW, EBW and TIG.	573
8.2(A)	Bar charts showing cumulative weight gain (mg/cm ²) for dissimilar weldment subjected to cyclic oxidation in air and molten salt environment for 50 cycles	575
8.2(B)	Bar charts showing parabolic rate constant K _p ((10 ⁻⁶ (gm ² Cm ⁻⁴ S ⁻¹)) for dissimilar weldment subjected to cyclic oxidation in air at and molten salt environment for 50 cycles	577
8.3(A)	The constituent of Cr ₂ O ₃ in the scale on friction weldment exposing in different environments at 600 °C.	579
8.3(B)	The constituent of Fe ₂ O ₃ in the scale on friction weldment exposing in different environments at 600 °C.	579
8.3(C)	The constituent of MnO in the scale on EBW weldment exposing in different environments at 600 °C.	580
8.3(D)	The constituent of NiO in the scale on EBW weldment exposing in different environments at 600 °C.	580
8.3(E)	The constituent of Cr ₂ O ₃ in the scale on TIG weldment exposing in different environments at 600 °C.	581
8.3(F)	The constituent of Fe ₂ O ₃ in the scale on TIG weldment exposing in different environments at 600 °C.	581
8.3(G)	The constituent of NiO in the scale on friction weldment exposing in different environments at 550 °C.	582
8.3(H)	The constituent of MnO in the scale on friction weldment exposing in different environments at 550 °C.	582
8.3(I)	The constituent of Cr ₂ O ₃ in the scale on friction weldment exposing in different environments at 500 °C.	583
8.3(J)	The constituent of Fe ₂ O ₃ in the scale on friction weldment exposing in different environments at 500 °C.	583
8.3(K)	The constituent of NiO in the scale on friction weldment exposing in different environments at 500 °C.	584
8.3(L)	The constituent of MnO in the scale on friction weldment exposing in different environments at 500 °C.	584
8.4(A)	The constituent of Cr ₂ O ₃ in the scale on EBW weldment exposing in different environments at 600 °C.	585
8.4(B)	The constituent of Fe ₂ O ₃ in the scale on EBW weldment exposing in different environments at 600 °C.	585
8.4(C)	The constituent of MnO in the scale on EBW weldment exposing in different environments at 600 °C.	586
8.4(D)	The constituent of NiO in the scale on EBW weldment exposing in	586

	different environments at 600 °C.	
8.4(E)	The constituent of MoO ₃ in the scale on EBW weldment exposing in different environments at 600 °C.	587
8.4(F)	The constituent of Cr ₂ O ₃ in the scale on TIG weldment exposing in different environments at 600 °C.	587
8.4(G)	The constituent of Fe ₂ O ₃ in the scale on TIG weldment exposing in different environments at 600 °C.	588
8.4(H)	The constituent of MnO in the scale on TIG weldment exposing in different environments at 600 °C.	588
8.4(I)	The constituent of NiO in the scale on TIG weldment exposing in different environments at 600 °C.	589
8.4(J)	The constituent of MoO ₃ in the scale on TIG weldment exposing in different environments at 600 °C.	589

LIST OF TABLES

Table No.	Particulars	Page No.
2.1	Friction Pressure for Different Metals	25
2.2	Weldability of dissimilar metal combinations using electron beam welding	41
2.3	Recent investigation concerning the EBW of dissimilar metals	43
2.4	Characterisation of coal gasification atmosphere at 1255 K (982 ⁰ C)	79
2.5	Formation reactions, Gibbs free energy changes and partial pressure for metal chlorides at 550 °C	103
3.1	Chemical composition of AISI 304 and AISI 4140	125
3.2	Mechanical Properties of Parent Metals	125
3.3	Welding parameters and their designation	126
3.4	EBW Welding parameters	129
3.5	TIG Welding parameters	129
4.1	Data on maximum hardness at the interface and minimum hardness in the low alloy steel adjacent to the interface.	167
4.2	Effect of burn-off length on impact strength	167
4.3	Effect of burn –off length on tensile strength	168
4.4	V notch Impact strength for Electron Beam Welded dissimilar metals	193
4.5	Tensile strength of Electron Beam Welded AISI 4140 and AISI 304	193
4.6	Tensile strength of TIG Welded AISI 4140 and AISI 304	225
5.1	The weight gain after 50 cycles/ 50 hours oxidation studies in air	234
6.1	Values of parabolic rate constant Kp	281
6.2	Values of parabolic rate constant Kp	359

6.3	Values of parabolic rate constant K_p	406
6.4	Values of parabolic rate constant K_p	459
7.1	Values of parabolic rate constant K_p	517
7.2	Values of parabolic rate constant K_p	520
8.1	The cumulative mechanical properties of AISI 4140 and AISI 304 dissimilar weldment made by FRW, EBW and TIG.	567
8.2	Oxidation data of friction weldment of dissimilar metals of AISI 4140 and AISI 304 in Air environment	568
8.3	Friction weldment of dissimilar metals of AISI 4140 and AISI 304 in $\text{Na}_2\text{SO}_4 + \text{V}_2\text{O}_5$ (60%) environment in cyclic condition	569
8.4	Friction weldment of dissimilar metals of AISI 4140 and AISI 304 in $\text{K}_2\text{SO}_4 + \text{NaCl}$ (60%) environment in cyclic condition	570
8.5	Friction weldment of dissimilar metals of AISI 4140 and AISI 304 in Na_2SO_4 (40%) + K_2SO_4 (40%) + NaCl (10%) + KCl (10%) environment in cyclic condition	571
8.6	Friction weldment of dissimilar metals of AISI 4140 and AISI 304 in $\text{Na}_2\text{SO}_4 + \text{NaCl}$ (50%) environment in cyclic condition	572

RESEARCH PAPERS PRESENTED/PUBLISHED/ UNDER PUBLICATION

1. Arivazhagan N, Surendra Singh, Satya Prakash and Reddy G.M, “High Temperature corrosion studies on friction welded dissimilar metals”, *Materials Science & Engineering: B journal*, 132 (2006), 222-227.
2. Arivazhagan N, Surendra Singh, Satya Prakash, G.M.Reddy “An Assessment of Hardness, Impact Strength and Hot Corrosion Behaviour of Friction Welded Dissimilar Weldments between AISI 4140 and AISI 304” *International Journal of Advanced Manufacturing Technology*, (accepted for publication).
3. Arivazhagan N, Surendra Singh, Satya Prakash, G.M.Reddy “High Temperature Oxidation In Air And Molten Salt ($\text{Na}_2\text{SO}_4 + 50\% \text{NaCl}$) Corrosion Of Friction Welded Low Alloy Steel And Stainless Steel Welds In Temperature Range of 500 – 600 C” *Materials Transation A*, (accepted for publication)
4. Arivazhagan N, Surendra Singh, Satya Prakash, “High Temperature Corrosion Studies on Dissimilar Welded AISI 304 and AISI 4140 in the Molten Salt Environment of $\text{K}_2\text{SO}_4 + \text{NaCl}$ (60%)” *International Journal of Pressure Vessels and Piping*, Under Review.
5. Arivazhagan N, Surendra Singh, Satya Prakash, “Hot Corrosion Studies on Dissimilar Friction Welded Low Alloy Steel and Austenitic Stainless Steel under Chlorine-Containing Salt Deposits under cyclic conditions” *Journal of Materials Processing Technology*, Under Review.
6. Arivazhagan N, Surendra Singh, Satya Prakash, “High Temperature Oxidation Exposed In Air And Molten Salt For Friction Welded Low And Stainless Steel” *Journal of Materials Engineering and Performance*, Under Review.
7. Arivazhagan N, Surendra Singh, Satya Prakash and Reddy G.M, “High Temperature Corrosion Studies on Friction Welded Dissimilar Metals”, *Symposium W, Advanced Materials and Polymers for Defense and Aerospace Applications*, July 2005, Singapore.
8. Satya Prakash, Surendra Singh and Arivazhagan.N. “Weldability and Corrosion Effect of Dissimilar Metal Combinations ISME 2003”, IIT Roorkee, India, 2003
9. Arivazhagan N, Surendra Singh, SatyaPrakash and Reddy G.M, “High Temperature Corrosion Studies on and Electron Beam and friction welded AISI 304 and AISI 4140

in the Molten Salt Environment of $K_2SO_4 + NaCl$ (60%)”, Accepted for Oral Presentation ICMAT 2007 Singapore.

10. Arivazhagan N, Surendra Singh, SatyaPrakash and Reddy G.M, “An Effect of Burn-off Length on Mechanical Properties and Hot Corrosion Behavior under $Na_2SO_4 + NaCl$ (50%) of Friction Welded AISI 4140 and AISI 304 Dissimilar Metals”, Accepted for Oral Presentation 3 rd Join Conference, Finland.

11. Arivazhagan N, Surendra Singh, SatyaPrakash and Reddy G.M, “High Temperature Corrosion Studies on Dissimilar Friction Welded and Electron Beam Welded AISI 304 and AISI 4140 in the Molten Salt Environment of $Na_2SO_4 + V_2O_5$ (60%)” , Accepted for Oral Presentation Materials Science & Technology 2007, Michigan (USA).

ABBREVIATIONS

FRW	Friction Welding
EBW	Electron Beam Welding
TIG	Tungsten Inert Gas Welding
B	Burn off length
BSEI	Back Scattered Electron Image
EDAX	Energy Dispersive X-ray Analysis
EPMA	Electron Probe Micro Analyser
GrA1	SA-210-Grade A1
hr	Hour
K_p	Parabolic rate constant
m.p.	Melting Point
mpy	Mils per year
SEM	Scanning Electron Microscopy
Wt%	Weight percentage
Wt. Gain	Weight Gain
XRD	X-ray Diffraction

CHAPTER 1

INTRODUCTION

Corrosion is a natural occurrence commonly defined as the deterioration of a substance (usually metal) or its properties as a consequence of its reaction with the environment. An estimated 40% of total US steel production goes to replacement of corroded parts and products. So far as India is concerned, the corrosion costs may touch Rs. 24000 crore (Rs. 240000 million). This cost is for the materials corrosion in building structures, bridges, chemical plants, offshore platforms, power plants, ships, pipe lines for transportation of hydrocarbon, electrical and electronics components (Gupta, 2003). However, unlike weather related disasters, corrosion can be controlled, but at a cost. The report further revealed that the 25% to 30% of annual corrosion costs in the U.S. could be saved if proper corrosion management practices were employed (Koch et al, 2002). According to a recent study, the total annual estimated direct cost of metallic corrosion in the U.S. is a staggering \$276 billion-approximately 3.1% of the Nation's Gross Domestic Product (GDP). This cost is more than the annual cost of weather related disasters, which is just averaging \$17 billion annually.

Metals and alloys get oxidised when they are heated to elevated temperatures in air or highly oxidising environments, such as a combustion gas with excess of air or oxygen. They often rely on the oxidation reaction to develop a protective oxide scale to resist corrosion attack, such as sulphidation, carburisation, ash/salt deposit corrosion etc. That is why oxidation is considered to be the most important high-temperature corrosion reaction. Further the rate of oxidation for metals and alloys increases with increasing temperature (Lai, 1990).

It is important to understand the nature of all types of environmental degradation of metals and alloys as vividly as possible so that preventive measures against metal loss and failures can be economically devised to ensure safety and reliability in the use of metallic components. Corrosion of metals had received

maximum attention of engineers and researchers in the field of environmental degradation of metals (Chatterjee et al, 2001).

Hot corrosion is the degradation of materials caused by the presence of a deposit of salt or ash in a general sense. In a more restricted sense, hot corrosion is the degradation of metals and alloys owing to oxidation process, which are affected by a liquid salt deposit. In hot corrosion, metals and alloys are subject to degradation at much higher rates than in gaseous oxidation, with a porous, non-protective oxide scale formed at their surface, and sulphides in the substrate.

Hot corrosion was first recognised as a serious problem in 1940s in connection with the degradation of fireside boiler tubes in coal-fired steam generating plants. Since then the problem has been observed in boilers, internal combustion engines, gas turbines, fluidized bed combustion and industrial waste incinerators (Khanna and Jha, 1998).

Hot corrosion became a topic of importance and popular interest in the late 60s as gas turbine engines of military aircraft suffered severe corrosion during the operation over sea water in the Vietnam war. Metallographic inspection of failed parts often showed presence of sulphides of nickel and chromium, so the mechanism was initially called as “sulphidation” (Rapp, 1986 and 2002).

It is believed that condensed alkali metal salts notably Na_2SO_4 , are a prerequisite to hot corrosion (Otero et al, 1992). The source of these salts may be:

- a) The direct ingestion of sea salt in a marine environment.
- b) Formation of Na_2SO_4 during the combustion of fuels containing both sodium and sulphur.
- c) The formation of (Na_2SO_4), during combustion from sodium contaminated airborne dust and sulphur in the fuel.

An excellent review by Stringer covered the work done in the field of hot corrosion up to about 1976 (1977). Most of the work was aimed at developing improved alloys and understanding the hot corrosion processes. Much of the mechanisms proposed

during that period were focused on thermochemistry. Bornstein and DeCrescente (1969 and 1971) and Bornstein et al (1973) proposed a hot corrosion mechanism based on the basic dissolution of the protective oxide scale by a reaction involving Na_2O , the basic minority component of the fused salt. Goebel and Pettit (1970A) also interpreted the hot corrosion of pure nickel in terms of basic dissolution and re-precipitation of NiO in the fused salt film. Goebel et al (1973) extended this mechanism to include acidic fluxing and oxide reprecipitation to account for the catastrophic oxidation caused by pure Na_2SO_4 for alloys containing strong acid components such as vanadium or molybdenum. The next important contribution in the fluxing model was made by Rapp and Goto (1981), who proposed that if the gradient in solubility of the protective oxide with distance into the salt layer becomes negative at the oxide/salt interface, accelerated attack could be sustained. Sodium vanadyl vanadate ($\text{Na}_2\text{O} \cdot \text{V}_2\text{O}_4 \cdot 5\text{V}_2\text{O}_5$), which melts at a relatively low temperature 550°C is found to be the most common salt deposit on boiler superheaters. Addition of Na_2O to liquid V_2O_5 causes an increase in the basicity of the melt with a corresponding increase in corrosivity with respect to the acidic oxides. Moreover, Na_2O has also been reported to decrease the viscosity. Therefore the protective oxides become porous and non-adherent. The formation of binary and tertiary low melting eutectics increase the surface attack thereby reducing the useful life of the component.

In energy generation processes the mechanism of hot corrosion is dependent on the formation of a liquid phase that is predominantly Na_2SO_4 or K_2SO_4 . The sulphur released from the coal, forms SO_2 with a minor amount of SO_3 and reacts with the volatilised alkalis to form Na_2SO_4 vapour, which then condenses together with fly ash on the superheater and reheater tubes in the boiler. Such a liquid phase dissolves the chromium oxide, which allows the base metal to react with sulphate ions to form sulphide ions and nonprotective oxides (Natesan, 1976 and Rapp et al, 1981).

Sulphur from fuel reacts with NaCl from ingested air during combustion in the combustor to form sodium sulphate which gets deposited on hot sections of turbine components resulting in accelerated oxidation attack. Sulphur in the fuel is

generally limited to 0.3 wt% for commercial jet engines and to 1.0 wt% for marine gas turbines. NaCl comes from seawater.

Corrosion problems caused by low-quality fuels are often tackled by decreasing the steam temperature in super heaters. For instance, in case of boilers burning low-chlorine fuels, such as coal, the steam temperature is usually limited to 570⁰C (Natesan, 1993), whereas boilers combusting high-chlorine fuels, like waste (Kawahara, 1997) or black liquor (Tran et al, 1988) operate with steam temperatures below 500⁰C. Unacceptable corrosion rates have occurred when biofuel fired boiler has been operated with steam temperature of 530⁰C. These lower steam temperatures drastically decrease the efficiency of electricity production. Furthermore, the high-temperature corrosion caused by such combustion environments is usually an accelerated oxidation or sulphidation process.

Due to depletion of high-grade fuels and for economic reason use of residual fuel oil in these energy generation systems is well known. Residual fuel oil contains sodium, vanadium and sulphur as impurities. Sodium and sulphur form Na₂SO₄ (melting point 884⁰C) by reactions in the combustion system. Whereas during combustion of the fuel, vanadium reacts with oxygen to form an oxide V₂O₅ (melting point 670⁰C). Thus V₂O₅ is a liquid at gas turbine operating temperature. These compounds (known as ash) deposit on the surface of the materials and induce accelerated oxidation (hot corrosion) in energy generation systems. When considering coal-gasification processes, hot corrosion is expected to be a problem because the gas environment generally has large sulphur activities and low oxygen activities and also contains substantial amount of salts (Natesan, 1976).

The operating temperatures in case of gas turbines are usually very high, which are expected to increase further with the advances in materials development and cooling schemes for the new-generation gas turbine engines. The combination of such high temperatures with an aircraft environment that contains contaminants such as sodium, sulphur, vanadium and various halides requires special attention to the phenomena of hot corrosion (Eliaz et al, 2002). Moreover, Goward (1998) has suggested that the corrosion in boilers and turbines had much in common.

According to a recent study conducted in U.S. it has been recommended that the U.S. must find more and better ways to encourage, support, and implement optimal corrosion control practices in spite of the fact that corrosion management has

improved over the past several decades. Moreover, corrosion prevention and control is critical to protecting public safety and the environment (Koch et al, 2002). A number of countermeasures are currently in use or under investigation to combat different types of corrosion. While selecting a particular corrosion control strategy it is always emphasised that the protection system must be practical, reliable and economically viable. So far as the hot corrosion problem of metals and alloys is concerned, it may be tackled by designing a suitable industrial alloy, controlling the process parameters, use of inhibitors, protective coatings and superficially applied oxides as per requirements in the given environment.

Controlling the various process parameters (air/fuel ratio, temperature, pressure etc.) of the boiler and gas turbine is useful to some extent to combat corrosion, but these parameters can be controlled only within certain limits. There are numerous inhibitors commercially available that are intended to reduce the severity of oil ash corrosion, particularly Mg and Mn-based inhibitors, which have proven to be effective (Paul and Seeley, 1991). Investigations in the area of inhibitors like MgO, CeO₂, CaO, MnO₂, etc. have already been done in the department and the decrease in the extent of hot corrosion in the most aggressive environment of Na₂SO₄-60%V₂O₅ at 900⁰C has been achieved. But the major problem being faced is how to inject these inhibitors along with the fuel in the combustion chamber in actual industrial environment (Tiwari and Prakash, 1998 and Gitanjaly et al, 2002).

High temperature corrosion of various coatings and boiler steels in oxidizing and reducing chlorine-containing atmospheres without deposits were reported by M.A. Uusitalo et al (2002). It was concluded that the corrosion resistance of bulk materials relied on properties of the oxide and sulfide scales formed at test conditions, whereas in case of coatings the coating structure and the coating composition determined the shielding capability of the coating.

Chlorine-containing ash deposits accelerate corrosion by several mechanisms. Firstly, chlorides lower the first melting temperature (FMT) of the deposits, and molten deposits may flux the protective oxide layer. It is reported that corrosion rate increases significantly, if the deposit temperature is above the FMT [K. Salmenoja et al (2000), N. Hiramatsu et al (1989), M.J. McNallan et al (1981), H.J. Grabke et al (1998), O.H.

Larsen et al (1996), J. Klower et al (1995), Y. Kawahara (1997)]. Chemical reactions are generally faster in liquid phase than as solid-solid reactions. The liquid phase also provides an electrolyte for ionic transport or electrochemical attack

There are many industries where austenitic stainless steel needs to be welded to low alloy steel, especially in the power generation industry [S.M. Shushan et al (1996) and A.Farkash et al (1989)]. Fossil-Fuel boilers and fossil – fuel fired power generating equipment experience hot corrosion problems in such components as steam generators, water walls surrounding the furnace, economizer assemblies, and in the front and rear portions of the super heater and reheater [Theus G.J. et al., 1983, NACE., 1982, and Wyatt , 1978]. These components are often made of carbon steel and low alloy steel which is welded with Austenitic stainless steel. In boiler austenitic stainless steels are used only if ferritic steels can not resist the temperature, load or corrosive environment. Transition joints between austenitic stainless steels and ferritic low alloy steels are utilized extensively in many high temperature applications in energy conversion systems.

In a nuclear water reactor, dissimilar metal welds are employed to connect the low alloy steel reactor pressure vessel and stainless steel pipe systems. Li.G.F., et al [2001] studied the effect of post weld heat treatment on stress corrosion cracking of a low alloy steel to austenitic stainless steel transition weld made by Manual-Metal Arc Welding. The dissimilar metal weldment joining boiler water reactor nozzles to safe ends is one of the more complex configurations in the entire recirculation system [Richard et al 2003].

Ferritic steel-austenitic stainless steel transition joint failure is a perennial problem in fossil-fired steam plants. The microstructure of a typical dissimilar alloy weld failure between low-alloy steel and austenitic stainless steel steam pipe has been studied by a number of investigators and factors that contribute to dissimilar alloy weld failure have been understood. Tucker et al (1956) summarized them as:

- (i) Cyclic thermal stresses caused by expansion differentials,
- (ii) Low oxidation resistance of the Low alloy steel,

(iii) Carbon migration, i.e., the diffusion of the carbon from the ferritic alloy across the interface to chromium rich austenitic stainless steel, and Metallurgical deterioration caused by elevated temperature service.

Low oxidation resistance of low alloy steel is a problem during welding. This is due to the absence of sufficient quantity of elements like chromium that impart oxidation resistance. Therefore, low alloy steels can not be used at high temperatures. Other problem with low alloy steel is that, they are generally subjected to post-weld treatments, which may not be suggested for the austenitic stainless steel as it results in undesired metallurgical changes in austenitic stainless steel. The problem with the dissimilar metal weld made between low alloy steel and austenitic stainless steel with an austenitic stainless steel filler metal is the carbide formation [Welding Handbook] due to higher carbon content of low alloy steels than that of austenitic stainless steel weld metal.

The relatively large amount of carbide forming elements, such as chromium, in stainless steel tends to lower the chemical activity of carbon. The chemical gradient of carbon in-addition to high affinity of carbon towards chromium promotes carbon diffusion from low alloy steel to stainless steel weld metal, which can occur during post weld heat treatment or during service at elevated temperatures. As a result, decarburization and coarse grain formation take place in the heat affected zone of the low alloy steel, that lower its mechanical properties [Erich Folkhard]. At the same time, the adjacent stainless steel weld metal is carburized and embrittlement takes place due to precipitation of brittle phase complex carbides.

The austenitic stainless steels are generally considered the easy weldable of stainless steels [Anik S et al (1991)]. Because of their physical properties, their welding behavior may be considerably different than those of the ferritic, martensitic, and duplex stainless steels [Satyanarayan VV et al (2005)]. It has been generally noted that the austenitic chrome-nickel stainless steels containing 12– 25% Cr and 8– 25% Ni are the most widely used for corrosion resistant applications and vessels, tubing, wire, medical and dental devices materials [Peel M et al (2003) and Baeslack W et al (1979)]. The ability to join austenitic steels itself and to other materials with conventional fusion welding process such as gas tungsten, laser, electron beam

welding opens up the possibility to produce unexpected phase propagation and a series negative metallurgical change such as delta ferrite phase, grain boundary corrosion, strain corrosion and sigma phase occurs at the welding interface. Therefore, extensive care and precautions like pre and post heat treatment or quick welding speeds are required [Tsuchiya K et al (1996), Baeslack W et al (1979), Sahin AZ et al (1998) and Yilmaz M et al (2002)].

In order to minimize joining problems of dissimilar materials, friction welding has represented the specific joint characteristic [Spindler DE (1995), Ozdemir N (2002) and Yilbas BS (1995)]. The advantages of this process are, among others, no melting, high reproducibility, short production time and low energy input [Ozdemir N et al (2005), Midling OT et al (1994), Behnken H (2000)]. Friction welding has advantage in materials that are hard to adopt fusion welding in that, it needs comparatively low thermal energy input in welding and causes minimal thermal degradation as base materials need not be fused for welding. In the practice, it is possible to bond a variety of dissimilar materials by friction welding processes.

Electron beam weiding (EBW) has been developed for many years and is being increasingly implemented in various industrial applications. Joining dissimilar metals using EBW has also been a subject of interest in recent years. Due to special features of EBW, e.g., high energy density and accurately controllable beam size and location, in many cases it has proven to be an efficient way of joining dissimilar metals. Numerous successful results have been achieved, and some of them have already been exploited in production. EBW continues to be the subject of investigations and further development, and improvements in the joining of dissimilar metals remain one of the aims. Since EBW is a fusion-welding process, metallurgical phenomena associated with fusion still exist and cause difficulties. However, these are often minor as compared to those in conventional arc welding.

R.K. Singh Raman et al (2002) reviewed of the non uniform scaling behaviour across microstructural gradients in weldments of pressure vessel steels in order to develop a global model for lifeassessment by relating oxide scale thickness with time–temperature history of in-service components. Also the author discussed about the

prevalence of in-service failures in the welds of chromium–molybdenum ferritic steels causes great concern in steam generating/handling systems of power plants, and components of petroleum/petrochemical industries. The researchers concluded that the accurate use of oxide scale thickness as a tool for life assessment of the welded components. Also the author recommends further investigations as listed below:

- examining the applicability of the recent practice of life assessment by scale thickness to the welded components, by establishing kinetics of the scale thickness growth across the broadly different (microstructural) zones (viz. weld metal, HAZ and base metal) of the steel weldments, in the environments of steam and air,
- developing a suitable model for life assessment by relating scale thickness with time–temperature history (and hence, creep damage) in the different zones of the steel weldments,
- testing the validity of the model for steam generators in fossil-fuel power plants,

For an improved understanding of the deterioration in the mechanical properties due to deleterious alloy microstructure, it will be necessary to carry out further investigations as listed below:

- characterising corrosion-assisted microstructural degradation in the alloy matrix across the broadly different (microstructural) zones (viz. weld metal, HAZ and base metal) of the steel weldments, in the environments of air and steam, and thus investigating the role of the environment in facilitating microstructural degradation,
- Examining the role of corrosion-assisted microstructural degradation, by conducting creep tests on the simulated weld metal and HAZ, in steam and inert environments.

Corrosion aspects of the similar and dissimilar joints of advanced materials made by different welding technologies Friction Welding, TIG welding and EBW welding still requires a vast amount of research and development.

The present study has been performed to evaluate the hot corrosion behaviour of dissimilar weldment of AISI 4140 and AISI 304 made by FRW, TIG and EBW temperature range from 500 to 900⁰C with and without salt mixture of Na₂SO₄+ V₂O₅ (60%); Na₂SO₄ + NaCl (50%), K₂SO₄ + NaCl (60%) and Na₂SO₄ (40%)+ K₂SO₄ (40%) + NaCl (10%)+ KCl (10%) under cyclic conditions.

CHAPTER 2

LITERATURE REVIEW

2.1. Weldability Aspects of Austenitic Stainless Steels

The presence of chromium greatly improves the corrosion resistance of the steel by forming a very thin stable oxide film on the surface, so that chromium-nickel stainless steels are now the most widely used materials in a wide range of corrosive environments both at room and elevated temperatures. Austenitic stainless steels have better ductility and toughness than carbon and low alloy steels because of the FCC crystal structure. Their notch toughness at cryogenic temperatures is excellent. These steels exhibit higher thermal expansion coefficient than low alloy steels, which means that distortion during welding can be greater.

Austenitic Stainless Steels possesses excellent weldability, provided they are welded with filler metals which yield an austenitic weld metal with delta ferrite contents in the range of about 5-15FN. It is a common practice to subject the austenitic steels to a solution annealing treatment, normally in the range of 1050-1100 °C. In the course of this heat treatment, M₂₃C₆ carbide, sigma phase and delta ferrite are completely dissolved and the annealing process produces a homogenous fully austenitic structure with a subsequent quenching treatment, this state is maintained down to ambient temperature which means that austenitic steels show prior to welding an austenitic structure without any delta ferrite.

When welding austenitic stainless steels greater distortion of the welded component must be expected, this is due mainly to the fact that the austenitic stainless steels have a higher coefficient of thermal expansion and lower thermal conductivity than the ordinary ferritic steels. Because of the lower thermal conductivity of the austenitic stainless steels below 800°C, dissipation of the welding heat into the base metal takes place more slowly; therefore an accumulation of heat may occur in the weld, which may lead to local overheating and severe distortion. A major concern, when welding the

austenitic stainless steels, is the susceptibility to solidification and liquation cracking. When Cr_{eq}/Ni_{eq} is less than 1.48 using the Schaeffler formula, solidification is austenitic and the susceptibility to cracking is high. With Cr_{eq}/Ni_{eq} between 1.5 and 1.95, the solidification is ferritic-austenitic; that is to say, the primary dendrites are ferritic and these transform to austenite by the peritectic reaction during solidification. The ferritic-austenitic mode is the most crack-resistant

Fig. 2.1 shows the time-temperature relationship for intergranular precipitation of carbides' in AISI 304 austenitic stainless steel and weld metal as a function of carbon content. Precipitation occurs between 425 and 800°C. Under welding conditions it is most rapid at about 650°C and occurs preferentially at grain boundaries, within the ferrite phase or along slip planes in cold-worked material. The carbide so formed is normally chromium carbide ($Cr_{23}C_6$) and it may be redissolved by heating between 1000 °C and 1100°C for a short period. During fusion welding, there is a region of the heat-affected zone that is heated within the carbide precipitation temperature range and this region is prone to intergranular corrosion known as sensitization. The severity of corrosion attack depends on the time and temperature of exposure, as well as the composition and prior heat treatment of the steel. Most austenitic stainless steel weldments do not require post weld heat treatment [Welding Handbook]. However, a heat treatment is sometimes used to improve corrosion resistance or to relieve stresses, or both. Corrosion problems associated with welds in austenitic stainless steels are often localized in the heat-affected zone. If the service environment is known to attack sensitized areas containing intergranular carbides or if maximum corrosion resistance is required, a post weld solution heat treatment at the annealing temperature should be used to re-dissolve the carbides.

2.2. Weldability Aspects of low alloy Steels

Low alloy steels can be classified as Heat Treatable Low Alloy Steel (HTLA), High Strength Low Alloy steel (HSLA) and Quenched and tempered Low Alloy Steel (Q&T LA). AISI 4130, 4140& 4340 belong to the heat treatable alloy steels, as these have to be heat-treated after welding. AISI 4140 steel has greater hardenability and strength than those of 4130

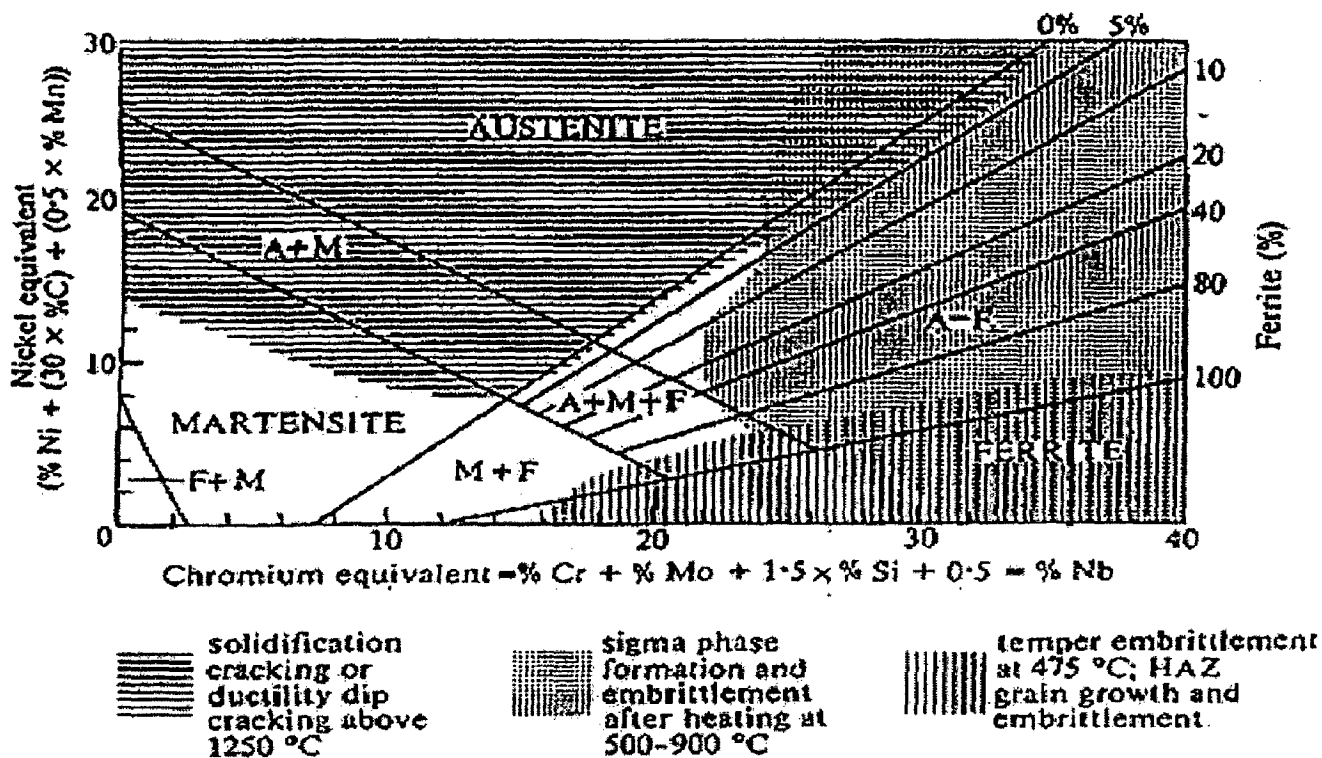


Fig.2.1 Schaeffler Diagram (Welding Hand Book (1975))

steel, but with some sacrifice in formability and weldability due to its higher carbon content [ASM International].

The combined carbon and alloy contents of the low alloy steels are sufficient to promote the formation of martensite from austenite when cooled rapidly to below the appropriate transformation temperature [Welding Handbook]. The carbon content is sufficiently high to form hard martensite that may be brittle (Fig. 2.2). During welding, a portion of the weld and HAZ will transform to austenite. If the weld metal and the austenitic HAZ are cooled too fast, they will transform to martensite or a combination of martensite and bainite, as illustrated in Fig. 2.3 for AISI 4340 steel [Kenneth Easterling]. The internal stresses that develop during cooling from both the contraction of the weld and HAZ and the transformation of austenite may cause hard martensite to crack. Since these steels are very sensitive to hydrogen induced cracking, the welding process and procedures should minimize the presence of hydrogen during welding as well as the formation of martensite. Since high carbon martensite is hard and brittle, proper preheating and low-hydrogen electrodes should be used to avoid underbead cracking [G.E. Linnert (1994)]. A convenient way of estimating the amount of preheating required is to use the so-called equivalent carbon content.

2.3 FRICTION WELDING

Friction welding is a solid state welding process, which produces coalescence of materials by the heat obtained from mechanically induced sliding motion between rubbing surfaces. Due to shorter welding times formation of intermetallic layer can be kept to a minimum enabling wide range of materials to be joined successfully[K.K.Wang (1975)].

2.3.1 Friction Welding Process

Initially one piece is mounted in the chuck and rotated to the required speed and the other piece is clamped. The process of Friction welding, in practice, is accomplished in three phases (Fig. 2.4) [R.S.Parmar]:

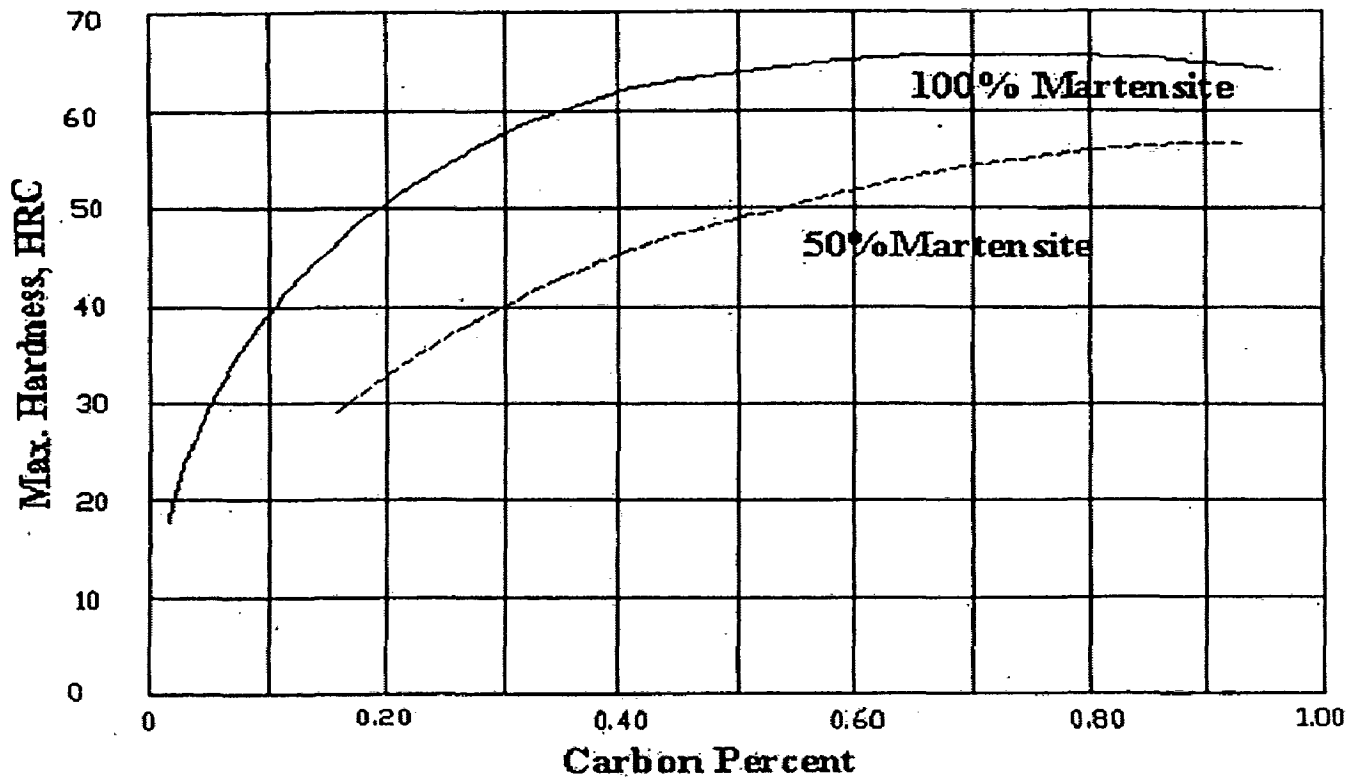


Fig.2.2 Relationship between carbon content and maximum hardness of steel with microstructures of 50 and 100% martensite.

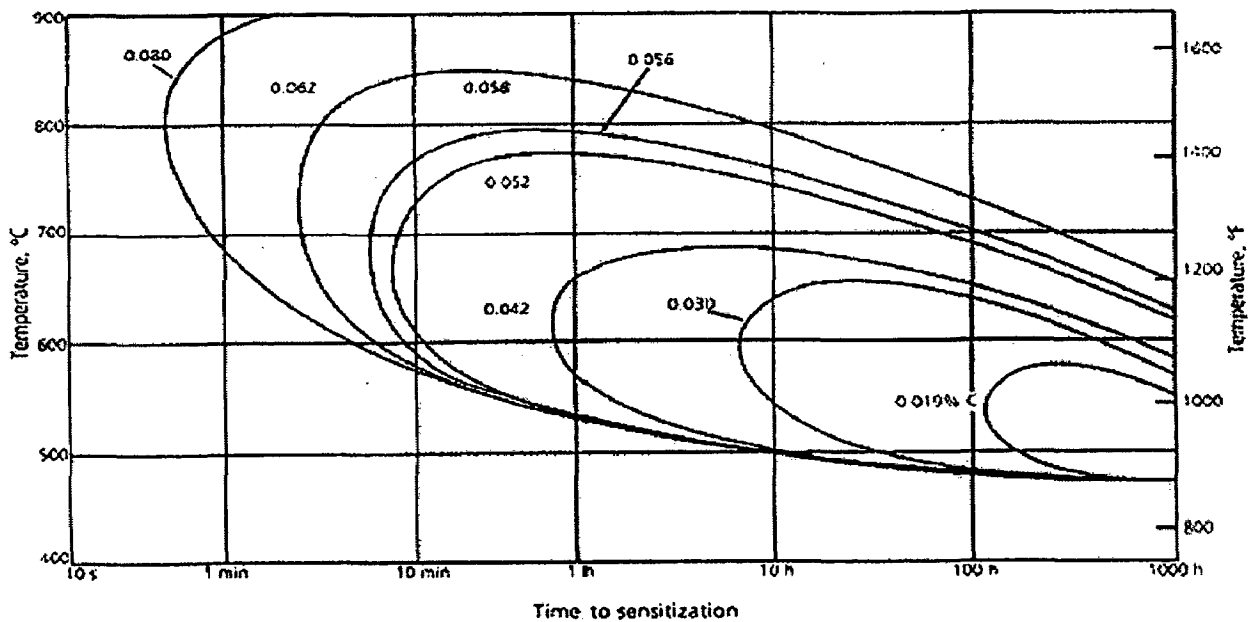
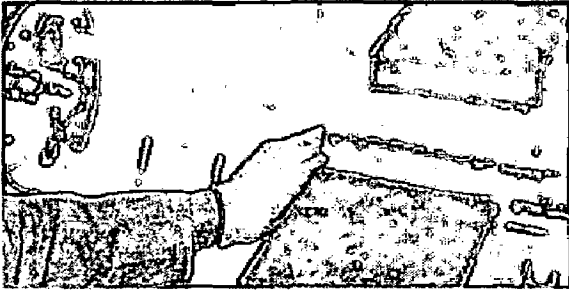
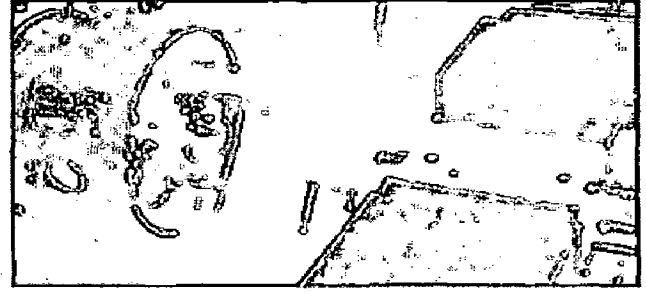


Fig.2.3 Time-Temperature relationship for intergranular precipitation of carbides in AISI 304 austenitic stainless steel and weld metal as a function of carbon content



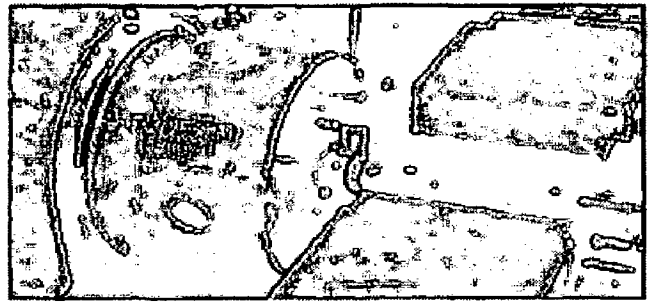
(a) Setup and Clamping



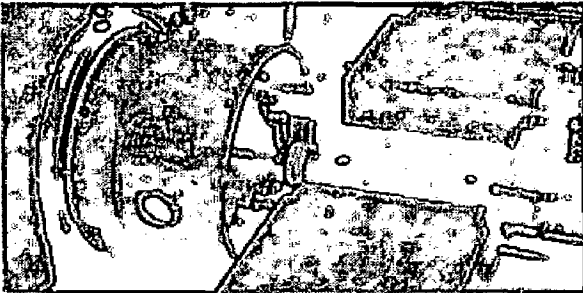
(b) Spindle starts rotating and slide advances



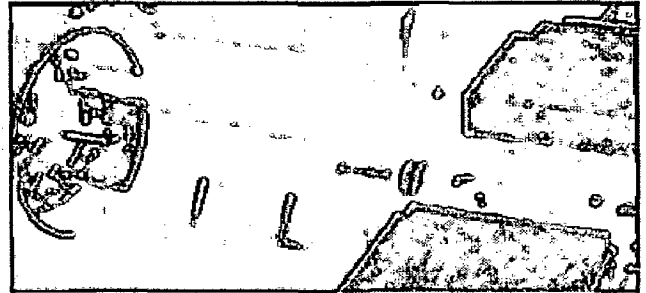
(c) First Friction



(d) Second Friction



(e) Forge



(f) Spindle retract, workpiece released

Fig 2.4 Sequence of friction welding process

Phase 1 (First Friction): Pieces are made to rub together, at low pressure (friction pressure), to accomplish a cleanup of the two surfaces to be welded. The force applied during First Friction is -30% of the Second Friction.

Phase 2 (Second Friction): The increased pressure brought about during second friction causes the metal to become "plastic" and flows outward from center to form the characteristic "Flash". Once the designed Flash is accomplished, the rotation is rapidly stopped. The Process then moves to the Forge Phase.

Phase 3 (Forge): The Forge is caused by the application of the highest pressure of the three process. The forge phase takes place while the components are at a complete rest. The pressure is maintained until the weld joint is sufficiently cooled. This step also promotes refinement of the microstructure of the weld.

2.3.2 Theoretical Considerations

Chudikov and Vill from Russia are credited with the successful application of friction welding to metals. The fundamental consideration of the process is based on Law of friction i.e., friction force F is proportional to the applied normal load, L . Thus

$$F = \mu L \dots\dots\dots (2.1)$$

Where (μ is the coefficient of friction, which increases with increase in load and is also dependent upon the speed.

According to Vill frictional force can be expressed by the following equation,

$$F = \alpha A + \beta L \dots\dots\dots (2.2)$$

Where A is the area of contact and α and β are constants. For high values of pressure the first term A is very small and thus $F = \beta L$ where β is nearly equal to μ and so the basic law of friction holds good.

Frictional force varies from the start of the operation till the completion of weld. To study its effects on the different phases of the process it is convenient to do so by analyzing the time-torque relationship shown in Fig.2.5. The initial peak in the torque curve is due to dry friction

but soon after it follows the second phase of the process wherein seizure and rupture takes place at the high points of the contact. The average temperature during the second phase is only 100-200°C. The quick rise of the torque and fluctuating nature of the curve is due to the change from marginal or boundary layer friction with $\mu = 0.1$ to 0.2 to pure friction with $\mu > 0.3$. The torque increases as the points of seizure increase and finally molten metal may appear at these points of contact and act as a lubricant and the average temperature of the interface may rise to 900-1100°C. Only 13% of the total heat is produced during the first two stages (T1+T2) while the rest is produced during the third stage (T3). Increasing the speed instead of reducing the duration of the process increases the temperature as it is evident from Fig.2.6. This is because enhanced speed results in decreased heating intensity. Heat energy generated per unit area of the faying surfaces is given by the following expression

$$H = \frac{2PK \times 10^2}{nR} W / mm^2 \quad (2.3)$$

Where,

H= heat generated, W/mm²

P= applied pressure, N/ mm²

R= work radius, mm

n= rpm

K= a constant $8 \times 10 \text{ mm}^2 / \text{min}^2$ for low carbon steel.

The second stage may cover nearly 30-70% of the axial pressure and the duration of the third stage is inversely proportional to the axial pressure. Thus, for optimal results the axial load should be kept low during the initial phase and be increased gradually or may be applied in two stages. The maximum temperature attained is controlled by the applied axial load as the metal with lower strength value will be squeezed out under a given specific load.

In friction welding of dissimilar metal combinations such as stainless steel to carbon steel, the plane of maximum temperature can move away from the interface; with the high speed of friction welding it moves into the stainless steel so that one-half of the flash is bimetallic. In

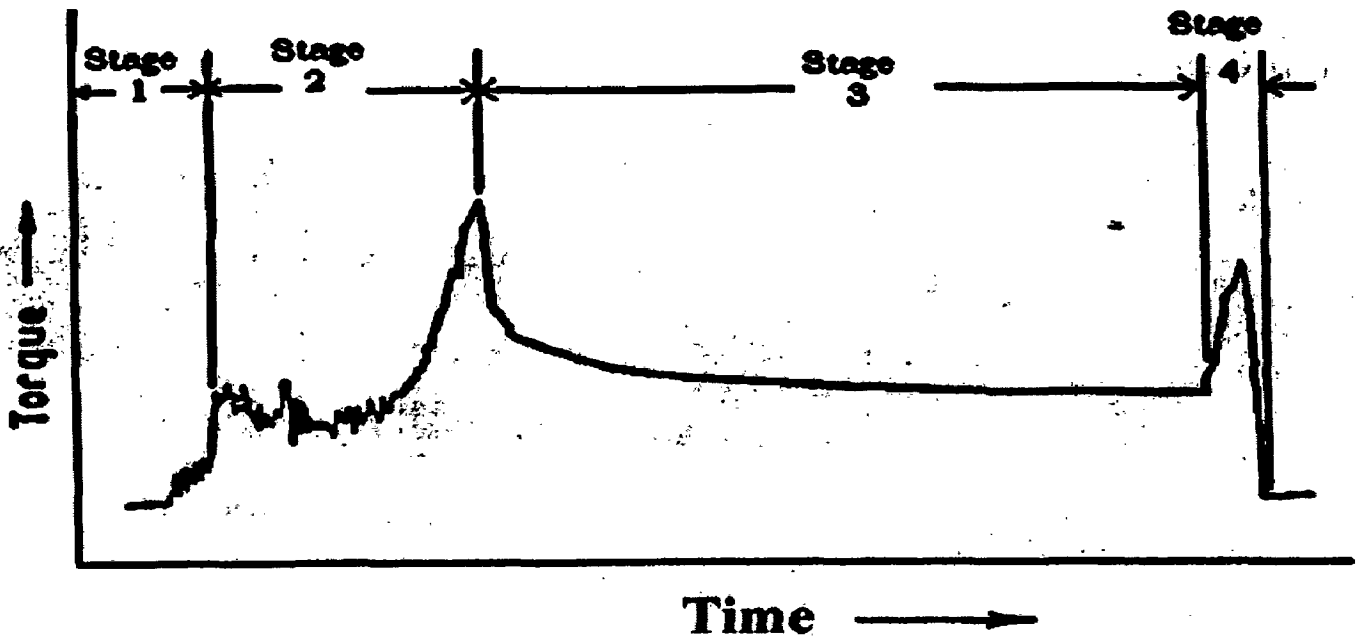


Fig 2.5 Time torque relationship for continuous drive friction welding process

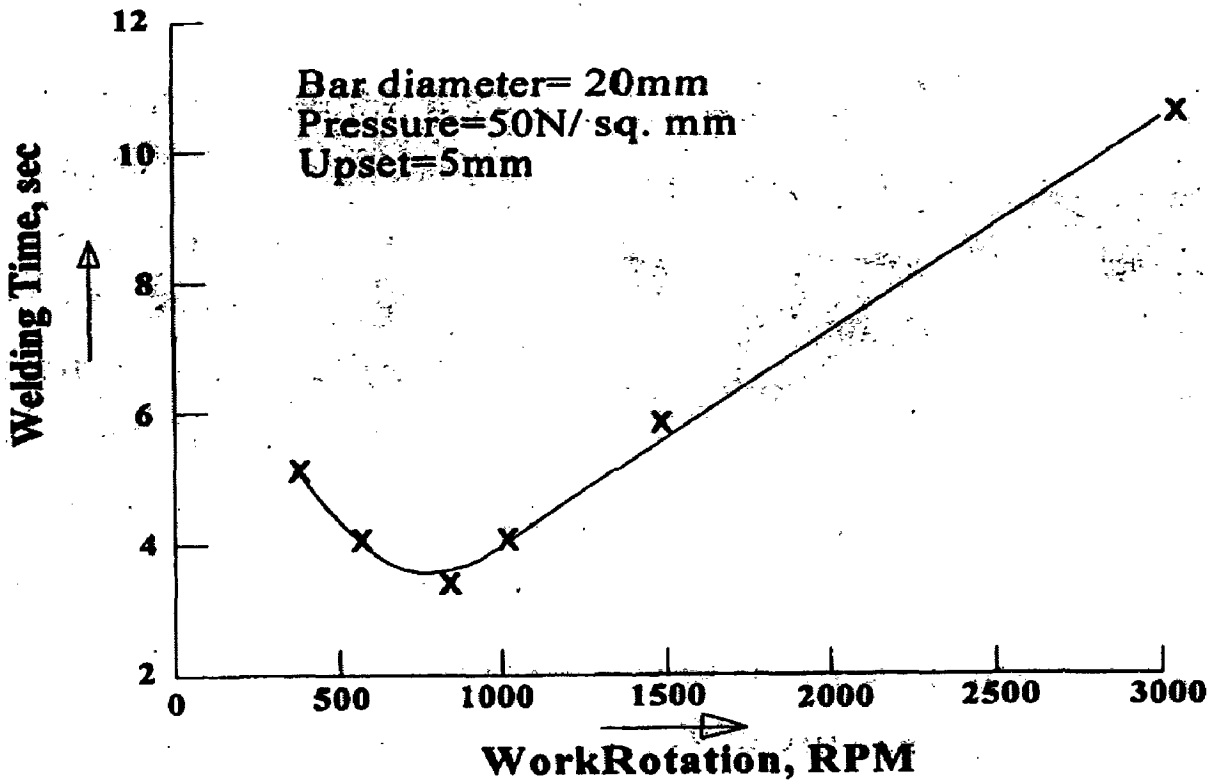


Fig 2.6 Effect of rotational speed on duration of welding

this case decreasing the rotational speed provides the desired result and at a certain lower speed the interface again becomes the plane of maximum temperature and thus a plane of maximum shear strain rate. The applied pressure is perhaps the most important single factor as it controls the temperature and determines the torque required. The heat input rate is proportional to the product of torque and the rotational speed. Rotational speed has to be such that certain minimum or threshold power is exceeded. If the power applied is just above the threshold it will take a long time for the required temperature to be reached and the heat-affected zone will be wide. The most important variable is the unit pressure applied during rotation and the recommended values for some of the metals are in Table 2.1

The sliding velocity varies from zero at the centre of the workpiece to a maximum at the peripheral surface, and the radius at 2/3 rd the diameter of the workpiece is used for the calculations. Longer heating times result in more material for forging and for optimal results there should be adequate heated material available for forging when the rotation is stopped. Excessive initial pressure results in excessive squeezing of heated metal leaving only relatively cold metal to be forged when the forging pressure is applied. This dilution leads to cold and low ductility joints.

Table 2.1 Friction Pressure for Different Metals

Metal	Friction Pressure (MPa)
Mild Steel	38
Medium Carbon Steel	48
Nickel-Chromium Steel	76
Aluminium alloys	55
Nimonic alloys (80/20 Ni/Cr)	97

2.3.3 Welding Characteristics of Continuous Drive Friction Welding:

Continuous Drive friction welding has more parameters to control [Vill.V.I]. These parameters, as referred to in Fig.2.7 are as follows:

Rotational Speed, Burn-off length, Friction Pressure, Upsetting or Forging Pressure, Frictional Heating Time, Forge Delay Time, and Upsetting or Forging Time. In practice,

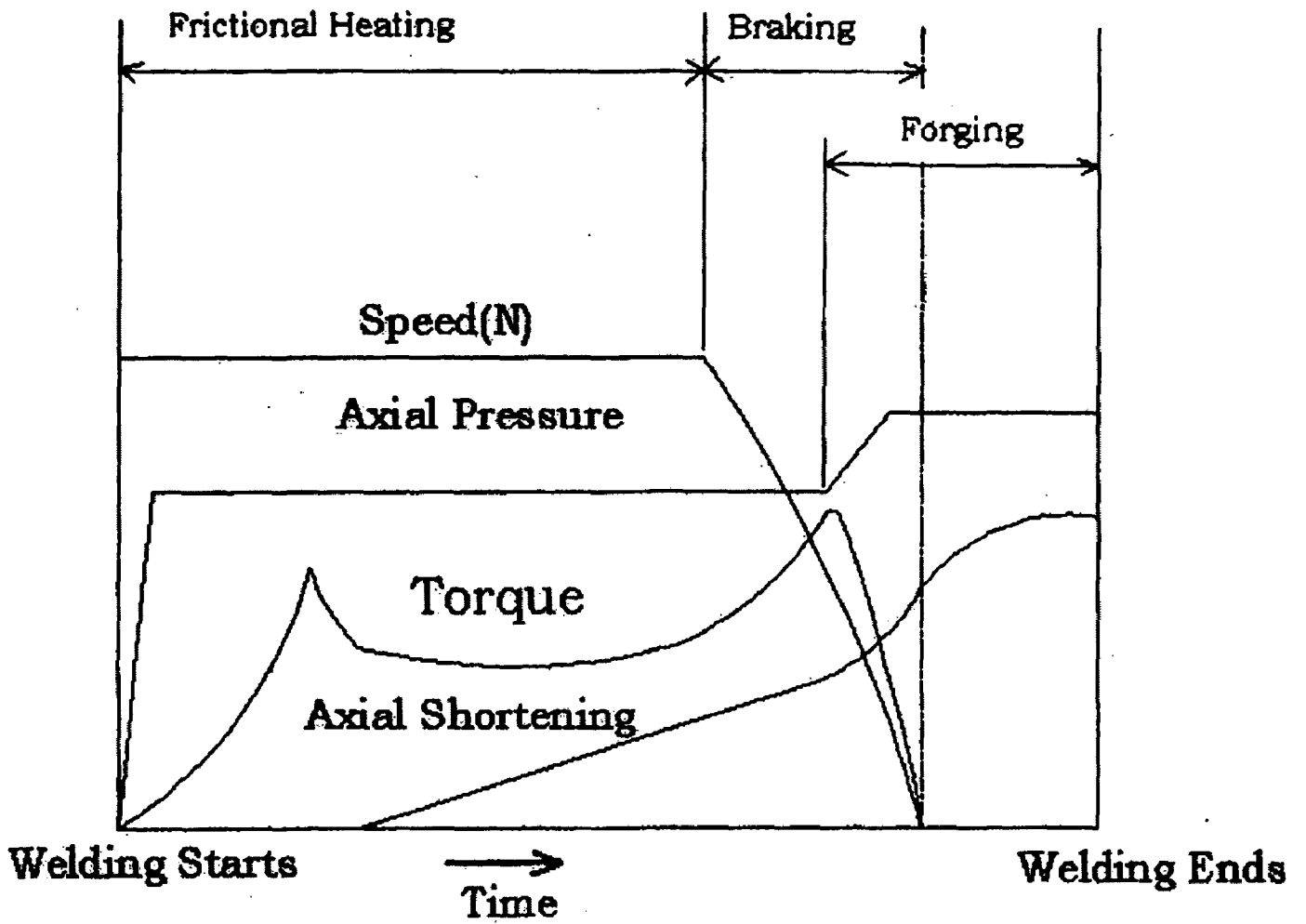


Fig 2.7 Variations of process parameters with time for continuous drive friction welding

however, not all the parameters need to be controlled. Usually only rotational speed, frictional heating time and forging pressure are considered for analyzing the process where as others are kept constant.

2.3.3.1 Rotational Speed

Rotational speed provides the necessary relative velocity at the faying surfaces. Its magnitude depends upon the metal being welded and for steels, the tangential velocity for both solid and tabular workpieces, should be in the range of 75-110 m/min [R.S.Parmar]. Tangential speeds lower than 75 m/min result in excessive torque with consequential clamping problems, non-uniform up-set and tearing of metal at the joint. Friction welding machines for production purposes, handling 50 to 100 mm diameter workpieces, usually operate at speeds varying between 90 to 200 m/min.

2.3.3.2 Frictional Heating Time

Heating time is controlled depending upon whether a fixed pre-set time is allowed for heating or the extent of the axial upset is to be within the specified limits [Vill.V.I]. Excessive heating time limits productivity and results in wastage of material; while insufficient time may result in uneven heating as well as entrapped oxide and unbounded areas at the interface.

2.3.3.3 Forging Pressure

The applied axial pressure controls the temperature gradient in the weld zone, the power required for the machine, and the axial shortening of the workpiece [Vill.V.I]. The specific pressure depends upon the metal being welded and joint configuration. It can be used to compensate for heat loss to a large body as in the case of tube-to-tube or tube-to-plate welds. Applied pressure must be high enough during the heating phase so as to keep faying surfaces in close contact to avoid oxidation. Properties of the joint may often be improved if the applied pressure is increased at the end of the heating phase.

2.3.4 Dissimilar-metal joints with Friction welding

The mechanical properties of dissimilar friction weldment of austenitic–ferritic stainless steel combination are compared by V.V. Satyanarayana et al (2005). Typical microstructure of

friction welded AISI 304 and 430 shown in Fig 2.8 (A). Evaluation of the joints for resistance to pitting corrosion revealed that the dissimilar welds exhibit lower resistance to pitting corrosion compared to the ferritic and austenitic stainless steel welds. They found that the central region consists of equiaxed grains and is confined to ferritic stainless steel. Adjacent to this region bent and elongated grains are observed on the ferritic stainless steel side. The austenitic stainless steel side consists of parallel banded features adjacent to the central equiaxed grain structure at the interface. The interface is narrow and straight in high burn-off welds. At low friction and low burn-off parallel bands are observed in the austenitic stainless steel side adjacent to the interface. The author concluded that the friction welding of austenitic–ferritic stainless steel, deformation is confined to ferritic stainless steel only. The mechanical properties of austenitic–ferritic stainless steel welds are similar to ferritic stainless steel welds. The toughness (16–28 J) and strength (600–697 MPa) properties of dissimilar metal welds are better than the parent metal ferritic stainless steel. Also the author investigated the effect of burn-off length with the hardness on the weldment. Highest hardness (265 Hv) and lowest hardness (195 Hv) were obtained at low burn-off and at high and low forge pressures, respectively. Impact toughness was on the higher side at high burn-off while notch tensile strength followed a reverse trend. Notch tensile strength ranged from a minimum of 600MPa to a maximum of 689MPa while impact toughness was in the range 15–28 J. Typical hardness distribution across the weld shown in Fig 2.8 (B) reveals that hardness is higher on austenitic stainless steel side of the interface.

N. O zdemir et al (2007) reported that the microstructural evaluation of friction-welded joints of AISI 304L to 4340 steel revealed four distinct zones across the specimens which were identified as Parent Metal (PM), Partial Deformed Zone (PDZ), Deformed Zone (DZ) and transformed and recrystallized fully Plasticized Deformed Zone (FPDZ) Fig 2.9 (A). Also the author concluded that the higher microstructural changes took place in the FPDZ and DZ region. The width of FPDZ region is mainly affected by the rotational speed. The use of higher rotational speed and shorter friction time increases the tensile strength of friction weld. It can be inferred that the width and formation of FPDZ which occurred as a result of the reactions taking place at the welding interface have a detrimental effect on the mechanical strength and consequently the quality of the friction-welded 304L/4340 steel couple and,

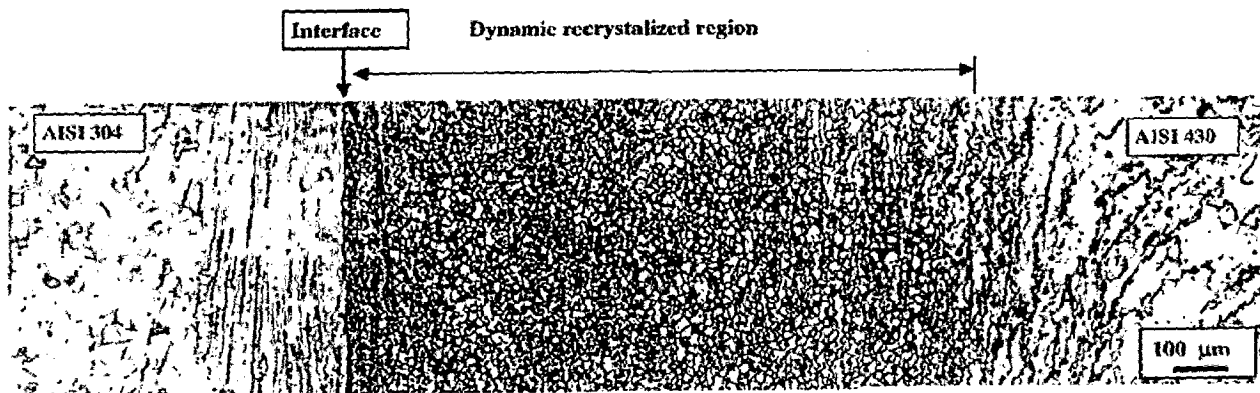


Fig 2.8 (A) Typical microstructure of friction welded AISI 304 and 430 (V V Satyanarayana et al (2005))

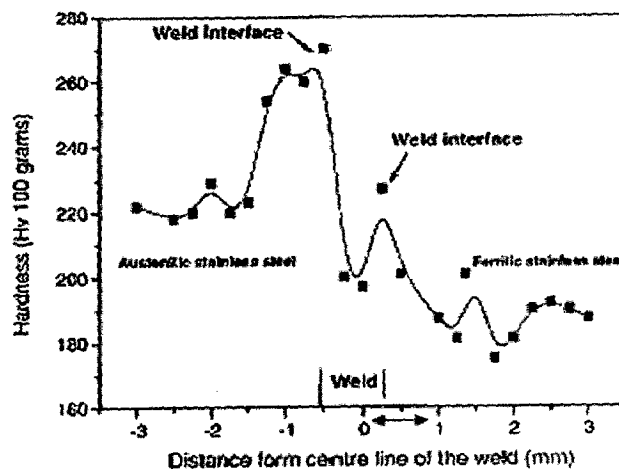


Fig 2.8 (B) Microhardness traverse along the bond line of a typical friction weldment (V V Satyanarayana et al (2005))

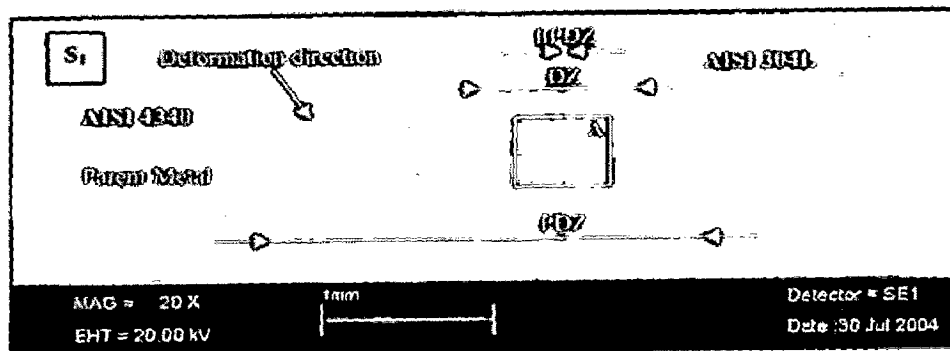


Fig 2.9(A) The macro SEM photo taken from welding interface of friction welded sample and representation of interface reactions (N.Ozedemir et al 2007)

therefore, must be controlled. The maximum hardness on the weldment obtained was 1000 HV and the ultimate tensile strength (UTS) was 95 (N/mm²) when the rotational speed of 2000 RPM.

S.D. Meshram et al (2007) investigated that the influence of interaction time on microstructure and tensile properties of the friction welding of five dissimilar metal combinations, namely Fe–Ti, Cu–Ti, Fe–Cu, Fe–Ni and Cu–Ni system. The author reported that the extended interaction time led to decreased strength due to thicker intermetallic layer formation in eutectoid forming systems (Fe–Ti and Cu–Ti) and insoluble system (Fe–Cu). Also in the soluble systems (Cu–Ni) strength increment is observed with an increased interaction time due to solid solution formation.

Bhole (1991) discussed about the microstructure and hardness in the heat affected zone of a friction weld between a mild steel bar and a high strength low alloy steel plate. The torsional shear and frictional heat generated during friction welding leads to phase transformations resulting in fine bainitic or martensitic microstructures. Hardness profile across the weld shows a sharp peak in hardness in the vicinity of the weld interface that could affect the properties of the weld.

Fickel (1964) studied the diffusion process in joints between dissimilar steels and it was shown that carbon migrates from ferritic steels across the interface in the direction of higher chromium content alloy like austenitic stainless steel. Evidence was obtained indicating that iron diffuses into an austenitic stainless steel from ferritic steel. Interpolation of a nickel barrier between a ferritic and an austenitic stainless steel reduces the transfer but does not prevent carbon migration.

C.J.Cheng (1963) investigated the transient heat conduction problems encountered in friction welding two dissimilar materials, which are in tubular form. It was observed that the temperatures near the interface are little affected by prolonged heating, once the peak of the heat input curve is obtained and during the welding cycle are mostly governed by the initial heat input history of the power cycle.

Hollander et al (1963) observed that type AISI 304 stainless steel can be friction welded to AISI 4140 alloy steel with joint strength in the as-welded condition equal to or greater than the stainless steel base metal. They also observed that, greater rates of heat

input can be achieved at lower speeds and/or higher pressures than are used in the optimum cycle, i.e., increasing the speed of rotation does not necessarily increase the amount of heat generated by friction.

2.3.5 Advantages of friction welding

Friction welding has emerged as a reliable process for high-production commercial applications, with significant economic and technical advantages [K.K.Wang (1975)]. Friction welding is clean, dry, hydraulically activated and Programmable Logic Control (PLC) and requires neither flux nor special atmosphere.

The advantages are both metallurgical and physical and they are:

1. A bonded joint is formed using no filler metal, flux or shield gas.
2. The process is environmentally clean; no arcs, sparks, smoke or flames are generated by clean parts.
3. Surface preparation/cleanliness is not significant with most materials since the process burns through and displaces surface impurities.
4. During the welding process there are narrow heat affected zones. The process is suitable for welding most engineering materials and is well suited for joining many dissimilar combinations. In most cases, the weld strength is as strong as or stronger than the weaker of the two materials being joined.
5. Operators are not required to have manual welding skills. Friction welding requires only simple integration into the manufacturing area.
6. The process is easily automated for mass production. Welds are made rapidly compared to other welding processes. Plant requirements (space, power, special foundation etc.) are minimal for the friction welding process.

2.3.6 Limitations of friction welding:

1. One workpiece must have axis of symmetry for rotation. This limitation is overcome by newer developments like linear friction welding and friction stir welding.

2. Preparation and alignment of workpiece may be critical for uniform rubbing and heating particularly for large diameter pieces.
3. High cost of the equipment.
4. In common with all other solid-state welds, lack of a reliable non-destructive testing method could be another deterrent to user's confidence.

2.4. ELECTRON BEAM WELDING

2.4.1. Electron beam welding process

Electron beam welding process has been amongst the most frequently investigated processes in the joining of dissimilar metals during the last decade. This trend may be attributed to several factors: (i) The rapid development of EBW equipment; (ii) The high quality requirements of the products which EBW can realize; (iii) The special features of the process which offer solutions that other alternative methods cannot provide; and (iv) The economic benefits obtained by using the process in mass production.

EBW, as an industrial welding process, was started in the late fifties. The process was used primarily in the nuclear, aircraft and aerospace industries, initially due to the requirements of high quality and reliability of the joints [D.E. Powers (1989)]. The principle of an EBW operation is to use the kinetic energy of electrons as the heating source to melt the metals to be joined. These electrons are generated by heating a negatively-charged filament (cathode) to its thermionic emission temperature range, upon which electrons are emitted. Such electrons, being accelerated by the electric field between the negatively-charged bias electrode located slightly below the cathode and the anode, pass through the hole in the anode and form a beam [Y. Arata (1985)]. The electron beam can be focused under vacuum, and strikes the metal surface at velocities of up to 70% of the speed light. About 95% of the electrons' kinetic energy is converted into heat. The electron beam can be focused on diameters in the range of 0.3-0.8 mm, and the resulting power density can be as high as 10^{10} Wm^{-2} . One of the key features of EBW is its ability to perform deep penetration welding with the 'key-hole' mechanism.

During the initial period of commercial application, the process was strictly limited to operations in a high vacuum chamber. However, the later development of the system permitted the option of welding in either a medium-vacuum chamber or a non-vacuum environment, which widened the use of EBW over a broad range of industrial applications [D.E. Powers et al (1989)]. Therefore, three modes of EBW are available at present: the high-vacuum mode ($<10^{-3}$ Torr); the medium-vacuum mode (10^{-25} Torr); and the non-vacuum mode (atmospheric). It should be noted that the use of non-vacuum EBW still remains very limited. The selection of EBW modes depends on the materials to be joined and the penetration requirement.

The primary processing parameters in the EBW are the beam current (current), the beam accelerating voltage (voltage), the focusing lens current (focal beam spot size), the welding speed, and the vacuum level. The quality of the joints depends on the selection of these parameters, although some secondary variables can, to some extent, refine the parameters, and thus produce welds with the desired properties. Some of the parameters particularly affect the results of dissimilar-metal joining. Other important parameters, such as the beam alignment relative to the joint centre line, and the focal beam spot size, could be dominating factors in dissimilar-metal joining due to their ability to control the desirable fusion ratio of the two metals. When using EBW, it is possible to weld particular dissimilar-metal combinations which were previously considered to be non-weldable with conventional fusion-welding processes. For instance, joints between Cu and Ti can be EB welded by locating the beam to the Cu side to minimize the melting of the titanium and increase the heat dissipation of the copper [M.M. Schwartz (1969)].

2.4.2. Dissimilar-metal joints with EBW

Dissimilar-metal joints are characterized particularly by compositional gradients and microstructural changes, which yield large variations in chemical, physical, and mechanical properties across the joint. The joining of dissimilar metals is, therefore, normally far more complex than the joining of similar metals. The difficulties encountered when joining dissimilar metals include the problems experienced when joining each base metal

individually, and the problems specific to the range of compositions, as well as to properties and their incompatibility possible in phases and/or compounds of the two metals in various proportions. Further complexity arises from the addition of filler or insert materials, which is a common practice in the joining of dissimilar metals [E.A. Brandes (1983)].

However, the large differences in physical properties also yield difficulties in joining the different metals together. Both physical and chemical mismatches easily result in incompatibility. For example, a large difference in the melting temperature between two metals makes the conventional fusion-welding processes unfit for welding due to the segregation of low-melting eutectics, which can cause hot cracking. Large differences in thermal expansion will, in turn, lead to the formation of large residual stresses, and thus reduce the joint strength and cause fatigue problems. A difference in the thermal conductivity of the two metals easily causes uneven heat dissipation. Furthermore, chemical mismatches in dissimilar-metal joints can result in the formation of brittle phases and the diffusion of particular elements.

Although EBW is a fusion-welding process and may still encounter these problems, it may, however, offer chances to reduce or overcome the problems to a certain extent, and hence, to produce satisfactory joints. For instance, EBW can solve the problem of the large difference in melting temperature more easily than, e.g., arc welding, due to the high-energy density resulting in a high heating and cooling rate. A low total-heat input per unit length of weld of EBW can also reduce the residual stresses substantially, as compared to arc welding. The thermal conductivity problem can be overcome by directing the beam correctly to the required location. The small weld bead size of EB welds minimizes the mixing of dissimilar metals, and thus, limits the brittle zones arising from the chemical mismatch, to some extent.

According to metallurgical compatibility and other factors, the EB-weldability of different metal combinations have been ranked as shown in Table 2.2, the data originating partly from phase-diagram information, and partly from practical experience [Welding Handbook].

Table 2.2: Weldability of dissimilar metal combinations using electron beam welding
[Welding Handbook]

Al	2																	
Au	1	5																
Be	5	2	5															
Co	3	5	2	5														
Cu	2	2	1	5	2													
Fe	3	5	2	5	2	2												
Mg	5	2	5	5	5	5	3											
Mo	3	5	2	5	5	3	2	3										
Nb	4	5	4	5	5	2	5	4	1									
Ni	2	5	1	5	1	1	2	5	5	5								
Pt	2	5	1	5	1	1	1	5	2	5	1							
Re	3	4	4	5	1	3	5	4	5	5	3	2						
Sn	2	2	5	3	5	2	5	5	3	5	5	5	3					
Ta	5	5	4	5	5	3	5	4	1	1	5	5	5	5				
Ti	2	5	5	5	5	5	5	3	1	1	5	5	5	5	1			
W	3	5	4	5	5	3	5	3	1	1	5	1	5	3	1	2		
Zr	5	5	5	5	5	5	5	3	5	1	5	5	5	5	2	1	5	
	Ag	Al	Au	Be	Co	Cu	Fe	Mg	Mo	Nb	Ni	Pt	Re	Sn	Ta	Ti	W	

1. Very desirable (solid solubility in all combinations), 2. Probably acceptable (complex structures may exist), 3. Use with caution (insufficient data for proper evaluation), 4. Use with extreme caution (no data available), and 5. Undesirable combinations (intermediate compounds formed).

The EB-solution can, furthermore, be associated with very precise control of filler-material addition typical of feeding units used in EBW, e.g., a CNC-controlled filler-wire feeding system has been successfully used in production [I. Meuronen (1994)]. Therefore, EBW does possess its own characteristics for dissimilar-metal joining. It should be emphasized that the data given here provide the user only with broad guidelines, because specific weldability may depend upon a number of factors, such as variation in alloy compositions, welding parameters, differences in component design, service requirements, etc. A recent survey about dissimilar-alloy combinations successfully welded by EBW O. Braun et al (1991). In the following, a few examples from Table 2.3 are introduced in greater detail to show how the advantages of EBW are realized, and how the problems are solved.

Dissimilar-metal EB-weldments of Cu/Ag joints used in low-temperature applications. This type of a joint requires proper thermal contact between the dissimilar metals at low temperature due to the working mechanism of the component. Although the Cu/Ag combination can also be easily welded with many fusion welding processes, a weld metal with poor thermal conductivity remains the main problem. For instance, TIG welding cannot meet this technical requirement of the products, because the larger newly formed fusion zone of the TIG weld will change the thermal conductivity of the contact area substantially. When using EBW, a very thin layer between the dissimilar metals is formed, thus ensuring a small contact resistance [S. Yin et al (1991)].

A study of the EBW of niobium to molybdenum thin sheets (0.5 or 1 mm thick) for the emitting electrodes of thermionic energy converters reports satisfactory joints [S. Lin et al (1986)]. EBW of niobium/copper joints is under consideration for a variety of applications, such as electrode plating drums, superconducting accelerating cavity components, microcomposite wires and sheets, and in the heat exchanger panels [R.J. Sinko (1993)]. It should, therefore, be concluded that EBW is a vital method for welding dissimilar-metal combinations involving metals having high thermal conductivities. It has been reported that 100 mm thick copper can be EB-welded with a single pass, due to its high energy density [G. Sayegh (1985)]. This feature of EBW can, certainly, be exploited to produce many other combinations with metals having high thermal conductivities in a wide range of plate thicknesses. A. Sanderson (2000) discussed the advanced welding process for fusion reactor fabrication. Also the author discussed the challenges of conventional welding processes, electron beam and laser beam welding technology.

Table 2.3 Recent investigation concerning the EBW of dissimilar metals (Z. Sun et al (1996))

Material combination	Potential Applications	Remarks	Ref
2 1/4Cr-1Mo/C-Mn steel	Steam turbine diaphragms Heavy	Beam deflection should be overcome	Y. Akutsu
SAE1136/1010 steel 1/4Cr-1 Mo/AISI 405	Heavy equipment equipment Power generation systems	Creep-fatigue property prediction was developed	G. Sayegh G. Sayegh , M. Okazaki
High speed/carbon or low mild steel High speed/ mild steel	Saw blades Cutting tools	Saving of high speed steels can be achieved Optimization of parameters	S. Elliott , Y. Liu A.M. Kosecek
20NiMoCr sintered powder/mild steel Inconel 713c/AISI 1045	Car industry Turbocharger impeller	Laser cutting and EBW	G. Sayegh S. Elliott , S. Matsui
13Cr steel/mild steel	Steam turbine nozzle diaphragms	Effect of oscillations of beam on microstructure was studied	A.P. Lopatko
Pearlitic steel 20/321 stainless steel		PWHT is beneficial	V.M. Nesterenkov
20Kh 12VNMF20KhN3M FA 321 stainless steel/ADI A1 21/4Cr-1 Mo/AISI 316	Power generation systems	Multi-pass welding was used Fatigue-property prediction was developed	G.M. Grigorenko M. Okazaki
2 1/4Cr-1 Mo, A204 and SS41/AISI 405	Power generation systems	Effect of PWHT, fracture toughness was investigated	Y. Itoh
2 1/4Cr-1 Mo/AISI 304 and 321 Cr-Ni alloy/EP517	Power generation systems Electromagnetic devices	Using nickei-base filler wire Optimization of parameters	J. Ruge , I. Decker V.K. Dragunov
EP288 austenitic-martensitic type steel/VZHL-14 Ni base stainless		Horizontal beam welding produce defect-free joints	N.P. Voronov
Vn-2AE Nb base alloy/321 stainless steel		Corrosion resistance was investigated	G.D. Nikiforov

Table 2.3: Conti..

Recent investigation concerning the EBW of dissimilar metals (Z. Sun et al (1996))

AISI 422/Inconel 600/Stellite alloy	Steam turbine blades	Optimization of parameters	F. Franchini
Cu/Ag	Low temperature applications	Contact resistance was studied	S. Yin
C10700/C17510 Cu alloy		Mechanical properties were investigated	T.A. Siewert
Beryllium copper/copper	Crimp-type connector contacts	The joints combine good spring properties (Be-Cu) with good formability (Cu)	R.J. Russell
Silver/copper	Switch contacts		R.J. Russell
Invar/stainless steel	Thermostatic bimetallic components	Finely defined weld zone with minimal HAZ	R.J. Russell, G. Israel
Steel/copper Cu-Cr-Zr alloy/NiCr15Fe Nb/Cu	Lead frames Nickel clad limiter Aerospace equipment	Beam was aligned to the copper side	R.J. Sinko
Nb/Mo and porous W/Mo	Emitting electrode, Ba-W cathode of microwave tubes	Optimization of parameters	S. Lin
Ta or Nb/321 stainless steel	Heating elements of high temperature vacuum furnace	Microstructural study	A. Detka
Gold/Phosphorus bronze	High reliability miniature switches		R.J. Russell
C-103Nb/Ti-6Al-4V		Evaluation of various properties of the joints	F. Franchini
Ta/Mo or W		High temperature annealing after welding is beneficial for bend strength	Y. Hiraoka
Ni-base superalloy/stainless steel	Marine engine valves	Good wear and corrosion properties	N.N.
EN 36/FV 520	Marine pump shaft		F.J. Becket

2.4.3. Weldability of austenitic/ferritic stainless steel with EBW

This material combination is widely used in many industrial applications, such as power-generation systems. When using conventional fusion-welding processes, nickel-based fillers have proven to be satisfactory. The theoretical background originates from the following two main factors. Firstly, the low diffusion-coefficient of carbon in nickel-based weld metal minimizes carbon diffusion across the ferritic steel/weld metal interface, and thereby reduces the tendency to form a soft decarburized zone in the ferritic steel. Secondly, the use of nickel-based fillers produces a weld having a thermal expansion coefficient very similar to that of ferritic steel. Therefore, the magnitude of ferritic steel/weld metal interfacial stresses can be reduced during the thermal cycling using nickel-based filler welds, as compared to autogenous welds or to welds made with austenitic stainless-steel fillers.

J.Ruge et al (1986) investigated this material combination with EBW. Type 304 austenitic stainless steel was EB-welded to 21Cr-1Mo ferritic steel with different procedures: (i) autogenous welding; (ii) welding with E308 austenitic stainless steel filler wire; and (iii) welding with Inconel 82 nickel-based filler wire. They concluded that best metallurgical quality of the dissimilar-metal joints, in terms of microstructure, was obtained, just as in conventional arc welding, when using nickel-based filler wire. They observed that autogenous welding, and welding with austenitic stainless-steel filler wire produced an inferior weld-metal microstructure, i.e., it yielded the formation of martensite with high hardness values. It is suggested by them that EBW with a suitable filler metal can be a good solution when tackling metallurgical problems for dissimilar-metal joints, although autogenous welding is often regarded as an obvious advantage of the EB process, especially in the joining of similar metals J.L. Ruge (1987). More generally, problems of metallurgical incompatibility and physical mismatches can be solved by the use of particular filler or transition materials.

The utilization of EBW to join dissimilar metals does not only originate from the avoidance of metallurgical problems faced by conventional fusion-welding processes, but also, in many cases, from special features of the process which meet the requirements of the product. For instance, the distortion caused by welding is a very common problem that is emphasized in the welding of dissimilar metals. Strictly speaking, there is no welding process

that can completely eliminate distortion. However, a process that minimizes distortion is increasingly preferred in many applications. EBW with a high energy density produces much smaller weld distortion than other conventional fusion-welding processes [P. Vartia (1993)].

Z. Sun (1996) reviewed that the High energy density beam (HEDB) welding processes, i.e. laser beam welding (LBW) and electron beam welding (EBW) have been developed rapidly and have been successfully used in many industrial applications; the potential of the HEDB process is continuously being exploited in further industrial sectors. The author concluded that using of EBW welding to produce ferritic/austenitic (Black/white joints) joints with nickel-based filler wire can be a potential process, although further data is still needed and improvements to the technique and in ensuring the quality of the joints.

Z. Sun et al (1996) reported that EBW has the potential of not only being able to weld material combinations, which often cause problems with conventional welding techniques, but also of showing functional advantages for some combinations which also can be produced with conventional welding processes. However, the use of the EBW process to join dissimilar metals is still at the development stage. Much more of the potential will be exploited in future via extensive R&D efforts. The limited amount of information available concerning the joinability of different dissimilar combinations, and the technical practice for potential weldable combinations, will stimulate many studies. The results of these studies should provide industries with competitive solutions and consequent benefits.

Although many combinations have been proven to have a good weldability, R&D for many difficult joint types are still required. Therefore, further R&D efforts should be directed, especially, to those combinations with which an alternative joining process cannot provide a technically and/or economically satisfactory result. EBW, with filler-metal addition, should be emphasized in these trials, because recent studies have demonstrated that this method can be applied to solve many problems associated with metallurgical incompatibility, although autogenous welding is often regarded as one of the advantages of the EB-process.

2.4.4 Advantages

1. Accurately controllable energy density and the small beam size makes it possible to control dilution, to weld with high precision, and thus, to weld both very thin and very thick metals, e.g., from 0.025-300 mm.
2. Possible accurate beam alignment at any position allows the two base metals to melt selectively to better satisfy the metallurgical compatibilities.
3. Low total heat input per unit length of weld produces a narrow weld bead and HAZ, and results in low residual stresses and minimum distortion, which can cause serious problems for conventional fusion welding processes.
4. It is possible to solve problems associated with metallurgical incompatibility more accurately with EBW when using a suitable filler material, although this can also be a possible solution for arc welding.
5. High purity environment (vacuum) for welding minimizes surface contamination of the metal by oxygen, nitrogen and hydrogen, which is particularly beneficial for reactive and refractory metals.
6. Dissimilar-metal combination involving high thermal conductivity metals such as copper can be welded without preheating.

2.4.5 Limitations

1. Problems related to melting and mixing of dissimilar metals during fusion welding still exist.
2. Possible beam deflection by electrostatic and magnetic fields due to dissimilar metals.
3. Vacuum environment normally necessary, impossible with metals vaporising easily.
4. High accuracy requirement in groove preparation.
5. Rapid solidification may result in brittleness of the weld, and defects, e.g., porosity.
6. Use of vacuum chamber may reduce product size and limit the product design.
7. Although beam oscillation can minimize the groove preparation requirement, it may cause problems for dissimilar-metal joining due to the possible uncontrollable fusion ratio of the two metals.
8. High equipment and running cost.

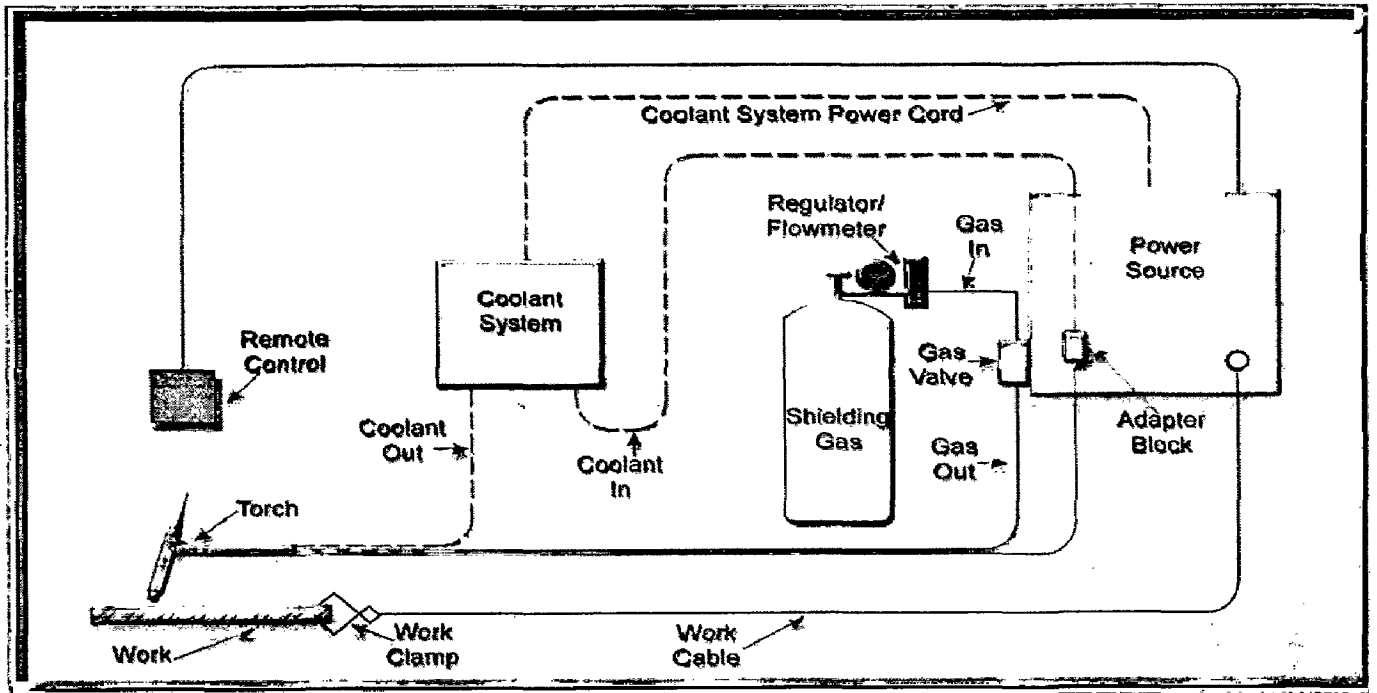


Figure 2.9 (B) The typical TIG welding process.

2.5 Tungsten Inert Gas Welding (TIG)

The necessary heat for Gas Tungsten Arc Welding (TIG) is produced by an electric arc maintained between a non consumable tungsten electrode and the part to be welded. The heat-affected zone, the molten metal, and the tungsten electrode are all shielded from the atmosphere by a blanket of inert gas fed through the GTAW torch. Fig 2.9 (B) shows the typical TIG welding process. Inert gas is that which is inactive, or deficient in active chemical properties. The shielding gas serves to blanket the weld and exclude the active properties in the surrounding air. It does not burn, and adds nothing to or takes anything from the metal. Inert gases such as argon and helium do not chemically react or combine with other gases. They possess no odor and are transparent, permitting the welder maximum visibility of the arc. In some instances a small amount of reactive gas such as hydrogen can be added to enhance travel speeds.

The greatest advantage of the GTAW process is that it will weld more kinds of metals and metal alloys than any other arc welding process. TIG can be used to weld most steels including stainless steel, nickel alloys such as Monel® and Inconel®, titanium, aluminum, magnesium, copper, brass, bronze, and even gold. GTAW can also weld dissimilar metals to one another such as copper to brass and stainless to mild steel. Some of the advantages of Pulsed GTAW are: Good penetration with less heat input; less distortion; Good control of the pool when welding out of position; Ease of welding thin materials; Ease of welding materials of dissimilar thickness

The main disadvantage of the GTAW process is the low filler metal deposition rate. Another disadvantage is that the hand-eye coordination necessary to accomplish the weld is difficult to learn, and requires a great deal of practice to become proficient. The arc rays produced by the process tend to be brighter than those produced by SMAW and GMAW. This is primarily due to the absence of visible fumes and smoke. The increased amounts of ultraviolet rays from the arc also cause the formation of ozone and nitrous oxides. Care should be taken to protect skin with the proper clothing and protect eyes with the correct shade lens

in the welding hood. When welding in confined areas, concentrations of shielding gas may build up and displace oxygen. Make sure that these areas are ventilated properly.

When using TIG welding of two dissimilar metals, there are a number of aspects that need to be addressed, in addition to those associated with welding similar materials. The difficulties in the welding of dissimilar materials can be summarized as follows [[S.Sunderesan (1976)]:

(i) Significant differences in physical and mechanical properties (e.g., coefficient of thermal expansion, thermal and electrical conductivity, melting temperatures etc) cause problems during welding as also during subsequent service. The wider the difference, the more severe is the difficulty.

(ii) It may not be possible to produce an adequate joint if the two materials are metallurgically incompatible. Metallurgical incompatibility may lead to uncontrollable weld metal/ HAZ cracking or a weld metal microstructure that cannot provide adequate mechanical or corrosion performance, e.g., containing unacceptable martensite or intermetallic phases.

(iii) When arc welding of dissimilar metals, arc blow or uncontrollable deflection of the arc may occur due to the flow of thermoelectric currents between the hot and cold parts of the joint, due to the varying thermal conductivity of the dissimilar metals, and hence the development of magnetic fields.

When two materials are metallurgically incompatible, it may be possible to make a satisfactory weld by addition of a suitable filler metal. This is exemplified by the joining of steels and stainless steels, when the Schaeffler diagram, or a modification of it, may be used to select a filler metal that is resistant to both solidification cracking and hydrogen cracking. Frequently, where a welding consumable with composition similar to one of the steels is not appropriate, a nickel-based filler may be adopted. In addition, these may be used for welding of steels to some copper alloys due to their tolerance to dilution by a range of alloying elements without a phase change. However, care must be taken to avoid Fe/Ni ratios giving sensitivity to solidification cracking, e.g. approximately 30% Fe, 30%

Ni is particularly susceptible. Where no satisfactory fusion welding process exists, e.g. between Fe and Ti alloys or Cu and Al alloys or nickel and Al alloys, it may be possible to produce a weld by a solid state process such as friction welding or explosive bonding.

J. Tusek et al (2001) investigated that the weldment of high alloy stainless steel and low-alloyed ferrite steel made by MIG and laser welding technique with and without filler material. The author reported that the laser welding of the above-mentioned materials without the addition of filler material cannot be performed or it is not possible to obtain a weld with satisfactory mechanical properties. The hardness of the laser weld is 300HV as compared to MIG welding which is 700HV.

T.W.Nelson et al (2000) investigated the nature and evolution of the fusion boundary in ferritic-austenitic dissimilar metal welds was made by Gas tungsten arc welding (GTAW). High purity iron was used as a base metal as it exhibits both the delta-gamma and gamma-alpha transformations that occur in C-Mn and low-alloy structural steels. A 70Ni-30Cu, single-phase (FCC) binary alloy with low impurity content was selected as the filler metal.

The author found several interesting microstructural characteristics that add insight into the evolution of the Type II boundaries were observed. Also the author observed the evidence of correlation between HAZ and Type II grain boundaries. The typical micrograph shows evidence of continuity between a prior austenite HAZ grain boundary and a Type II boundary at the fusion boundary can be observed. Another interesting characteristic of the Type II boundary is manifested by the nature of the solidification grain boundaries (SGBs) and solidification sub grain boundaries. Based on the results of this investigation the authors proposed the model for the formation of the Type II boundary and resulting fusion boundary orientation relationships.

A. Celik (1999) studied the GTAW weldment of ferritic steel (St37-2) and an austenitic stainless steel (AISI 304) by using an austenitic filler metal. The ultimate tensile strength values of the ferritic-austenitic dissimilar joints were obtained 402 MPa and the micro hardness on the weld zone contains 275-220 HV. The microstructure of the ferritic side predominantly ferritic and pearlitic. On the austenitic side, it mainly shows an austenitic

dendritic structure. The microstructure of the dissimilar weld joint contains coarse and malformed lamellae of pearlite in the ferritic region.

Ahmet Durgutlu (2004) was investigated the effect of hydrogen in argon as shielding gas for tungsten inert gas (TIG) welding of 316L austenitic stainless steel. The author reported that the ultimate tensile strength (695 MPa) obtained from 1.5%H₂-Ar as gas shielding. The hardness of weld metal is Lower (310 HV) than that of the HAZ and base metal.

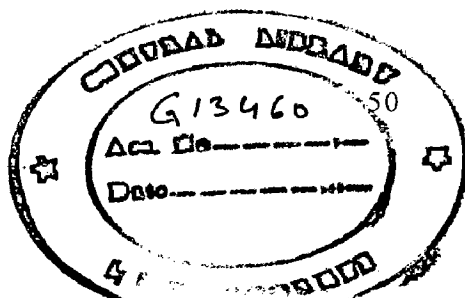
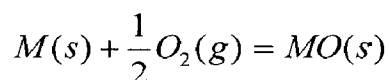
2.6 HIGH TEMPERATURE OXIDATION

Metals and alloys still constitute the most important group among engineering materials and the demand for metallic materials with higher strength and special properties is on the increase with the advancement of technology. However, a serious drawback of metallic material (and of other materials too) is the deterioration in properties originating from their interaction with the environments in which they are to perform. Often this leads to a premature failure of metallic components with the allied hazards of plant shutdown and loss of economy, environmental pollution and risk to human lives. The annual direct loss of natural resources, i.e. metals, due to environmental degradation is also substantial (Chatterjee et al, 2001).

Oxidation is a type of corrosion involving the reaction between a metal and air or oxygen at high temperature in the absence of water or an aqueous phase. It is also called dry-corrosion. The rate of oxidation of a metal at high temperature depends on the nature of the oxide layer that forms on the surface of metal. Both the mechanical properties as well as oxidation resistance are important for consideration of a material for high temperature applications. Creep, mechanical fatigue, thermal fatigue, oxidation and sulphidation are the main possible causes of failure of a turbine blade in a hot station (He et al, 2001).

2.6.1 Mechanism of Oxidation

From the consideration of the equation:



It is obvious that the solid reaction product MO will separate the two reactants as shown below:



In order for the reaction to proceed further, one or both reactants must penetrate the scale, either metal must be transported through the oxide to the oxide-gas interface and react there or oxygen must be transported to the oxide-metal interface to react (Birks and Meier, 1983). Kofstad (1990) has explained diffusion processes with the help of neat sketches shown in Fig. 2.10, which illustrate the growth of chromia scales in the presence or absence of oxygen active elements. When inward oxygen diffusion predominates, oxide formation takes place at the scale-alloy interface, reducing void or cavity formation and thereby increased scale adhesion is achieved.

2.7 HOT CORROSION

Metallic corrosion is the surface wastage that occurs when metals are exposed to reactive environment. The chemical compounds that constitute the products of such wastage are close cousins of the metalliferous mineral rocks that we find in the earth's crust. In other words, corrosion reactions cause metals to revert to their original ores. At temperatures above 200⁰C there is usually significant reaction of most metals in dry air, and the rate and extent of reaction progressively increase either, as the temperature is raised or the air is contaminated by other gases. In general, it may be said that the degree of wastage is largely governed by the ionic conducting properties of the corrosion product when it is present as a solid scale by its mechanical strength and adherence to the underlying metal. The study of high temperature corrosion products is therefore, a study of semiconducting oxides, sulphides and so on and the influences of temperature, pressure and ionic contaminants on their mechanical coherency, stability and permeability (West, 1986).

According to Hancock (1987), hot corrosion is an accelerated form of oxidation which occurs when metals are heated in the temperature range 700-900⁰C in the presence of sulphate

deposits formed as a result of the reaction between sodium chloride and sulphur compounds in the gas phase around the metals.

If the concentration of the sulphate exceeds the saturation vapor pressure at the operating metal temperature for turbine blades and vanes (700-1100⁰C), then deposition of the Na₂SO₄ will occur on the surface of these components. At higher temperatures the deposits of Na₂SO₄ are molten (m. p. = 884⁰C) and can cause accelerated attack of the Ni- and Co-base superalloys. This type of attack is commonly called "Hot Corroison". The accelerated corrosion can also be caused by the other salts, viz. vanadates or sulphate-vanadate mixtures and in the presence of solid or gaseous salts such as chlorides.

2.7.1 Mechanisms of Hot Corrosion

Hot corrosion can occur at high temperatures where the deposit is in the liquid state right from the beginning or the solid deposit turns into liquid during the exposure as a result of reaction with the environment. These two types of hot corrosion processes are termed as High Temperature Hot Corrosion (HTHC) or Type I and Low Temperature Hot Corrosion (LTHC) or Type II respectively (Khanna and Jha, 1998).

Type I Hot Corrosion

High temperature (type 1) hot corrosion (HTHC) is normally observed in the temperature range of about 825-950⁰C when the condensed phase is clearly liquid. The typical microstructure for HTHC shows the formation of sulphides and a corresponding depletion of the reactive components in the alloy substrate. The external corrosion products consist of oxide precipitates dispersed in the salt film. The presence of the pore, crevice or crack across a protective film can lead to the sulphidation of the alloy substrate. This results in a significant shift in the basicity of the salt film. Once the fused salt contacts the alloy substrate, the rate and duration of the rapid corrosion kinetics is decided by the magnitude and gradient of salt basicity relative to the local solubilities for the oxide scale phases (Rapp and Zhang, 1994).

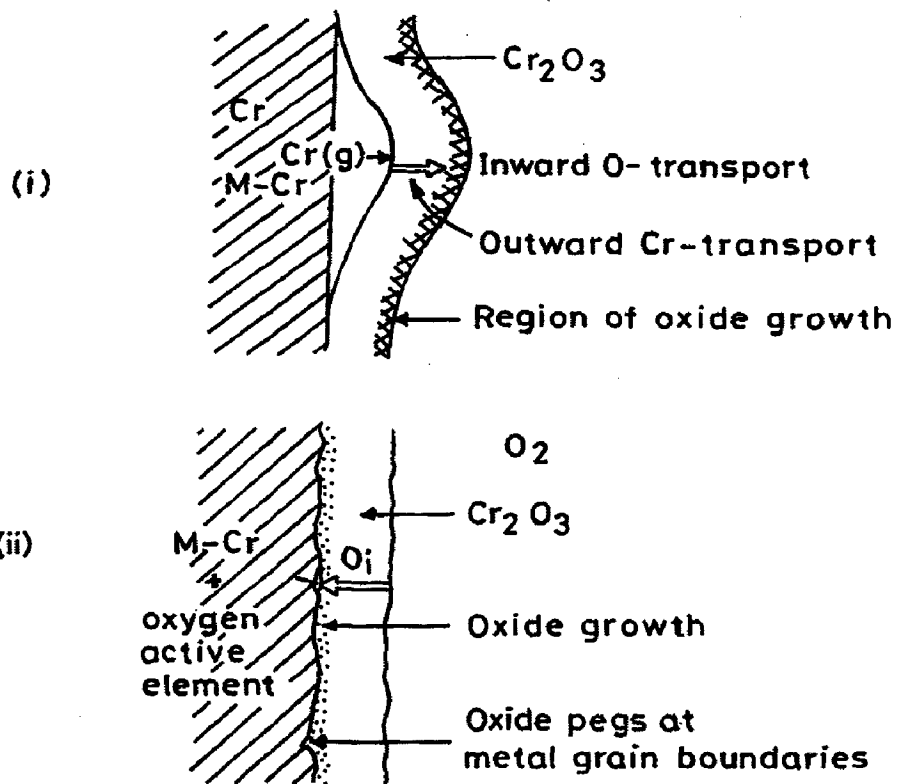


Fig. 2.10 Schematic illustration of the growth of chromia scales in (i) the absence of oxygen active elements and with predominant outward transport of chromia through the scale, and (ii) the presence of oxygen active elements and with predominant inward transport of oxygen (Kofstad, 1990).

Type II Hot Corrosion

The low temperature hot corrosion (LTHC) occurs well below the melting point of Na_2SO_4 (884°C). The reaction product morphology is characterised by a non-uniform attack in the form of pits, with only little sulphide formation close to the alloy/scale interface and little depletion of Cr or Al in the alloy substrate (Rapp and Zhang, 1994).

Luthra (1985) reported LTHC behaviour for a number of Co-Cr, Co-Al and Co-Cr-Al alloys. After a low melting $\text{CoSO}_4\text{-Na}_2\text{SO}_4$ liquid phase was formed, the acidic dissolution of CoO at the oxide/salt interface supported the precipitation of either Co_3O_4 or CoSO_4 near the salt/gas interface. The negative solubility gradient was maintained by gradients in the basicity and oxygen activity in the salt film. For sufficient acidic cobalt-solute ions in the salt film, counter-transportation of $\text{Co}^{2+}/\text{Co}^{3+}$ ions carried the reduction reaction to the salt/gas interface. In this case the dissolution/precipitation of cobalt compounds prevent the formation of protective scale of Cr_2O_3 or Al_2O_3 .

2.7.2 Hot Corrosion Degradation Sequence

When superalloys undergo hot corrosion degradation, this process almost always consists of two stages (Pettit and Giggins, 1987; Pettit and Meier, 1984). It is a fact that all corrosion resistant alloys degrade via such a sequence and it is the result of using selective oxidation to develop oxidation or corrosion resistance. It is convenient to place emphasis on the two stages, namely, an initiation stage during which the alloys behave as they would have behaved in the absence of the deposit and a propagation stage where the deposit has caused the protective properties of the oxide scales to become significantly different than what they would have been, had no deposit been present.

(i) The Initiation Stage

During the initiation stage of hot corrosion elements in the alloy are oxidised and transferred from metallic atoms to the reducible substances in the deposit. To develop resistance to hot corrosion one should strive to have the superalloys which can remain in the initiation stage as long as possible.

In some cases of hot corrosion an increasing amount of sulphide particles becomes evident in the alloy beneath the protective reaction product barrier. In other, small holes become evident in the protective reaction product barrier where the molten deposit begins to penetrate it. Eventually the protective barrier formed via selective oxidation is rendered ineffective and the hot corrosion process enters into the propagation stage (Pettit and Giggin, 1987).

(ii) The Propagation Stage

The propagation stage of the hot corrosion sequence is the stage for which the superalloy must be removed from service since this stage always has much larger corrosion rates than for the same superalloy in the initiation stage. Before describing the types of propagation modes by which superalloys undergo hot corrosion attack, it is of value to examine how deposits upon the surfaces of superalloys may affect their corrosion behaviour. In Fig. 2.11 a deposit of Na_2SO_4 is depicted schematically upon the surface of a superalloy.

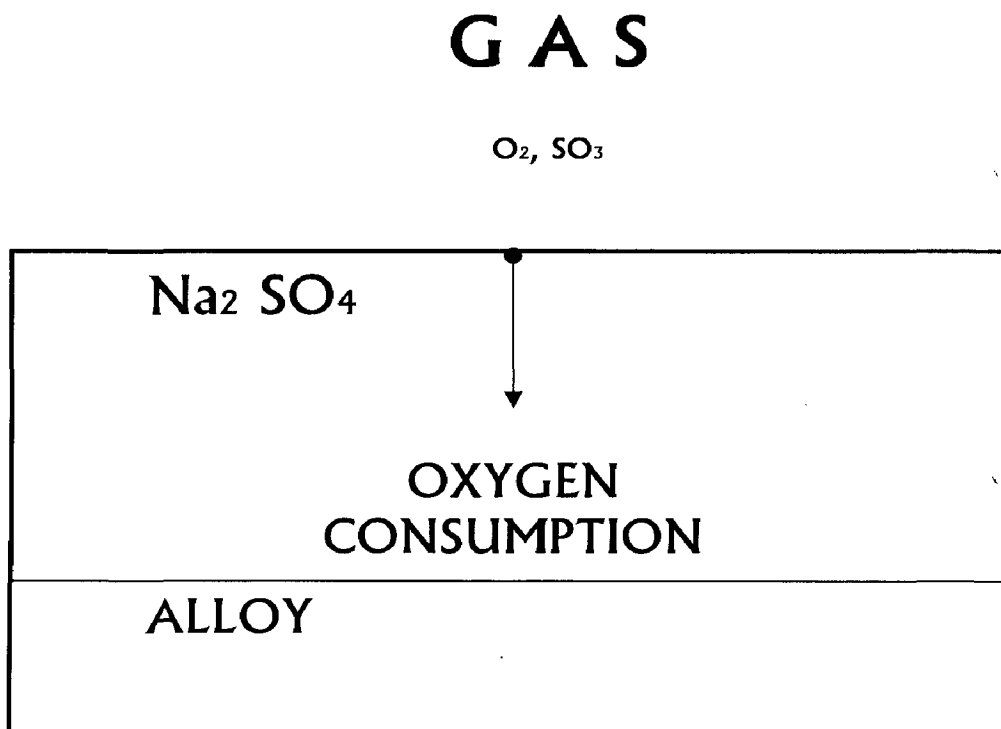
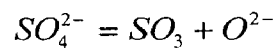


Fig. 2.11 Schematic diagram showing a Na_2SO_4 deposit upon an alloy separating the alloy from the gas phase (Pettit and Meier, 1984).

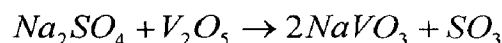
As indicated in the figure superalloy will react with elements in the deposit provided that the deposit prevents free access of the gas. Since superalloys always contain elements that have high affinities for oxygen, an oxygen gradient is established across the deposit. Hence, an important effect of the deposit is to separate the super alloy from the gas environment. This situation usually results in a lower oxygen activity over the surface of the alloy than what would have been established in the absence of a deposit (Pettit and Meier, 1984; Pettit and Giggin, 1987).

2.7.3 Salt Fluxing

The salt fluxing reactions for superalloys may be either acidic or basic in nature. The deficiency of oxide ions in the processes by which the reaction product barrier becomes non-protective due to the formation of species, which are soluble in the liquid deposit, are called “fluxing” reaction. In a molten sulphate deposit the following equilibrium can be used to define the acidity or basicity:



With the equilibrium constant, $K = P_{SO_3} \cdot a_{O^{2-}}$ where P_{SO_3} is the pressure of SO_3 and $a_{O^{2-}}$ is the activity of the oxide ions in the melt. In sulphate melts, the acidity is determined by the SO_3 pressure and the acidity increases as the SO_3 pressure is increased. The acidity need not only be controlled by the SO_3 pressure in the gas since there are other ingredients in same systems that may affect acidity. For example V_2O_5 can react with Na_2SO_4 to increase the acidity of the melt via reaction:

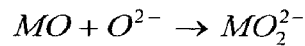


Molybdenum and Tungsten in the alloy can create similar effects when their oxides are formed as corrosion products (Pettit and Giggins, 1987).

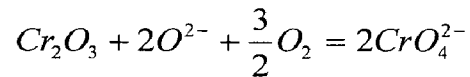
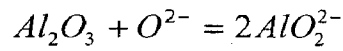
The initial concept of basic fluxing was first proposed by Bornstein and Decrescent (1970) and then described in thermodynamic terms for the hot corrosion of nickel by Goebel and Petit (1970).

Pettit and Giggins (1987) have suggested that essential feature of this process is that oxide ions are produced in the Na_2SO_4 deposit due to removal of oxygen and sulphur from the

deposit via reaction with the alloy and metal. Furthermore, oxide scales (MO) that normally would form as protective barrier on the surface of these alloys can react with oxide ions via reaction such as:



The protective oxide scales, e.g. Al_2O_3 or Cr_2O_3 can react with O^{2-} ions to form soluble aluminates or chromate ions, respectively,



and their protective properties are destroyed. Such basic fluxing has a number of distinct features. Sulphides are usually found in the alloy substrate as a result of S removal from Na_2SO_4 to produce oxide ions. The amount of attack depends upon the production of oxide ions by the melt. Hence a supply of Na_2SO_4 is necessary for the attack to continue and the type of fluxing is often not self-sustaining. This form of attack is usually restricted to high temperatures ($900^{\circ}C$) since the O^{2-} ion production is slow at lower temperatures and is more likely to be important in gases without an acidic component (e.g. SO_3). However according to Rapp and Goto (1981) basic fluxing can also occur in gases with acidic components. They have proposed that protective scales on alloy could be made non-protective when the solubility gradients of the protective oxides in the molten deposit were negative since continuous dissolution and reprecipitation of oxide is then possible. Their mechanism permits fluxing to be either basic or acidic, within the need for a source or sink for O^{2-} ions which means that attack may continue without the additional supply of the deposit. But Shores (1983) has examined the Rapp-Goto precipitation criteria for a variety of conditions and remarked that basic fluxing reactions are not always self sustaining.

Rapp and Goto (1981) proposed that, if the gradient in solubility of the protective oxide with distance into the salt layer was negative at the oxide /salt interface, accelerated attack could be sustained. This provides a quantitative expression of the earlier concepts of solubility gradients and oxide precipitation, that is, when

$$\left(\frac{d(\text{solubility of oxide})}{dx} \right)_{x=0} < 0$$

Oxide can dissolve at the oxide /salt interface, migrate down a concentration gradient away from that side to a region of low solubility and precipitate. At steady state, oxide dissolves and is transferred away from the oxide/salt interface, just as fast as the oxide layer grows Fig. 2.12.

They recognised that such a gradient can be established across a thin salt film and that it need not be a consequence of the removal of sulphur from Na_2SO_4 or the introduction of acidic ions from the corrosion products as required by the Goebel and Pettit (1970) model. When Rapp-Goto (1981) criterion for the oxide solubility is satisfied, fluxing is expected. The solubility of an oxide depends on the acidity or basicity of the melt and in some cases on p_{SO_3} as well. In basic fluxing the solubility decreases with increasing p_{SO_3} (decreasing activity of $\text{O}^{2-\text{ve}}$). In acidic fluxing the solubility increases with increasing p_{SO_3} (decreasing activity of $\text{O}^{2-\text{ve}}$). Rapp and Goto (1981) suggested that the electrochemical reduction reaction should generally be expected to create a condition of local high basicity, because reduction reactions may generate oxide ions as reaction products.

(i) The Basic Fluxing Mode

Basic fluxing reactions occur because sulphur is removed from the Na_2SO_4 and consequently oxide scale. It is important to notice that the concentration of oxide ions available for basic fluxing is limited by the amount of the deposit present upon the surface of the superalloy. Hence, basic fluxing reactions are not self-sustaining, but require a continuous source of Na_2SO_4 in order for this type of degradation to proceed indefinitely (Pettit and Meier, 1984).

(ii) The Acidic Fluxing Mode

The acidic fluxing reactions involve the development of non protective reaction products on superalloys as a result of a liquid deposit on the surface of the superalloy which has a deficiency of oxide ions. The deficiency of oxide ions in the Na_2SO_4 can arise due to an

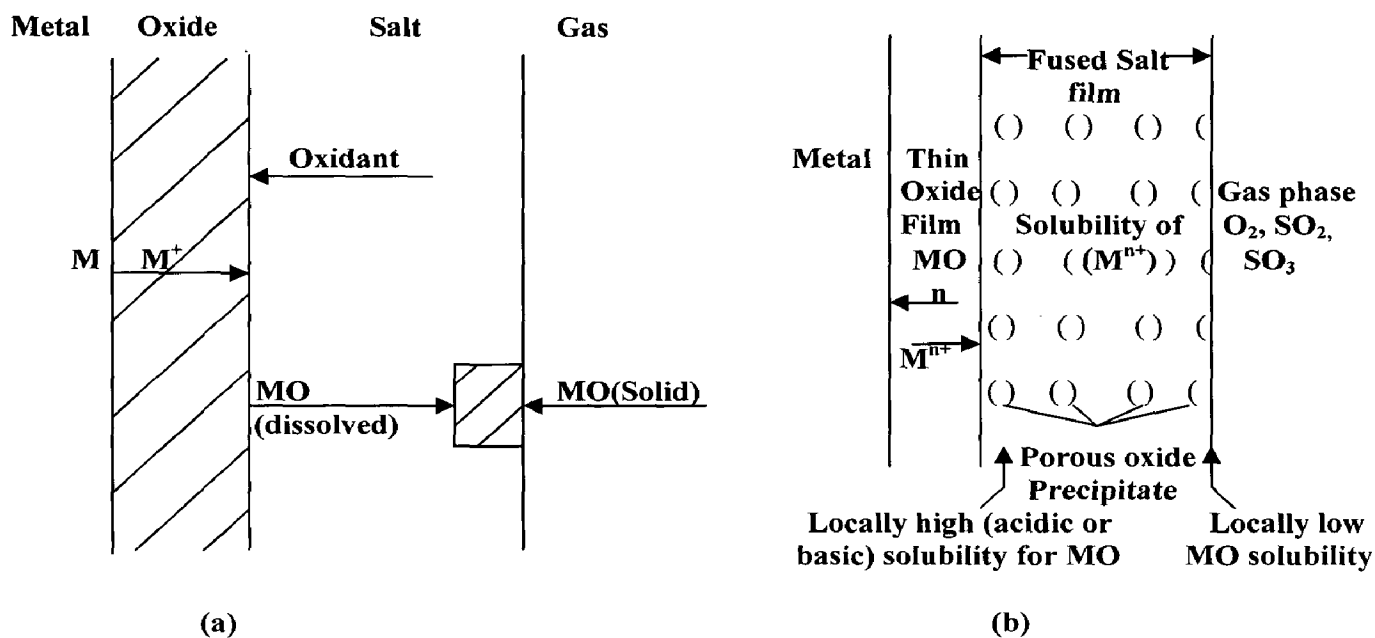


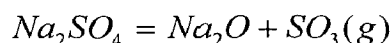
Fig. 2.12 (a) Schematic diagram for fluxing showing dissolution of metal oxide at the oxide/salt interface (Shores, 1983) and (b) Precipitation of a porous MO oxide supported by the solubility gradient in a fused salt film (Rapp and Zhang, 1994).

acidic component present in the gas or an acidic phase formed as an oxidation product upon the superalloy. When the acidic component is present in the gas the nonprotective oxide scale ensues due to rapid transport of certain ionic species in the acidic melt. If the melt becomes acidic due to formation of an oxide from an element in the superalloy, the attack becomes self-sustaining even with a small amount of Na_2SO_4 . The refractory elements Mo, W and V form oxides that cause Na_2SO_4 to become acidic and hence, these elements when oxidised in the presence of Na_2SO_4 deposit on superalloys usually cause catastrophic self-sustaining hot corrosion via acidic fluxing (Pettit and Meier, 1984).

2.8 Salt Chemistry

2.8.1 Sulphate Solution Chemistry

As described by Rapp (1986 and 2002) oxyanion melts of alkali nitrates, carbonates, hydroxides and sulphates exhibit an acid base character. Whereby the acid components may be considered as $\text{NO}_2(\text{g})$, $\text{CO}_2(\text{g})$, $\text{H}_2\text{O}(\text{g})$ or $\text{SO}_3(\text{g})$ respectively. Although the use of the Flux-Fluid selection of NO_3^- , CO_3^{2-} , OH^- and SO_4^{2-} as the basic components is common for such fused salts. The oxide ion can be alternatively changed as the Lewis base is common for all of these salts. For a melt of pure Na_2SO_4 , the equilibrium:



In examining the expected stability of the protective oxide Cr_2O_3 , they explained with respect to dissolution either as acidic solutes such as $\text{Cr}_2(\text{SO}_4)_3$ or as basic solutes such as Na_2CrO_4 or NaCrO_2 . The phase stability diagram for the Cr-S-O system can be superimposed on that for Na-S-O, as shown in Fig. 2.13. Under no conditions, the metal chromium remains stable in contact with Na_2SO_4 at 1200 K (927°C).

2.8.2 Vanadate Solution Chemistry

Figure 2.14 is the phase stability diagram for the Na-V-S-O system at 900°C . The dashed lines are isoactivity lines for the vanadate species in the salt solution. The dependence of the equilibrium concentrations of various vanadate solutes in sodium sulphate-vanadate

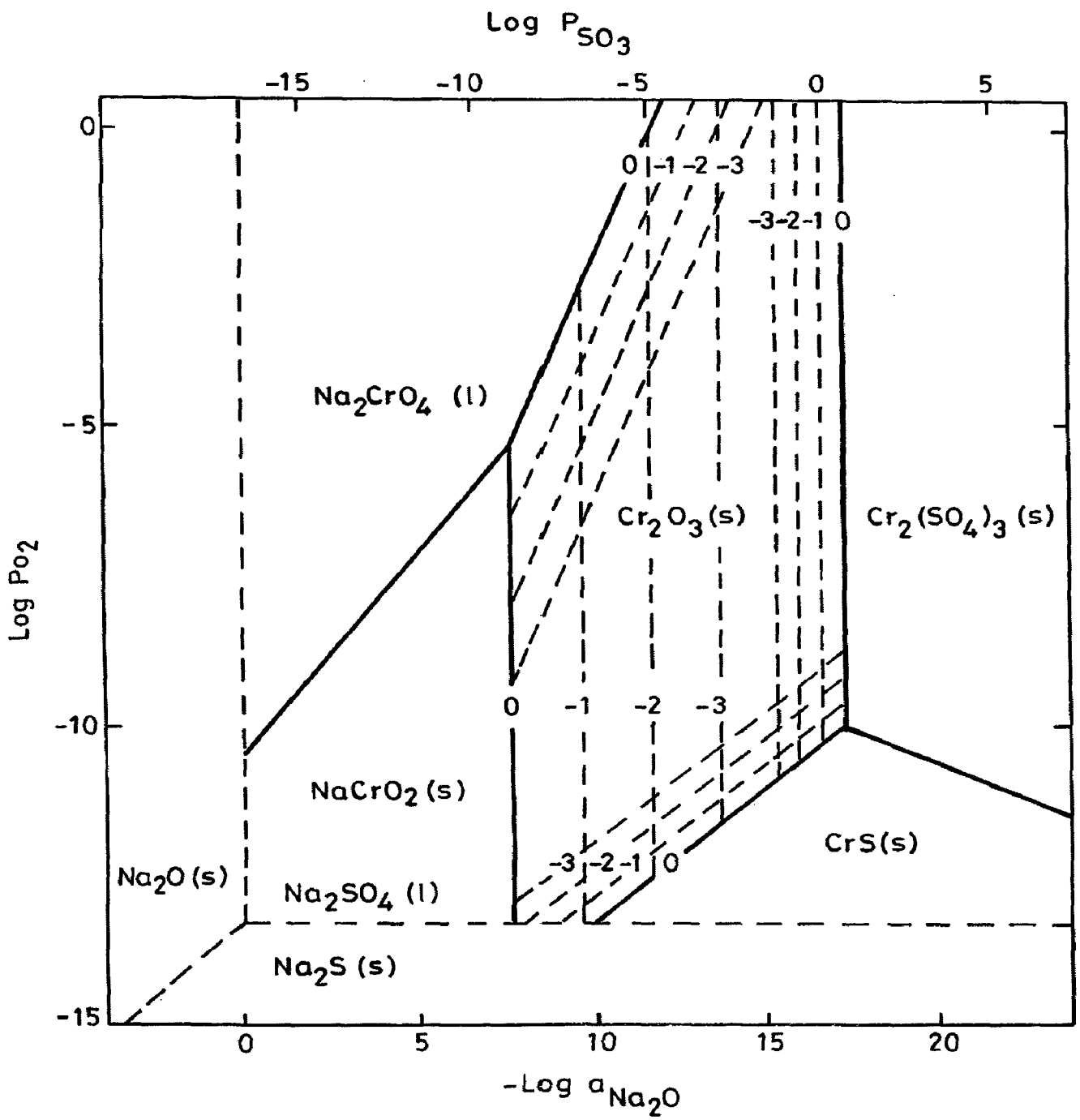


Fig. 2.13 Na-Cr-S-O phase stability diagram for 1200 K (Rapp, 1986).

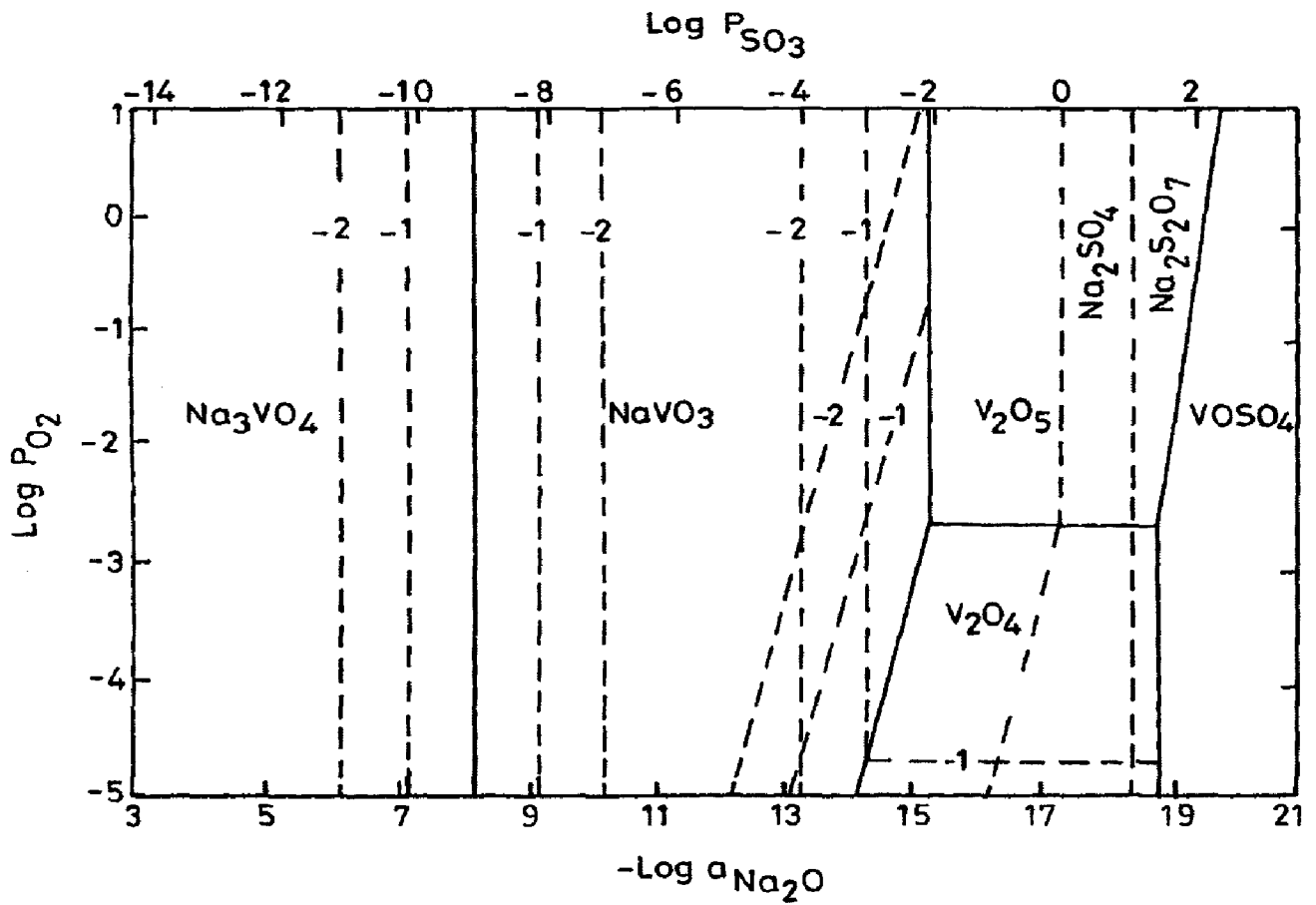
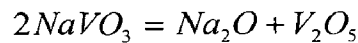
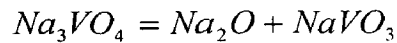
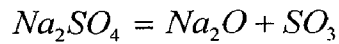


Fig. 2.14 Phase stability diagram for Na-V-S-O system at 900 °C (Hwang and Rapp, 1989).

solutions on the melt basicity, defined as $-\log a_{Na_2O}$, is determined by considering the equilibrium reactions:



The equilibrium concentration of each vanadium compound varies continuously with melt basicity. Na_3VO_4 is the dominant component in the melt at basicity less than 8.2 and V_2O_5 is dominant at basicity greater than 16.3. For basicities between 8.2 and 16.3, $NaVO_3$ is the most important vanadium solute (Hwang and Rapp, 1989).

2.9 HOT CORROSION IN ENERGY GENERATION AND COAL GASIFICATION SYSTEMS

Boilers and other steam power plant equipments are subjected to a wide variety of failures involving one or more of several mechanisms. Overheating is the main cause of failure in steam generators. A survey compiled by one laboratory over a period of 12 years, encompassing 413 investigations, listed overheating as the cause in 201 failures or 48.7% of those investigated. Fatigue and corrosion fatigue were listed as the next most common causes of failure accounting for a total of 89 failures or 21.5%. Corrosion, stress corrosion and hydrogen embrittlement caused a total of 68 failures or 16.5%. Defective or improper material has been cited as the cause of most of the remaining failures (13.3%). Although “defective material” is often blamed for a failure but this survey indicates that statistically it is one of the least likely cause of failure in power plant equipments (Metals Handbook, 1975).

Yuuzou Kawahara (2002) described the corrosion mechanisms and the effects of alloying elements. The corrosion products were analyzed for Cr-Mo steel and alloy 625, which were the typical materials practically used for the superheater of high efficiency plants.

The test was conducted at 600°C for 200 h in practical boiler-simulating gas. The author concluded that both T12 steel and alloy 625 form corrosion products having lamellar oxide structures according to environmental change during operation and the existence of comparatively soft chlorides, oxides, and sulphides. It is considered that oxychlorination is the main reaction of corrosion, while, molten salt corrosion occurs at the initial stage of reaction, especially in break-away position of protective film by the M-Cl-O phase diagram soft metallic elements.

Prakash et al (2001) have studied the boiler tube failure in coal fired boilers. A case study covering one-year duration has been conducted by them for a coal fired power plant in northwestern region of India. The number of failures occurred in the study year have been found to be 89 and out of which 50 failures were attributed to the hot corrosion and erosion of ash. They further investigated five samples of failed boiler tubes which were randomly selected from the same installation. The main cause of tube failures was found to be overheating which may be due to one or the other reason as out of five three failures were reportedly attributed to the overheating.

Severe pitting corrosion of carbon steel tube was observed in the air preheater of a power plant by Krishna and Sidhu (2002). They suggested that the extended non operation of the plant resulted in the settlement of corrosive species on the tube surface. The complete failure reportedly occurred due to diffusion of these elements into the base metal and precipitation of potassium and chlorine compounds along the grain boundaries with subsequent dislodging of grains.

The variation of corrosion rate of mild steel as a function of moisture content of the coal and iron ore has been investigated by Gardiner and Melchers (2002). Two types of black coal sieved to three different size fractions up to 2360 μm particle diameter and one type of iron ore of 600-1180 μm particle diameter were tested. A pronounced increase in corrosion rate was observed at moisture content between 60% and 80% of the maximum water holding

capacity for all samples. The corrosion rate was also reported to increase with decreasing particle size distribution.

Moujahid (1987) has observed the ash corrosion, mechanical deformation and cracks on the cast iron chains of moving grate used to air burning of coal. The material design reportedly does not pay enough attention to the structure behaviour during the thermal cycling. Liquid coal ash at 1300⁰C strongly acidic has been observed to dissolve the basic wustite/spinel layers which got formed on the chains at elevated oxidation temperature. The fused ash embeds coal particles and also reduces the thermal efficiency of the equipment. Drastic enhancement in ash corrosion rate has been attributed to the mechanical damages.

Coal gasification systems operate at temperature of up to 2000 F (1093⁰C) and at a pressure of up to 100 atm depending on the specific process and the product, coal gas generates the greatest problems. In addition to hydrogen and carbon-containing gaseous species, there are many undesirable species including sulphides, sulphites, sulphates, ammonia, cyanides, volatilised oils, phenols and aggressive trace elements such as potassium, sodium, vanadium and lead (Rapp et al, 1981). Metallic components in coal gasification pilot plants are exposed to severe corrosive atmospheres and high temperatures. The corrosive nature of the gaseous environments which contain oxygen, sulphur and carbon may cause rapid material degradation and result in the premature failure of components (Danyluk and Park, 1979, and Wang, 1988).

If the temperature of the metal surface is above the melting point of the salt's eutectic composition, very corrosive conditions develop with the molten salts fluxing the protective oxide scales or directly dissolving the metal. This corrosion mechanism is very often encountered in waste incinerators, black liquor recovery boilers in the pulp and paper industry, fluidised bed boilers burning fuels with higher chlorine contents and also engine exhaust systems when oils with higher amounts of vanadium are burnt (Heath et al, 1997). Figure 2.15 shows the various examples of ash-deposition induced hot corrosion.

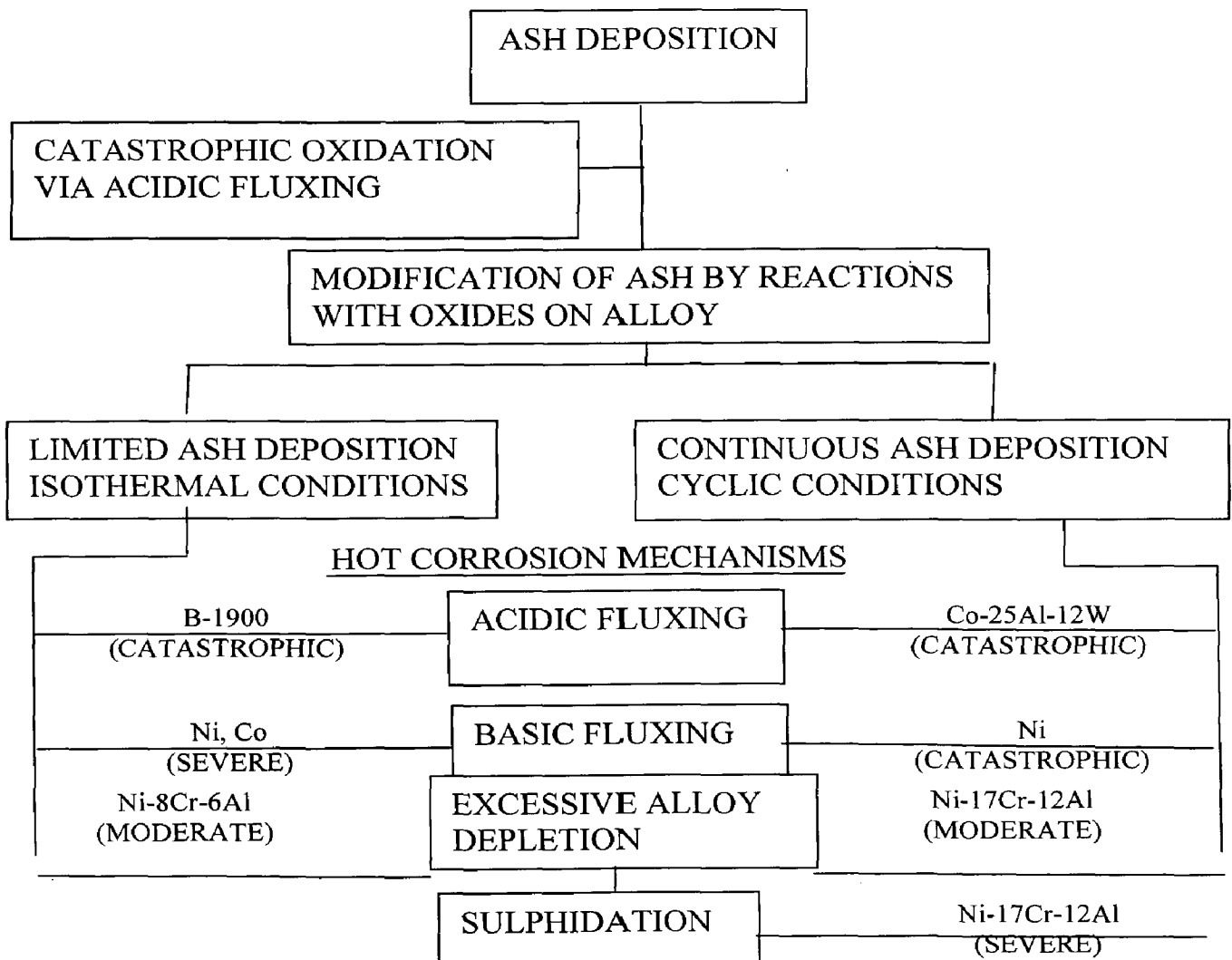


Fig. 2.15 Schematic of hot corrosion mechanisms (Natesan, 1976).

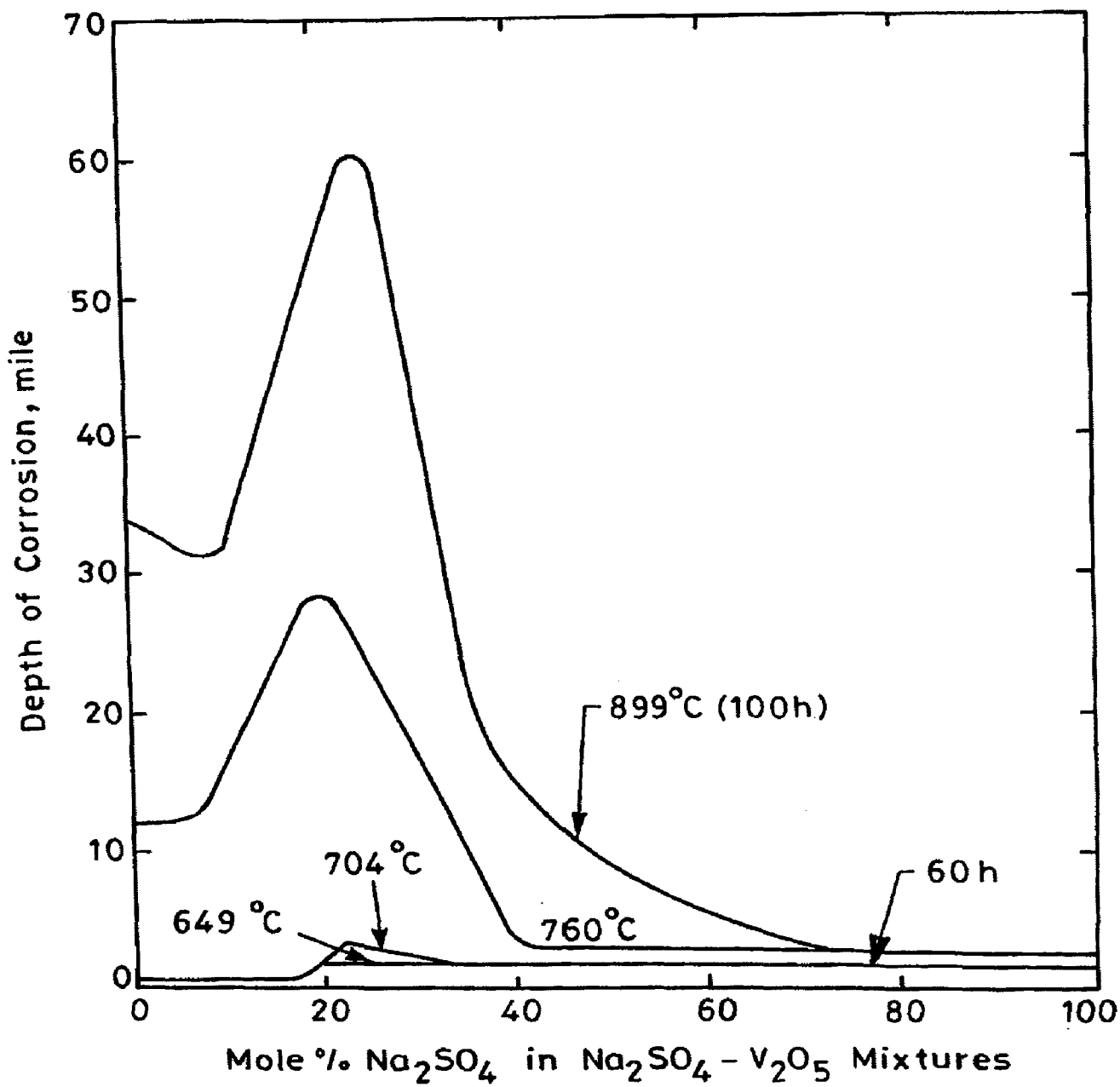


Fig. 2.16 Corrosion rate of Type 304 stainless steel in different mixtures of $\text{Na}_2\text{SO}_4\text{-V}_2\text{O}_5$ (Natesan, 1976).

Vanadium pentoxide alone or in mixture with sodium sulphate in ash can also cause hot corrosion. Fuels that contain only 50 ppm vanadium have been found to cause severe attack on stainless steels. Figure 2.16 shows the corrosion rate of Type 304 stainless steel in different V_2O_5 - Na_2SO_4 mixtures at temperatures between 790 and 900 °C. At temperatures below the melting point of ash, the rate of attack of stainless steel is low and follows the normal oxidation rate. All stainless steels and other common engineering alloys are severely attacked by fuel ash that contains vanadium with or without sulphates (Natesan, 1976). The most common deposit found on boiler super-heaters is the sodium vanadyl vanadate, $Na_2O.V_2O_4.5V_2O_5$, which melts at a relatively low temperature, 550°C. Above the melting point, this ash material corrodes metals by long term contact (Barbooti et al, 1988).

2.9.1 Characterization of Gasification Environments

When considering coal-gasification processes, hot corrosion is expected to be a problem because the gas environment generally has large sulphur activities and low oxygen activities and also contains substantial amounts of salts. However, the plausible mechanisms of hot corrosion are fairly well established and any one or more of these mechanisms may be operative in the degradation of a given alloy. At present, methods to minimise the extent of hot corrosion have been identified, however considerable research effort is needed for a quantitative evaluation of these methods under conditions of interest in the coal-gasification processes (Natesan, 1976).

The characterisation of complex industrial atmospheres, both with respect to composition and oxidation, carburisation and sulphidation potentials is important in the design and operation of laboratory tests for materials evaluation (Kane, 1980). The gas environments that result from the reaction of coal with steam and oxygen or air are mixtures that include CO , CO_2 , CH_4 , H_2 , H_2S , H_2O , NH_3 and N_2 . In coal gasification atmospheres that involve species such as oxygen, sulphur and carbon, it has been well established that the reliable performance of various components is strongly dependent on the sulphur contents of the gas phase, duration

and temperature of exposure (Natesan, 1985). Table 2.4 enlists the characterisations similar to those prevailing in coal gasification systems.

2.9.2 Chemistry of Salts in Combustion of Coal/Fuel Oils

The sulphur present in coal and fuel oils yields SO_2 on combustion which is partially oxidised to SO_3 . The NaCl (either as impurities in the fuel or in the air) reacts with SO_3 and water vapours at combustion temperatures to yield Na_2SO_4 as below:

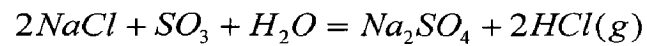
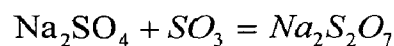


Table 2.4 Characterisation of coal gasification atmosphere at 1255 K (982°C), (Kane, 1980).

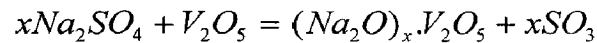
	Inlet Mole Fraction	1 Atm Mole Fraction	Outlet Mole Fraction	68 Atm Partial Pressure, Atm
H ₂	0.24	0.367	0.340	23.1
CO ₂	0.12	0.124	0.189	12.85
H ₂ S	0.01	8.8 x 10 ⁻³	9.16 x 10 ⁻³	0.623
H ₂ O	0.39	0.301	0.324	22.03
CH ₄	0.05	5.05 x 10 ⁻⁶	1.61 x 10 ⁻²	1.09
CO	0.18	0.202	0.121	8.25
NH ₃	0.01	-	-	-
SO ₂	-	2.9 x 10 ⁻⁷	6.5 x 10 ⁻⁹	4.4 x 10 ⁻⁷
COS	-	1.7 x 10 ⁻⁴	1.8 x 10 ⁻⁴	1.2 x 10 ⁻²
H	-	3.3 x 10 ⁷	3.8 x 10 ⁻⁸	2.6 x 10 ⁻⁶
CS ₂	-	2.7 x 10 ⁻⁸	2.8 x 10 ⁻⁸	1.9 x 10 ⁻⁶
S ₂	-	2.51 x 10 ⁻⁶	4.69 x 10 ⁻⁸	3.18 x 10 ⁻⁶
O ₂	-	1.01 x 10 ⁻¹⁵	2.0 x 10 ⁻¹⁷	1.37 x 10 ⁻¹⁵
log PS ₂	-	-5.599		- 5.496
log PO ₂	-	-14.994		- 14.863
log PC	-	-24.032		- 22.296

Log PC for soot formation = - 21.585 at 1255 K.

At lower temperatures Na₂SO₄ can further react with SO₃ to form sodium pyrosulphate, Na₂S₂O₇ with melting point (m. p.) of 401°C:



Small amounts of vanadium may be present in fuel oils, which on combustion forms V_2O_5 . This may further react with Na_2SO_4 to form low melting sodium vanadates, which are highly corrosive.



Thus metals and alloys in combustion gases are exposed to various corrosives such as O_2 , SO_2/SO_3 , molten salts, e.g. Na_2SO_4 or sulphate mixtures, sodium vanadates, $NaCl$ etc (Khanna and Jha, 1998).

2.10 BEHAVIOUR OF METALS AND ALLOYS IN VARIOUS OXIDISING ENVIRONMENTS

2.10.1 Air

The establishment of an oxide scale on an alloy occurs by a nucleation and growth process. When the clean component is exposed to an oxygen-rich gas, small, impinging nuclei of all the thermodynamically stable oxides develop on the surface. These initial nuclei of oxide coalesce rapidly to give a complete layer. During this initial or transient stage the rate of oxidation is rapid. All the elements in the alloy oxidise and the amounts of the various oxides in the layer are approximately proportional to the concentration of the elements in the alloy. Once the transient oxide layer has been established, it continues to grow following diffusion of metal ions to the scale/gas interface or oxygen to the scale/alloy interface. The rate of thickening of the layer is determined by the temperature, the oxygen pressure and the spatial distribution, the amount, the composition and the structure of the initial oxide phases (Stott, 1998).

The high temperature behaviour of pure metals, as well as Fe-Cr binary and ternary Fe-Cr-Ni alloys is strongly dependent on the method of their surface preparation procedure (Kuiry et al, 1994). They have further reported that mechanically polished surfaces exhibit a shorter incubation period for initial oxidation but better oxidation resistance during isothermal

holding at 1423 K (1150⁰C) as compared to electropolished surfaces. This has been reportedly attributed to the enhanced outward diffusion of Cr and establishment of Cr-rich oxide layer on mechanically polished surfaces.

Nickel base alloys have been tested at 1093⁰C in cyclic oxidation tests using a tube furnace and burner rig by Levy et al (1989). The same ranking of the alloys was reported in both tests with the single-crystal superalloys having better oxidation resistance than the directionally solidified alloy DS Mar M 200. They further reported that tube furnace tests can be used in place of burner-rig tests to rank alloys. All the alloys were reported to be severely degraded when a liquid sulphate deposit was placed upon their surfaces at 900⁰C and 704⁰C respectively. They proposed that coatings are required if the alloy is exposed to any type of hot corrosion conditions at 704⁰C or higher temperature.

Seal et al (1994) has studied the oxidation behaviour of three grades of austenitic stainless steel (AISI-316, -321 and -304) in dry air with and without superficially applied CeO₂. The linear heating rate employed was 6 K min⁻¹ up to maximum temperature of 1423 K (1150⁰C) and the isothermal holding temperature was 1273 K (1000⁰C). In the bare condition 321-grade steel was reported to exhibit best performance whereas in the presence of coatings the performance of 316 and 321 grades was identical. Roy et al (1995) have also studied the role of the similar type of coatings on AISI 347 and reported identical results.

Sadique et al (2000) have studied the oxidation behaviour of Fe-10Cr alloy, containing aluminum in the range 2-8% by weight in pure oxygen at 1 atm under cyclic conditions. The cyclic oxidation resistance was reported to be improved with increasing aluminum contents and decreased with increase in temperature at a particular content of aluminum.

Further Hiramatsu and Stott (2000) reported that thin foils of Fe-20Cr-5Al alloys are susceptible to breakaway oxidation once the aluminum content of the substrate falls below some critical value. It reportedly led to the formation of iron-rich oxides that engulfs the specimen. According to them the combined addition of 0.1 wt% lanthanum and 0.1 or 2 wt% molybdenum has a beneficial effect on the high-temperature oxidation of such foils.

The effect of long duration exposure of laser surface engineered composite boride coating on plain carbon steel in air at high temperature has been investigated by Agarwal et al (2000). Exposures at 600, 800 and 1000⁰C for 10, 30 and 50 hours of composite-TiB₂ coated samples were conducted to study oxide scale growth and morphology. They have used thermogravimetric technique to study the kinetics of oxidation at elevated temperature. Oxidation rate for all the samples was observed to be parabolic in nature and oxidation kinetic rate constant was reported to increase with increasing temperature of exposure.

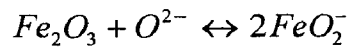
The effect of Ti addition on the cyclic oxidation behaviour of aluminide coatings on the Co-base superalloy has been studied by Liu et al (2001) at 1000⁰C. Ti addition reported to promote the cracking and spalling of the oxide scale and accelerate the degradation of the CoAl phase of the coating. Mechanical properties and oxidation resistance of TiAl based alloys has further been studied by Wu and Hwang (2002) with Y-modifications. The alloys with Y addition were reported to have higher ultimate tensile strength, elongation and oxidation resistance than the Y-free alloy. They further reported that in an oxidation test in air at 800⁰C, the Y-containing alloys showed a significantly low weight gain as compared with the Y-free alloys.

Haugsrud (2003) has reported the oxidation properties of nickel. According to him nickel above 1100⁰C behaves according to a parabolic rate law and the oxidation rate is governed by the outward lattice diffusion of Ni via either singly or doubly charged Ni vacancies. The dominating outward growth was observed by them and with decrease in temperature the oxidation mechanism of Ni was found to be more complex.

2.10.2 Pure Na₂SO₄

To understand the accelerated oxidation of metals and alloys under sulphate salt coating wide ranges of corrosion kinetics and morphologies have been observed by Shi (1993) under controlled laboratory conditions and several kinds of mechanisms have been proposed by him. The Na₂SO₄-Na₂O eutectic melt was reported to be responsible for the formation of the abundant sulphide in the scale and believed to play an important role in the

present form of accelerated corrosion. Moreover Fe_2O_3 can dissolve into the eutectic melt according to the reaction:



According to him the reduction of sulphate ions occurs at the scale/melt interface a negative gradient of concentration of O^{2-} and thereby of $2FeO_2^-$ could be established across the melt. Further fluxing of Fe_2O_3 with the dissolution of Fe_2O_3 at the scale/melt interface and reprecipitating at the melt/gas interface was proposed by him.

The mechanism of Na_2SO_4 induced hot corrosion for nickel base superalloys has been reported by Goebel et al (1973) in temperature range 650-1000°C and by Misra (1986) in the temperature range of 750-950°C. According to them the alloys underwent catastrophic corrosion. The accelerated oxidation has been ascribed to the formation of the liquid flux based on Na_2SO_4 which normally dissolves the protective oxide scales. They proposed the occurrence of catastrophic or self-sustaining rapid oxidation in alloys which contain Mo, W or V because solution of oxides of these elements with Na_2SO_4 decreases the oxide ion activity of the molten salts which further produces the melts which are acidic fluxes for oxide scales.

The effect of Mo on the hot corrosion of superalloys has been further reported by Peters et al (1976), Pettit and Meier (1984), and Fryburg et al (1984). They observed the alloy containing Mo suffers catastrophic oxidation. It has been reported that MoO_2 reacts with Na_2SO_4 to produce an acid (SO_2 -rich) salt, leading to acidic fluxing. The MoO_3 gets incorporated into the Na_2SO_4 via the formation of compounds such as Na_2MoO_4 , $Na_2MoO_4 \cdot MoO_3$ and $Na_2MoO_4 \cdot 2MoO_4$. All these phases are liquid and reported to have high solubility for Al_2O_3 and Cr_2O_3 .

The high temperature oxidation behaviour of Nimonic alloys (75, 80A, 90 and 105) has been investigated in presence of varying amounts of Na_2SO_4 in air environment by Malik and Ahmad (1983). The effect of $Cr_2(SO_4)_3$, $NiSO_4$ or $CoSO_4$ additions in presence or absence of Na_2SO_4 has also been investigated. Upto 800°C, the lower oxidation rates for Na_2SO_4

coated alloys have been attributed to a scale morphology consisting of inner scales of Cr_2O_3 acting as a protective oxide film and external scales of NiO .

The kinetics of corrosion and the morphology of the scales formed on pure iron, manganese and chromium with Na_2SO_4 deposits have been studied in the temperature range of $600\text{-}800^\circ\text{C}$ under 1 atmosphere of a gas mixture containing O_2 (3.6%), SO_2 (0.25%) and N_2 (balance) by Nanni et al (1987). At all the temperatures salt coated iron has been observed to exhibit accelerated attack whereas the corrosion rate of chromium was not appreciably affected by the deposited salt. They have further suggested that the enhanced corrosion phenomena is due to low melting liquid sulphate formation.

The interactions of some metal oxides such as Co_3O_4 , NiO , Al_2O_3 , Cr_2O_3 , Fe_2O_3 and SiO_2 etc. with Na_2SO_4 have been studied by Malik and Mobin (1987) in the temperature range $900\text{-}1200\text{ K}$ ($627\text{-}927^\circ\text{C}$) and Mobin et al (1996) at temperatures 1100 and 1200 K ($827\text{-}927^\circ\text{C}$). According to them the high temperature reaction products usually contain 3-phase structure namely, $\text{Na}_2\text{O-MO-M}_2\text{O}_3$ and metal sulphide and or metal sulphate. The formation of $\text{Na}_2\text{O-M}_2\text{O}$ was further reported to be dependent upon the solid state solubility of metal oxide in the molten salt at high temperature and under limited solubility conditions $\text{Na}_2\text{O-M}_2\text{O}$ was invariably formed, but as soon as conditions got relaxed the oxide M_2O_3 precipitated and was observed to form a separate phase.

Further the phenomena and mechanism of sub-melting point hot corrosion (Type II hot corrosion) of nickel and cobalt base alloys including M-Cr-Al-Y coatings caused by Na_2SO_4 deposit has been reviewed by Shih et al (1989). Where the mechanism of low temperature hot corrosion of iron, AISI 304 stainless steel and Fe-Cr alloys under $\text{K}_2\text{SO}_4\text{-Na}_2\text{SO}_4$ deposit has been described as the dissolution of iron at the oxide-melt interface and reprecipitation of Fe_2O_3 as porous particles at the melt-gas interface. Further they have described the catastrophic hot corrosion of B-1900 alloy under Na_2SO_4 deposit at 750 and 827°C where it has been proposed that MoO_3 plays a role in the reduction reaction probably as $\text{Mo}_2\text{O}_7^{2-}$.

The high temperature corrosion behaviour of alloy 800H has been studied by Xu et al (1994) in an oxidising and a reducing sulphidising environment at 750°C and 850°C respectively.

When corroded in $\text{SO}_2\text{-O}_2$, the protective chromia scale which developed on the alloy in the early stages was found to crack and spall in quite a short time period. According to them this has further led to the growth of iron and nickel sulphides beneath the chromia layer thereby causing more chromia spallation.

Shi (1995) has studied the possibility of $\text{Na}_2\text{SO}_4\text{-Na}_2\text{O}$ eutectic melt being formed on metals deposited with Na_2SO_4 in oxygen and air at temperature of 750°C . In case of Ni, Co, Al, Cr and their alloys they could not detect formation of $\text{Na}_2\text{SO}_4\text{-Na}_2\text{O}$. In case of iron base alloy with high Cr or Al content where Cr_2O_3 or Al_2O_3 again $\text{Na}_2\text{SO}_4\text{-Na}_2\text{O}$ eutectic was not observed but at lower Cr or Al content this eutectic melt was found and it might be resulting accelerated rate of corrosion.

High temperature corrosion of Inconel-600 tube used as a furnace accessory has been reported by Krishna and Sidhu (2001). The corrosion of the tube was analysed to be due to severe oxidising and sulphidising atmospheres generated by inter-diffusion of base metal constituents and sulphur through the microchannels.

2.10.3 Vanadium Pentoxide (V_2O_5)

Pantony and Vasu (1968) reported that under sufficient quantities of molten vanadium to cover the specimens, metals such as iron, cobalt, titanium, molybdenum, tungsten and vanadium show a corrosion rate which is linear with respect to time. Nickel which was considered to be more resistant was observed to obey approximate logarithmic rate law while chromium was found to be the most resistant to corrosion. In these two cases a coherent corrosion layer, which was a protective barrier has been observed by them. In all cases corrosion rates vary inversely with the depth of melt. The inward diffusion of oxygen and outward diffusion of corrosion products has also been observed. According to them attempts to prevent vanadic corrosion of the pure metals either electrochemically or by means of additives are largely unsuccessful owing to the transition semiconductance of molten vanadium pentoxide.

Suito and Gaskell (1971) studied the thermodynamic of melts in the system $\text{VO}_2\text{-V}_2\text{O}_5$ and suggested that the nonstoichiometric liquid oxide may act as a corrosive medium.

Corrosion resistance of various metals and alloys has also been analysed by Kerby and Wilson (1973) in the liquid vanadates. They found that the stainless steels and particularly 440 stainless steel (25 wt% Cr) shows the best corrosion resistance to liquid V_2O_5 . The rate of corrosion of Armco iron by liquid V_2O_5 has been reported to be controlled initially by the diffusion of oxygen across the metal oxide-liquid vanadate interface. As the available oxygen ions get depleted from the melt, the rate controlling mechanism is observed to be changed to the sorption of oxygen at the liquid vanadate gas phase interface.

A 50Cr-50Ni alloy has been corroded in pure V_2O_5 and sodium vanadates in the temperature range 750-950⁰C in a rotating disk apparatus by Dooley and Wilson (1975). In pure V_2O_5 at 810⁰C, a Cr_2O_3 scale has been observed on the alloy which subsequently got dissolved slowly into the liquid melt and was thus proposed as a barrier layer by them.

The association of the high temperature corrosion of superalloys with contaminants has been reported by Hancock (1987). He proposed that to compare contaminant conditions the contaminant flux rate (CFR) rather than the contaminant level in the fuel or environment should be considered. He further suggested that at temperatures above 700⁰C where vanadates cause fluxing of the protective oxide scales, corrosion could be determined by the CFR and temperature rather than by material selection.

Iyer et al (1987) have carried out investigations on the high temperature corrosion of a nickel base superalloy by vanadium at 700⁰C. They reported that vanadium, present as vanadium pentoxide attacked the alloy severely at this temperature of investigation. Their study of ternary oxide system and spot tests showed that two low melting eutectics, namely, NiO- V_2O_5 - Cr_2O_3 melting at 550⁰C and V_2O_5 - Cr_2O_3 - Fe_2O_3 melting at 480⁰C, were formed. The formation of these liquid eutectics and the presence of corrosive V_2O_5 were reported to have caused severe damage to the superalloy.

Swaminathan et al (1993) studied the hot corrosion attack of different amounts of V_2O_5 on nickel based superalloy namely Nimonic 80A, Hastelloy C-276 and Superni 600 for a period of 100 hours at 923, 973 and 1023 K (650, 700 and 750⁰C) in air. Parabolic rate law

was applicable for two different ranges of temperatures at 973 and 1023 K (700 and 750°C) and the protection was ascribed to the formation of a solid $\text{Ni}_3\text{V}_2\text{O}_8$ layer.

2.10.4 Molten Salt ($\text{Na}_2\text{SO}_4\text{-V}_2\text{O}_5$) Environment

Vanadium and sodium are common impurities in low-grade petroleum fuels. Molten sulphate-vanadate deposits resulting from the condensation of combustion products of such fuels are extremely corrosive to high temperature materials in the combustion systems. Thermodynamic calculations for the equilibrium concentrations of Na_3VO_4 , NaVO_3 and V_2O_5 in a mixed sodium sulphate-vanadate solution containing 30 mol % vanadate as a function of melt basicity have been reported by Hwang and Rapp (1989). They suggested that vanadate ions greatly increase the acidic solubility of all metal oxides compared to that in pure Na_2SO_4 .

The kinetics of the reactions between Na_2SO_4 (X) and V_2O_5 (Y) has been studied by Kolta et al (1972). They have concluded that the rate of the reaction depends both on the temperature (600-1300°C) and the molar ratios of X : Y. They further found that with increase in the reaction period (>30 min.) there was decrease in reaction rate which finally reached to zero order. This decrease in the reaction rate has been attributed to the formation of vanadosulphate complexes such as $(\text{NaV}_3\text{O}_8)_2\cdot\text{Na}_2\text{SO}_4$ and $(\text{NaVO}_3)_2\cdot\text{Na}_2\text{SO}_4$ which get decomposed at higher temperatures giving the meta- and pyro-vanadates respectively.

The effect of vanadium and sodium on the accelerated oxidation of nickel base alloys has been reported by Bornstein et al (1975). They observed the initial rapid rate of oxidation between V_2O_5 and metal substrate which is attributed to the reduction of V_2O_5 by the substrate. Intermetallic systems Ni_3Al and NiAl were particularly found to be susceptible to V_2O_5 corrosion. According to them the sulphidation attack alters the composition of the melt to produce more oxide ions i.e. $M + \text{SO}_4^- = \text{MS} + \text{O}^- + 3/2 \text{O}_2$. Severity of attack is found to decrease with increase in the initial oxide ion content of the melt. Oxides such as Cr_2O_3 have been suggested to react preferentially with oxide ions.

Thermogravimetric studies which delineate the conditions for simultaneous sulphate and vanadate induced corrosion at 650 to 800⁰C have been carried out by Seiersten and Kofstad (1987). They found that the corrosion caused by sodium sulphate/sodium vanadate mixtures have a complex mechanism. Samples coated with sodium vanadate were exposed to O₂ + 4% SO₂ and the initial reaction was observed to be same as that observed in pure oxygen. After an incubation period the duration was found to decrease with increasing temperature and sufficient SO₃ had got dissolved in the molten vanadate which resulted in formation of a mixture of NiSO₄ and Na₂SO₄ near the metal. When a molten NiSO₄-Na₂SO₄ solution containing small amounts of vanadate was formed as an intermediate layer the reaction reportedly proceeded as sulphate-induced hot corrosion. The corrosion mechanism was observed to be changed from initial vanadate-induced to essentially sulphate induced hot corrosion when the sulphur trioxide pressure was high enough to form sodium sulphate.

According to Otero et al (1987) Na₂SO₄-60%V₂O₅ deposit was detected on a number of components in actual service which were operated at high temperature and were in contact with high-temperature gases from combustion of dirty fuels, containing certain amounts of impurities, i.e. Na, V, S etc. The presence of sulphur and its oxidised compounds were reported to favour the formation of isolated lobes with radial morphology having great permeability to facilitate the access of oxygen which further led to reduction in the protector character of scale. The presence of vanadium and its oxidised products was observed to generate compounds with aciculate morphology, identified to look like alkaline vanadate complexes. These aciculated shapes further contribute to reduce the protective character of the scale. The equilibrium diagram for varying composition of Na₂SO₄ is shown in Fig. 2.17 and the mixture of Na₂SO₄-60%V₂O₅ is seen to be the lowest eutectic temperature.

In this aggressive environment (Na₂SO₄-60%V₂O₅) the hot corrosion behaviour of Superalloy IN-657 at 1000 K (727⁰C) has been investigated by Otero et al (1990 and 1992). They reported that corrosion rate of the alloy in contact with molten salt mixtures has been approximately reduced by one order of magnitude over exposure times of 210 hrs when the

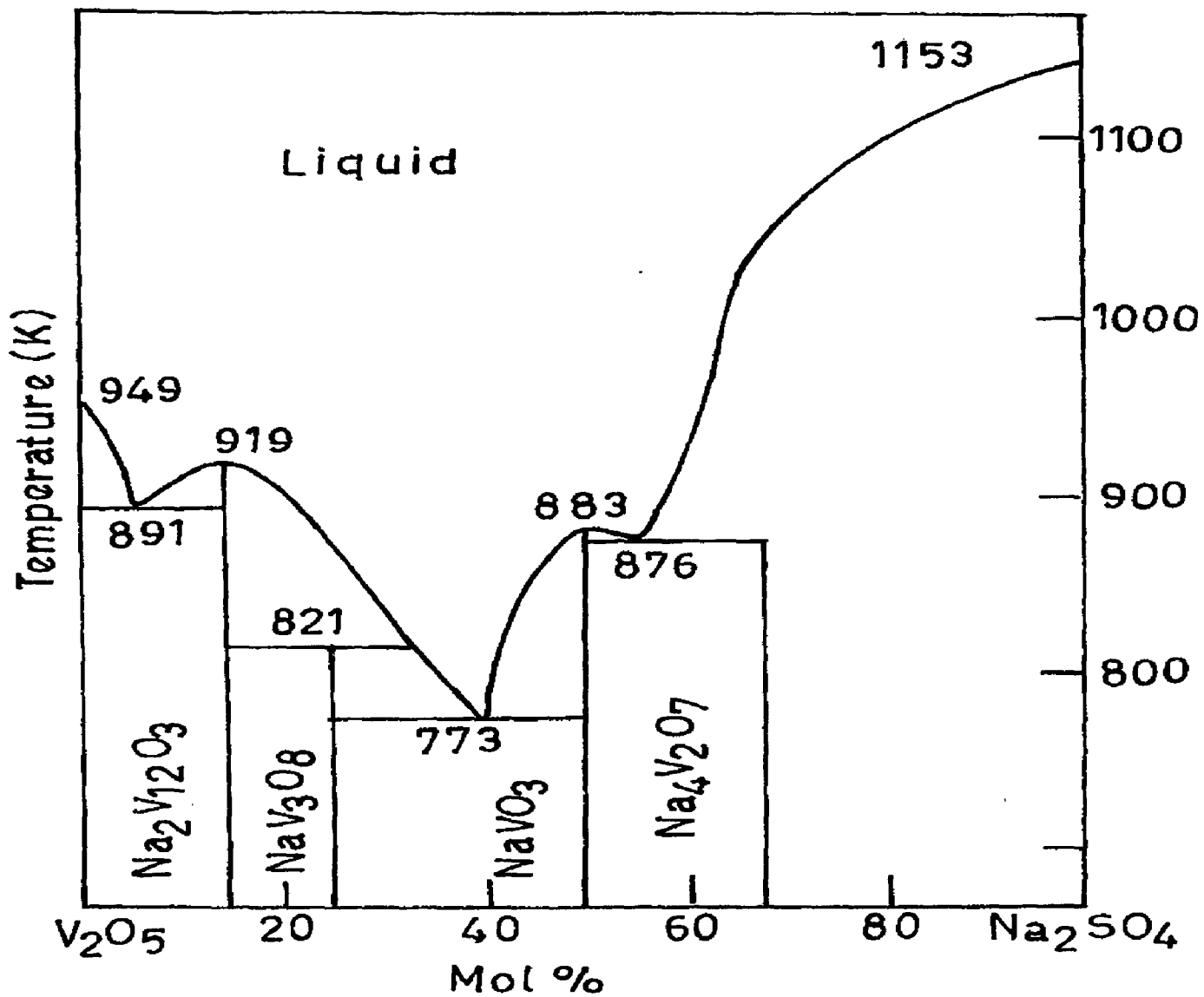


Fig. 2.17 Phase Diagram for Na_2SO_4 - V_2O_5 System (Otero et al, 1987).

amount of molten salt is kept constant. During the initial stages of the exposures the corrosion rate was found to be increased with increasing the temperature up to 1000 K (727^oC) and further reported to have decreased at higher temperature. After 100 hours of exposure the influence of temperature was insignificant.

Tiwari and Prakash (1996 and 1997) and Tiwari (1997) have also reported studies on superalloys in temperature range 700-900^oC in pure Na₂SO₄, Na₂SO₄-15%V₂O₅ and Na₂SO₄-60%V₂O₅. They observed accelerated corrosion rates for Na₂SO₄-60%V₂O₅ composition i.e. eutectic with melting point of 500^oC.

Oxidation and hot corrosion in sulphate, chloride and vanadate environment of a cast nickel base superalloy have been reported by Deb et al (1996). Weight gain studies were carried out in air for the uncoated samples and coated with 100% Na₂SO₄, 75% Na₂SO₄ + 25% NaCl and 60% Na₂SO₄ + 30% NaVO₃ + 10% NaCl. The presence of sulphur in the form of sulphates has been reported to cause internal sulphidation of the alloy beneath the external oxide layer. They observed the formation of volatile species by chlorides which further led to formation of voids and pits at grain boundaries those reportedly provide easy path for flow of corrodents. The presence of vanadate in conjunction with sulphate and chloride is proposed to provide additional fluxing action. According to them this destroys the integrity of the alloy and weakens its mechanical properties.

Almeraya et al (1998) carried out electrochemical studies of hot corrosion of steel AISI-SA-213-TP-347H in 80 wt% V₂O₅ + 20 wt% Na₂SO₄ at 540^oC–680^oC and reported the corrosion rate values of around 0.58-7.14 mm/year. They further observed an increase in corrosion rate with time. However they also observed that corrosion potential decreases with increase in temperature from 540 to 680^oC.

Lee and Lin (1999) studied the oxidation, mixed oxidation-sulphidation and hot corrosion of ductile iron aluminide Fe₃Al with Cr addition at temperatures 605-800^oC. They observed that hot corrosion of iron aluminide was significantly more severe than oxidation and mixed-oxidation-sulphidation which according to them can be attributed to the formation

of aluminide sulphide at the interface of the metal-salt as a result of high sulphur potential in the molten salt at the oxide-metal interface.

2.10.5 Molten Salt Environment (40 wt% K₂SO₄, 60 wt% NaCl.)

Sodium and potassium impurities presented in the form of chloride or sulfates are very corrosive constituents under certain combustion conditions such as waste incinerators and biomass-fired boilers [H.J. Grabke et al (1995)]. The influence of individual KCl, NaCl and their mixtures with heavy metal chlorides or sulfates on the corrosion behaviour of a series of alloy systems has been studied in detail by Y.S. Li et al (2005). Also the author reported that generally realized that Cr is not an effective element for corrosion resistance improvement of Fe-base and Ni-based alloys due to chloride salt attack. Also he presented the degradation behaviour of various Fe–Cr, Fe–Al and NiAl alloys beneath a NaCl–KCl melt coating in air at 670 °C. The author concluded that the different corrosion performances of the Al and Cr modified alloys primarily result from the high reactivities of Cr and Cr₂O₃ with the alkali chloride whereas Al₂O₃ is relatively inert. S. Akila et al (1993) investigated the melting point of the K₂SO₄-NaCl system. Fig 2.18 shows the phase diagram for the above said system.

From the extensive literature survey, the high temperature corrosion of steels by chlorine and chlorides plays a detrimental role in power plants where municipal waste or coal containing chlorides are used as a fuel. In the incineration atmospheres of such plants, rapid wastage is observed in the heat exchanger tubes which are generally made of low alloy steels. The tubes are covered with thick layers of deposits, formed by deposition of fly ash on the oxide scale of the steel surface. In failure cases a layer of the condensed chloride FeCl₂ has been observed at the metal/oxide interface and the oxide layer above the chloride precipitates was very porous and loose, i.e. it could not serve as a protective layer. The effects of HCl and chlorides on the high temperature oxidation of iron and steels have been previously studied. The most striking effect in these studies is the rapid response of the corrosion phenomena on the introduction of the chlorine containing contamination into the environment. As soon as sodium chloride is introduced, as a vapour into the oxidizing atmosphere or as a grain on to the oxide scale of steel, the oxidation is strongly accelerated. A vibrational technique indicated that the main effect is considerable damage to the oxide scale. In a hot stage microscope blistering and

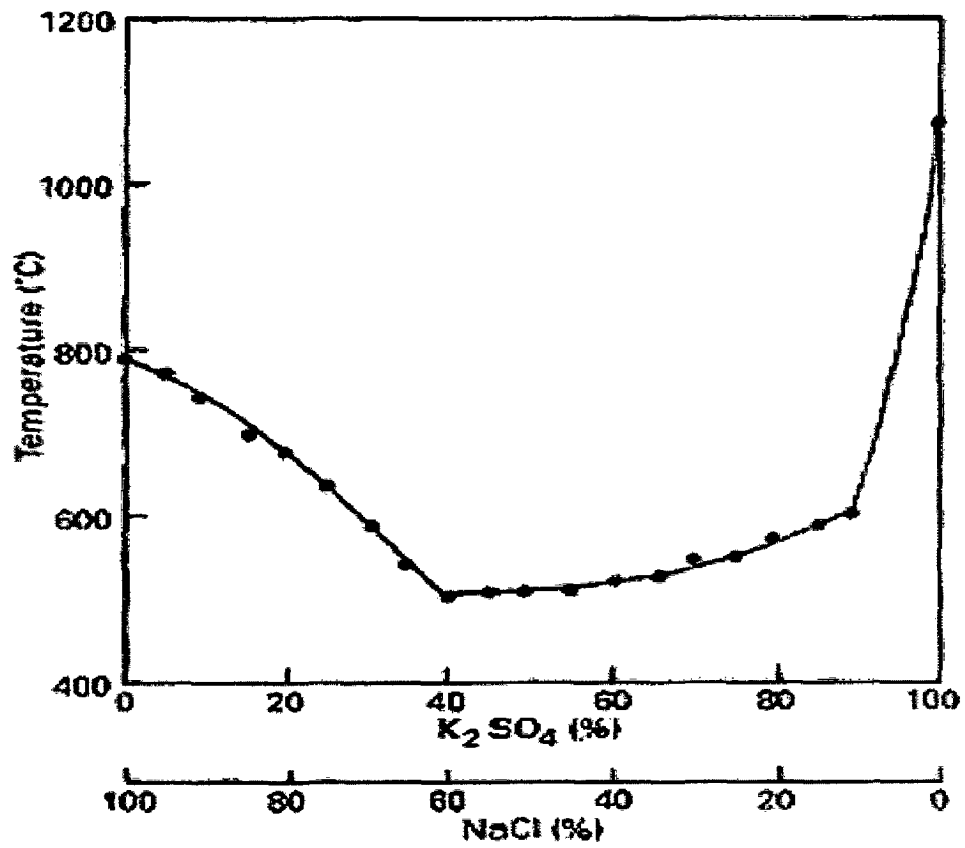


Fig. 2.18 Phase Diagram for K₂SO₄-NaCl System (S. Akila et al (1993)).

cracking of the oxide scale was observed upon depositing sodium chloride on the sample [J. Grabke (1991)].

Thermogravimetric studies have been conducted by H. J. Grabke et al (1995) on the oxidation of low alloy steel at 500 C and high alloy steels at 600 and 700 C under NaCl or fly ash. The author reported that the role of chlorine with accelerated oxidation. The presence of HCl in the atmosphere causes a sulfation of chlorides and the generation of chlorine. The presence of HCl in the atmosphere causes a transformation of sulfates in the deposits into chlorides, which induce enhanced active oxidation. The author concluded that the formation of chlorine at the scale surface, penetration of chlorine (or Cl) into the scale to the oxide/metal interface, the formation of chlorides of the alloy components mostly FeCl_2 which continuously evaporates and is oxidized to Fe_3O_4 and Fe_2O_3 during its diffusion to the scale surface, forming a non-protective scale. The chlorine returns partially to the scale/metal interface. A reaction circuit exists in which chlorine acts as a catalyst, accelerating the oxidation. After the start, the rate of the active oxidation is controlled by the outward diffusion of $\text{FeO}_2(\text{g})$ through the open ways in the scale to the surface, i.e. it depends on the open space, on the diffusivity of $\text{FeCl}_2(\text{g})$ and vapour pressure of the $\text{FeCl}_2(\text{s})$ and is inversely proportional to the thickness of the oxide scale. In the temperature range around 500°C the sulfates are harmless compared to the chlorides. At somewhat higher temperatures chromia forming steels are applied. But from the reaction of Cr_2O_3 (or FeCr_2O_4) with chlorides chlorine is generated, penetrating into the oxide scales and causing active oxidation. Different steels were investigated, and the inverse dependence on the oxide scale thickness was confirmed. Steel forming a relatively thin scale was found to be very susceptible to active oxidation.

M.C. Mayoral et al (2006) Studied the sulphidation and chlorination on oxidized SS310 and plasma-sprayed Ni-Cr coatings as simulation of hot corrosion exposed under pyrite, potassium sulphate and potassium chloride attack in inert atmosphere at 900°C , as simulation of fouling and slagging in co-firing coal with biomass. The author reported that Ni-Cr coatings have been proved to be more resistant to sulphidation attack than the chromia layer generated by preoxidation over austenitic SS310 steel. Sulphur from molten iron

sulphide is able to penetrate through the coatings forming chromium sulphides, but sulphidation is prevented in the steel matrix underneath the coatings. The resistance of these materials against chlorination was dependent on the chromia outer layer; preoxidised SS310 was deeply corroded by the KCl salt, with the formation of voids and scale spallation.

Bani P et al (2004) reported that the role of chlorides in hot corrosion of a cast Fe–Cr–Ni alloy exposed under (K,Na) sulfate or (K, Na) sulfate +chloride at different temperature (500 to 900 °C). the author reported that corrosion rate is significant above 600 °C and increases up to 900 °C. When thermal cycling is superimposed on hot corrosion, spallation of the oxide scale upon cooling causes additional damage, and the spallation was found to be more extensive in the presence of alkali chlorides. Also the author concluded that The presence of alkali chlorides in the deposit causes much more aggressive hot corrosion attack than a salt deposit containing only alkali sulfates, and the mechanism of attack changes. Active oxidation, involving transport of metal chlorides in the liquid salt phase, destroys the normally protective Cr₂O₃ scale, if one is pre-formed, and prevents the re-establishment of a protective scale.

2.10.6 Molten Salt Environment (40 wt% K₂SO₄, 40 wt% Na₂SO₄, 10 wt% KCl, and 10 wt% NaCl.)

Corrosion, fouling and slagging of superheaters are serious problems in boilers utilizing fuels with high alkali and chlorine content. Combustion of biomass [K. Salmenoja (2000), H.P. Nielsen et al (2000)], waste [H.J. Grabke et al (1995)], black liquor [H.N. Tran et al (1988)], and high-chlorine coals [J.E. Oakey et al (1991), P.L. Daniel et al (1989)] are reported to cause severe materials wastage in super heaters. High temperature corrosion of superheaters caused by chlorine-containing flue gases in combustors is usually accelerated oxidation or sulfidation. High temperature corrosion of various coatings and boiler steels in oxidizing and reducing chlorine-containing atmospheres without deposits were reported by M.A. Uusitalo et al (2002). It was concluded that the corrosion resistance of bulk materials relied on properties of the oxide and sulfide scales formed at test conditions, whereas in case of coatings the coating structure and the coating composition determined the shielding capability of the coating.

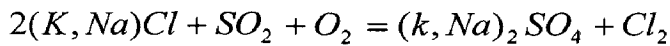
Tetsuo Ishitsuka et al (2002) investigated the solubility measurements of Cr_2O_3 , NiO , Co_3O_4 , Fe_3O_4 and SiO_2 in molten NaCl-KCl and $\text{NaCl-KCl-Na}_2\text{SO}_4\text{-K}_2\text{SO}_4$ were conducted in roughly and widely varied basicity in order to elucidate the corrosion mechanism of boiler tubes in a waste incineration environment and to develop a highly corrosion resistant boiler tube. And the author concluded that the dissolution behavior of oxides in molten chlorides has almost the same tendency as that in molten Na_2SO_4 . In a waste incineration environment, a protective Cr_2O_3 film easily dissolves in the molten chlorides as CrO^{2-}_4 because $p\text{O}^{2-}$ of the molten chlorides in the deposit tends to have a small value due to the effect of water vapor contained in the combustion gas. Molybdenum and silicon were effective for improving the corrosion resistance of 25% Cr-25% Ni. The effect of silicon is smaller than that of molybdenum. Scale analysis suggests that the relatively small effect of silicon is due to discontinuity of the silica layer, but the effects of molybdenum cannot be explained completely by only an increase of $p\text{O}^{2-}$ in the molten chloride by the basic dissolution of MoO_3 .

Corrosion of superheaters is even more severe below chloride-containing ash deposits than in chlorine-containing atmosphere without deposits [K. Salmenoja (2000), H.P. Nielsen et al (2000), H.J. Grabke et al (1995)]. Gaseous HCl is less corrosive than alkali chlorides condensed on superheaters. It is claimed that even high partial pressure of HCl in flue gases (1000 vppm) does not cause severe gas phase corrosion attack [Nielsen et al (2000)].

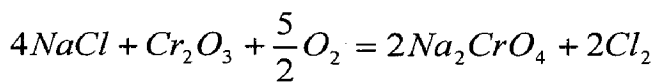
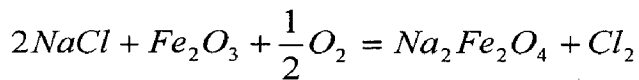
Chlorine-containing ash deposits accelerate corrosion by several mechanisms. Firstly, chlorides lower the first melting temperature (FMT) of the deposits, and molten deposits may flux the protective oxide layer. It is reported that corrosion rate increases significantly, if the deposit temperature is above the FMT [K. Salmenoja et al (2000), N. Hiramatsu et al (1989), M.J. McNallan et al (1981), H.J. Grabke et al (1998), O.H. Larsen et al (1996), J. Klower et al (1995), Y. Kawahara (1997)]. Chemical reactions are generally faster in liquid phase than as solid-solid reactions. The liquid phase also provides an electrolyte for ionic transport or electrochemical attack.

Secondly, the partial pressure of chlorine may be significant below the chloride-containing deposits, even below the FMT, and chlorine is able to attack the metal surface with mechanism similar to gas phase corrosion. The origin of gaseous chlorine is attributed to sulfation of alkali chlorides in deposits by SO_2 in flue gases [K. Salmenoja (2000), H.J. Grabke (1998), O.H.

Larsen et al (1996), K. Salmenoja et al (1996)], and to reactions between solid chlorides and the oxide scale [H.J. Grabke (1998)], but also presence of solid NaCl or KCl in deposits creates an atmosphere rich in gaseous chlorine-containing species. The partial pressures of gaseous KCl and NaCl in equilibrium with solid chlorides are in the range of 10^{-7} bar at 550 °C. Chlorine is released by sulfation of chloride-containing deposits according to the reaction [H.J. Grabke (1995)].



Or from reactions of condensed chlorides with oxide scale



The phase stability diagram of the (Fe, Cr, Ni)-O-Cl system at 550 °C is presented in Fig. 2.19 According to Grabke et al (1995)] the partial pressure of Cl_2 below chloride-containing deposits is in the range of 10^{-10} - 10^{-13} bar. In oxidizing combustion atmospheres metal oxides are stable, even if gaseous chlorine is present. However, the partial pressure of oxygen below the oxide layer is low, corresponding to the partial pressure needed for oxide formation. According to thermodynamics, metal chlorides can be formed in low oxygen environment at the oxide/metal interface, if chlorine can penetrate through the oxide layer. Penetration of chlorine through the oxide layer has been reported in numerous publications. The presence of chlorine at the metal/oxide interface has been detected frequently, but the route of chlorine through the oxide is not clear [K. Salmenoja (2000), H.J. Grabke (1995)].

When chlorine has reached the metal surface, it reacts with metals forming metal chlorides. Gibbs free energies for metal chloride formation are strongly negative, which means that metal chlorides can form. The partial pressures of gaseous metal chlorides at 550 °C are significant and continuous evaporation of metal chlorides takes place in an open system. Gibbs free energies for metal chloride formation and partial pressures of metal chlorides at 550 °C for Fe, Cr and Ni calculated with HSC Chemistry [A. Roine (1999)] are presented in Table 2.5

High temperature corrosion tests were performed by M.A. Uusitalo et al (2004) on low-alloyferritic steel and austenitic stainless steel, five high velocity oxy -fuel (HVOF) coatings, a laser cladding, and a diffusion chromized steel. Test conditions simulated superheater conditions of biofuel- fired boiler. The samples were exposed to synthetic salt containing 40 wt% K_2SO_4 , 40 wt% Na_2SO_4 , 10 wt% KCl , and 10 wt% $NaCl$ at 550 °C for 100 hours. The author found that active oxidation caused accelerated corrosion in oxidizing conditions. In reducing conditions metal chlorides formed and evaporated into the atmosphere, and a layer depleted in chlorine was formed adjacent to the metal surface, retarding the corrosion rate. Also the researchers reported that the corrosion resistance of nickel-based, high chromium coating materials was satisfactory in test conditions.

Hot corrosion of an electrodeposited Ni-11 wt % Cr, Nanocomposite under Molten Na_2SO_4 - K_2SO_4 - $NaCl$ in air at 700 °C studies by C. Zhang et al (2005) showed that rapid formation of a continuous chromia-rich scale is essential for hot corrosion protection. The author reported that the protection mechanism lies in the fast formation of a continuous chromia scale on the nanocomposite, due to the easy nucleation of chromia on both chromium nanoparticles and abundant nickel grain boundaries, and then fast linking of the nuclei as a result of enhanced diffusion of Cr through those grain boundaries. Also the author compared the hot corrosion of the nanocomposite and the arc-melted Ni-10Cr and Ni-20Cr alloys in air at 700°C under molten Na_2SO_4 - K_2SO_4 - $NaCl$ demonstrated that the hot corrosion resistance of the three materials, from worst to best, is in the order of Ni-10Cr < Ni-20Cr < Ni-11Cr nanocomposite.

The existence of volatile metal chlorides, such as $CrCl_2$ (g), was predicted from thermodynamic calculations based on single chemical reactions. Such species were postulated to enhance the transport of metal through the corrosion product layer [H.J. Grabke (1991)]. Calculations of multi-component thermochemical equilibria in systems involving (initially) metal/salt/gas as a function of local oxygen activity can help identify the important hot corrosion reactions David A et al (2004). Such calculations for four pure salts (KCl , $NaCl$, Na_2SO_4 , and K_2SO_4) and a mixture of these salts in contact with an Fe-20%Cr alloy at 800 °C are presented by author. The results predict that the compositions of gas, oxide, (sulfide, when

sulfate was input) and salt phases depend strongly upon the salt chosen and upon the local oxygen activity.

Also the author support faster hot corrosion rates in an alkali chloride + sulfate salt compared to that in alkali sulfate alone. First, alkali chlorides, unlike sulfates, support a continuous salt pathway from ambient to the metal/scale interface, allowing oxidant to be efficiently transported to oxidize metal. Secondly, under oxidizing conditions alkali chlorides have a higher solubility of dissolved Fe- and Cr-containing species than that in alkali sulfates. Both of these factors support higher transport rates, which according to the fluxing theory of hot corrosion will lead to faster corrosion.

The presence of both salt species increases chemical complexity and makes it imperative to consider the problem of competitive reactions. For example, in the presence of a limited quantity of salt, containing both alkali sulfate and alkali chloride, how will Cr partition among several possible phases and species, such as Cr (in metal), Cr_2O_3 (s), CrCl_3 (g), CrCl_2 (g), CrS (s) and Na_2CrO_4 (dissolved)? This and related questions can be addressed by calculating the multicomponent equilibrium for a model system that simulates the local metal-salt-corrosion product environment. To help clarify reactions in the complex salt mixture, we have also calculated equilibria in single salts (KCl, NaCl, Na_2SO_4 , and K_2SO_4) under comparable conditions of temperature, pressure and alloy composition. The author concluded that chloride+ sulfate salts were much more aggressive than sulfate salts, two factors have emerged from the equilibrium calculations. First, the presence of chlorides has allowed a salt phase to exist at the metal/ scale interface. Importantly, this also means that a continuous salt phase pathway exists to deliver oxidant directly to the metallic phase, and in parallel, to move dissolved metal species away from the reaction site. Secondly, the equilibrium calculations show that chloride salts and even the chloride+ sulfate mixture supported a higher concentration of dissolved Cr and Fe than sulfate only salts. Since high temperature corrosion rates typically are expected to be controlled by transport according to the fluxing model [K.N. Lee et al (1990)], both of these factors argue for a faster corrosion rate in chlorides.

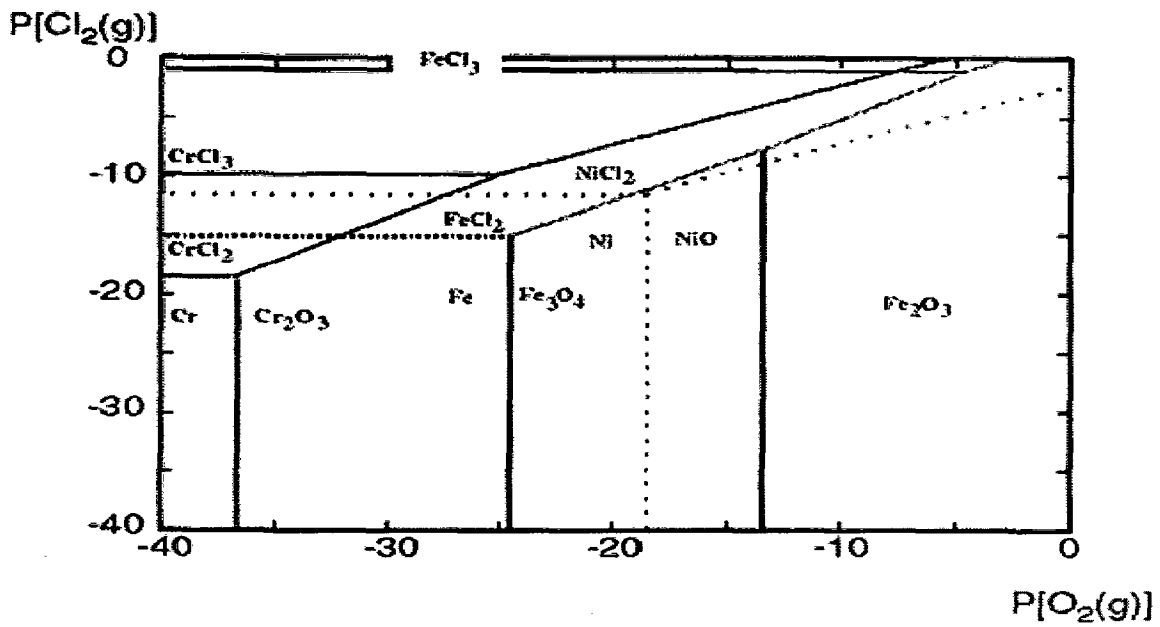


Fig 2.19 Superimposed stability diagram of the (Fe, Cr, Ni)-O-Cl system at 550 C. calculated with HSC Chemistry [A. Roine (1999)]

Table 2.5 Formation reactions, Gibbs free energy changes and partial pressure for metal chlorides at 550 °C

Reaction	°C (kJ/mol)	Partial pressure of MCl ₂ at 550 ° C (bar)
Fe + Cl ₂ = FeCl ₂	-238	2.1 x 10 ⁻⁴
Cr + Cl ₂ = CrCl ₂	-292	2.0 x 10 ⁻⁷
Ni + Cl ₂ = NiCl ₂	-181	1.3 x 10 ⁻⁵

The evaporated chlorides diffuse outward through cracks and pores in the scale. On their way outwards, the regions of higher oxygen pressure are reached, where the chlorides are oxidized. The oxides formed in this process are porous and non-protective. If oxidation of gaseous metal chlorides takes place in the vicinity of the metal surface, part of the chlorine released in oxidation process will diffuse back to metal/oxide interface and the oxidation process will proceed. The process of chlorine-activated corrosion is called active oxidation, because no passivation of metal surface occurs. More detailed description of the active oxidation process and associated thermodynamics are presented in article by Zahs et al (2000)].

The atmosphere in contact with deposits affects the corrosion reactions, because the composition of the atmosphere determines the composition of the deposits. In laboratory experiments the formation of volatile metal chlorides may cause depletion of chlorine in deposits. HCl in atmosphere accelerates corrosion below the deposits [H.J. Grabke (1995)], presumably by stabilizing chlorine-containing species.

Material temperatures in superheaters are set as high as possible, because the steam temperature and pressure determine the maximum efficiency of the boiler. High corrosion rates are experienced in boilers combusting high-chlorine fuels with high material temperatures. Corrosion rates can be reduced by lowering the material temperatures or by applying highly alloyed materials. Low-alloy steels suffer from severe corrosion in chlorine-containing environments, because partial pressure of iron chloride is high at elevated temperatures. Nickel-based alloys are more resistant than steels because partial pressure of nickel chloride is significantly lower than partial pressure of iron chlorides, and the Gibbs free energy change of NiCl₂ formation is less negative than that of FeCl₂ formation [Zahs et al (2000)]. Alloying with chromium [Zahs et al (2000), K. Salmenoja et al (1999)] and silicon are reported to increase corrosion resistance of steels and nickel-based alloys [N. Hiramatsu et al (1989), J. Klower et al (1995), A. Zahs et al (2000), E.P. Latham et al (1989)]. Materials with satisfactory corrosion

resistance in chlorine-containing high temperature environments are highly alloyed [K. Salmenoja (2000)]. Low-alloy ferritic tube coated with a thin layer of corrosion resistant material is an interesting option because of difficulties associated with mechanical properties, workability and high material price of highly alloyed materials [E.P. Latham (1989)].

2.10.7 Hot corrosion by NaCl/Na₂SO₄ mixtures

The mixtures with compositions of 50 wt % Na₂SO₄ + 50 wt % NaCl were partially melted at 500-550 °C, indicating that Na₂SO₄ acidic- and basic-fluxing mechanism which would induce accelerated oxidation of weldment possibly takes place. Figure 2.20 shown the phase diagram for Na₂SO₄ and NaCl system.

The presence of NaCl in the mixtures of NaCl/Na₂SO₄ could initiate attack in high chromium content in the interface which is diffuse from austenitic stainless steel to low alloy steel as reported by Johnson et al (1975).

In a molten salt environment, sulfur was incorporated into scale and proceeds to a sulfide formation in the alloy substrate. Therefore, as the formation of protective oxide scale was inhibited by the presence of NaCl, chlorides and sulfides tend to form in the alloy substrate as indicated leading to the propagation of hot corrosion as suggested by Charng-Cheng Tsaura et al (2005).

Various stainless steels were examined N. Hiramatsu et al (1989) to investigate the effects of alloying elements on NaCl induced hot corrosion properties at temperatures below its melting point. The corrosion rate increases with increasing testing temperature from 450 °C to 750 °C. The author concluded that the weight loss by corrosion increases almost rectilinearly with increasing number of cycles. Weight loss increases as the test temperature increases. At 450 °C corrosion is so slight that the corrosion morphology cannot be clarified. At 650 °C, however, corrosion proceeds rapidly and all materials exhibit intergranular corrosion. The outermost layer was very rough because of the removal of grains at the surface layer by

NaCl - Na₂SO₄

Data from FACT database - www.crct.polymtl.ca

FactSage

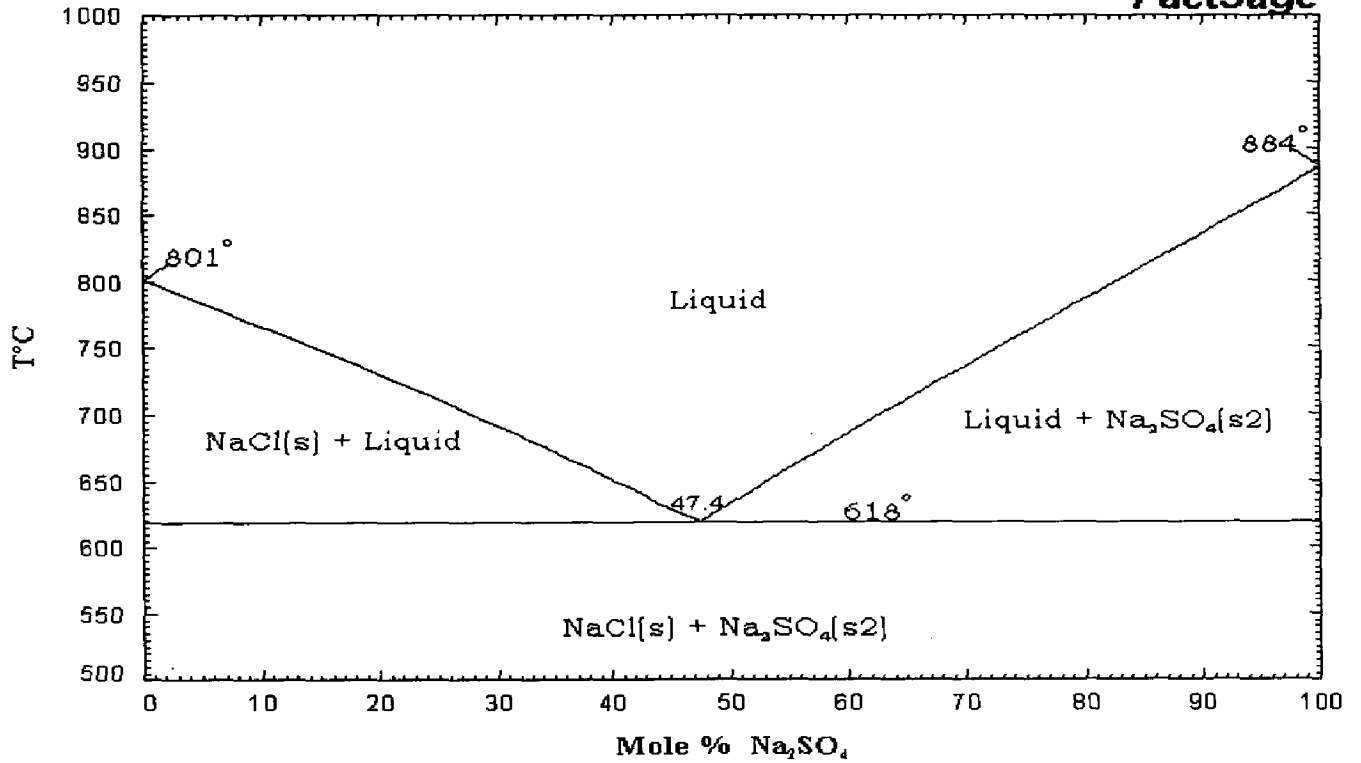


Fig 2.20 Phase Diagram for NaCl and Na₂SO₄ system

corrosion. Fe_2O_3 and spinel oxides were detected in the corrosion products. Austenitic stainless steels exhibit better hot corrosion resistance than ferritic stainless steels. Silicon improves the hot corrosion resistance of austenitic stainless steel, and nickel is also effective. Corrosion is increased when Cr_2O_3 reacts with NaCl to form Na_2CrO_4 instead of a protective scale. Also the findings of Cl_2 or HCl which are formed by that reaction accelerate the corrosion.

Aircraft engines and the boilers at off-shore industrial rigs undergo hot corrosion when the sodium chloride from the ocean breeze mixes with Na_2SO_4 from the fuel and deposits on hot-section components. This leads to accelerated attack on the alloy substrate. The hot corrosion often increases the corrosion loss of heat resisting alloys by over hundred times [Y. Shinata et al (1987)].

Studies of hot corrosion induced by mixtures of $\text{NaCl}/\text{Na}_2\text{SO}_4$ have generally focused on Ni- and Co-base super alloys, and Ni-Cr alloys used in turbine engines or gas turbines [G.Y. Lai (1990), D.M. Johnson et al (1975)]. The addition of 10 wt. % NaCl in Na_2SO_4 coatings can easily cause the degradation of protective Cr_2O_3 layers and increase the amount of sulfur incorporated into the substrate, accelerating the corrosion of alloys [D.M. Johnson et al (1975)]. It has been reported that the most severe hot corrosion attack is observed on Ni- and Co-base alloys at 900 °C in still air with mixtures of $\text{NaCl}/\text{Na}_2\text{SO}_4$ containing 40 wt, % NaCl [D.M. Johnson et al (1975)]. The 310SS is a good candidate used in most parts of the waste incinerator. The chromic scale can be yet formed with adequate amounts of chromium content, and act as a protective barrier in oxygen-containing atmospheres. Low alloy steel and austenite stainless steel is extensively used for boiler tubing application at elevated temperatures because of its relatively low cost, good weldability and creep resistance [Wyatt L.M (1982)]. It finds wide use in the low temperature region of the superheaters. Welding of tubes is commonly employed in boiler fabrication and these joints are weak points where failure can happen [Saxena A et al (1987)].

Heat exchanger pipes are found to be corroded via oxidation, sulfidation, and molten salt corrosion. Molten salt corrosion occurs by the formation of alkali-iron sulfate as reaction products of sulfur oxide in fuel gas and sodium chloride from seawater. Many integrated steel

mills are located near the sea for convenience of transportation. Salt from the seawater can affect the corrosion of the heat exchanger pipes by inducing hot corrosion. The inter-lamella pores may act as passages for molten salts. Therefore, the coatings should be carefully sprayed so that the molten salts do not penetrate into the coating layer Byeong Geun Seonga (2000). The author investigated the scales and heat exchanger pipe materials of recuperators used in a hot rolling mill located near the sea, the corrosion process that occurred on the heat exchanger pipes is a form of hot corrosion induced by salt deposits. The source of the salt is the marine environment for alkali metals, Na and K, and fuel gas for sulfur. The fluxing action of the molten salt is mainly due to the formation of alkali-iron trisulfates. This fluxing action of the trisulfates is responsible for severe attacks on the heat exchanger pipes by making the oxide layer porous and non-protective.

Hot corrosion tests were carried out by I. Gurrappa (1999) on CM 247 LC alloy half-immersed in silica crucibles containing Analar grade Na_2SO_4 y NaCl mixtures in the temperature range of 700 to 1000°C for periods of 4 to 70 hr. The author reported that bare CM 247 LC was severely corroded in just 4 hr, while it was completely consumed in 70 hr when tested in 90% Na_2SO_4 +10% NaCl at 900°C. The results show that a chloride containing melt is more corrosive than pure sodium sulfate. The weight loss is linearly related to $t^{1/2}$ (time) and temperature in the different environments studied. The hot corrosion rate is negligible in pure sodium sulfate and appreciable in chloride containing environments. Where as high corrosion rate recorded in Na_2SO_4 containing either 5 or 20% NaCl and a minimum at 10% NaCl.

Charng-Cheng Tsaura et al (2005) has been studied the high-temperature corrosion behavior of 310 stainless steel at 750 °C in air with 2mg cm^{-2} mixtures of various NaCl/ Na_2SO_4 ratios. The author reported that weight gain kinetics in simple oxidation reveals a steady-state parabolic rate law after 3 h, while the kinetics with salt deposits display multi-stage growth rates. NaCl is the main corrosive specie in high temperature corrosion involving mixtures of NaCl/ Na_2SO_4 and is responsible for the formation of internal attack. Uniform internal attack is the typical morphology of NaCl-induced hot corrosion, while the extent of intergranular attack is more pronounced as the content of Na_2SO_4 in the mixture is increased.

From the investigation the author concluded that the fact that mixtures with 75% NaCl showed the most severe corrosion due to molten eutectic salt and capillary transport. Also the author find Fe_2O_3 , $(\text{Fe,Cr})_2\text{O}_3$, and Cr_2O_3 are main corrosion products in the external scale. Minor spinels such as FeCr_2O_4 and NiCr_2O_4 are formed on the external scale-subscale interface. Sulfides such as NiS, FeS, and chromium sulfides are found with increasing Na_2SO_4 content in the coating layer.

The oxidation behaviour of two Na_2SO_4 -coated, chromia-forming, iron-based alloys at 900°C has been studied by D. N. H. Trafford et al (1980). The author reported that Na_2SO_4 coatings markedly enhance the oxidation rates of both alloys and result in the formation of thick, compact, stratified scales. The salt/scale reactions result in the formation of sodium--iron oxide, which is capable of assisting in the corrosion reaction, albeit in a minor way. Also the author investigated the role of NaCl additions during Na_2SO_4 induced corrosion.

2.10.8 Hot corrosion with 100% NaCl

Hot corrosion requires a molten salt to be in contact with the specimen. If there are no molten phases, the corrosion rate will be low. It is possible that a molten phase is formed for the $\text{Na}_2\text{SO}_4 + \text{NaCl}$ (50%) salt. Many researchers have pointed out that the formation of sodium chromate, Na_2CrO_4 , could result from oxychloridation in which chromium or chromium oxide reacts with NaCl and oxygen even when the temperature is lower than the melting point of salt deposits [M.K. Hossain et al (1978), N. Hiramatsu et al (1989)]. As the Na_2CrO_4 is formed, the salt will wet the specimen surface due to the low-melting eutectic $\text{NaCl-Na}_2\text{CrO}_4$ (500°C) and lead to a mechanism of hot corrosion dominated by molten salt. Oxychloridation, in which NaCl reacts with metal and the oxygen dissolved in molten salts to form metal oxides, sodium-containing oxides, and chlorine, is believed to be the initial reaction of NaCl-induced hot corrosion. There are three ways that chlorine may be further reacted in this study:

- (1) Escaped to atmosphere
- (2) Dissolved into Cr_2O_3 lattice increasing the content of cation vacancies and accelerating the oxidation of alloy.

(3) Reacted with alloy substrate to form metal chlorides.

The metal-chloride generated by the reaction between metal and chlorine produced from the oxychloridation evaporates, diffuses out and oxidizes in a place with appropriate partial pressure of oxygen to form metal-oxide and chlorine which is returned back to the process again. Hence, during the cyclic chloridation/oxidation reaction process, the chlorine acts as catalyst to accelerate corrosion [N. Hiramatsu 1989].

The hot corrosion behaviors of hot dip aluminized low carbon steel, SUS310 and Fe–Mn–Al–Cr–Si–C alloy with 9 mg cm² of NaCl deposition was studied by C.J. Wang (2003) at 900 °C for 1–144 h in dry air. The high solubility of aluminum in the Fe–Mn–Al–Cr–Si–C alloy, the coated aluminum diluted rapidly and complex phase transformations were induced by the interdiffusion of the aluminum and alloy matrix. The corrosion resistance of hot-dip aluminum coated Fe–Mn–Al–Cr–Si–C alloy was thus degraded. The author reported that the preoxidation treatment increased the thickness of the aluminized layer, yet reduced the corrosion resistance of three alloy systems due to the formation of microcracks during the cooling and the further heating to elevated temperature.

Morphological development of subscale formation in Three types of stainless steel (430, 304, and 310) with a coating of NaCl, NaCl/AlCl₃, or NaCl/Al₂(SO₄)₃ are exposed at 750 and 850°C investigated by Chaur-Jeng et al (2002). The author reported that NaCl has a major effect on corrosion and sulfur plays an important role in intergranular corrosion. After high-temperature exposure with a 100% NaCl coating, the morphologies of alloys 304 and 310 show typical uniform subscale attack the depths of attack increasing with temperature, while alloy 430 showed a planar attack. Alloy 310 has the highest chromium content and has the least metal loss. After high-temperature exposure with a NaCl/AlCl₃ coating, the corrosion morphologies and depths of attack are similar to those associated with an NaCl coating, but only voids are larger in the subscale. When coated with NaCl/Al₂(SO₄)₃, the alloys are attacked simultaneously by sulfur and chlorine at 750°C, resulting in a typical sulfur-attack intergranular corrosion. However, as the temperature increases to 850°C, the corrosion morphology changes to a uniform subscale attack. The author concluded that Fe–Cr ferritic

stainless steel 430 shows a nearly planar-attack type, while those of Fe–Cr–Ni austenitic stainless steels 340 and 310 reveal intergranular attack or uniform internal attack patterns due to the selective leaching of Cr and Fe by chlorination reactions, followed by volatilization of these metal chlorides. All three alloys have similar corrosion products under all test conditions. In all the cases the corroded products contain Fe_2O_3 , $(\text{Fe}, \text{Cr})_2\text{O}_3$, Cr_2O_3 , NiFe_2O_4 , NiCr_2O_4 .

The hot corrosion behaviour of NaCl-coated SUS-430, SUS-304, SUS-316 and SUS-329J1 stainless steels was examined by Yutaka Shinata et al (1987) in a temperature range from 650 to 900 °C. The author reported that corrosion of these stainless steels is markedly accelerated by the presence of NaCl at every temperature, but the rate of acceleration is considerably higher above the melting point of NaCl. In hot corrosion, chromium is oxidized selectively, forming a non-protective Cr_2O_3 scale. The nickel contained in the steels restricts the detrimental effect of chromium. In the SUS-329J1 two-phase stainless steel, the ferritic phase is attacked more than the austenitic phase because the ferrite has high chromium content and a low nickel content. Also the author concluded that the chromium contained in these steels is oxidized preferentially, forming a nonprotective Cr_2O_3 scale. Consequently, high chromium steels such as SUS-329J1 are more severely corroded than lower chromium steels. Nickel in steels restricts the detrimental effect of chromium slightly. Chromium is oxidized in the presence of chlorides, forming non protective Cr_2O_3 [Y. Shinata et al (1986)]. This accelerated oxidation occurs at temperature both below and above the melting point of NaCl. Nickel is also oxidized quickly in the presence of NaCl, but only above the melting point [Y. Shinata et al (1985)]

2.11. Hot corrosion on the weldment

Dissimilar-metal joints are used widely in various industrial applications due to both technical and economic reasons. The adoption of dissimilar-metal combinations provides possibilities for the flexible design of the product by using each material efficiently, i.e., benefiting from the specific properties of each material in a functional way. Fusion welding is by far the most important process used in the fabrication of modern boilers. Components are joined by the formation of a molten pool of metal between them. The production of high

quality welds with a high degree of consistency is readily achievable. However, defects are more likely to occur in welds than in wrought material. In all arc welding processes, the intense heat source produced by the arc and the associated local heating and cooling results in a number of consequences in material corrosion behaviour and several metallurgical phase changes occur in different zones of a weldment. Because the occurrence of corrosion is due to electrochemical potential gradient developed in the adjacent site of a weld metal, the author proposed to study the effects of welding on the corrosion behaviour G.E. Linnert et al (1994).

Fusion welding is one of the most widely used methods for the joining of metals. Therefore, continuous efforts are made to apply these methods to the joining of dissimilar-metal combinations also, despite the many difficulties encountered. These difficulties include problems associated with metallurgical incompatibility, e.g., the formation of brittle phases, the segregation of high- and low-melting phases due to chemical mismatch, and possibly large residual stresses from the physical mismatch.

There are several choices amongst the fusion welding processes, such as common conventional shielded metal arc, gas tungsten arc, gas metal arc, and submerged arc welding. They also include processes characterized by high energy density, such as plasma arc, electron beam, and laser beam welding. In addition to fusion welding, several other types of joining techniques are also available, and may often be associated with less difficulty for producing dissimilar-metal joints. These are pressure welding, e.g., friction, resistance and diffusion welding, as well as brazing and soldering, adhesive bonding, and mechanical joining. Most of these techniques can eliminate the fusion problems because the base metals remain in the solid state during joining. Therefore, they are better than fusion welding in this respect.

However, the service conditions may make particular processes unsuitable, e.g., for high-temperature applications, soldering and adhesive bonding cannot be candidates, and for leak-tight joints, mechanical joining is not acceptable. Furthermore, the required joint geometry can make, e.g., friction welding difficult to apply. Diffusion welding often provides superior technical benefits for joining small dissimilar-metal parts, but the process is rather

time consuming. Therefore, solutions relying on high energy density processes, e.g., electron beam welding (EBW) and laser beam welding (LBW), are still of great industrial interest.

Low alloy steel and austenitic stainless steel possess a good combination of mechanical properties, formability, weldability, and resistance to stress corrosion cracking and other forms of corrosion. Owing to these attributes at moderately high temperatures, Cr-Mo steels are an extensively used family of engineering materials for applications such as steam generation/handling, petroleum processing/refining, thermal reforming/polymerization/cracking. However, the strength of the weldments of Cr-Mo steels is generally inferior, and most of the in-service failures are reported to take place in the weld region ASME (1986). Given that the weldments are an indispensable part of most component fabrication, the frequent occurrence of weld failures has ensured ongoing research interest in the past few decades. However, most of the research effort has been directed to the correlation of the in-service failure of these steels to the microstructural degradation caused during welding. In recent years, first-ever systematic investigations have been initiated to study the influence of variation in alloy microstructure on gaseous corrosion of Cr-Mo steel weldments, with a view to developing a rather complete understanding of the complex interplay of the mechanical stress, microstructure, and environment which result in weld failure R K Singh Raman et al (1999).

2.11.1. Weldment corrosion of Cr-Mo Steel

Microstructures of Cr-Mo steel are very susceptible to thermo mechanical treatments [J. Pilling et al (1982)]. This microstructural susceptibility is often exploited to develop carbide precipitates of the required chemistry, morphology, and distribution to effect precipitation hardening. However, due to the meta-stable nature of the composition and the morphology of the strengthening precipitates, the secondary precipitates could undergo undesirable transformations during elevated-temperature service and/or during thermomechanical treatments experienced during fabrication, viz., welding, forging, hot rolling, etc [T. Wada et al (1981)]. Microstructural changes due to welding include variations in the grain size in the area adjoining the weld metal (*i.e.*, the heat-affected zone (HAZ)) and enrichment of Cr in the existing secondary precipitates and/or additional Cr-rich precipitate

formation. Trapping of "free" chromium (from the matrix) through Cr-rich precipitate formation is reported to alter the oxidation resistance of low-Cr alloys, whereas the increase in grain size is found to facilitate internal oxidation. [R.K. Singh Raman et al (1992)] The surface-scaling-rate data are generally of secondary importance to design engineers (primarily because surface scaling of steels follows parabolic kinetics and the scaling rate decreases considerably after the initial period). Low-chromium steels are also known to undergo internal oxidation, resulting in distinct "subscale" formation (subscale is the region underneath the external oxide scale) N. Birks et al (19820).

2.11.2. Internal Oxidation of Low alloy steel

Low-Cr steels invariably form an external scale during high-temperature oxidation. In addition to the continuous and uniform external oxide scale, under certain environmental and alloy conditions, isolated oxide precipitates are also formed in the alloy matrix underneath the external scale. It takes a specific combination of oxygen partial pressure underneath the external scale, alloy microstructure, oxidation temperature, and nature of the resulting external scale to establish and sustain internal oxidation. Internal oxidation is, therefore, governed by the nature of the oxidant and its access underneath the scale, [N. Birks et al (19820).] which, in turn, will be governed by the the physical and chemical characteristics of the external scale in terms of diffusion of the oxidant through the scale. Depending on the oxygen partial pressure in the environment and temperature, an iron-chromium alloy can form significantly different types of external scales in which diffusion of oxidants can vary considerably, also the author is well established that the physical and chemical characteristics of the scales formed over micro structurally different regions of the weldment do vary considerably; it may be relevant to compare the combined role of this variation and environment on the internal oxidation behavior R.K. Singh Raman (1998).

2.11.3. Internal Oxidation in Weldment

Internal oxidation can particularly deteriorate the creep and fatigue lives of alloys due to phenomena such as crack initiation at grain boundaries; selective leaching of alloying elements from the areas adjacent to grain boundaries; vacancy and void formation, which can assist crack propaga-tion: [C. Phaniraj et al (1984)] and grain-boundary cavitation resulting

from annihilation of vacancies created by selective leaching [W.R. Johnson et al (1972)] A less protective inner scale formed during oxidation of the HAZ region of Cr-Mo steel weldments, as established earlier, may be important for establishing and sustaining internal oxidation. However, no systematic studies have been carried out to understand the combined role of alloy microstructure and environment on internal oxidation (and subscale formation) and the associated micro-structural degradation of Cr-Mo steels and their weldments. In this regard, it is important to note that most of the creep-rupture data on Cr-Mo steels are generated for air environments, and the influence (if any) due to the actual in-service environment, such as steam, seems to have been ignored R.K. Singh Raman et al (1993 and 1994).

2.11.4. High temperature corrosion on dissimilar weldment

R.K. Singh Raman et al (2002) reviewed of the non uniform scaling behaviour across microstructural gradients in weldments of pressure vessel steels in order to develop a global model for life assessment by relating oxide scale thickness with time-temperature history of in-service components. Also the author discussed about the prevalence of in-service failures in the welds of chromium-molybdenum ferritic steels causes great concern in steam generating/handling systems of power plants, and components of petroleum/petrochemical industries. The researchers concluded that the accurate use of oxide scale thickness as a tool for life assessment of the welded components. Also the author recommends further investigations as given:

(i) examining the applicability of the recent practice of life assessment by scale thickness to the welded components, by establishing kinetics of the scale thickness growth across the broadly different (microstructural) zones (viz. weld metal, HAZ and base metal) of the steel weldments, in the environments of steam and air; (ii) developing a suitable model for life assessment by relating scale thickness with time-temperature history (and hence, creep damage) in the different zones of the steel weldments; (iii) testing the validity of the model for steam generators in fossil-fuel power plants,

For an improved understanding of the deterioration in the mechanical properties due to deleterious alloy microstructure, it will be necessary to carry out further investigations as listed below: (i) characterising corrosion-assisted microstructural degradation in the alloy matrix across the broadly different (microstructural) zones (viz. weld metal, HAZ and base metal) of the steel weldments, in the environments of air and steam, and thus investigating the role of the environment in facilitating microstructural degradation; (ii) Examining the role of corrosion-assisted microstructural degradation, by conducting creep tests on the simulated weld metal and HAZ, in steam and inert environments.

Arivazhagan et al (2006) investigated the behaviour of dissimilar friction weldment of AISI 4140 and AISI 304 exposed under $\text{Na}_2\text{SO}_4 + \text{V}_2\text{O}_5$ (60%) at 500 and 550 °C. The author reported that the scale thickness on low alloy steel side was found to be more and was prone to spalling. Weld region has been found to be more prone to degradation than base metals due to inter diffusion of element across the interface and the formation of intermetallic compound. Also they reported that the corrosion product contains Cr_2O_3 and Fe_2O_3 on scale over weld zone may be due to enrichment of this zone with Fe and Cr. It is suggested by them that for better hot corrosion resistance, the heat-generating phase has to be kept to a minimum by keeping optimum Burn-Off length as it will decrease the amount of intermetallics and maintain better uniformity of microstructure.

High temperature corrosion tests were performed by M.A. Uusitalo et al (2004) on low-alloy ferritic steel and austenitic stainless steel, five high velocity oxy -fuel (HVOF) coatings, a laser cladding, and a diffusion chromized steel. Test conditions simulated superheater conditions of biofuel- fired boiler. The samples were exposed to synthetic salt containing 40 wt% K_2SO_4 , 40 wt% Na_2SO_4 , 10 wt% KCl , and 10 wt% NaCl at 550 °C for 100 hours. The author found that active oxidation caused accelerated corrosion in oxidizing conditions. In reducing conditions metal chlorides formed and evaporated into the atmosphere, and a layer depleted in chlorine was formed adjacent to the metal surface, retarding the corrosion rate. Also there researchers reported that the corrosion resistance of nickel-based, high chromium coating materials was satisfactory in test conditions.

S. Ahila et al (1993, 1994) studied the hot corrosion of 2.25 Cr-1Mo steel weldment made by manual metal arc welding, induction pressure welding. The weldment exposed under eutectic mixture of 40 wt% K_2SO_4 and 60 wt% NaCl at 550 and 650 °C. From the investigation the author concluded that the welded specimens showed a lower degree of attack in both coated and uncoated conditions. Attack on coated specimens was due to the formation of a liquid phase which could flow along the grain boundaries and weaken them. This led to accelerated corrosion. Also the author investigated the hot corrosion on dissimilar weldment of 2.25Cr-1 MO steel-347H made by transition joint using a nickel-based filler metal (INCO 82) in a mixture containing Na_2SO_4 and 60% NaCl. The author reported that the hot corrosion attack led to the formation of oxides of iron on the surface and sulphides of iron and chromium on the subsurface. Also the author concluded that the mixture of molten salt indicates an enhanced degradation of Cr-Mo side of the joint. The surface is oxidised and the subsurface is sulphidised. Due to this, the material is continuously lost from the surface leading to reduced section thickness of the Cr-Mo side. The salt deposit contained the 50 wt % Na_2SO_4 + 50 wt % NaCl and low-melting eutectic NaCl/ Na_2SO_4 action time on the weldment is the longest, resulting in generating the highest rate of corrosion at 500-550 C. whereas the temperature more than 600 C, the salt mixtures exist in a completely liquid phase where the fast evaporation characteristics of NaCl led to a residue of solid Na_2SO_4 on the weldment surface as suggested by Charng-Cheng Tsaura et al (2005).

It is widely agreed that the hot corrosion weight gain will be more severe when the temperature is higher than the melting point of salt deposits. Although the testing temperature in this study is lower than the melting point of salt deposit (50 wt % Na_2SO_4 + 50 wt % NaCl (600 °C), the corrosion rate is at least three orders of magnitude higher than that of air oxidation. Corrosion morphology of the weldment shows typical uniform subscale implying that NaCl coating plays an important role in hot corrosion behavior, even at temperatures lower than 600 °C as reported A.U. Seybolt (1970), Y. Shinata (1987).

Murti and Sundaresan (1985) examined the transition joints between low alloy steel and stainless steel in the superheater section of a steam power plant boiler, which were made using friction welding. The joints were subjected to a variety of thermal conditions, including thermal cycling and isothermal loads. It was found that, thermal aging or cycling without an external load causes another interface layer to develop on the low alloy steel side, and this is believed to consist of intermetallic phases. It has been reported that thermal cycling leads to predominant carbon depletion than in any other thermal exposure conditions.

R.L.Kleuh et al (1982) examined the dissimilar alloy weld failure problem that is quite common in fossil-fired boilers for transition joints between ferritic steels and austenitic stainless steel. The microstructure that develops at a weld metal ferritic steel interface during welding and elevated temperature service was examined in the as-welded, as-welded-and-tempered, and as-welded-and-aged conditions and in failed and un failed joints that had been in service in fossil-fired boilers for more than 100,000hr and developed a mechanism by which the interface microstructure forms during welding, how it evolves during elevated temperature service, and how this microstructure leads to failure.

2.12 FORMULATION OF PROBLEM

There are many industries where austenitic stainless steel needs to be welded to low alloy steel, especially in the power generation industry S.M. Shushan et al (1996). Low alloy steel and austenite stainless steel is extensively used for boiler tubing application at elevated temperatures because of its relatively low cost, good weldability and creep resistance Wyatt L.M (1982). It finds wide use in the low temperature region of the superheaters. Welding of tubes is commonly employed in boiler fabrication and these joints are weak points where failure can happen [Saxena A et al (1987)].

Corrosion aspects of the similar and dissimilar joints of advanced materials made by friction welding (FRW) technologies still require a vast amount of research and development. Unfortunately, Dissimilar Metal Welding (DMW) has several fabrication and metallurgical drawbacks that can often lead to in-service failures. The most pronounced fabrication faults are hot cracks due to inadvertent use of incorrect welding electrodes. Use of the carbon steel

welding electrodes results the formation of a very hard, crack susceptible bulk structure on the stainless steel side of the DMW joint [Omar A (1991), Welding Handbook (1982)]. However, the most trouble-some drawback of DMWs is the inherent formation of discontinuous brittle and hard zones primarily along the fusion line of the ferritic side of the joint. Such hard and brittle zones may render DMWs susceptible to localized pitting corrosion attack, hydrogen embrittlement, sulfide stress cracking (SSC) and stress rupture, which often occurs in the weakened structure of the heat affected zone (HAZ) of ferritic material of the DMW. Indeed, several in-service failure have been reported in the open literature [Schaefer A (1979), Klueh R.L et al (1982), Sakai T et al (1982), Avery R.E et al (1991)]. In addition no attempt is made to study the high temperature molten salt corrosion and oxidation kinetics of iron – chromium alloys DMW obtained by FRW.

Fossil -fuel boilers and fossil-fuel fired power generating equipment experience hot corrosion problems in components of steam generators, water walls surrounding the furnace, economizer assemblies, and front and rear portions of the super heater and re-heater [G.J. Theus et al (1983), NACE (1982), Wyatt (1978)]. M.H.Hurdus (1990) noticed that the fine grain size result in an increase in the active area of chemical reaction, quicker formation of protection scales and self healing, increase in the sites for oxide nucleation, as well as increase in the regions with difference in morphology and growth of the scales at the grain boundaries and with in the grains.

Apart from the welding defects, microstructural changes in the HAZ may induce corrosion damage on the weldment. The steel's performance in oxidizing environments is well established, but its behavior of weldment in corrosive environments, particularly those containing sulfidizing species and/or chlorides have not been studied extensively. Thus, the hot corrosion behavior of dissimilar weldment under eutectic mixture of NaCl (50%) and Na₂SO₄ (50%) is studied. Both kinetics evolution and morphological development are investigated by means of thermal gravimetric analyses, measurements of corrosion attack, metallographic examination, and the identification of the corrosion products. The relationship between the corrosion morphology and composition of deposited salt layers is also explored. Life extension of ageing plants is largely concerned with degradation of high temperature components. It is important to understand the nature of all types of environmental degradation

of metals as well as weldment as intensely as possible so that preventive measures against metal loss and failures can be economically devised to ensure safety and reliability in the use of metallic components [EPR (1993)].

Low alloy steels are used extensively in the steam generating and handling systems of power plants (in the temperature range of 623–873 K). Common applications of 'Cr– Mo' steels also include reactors for refining and processing of petroleum, high-temperature, high-pressure vessels for thermal reforming, polymerisation, alkylation, hydro cracking and coal-gasification [Bland J (1956), Mandich LS et al (1956), Colebeck EW et al (1952)]. The strength of the weldments of these steels is reported to be poor [Laha K et al (1990), ASME (1986)]. About 80% of the failures are reported to take place in the weld region [Chew B et al (1979)]. This has led to widespread use of nickel-based filler materials for such welds, but even with these joints service failures due to carbide precipitates in the ferritic steel close to the weld interface have been reported [P.E. Haas (1982), A.T. Price (1982), R.D. Nicholson (1984)]. Considerable research work of the past 3–4 decades has often indicated the inferior creep rupture of the weldments to result primarily from the microstructural degradation of the heat affected zone (HAZ). However, there is little information available on the high temperature corrosion-assisted microstructural degradation and their specific contribution in damaging service life of the DSW between AISI 4140 low alloy steels and AISI 304 stainless steel. Because of their acceptable corrosion resistance, good mechanical properties and being economic, low alloy steel has become increasingly attractive to a number of industrial sectors. Austenitic stainless steel has been widely preferred by industry due to its good mechanical properties and outstanding corrosion resistance in a wide range of environment.

It is well known that in such a joint, diffusion occurs at increased temperatures, and diffusional layers are formed that may cause crack formation within a short service time. Diffusional layers are the zones formed due to the inter diffusion of carbon, chromium, iron and nickel across both side of the interface between the weld and the heat-affected zone (HAZ), typically carbide layers and decarburized zones and intermetallic compounds. The microstructure of these diffusional layers significantly differs from the neighboring area of the joints. The characteristic dimension of these layers is the thickness, i.e., the size perpendicular to the weld interface between the weld and the HAZ. The rate of dimensional change of these layers is relative to the chemical composition: the greater the composition (first of all Cr)

differences between weld and base metals, the greater are the dimensional change. Temperature of exposure and burn-off length also has the same effect on this rate [L. Beres et al (2003)]. In a DSW the acceptable service temperature cannot be as high as would be possible for homogeneous joints. Increasing application of these steels will require a better understanding of the issues associated with welds of dissimilar metals (DSM). The joining of DSM is generally more challenging than that of similar materials because of differences in the physical, chemical and mechanical properties of the base metals to be welded. These differences may also complicate the selection of filler metals which has to be compatible to both the base metals [Barnhouse EJ et al (1988)].

Research in the area of super alloys, boiler tube steels etc. has already been done in the department and the decrease in the extent of hot corrosion using inhibitors and coatings in the most aggressive environment of Na_2SO_4 -60% V_2O_5 at 900°C has been achieved. But the major challenge in this area is shortage of literature to study the hot corrosion behaviour of dissimilar weldment. The dissimilar weldments made by FRW, TIG and EBW under study were done at Defence Metallurgical Research Laboratory (DMRL-Hyderabad).

So far, most studies on the hot corrosion of metal and alloys have solely considered Na_2SO_4 environments. Comparatively less information is available on the combined effect of vanadium oxide and sodium sulphate. Vanadium oxide can react with Na_2O to form sulphate-vanadate compounds, which modify the attack rate of the oxide layer or even attack the alloy (Lambert et al, 1991).

The steel's performance in oxidizing environments is well established, but its behavior of weldment in corrosive environments, particularly those containing sulfidizing species and/or chlorides have not been studied extensively. The presence of solid NaCl or KCl in deposits creates an atmosphere rich in gaseous chlorine-containing species. The partial pressures of gaseous KCl and NaCl in equilibrium with solid chlorides are in the range of 10^7 bar at 550°C [A. Roine (1999)]. Thus, the hot corrosion behavior of dissimilar weldment under eutectic mixture of $\text{Na}_2\text{SO}_4 + \text{V}_2\text{O}_5$ (60%); $\text{Na}_2\text{SO}_4 + \text{NaCl}$ (50%), $\text{K}_2\text{SO}_4 + \text{NaCl}$ (60%) and Na_2SO_4 (40%) + K_2SO_4 (40%) + NaCl (10%) + KCl (10%) is studied.

Corrosion of superheaters is even more severe under chloride-containing ash deposits than in chlorine-containing atmosphere without deposits. The presence of chlorine at the metal/oxide interface has been detected frequently, but the route of chlorine through the oxide is still not clear [K. Salmenoja (2000), H.J. Grabke (1995)].

Most industrial processes involve the use of metals and alloys at elevated temperature followed by cooling to room temperature numerous times. The operating conditions in such plants conform more to cyclic, rather than to isothermal processes. Therefore oxidation under cyclic conditions constitutes a more realistic approach towards solving the problem of metal corrosion (Sadique et al, 2000). Relatively fewer studies are reported under cyclic conditions, which actually simulate the working conditions of boilers and gas turbines. In cyclic conditions, high thermal stresses are developed.

Hence it is decided to select 50 cycles (cycle of 1 hour heating followed by 20 minutes cooling) to study the behaviour of dissimilar weldment in the temperature range from 500 to 900 °C in laboratory furnace in air without and with aggressive environments.

Dissimilar weldment of low alloy steel (AISI 4140) and austenitic stainless steel are taken up to evaluate the hot corrosion aspects keeping in view their proposed usage in Energy conversion systems / Power generation industry, widely used in boilers and nuclear reactors. In a nuclear water reactor, dissimilar metal welds are employed to connect the low alloy steel reactor pressure vessel and stainless steel pipe systems. The dissimilar metal weldment joining boiler water reactor nozzles to safe ends is one of the more complex configurations in the entire recirculation system.

Corrosion, fouling and slagging of super heaters are serious problems in boilers utilizing fuels with high alkali and chlorine content (like Na₂SO₄, V₂O₅, NaCl, K₂SO₄ and KCl). Combustion of biomass waste, black liquor and high chlorine coals are reported to cause severe material wastages in super heaters.

So the environment created by the mixture of varying composition of Na₂SO₄, V₂O₅, NaCl, K₂SO₄ and KCl. So far, most studies on the hot corrosion have solely considered base metals. Little information is available on the dissimilar welded metals. In addition, no high

temperature corrosion studies are reported on dissimilar friction welded low alloy steel and stainless steel as per the open literature. Hence, this study assumes significance.

The present study is an attempt to evaluate the hot corrosion behaviour of dissimilar weldment of AISI 4140 and AISI 304 made by FRW, TIG and EBW temperature range from 500 to 900⁰C with and without salt mixture of Na₂SO₄+ V₂O₅ (60%); Na₂SO₄ + NaCl (50%), K₂SO₄ + NaCl (60%) and Na₂SO₄ (40%)+ K₂SO₄ (40%) + NaCl (10%)+ KCl (10%) under cyclic conditions.

It was also proposed to measure weight change to study the corrosion kinetics and to use X-ray Diffractometer (XRD), Scanning Electron Microscope (SEM), Energy Dispersive X-ray Analysis (EDAX) and Electron Micro Probe Analyser (EPMA) to characterise the corrosion products and to make an attempt to understand the mechanism of corrosion.

CHAPTER 3

EXPERIMENTAL PROCEDURE

In this chapter the experimental details used for the study has been summarised. It includes the parent metal chemical compositions, welding parameter details, mechanical testing, metallographic examination, the hot corrosion studies and the characterization of final corrosion products.

3.1 WELDMENT CHARACTERISATION

3.1.1 Selection of Base Materials

The parent metals employed in the study are AISI 304 stainless steel, AISI 4140Cr-Mo steel. Microstructures of parent metals are shown in Fig. 3.1. The micro structure of 304 SS consists of equiaxed and coarse austenite grains whereas low alloy steel consists of ferrite and pearlite. The chemical composition and mechanical properties of the low alloy steel, stainless steel and nickel interlayer are presented in Tables 3.1 and 3.2 respectively.

Table 3.1 Chemical composition of AISI 304 and AISI 4140 (wt%)

Name of Alloys	C	Cr	Mn	Ni	Si	Mo	Fe
AISI 304	0.06	18.4	1.38	8.17	0.32	----	Balance
AISI 4140	0.40	1.1	0.75	----	0.31	0.28	Balance

Table 3.2 Mechanical Properties of Parent Alloys

Mechanical Property	AISI 304	AISI4140
Tensile Strength (MPa)	515	655
Yield Strength (MPa)	205	417
Elongation in 50mm gauge length (%)	40	25.7
Hardness (Hv)	150	200
Izod Impact Strength	210	85

3.1.2 Friction Welding (FRW)

A 150 KN capacity continuous drive friction welding machine, manufactured by ETA Pvt, Ltd, Bangalore (India) (Fig. 3.2) was used in the experiments. This machine has provision for holding the work pieces from 6 to 25.4 mm diameter and with continuously varying rotational speed from 0 to 2400 rpm and operates on bum-off length or friction time modes. The machine works on step less adjustment of friction pressure, forge pressure, bum off, feed rate, brake delay time, upset delay time and upsetting time. Friction welding had been carried out at Defense Metallurgical Research Laboratory (DMRL-Hyderabad). Friction welding was performed between rods AISI 4140 and AISI 304 of 25 mm diameter and 100 mm length at constant speed, friction force and upset force by keeping the bum-off as a variable parameter. The parameter details and the joints that are made are designated as in given the Table 3.3.

Table 3.3 Welding parameters and their designation.

Joint Designation	Welded Joint	Bum-off, (mm)	Friction Force, KN	Upset Force, KN	Rotational Speed, rpm
B5	304-4140	5	37.5	50	1500
B7	304-4140	7	37.5	50	1500
B9	304-4140	9	37.5	50	1500
B12	304-4140	12	37.5	50	1500

3.1.3 Electron Beam Welding (EBW)

The base alloys (AISI 4140, AISI 304) used for electron beam welding were taken from the same lot (25 mm diameter and 200 mm length) used for FRW. These were hot forged to thickness of 6 mm sheets which has been used for electron beam welding. Before welding, the oxide layer was removed from the surfaces and the specimens were cleaned with acetone. All welding experiments were conducted using Low KV Electron Beam Welding machine, manufactured by TECHMETA (France) at Defense Research and Development Laboratory (DRDL), Hyderabad. The weldment made by autogenous

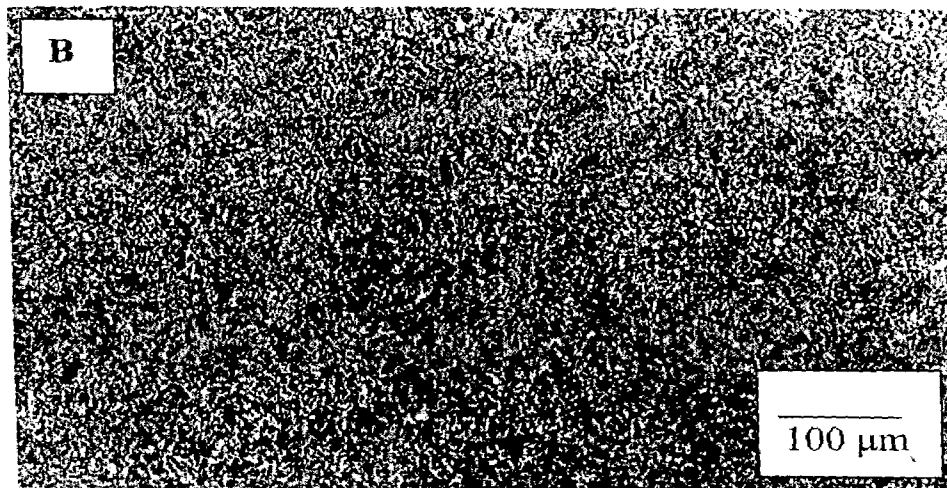
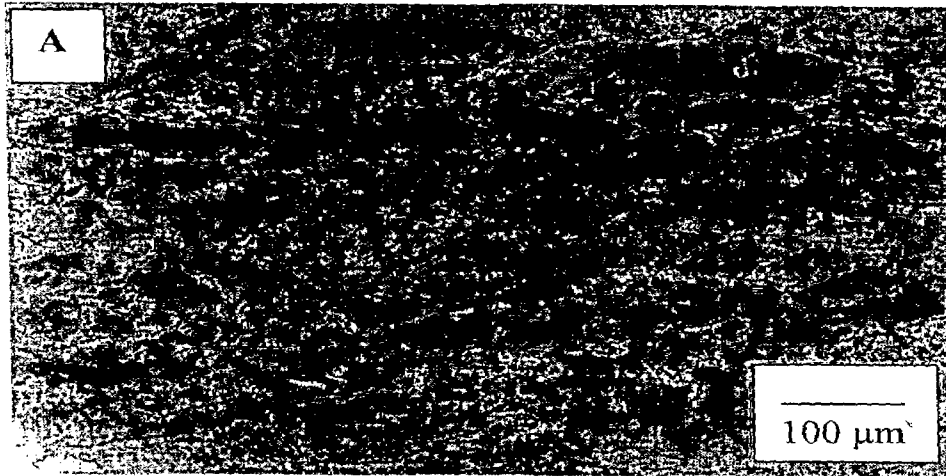


Fig 3.1 Microstructure of parent metals (A) AISI 304, (B) AISI 4140

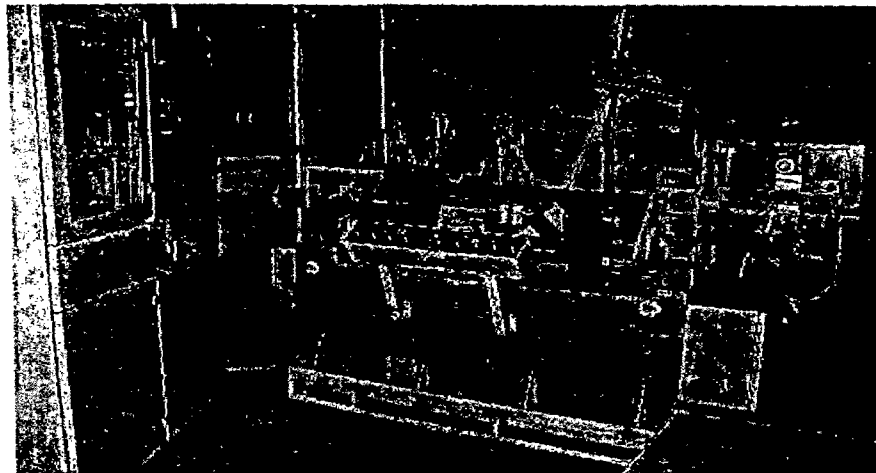


Fig 3.2 Friction welding equipment

method (without filler metal). The parameter details and the joints that are made are designated as in given the Table 3.4.

Table 3.4 EBW Welding parameters

Welding parameter	Value
Work distance (mm)	275
Accelerating voltage (kV)	55
Beam current (mA)	50
(Beam focus slightly above the surface)	
Travel speed (m/min)	1
Vacuum level (mbar)	10^{-4}

3.1.4 Tungsten Inert Gas Welding (TIG)

The base alloys (AISI 4140, AISI 304) used for tungsten inert gas welding were taken from the same lot (25 mm diameter and 200 mm length) used for FRW which were hot forged to the thickness of 10 mm. Before welding, the oxide layer was removed from the surfaces and the specimens were cleaned with acetone. All welding experiments were conducted at Defense Metallurgical and Research Laboratory (DMRL), Hyderabad. The weldment made by autogenous method (without filler metal). The taken welding parameters are given in table 3.5.

Table 3.5 TIG Welding parameters

Welding parameter	Value
Current (DCSP) (Amp)	300
Voltage (volt)	23
Argon pressure (bar)	2.1
Torch traveling Speed (cm/ sec)	0.2

3.1.5 Optical microscopy

Welded 304-4140 joints were sectioned and mounted in Bakelite and were mechanically polished using 120 to 800 grit SiC papers and then polished using alumina paste on rotating wheels. Etching was done by using Nital's reagent for low-alloy steel, Aqua Regia's reagent for austenitic stainless steel. A Zeiss Axiovert 200 MAT inverted optical microscope, fitted with Zeiss Axiovision Release 4.1 imaging software (Germany) was used for observing the microstructure at different zone of the weldment.

3.1.6 Scanning Electron Probe Micro Analysis (EPMA)

304-4140 welds sectioned and mounted in Bakelite and were mechanically polished using 120 to 800 grit SiC papers and then polished using alumina paste on rotating wheels. These samples were then subjected to scanning electron probe micro analysis. EPMA is done to analyze the elemental composition at micron level and also to know the possible combinations of carbides formed due to carbon and chromium migration.

3.1.7 Hardness Test

The samples were cut to required size, mounted in Bakelite and then polished. Micro-hardness survey was carried out using a Vickers digital micro-hardness tester along the weld joint (Fig. 3.3). A load of 100 gms was applied, for a duration of 10 seconds. Hardness was measured at intervals of 0.05mm across the interface and 0.5mm along the base metal. Hardness survey was performed across the weld in the axial direction.

3.1.8 Impact Test

The welded samples were machined to square section as per ASTM E 23 (Fig. 3.4) with a notch at the interface and then Charpy 'V' notch impact testing was performed at the room temperature on welded samples. The test was carried out by impact machine BLUE STAR (SL No 423/25), made in the German Democratic Republic.

3.1.9 Tensile Test

The friction welded samples were machined by EDM wire cut to required size (ASTM E18) by keeping weld interface at center shown in Fig. 3.5 and 3.6. tensile specimen for EBW and TIG (Fig 3.7) welded sample machined by milling operation and then tensile testing was performed at the room temperature on samples of different welded samples. The test was carried out by tensile testing machine made by Hounsfield, S-series (H25K-S) (U.K).

3.1.10 Scanning Electron Microscopy (SEM)

Scanning electron microscopy is carried out to examine the surfaces of fractured impact specimens and tensile specimen of the different welded sample at various magnifications. The fractured impact and tensile samples are first cut to required size and are then ultrasonically cleaned and degassed before loading in SEM chamber. A scanning electron

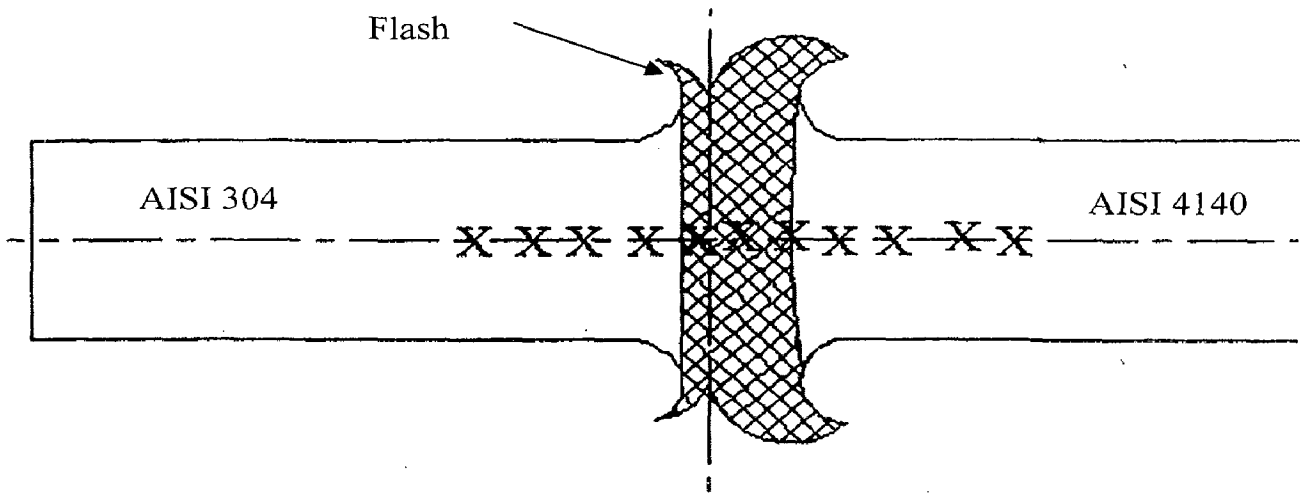


Fig 3.3 Hardness measurement along the weld

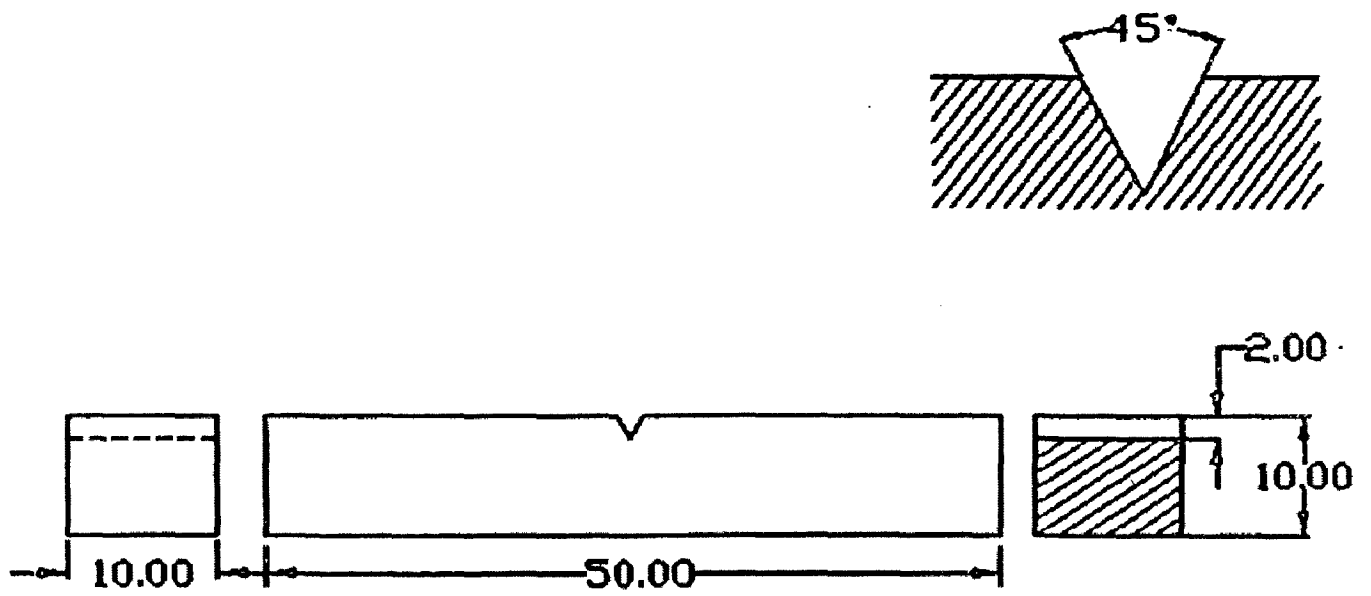
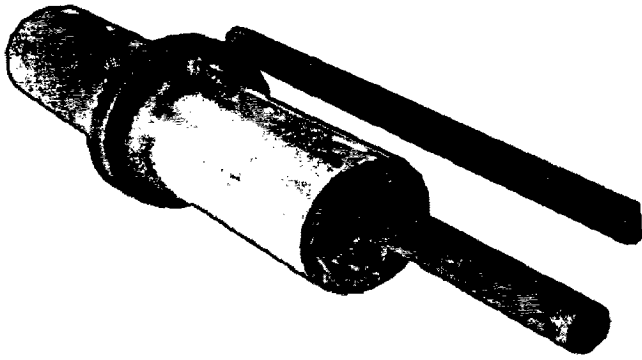
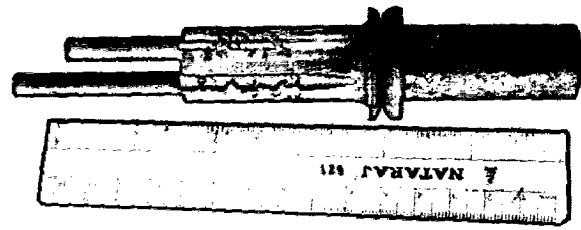


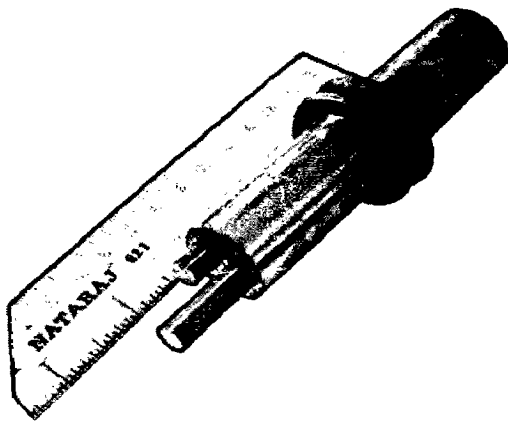
Fig 3.4 Charpy 'V' notch impact test sample



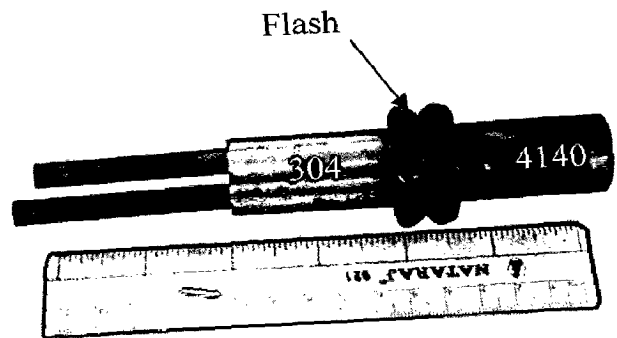
(i) Burn-off length 5 mm



(ii) Burn-off length 7 mm



(iii) Burn-off length 9 mm



(iv) Burn-off length 12 mm

Fig 3.5 Tensile specimen preparation by EDM wire cut

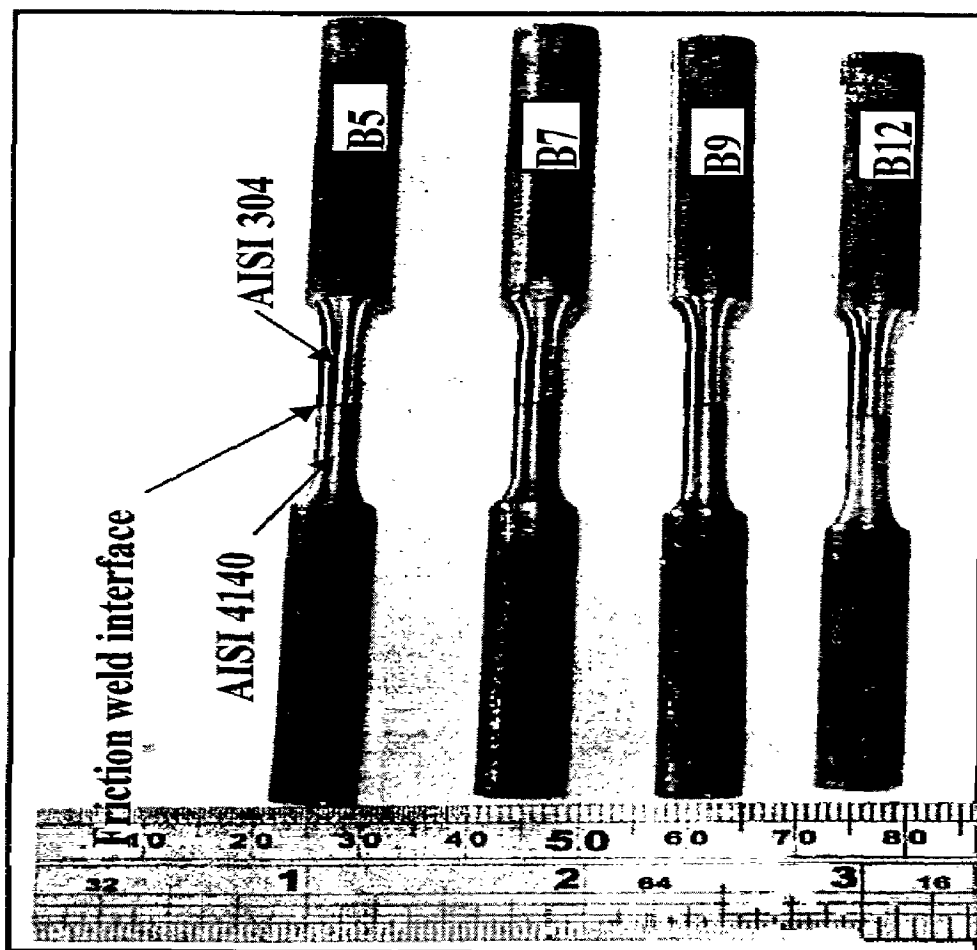


Fig 3.6 Tensile specimen for friction weldment,
Burn off length 'B' 5, 7, 9 and 12 mm

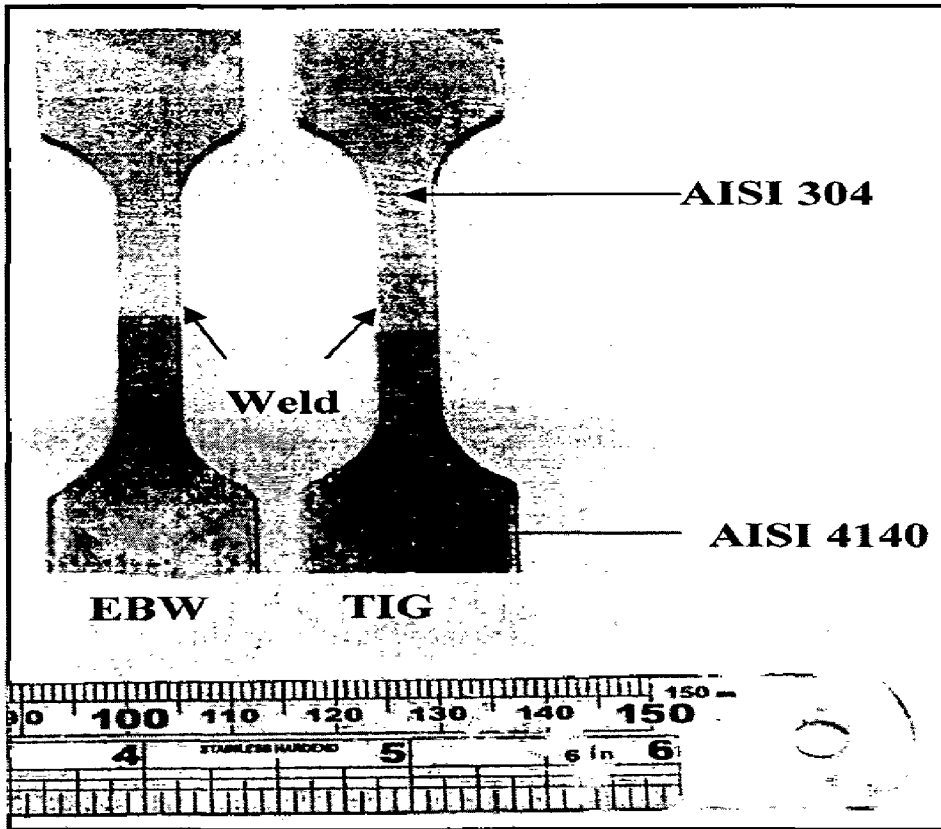


Fig 3.7 Tensile specimen for EBW and TIG welded sample

microscope (JEOL, JSM-5800) with EDAX attachment (Oxford, Model-6841, England) was used for SEM analysis.

3.2 HIGH TEMPERATURE OXIDATION AND HOT CORROSION STUDIES

3.2.1 Experimental Setup

Oxidation and hot corrosion studies were conducted at the exposed temperature from 500 to 900⁰C in the laboratory silicon carbide tube furnace, Digitech, India make. The furnace was calibrated with the variation of $\pm 5^{\circ}\text{C}$ using Platinum-Rhodium thermocouple and temperature indicator of Electromek (Model-1551 P), India. Al₂O₃ boat was pre heated upto 1200⁰C for 6 h with the assumption that its weight would remain constant during the cycle of study. The samples were prepared by electrical discharge machining (EDM) wire cut, each measuring 20mm×15mm×5mm by keeping the weld at the approximate centre. The specimens were subjected to mirror polishing also subjected to wheel cloth polishing for 5 minutes before study. After polishing the samples were washed properly and dried in the hot air to remove the moisture. The sample was kept in the boat, weight of boat and sample was measured before inserting into the hot zone of the furnace. The holding time in the furnace was one hour and after one hour the boat with sample was taken out and cooled at the ambient temperature for 20 minutes. Weight of the boat along with sample was measured and this constituted one cycle. Air oxidation and molten salt hot corrosion studies carried out for such 50 cycles. Any spalled scale in the boat is taken into consideration for the weight change measurements. The Electronic Balance Model CB-120 (Contech, Mumbai, India) with a sensitivity of 1 mg was used to measure the weight change values.

3.2.2 Oxidation Studies in Air

The oxidation tests at the exposed temperature from 500 - 900⁰C were performed on the weldment in laboratory furnace up to 50 cycles as discussed in section 5.1. Visual observation for the oxide scale was recorded after each cycle along with the weight change measurements.

3.2.3 Hot Corrosion Studies in Molten Salt.

The hot corrosion studies were performed on the weldments exposed at the temperature from 500 to 600 °C under the following mixture of molten salt for 50 cycles.

(i) $\text{Na}_2\text{SO}_4 + \text{V}_2\text{O}_5$ (60%)

(ii) $\text{K}_2\text{SO}_4 + \text{NaCl}$ (60%)

(iii) Na_2SO_4 (40%)+ K_2SO_4 (40%)+ NaCl (10%) + KCl (10%)

(iv) $\text{Na}_2\text{SO}_4 + \text{NaCl}$ (50%)

3.2.3.1 Molten Salt coating

The weldments were prepared for studies as discussed in section 6.1. The samples were heated in the oven upto 250 °C and the above mentioned salt mixtures were dissolved in distilled water and applied on the warm polished samples with the help of a camel hair brush. The amount of the salt coating varied from 3.0 -5.0 mg/cm². The coated samples were then dried at 110 °C for 3-4 hours in the oven and weighed along with the Al_2O_3 boat.

3.2.3.2 Hot Corrosion Studies

The salt coated samples were subjected to hot corrosion study in the laboratory furnace at temperatures of 500, 550 and 600 °C respectively for 50 cycles each. At the end of each cycle critical observations were made regarding the nature of corrosion products along with the weight change measurements.

3.3 ANALYSIS OF CORROSION PRODUCTS OF OXIDATION IN AIR, MOLTEN SALT ENVIRONMENT

All the hot corroded weldments were analysed for the identification of corrosion products for both the surface as well as cross-section. Corroded samples were subjected to XRD, SEM, EDAX, measurement of scale thickness and EPMA analysis.

3.3.1 Visual Observation

Visual examination was made and recorded after each cycle for any change in colour, lustre, adherence, spalling tendency and development of cracks on the surface of the scale etc. After the completion of 50 cycles (each cycle of 1 hr heating and 20 minutes cooling) in laboratory were finally carefully examined and then their macrographs were taken.

3.3.2 Thermogravimetric Studies

The weight change values were measured at the end of each cycle with the aim to understand the kinetics of corrosion. The data was plotted with respect to number of cycles for each sample and the plots are given in the subsequent chapters. In many cases spalling and scaling occurred in the alumina boat and the same was also added in the weight change values.

3.3.3 Measurement of Scale Thickness

After exposure at different temperature of 500, 550 and 600 °C in laboratory furnace, the samples were cut across the cross-section by keeping weld at center and polished as discussed in section 5.2.4. Scanning Electron Microscope (LEO 435VP) with attached Robinson Back Scattered Detector (RBSD) was used to obtain the BSE images. The average thickness of the scale was determined from the measurements taken on BSE images.

3.3.4 X-Ray Diffraction (XRD) Analysis

XRD studies performed on the weldment for identification of the different phases formed during hot corrosion studies identify the phases present on the surface of the scale. The diffraction pattern is scanned by Philips X-ray diffractometer, model PW 1140/90 using Cu target and nickel filter at 20 mA under a voltage of 35 kV. The samples were scanned in the range (2θ), 10 to 120° and recorded at a chart speed of 1 cm/min and the Goniometer speed 1°/min. For the intensity peaks and corresponding values of 2θ, the interplanar spacing 'd', has been calculated using Bragg's law

$$2d \sin \theta = n\lambda$$

Where, λ is the wave length of Cu K_{α} radiation used for the diffraction and is taken as 1.54 Å for estimating the 'd' values which is finally used for identification of various

phases with the help of inorganic ASTM X-ray diffraction data cards. 'd' values were calculated for all the prominent peaks in the usual manner. Assuming the height of the most prominent peak as 100%, the relative intensities were calculated for all the peaks.

3.3.5 SEM/EDAX Analysis

3.3.5.1 Surface morphology

SEM / EDAX analysis of corroded sample surfaces were performed at CRF, Indian Institute of Technology, Kharagpur (India) and the details regarding the equipment was already provided in section 3.4.3. Samples were scanned under the SEM and the critical areas of interests were photographed with an aim to identify the inclusions, microcracks and morphology of the surface scale. Point analysis was performed on various locations on these identified areas of interest on corroded surfaces of the samples with an aim to identify the various corrosion products.

3.3.5.2 Cross-section morphology

In case of studies the thickness of the scale and cross section morphology data could not be used for predicting corrosion behaviour due to brittle and spalling nature of the scale. After exposure at different temperature of 500, 550 and 600 °C in laboratory furnace, the welded samples were cut across the cross-section by keeping weld at center and polished as discussed in section 3.4.4. Scanning Electron Microscope (LEO 435VP) with attached Robinson Back Scattered Detector (RBSD) was used to obtain the BSE images. The average thickness of the scale was determined from the measurements taken on BSE images.

3.3.6 Electron Probe Micro Analyser (EPMA)

For the detailed cross-sectional analysis the samples were cut along the cross-section by keeping weld at center, mounted and polished as per the procedure already discussed in section 3.4.4 and subjected to EPMA analysis. The mounted samples were subjected to gold coating before performing the EPMA analysis. The elemental X-ray mapping was obtained for the critical area of interest on each sample. The selected area could have the three i.e. base sample, oxide scale and some epoxy region at the top of the scale. First Backscattered Electron Image (BSEI) was photographed and then elemental X-

ray mapping was taken for various elements. The elements selected for X-ray mapping were as per the composition of the base steels, type of coating and environment of study. Most of the EPMA analysis was done at Institute Instrumentation Centre (IIC), Indian Institute of Technology, Roorkee (India) on JXA-8600M microprobe.

For some of selected samples EPMA analysis was carried out and detailed analysis was made for distribution of oxygen and other elements in the scale and the substrate. Elemental line profiles were also obtained to understand the basic structure of the scale at Materials Division, BARC, Trombay (India) using Camaca SX100, 3 Wavelength Dispersive Spectrometer, France make.

CHAPTER 4

CHARACTERISATION OF WELDMENT

The chapter deals with micro structure and mechanical property determination of the weldments made by AISI 4140-AISI 304 by Friction Welding (FRW), Tungsten Inert Gas (TIG) and Electron Beam Weld (EBW). The results of metallographic examination of dissimilar weldment as well as the microhardness, impact toughness and tensile strength of as dissimilar weldments have been reported and discussed with respect to the existing literature.

4.1 FRICTION WELDING

4.1.1 Visual Examination

The Friction Welded dissimilar joints for four welding combinations are presented in Fig. 4.1. It can be observed that at lower burn-off length AISI 4140 undergoes less deformation as compared to AISI 304 but with increase in burn-off length this difference in the deformation decreases. At 12 mm burn-off both the steels show similar flash width. From these pictures it is also evident that the total flash width increases with increase in burn-off and the flash width is maximum in 12 mm burn-off welds. It is to be noted that at lower burn-off the flash on 4140 side exhibits edge cracks.

4.1.2 Macro structure

Macrographs for longitudinal cut sections for the welds are presented in Fig. 4.2. From these figures it is noted that the flash lips tend to attain curved shape with increase in burn-off length. The interface in all the friction welds is small. Curved deformation lines similar to those generally observed in forging flow lines are noticed in the AISI 304 steel adjacent to the weld interface. The interfaces in all welds are corrugated at the periphery while they are comparatively smoother in the centre region. The central regions of 7, 9 and 12 mm burn-off length welds contain distinct interface phase while the same is absent in 5 mm burn-off length weld.

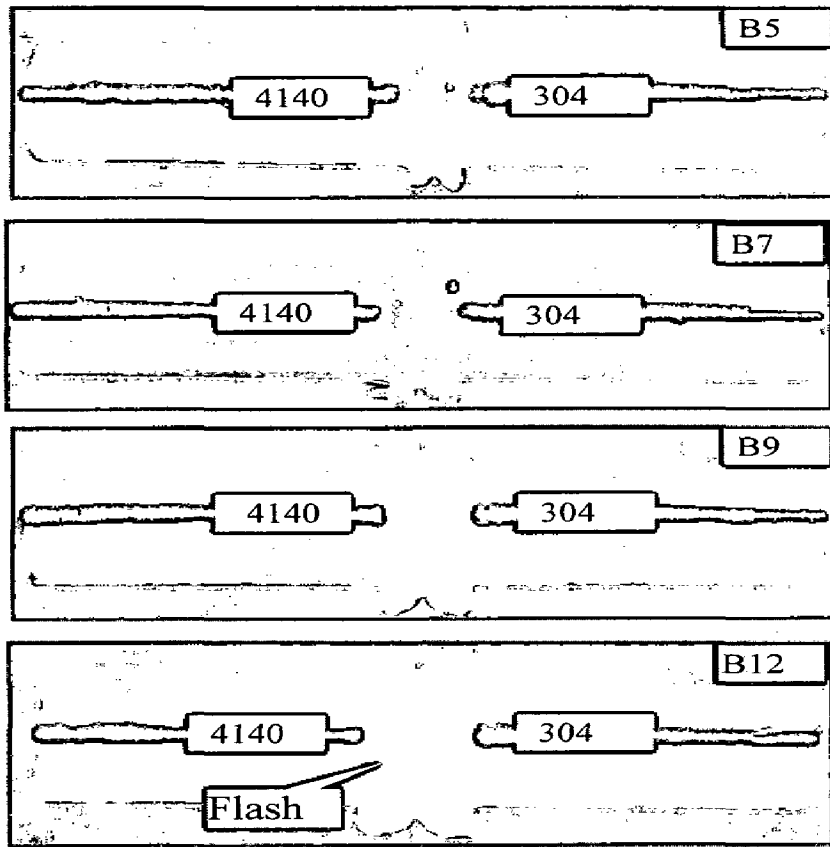


Fig 4.1 Friction welded specimen (Burn-off length B5, B7, B9 and B12)

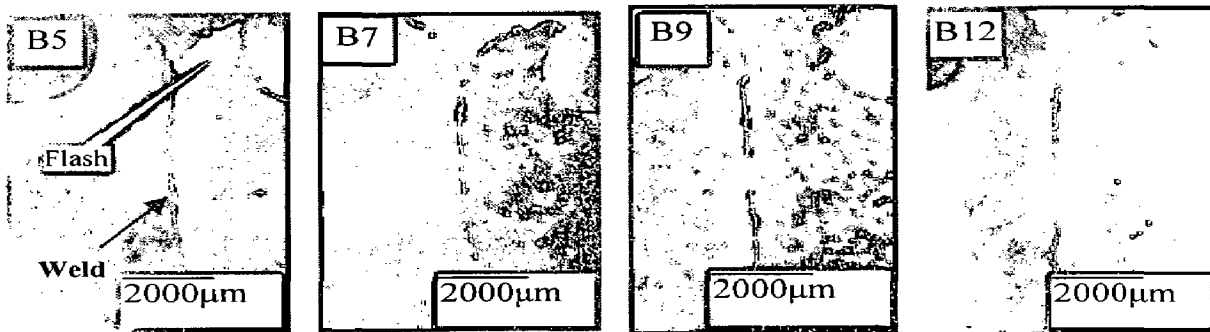


Fig 4.2 Effect of burn – off length on flash formation (Material on left side in the macrographs is AISI 304 stainless steel.) burn-off length: B5, B7, B9 and B12.

4.1.3 Microstructure

The microstructures from the centre and periphery regions of the welds are shown in Fig 4.3. The interface of centre regions of the weld of 5 mm burn-off length is nearly straighter while with increase in burn-off length the interface becomes irregular and the intermixing between 304 and 4140 steels increases. The microstructure of 4140 steel adjacent to the weld interface exhibits coarser features with increase in burn-off length. The peripheral regions of the welds exhibit greater degree of irregular interface. The interface is wavy in 5 and 7mm burn-off length welds while for 9 and 12 mm burn-off length welds exhibits alternate layers of 304 and 4140 steels implying extensive inter mixing of the steels with increase in burn-off length. It may be mentioned that in all the welds the microstructure of 4140 adjacent to the interface contains coarser martensitic features and the coarseness of these features increases with increase in burn-off length. This martensitic microstructure is comparatively coarser in the peripheral regions of the welds than in the centre regions of the welds.

In Fig. 4.4 the microstructures in different regions of AISI 304 stainless steel by keeping 12 mm burn-off length weld are shown. Extensive grain growth with well developed grain boundaries are noted adjacent to the weld interface and by the side of this region there predominant precipitation observed along the grain boundaries. In Fig. 4.4 gives the microstructures of central and peripheral regions of 12 mm burn-off welds in as-welded condition. Prominent deformation bands are noted in AISI 304 stainless steel side adjacent to the interface.

4.1.4 XRD ANALYSIS

X-Ray Diffraction studies were carried out to analysis the phases formed on dissimilar weldment in as welded condition for 5, 7, 9 and 12mm burn-off length as shown in Fig 4.5 (a) and 4.5 (b). As welded condition, high intensity peaks of FeNi and Ni_3C have been observed with for 5 mm burn-off length. At 7 mm burn-off length many intermetallics (FeNi, Cr-Ni-Mo and CrNiFe) and carbides (Ni_3C , Cr-Si-C etc.,) were indicated.

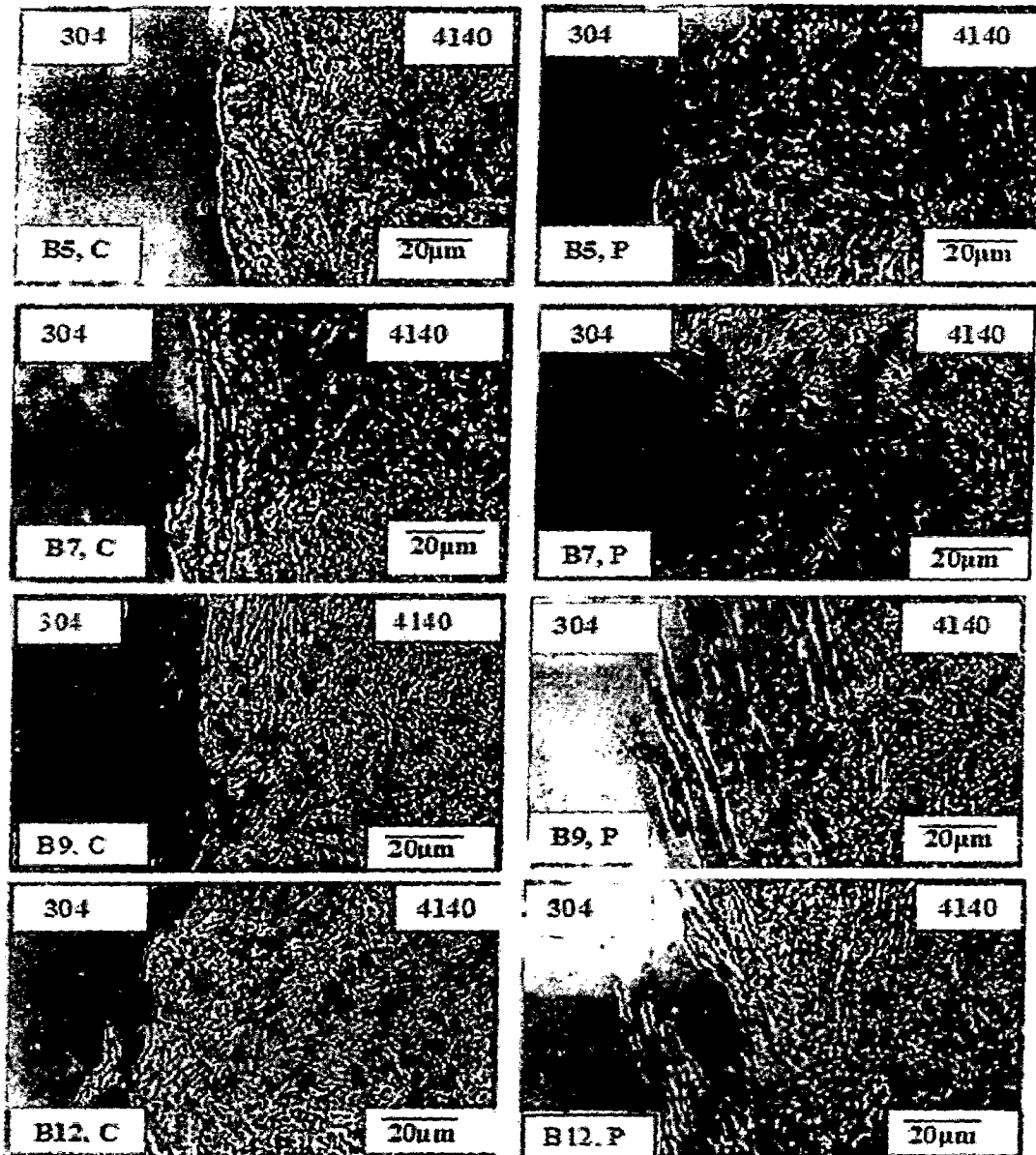


Fig 4.3 Microstructure at centre and periphery of the friction weld joint for B5, B7, B9 and B12. (B-Burn off length in mm)

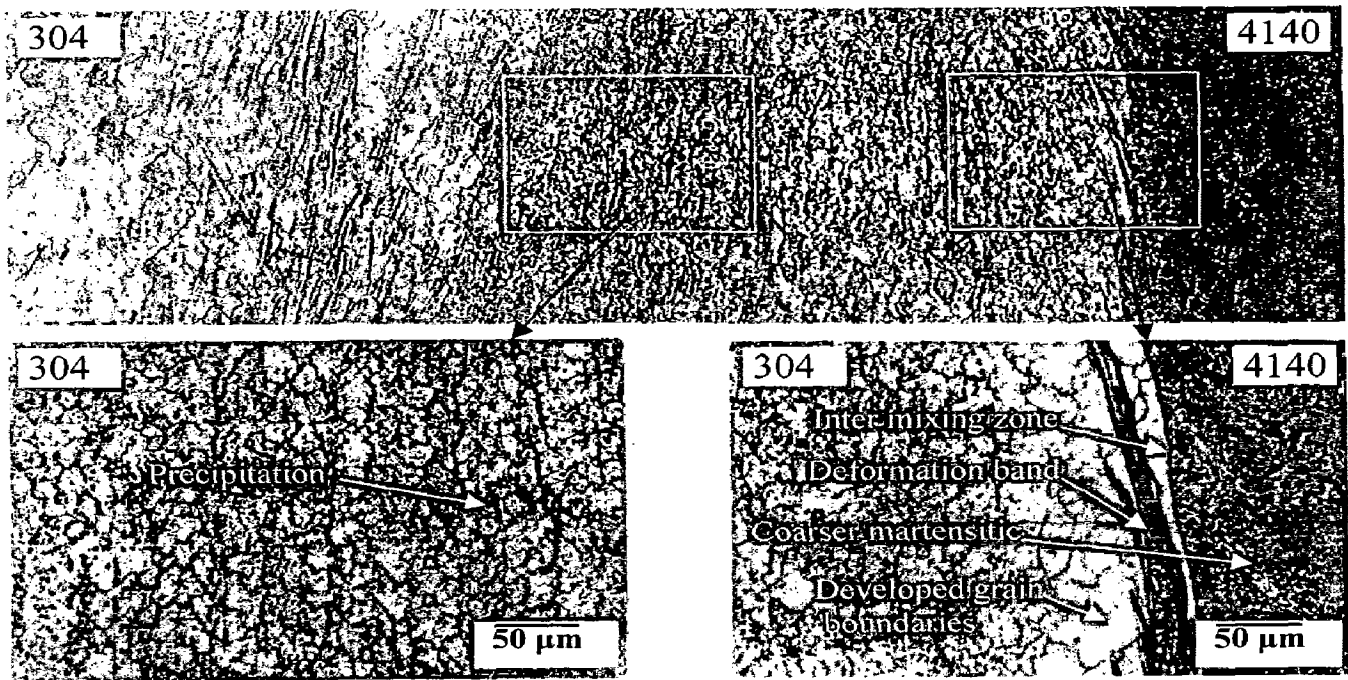


Fig 4.4 Microstructures in different regions of AISI 304 in burn-off length 12

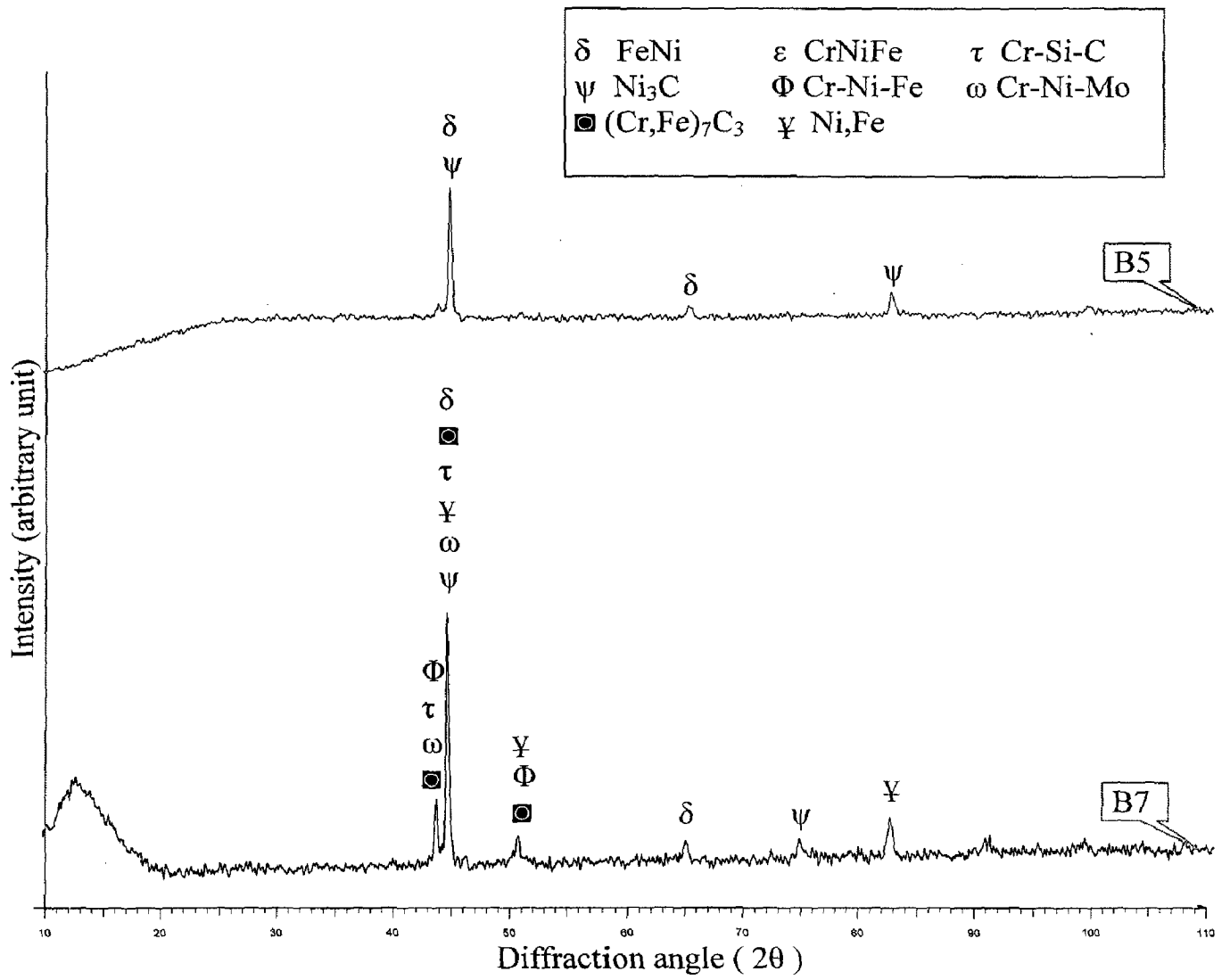


Fig. 4.5(a) X-Ray diffraction patterns for friction weldment as welded condition burn-off length B5 and B7

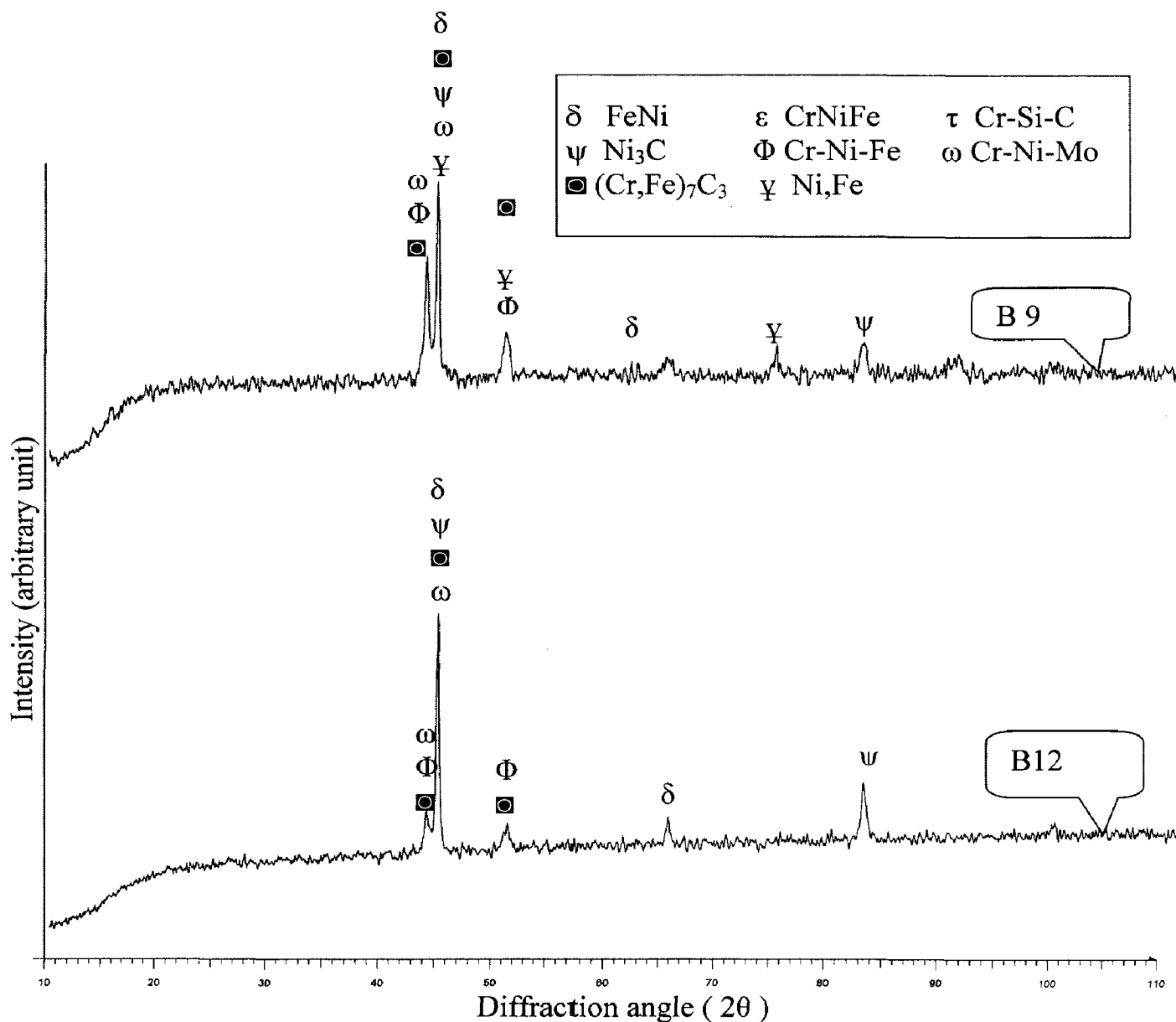


Fig. 4.5(b) X-Ray diffraction patterns for friction weldment as welded condition
Burn-off length B9 and B12

4.1.5 Electron probe micro analysis

The influence of burn-off length in case of 5 and 12 mm burn-off length welds on elemental distribution across the welds is shown in Fig. 4.6. From these figures it is observed that chromium and nickel diffuse towards low alloy steel from the stainless steel and diffusion of iron from low alloy steel side towards stainless steel. The extent of diffusion is more in case of 12 mm burn-off length welds. A distinct weld region with enrichment of chromium, nickel and iron develops in 12 mm burn-off length welds. This weld region exhibits nearly similar composition without much compositional gradient, while a similar region in 5 mm burn-off length welds exhibits compositional gradient.

4.1.6 Micro Hardness

The hardness data across the welds in the central region for the four parameter combinations are presented in Fig. 4.7 (a, b). In general the weld interface is harder than the respective parent metals. In the interface region two high hardness peaks are seen with lower hardness region between them. In general, maximum hardness peak is observed on the stainless steel side, while the other second hardness peak is in the low alloy steel side. Lower hardness in between the two peaks is also located in the low alloy steel side. However, it may be added that only one maximum hardness is observed in 5 mm burn-off length welds. This weld does not contain any low hardness region in the low alloy steel side adjacent to the interface. These observations are consistent with the distinct interfaces observed in higher burn-off length welds and may be due to decarburization.

It may also be added that the peak hardness increases with increase in burn-off length. Whereas the hardness values an adjacent low alloy steel further falls with an increase in burn-off length (Table 4.1). It may be noted that with increase in burn-off length a soft region appears on the stainless steel adjacent to the interface. In general, the width of the hardened region also decreases with increase in burn-off length. The formation of soft region of low alloy steel side can be attributed to decarburization while on the stainless steel it is thought to be due to softening of the material due to heat buildup as a result of low thermal conductivity of the material. The reduction in the width of hard zones is due to loss of material in the form of flash with increased burn-off length. The peak hardness at the interface and reduces overall hardness as

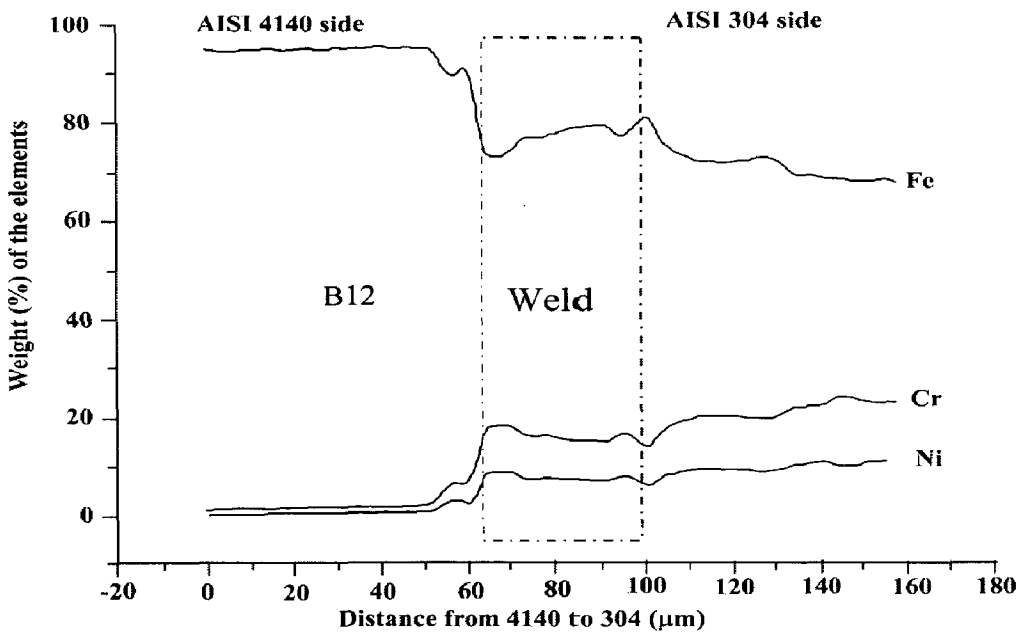
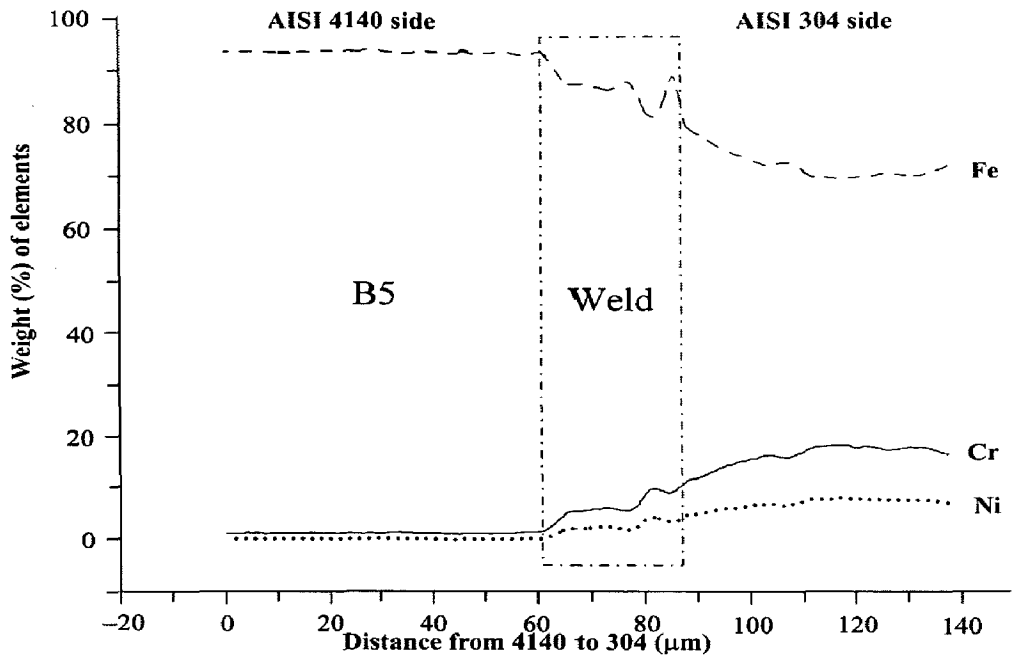


Fig 4.6 Elemental distribution across the weld centre in 4140-304 weld joint (B5 and B12)

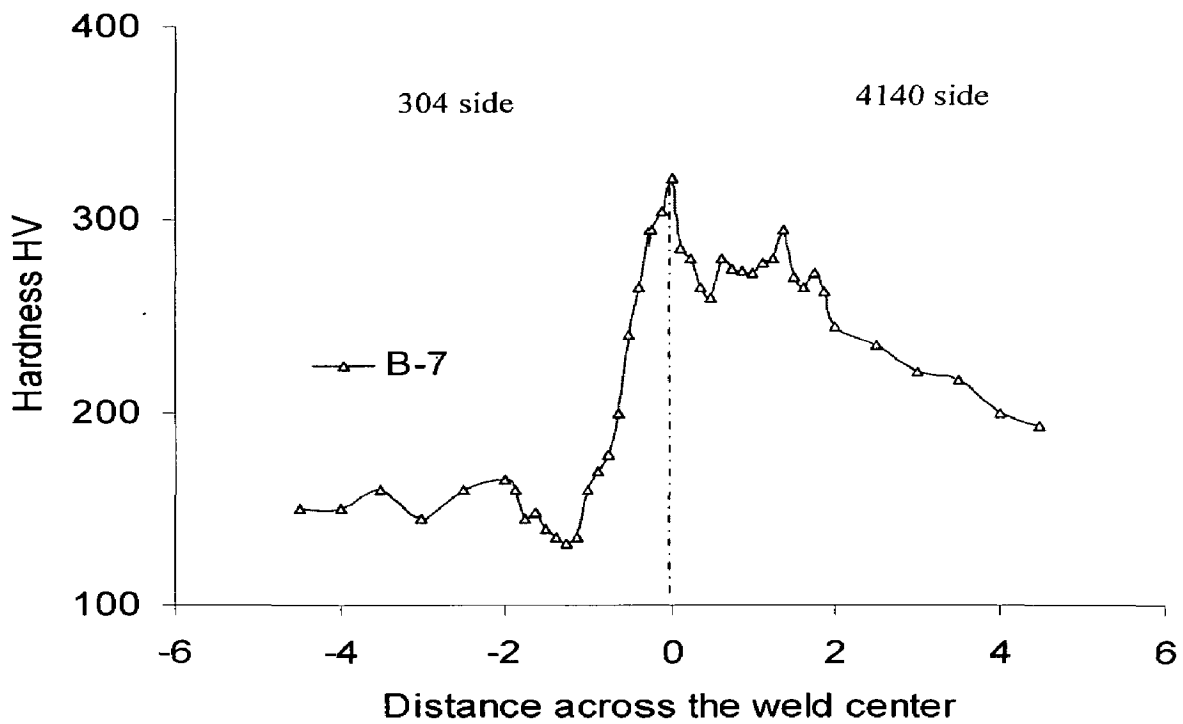
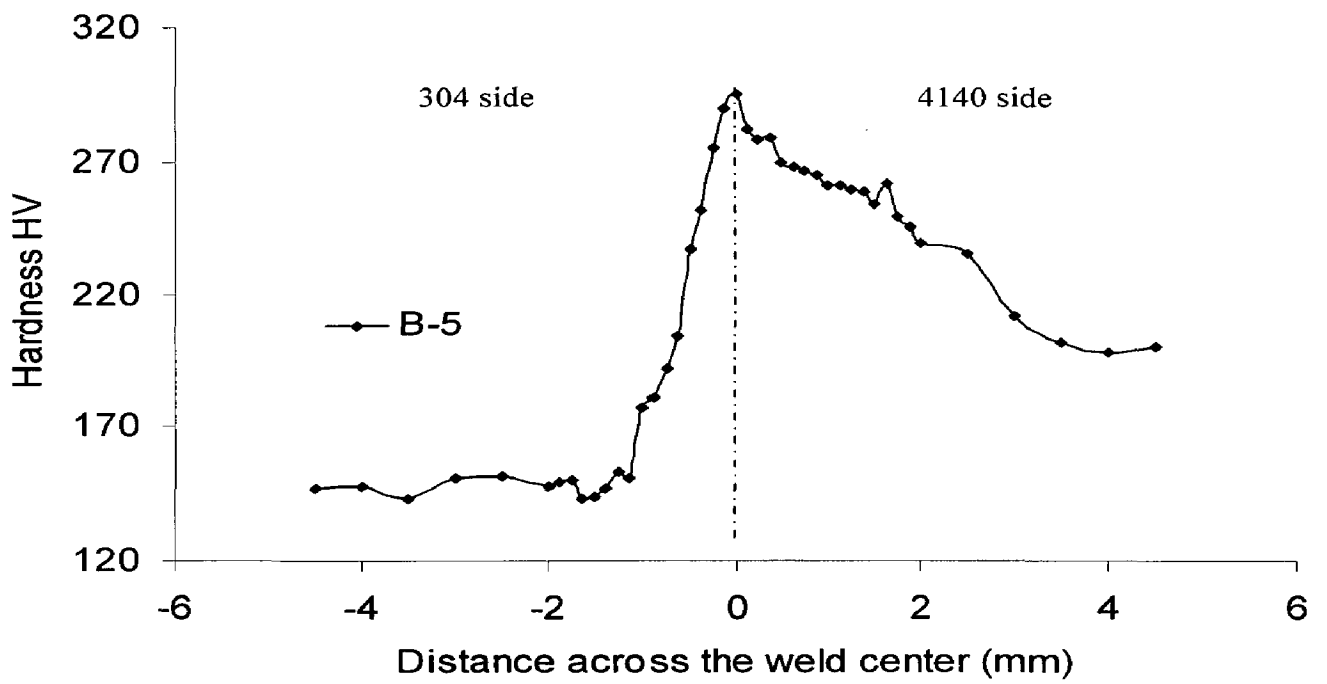


Fig.4.7 (a) Effect of burn-off length (B5 and B7) on hardness distribution across the weldment.

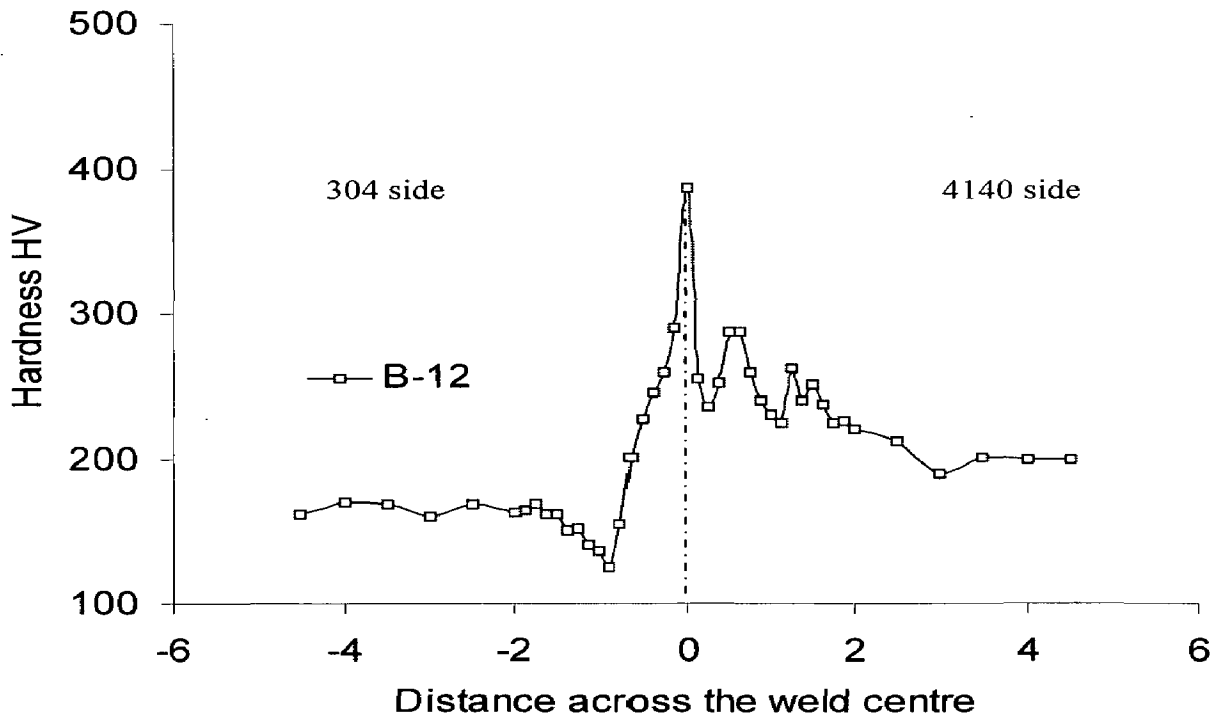
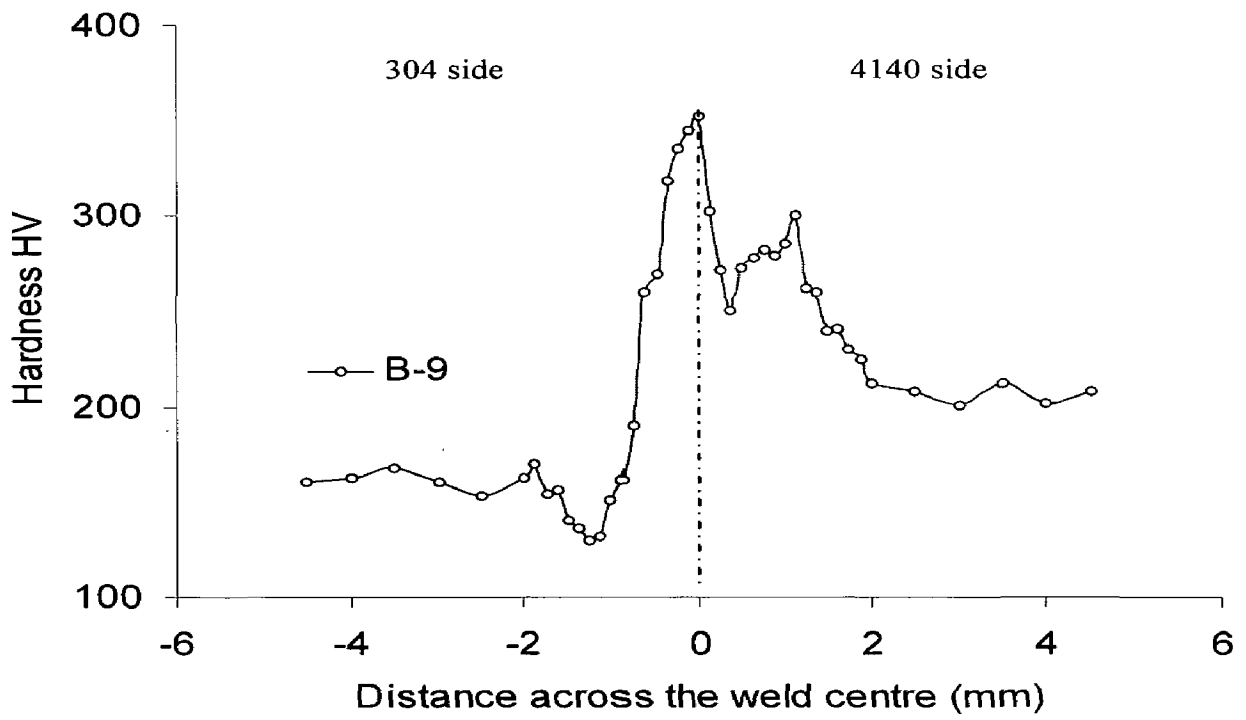


Fig.4.7 (b) Effect of burn-off length (B9 and B12) on hardness distribution across the weldment.

well as soft zone hardness on the low alloy steel side of the interface (Table 4.1). This behavior can be attributed to carbon migration from the low alloy steel side to stainless steel side.

Table 4.1 Data on maximum hardness at the interface and minimum hardness in the low alloy steel adjacent to the interface.

Joint	Max. Hardness (Hv, 100gms) at the interface	Min. Hardness (Hv, 100 gms) on low alloy steel side of interface
B5	305	276
B7	322	262
B9	351	249
B12	386	238

4.1.7 Impact Toughness

The impact toughness data of welds is presented in Table 4.2. The table depicts impact toughness of parent metals also. From the data it is observed that there is reduction in toughness with increase in burn-off length.

In general the impact toughness values are lower than those of low alloy steel in the as received condition (65J). At the lowest burn-off length at the 5 mm the impact toughness is around 40% of the parent metal while, at the highest burn-off length 12mm it is as low as 10J, which is 1/6th of the parent low alloy steel.

Table 4.2 Effect of burn-off length on impact strength:

Joint	Impact Strength, J
AISI 304 Base	210,215
AISI 4140 Base	65, 67
FRW-B 5	24,26
FRW-B 7	20,22
FRW-B 9	15, 16
FRW-B12	10, 11

Fractographs of parent metals AISI 304 and AISI 4140 are presented in Fig. 4.8. Fig. 4.8 show predominantly well developed micro void ductile fracture features

in AISI 304, while AISI 4140 steel exhibits quasi cleavage fracture with small facets and smaller facets embedded within the small facets.

Fractographs of the impact tested specimens of welds are presented in Fig. 4.9 (a, b). As-welded condition exhibit predominantly cleavage fracture with an increase in cleavage facet size with increase in burn-off length. In 12 mm burn-off length welds long facets and with some areas showing microvoid features. Increase in facet size indicates low energy fracture and supports the decrease in toughness with increase in burn-off length. The elongated facet features observed in the fractographs support the lowest toughness obtained for 12 mm burn-off length.

4.1.8 Tensile Testing

The tensile strength of welds presented in Table 4.3. From the data it is observed that yield stress decreases with increase in burn-off length 12mm.

In general the yield stress values for all the friction welded samples are more than those of low alloy steel in the as received condition (417 MPa).

Table 4.3 Effect of burn –off length on tensile strength

Burn off length	Proof Stress (MPa)	Max Stress (MPa)	Ext. Yield (%)
B-5.1	301.8	487.2	18.15
B-5.2	308.9	483.4	17.97
B-7.1	283.2	496.5	18.89
B-7.2	277.4	490.9	18.33
B-9.1	287.6	472.7	15.20
B-9.2	299.5	476.0	17.15
B-12.1	291.3	474.8	18.30
B-12.2	286.0	478.0	17.86

The photograph of tensile tested specimen of friction welded AISI 304 and AISI 4140 are presented in Fig. 4.10. Fractographs of friction welded AISI 304 and AISI 4140 with different burn off length are presented in Fig. 4.11- 4.14, shows predominantly well developed micro void ductile fracture features in the weldment for all the burn off lengths. From the data it was observed that no much variation in yield stress and the stress Vs strain curve shown in Fig 4.15.

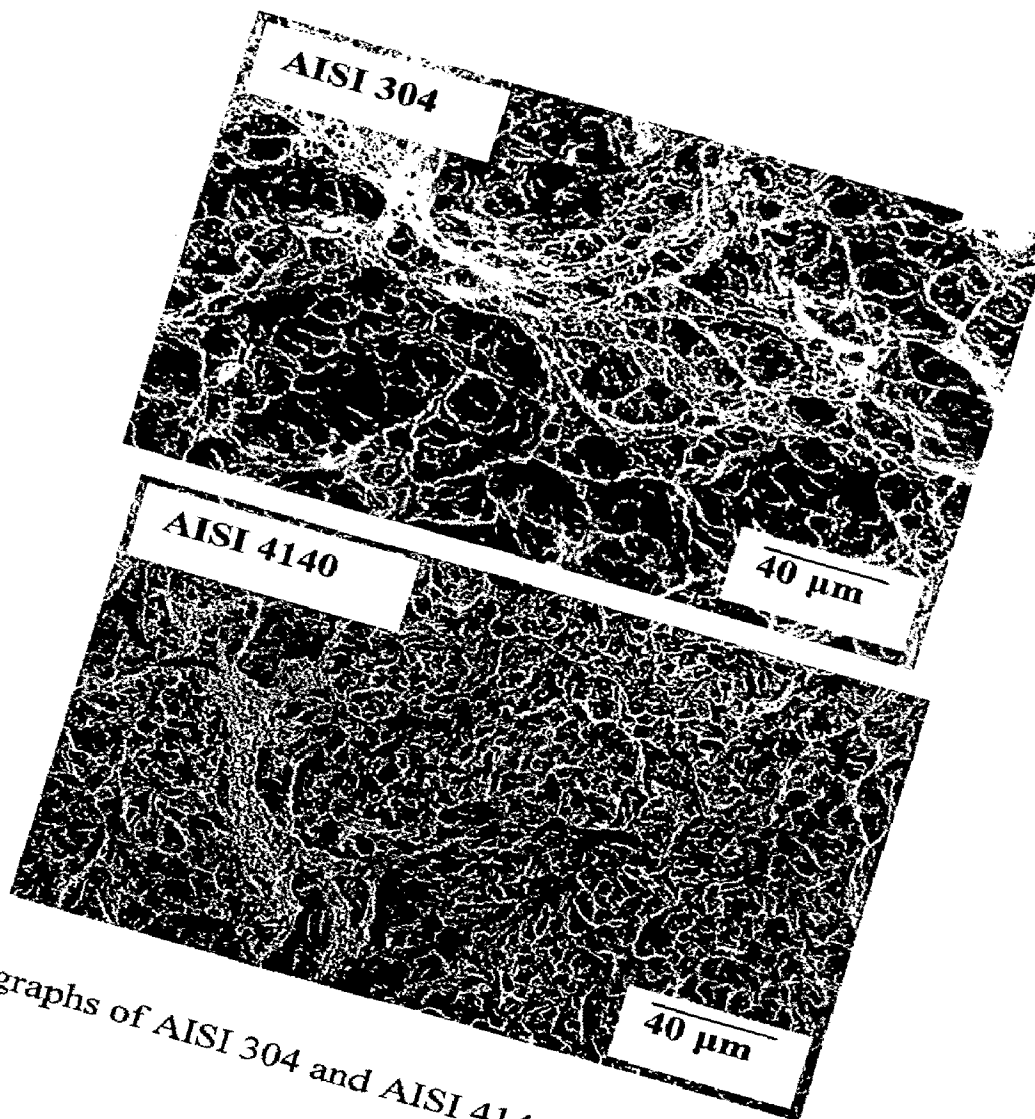


Fig 4.8 Fractographs of AISI 304 and AISI 4140 parent metal at the center

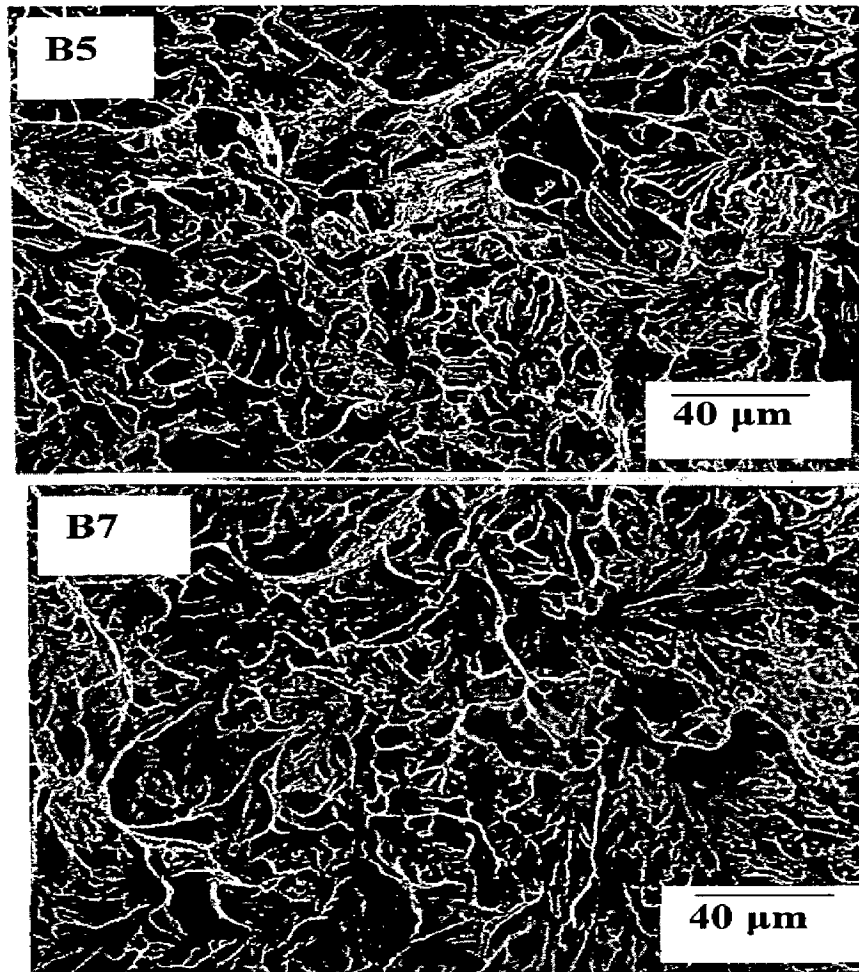


Fig 4.9 (a) Fractographs of 304 - 4140 weld, B5, B7 at the center (Burn-off length 5, 7 mm)

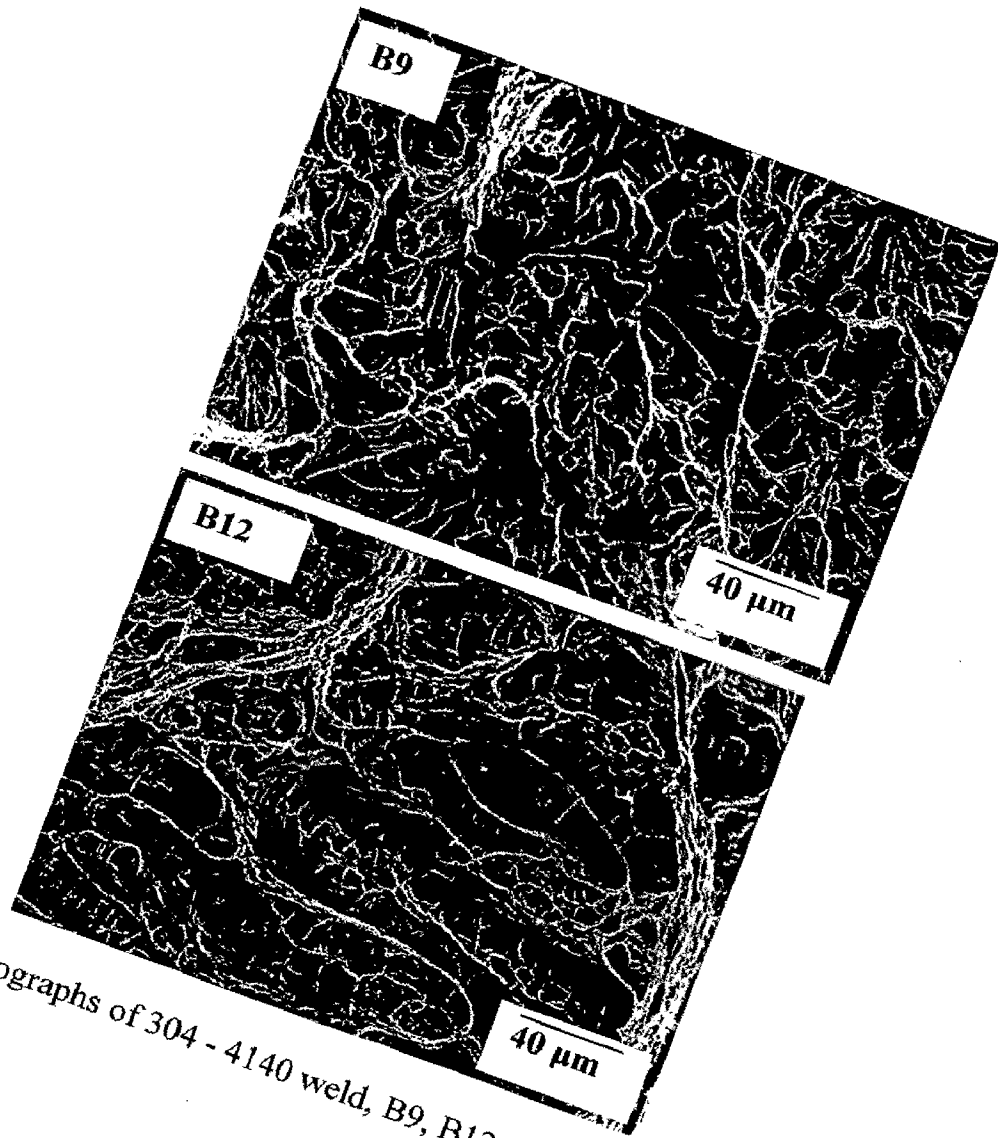


Fig 4.9 (b) Fractographs of 304 - 4140 weld, B9, B12 at the center (Burn-off length 9, 12 mm)

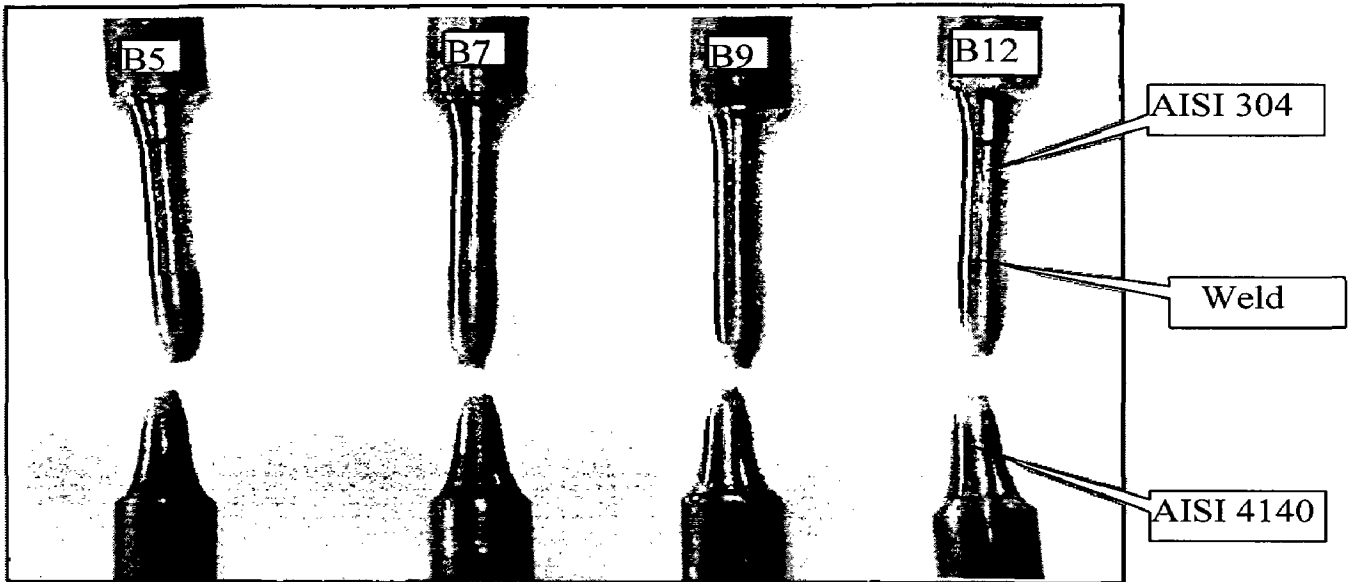


Fig 4.10 Photograph for fractured tensile specimen of friction welded specimen

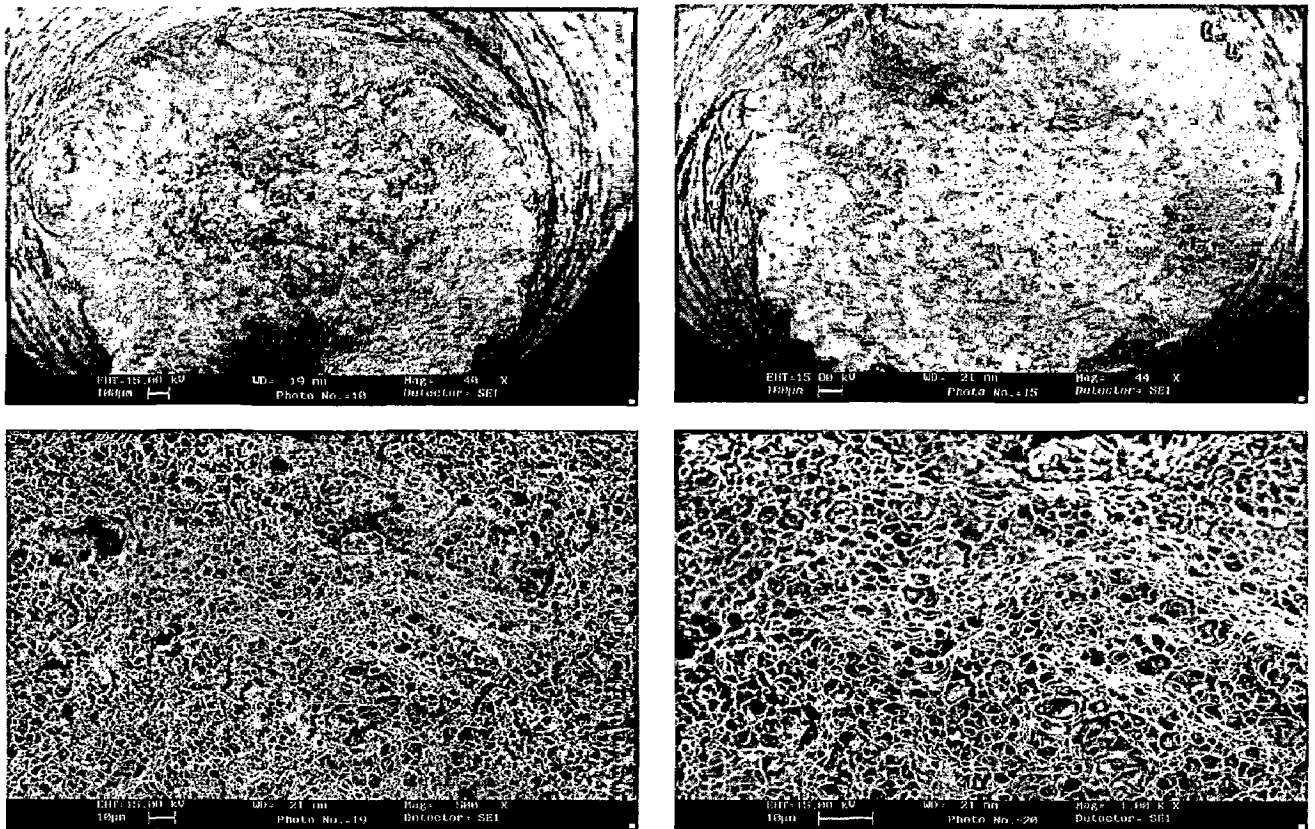


Fig 4.11 Tensile Fractographs of friction welded AISI 304 and AISI 4140 by keeping burn off length 5 mm.

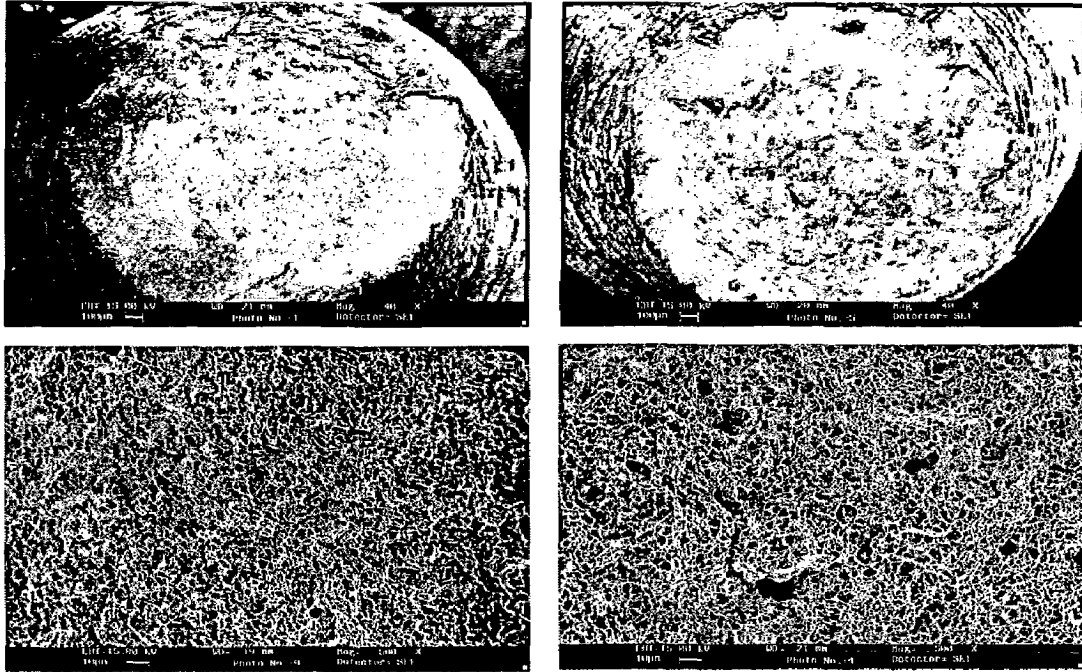


Fig 4.14 Tensile Fractographs of friction welded AISI 304 and AISI 4140 by keeping burn off length 12 mm.

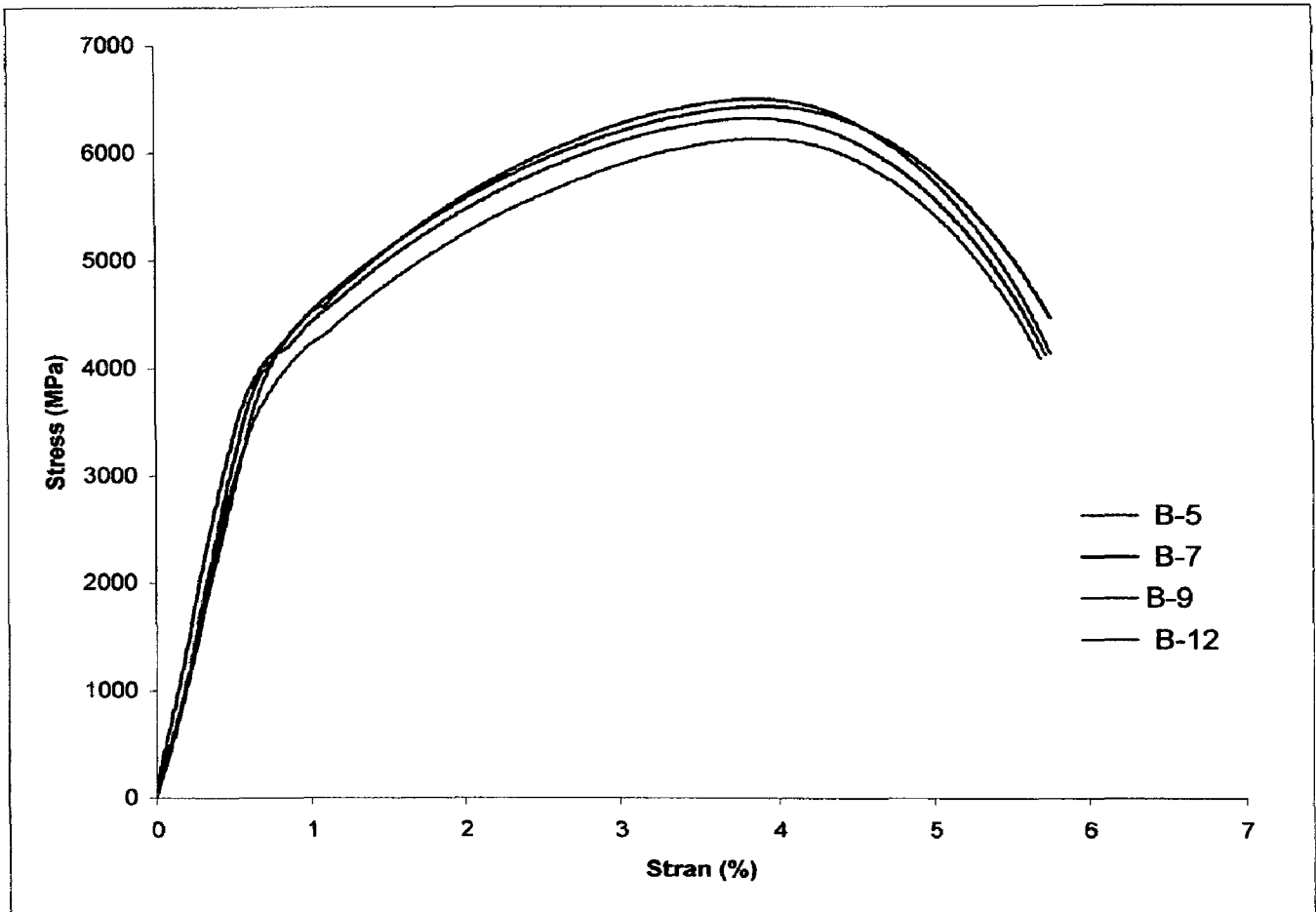


Fig 4.15 Stress Vs Strain curve for tensile specimen for friction welded AISI 4140 and AISI 304

4.1.9 Discussions

Investigation on the effect of burn-off length on mechanical properties of AISI 4140-AISI 304 dissimilar welds revealed that in general the toughness of these welds is very low while the hardness is high. The inverse relation between hardness and toughness is as per the established trends. The reduction in toughness and increase in hardness with increase in burn-off length may be attributed to increased carbon migration from the low alloy steel side towards stainless steel due to increase temperatures that prevail around the interface region with increase in burn-off length. Increased burn-off length leads to increased friction time that aids in raising the temperature of the surroundings of the interface [C.J.Cheng (1963), KK.Wang (1975)]. This condition promotes diffusion of elements. The soft zone observed on the low alloy steel side is mainly due to carbon depletion. Whereas carbon enrichment on stainless steel side leads to high hardness due to carbide formation. These microstructure features are mostly responsible for the low toughness observed in these welds. The elemental migration would increase with increased burn-off length, due to high temperatures prevailing under these conditions. Elemental distribution across the interface and predominantly cleavage fracture features suggest interdiffusion of elements leading to brittle microstructure features responsible for the low ductility quasi cleavage fracture.

Under the given welding conditions, the AISI 4140-AISI 304 dissimilar FRW revealed sound welds without any cracks. The measured value of hardness is in good agreement with previous findings by other researchers [Yenni C et al (1996), Cam G et al (1998)]. Also the hardness at the weld interface obtained in the present study is less than one reported for laser beam welding [Cam G et al (1999)]. This may be attributed to lesser tendency of carbide precipitation and intermetallics formation in the weld region of FRW weldments. The soft zone observed on the low alloy steel side can be ascribed to carbon depletion whereas enrichment of stainless steel side results in hard and brittle carbide formation (Fig. 4.7), which is also supported by Kuchuk and Lippold J.C. et al [Kuchuk (1990), Lippold J.C(1984)]. Increased burn-off length is equivalent to increased friction time that aids in migration of Fe, Ni and Cr with rise in the temperature of the surroundings of the interface. The higher hardness at weld interface may be due to enrichment of this zone with Fe, Ni and Cr

and subsequent formation of intermetallic FeNi / CrNiFe which is also supported by EPMA and XRD (Fig 4.5 and 4.6) which also supported by C.D. Lundin (1982), K.G.K. Murti et al (1985), R. Viswanathan (1982). Elemental distribution across the interface and predominantly cleavage fracture features suggest that inter-diffusion of elements has lead to creation of brittle microstructure features responsible for the low ductility quasi cleavage fracture (Fig 4.14). Similar observation has been made by Cheng C.J and Wang K.K [Cheng C.J (1963), Wang K.K (1975).

At lower burn-off length the weldment attains to lower interface temperature at which metal starts getting extruded resulting in less susceptibility to formation of intermetallics and carbide precipitation. Whereas with increase in the burn-off length, the welding time is increased thereby allowing more time for precipitation of carbide and intermetallics compound which may lead to reduced corrosion resistance as also has been suggested by Hasue et al (1968).

4.2 ELECTRON BEAM WELDING

4.2.1 Visual Examination

The Electron Beam Welded dissimilar joints are presented in Fig 4.16. From the joints it is observed that the heat affected zone on the AISI 4140 is wider as compared to AISI 304 side. The width of the weld zone is wider than that of friction welded specimens.

4.2.2 Macrostructure

Electron beam welded AISI 4140 and AISI 304 weldment represents nail-shaped penetration. The macrograph of weld cross-sections is shown in (Fig 4.17) that the deep and narrow fusion zone can be obtained when the focal location is slightly above the surface of work piece. The HAZ on AISI 304 is thinner as compare to one of AISI 4140 side.

4.2.3 Microstructure

The microstructure of the dissimilar weld at five different regions is depicted in Fig.4.18. From the AISI 304 side, HAZ (304), weld, HAZ (4140) and AISI 4140

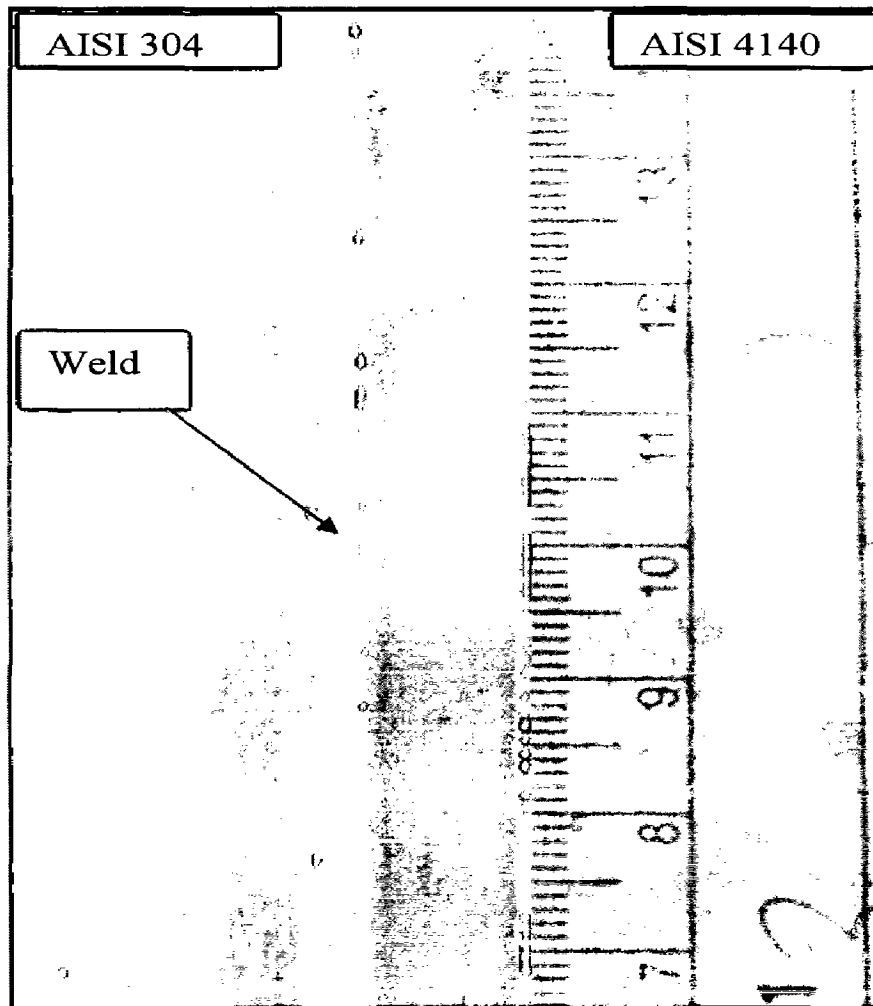


Fig 4.16 photograph of Electron Beam Welded specimen

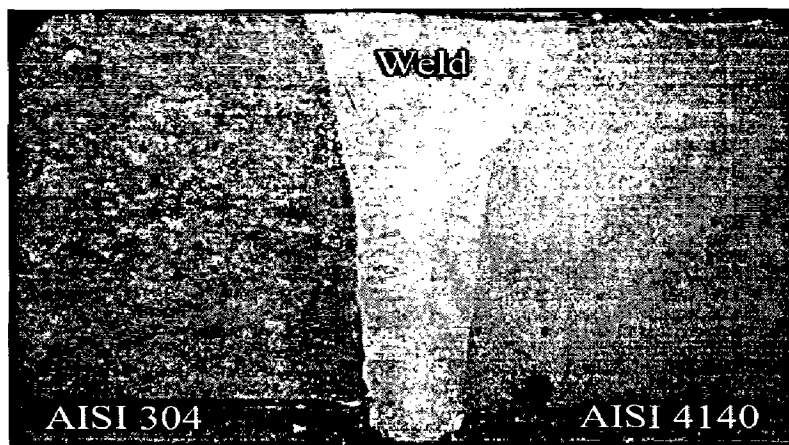


Fig 4.17 Macro structure of electron beam welded AISI 4140 and AISI 304 dissimilar metals.

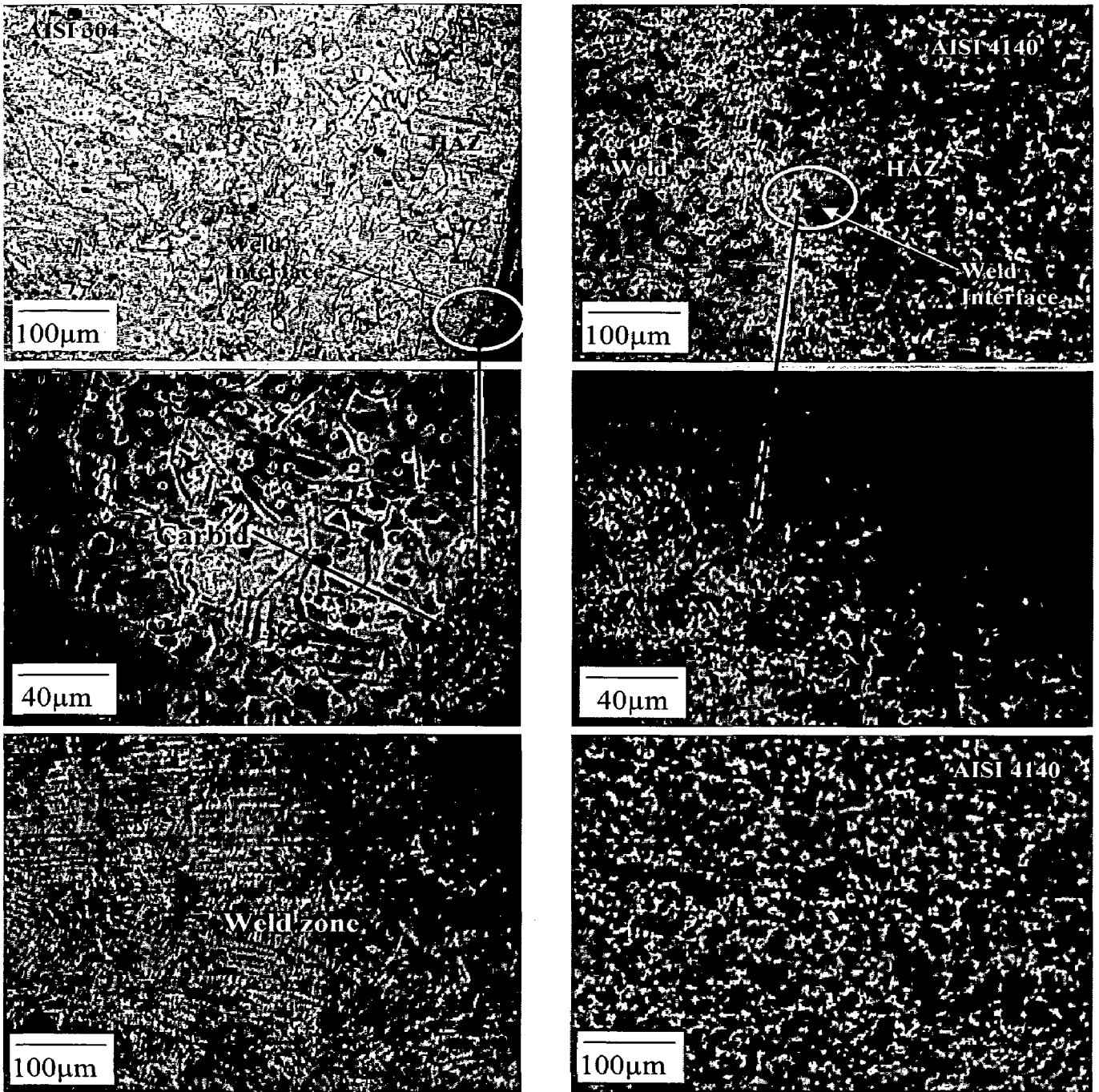


Fig 4.18 Microstructure of electron beam welded dissimilar AISI 4140 and AISI 304 metals

shows changes in microstructure. The microstructure of the low alloy steel side is expected to be ferritic and pearlitic. On the austenitic side, it mainly shows twin structure with mixtures of austenite and some ferrite. The regions that have large amounts of Cr and Ni have mainly an austenitic-ferritic structure. The micro structural changes occurring in the HAZ at the low alloy steel side depend on the kinetic formation of austenite and its grain size according to the continuous cooling transformation.

The microstructure of the austenitic steel close to the weld interface shows evidence of the small amount of grain recrystallization that took place during the welding process. Also revealed was a little carbide precipitation, this despite the fact that the austenitic steel has a relatively low carbon content and a high cooling rate was applied to the austenitic side. At the weld interface on the low alloy steel side the microstructure was coarse, and contained malformed lamellae of pearlite. In addition, there was a lot of variation in grain size in the HAZ of the low alloy steel, caused by variations in cooling rate. A comparison of different zone of the weldment indicates that the microstructures in the interface are extremely heterogeneous and observed dendrite structure. Although only small areas contain excess phases exist along the fusion line in the both side of weld metal.

4.2.4 XRD Analysis

X-Ray Diffraction studies were carried out to analysis the phases formed on dissimilar electron beam weldment in as welded condition as shown in Fig 4.19. As welded condition, $(Cr,Fe)_7C_3$ and Cr-Ni-Mo have been observed with high intensity peaks with Ni_3C , FeNi etc., in as low intensity peaks

4.2.5 Electron Probe Micro Analysis

The elemental distribution line profile across the welds is shown in Fig. 4.20. From these figures it is observed that the chromium and nickel diffuse across the weld towards low alloy steel side. Whereas iron diffuses from low alloy steel side towards stainless steel.

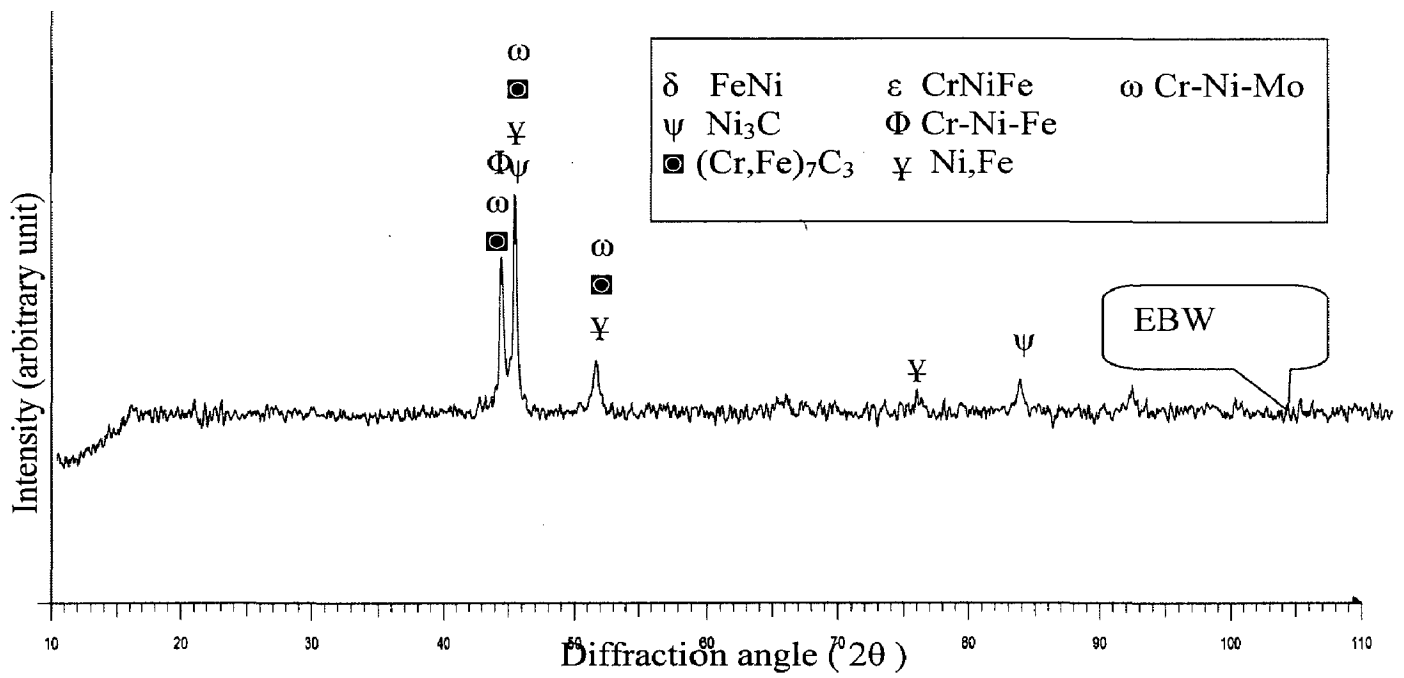


Fig. 4.19 X-Ray diffraction patterns for Electron Beam weldment as welded condition.

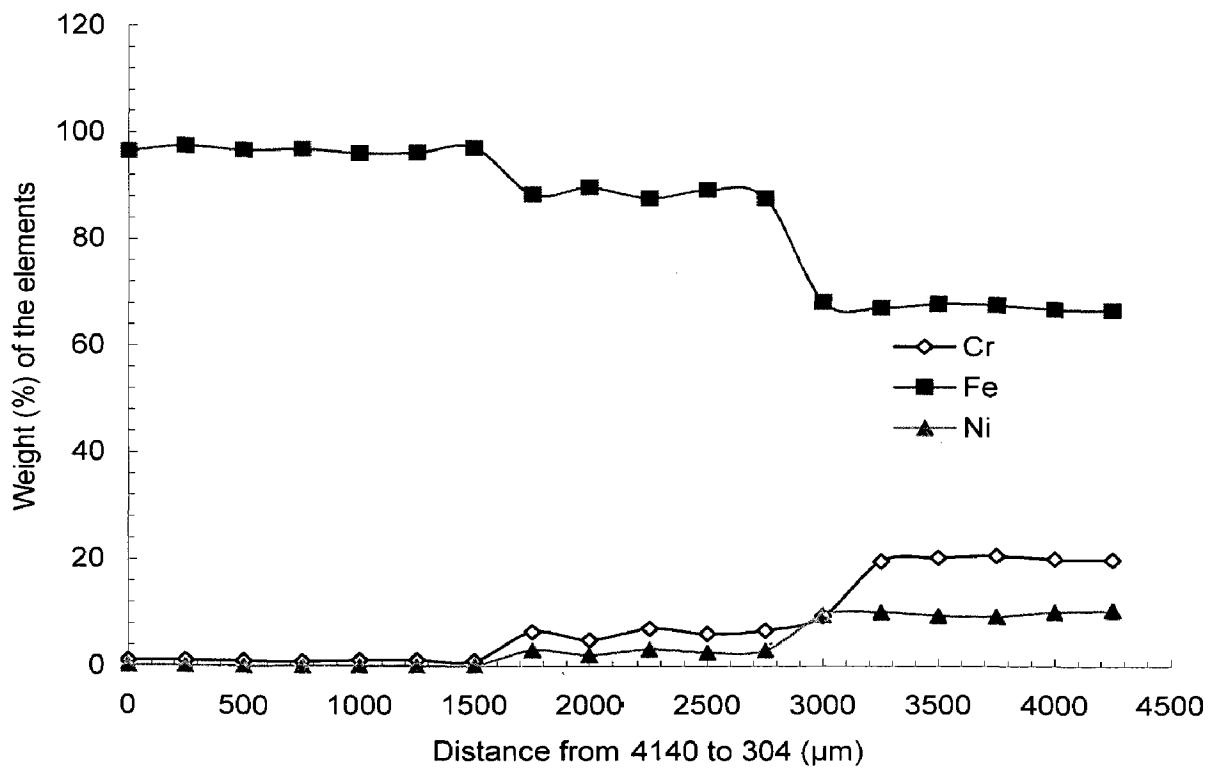


Fig 4.20 Elemental distribution across the weld centre in 4140-304 of Electron Beam Weld joint

4.2.6 Micro Hardness

Hardness distribution across the Electron beam welded AISI 4140 and AISI 304 dissimilar metals are presented in Fig 4.21. The hardness of the weld region is in the range 600 Hv (min) to 700 Hv (max).

4.2.7 Impact Toughness

The impact toughness of dissimilar weldment of AISI 4140 and AISI 304 made by electron beam welding technique were shown in table 4.4 welds. The photograph of impact tested specimen of electron beam welded AISI 304 and AISI 4140 are presented in Fig. 4.22. From the data it is observed that the toughness in the range of 18 to 23 J. Fractographs of the impact tested specimens of welds are presented in Fig. 4.23 (i-iii). In all the case the dimple structure (ductile fracture) was observed.

Table 4.4 V notch Impact strength for Electron Beam Welded dissimilar metals:

Joint Trial	Impact Strength, J
EBW-1	22
EBW-2	23
EBW-3	18

4.2.8 Tensile Testing

The tensile strength of welds made by EBW presented in Table 4.5. In general the yield stress values are more than those of low alloy steel in the as received condition (417 MPa).

Table 4.5 Tensile strength of Electron Beam Welded AISI 4140 and AISI 304

Weld Trial	Proof Stress (MPa)	Max Stress (MPa)	Ext. Yield (%)
EBW-1	585	693	21.64
EBW-2	494.3	670	38.88
EBW-3	508	681	35.40

The photograph of tensile tested specimen of Electron Beam welded AISI 304 and AISI 4140 are presented in Fig. 4.24. In all the sample the fracture occurred on the heat affected zone of AISI 4140 side and the range of yield strength (670 to 693

MPa) were noted. Fractographs of Electron Beam welded AISI 304 and AISI 4140 by keeping different magnification are presented in Fig. 4.25 and 4.26. Fig. 4.25 and 4.26 showed predominantly well developed micro void ductile fracture features in the weldment made by Electron Beam Welded specimen. The stress Vs strain curve shown in Fig 4.27.

4.2.9 Discussions

The results of this evaluation indicate the autogenous welding of dissimilar metals of AISI 4140 and AISI 304 by electron beam welding technique can produce satisfactory joints in terms of weldability and room temperature mechanical properties. However autogenous welding is not considered to be suitable for this type of joints in terms of service properties, particularly in the weld metal. The fractography shows that with both tensile and impact toughness test ductile fracture is obtained. Since the failure of tensile specimen at the HAZ on AISI 4140 side, the weld strength is equal or more than 693 (MPa) and the maximum impact toughness (23 J) were noted. Dendrite region observed in weld zone which is supported by (Sun Z et al (1994)) who also reported that austenitic is absent in autogeneous welding. The microhardness curves in Fig. 4.21 indicate that some oscillation in microhardness occurs and that this varies with the different zone of the weldment. Higher hardness indicate the enrichment of C, Cr, Ni, and Fe which may be leading to precipitation of carbide and formation of intermetallic compounds at interface which is further supported by EPMA and XRD analysis.

The reasons that no weld cracking was found in this study may be partly due to the good crack resistance and the welding conditions provided in electron beam welding. Sufficient mechanical properties at elevated temperature are important for this dissimilar joint due to their operating condition. Furthermore, it has been reported that electron beam welded 2.25 Cr-1 MO and 1.25 Cr-0.5 MO similar steel joints possess satisfactory strength at both room and elevated temperatures, i.e. all the fractures occurred in the base metals (Kita et al (1987)). However the capital and running cost of equipment is much higher for electron beam welding. Electron beam welding of AISI 4140 and AISI 304 joints can provide several advantages. These include low distortion, less residual stresses, smaller HAZ and fusion zone, high

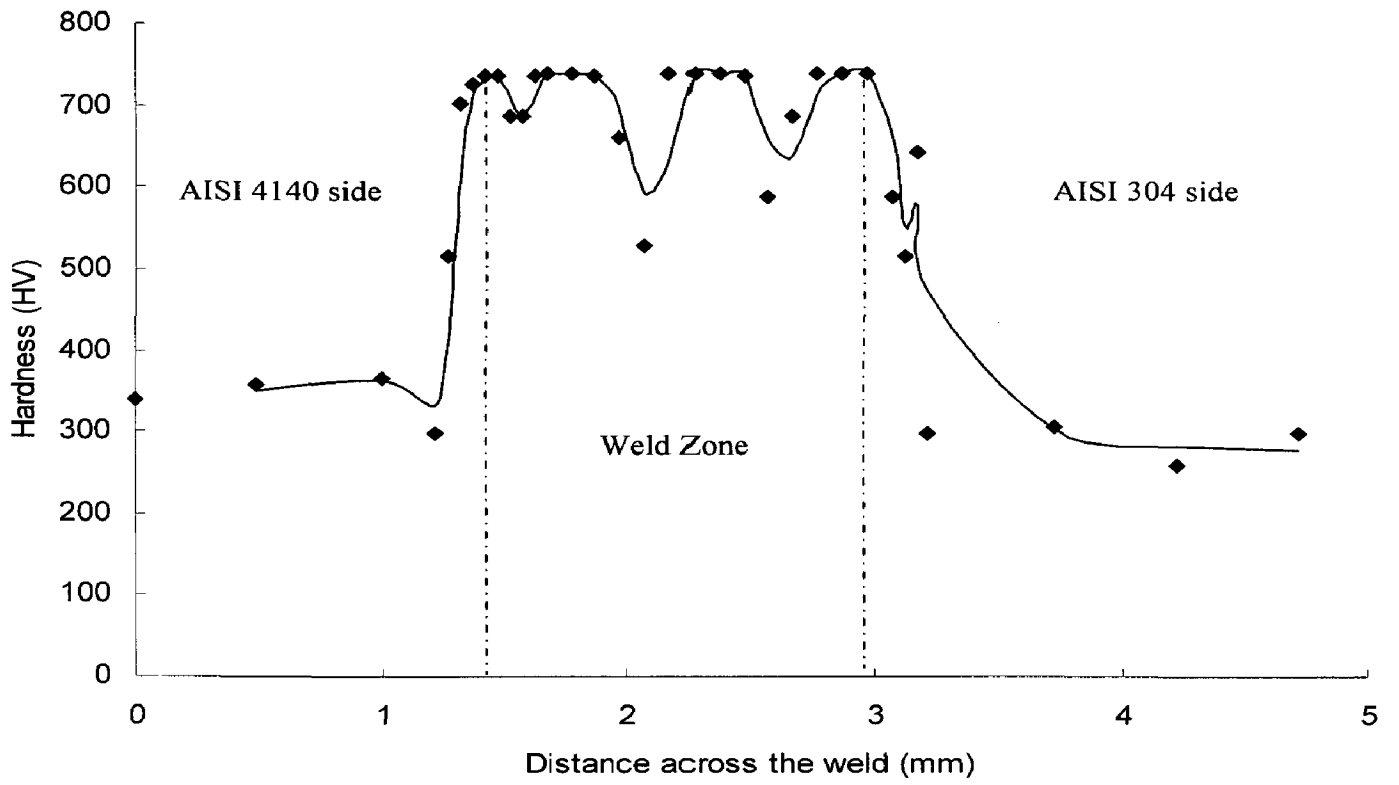


Fig 4.21 Hardness distribution across the EBW weldment of AISI 4140 and AISI 304

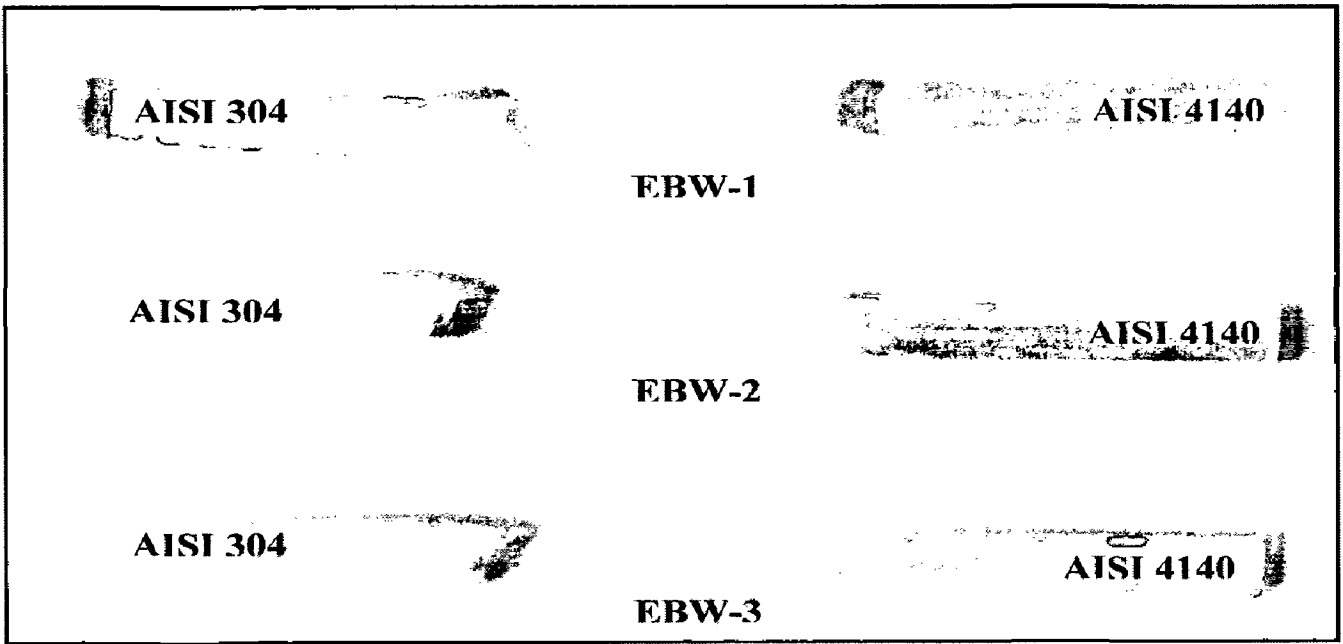


Fig 4.22 Photograph of Charpy 'V' notch tested sample for Electron Beam Welded Sample

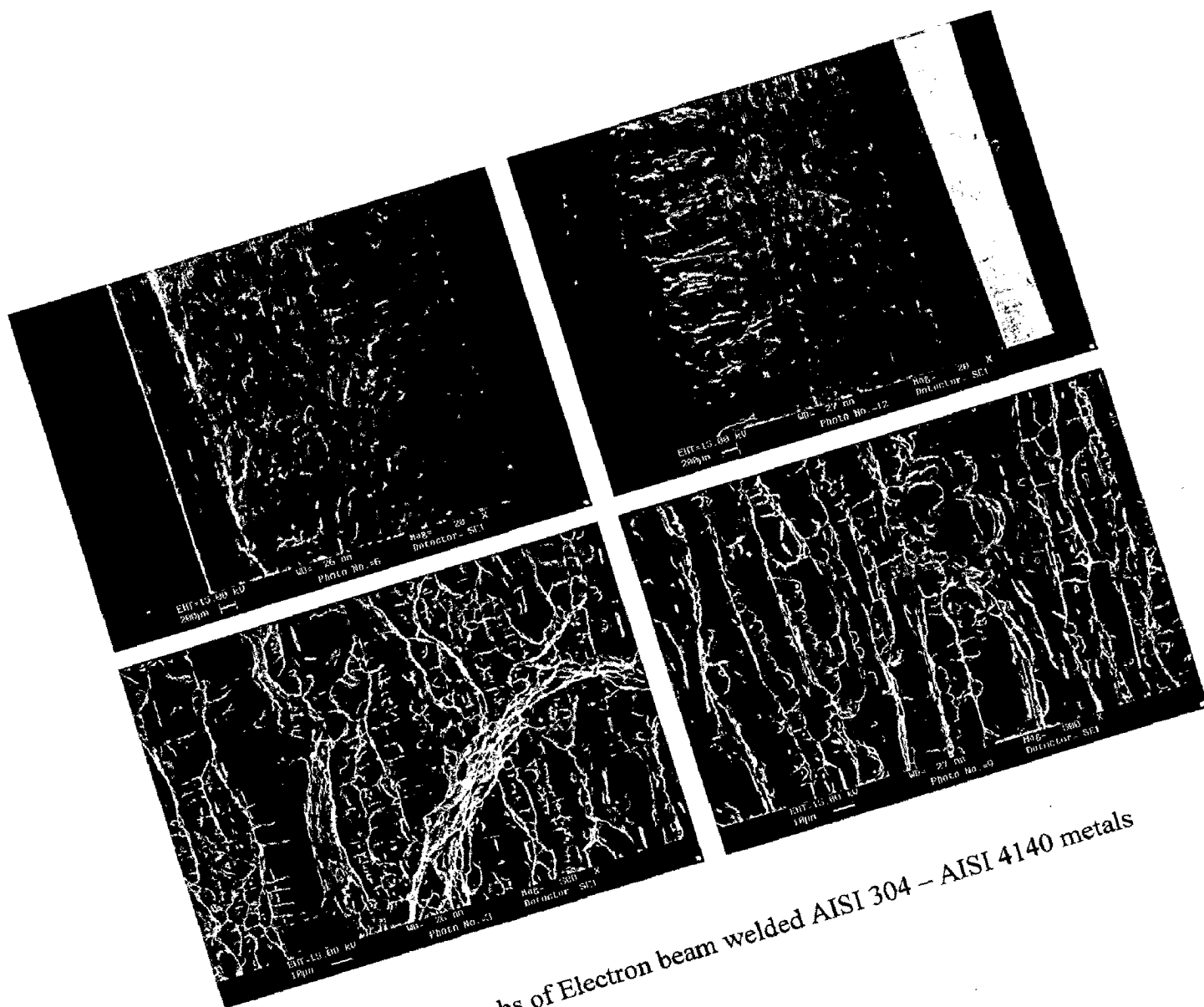


Fig 4.23(i) Fractographs of Electron beam welded AISI 304 – AISI 4140 metals

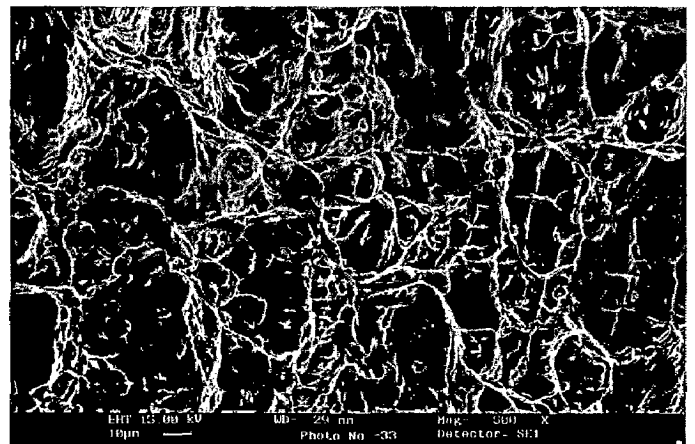
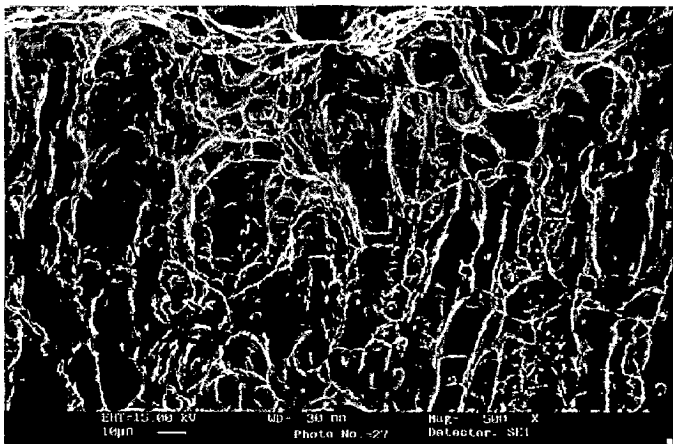
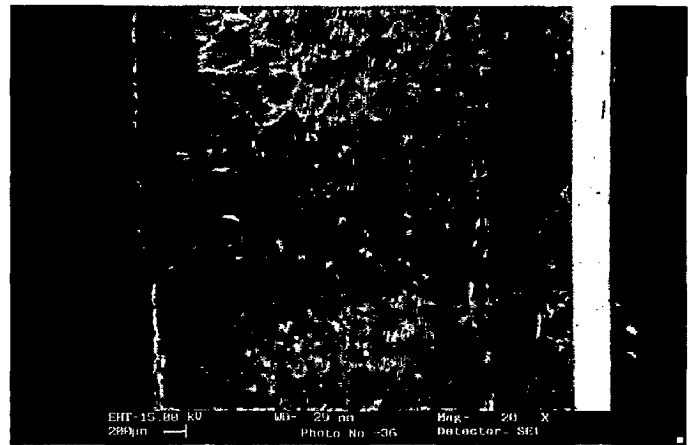
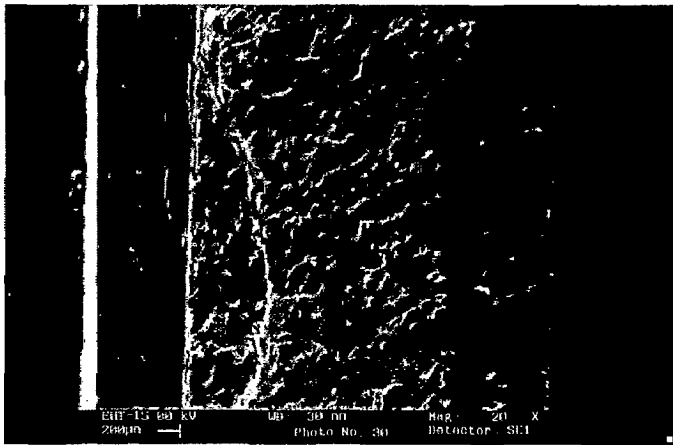


Fig 4.23 (ii) SEM Fractographs of Electron beam welded AISI 304 – AISI 4140 metals

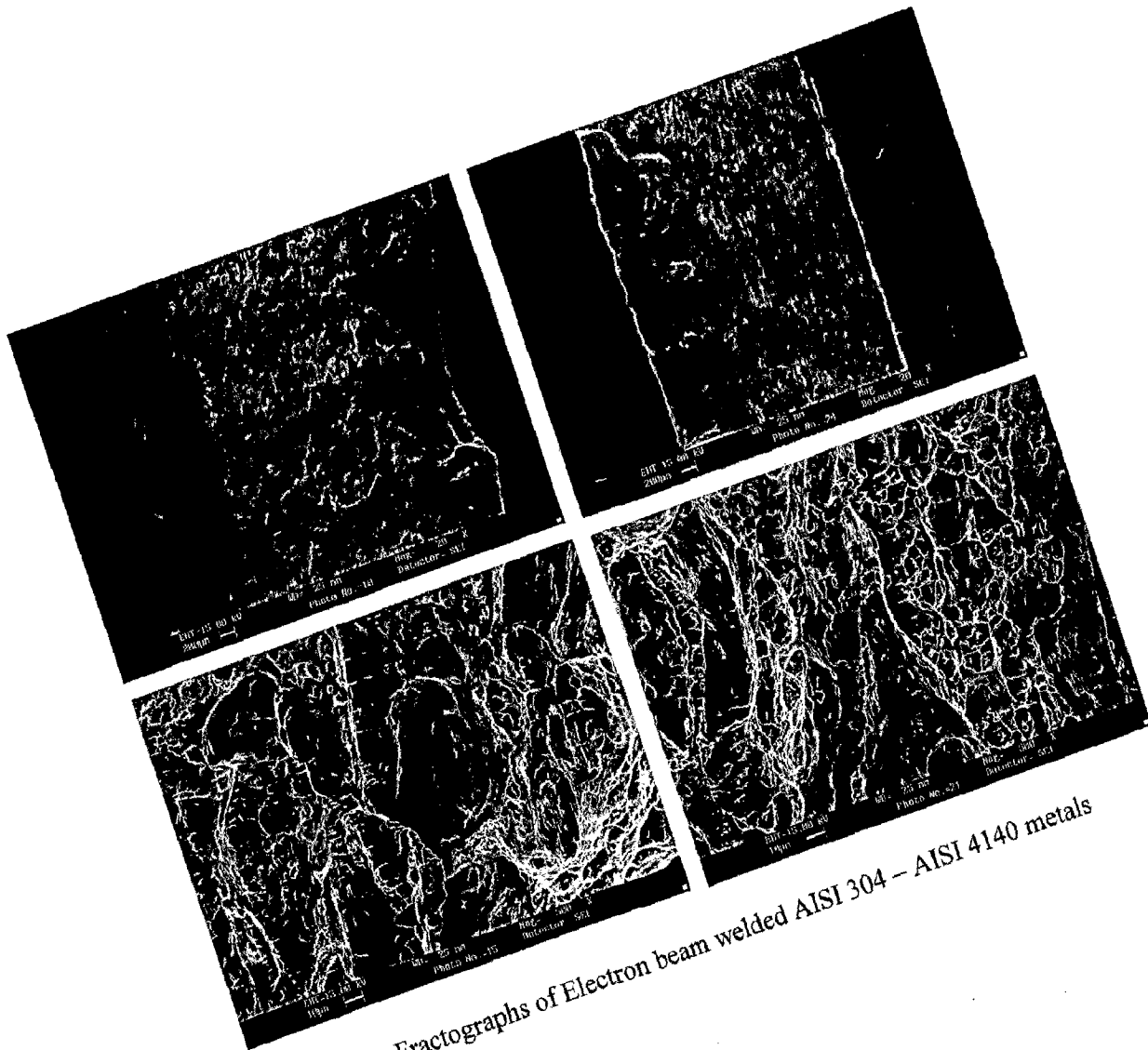


Fig 4.23(iii) Fractographs of Electron beam welded AISI 304 – AISI 4140 metals

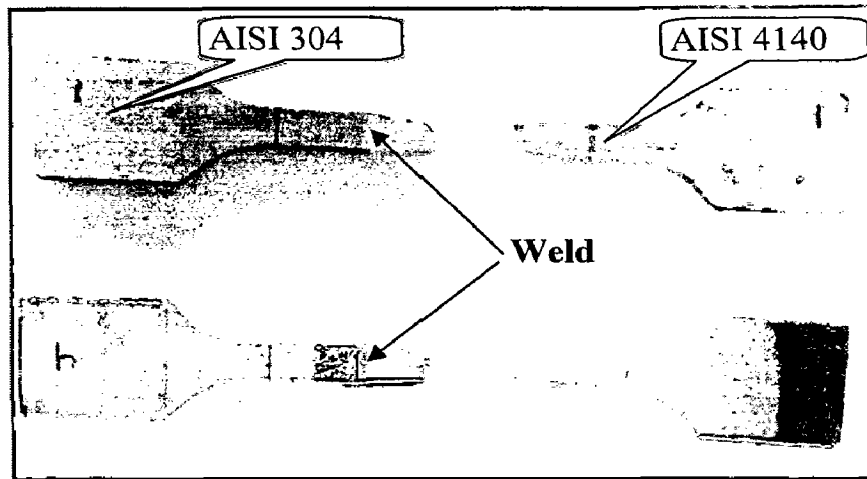


Fig 4.24 Photograph for tensile fractured weldment made by EBW

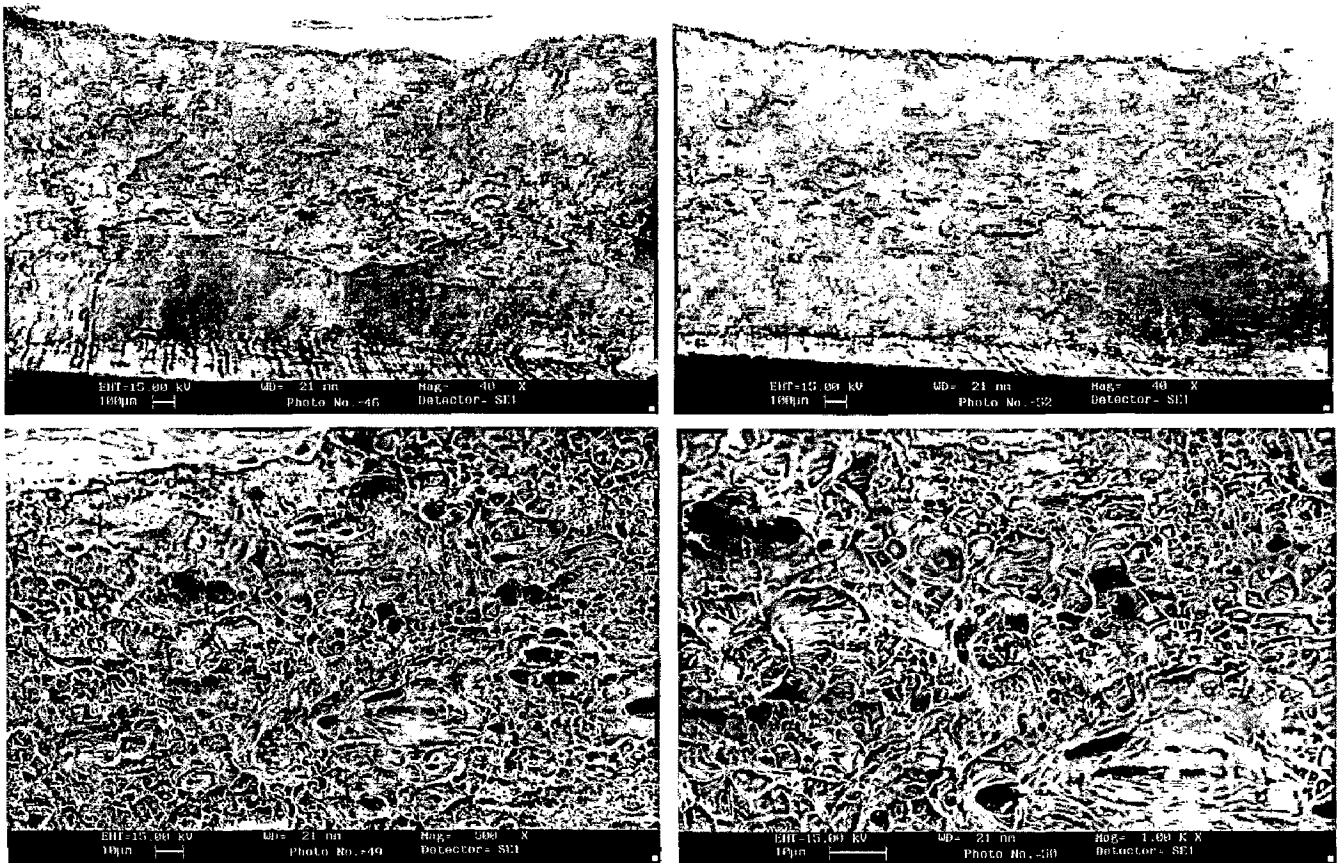


Fig 4.25 SEM fractographs for tensile specimen for EBW welded AISI 4140 and AISI 304

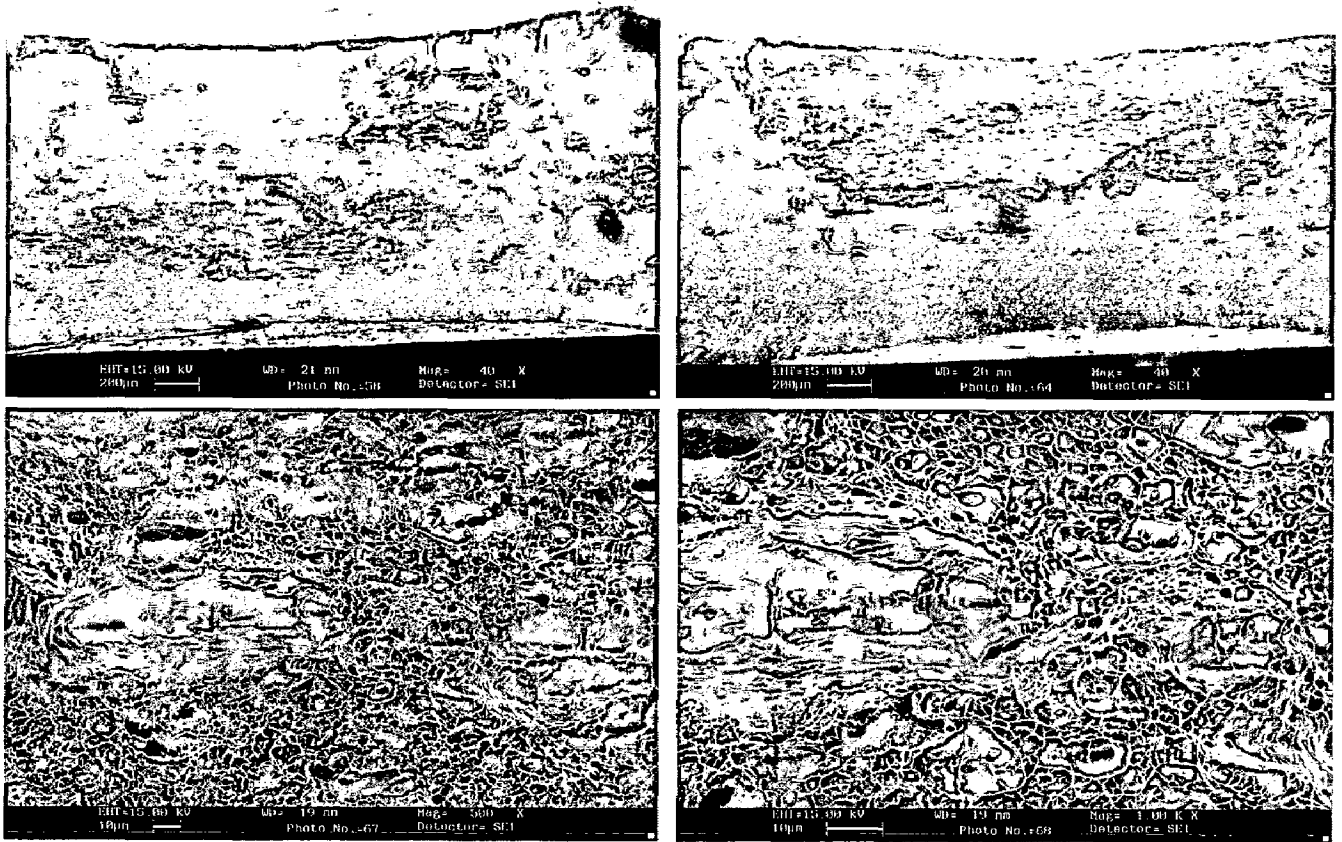


Fig 4.26 SEM fractograph for tensile specimen for EBW welded AISI 4140 and AISI 304

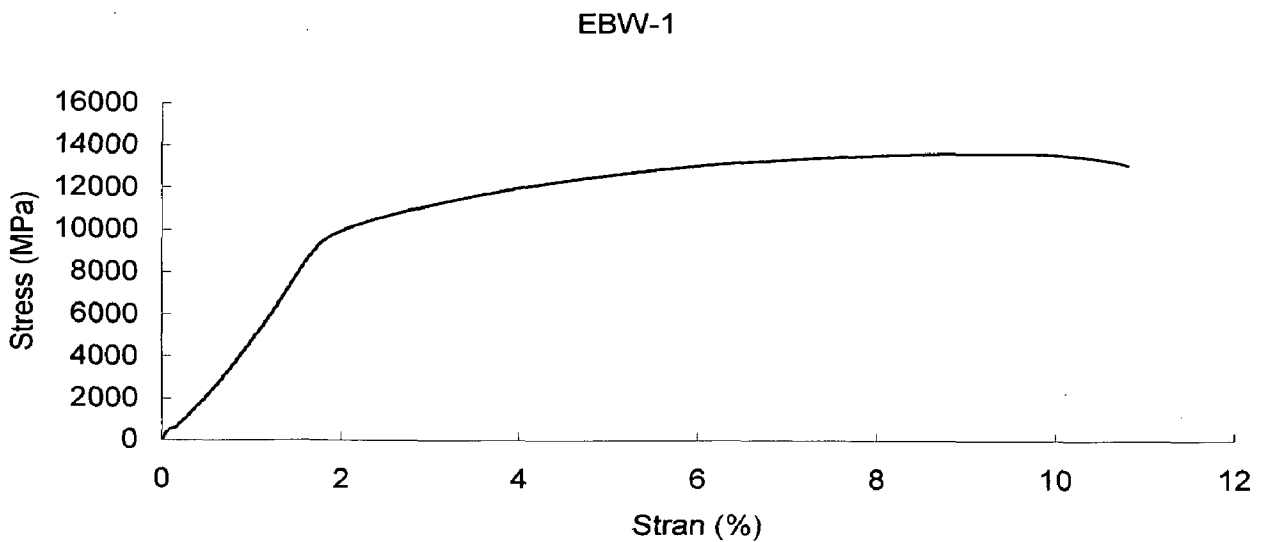


Fig 4.27 Stress Vs Strain curve for EBW welded AISI 4140 and AISI 304 weldment

welding speed, reproducible weld quality and reduced material usage. However, a few drawbacks may still limit its use in practice. Nevertheless, continuous development of electron beam technology may provide possibilities in the future. It should be noted that this study is based on a dissimilar weldment, which is used in power plant environment. Further study may be extended to the tri-metallic joint configuration with the same process in order to achieve even better results.

4.3 TUNGSTEN INERT GAS WELDING

4.3.1 Visual Examination

The Tungsten Inert Gas (TIG) welded dissimilar joints are presented in Fig 4.28. From the joints it is observed that in all the cases the heat affected zone of the AISI 4140 and AISI 304 weld on both sides is wider than that for EBW and FRW dissimilar welds. The width of the weld zone is comparatively large as compared with EBW and FRW.

4.3.2 Macrostructure

The macro structure of TIG welded AISI 4140 and AISI 304 dissimilar metals shows desirable penetration (Fig 4.29). The macrograph of weld cross-sections showed that the deep and wide weld zone. In this study no weld defects were observed on the surface.

4.3.3 Microstructure

The microstructure of low alloy steel (AISI 4140) and austenitic stainless steel (AISI 304) dissimilar weldment is heterogeneous. Fig 4.30 shows the different zone of the weldment. This phenomenon is the result of the thermal cycle associated with TIG welding. The microstructure of the heat affected zone of austenitic steel close to the weld zone shows evidence of the small amount of grain recrystallization that took place during the welding process. Also revealed was a little carbide precipitation, at interface of AISI 304 stainless steel side. At the weld interface on the low alloy steel side the microstructure was coarse, and contained malformed lamellae of pearlite. Also small amount of precipitation noted at the interface of low alloy steel side. In addition, there was a lot of variation in grain size in the HAZ of the low alloy steel, caused by variations in cooling rate. Weld metal grains were formed as dendrites. Further some directionality has been observed near fusion boundary, but not at the center portion of TIG weld.

This may be due to local variation in solidification mode and growth velocity at fusion boundary and center portion of the weld.

4.3.4 XRD Analysis

X-Ray Diffraction studies were carried out to analyse the phases formed on dissimilar TIG weldment in as welded condition as shown in Fig 4.31. As welded condition, $(Cr,Fe)_7C_3$ has been indicated with high intensity peak whereas Cr-Ni-Mo, CrNiFe, Ni_3C , FeNi etc., are having low intensity peaks.

4.3.5 Electron Probe Micro Analysis

The elemental line profile across the welds is shown in Fig. 4.32. From the data it was observed that the Cr and Ni diffuse from AISI 304 to AISI 4140 side, whereas Fe diffuses to AISI 304 side. There is an enrichment of Cr, Ni, and Fe in the weld zone.

4.3.6 Micro Hardness

Hardness distribution across the TIG welded AISI 4140 and AISI 304 dissimilar metals are presented in Fig 4.33. The hardness of the weld region is in the range 473 Hv (min) to 513 Hv (max). Highest hardness (698 Hv) observed at interface of AISI 304 side.

4.3.7 Impact Toughness

The impact toughness of TIG weldment made by dissimilar metals of AISI 4140 and AISI 304 was observed to be 20 and 31 (J). Fractographs of the impact tested TIG welds are presented in Fig. 4.34 (i-ii). From the fractographs it was observed that the structure exhibits predominantly cleavage fracture with occasional appearance of microvoid features. Figure 4.34 (i) shows the elongated facet features observed in the fractograph supports the lowest toughness (20 J). Also Fig 4.34(ii) shows the dimple structure (ductile fracture) shows the maximum impact strength of 31 (J).

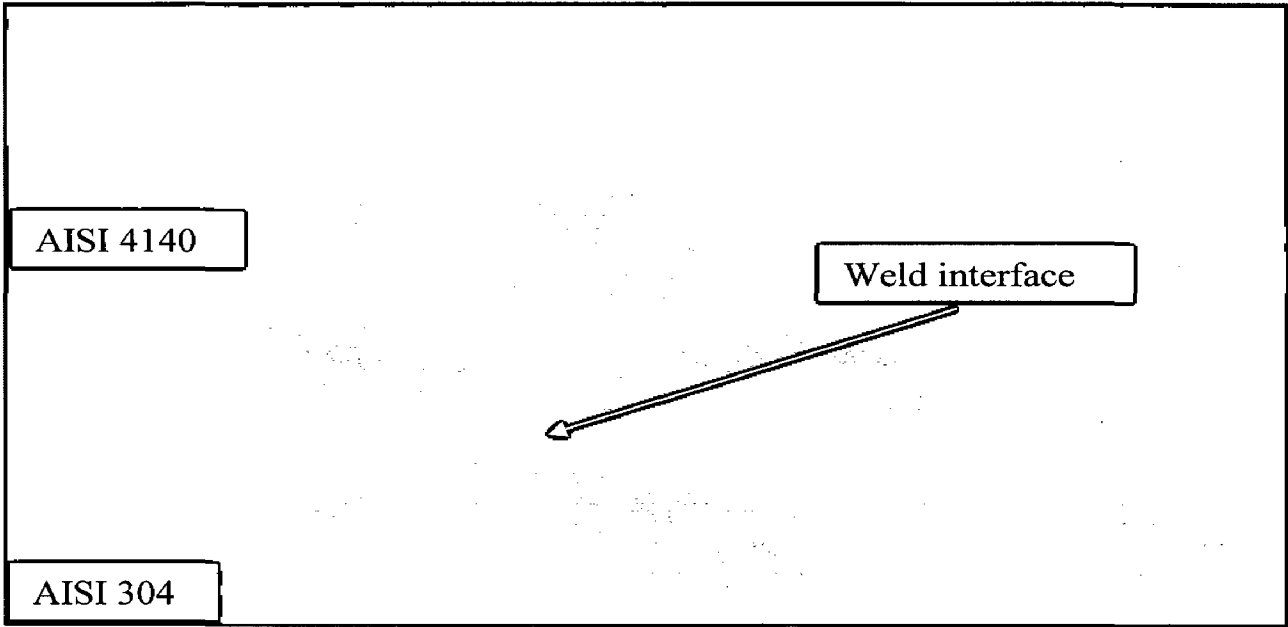


Fig 4.28. TIG Welded specimen

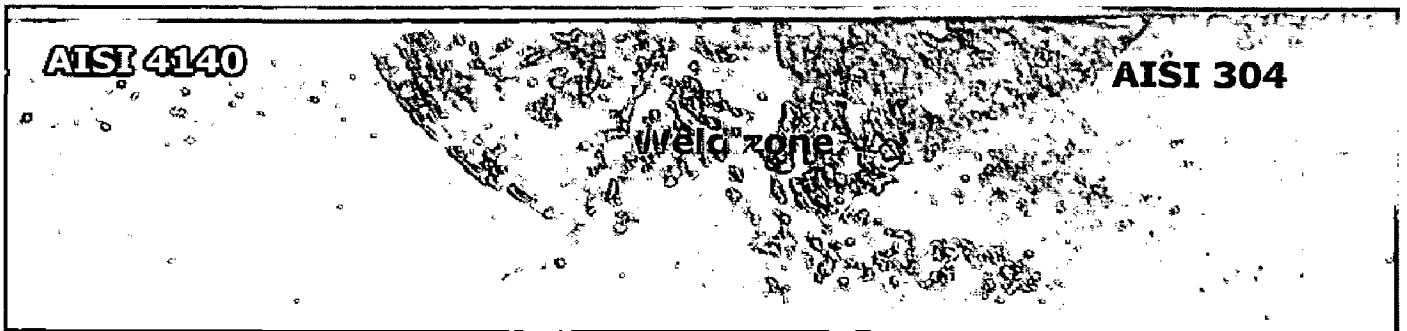


Fig 4.29 Macro structure of TIG welded AISI 4140 and AISI 304 dissimilar metals

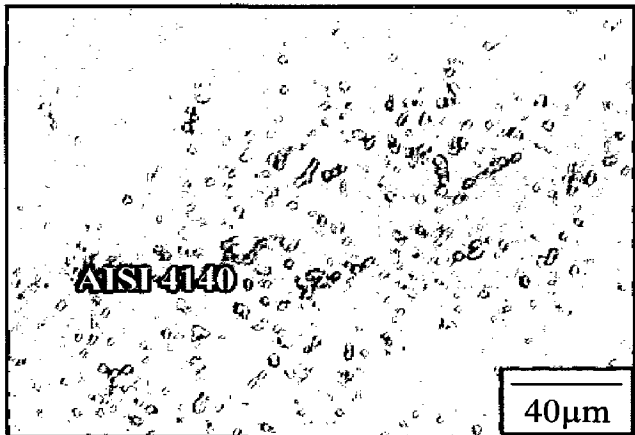
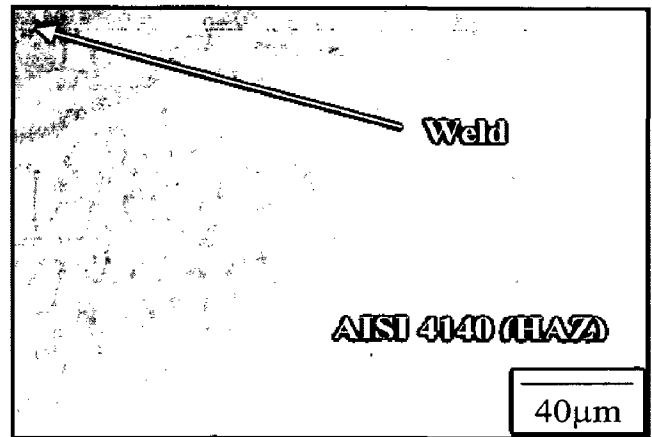
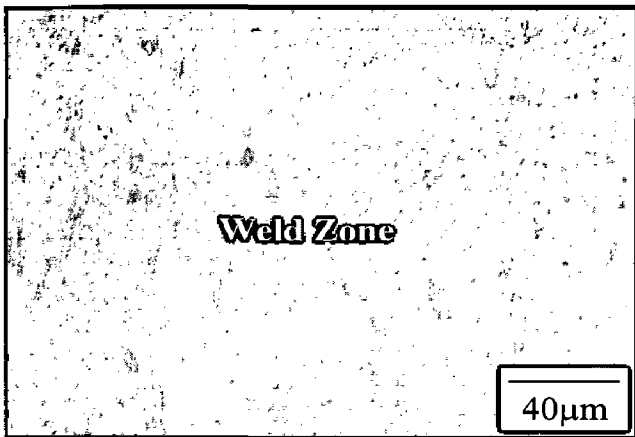
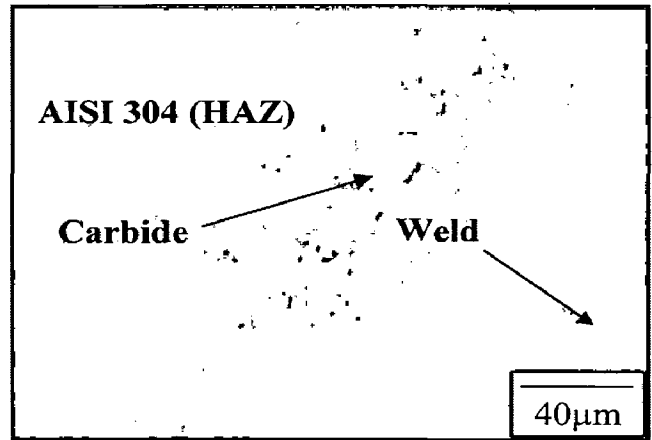


Fig 4.30 Microstructure of TIG welded AISI 4140 and AISI 304 dissimilar metals

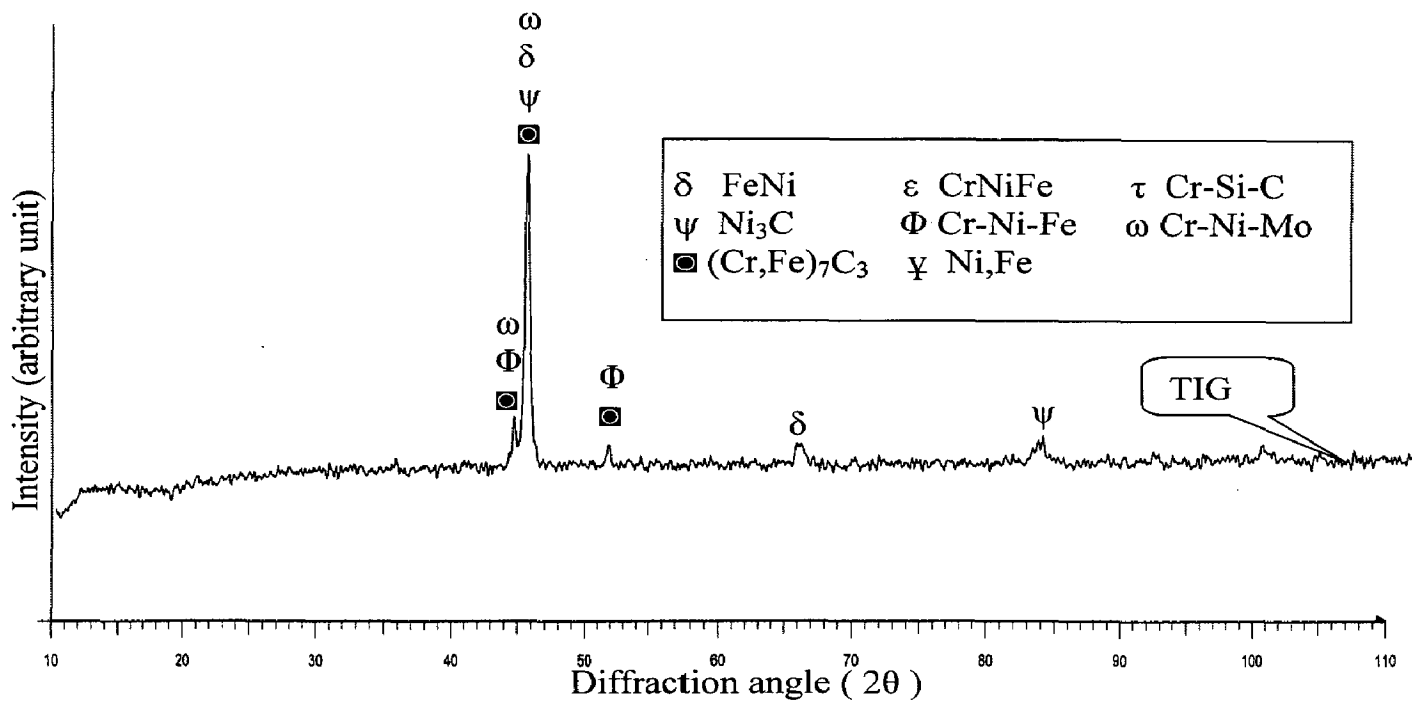


Fig. 4.31 X-Ray diffraction patterns for TIG weldment as welded condition.

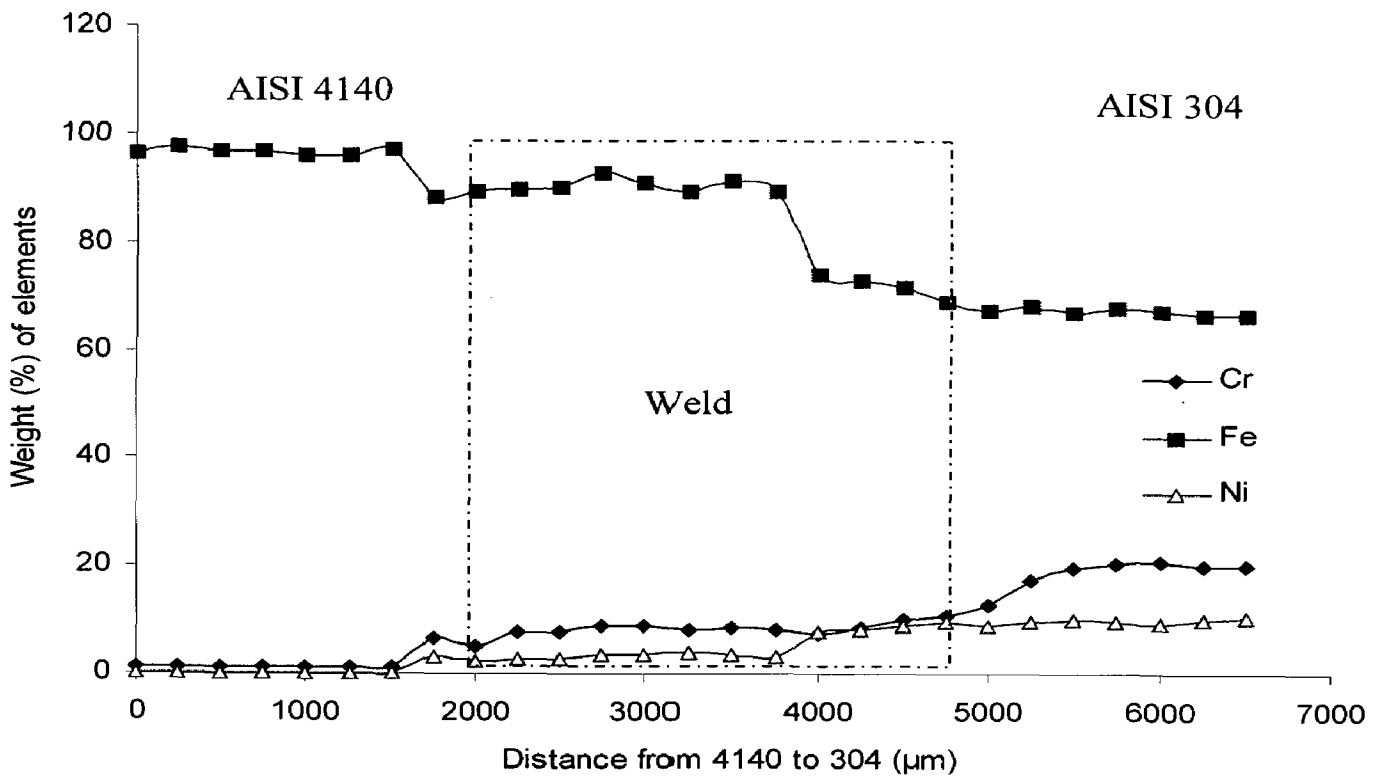


Fig 4.32 Elemental distribution across the weld centre in 4140-304 TIG weld

joint

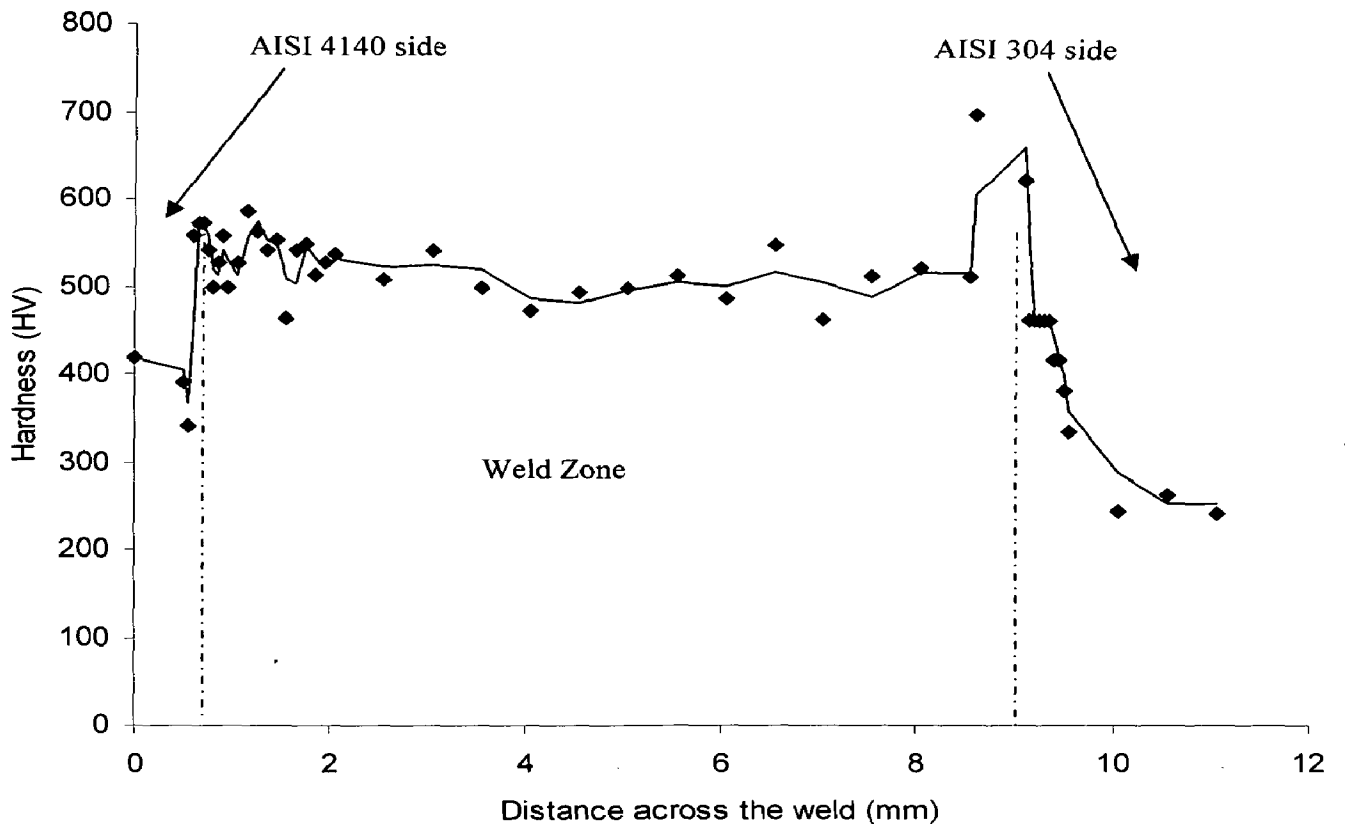
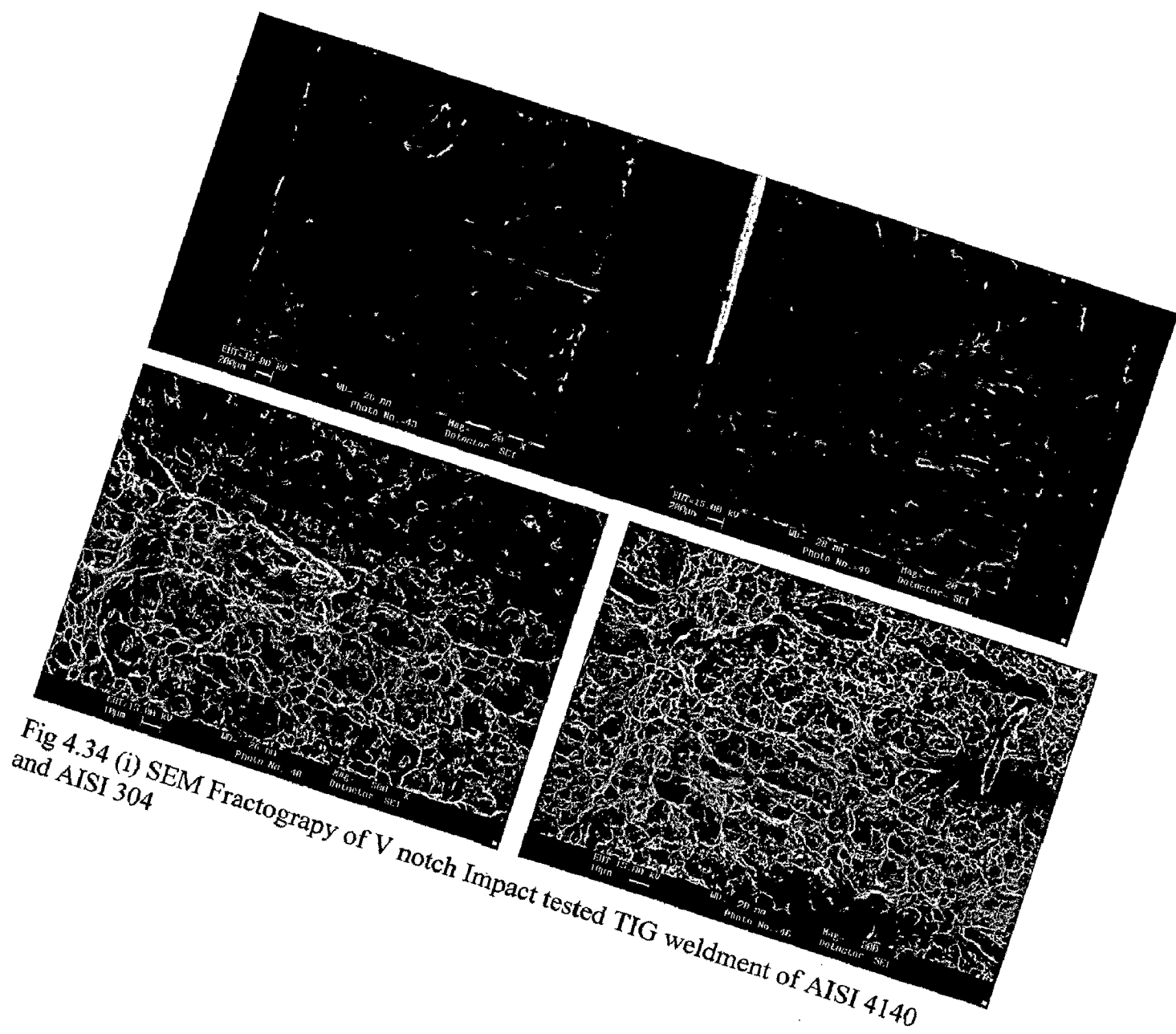


Fig 4.33 Hardness distribution across the TIG weldment of AISI 4140 and AISI 304



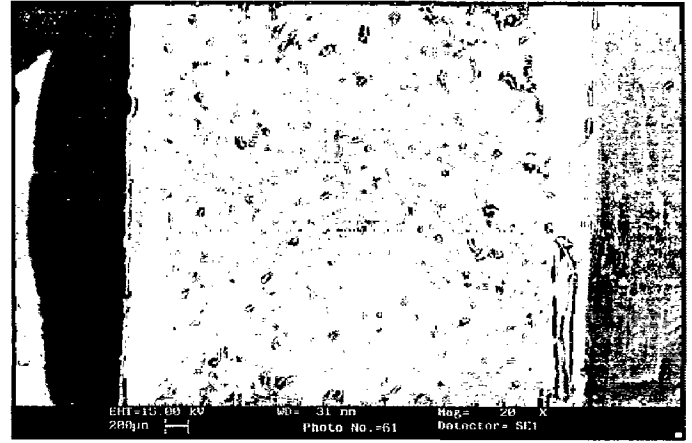
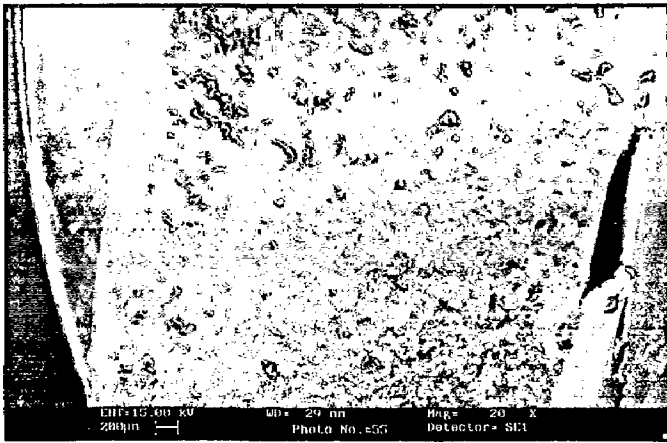


Fig 4.34 (ii) SEM Fractography of V notch Impact tested TIG weldment of AISI 4140 and AISI 304

4.3.8 Tensile testing

The tensile strength of welds made by TIG presented in Table 4.6. In general the yield stress values that are more than those of low alloy steel in the as received condition (417 MPa).

Table 4.6 Tensile strength of TIG Welded AISI 4140 and AISI 304

Test Trial	Proof Stress (MPa)	Ext. Yield (%)	Max Stress (MPa)
1	542	28.28	676
2	585	21.64	693

The photograph of tensile tested specimen of TIG welded AISI 304 and AISI 4140 are presented in Fig. 4.35. In all the samples the fracture occurred on the heat affected zone of AISI 4140 side and yield stress was in the range of 576 to 693 MPa. Fractographs of TIG welded AISI 304 and AISI 4140 are presented in Fig. 4.36. SEM micrographs shows predominantly well developed micro void ductile fracture features in the weldment made by TIG Welded specimen and the stress Vs strain curve shown in Fig 4.37.

4.3.9 Discussions

Micrographs of the transition zone of the samples which were welded by TIG are given in Fig. 4.30. Grains in the weld metal oriented parallel to the heat flow. Durgutlu A (1999) also reported similar result about grain orientation. Weld metal contained as dendrites. TIG welding it leads to longer solidification time for the weld metal as there is increased heat input to the weld metal. The longer solidification time may be responsible for the grain orientations in different directions depending on the flow from weld metal. The maximum hardness was noted at the weld interface adjacent to AISI 304 sides may be due to carbon enrichment leading to carbide precipitation. From the fractograph of impact test TIG weldment shows that the fracture during impact loading propagated in the weld metal near the toe of the weld. Fracture surfaces after impact are parallel to the loading direction. Microstructure of the weldment is free from cracks. The minimum impact strength (20 J) of the TIG welds may be due to low melting eutectics, carbide precipitation and intermetallics formation which is supported by XRD and EPMA analysis (Fig 4.31, 4.32). The tensile test shows that the failure was observed at the interface of the AISI 4140 as shows in Fig 4.35 may be

due to excess phase formation which is supported by microstructure analysis Fig 4.30. From the fractographs of tensile tested weldment some porosity and micro cracks observed where the specimen leading to low yield stress (576 MPa). The TIG welded dissimilar weldment between AISI 4140 and AISI 304 are satisfactory.

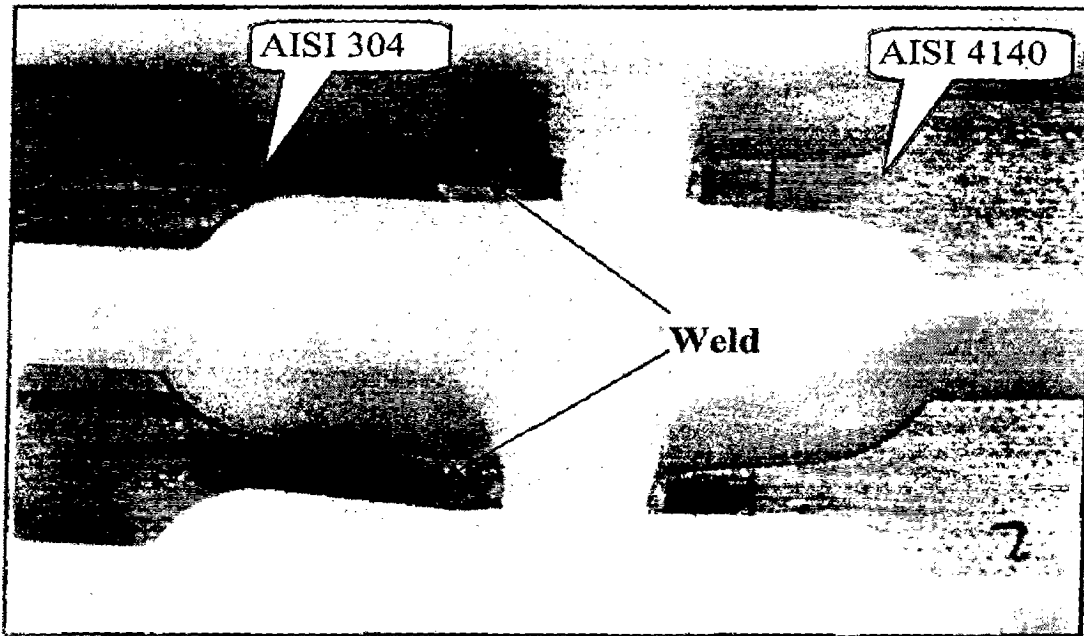


Fig 4.35 Photograph for tensile fractured TIG welded AISI 4140 and AISI 304

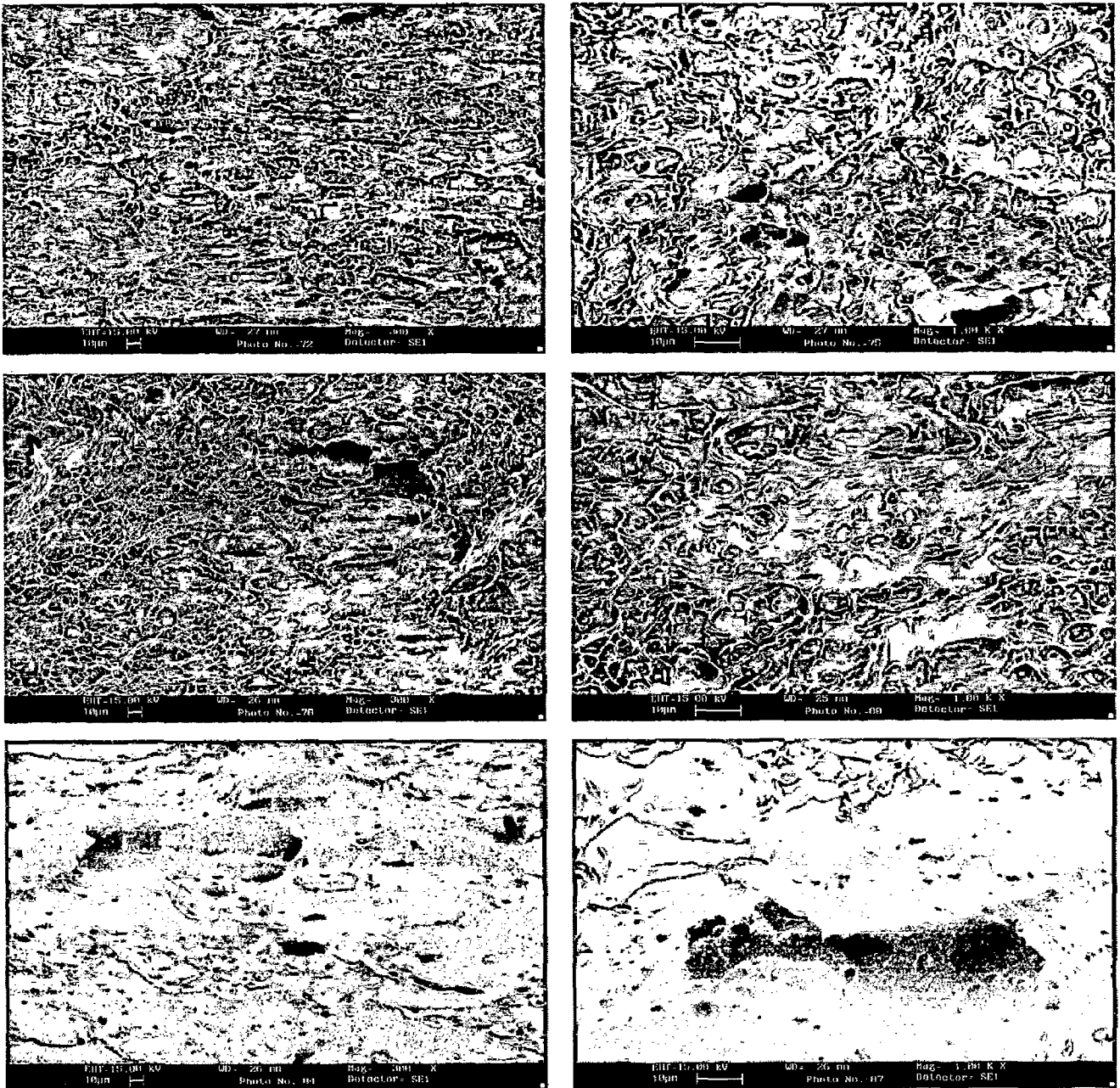


Fig 4.36 SEM fractograph for TIG welded AISI 4140 and AISI 304 tensile specimen

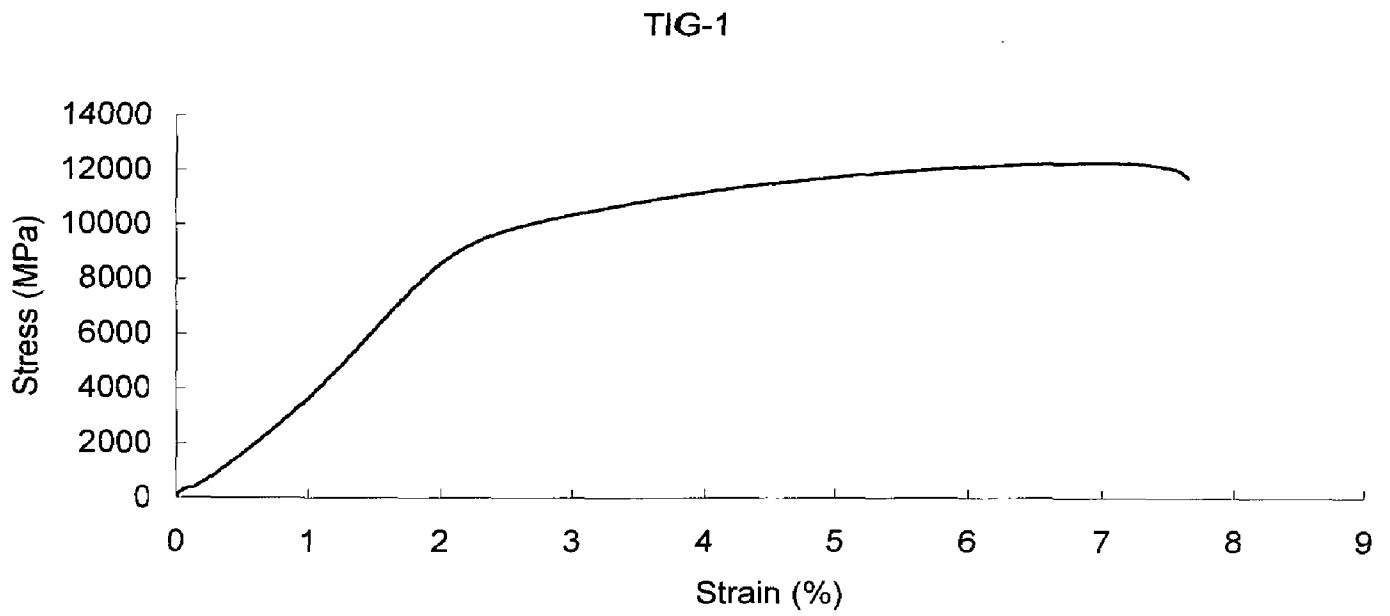


Fig 4.37 Stress Vs Strain curve for TIG welded tensile specimen

OXIDATION STUDIES OF FRICTION WELDED DISSIMILAR WELDMENT IN AIR

This chapter deals with the critical examination of corrosion products of dissimilar weldment when subjected the cyclic and isothermal oxidation at 500 to 900 °C in air. Visual observations were recorded and gravimetric data were collected at the end of each cycle during study. Efforts have been made to understand the mechanism of corrosion. The corrosion products were analysed with XRD, SEM/EDAX and EPMA. The parabolic rate constants and scale thicknesses have been evaluated.

5.1 AIR OXIDATION TEST

Oxidation studies were performed on the dissimilar friction welded (FRW) specimen under following condition.

(a) **Cyclic oxidation in air** (Each cycle consisting of 1 hour heating followed by 20 min cooling which was carried out at temperature 500 and 600 °C)

(b) **Isothermal oxidation in air** (At 500, 700 and 900 °C for 50 hours)

The aim of cyclic oxidation is to create severe conditions which are near to the actual service conditions. The high temperature corrosion studies were performed for FRW samples by keeping constant weld parameter (B5). The welded samples were mirror-polished, down to 1 µm alumina wheel cloth polishing before corrosion studies. Weight-change measurements were taken at the end of each cycle using an electronic balance (model 06120) with a sensitivity of 1 mg for cyclic oxidation whereas continuous oxidation at the end of 50 hours. At the time of weighing, even the spalled scale was also included to determine the total rate of corrosion. Efforts were made to formulate the kinetics of corrosion. The surface of the corroded specimens was visually observed to record color of the scale, spalling and peeling of scale during cyclic corrosion. The samples after corrosion run were examined by SEM, EDAX and XRD for surface analysis.

5.2 RESULTS

5.2.1 Visual Examination

During cyclic study at 500 and 600 °C the colour of scale for the entire low alloy steel (AISI 4140) steels was light purplish grey during first few cycles and turned to dark grey after fifth cycle. In case of stainless steel (AISI 304) side blue colour patch started increasing just after 4th cycle. In the weld interface showed light grey colour after 8 th cycle. No much interesting observation was noticed for all the cases up to 50 cycles. Fig 5.1 shows the photographs of the weldment after hot corrosion exposed under air.

5.2.2 Thermogravimetric Data

The weight gain (per unit area) during corrosion test for the dissimilar FRW (AISI 304 and AISI 4140) in the air oxidation at the temperature of 500 and 600 °C, have been plotted and is shown in Fig. 5.2 indicating parabolic behavior. The parabolic rate constant $K_p \times 10^{-6}$ ($\text{g}^2 \text{cm}^{-4} \text{S}^{-1}$) were obtained from the slope of the linear regression fitted line (cumulative weight gain / area)² Vs. number of cycles at 500 and 600 °C were 0.297 and 0.383 respectively. The weight gains after cyclic and isothermal oxidation were shown in the table 5.1.

Table 5.1. The weight gain after 50 cycles/ 50 hours oxidation studies in air

Type of hot corrosion	Temperature (°C)	Weight gain after 50 cycles/ 50 hours $\times 10\text{g/cm}^2$
Cyclic Oxidation	500	0.022
	600	0.027
Isothermal Oxidation	500	0.001
	700	0.150
	900	0.446

5.2.3 X-ray Diffraction Analysis

X-Ray diffraction studies were carried out to analyse the phases formed on the oxidized DSW. Fe_2O_3 was identified be the major oxide with NiFe_2O_4 and NiCr_2O_4 as a minor constituent (Fig 5.3(A,B)) for all three temperatures of exposure. At 500 °C oxidation for both cyclic and isothermal condition, FeNi intermetallic compound was indicated with

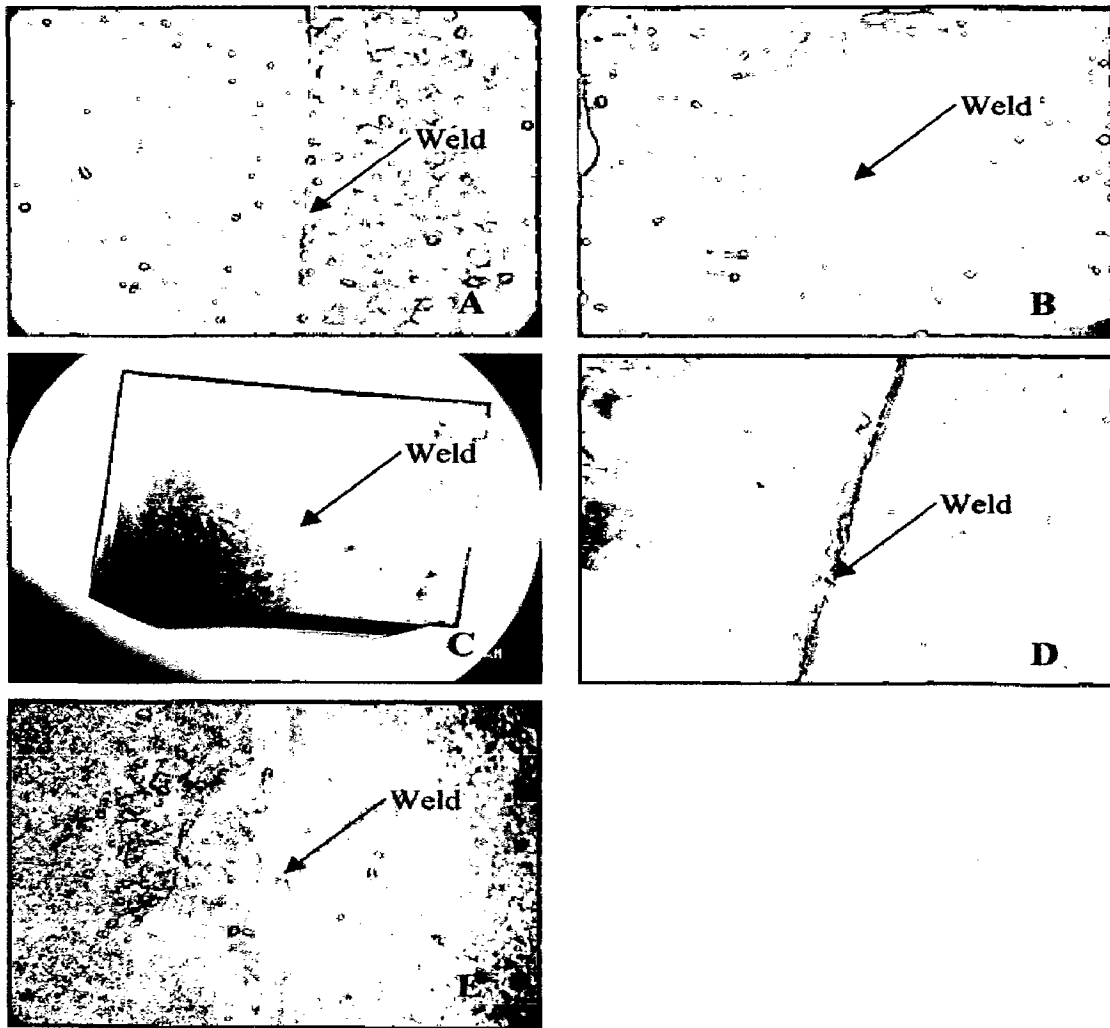


Fig 5.1 Photograph after complete the high temperature corrosion of friction welded AISI 4140 and AISI 304, exposed under air. (A) Cyclic oxidation at 500 °C, (B) Cyclic oxidation at 600 °C, (C) Isothermal Oxidation at 500 °C, (D) Isothermal Oxidation at 700 °C, (E) Isothermal Oxidation at 900 °C.

Note: Right side of the specimen indicates AISI 304.

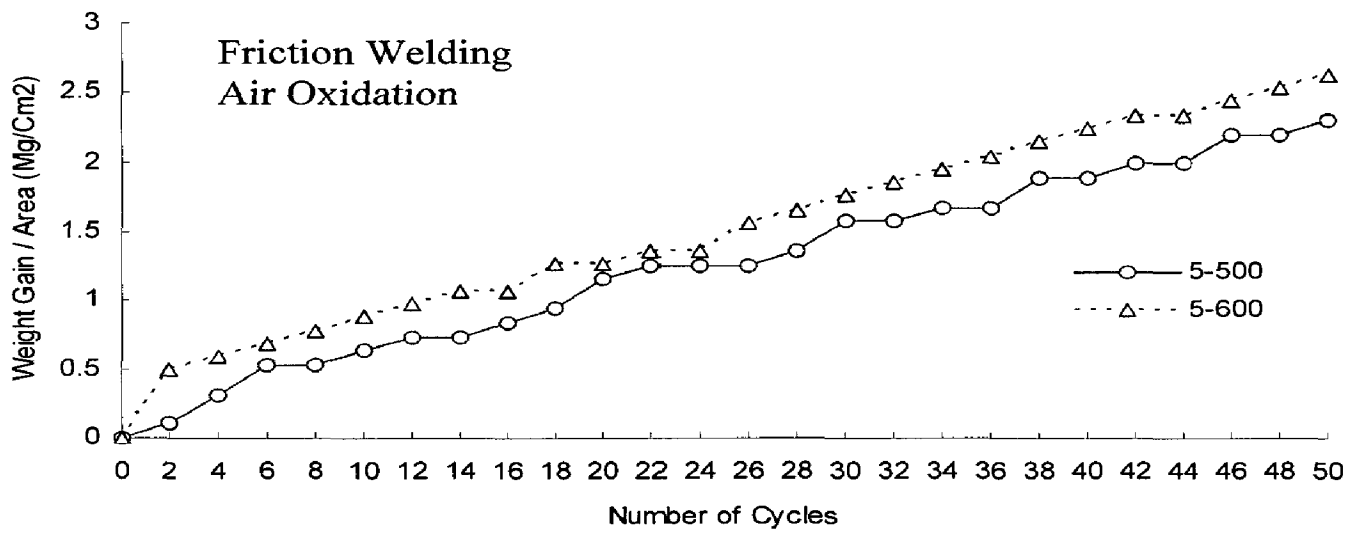


Fig 5.2. Plots of cumulative weight gain (mg/cm^2) as a function of time (number of cycles) for 500 and 600 °C after 50 cycles

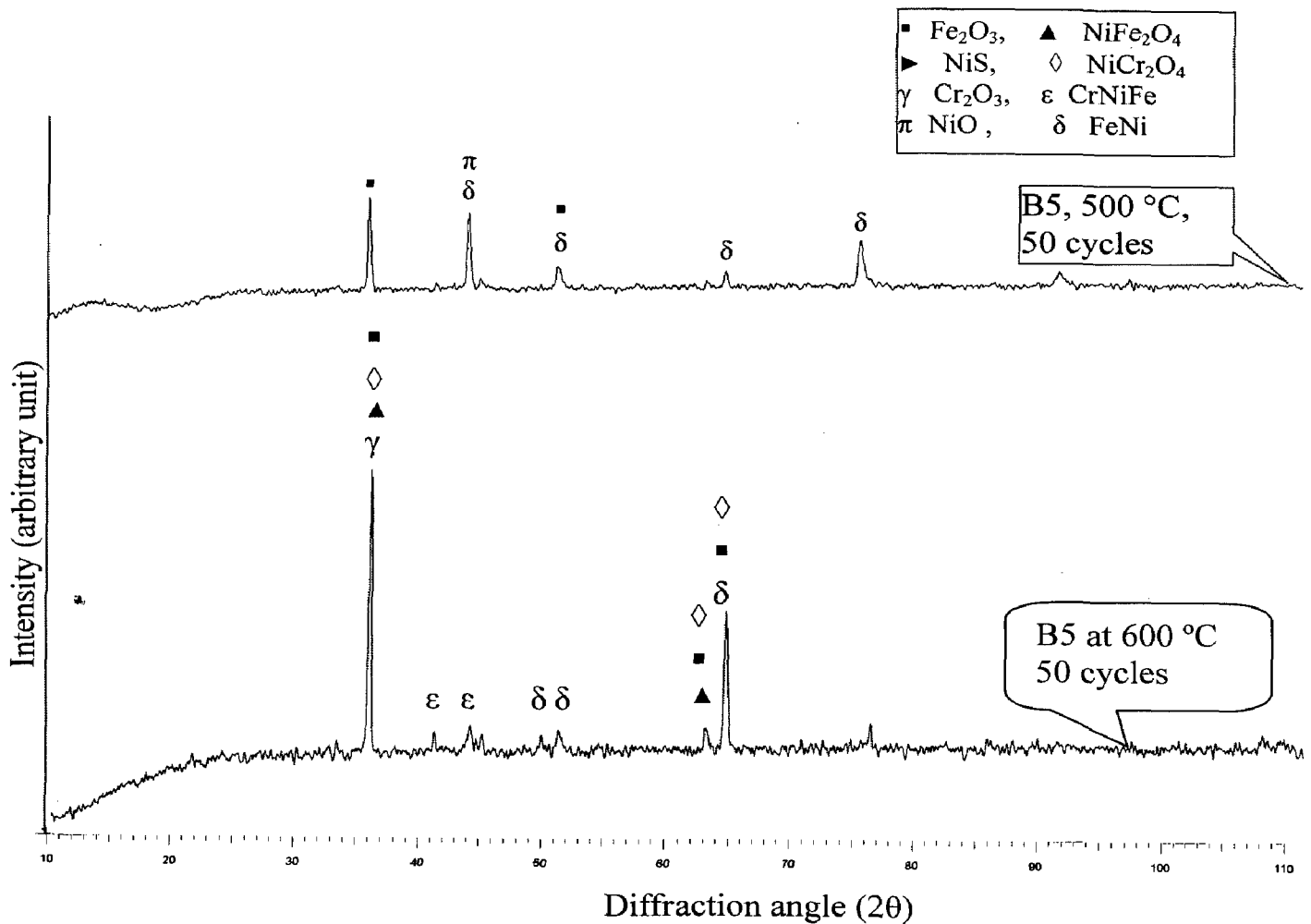
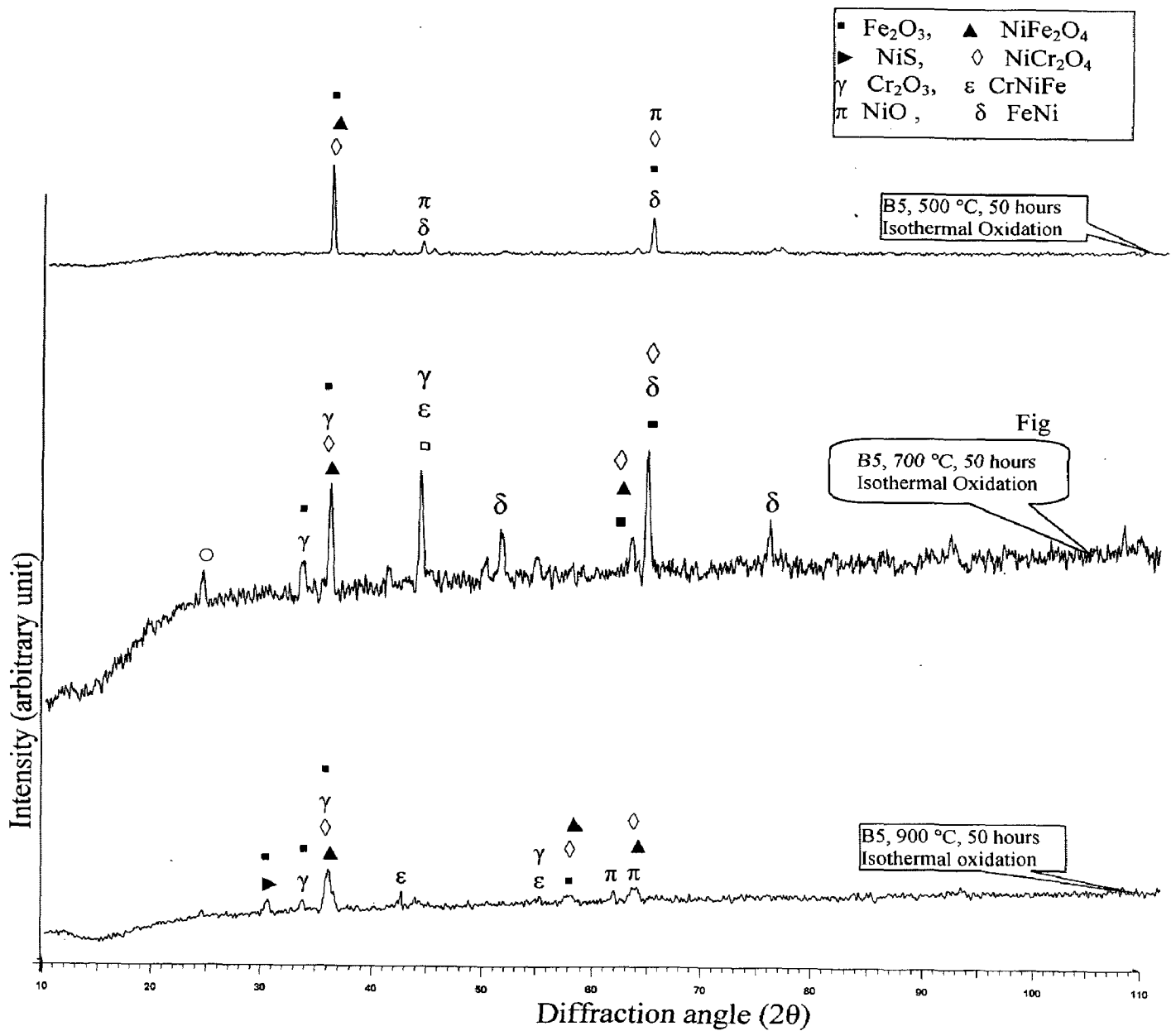


Fig 5.3(A). X-Ray diffraction patterns for dissimilar friction weldment made by AISI 4140 and AISI 304, exposed under cyclic air oxidation at 500 and 600 °C



5.3 (B). X-Ray diffraction patterns for dissimilar friction weldment made by AISI 4140 and AISI 304, exposed under isothermal oxidation at 500 700 and 900 °C (isothermal)

Fe₂O₃ whereas the Cr₂O₃ was absent. At 900 °C for isothermal oxidation, the scale on the weldment contained Cr₂O₃, CrNiFe intermetallic with NiS whereas FeNi was absent.

5.2.4 Scale Thickness Measurement

The samples were cut across the cross-section after exposure to air at 500 and 600 °C for 50 cycles and mounted. The scale thickness was measured from SEM back scattered images as shown in Fig. 5.4. The scale thickness values are 21.42 μm and 32.14 μm at 500 and 600 °C for dissimilar friction welded dissimilar weldment respectively. Whereas, in the case of isothermal oxidation at 700 and 900 °C the average scale thickness on low alloy steel side. Since the scale more prone to brittle and spalling nature, the exact scale thickness could not be noted.

5.2.5 SEM/EDAX Analysis

SEM photographs showing surface morphology of the DSW after cyclic and isothermal oxidation in air for 50 hours are shown in Fig 5.5 (a-e). The EDAX analysis of the scale formed on weldment after cyclic and isothermal oxidation in air at 500 °C, Fe₂O₃ is found to be the predominant phase. Fe₂O₃ content is in the scale higher on the base metal 4140 and tends to decrease as we move towards HAZ-4140 → weld → HAZ-304 → 304 base metal. Whereas Cr₂O₃ content of scale is reducing as we move from 304 → HAZ-304 → weld → HAZ-4140 → 4140 base metal. Little amount of NiO is obtained on 304 side whereas it was negligible on 4140 side, whereas it is maximum at the interface. At 700 °C isothermal oxidation, the percentage of Fe₂O₃, Cr₂O₃ and NiO observed in the scale on the weldment follows the same trend as at 500 °C. At 900 °C oxidation the percentage of Cr₂O₃ becomes higher in the scale on HAZ-304 as compared Fe₂O₃.

5.2.6 EPMA Analysis

EPMA analysis had been done only selected sample which contained thicker scale thickness. BSEI and X-ray mapping for a part of oxide scale of dissimilar weldment after

isothermal oxidation by exposing at 700 and 900 °C temperature is shown in Fig. 5.6 to 5.10. It can be inferred from the EPMA results that the scale mainly consists of iron oxide.

The detailed X-ray mapping and elemental distribution analysis had been done on the air oxidized specimen. The cross section of the specimen cleaned by ultrasonic method. The figure 5.11 and 5.13 shows the X mapping analysis on the isothermal air oxidized dissimilar weldment exposed at 700 and 900 °C respectively. From the micrographs it was observed that the Cr, Ni, Fe and carbon got enriched more on the weld zone as well as in the scale. With increase the temperature to 900 °C it was noted that the amount of enrichment was also more. The BSEI and EDS curve also supported the above. (Fig 5.12 and 5.14).

5.2.7 Discussion

From the oxidation studies weight gain curves tendency for oscillation type reaction weight gain rate has been observed (Fig.5.2) perhaps due to changes in reaction rate which are associated with the formation of a laminated, inner-oxide layer, made up of bands of fine and coarse grain oxide spinel, as suggested by M.H.Hurdus et al [1990].

From the SEM/EDAX data, the percentage of change in Fe_2O_3 in the scale remain constant from base metal (4140) → 4140-HAZ and tend to decrease from 4140-HAZ to weld zone. This trend is almost same for all the temperature of exposure. At 500 C cyclic oxidation this Fe_2O_3 further decreases as one moves from Weld → 304-HAZ and increases from 304-HAZ → 304 base metal. Whereas at 600 °C oxidation Fe_2O_3 increases from weld → 304(HAZ) and decreases from 304(HAZ) → 304 base metal (Fig.5.5 (a, b)). At 500 and 700 °C for isothermal oxidation, the Fe_2O_3 is decreases as one moves from Weld → 304(HAZ) → 304 base metal (Fig.5.5(c, d)).

At 500 °C and 700 °C isothermal oxidation the percentage of Cr_2O_3 in the scale increases from Weld → 304 (HAZ) → 304 base metal whereas at 900 °C oxidation Cr_2O_3 observed higher in the scale on 304 (HAZ) (Fig 5.5 (e)).

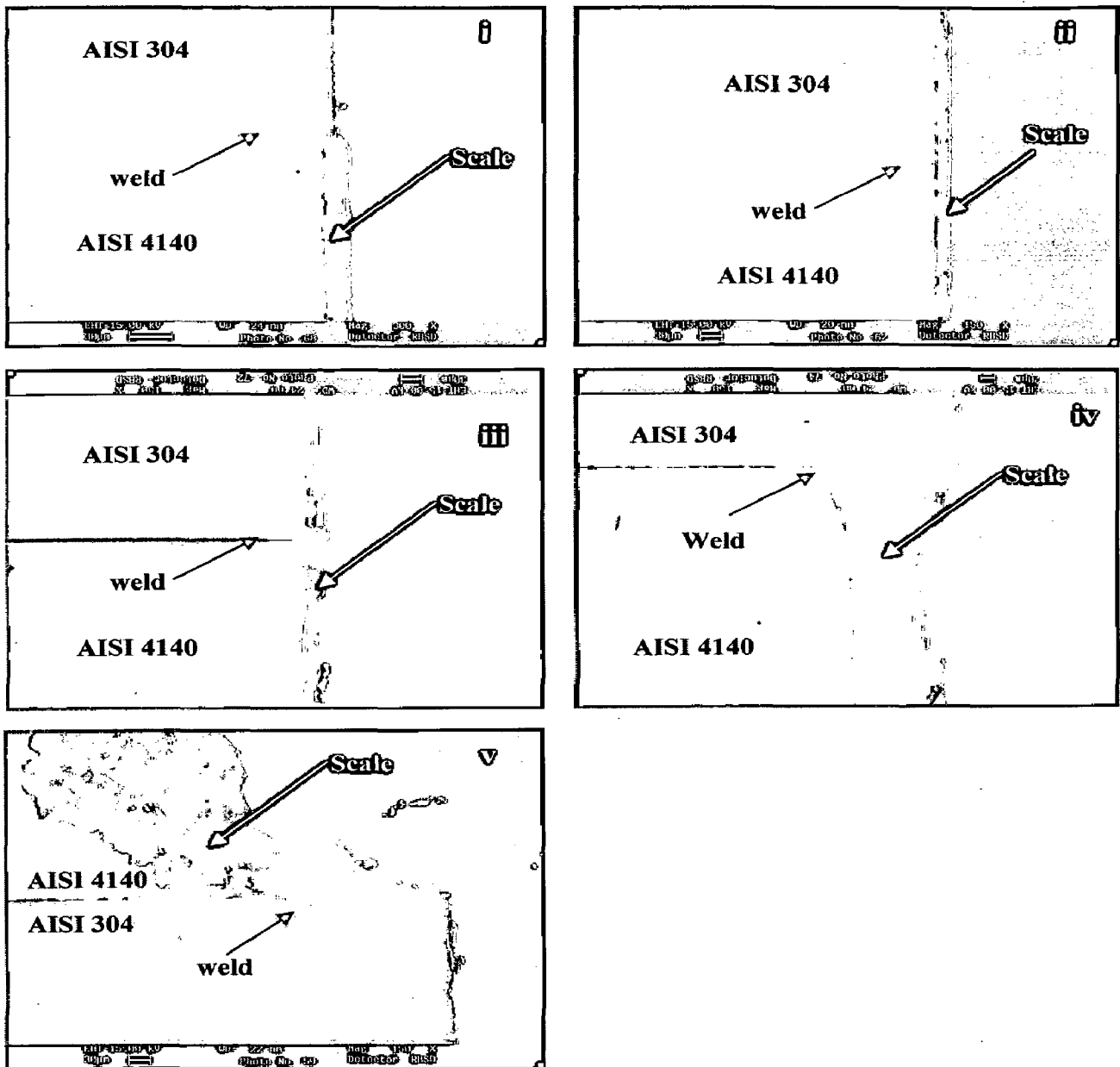


Fig 5.4 Back Scattered Image after complete the high temperature corrosion of friction welded AISI 4140 and AISI 304, exposed under air. (i) Cyclic oxidation at 500 °C, (ii) Cyclic oxidation at 600 °C, (iii) Isothermal Oxidation at 500 °C, (iv) Isothermal Oxidation at 700 °C, (v) Isothermal Oxidation at 900 °C.

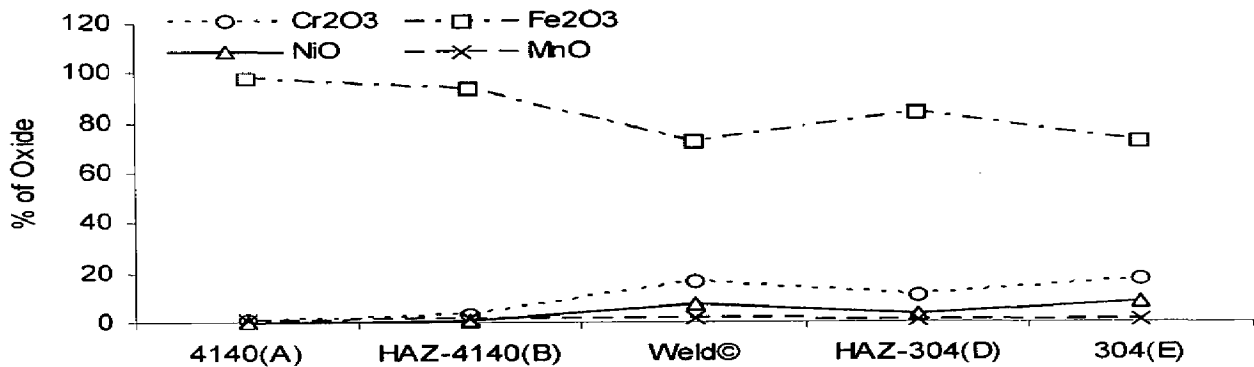
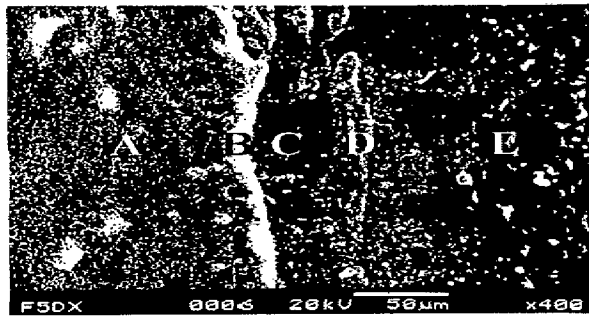


Fig.5.5(a). EDAX on the weldment of 4140-304. Note: 500 °C cyclic oxidation, A- 4140, B- HAZ (4140), C-Weld, D- HAZ (304), E- 304.

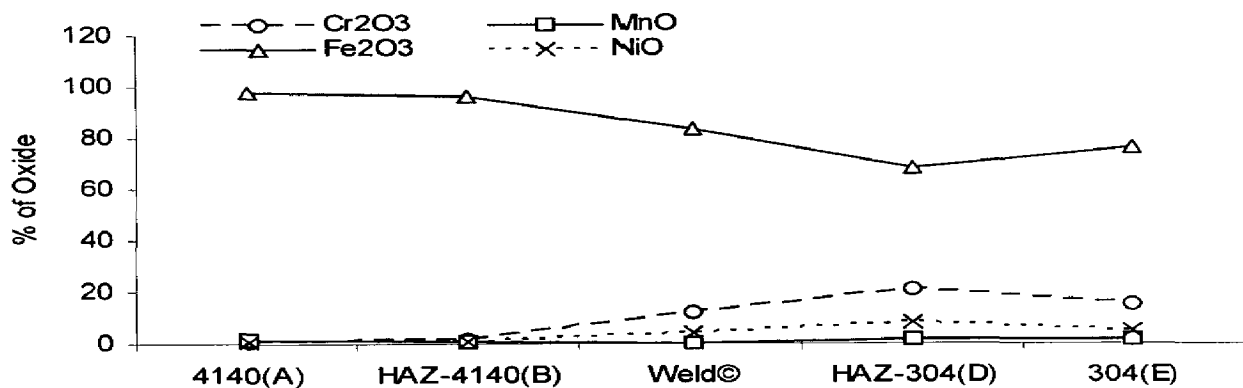


Fig.5.5(b). EDAX on the weldment of 4140-304. Note: cyclic oxidation at 600 °C, A- 4140, B- HAZ (4140), C-Weld, D- HAZ (304), E- 304.

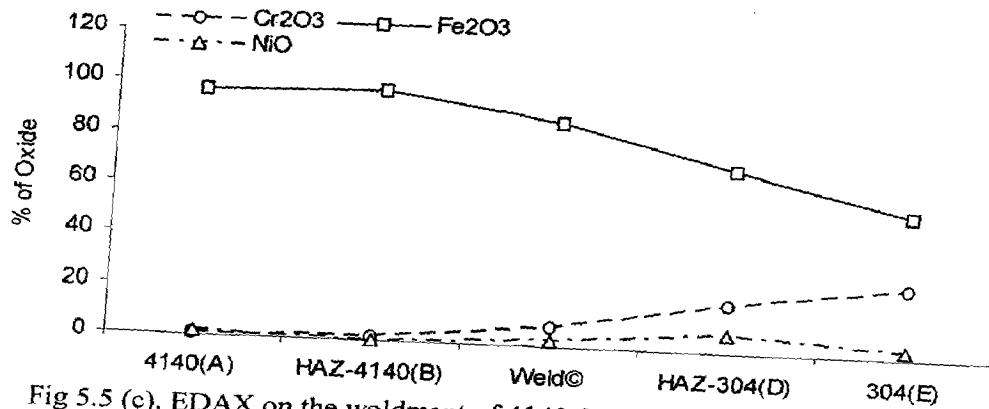
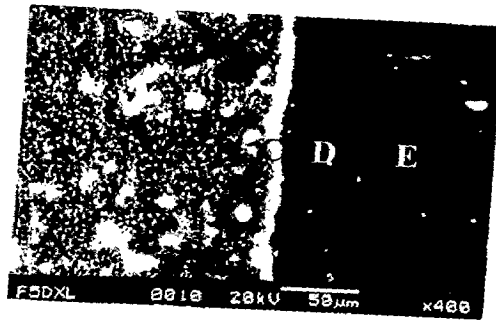


Fig 5.5 (c). EDAX on the weldment of 4140-304. Note: 50 hours Isothermal oxidation at 500 °C. A- 4140, B- HAZ (4140), C-Weld, D- HAZ (304), E- 304.

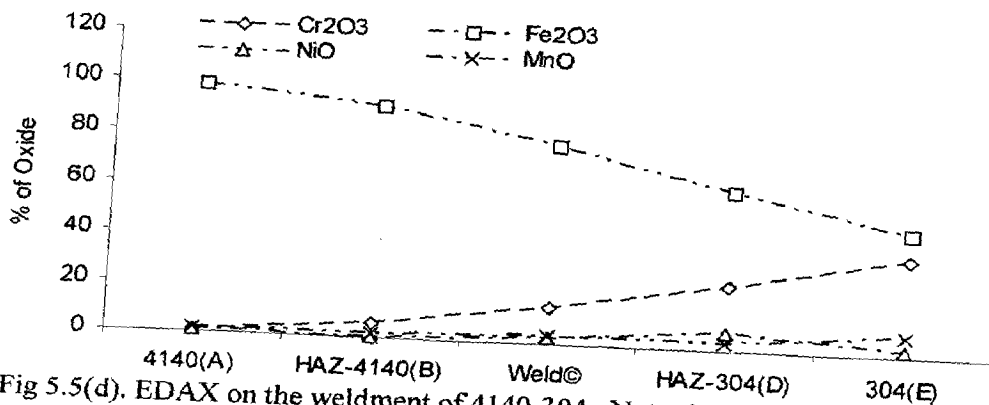
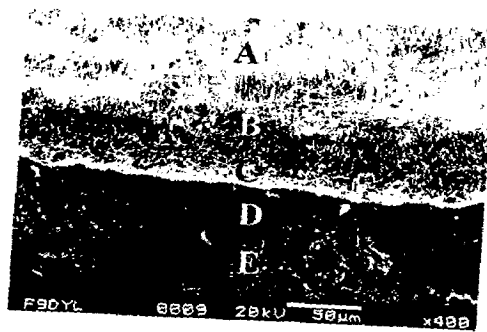


Fig 5.5 (d). EDAX on the weldment of 4140-304. Note: 50 hours Isothermal oxidation at 700 °C. A- 4140, B- HAZ (4140), C-Weld, D- HAZ (304), E- 304.

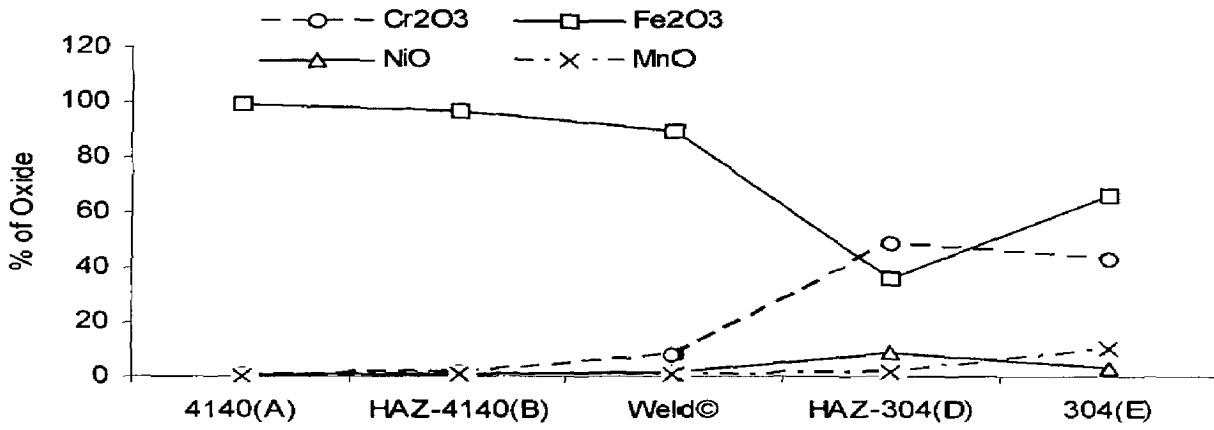
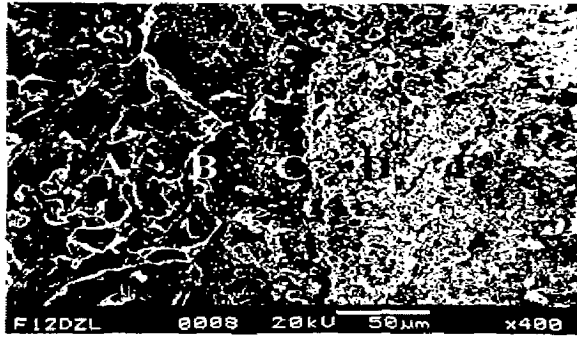


Fig 5.5(e). EDAX on the weldment of 4140-304. Note: 50 hours Isothermal oxidation at 900 °C. A- 4140, B- HAZ (4140), C-Weld, D- HAZ (304), E- 304.

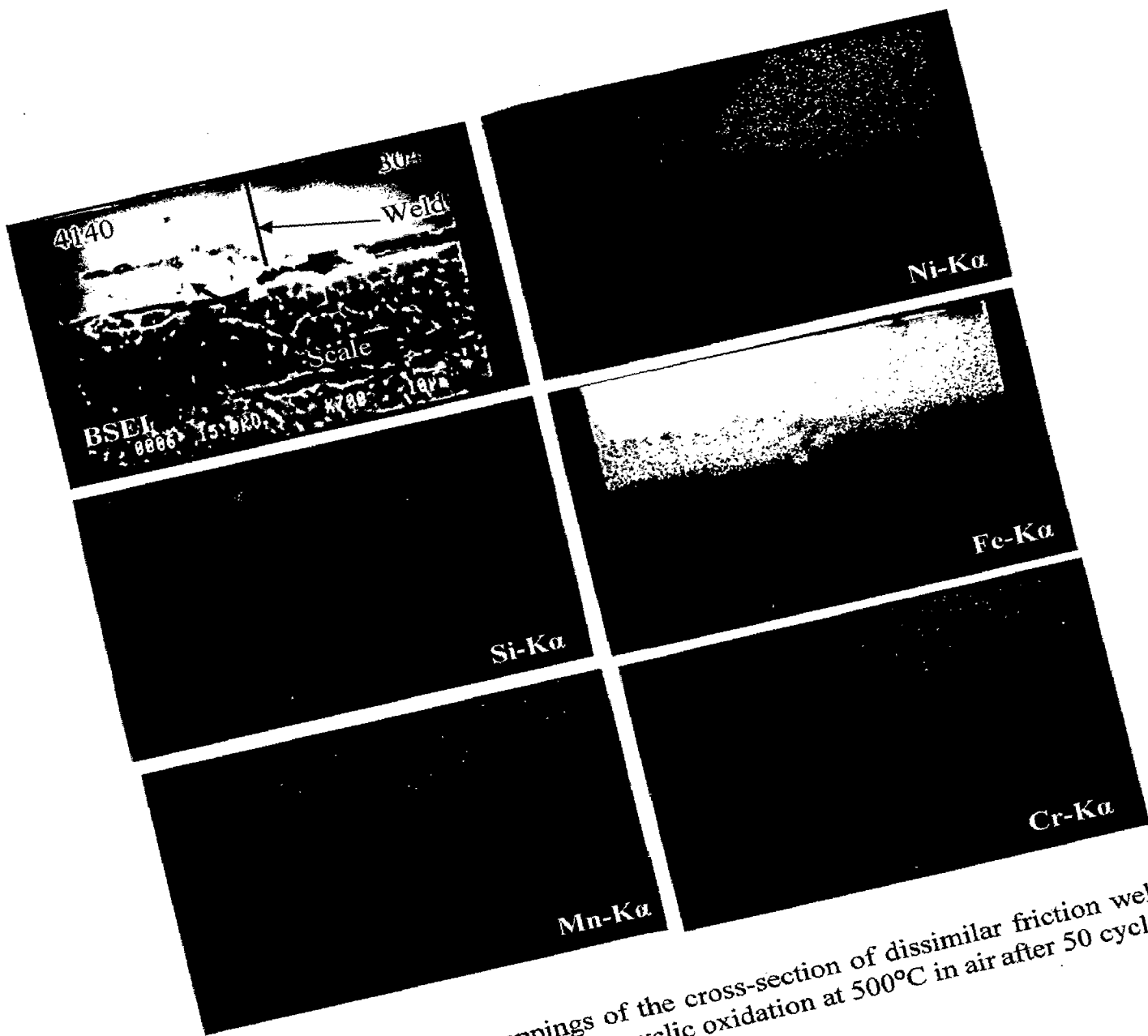


Fig. 5.6 BSEI and X-ray mappings of the cross-section of dissimilar friction welded AISI 4140 and AISI 304 subjected to cyclic oxidation at 500°C in air after 50 cycles.

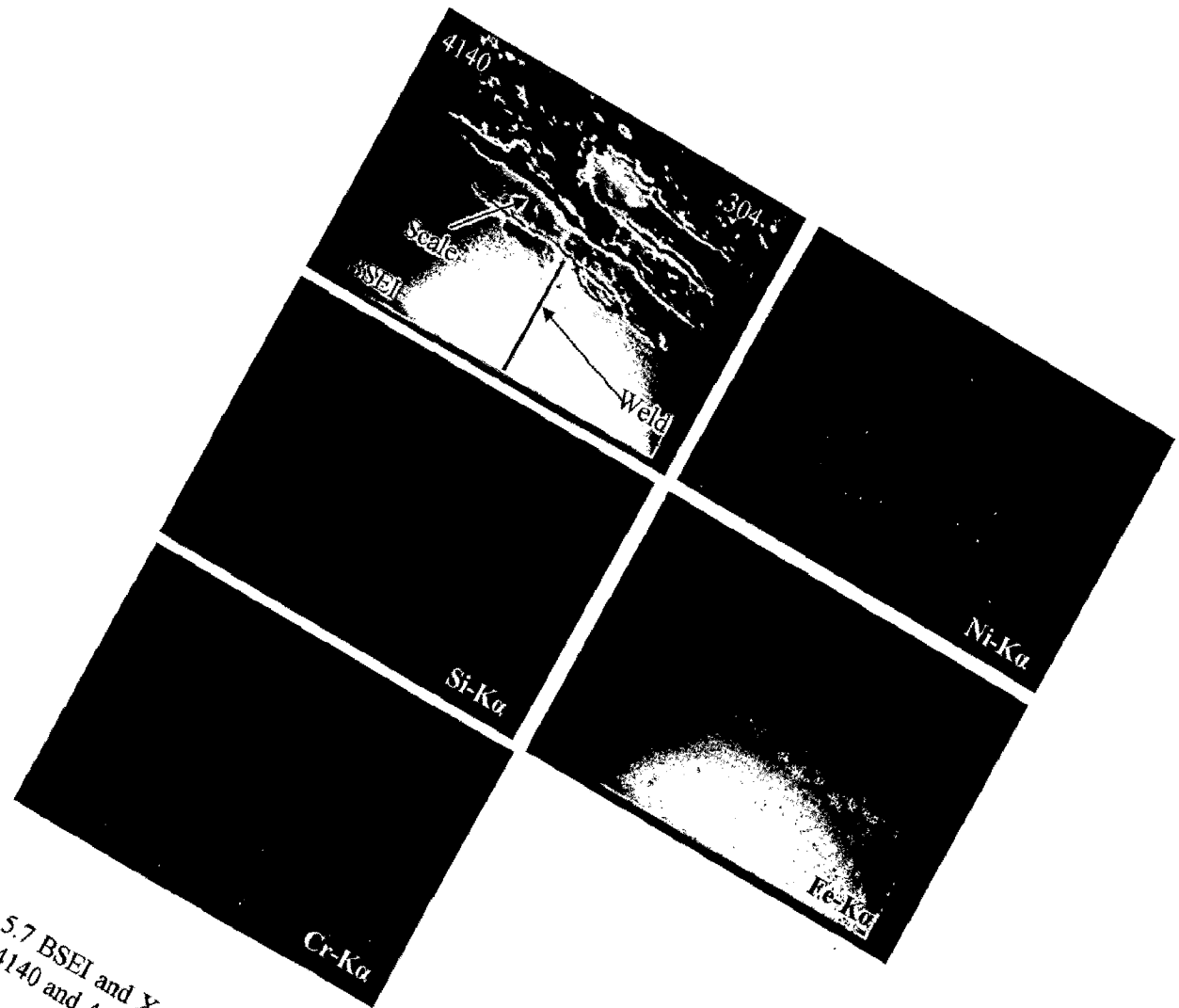


Fig. 5.7 BSEI and X-ray mappings of the cross-section of dissimilar friction welded AISI 4140 and AISI 304 subjected to cyclic oxidation at 600°C in air after 50 cycles.

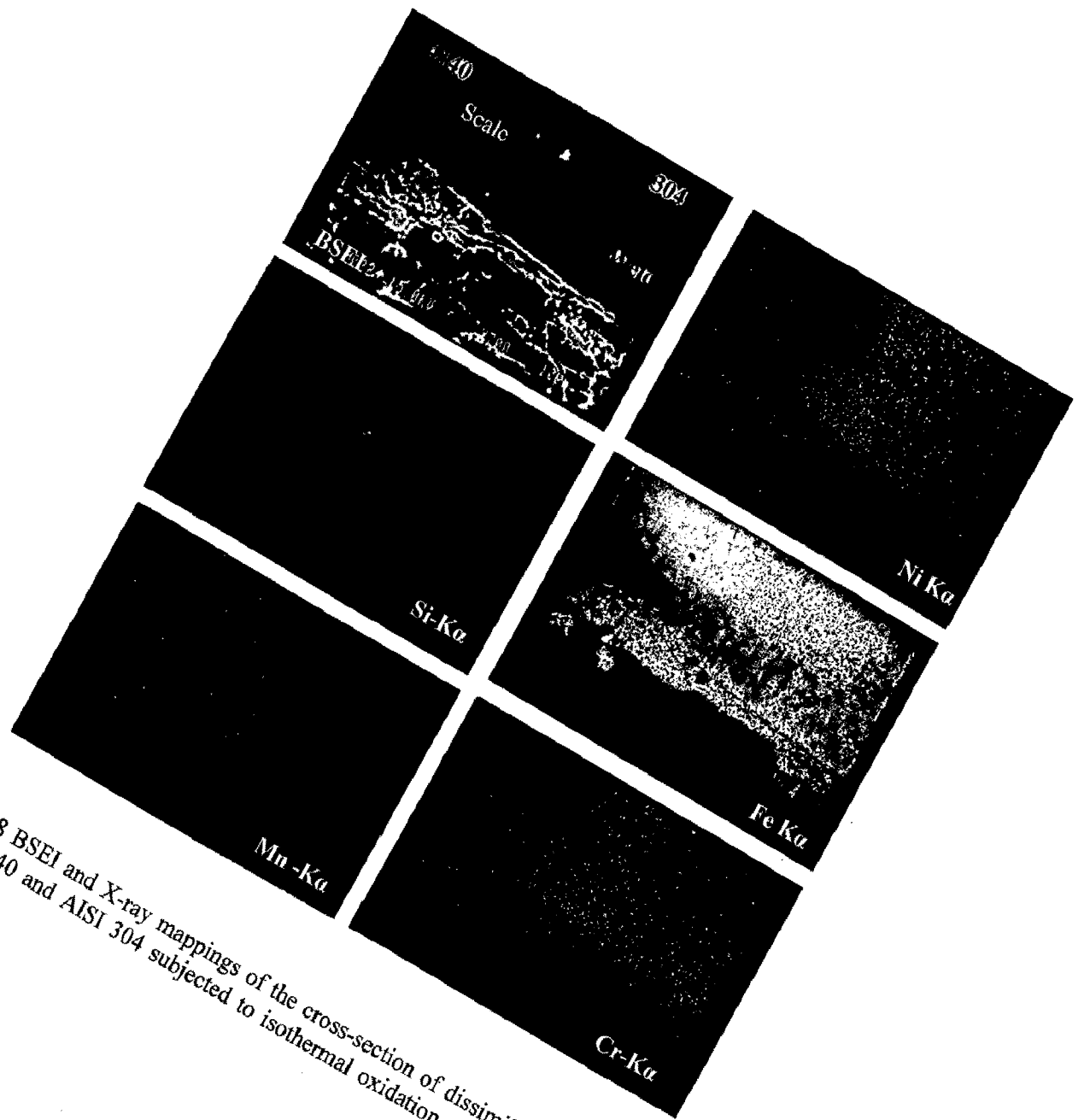


Fig. 5.8 BSEI and X-ray mappings of the cross-section of dissimilar friction welded AISI 4140 and AISI 304 subjected to isothermal oxidation at 500°C in air after 50 cycles.

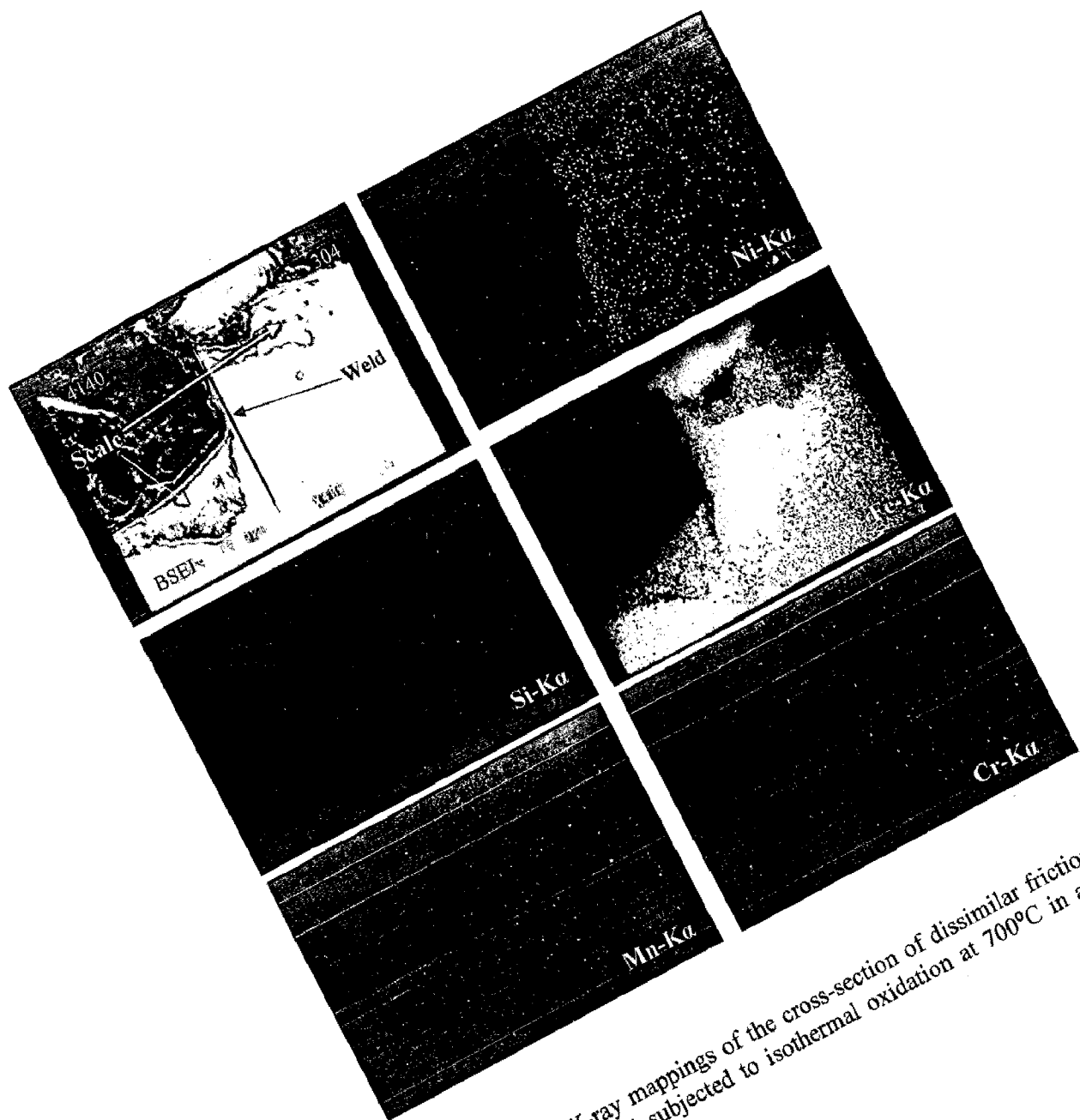


Fig. 5.9 BSEI and X-ray mappings of the cross-section of dissimilar friction welded AISI 4140 and AISI 304 subjected to isothermal oxidation at 700°C in air after 50 cycles.

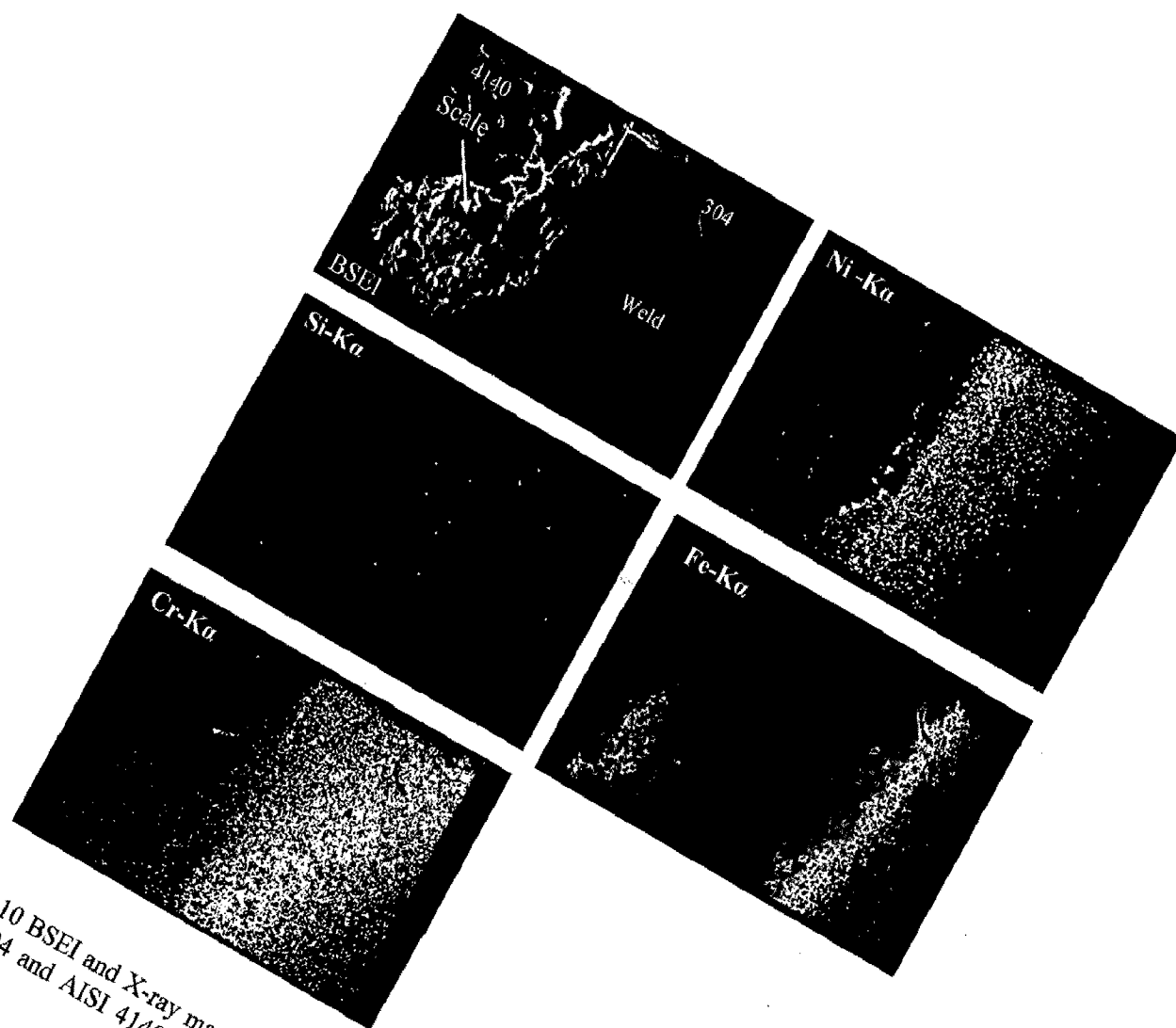


Fig. 5.10 BSEI and X-ray mappings of the cross-section of dissimilar friction welded AISI 304 and AISI 4140 subjected to isothermal oxidation at 900°C in air after 50 cycles.

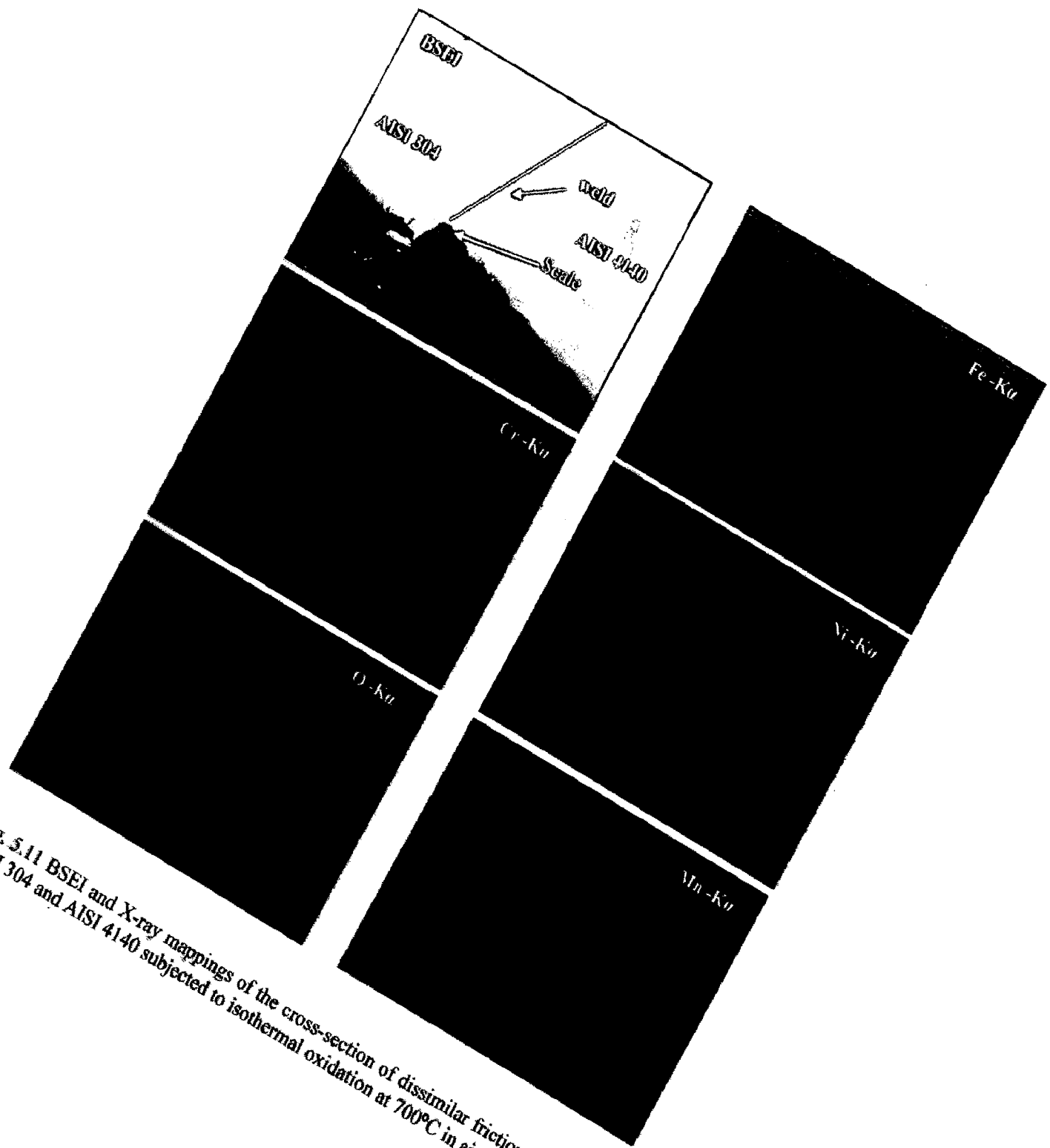


Fig. 5.11 BSEI and X-ray mappings of the cross-section of dissimilar friction welded AISI 304 and AISI 4140 subjected to isothermal oxidation at 700°C in air.

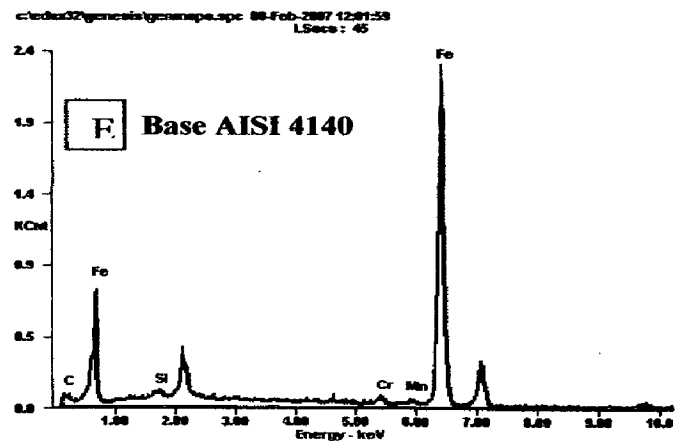
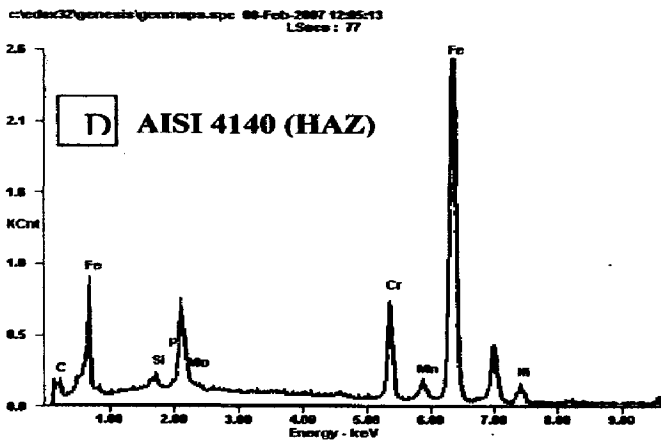
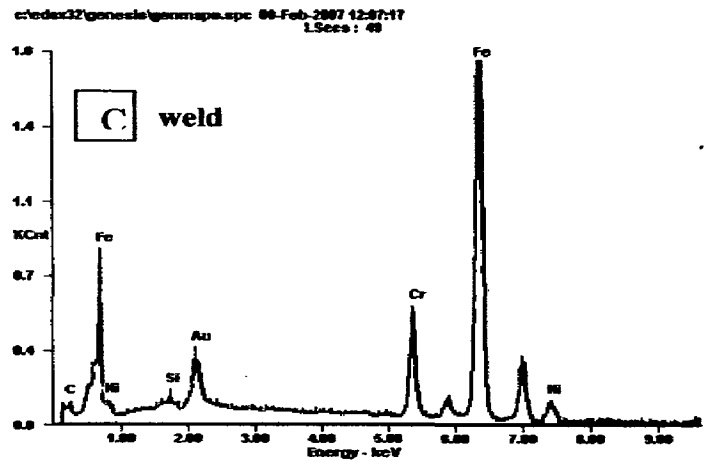
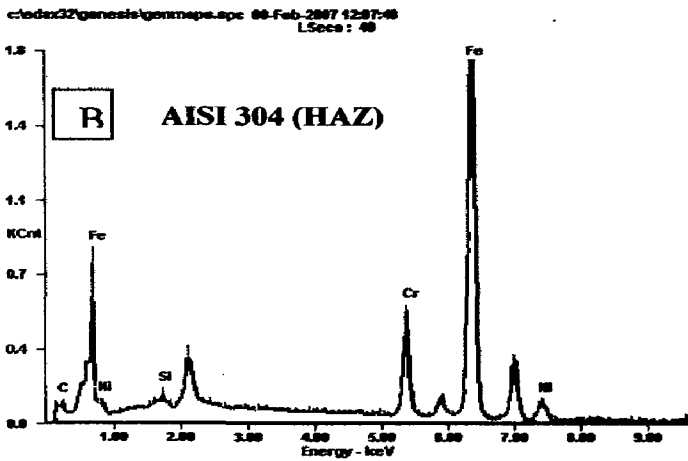
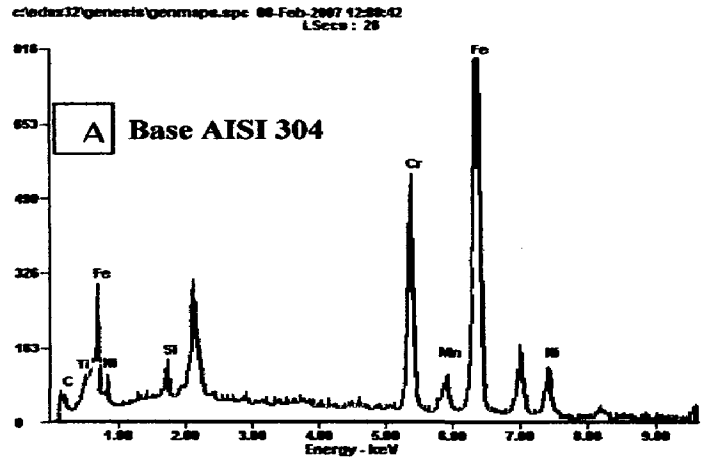
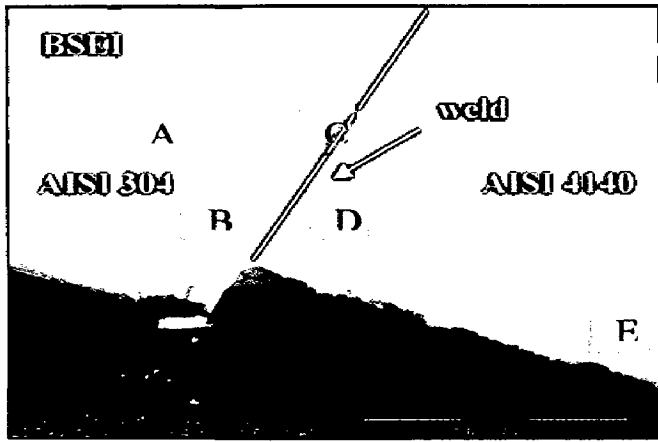


Fig 5.12 BSEI and Elemental Distribution curve on the cross-section of dissimilar friction welded AISI 304 and AISI 4140 subjected to isothermal oxidation at 700°C in air.

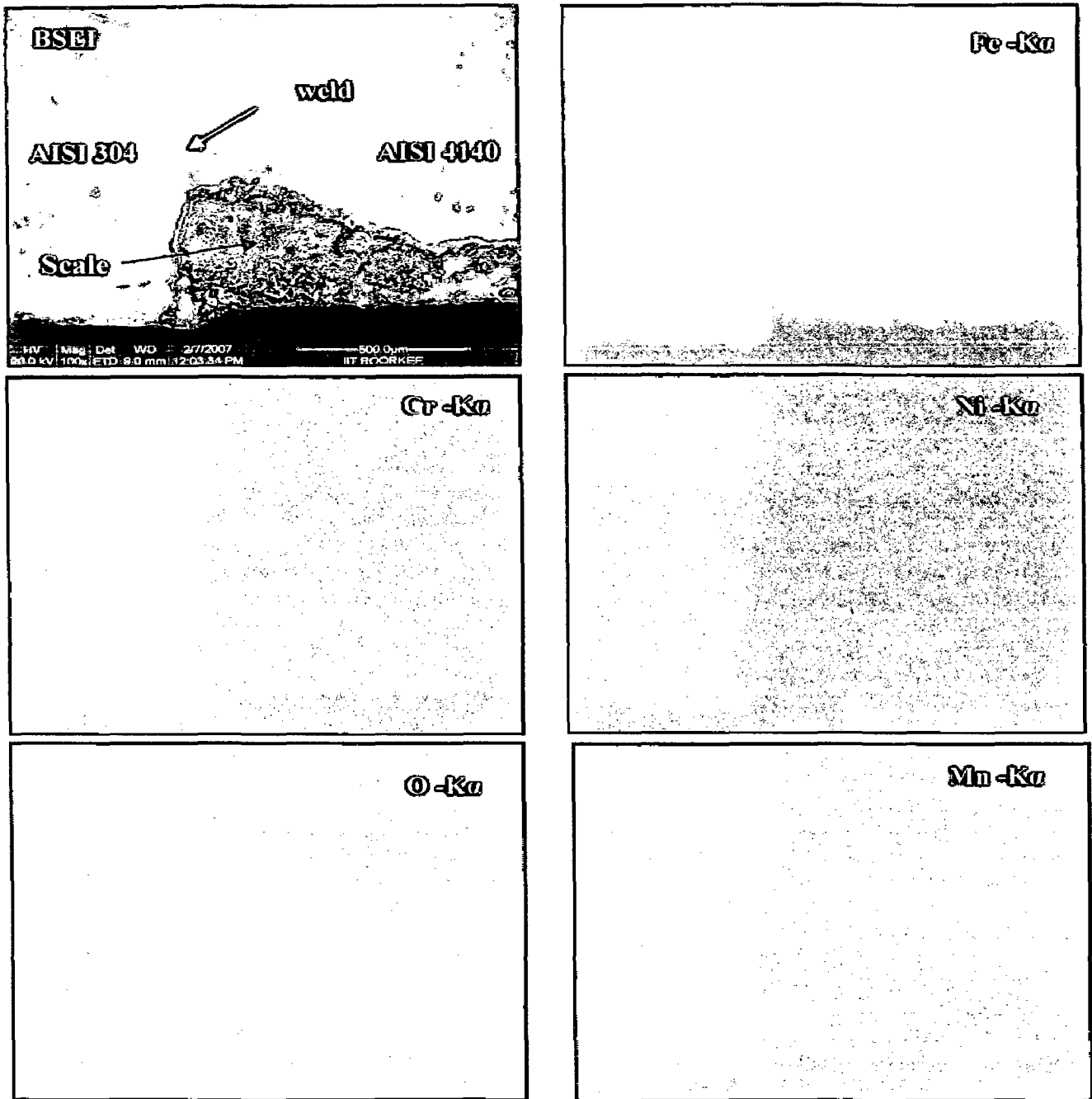


Fig. 5.13 BSEI and X-ray mappings of the cross-section of dissimilar friction welded AISI 304 and AISI 4140 subjected to isothermal oxidation at 900°C in air

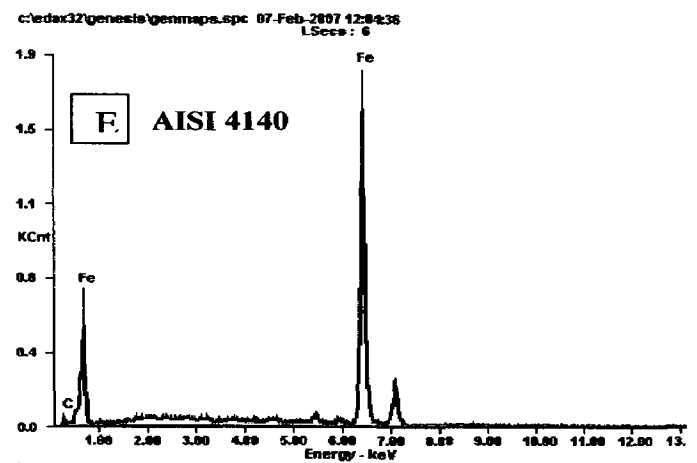
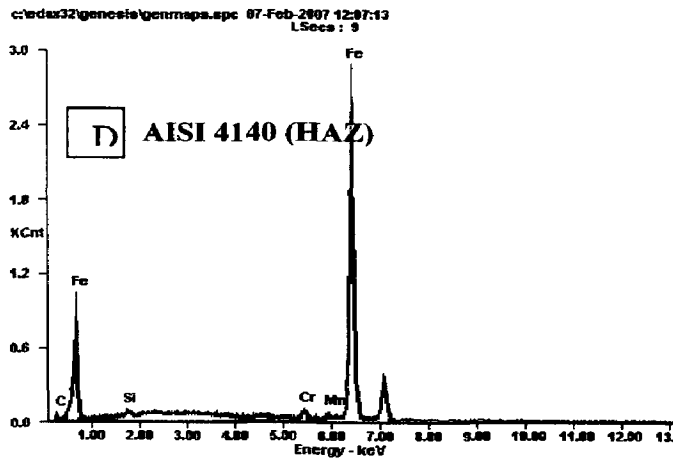
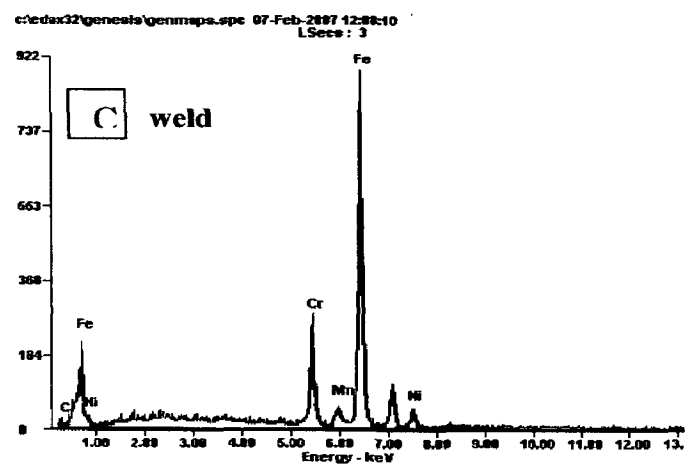
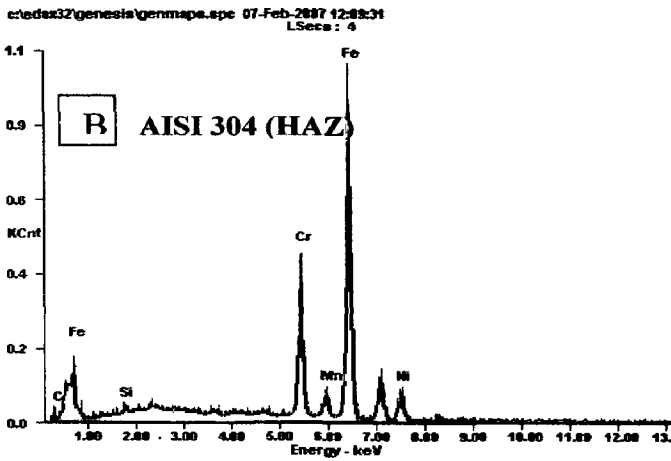
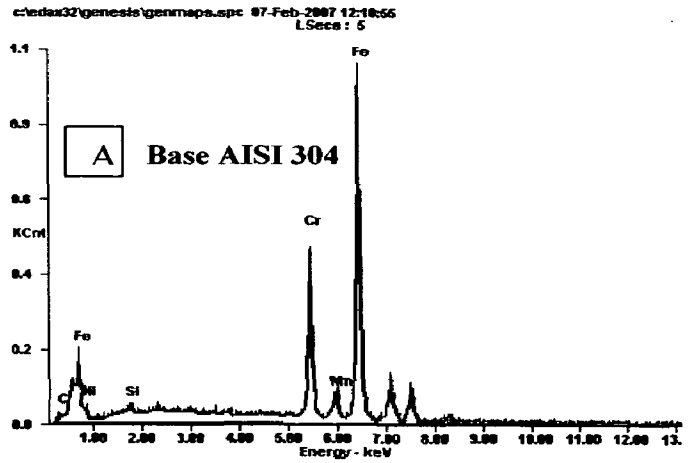
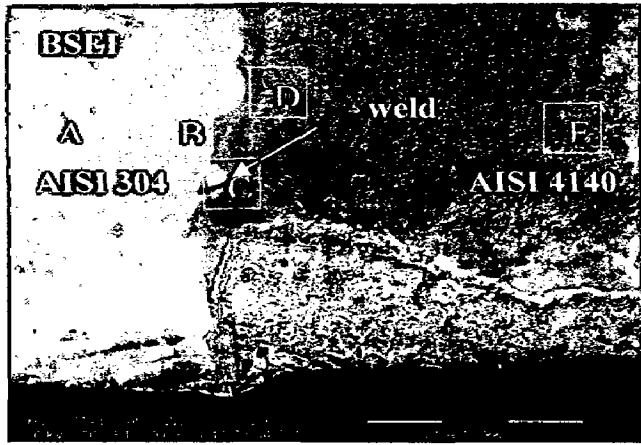


Fig 5.14 BSEI and Elemental Distribution curve on the cross-section of dissimilar friction welded AISI 304 and AISI 4140 subjected to isothermal oxidation at 900°C in air.

FeO is not detected in the scale of the weldment exposed to all the three temperatures. This may be due to increase in the Cr_2O_3 content of scale on the weldment. Similar observation has been made by Moretimer et al [1969]. The iron oxidized in preference of Cr in the alloy 4140 where Cr content is only 1.1% and the part of this Cr is present as carbide. This amount of Cr is not sufficient for forming a protective layer of Cr_2O_3 on the surface. There is little migration of Cr from the interior as its diffusion coefficient is small. Oxygen diffuses through the outer scale of iron oxides and reacts with chromium to form Cr_2O_3 at the inner layers which exist as particles and not as continuous layers.

The amount of Fe_2O_3 is higher in the scale on the weldment where as the presence of chromium in the inner scale has been observed for all the temperatures of exposure. Similar findings also reported by Lai et al [1990]

The scale on the weldment was observed to be fragile and had tendency for spalling perhaps due to differences in the thermal-expansion coefficients of interface, and the two base metals and their oxides. The scale thickness more on low alloy steel side which increased with increase in temperature, also it was observed that the rate of corrosion was more in the weld region as compared to base metal as can be observed in Fig 5.4.

The phenomena of cracking of the scale on the low alloy steel side may be as the result of the presence of Mo in low alloy steel. The oxide protrusions appeared from beneath through the cracks is perhaps of greater specific-volume of iron oxide which also observed by Bornstein et al [1971].

The presence of chromium oxide as revealed by XRD analysis in the scale on the dissimilar weldment under isothermal oxidation at 700 and 900 °C. This may be due to spalling of top Fe_2O_3 layer of the scale. Presence of only iron oxide in the scale on weld interface has further been confirmed by EDAX indicating upper scale of Fe_2O_3 for weldment which is followed by subscale where Fe_2O_3 and Cr_2O_3 are coexisting. This can

be attributed to depletion of iron from the metal subscale thereby leaving behind chromium rich pockets which further gets oxidised to form oxides of chromium in the inner scale. Sadique et al. [2000] have suggested similar behaviour.

From the mapping and elemental analysis on hot corroded sample, it was observed that the enrichment of Fe, Cr, Ni in the weld region as well as in the scale of low alloy steel side (Fig 5.11 to 5.14), which leads to formation of intermetallic FeNi / CrNiFe which also supported by EPMA and XRD (Fig 5.3).

CHAPTER 6

HOT CORROSION STUDIES OF FRICTION WELDED DISSIMILAR METALS IN MOLTEN SALT ENVIRONMENT

This chapter deals with the critical examination of corrosion products and the behaviour of friction welded dissimilar weldment. The hot corrosion studies were performed on the weldments exposed at the temperature from 500, 550 and 600 °C under the following mixture of molten salt for 50 cycles.

- (i) $\text{Na}_2\text{SO}_4 + \text{V}_2\text{O}_5$ (60%)
- (ii) $\text{K}_2\text{SO}_4 + \text{NaCl}$ (60%)
- (iii) Na_2SO_4 (40%) + K_2SO_4 (40%) + NaCl (10%) + KCl (10%)
- (iv) $\text{Na}_2\text{SO}_4 + \text{NaCl}$ (50%)

The samples were visually examined at the end of each cycle for any change in the colour, lustre, adherence of scale to the substrate and spalling tendency. The weight change measurements were made at the end of each cycle. Efforts have also been made to understand the mechanism of corrosion wherever possible.

The corrosion products were analysed with the help of XRD, SEM/EDAX and EPMA. The results for different environment of molten salt mixture have been reported under different subheadings. In view of comparison the thermogravimetric data for each environment along with different temperature of exposure were recorded. The parabolic rate constants and scale thickness values have been evaluated after 50 cycles of exposure.

6.1 RESULTS

6.1.1 Friction Welded Dissimilar Metals Exposed to $\text{Na}_2\text{SO}_4 + \text{V}_2\text{O}_5$ (60%)

This subheading deals with the critical examination of corrosion products and the behaviour of friction welded dissimilar weldment made by different burn-off length namely 5, 7, 9, and 12 mm. The hot corrosion studies were performed on the weldments exposed at the temperature from 500, 550, 600, 700 and 900 °C under the $\text{Na}_2\text{SO}_4 + \text{V}_2\text{O}_5$

(60%) mixture of molten salt for 50 cycles. In view of comparison the thermogravimetric data of each environment along with different temperature of exposure were recorded. The parabolic rate constants and scale thickness values have been evaluated after 50 cycles of exposure.

6.1.1.1 Visual Examination

In the hot corrosion study of the friction welded 4140 low alloy steel and 304 Stainless steel weldment, after first cycle indicated a light rough scale having brown patches. These numbers of patches are more on 4140 side than 304 side. After completion of 10 cycles the scale becomes thicker and with dark brown colour on low alloy steel and there is extensive spalling. Whereas on 304 sides the scale was light brown and adherent. With further increase in number of cycles, the scale becomes darker. The color and texture of scale at weld region was different from that on the base metals. With increase in the temperature from 500 to 550 °C and then 600 °C the thicker scale was observed on HAZ of 4140 side which was light grey in colour, whereas the scale on the HAZ of 304 was of darker grey colour. As the temperature of exposure increased from 500 to 600 °C extent of spalling got increased. At high temperature of exposure the scale more brittle and extensive spalling was observed. When the dissimilar weldment were exposed at 700 and 900 °C the weld zone as well as low alloy steel side shows high degrading. Fig.6.1 (i-v) shows the typical macrographs of hot corroded samples after 50 cycles.

6.1.1.2 Thermogravimetric Data

The plots of cumulative weight gain (mg/cm^2) as a function of time (number of cycles) for four FRW parameters (burn-off length 5,7,9 and 12 mm) at the temperature of 500, 550 and 600 °C in Na_2SO_4 (40%) + V_2O_5 (60%) up to 50 cycles are shown Fig 6.2. Hot corrosion studies also carried out at the temperature of 700 and 900 °C for the above mentioned environment (Fig 6.3). B12 weldment showed the maximum weight gain whereas B5 weldment showed the least weight gain. The parabolic rate constants, K_p for B5, B7, B9 at the different exposure of temperature (500, 550, 600, 700, 900°C)

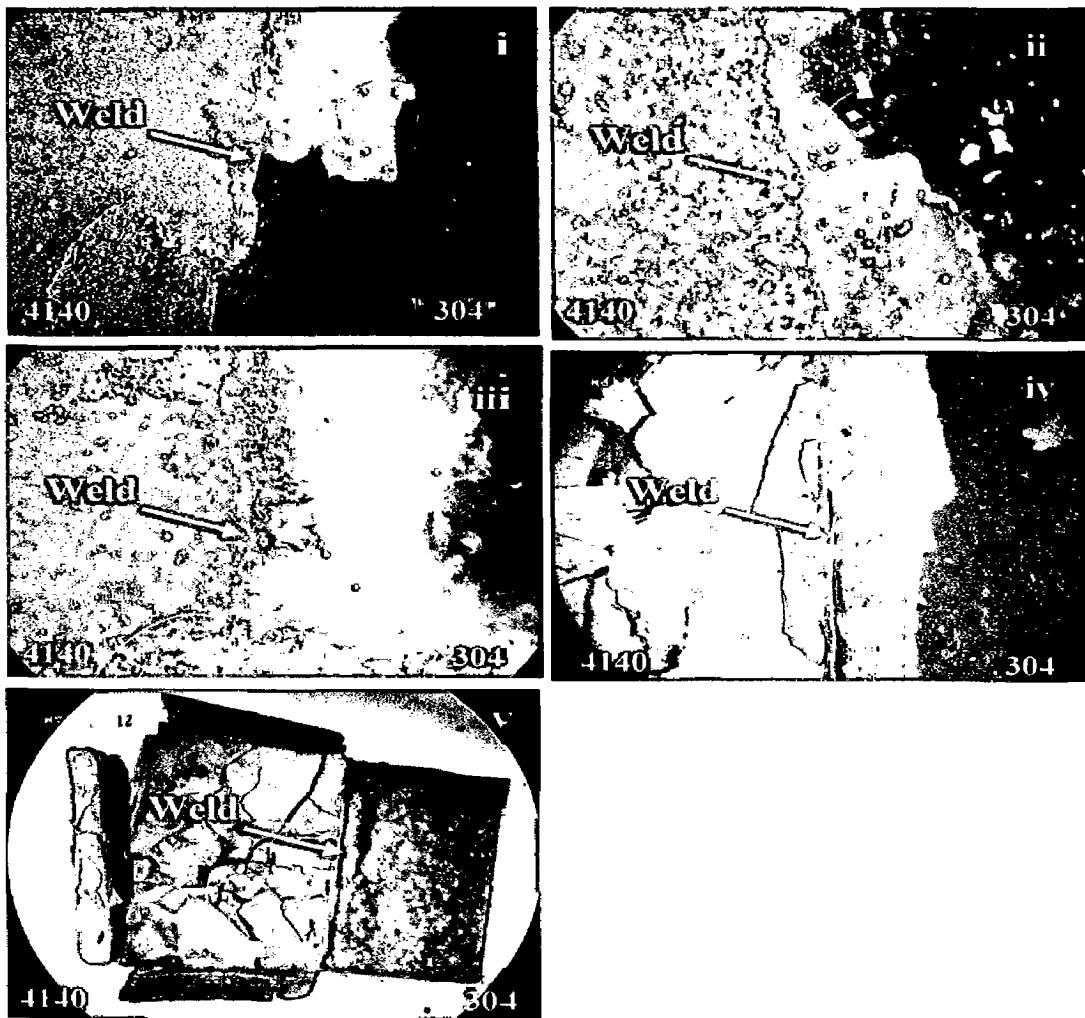


Fig. 6.1 Macrographs dissimilar friction welded AISI 4140 and AISI 304 subjected to cyclic hot corrosion exposed under Na_2SO_4 (40%) + V_2O_5 (60%) at 500, 550, 600, 700 and 900 °C after 50 cycles.

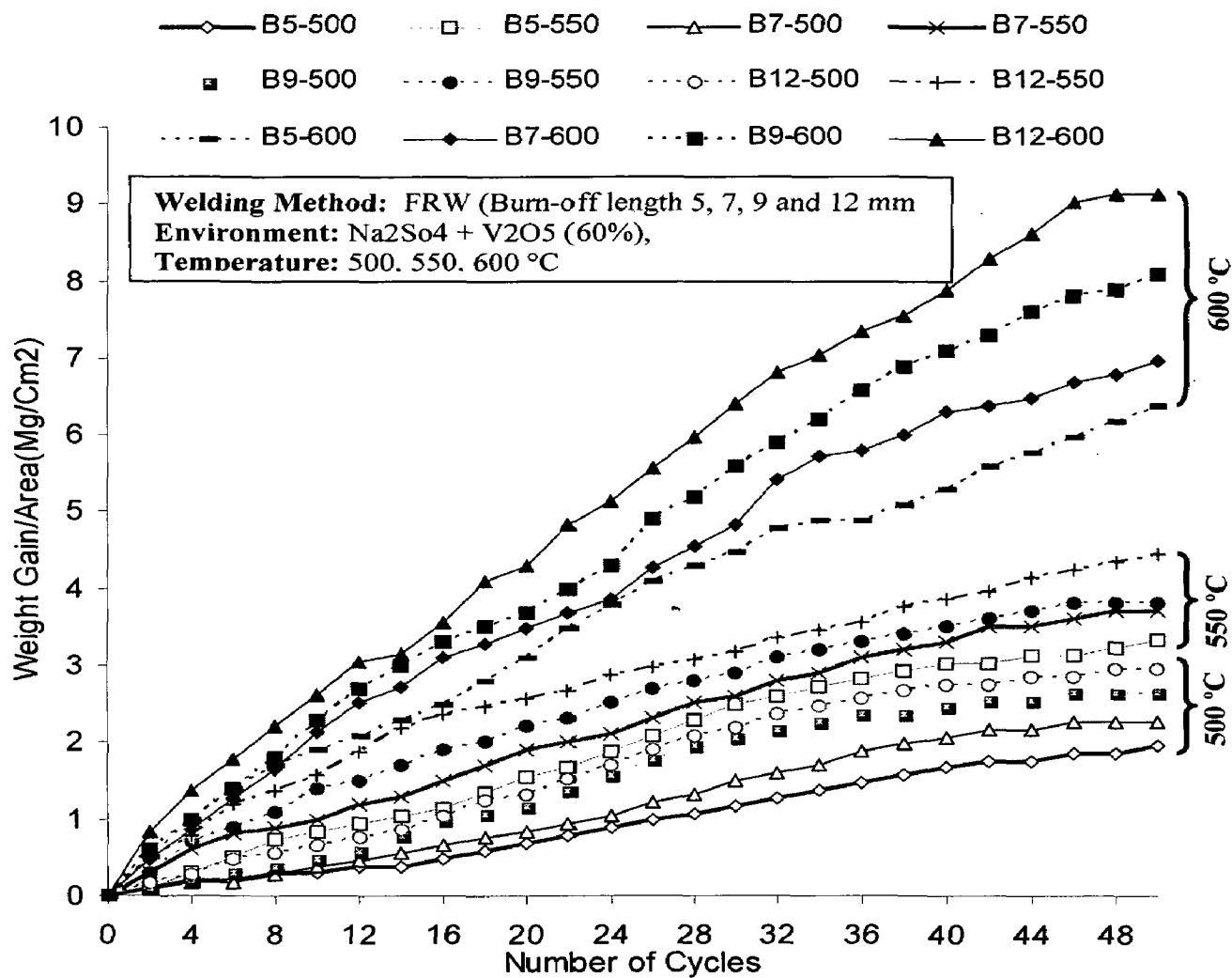


Fig 6.2. Plots of cumulative weight gain (mg/cm²) as a function of time (number of cycles)

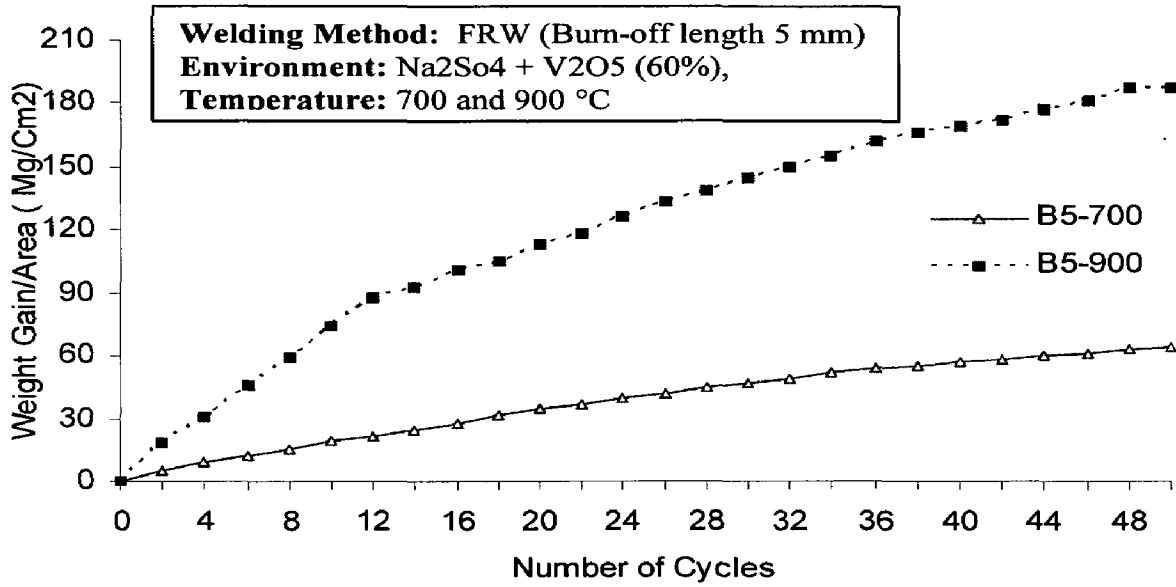


Fig 6.3. Plots of cumulative weight gain (mg/cm²) as a function of time (number of cycles)

are given in Table 6.1 The parabolic rate constant for corrosion of dissimilar weldment made by burn-off length 'B' 12mm is around 2.5 times of that for B5 weldment. When increasing the temperature of exposure was increased from 500 to 600 °C, the parabolic rate constant approximately 15 times than that of at 500 °C. when the weldment were exposed to given corrosive mixture at 700 and 900 °C, the rate of corrosion is increased drastically and the Kp values are increased 50 and 400 times respectively.

Table 6.1 Values of parabolic rate constant Kp

Temperature (°C)	Description		Kp ($10^{-6}(\text{gm}^2\text{Cm}^{-1}\text{s}^{-1})$)
	Burn off length (mm)		
500	5		0.229
	7		0.336
	9		0.477
	12		0.575
550	5		0.697
	7		0.858
	9		0.916
	12		1.100
600	5		2.32
	7		2.96
	9		3.96
	12		5.09
700	5		250.000
900	5		2099.000

6.1.1.3 X-ray Diffraction Analysis

The XRD patterns for the hot corroded surfaces of welded samples by keeping four different burn-off length (B5, B7, B9 and B12 mm) exposed to the Na₂SO₄- 60% V₂O₅ environment at exposure temperature of 500, 550 and 600 °C after 50 cycles are shown in Fig. 6.4 - 6.6. It is evident from the diffraction patterns that the hot corroded

weldment has Fe_2O_3 as the main phases along with relatively weak peaks of Cr_2O_3 . Corroded weldment also reveals the formation of similar phases with different burn off length B5 to B12. The peak intensity increase with temperature and burn -off length. However, in the case of B12 at 600 °C the peak of the NiFe, $(\text{Cr}, \text{Fe})_2\text{O}_3$ and SiO_2 peaks are found which are absent with exposure at 500 and 550 °C. When the temperature of expose increase to 700 and 900 °C, the intensity of Fe_2O_3 peak increases with weak indicate of Cr_2O_3 FeNi and CrNiFe are observed (Fig 6.7).

6.1.1.4 Scale Thickness Measurement

The samples were cut across the cross-section after exposure to molten salt at 500, 550 and 600 °C for 50 cycles and mounted. The precise scale thickness values were measured from SEM back scattered images shown in Fig. 6.8. Fig 6.9 shows the BSEI for friction weldment exposed at the temperature of 700 and 900 °C under molten salt of Na_2SO_4 - 60% V_2O_5 . The exact oxide scale thickness could not be measured for all the weldments due to intense spalling and sputtering. The SEM micrograph shows the fragile and cracked scale for all the weldment.

6.1.1.5 SEM/EDAX Analysis

SEM micrographs of the FRW specimens with four burn of length(B5, B7, B9 and B12) showing surface morphology after cyclic hot corrosion for 50 cycles at 500, 550, and 600 °C, are shown in Fig.6.10 (A to L). The micrographs of all the corroded weldments clearly indicate the tendency spalling of the scale. The oxide grains of the scale over the upper portion of the weld metal were generally fine-grained compared to those over HAZ and base metal region of dissimilar weldment. The SEM micrograph of the top surface of the weldment indicates a sharp difference in their morphologies of the scale which fine grained and coarse grained over the weld and HAZ respectively. The EDAX analysis of the scale for the weldment shows Fe_2O_3 to be the predominant phase, with small amounts of Cr_2O_3 , NiO, MnO and SiO_2 . From EDAX analysis (Fig 6.10 (A-L)) across the low alloy steel 4140, HAZ-4140; weld, HAZ-304 and Stainless steel 304 with B5 heated at 500 °C at given molten salt indicate maximum amount of Cr_2O_3 is in

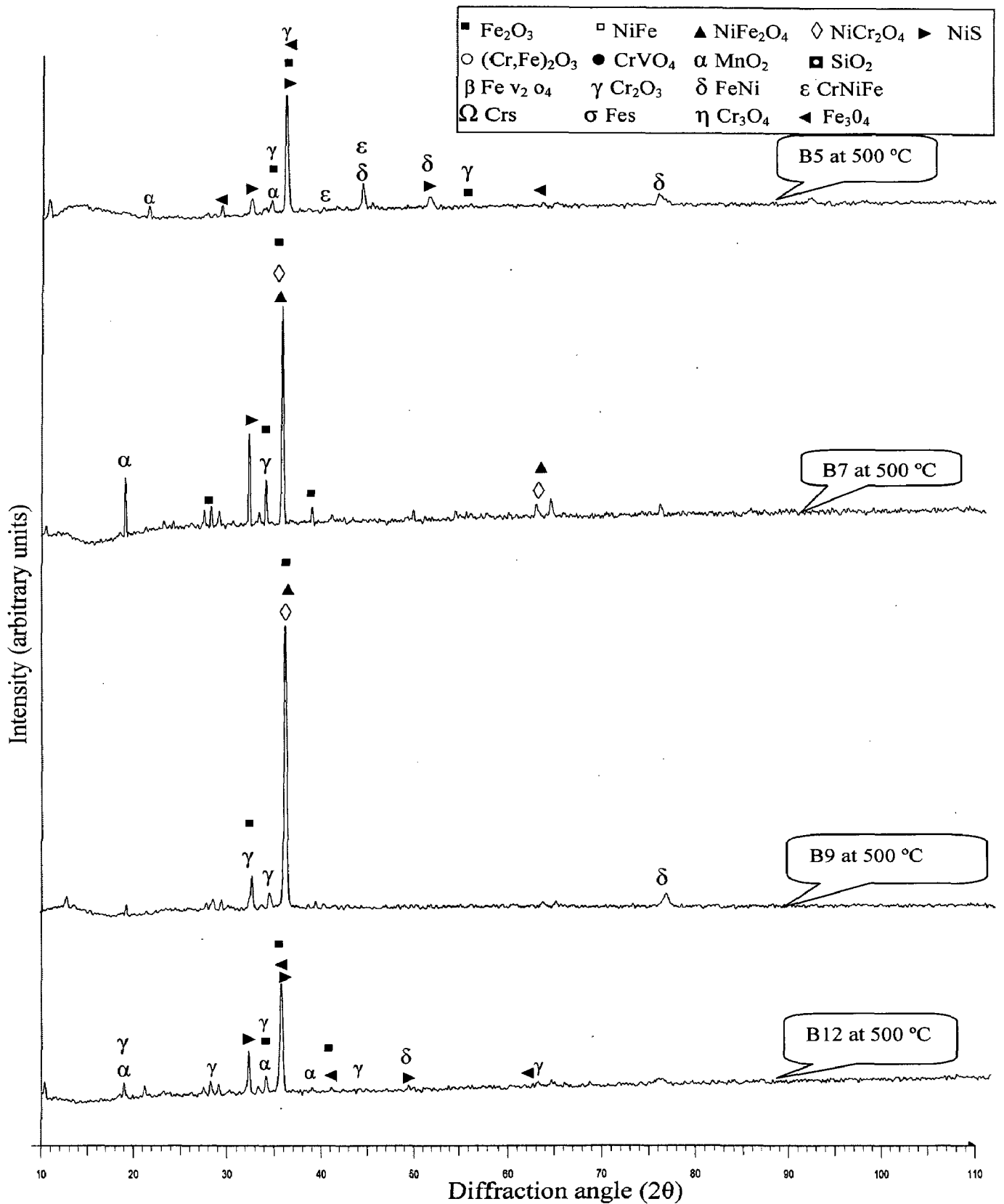


Fig. 6.4 X-ray diffraction patterns for the hot corroded surfaces of friction welded samples by keeping for different burn-off length (B5, B7, B9 and B12 mm) exposed to the Na_2SO_4 -60% V_2O_5 environment exposure temperature of 500 after 50 cycles.

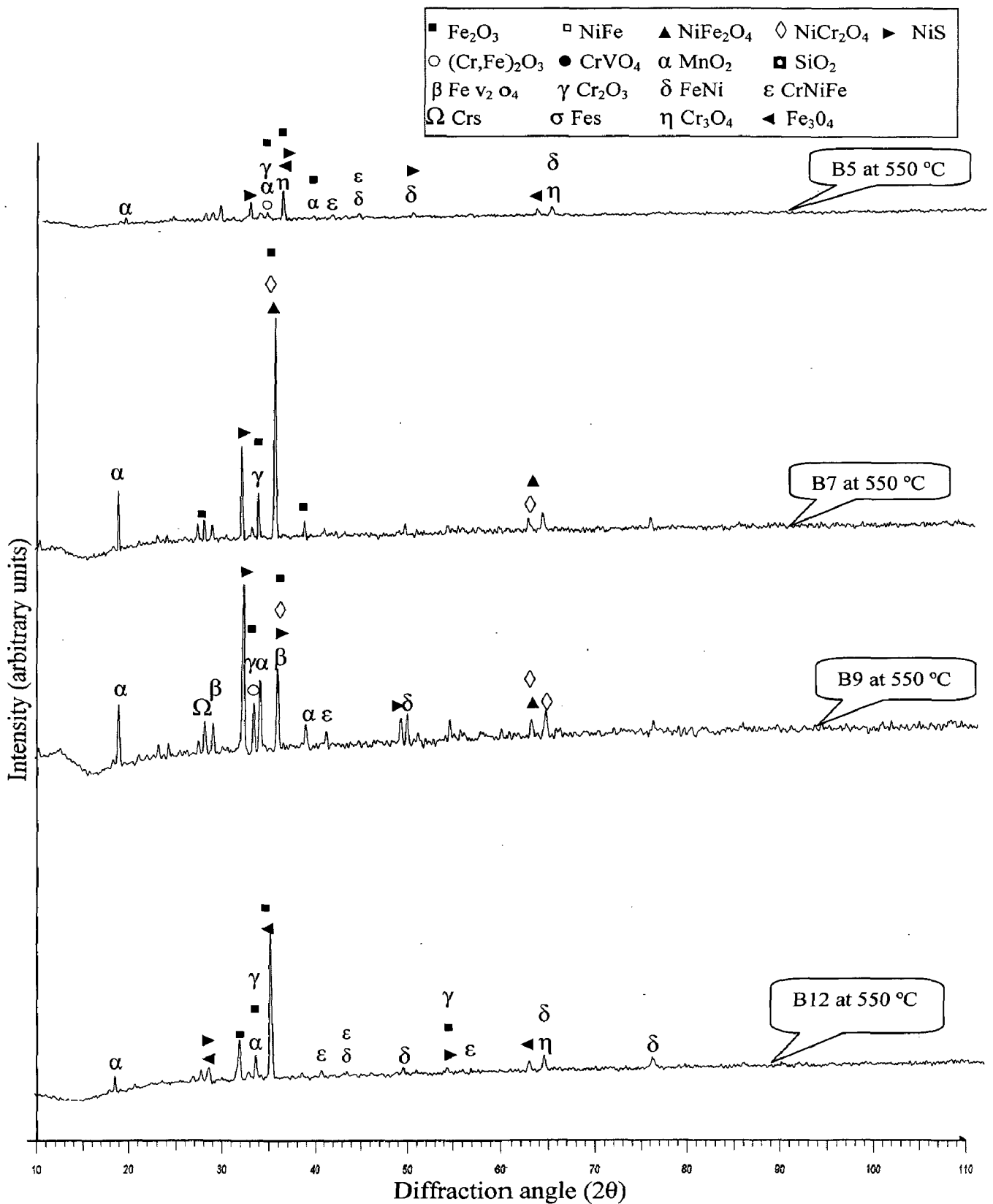


Fig. 6.5 X-ray diffraction patterns for the hot corroded surfaces of friction welded samples by keeping for different burn-off length (B5, B7, B9 and B12 mm) exposed to the Na₂SO₄- 60% V₂O₅ environment exposure temperature of 550 after 50 cycles.

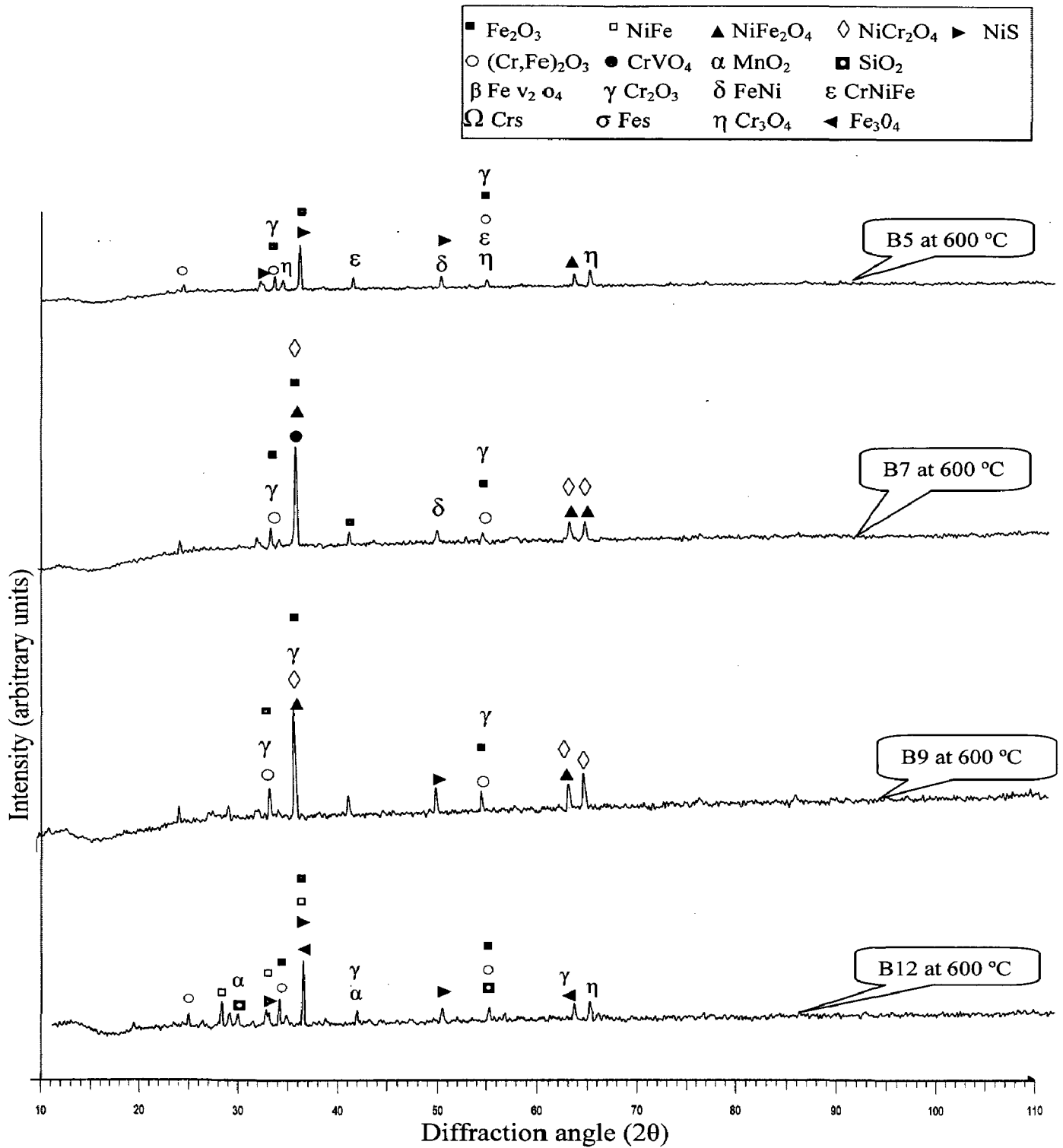


Fig. 6.6 X-ray diffraction patterns for the hot corroded surfaces of friction welded samples by keeping for different burn-off length (B5, B7, B9 and B12 mm) exposed to the Na₂SO₄- 60% V₂O₅ environment exposure temperature of 600 after 50 cycles.

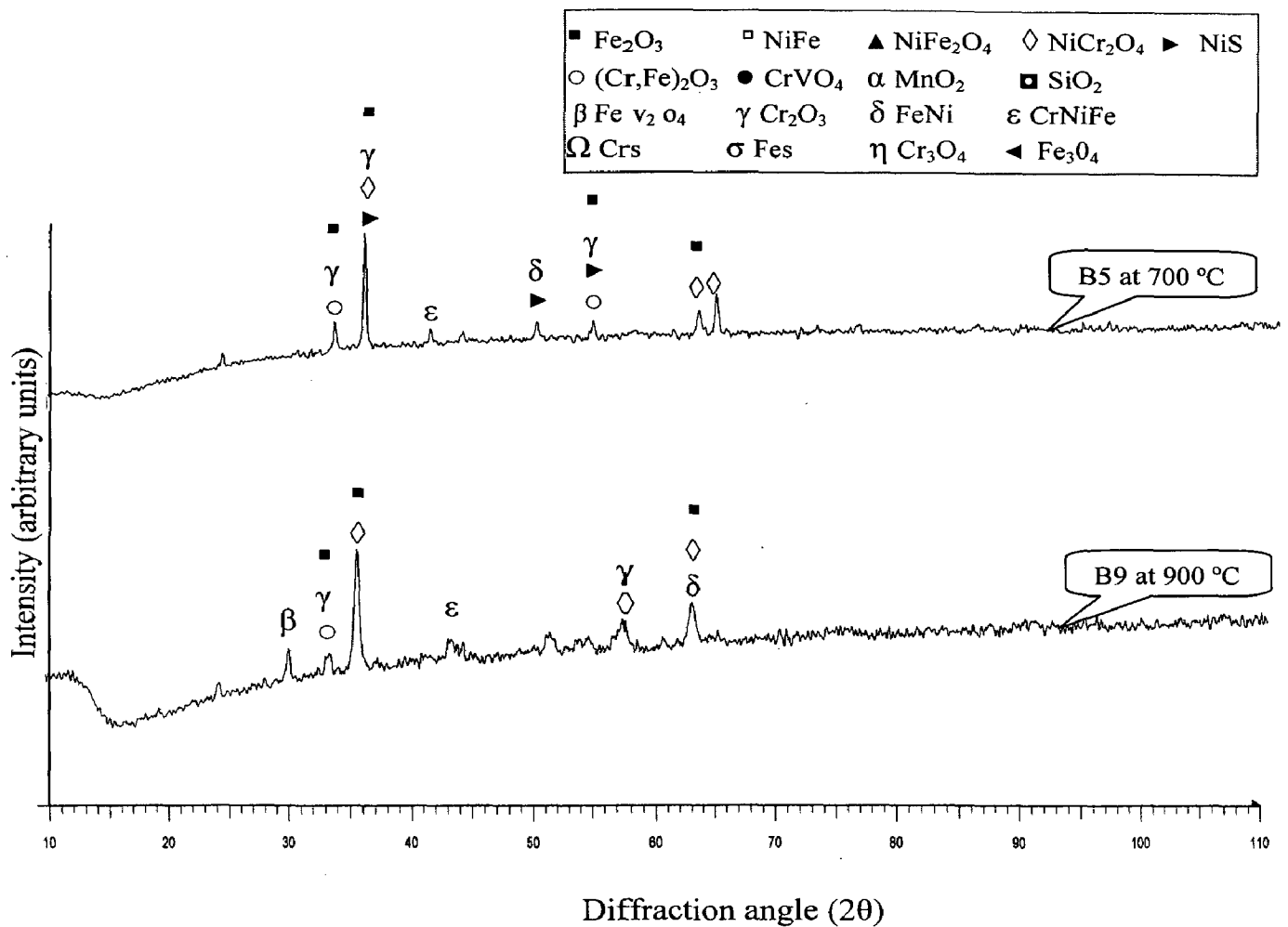


Fig. 6.7 X-ray diffraction patterns for the hot corroded surfaces of friction welded samples by keeping four different burn-off length (B5 mm) exposed to the Na₂SO₄- 60% V₂O₅ environment at exposure temperature of 700 and 900 °C after 50 cycles.

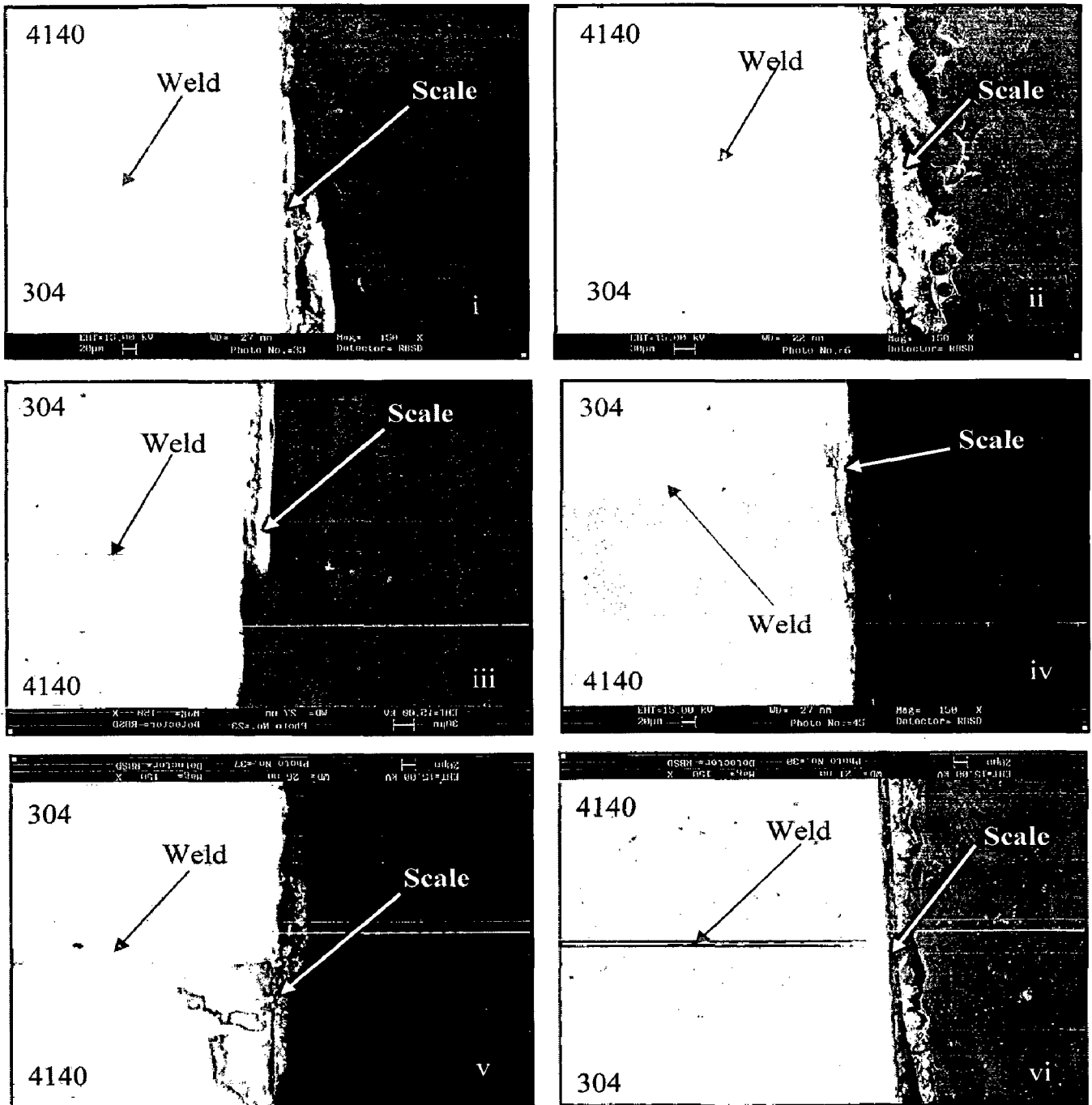


Fig 6.8 BSEI for hot corroded friction weldment exposed temperature of 500, 550, 600,

(i), (ii) and (iii): Exposed temperature 500, 550 and 600 °C respectively for weldment made by keeping 5 mm Burn off length.

(iv), (v) and (vi): Exposed temperature 500, 550 and 600 °C respectively for weldment made by keeping 12 mm Burn off length.

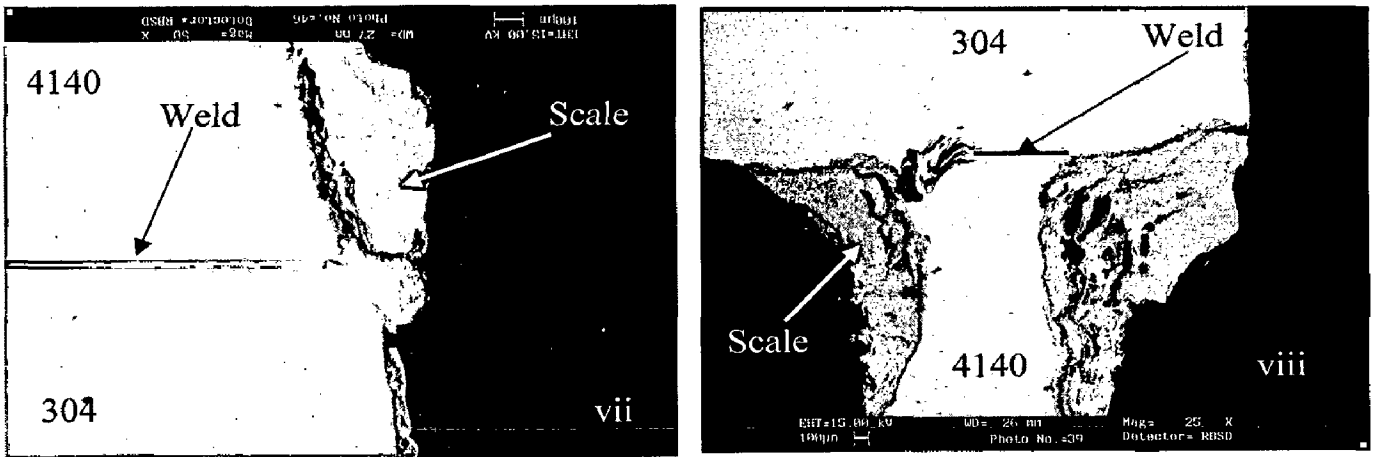
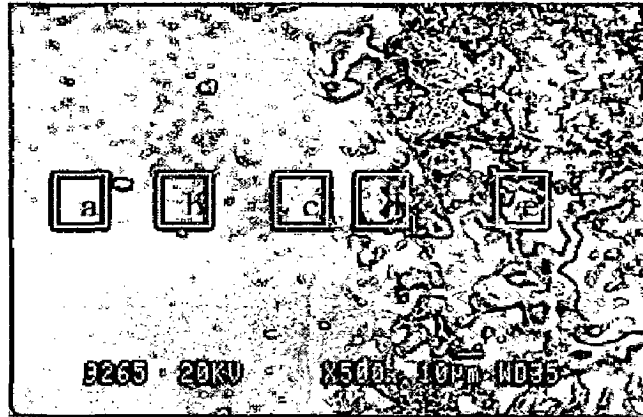


Fig 6.9 BSEI for hot corroded friction weldment exposed temperature of 700 and 900 °C (vii) and (viii) Exposed temperature 700 and 900 °C respectively for weldment made by keeping 5 mm Burn off length.



A

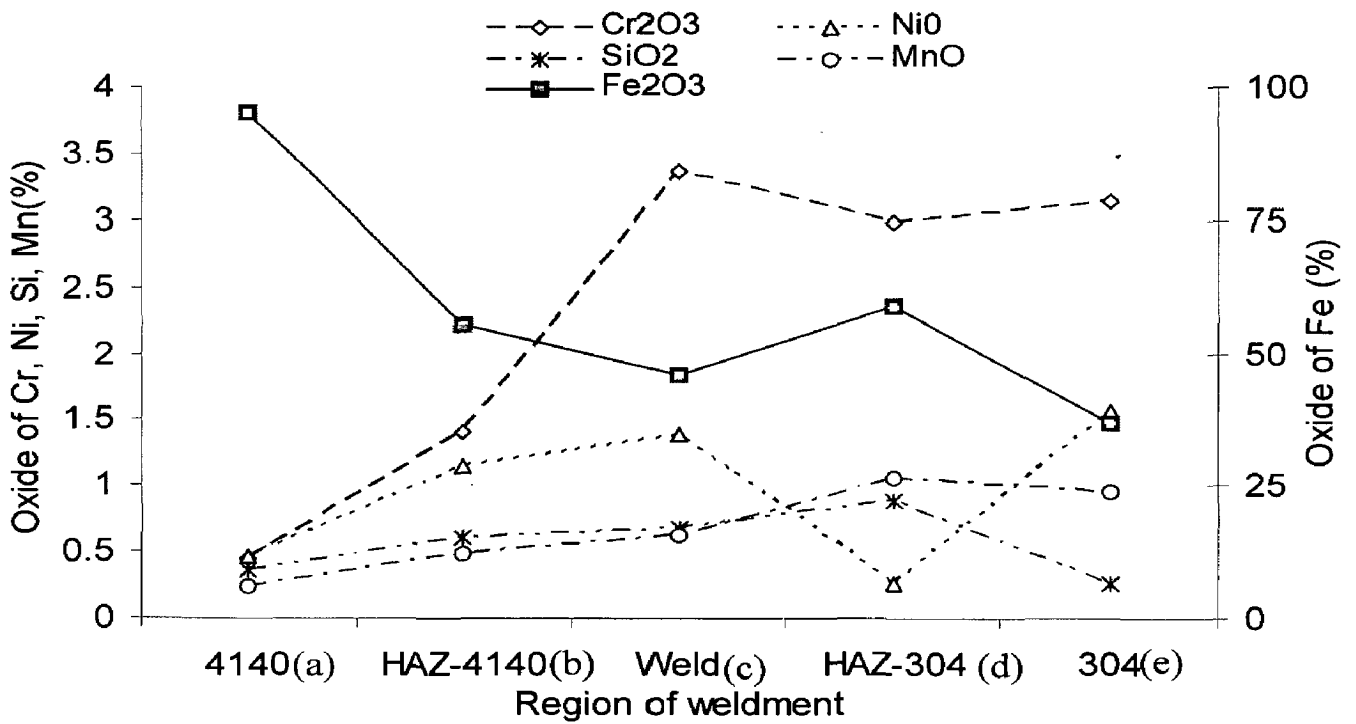
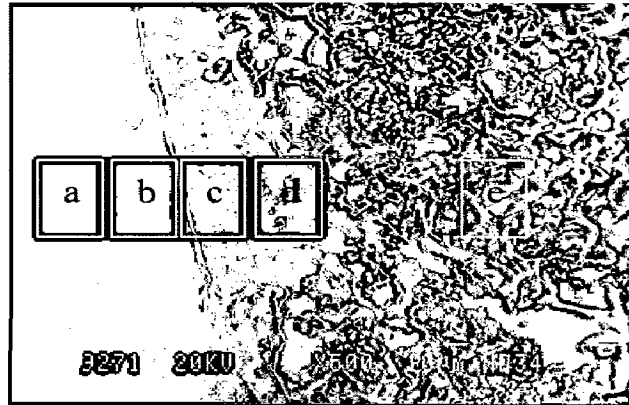


Fig 6.10(A) SEM/EDAX graph shows the friction weldment by keeping 5 mm burn off length, exposed at 500 °C under Na₂SO₄- 60% V₂O₅ after 50 cycles



B

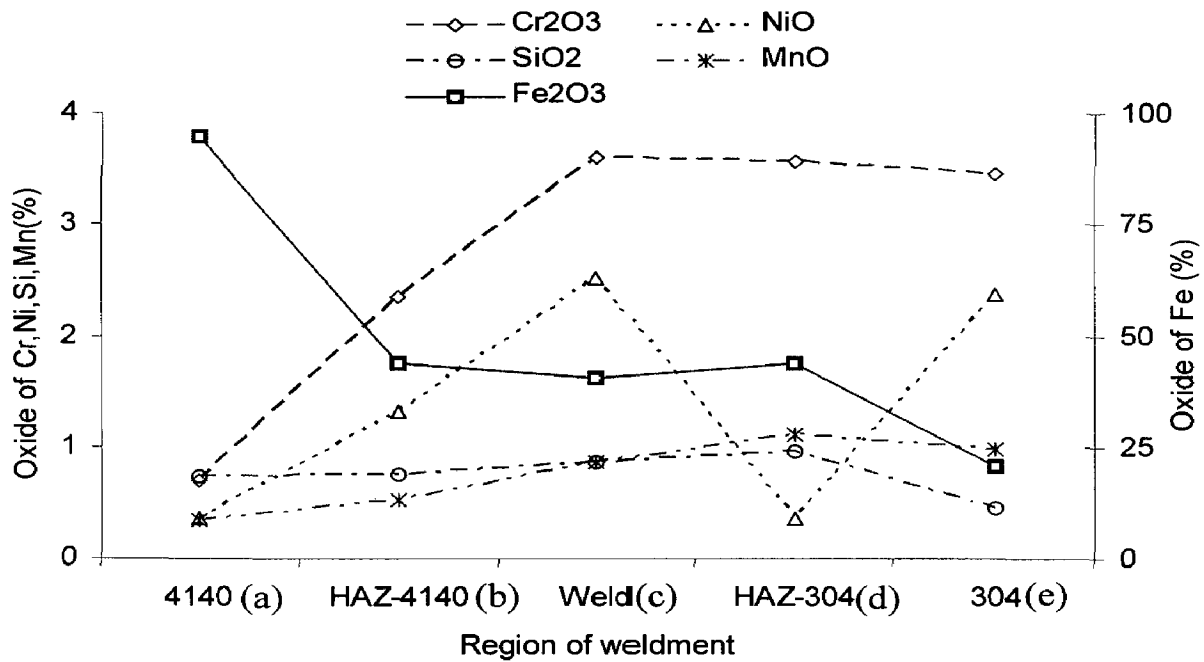
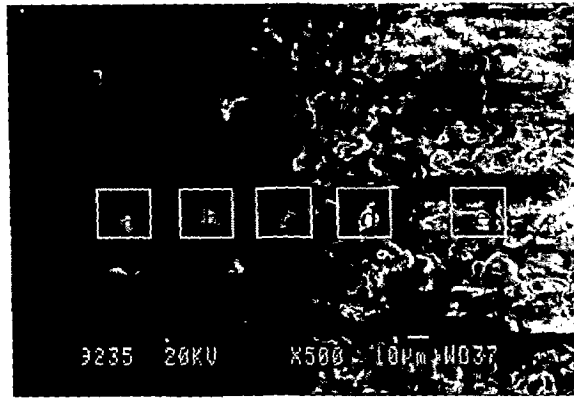


Fig 6.10(B) SEM/EDAX graph shows the friction weldment by keeping 7 mm burn off length, exposed at 500 °C under Na₂SO₄- 60% V₂O₅ after 50 cycles



C

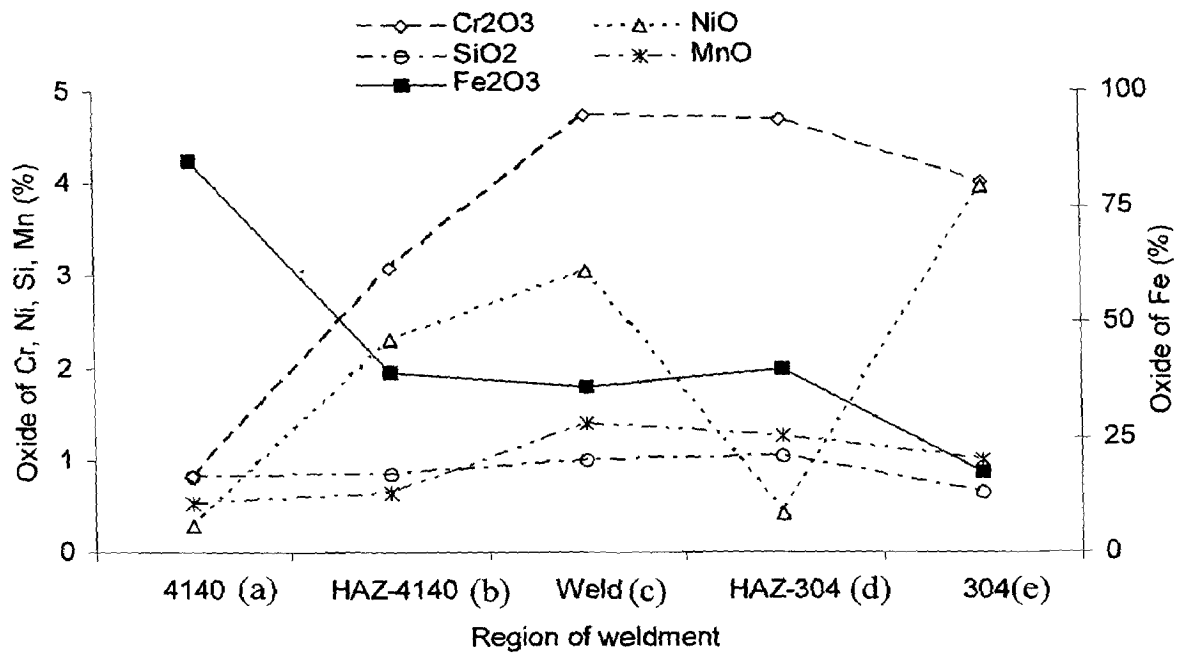
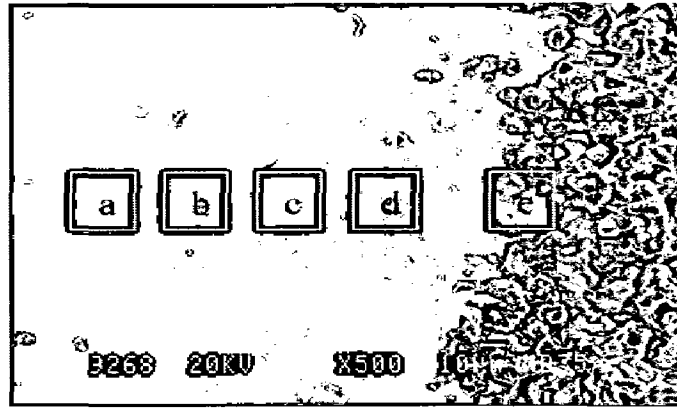


Fig 6.10(C) SEM/EDAX graph shows the friction weldment by keeping 9 mm burn off length, exposed at 500 °C under Na₂SO₄- 60% V₂O₅ after 50 cycles.



D

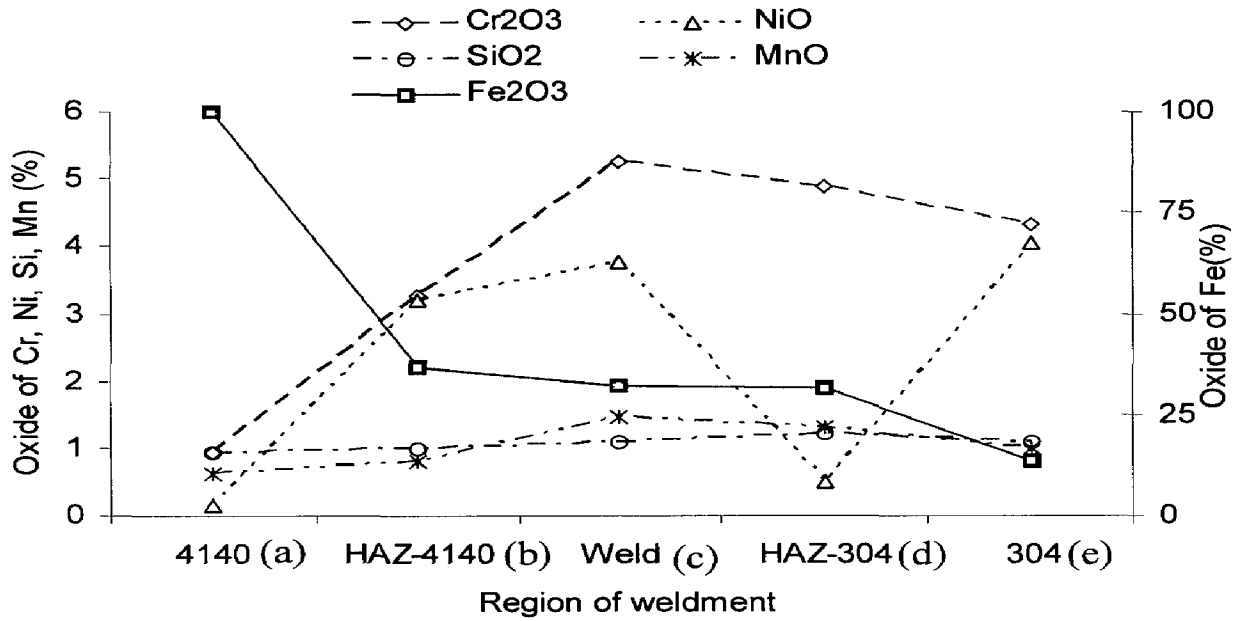
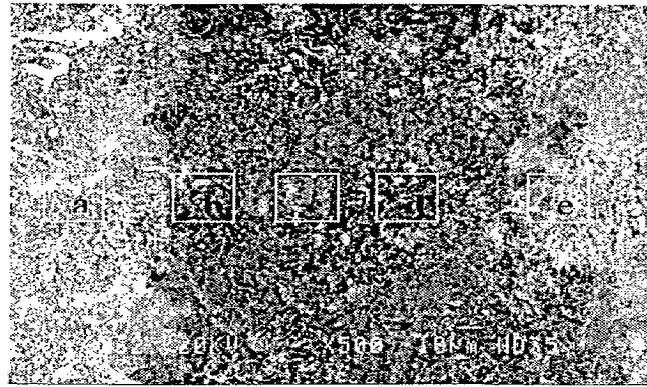


Fig 6.10(D) SEM/EDAX graph shows the friction weldment by keeping 12 mm burn off length, exposed at 500 °C under Na₂SO₄– 60% V₂O₅ after 50 cycles



E

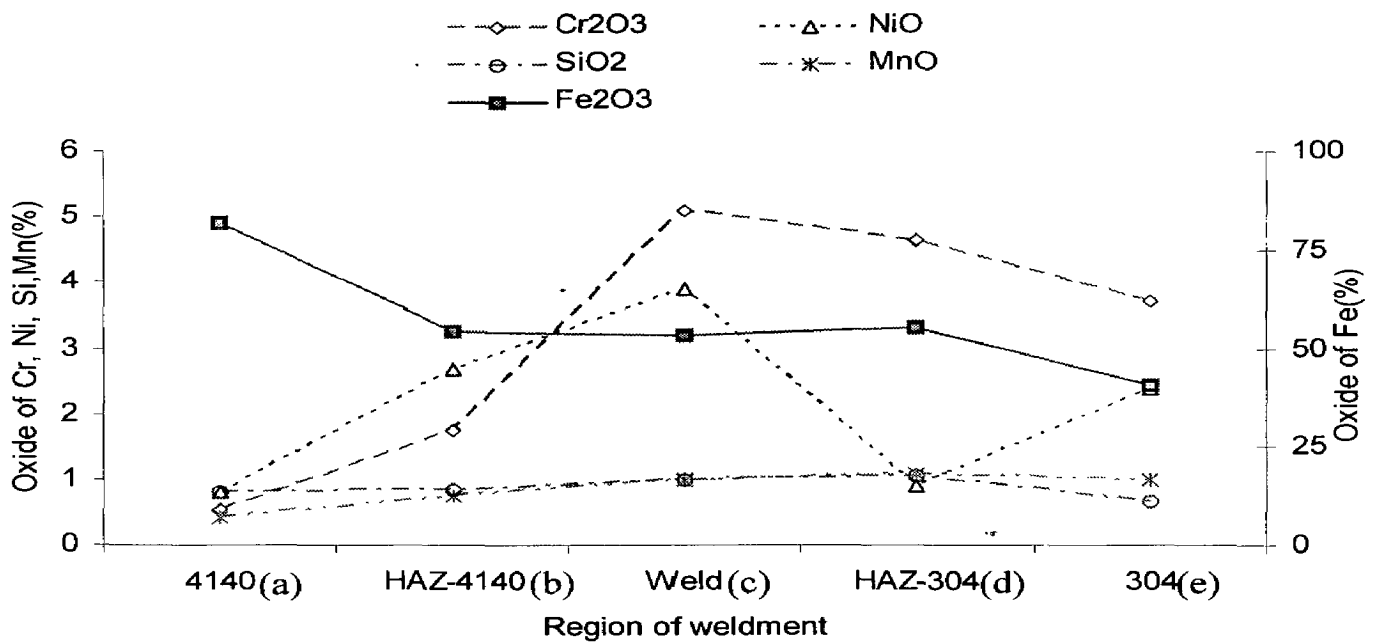
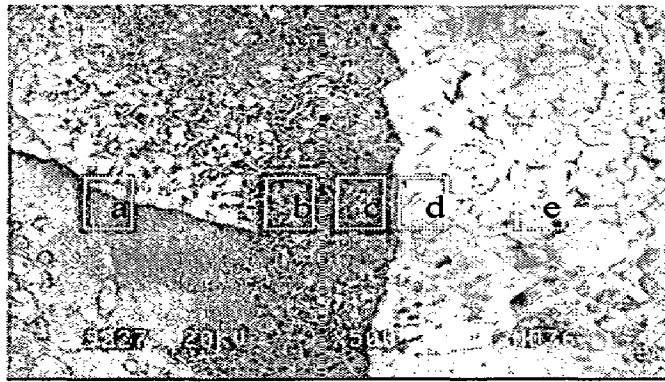


Fig 6.10(E) SEM/EDAX graph shows the friction weldment by keeping 5 mm burn off length, exposed at 550 °C under Na₂SO₄- 60% V₂O₅ after 50 cycles



F

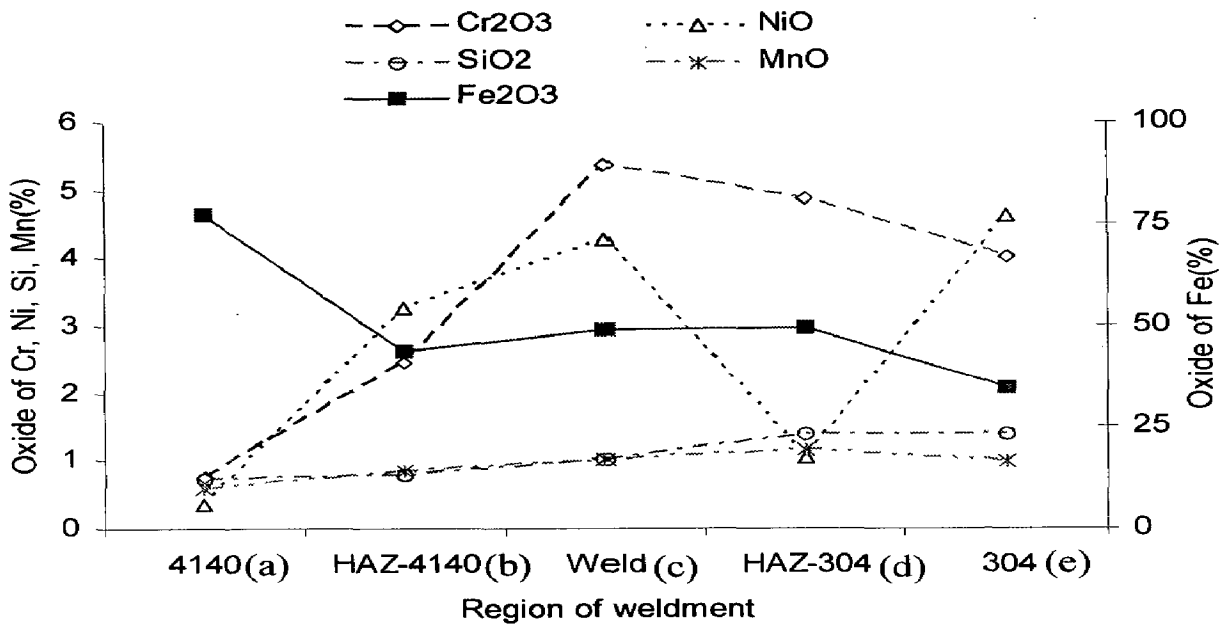
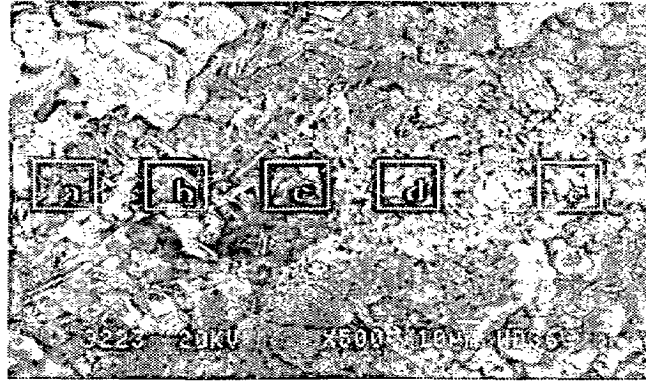


Fig 6.10(F) SEM/EDAX graph shows the friction weldment by keeping 7 mm burn off length, exposed at 550 °C under Na₂SO₄– 60% V₂O₅ after 50 cycles



G

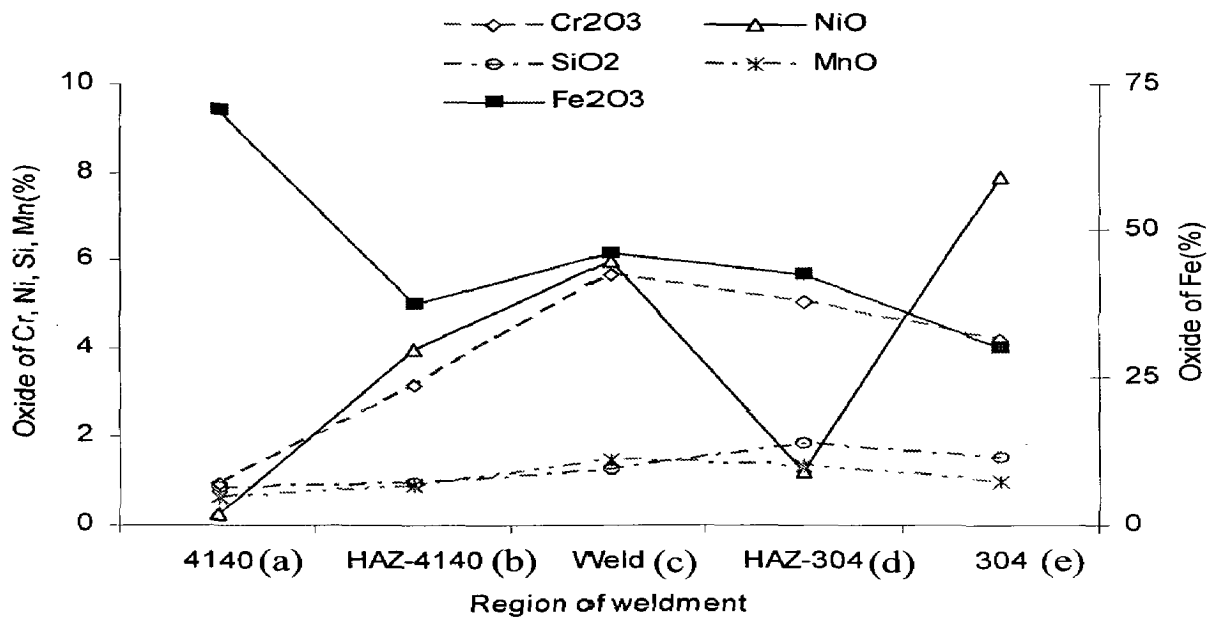
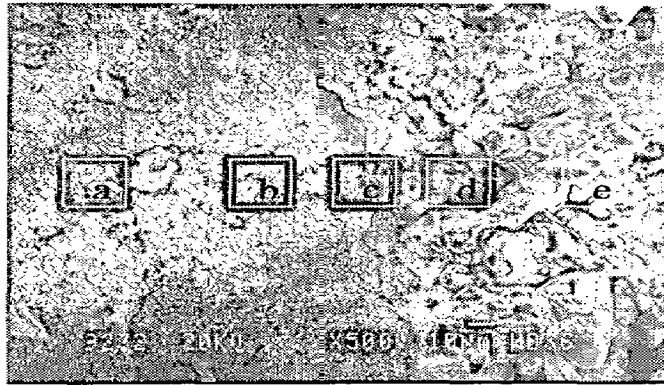


Fig 6.10(G) SEM/EDAX graph shows the friction weldment by keeping 9mm burn off length, exposed at 550 °C under Na2SO4– 60% V₂O₅ after 50 cycles



H

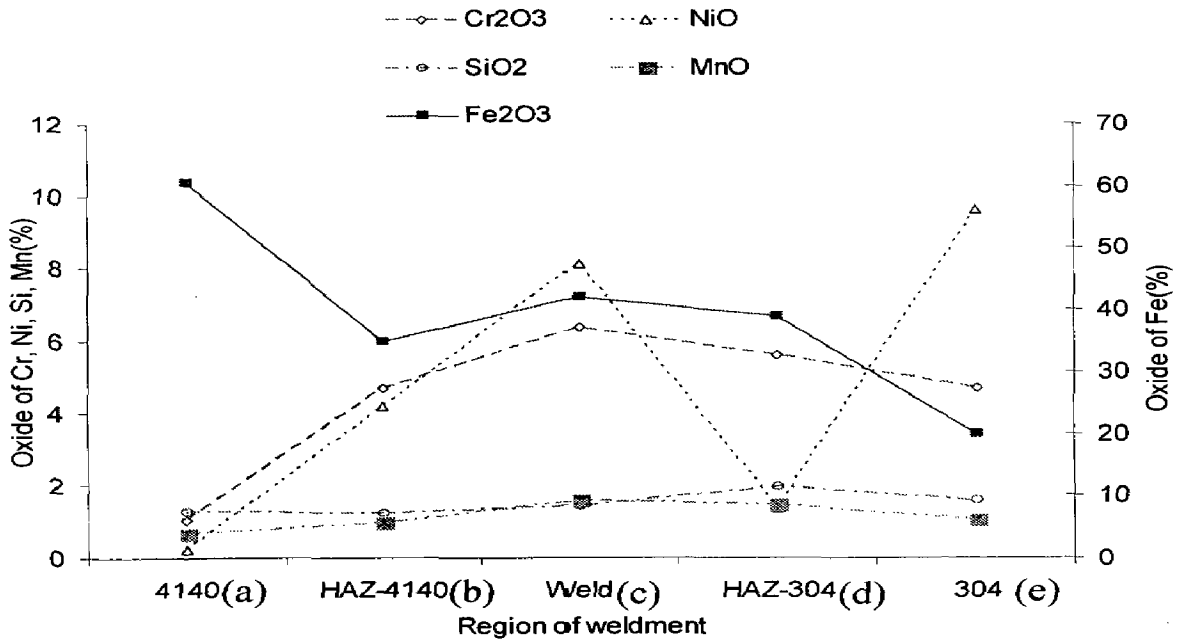
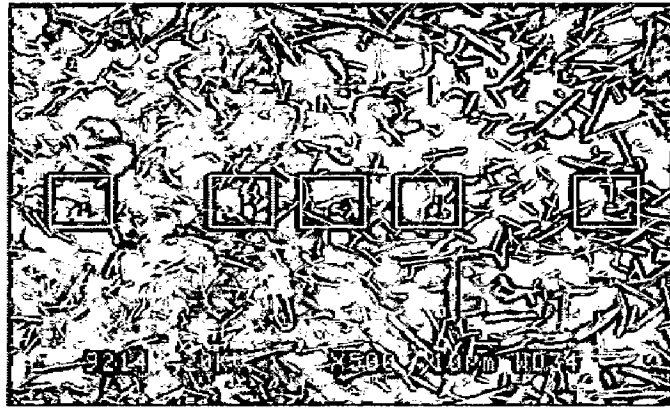


Fig 6.10(H) SEM/EDAX graph shows the friction weldment by keeping 12 mm burn off length, exposed at 550 °C under Na₂SO₄– 60% V₂O₅ after 50 cycles



I

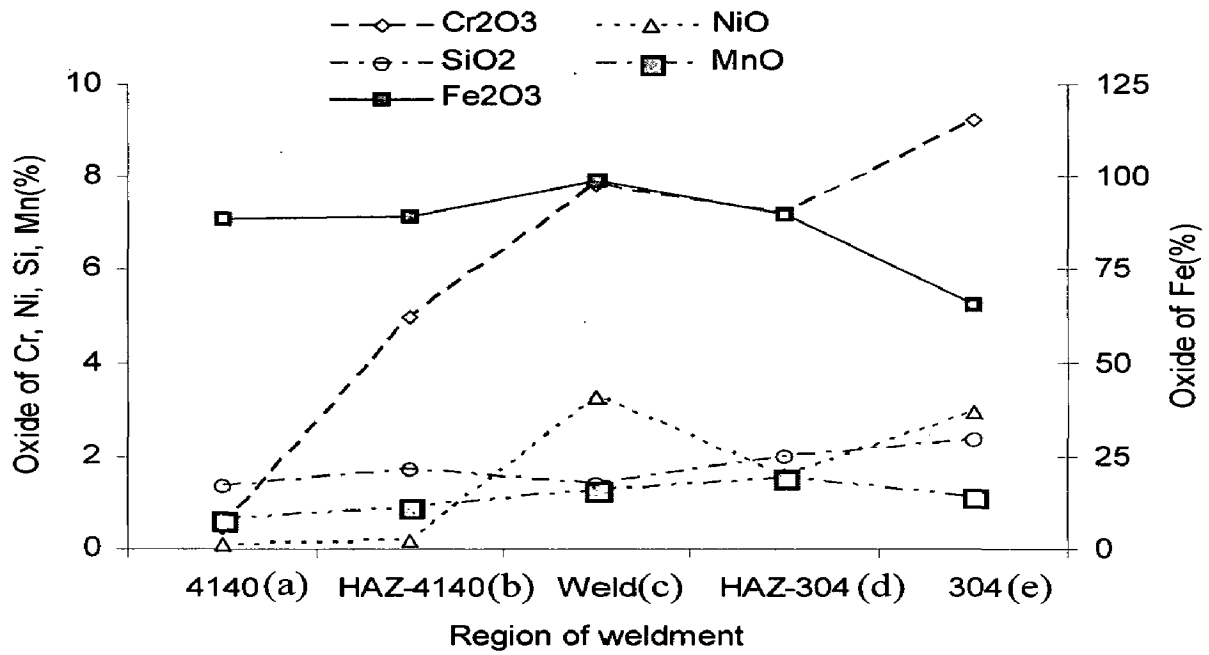
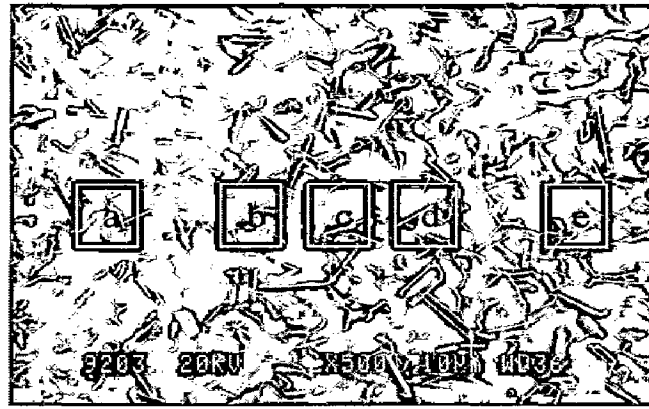


Fig 6.10(I) SEM/EDAX graph shows the friction weldment by keeping 5 mm burn off length, exposed at 600 °C under Na₂SO₄- 60% V₂O₅ after 50 cycles



J

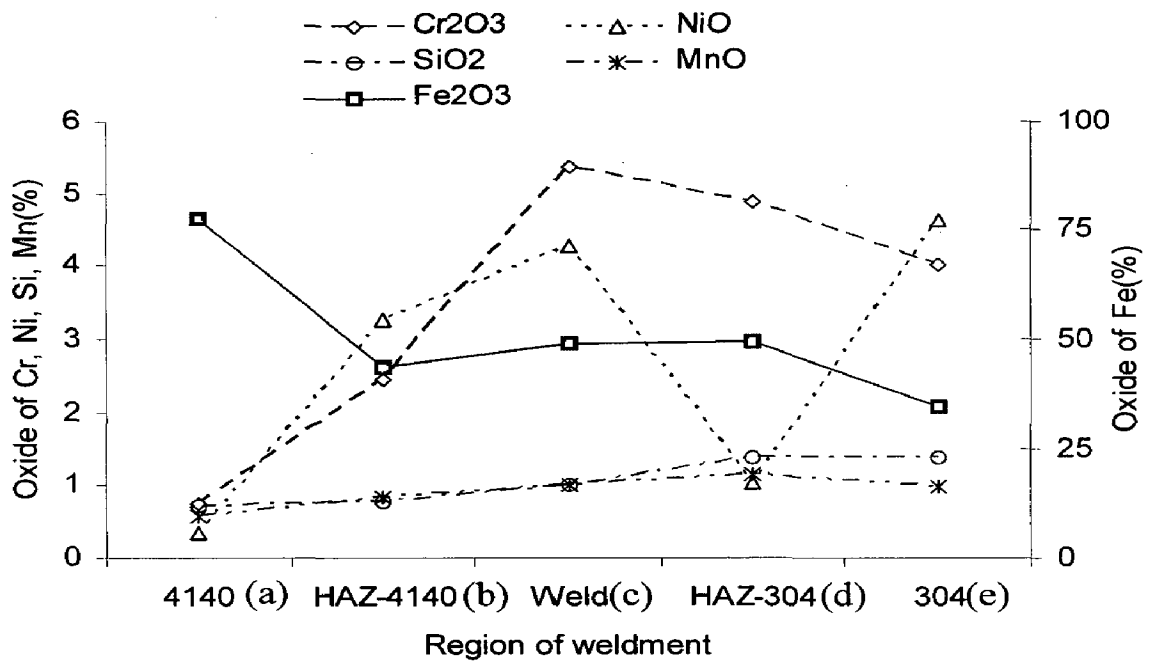
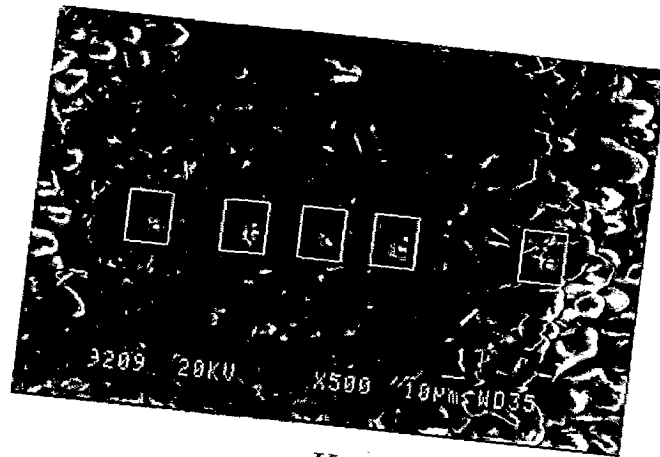


Fig 6.10(J) SEM/EDAX graph shows the friction weldment by keeping 7mm burn off length, exposed at 600 °C under Na₂SO₄– 60% V₂O₅ after 50 cycles



K

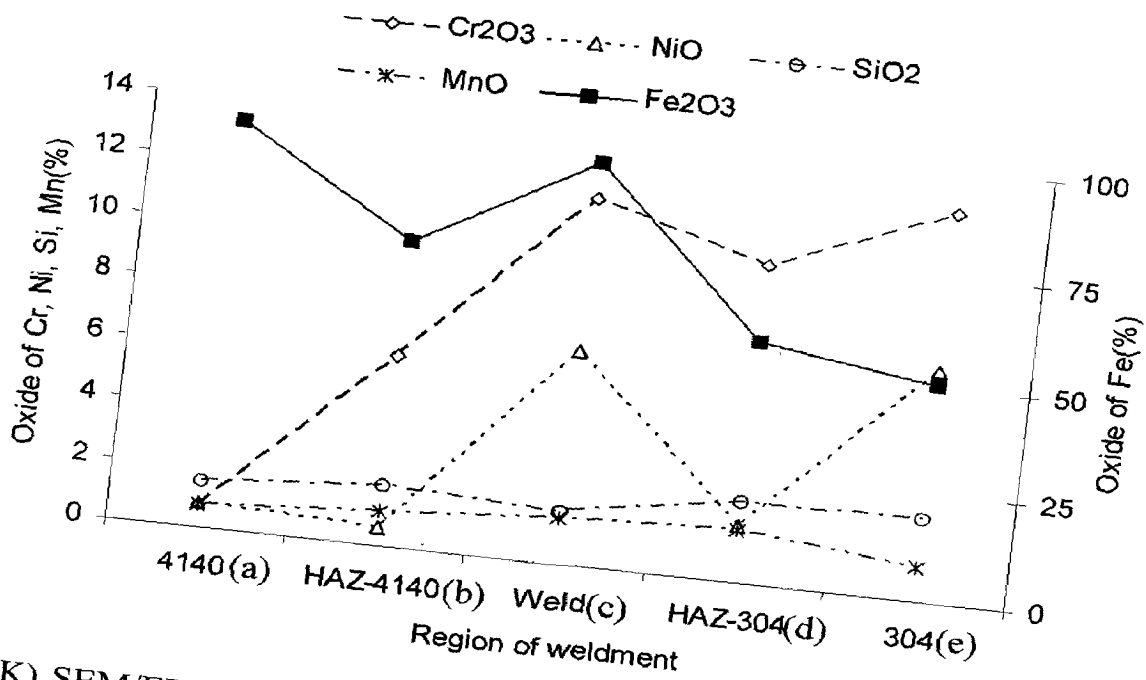
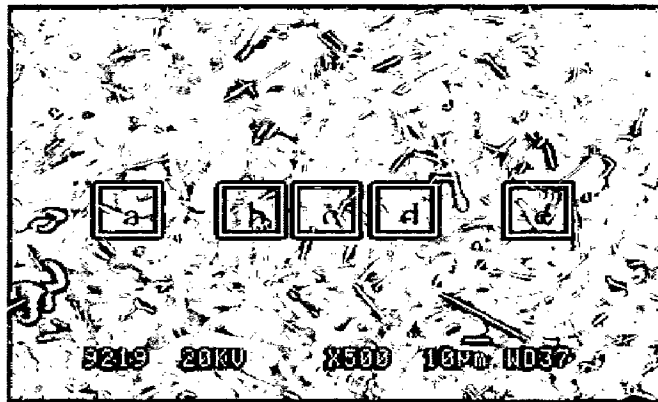


Fig 6.10(K) SEM/EDAX graph shows the friction weldment by keeping 9 mm burn off length, exposed at 600 °C under Na2SO4- 60% V2O5 after 50 cycles



L

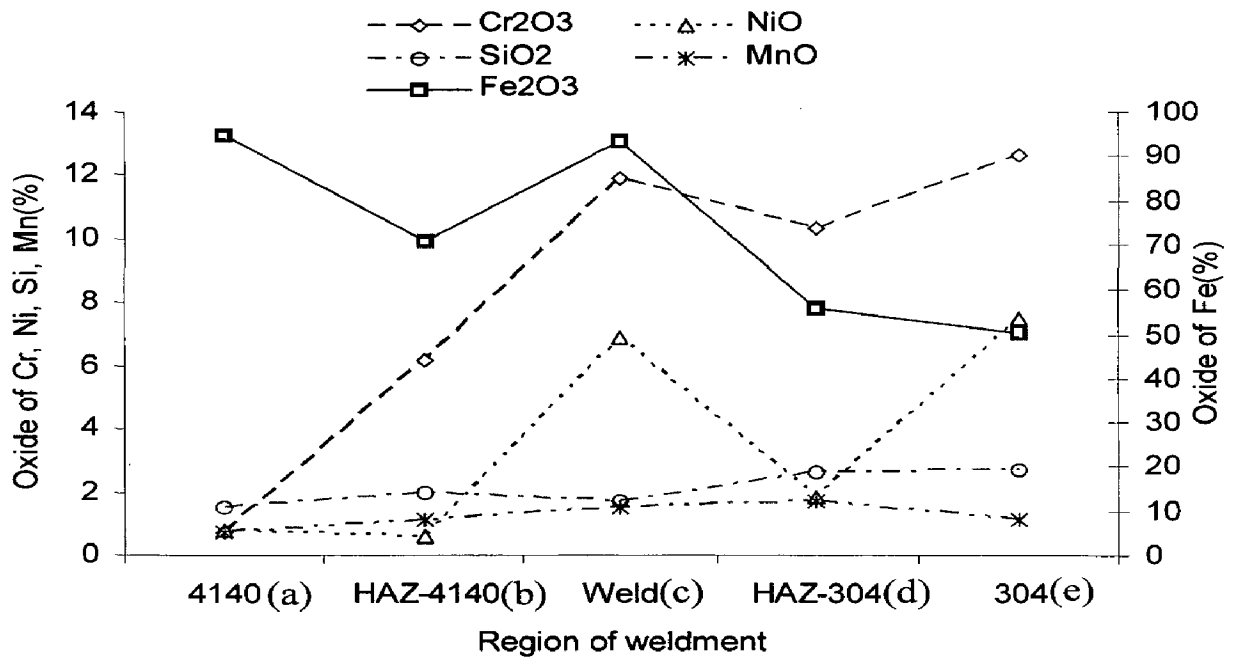


Fig 6.10(L) SEM/EDAX graph shows the friction weldment by keeping 12 mm burn off length, exposed at 600 °C under Na₂SO₄– 60% V₂O₅ after 50 cycles

the scale above the weld, It decreases as we move to the HAZ on the low alloy steel side and is negligible in the low alloy steel side. Where as scale on the low alloy steel 4140 mainly consists of Fe_2O_3 and this Fe_2O_3 goes on decreasing as we move towards the HAZ-4140, weld, HAZ-304 and base 304 steel. The same trend is observed with burn off length B7, B9 and B12 at 550 and 600 °C exposures. EDAX analysis shows NiO in the weld region and AISI 304 base metal. It further increase with increase either burn-off length or temperature. Where as SiO_2 gradually increasing as one move towards the HAZ-4140, weld, HAZ-304 and base 304 steel. The concentration of V_2O_5 , Na_2O_5 is observed on the stainless steel side there by indicating un-reacted salt. At 700 and 900 °C the scale on the weld zone as well as HAZ of 304 contains more Cr_2O_3 as compared with other lower temperatures Fig 6.11 (A, B). From the EDAX data, the effect of temperature and burn off length on the formation of oxides in the scale on the weldment shown in Fig 6.11 (C-H).

6.1.1.6 EPMA / EDAX Analysis

The scale on the friction welded dissimilar metal weldment was found to be fragile Even though by using slow speed cutting machine some of the scale was gone lost, so BSEI and X- ray mapping have been analyzed selectively.

BSEI and X-ray mapping for cross-section of corroded dissimilar weldment exposed to Na_2SO_4 -60% V_2O_5 at 500, 550, 600, 700 and 900 °C for 50 cycles. The EPMA of the cross-section of corroded dissimilar weldment made by friction welding by keeping different burn-off length (5, and 12mm) indicates that scale is mainly consisting of Fe, Cr and Ni Fig. 6.12(A-E). Figure 6.12 (F to L) shows the X ray mapping and elemental distribution analysis done by EDAX. Figure 6.12 (F and G) shows that oxygen penetration in the scale of friction weldment of burn-ff length 5, 7 mm respectively exposed at 600 °C under molten salt environment. Also it was observed that the scale mainly consisting with Fe, Cr and Ni. The elemental distribution in the weldment shown in Fig 6.12 (H), it was noted that the Cr content is more in the weld zone as well as the both side of HAZ. Fig 6.12 (I to L) shows that the X – ray mapping and elemental distribution on the weldment after exposed at 700 and 900 °C.

6.1.2 Friction Welded Dissimilar Metals Exposed to $K_2SO_4 + NaCl$ (60%)

This subheading deals with the critical examination of corrosion products and the behaviour of friction welded dissimilar weldment made by different burn-off length namely 5, 7, 9, and 12 mm. The hot corrosion studies were performed on the weldments exposed at the temperature from 500, 550 and 600 °C under the $K_2SO_4 + NaCl$ (60%) mixture of molten salt for 50 cycles. In view of comparison the thermogravimetric data of each environment along with different exposure of temperature. The parabolic rate constants and scale thicknesses values have been evaluated after 50 cycles of exposure.

6.1.2.1 Visual Examination

In the hot corrosion study of the friction welded 4140 low alloy steel and 304 Stainless steel weldment, after first cycle the white colour salt coating changed in to brown colour with some small black spots seen on the low alloy steel side. Negligible reaction has taken place on the stainless steel side. After completion of 15 cycles the scale becomes thicker and is of dark brown colour on low alloy steel and most of it scale spalled out. Whereas on 304 sides the scale was light brown and adherent and on the weld area the salt coating remain unreacted. With further increase in number of cycles, all the scale spalled out from low alloy steel side, leaving behind black colour subscales. The color and texture of scale at weld region was different from that on the base metals. With increase in the temperature from 500 to 550 °C and then 600 °C the thickness of scale was observed on the 4140 steel side with extensive spalling. Figure.6.13 (i-iii) shows the macro structure of hot corroded samples after 50 cycles.

6.1.2.2 Thermogravimetric Data

The weight gain (per unit area) during corrosion test for the dissimilar friction weldment made by changing burn-off length (5,7,9 and 12 mm) in the presence of a salt layer of K_2SO_4 (40%) and $NaCl$ (60 %) mixture at different temperature (500, 550 and 600 °C) have been plotted and is shown in Fig 6.14. Higher the burn-off length shows a higher weight gain throughout the entire range up to 50 cycles for all the temperatures of exposure. The parabolic rate constants K_p were obtained from the slope of the linear regression fitted line (cumulative weight gain / area)² Vs. number of cycles and is shown

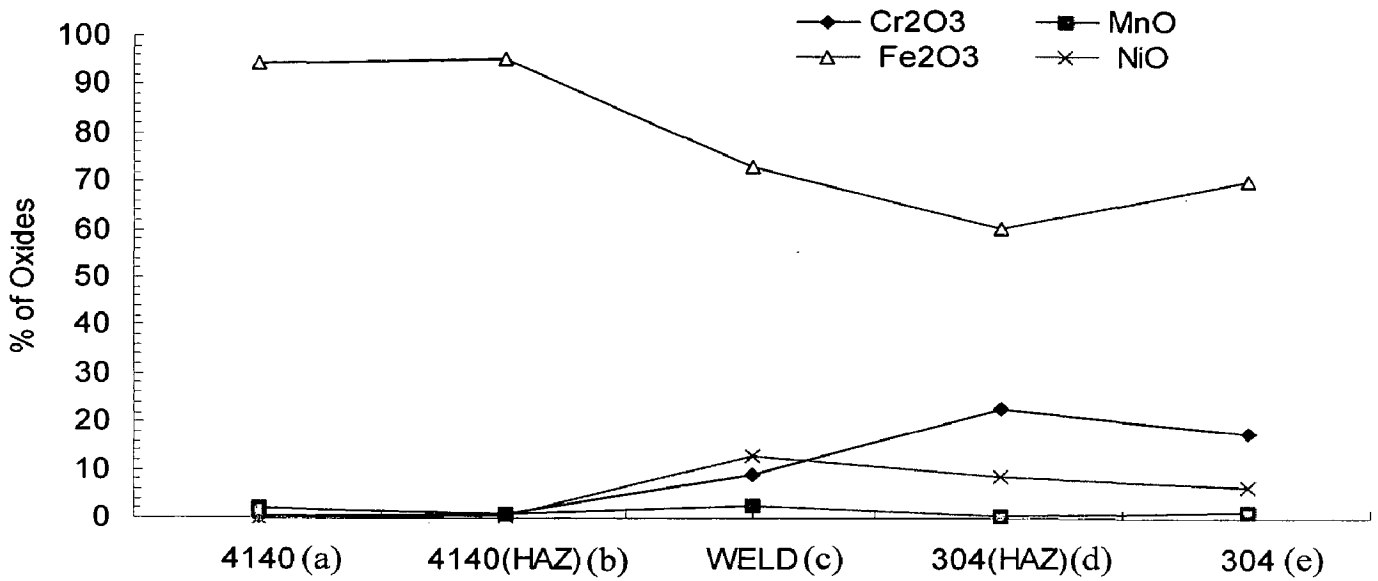
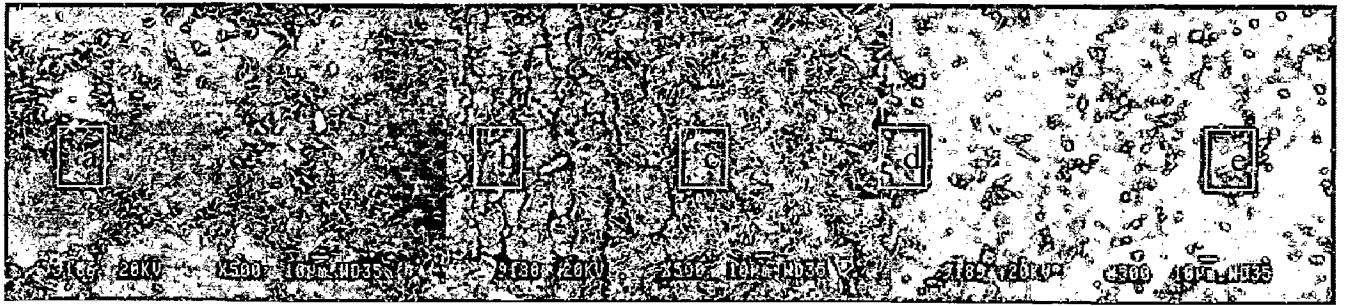


Fig 6.11(A) SEM/EDAX graph shows the friction weldment by keeping 5 mm burn off length, exposed at 700 °C under Na₂SO₄- 60% V₂O₅ after 50 cycles.

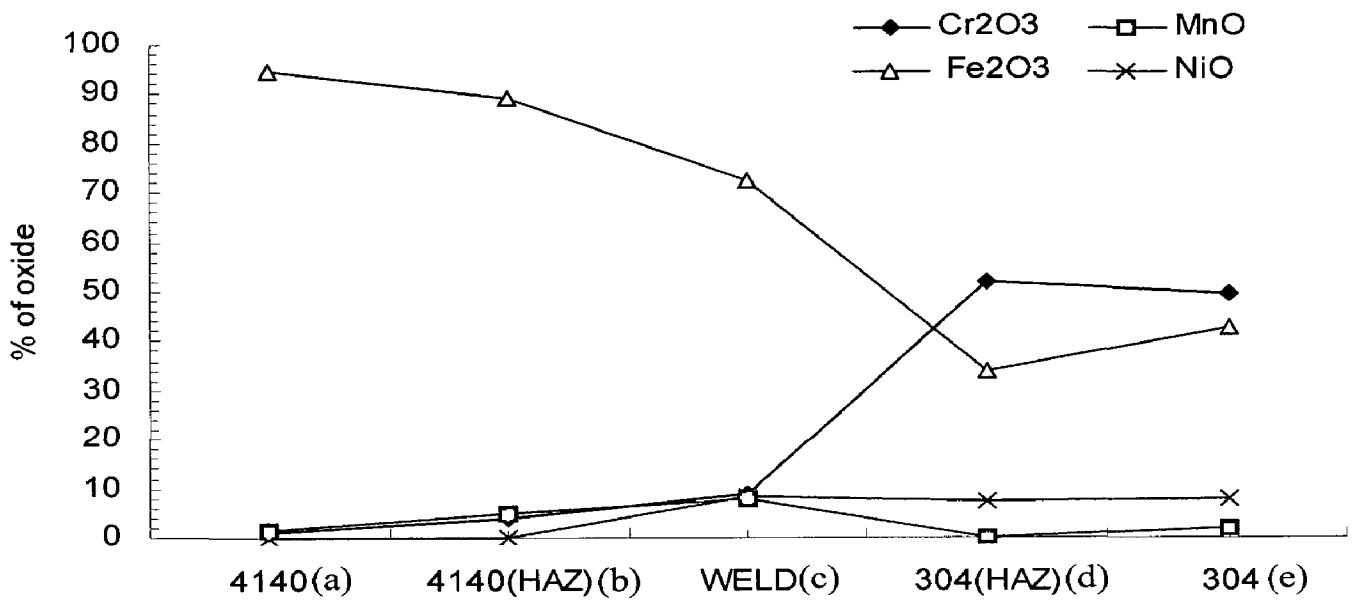
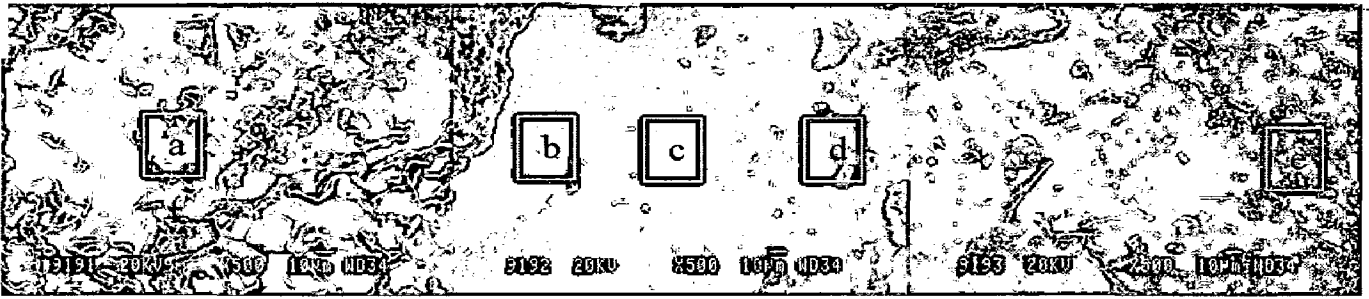


Fig 6.11(B) SEM/EDAX graph shows the friction weldment by keeping 5 mm burn off length, exposed at 700 °C under Na₂SO₄– 60% V₂O₅ after 50 cycles.

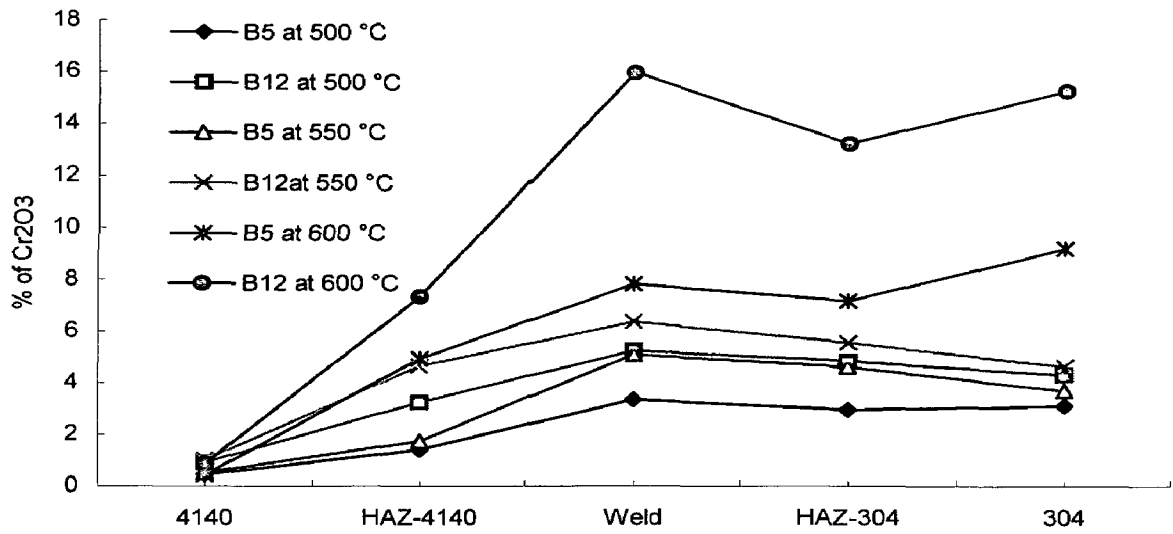


Fig 6.11 (C) EDAX data shows the effect of burn off length and temperature on formation of Cr₂O₃ on the friction weldment under molten salt environment of Na₂SO₄-60% V₂O₅.

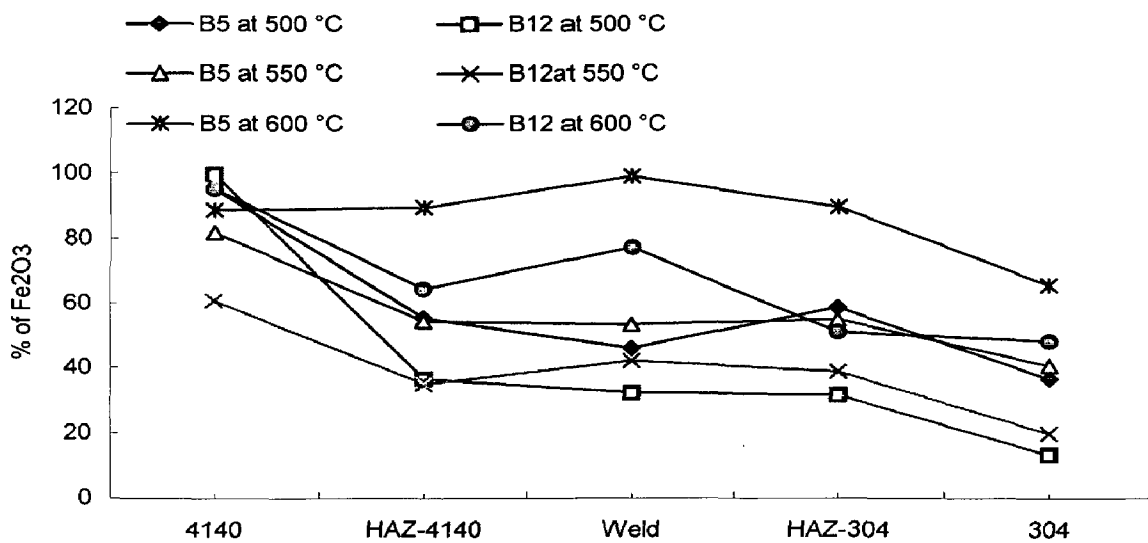


Fig 6.11 (D) EDAX data shows the effect of burn off length and temperature on formation of Fe₂O₃ on the friction weldment under molten salt environment of Na₂SO₄-60% V₂O₅.

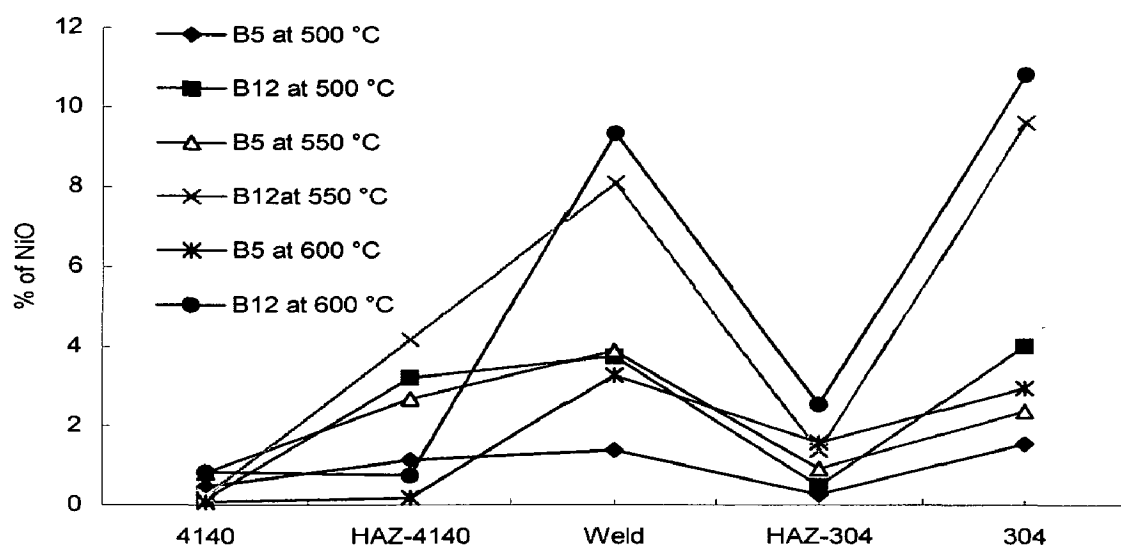


Fig 6.11 (E) EDAX data shows the effect of burn off length and temperature on formation of NiO on the friction weldment under molten salt environment of Na_2SO_4 -60% V_2O_5 .

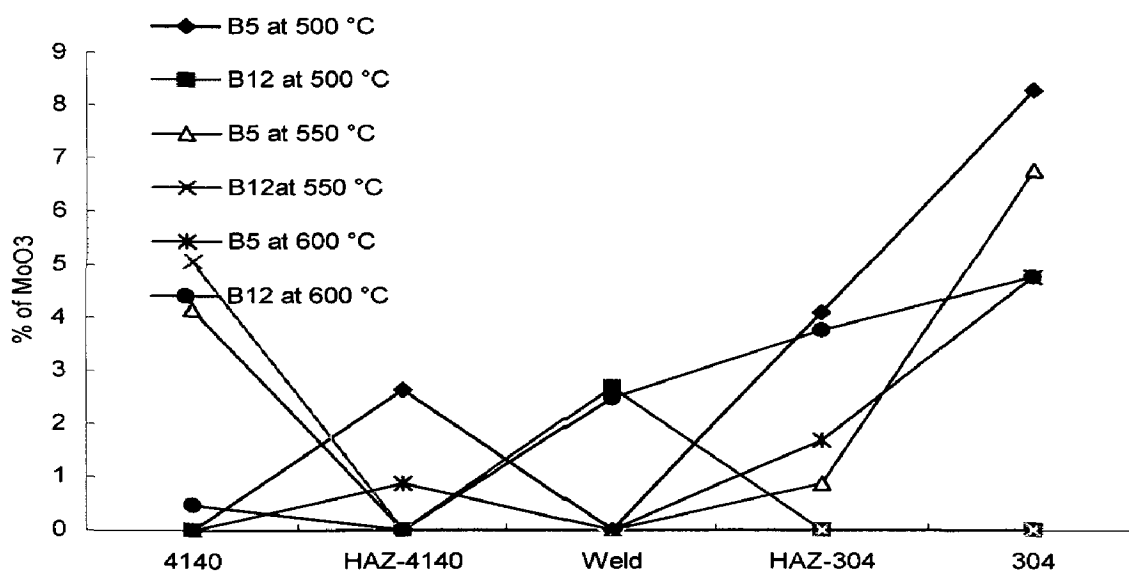


Fig 6.11 (F) EDAX data shows the effect of burn off length and temperature on formation of MoO₃ on the friction weldment under molten salt environment of Na_2SO_4 -60% V_2O_5 .

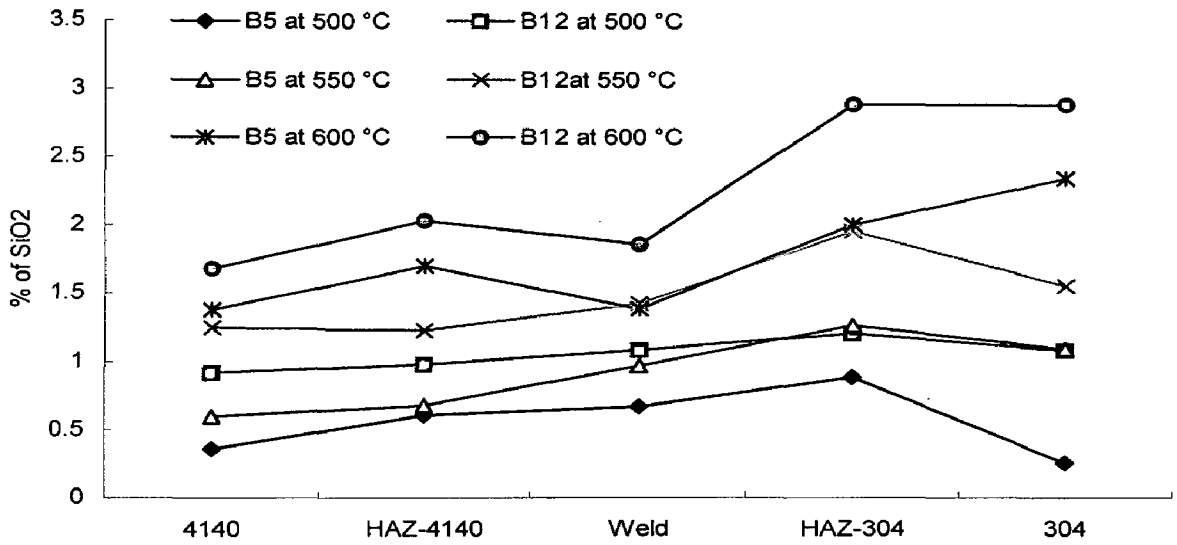


Fig 6.11 (G) EDAX data shows the effect of burn off length and temperature on formation of SiO₂ on the friction weldment under molten salt environment of Na₂SO₄-60% V₂O₅.

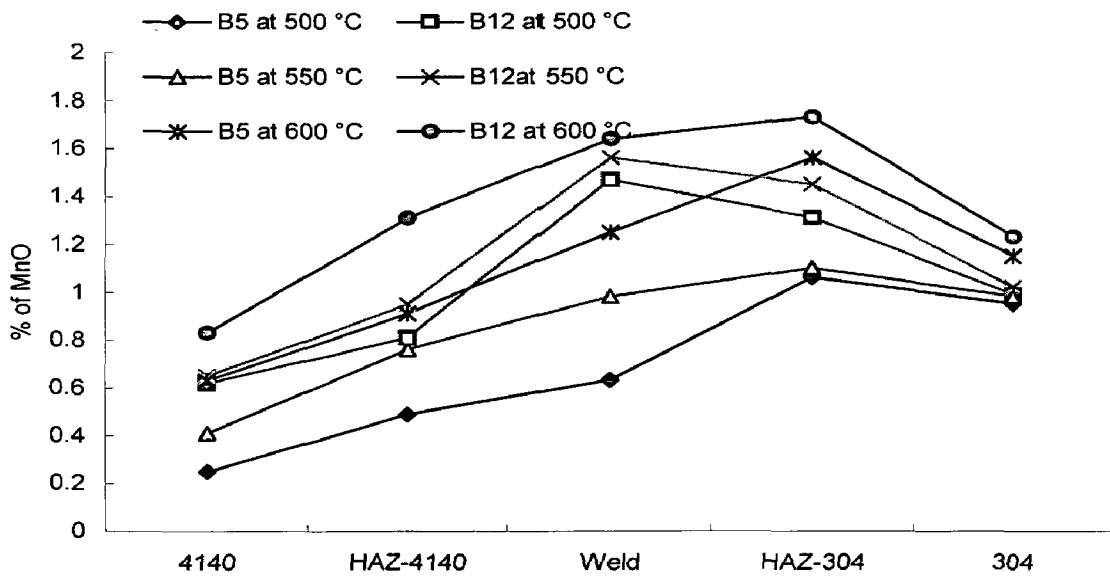


Fig 6.11 (H) EDAX data shows the effect of burn off length and temperature on formation of MnO on the friction weldment under molten salt environment of Na₂SO₄-60% V₂O₅.

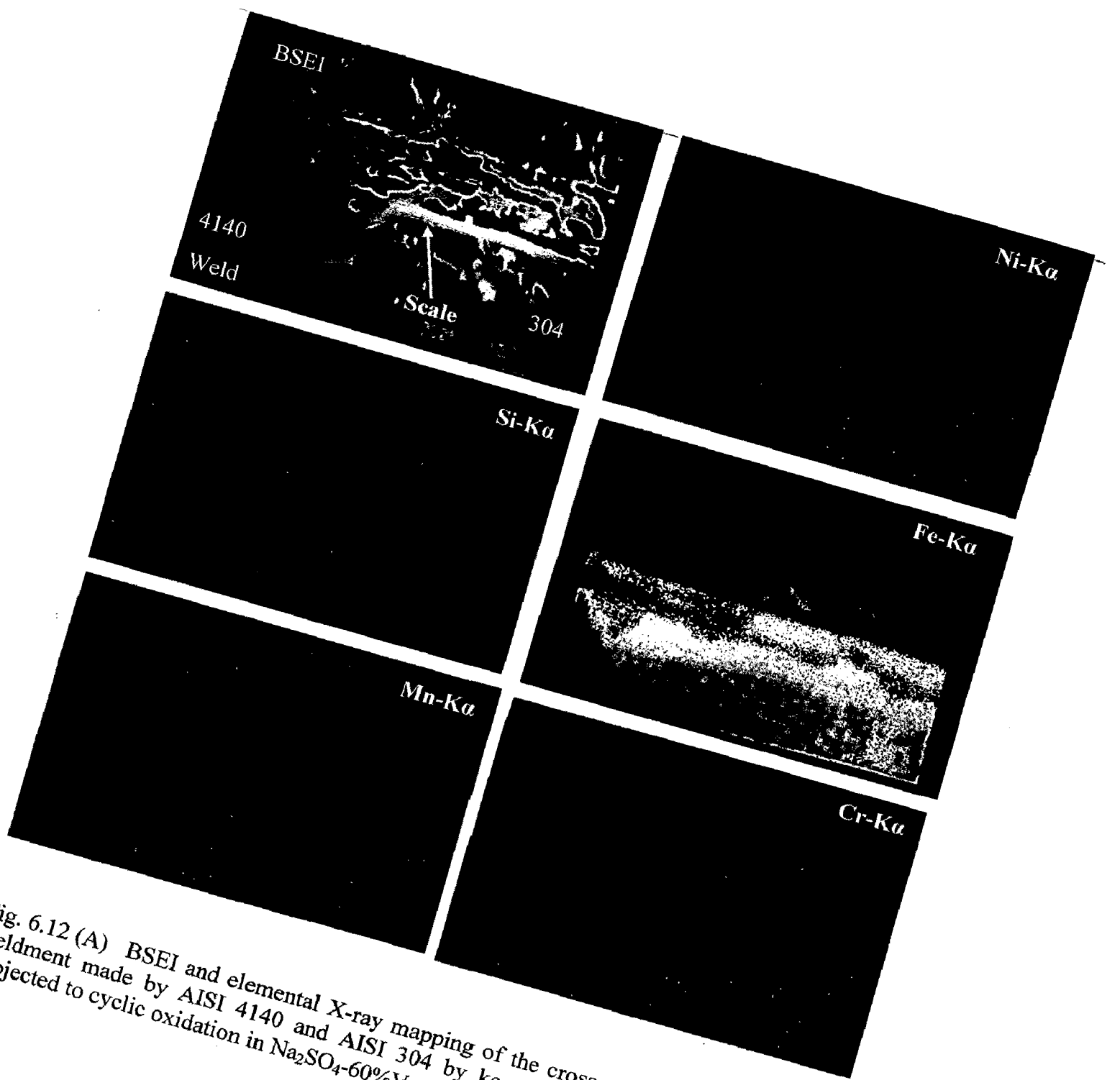


Fig. 6.12 (A) BSEI and elemental X-ray mapping of the cross-section of dissimilar weldment made by AISI 4140 and AISI 304 by keeping burn off length 5 mm, subjected to cyclic oxidation in Na_2SO_4 -60% V_2O_5 at 500°C for 50 cycles, 800 X.

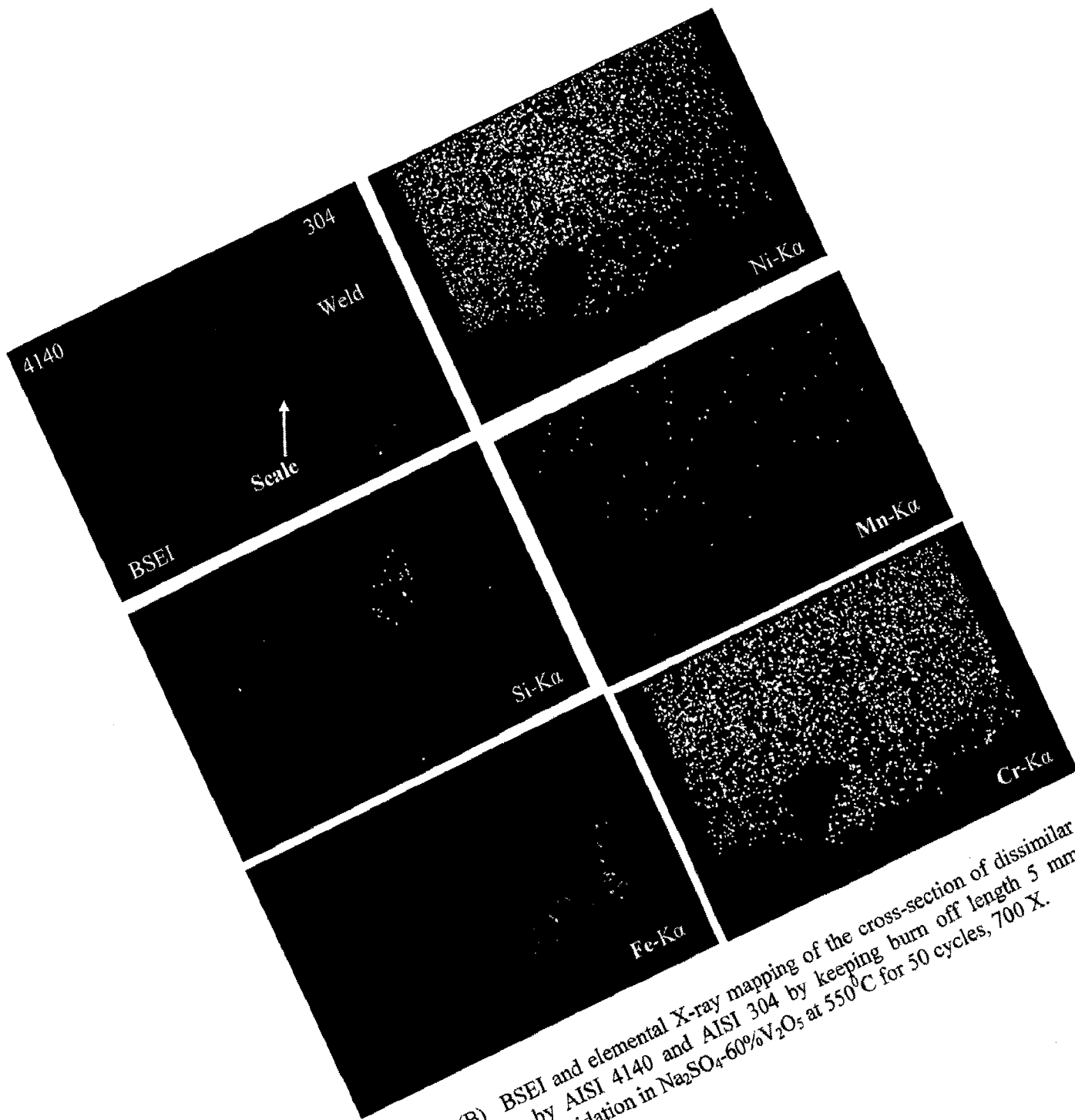


Fig. 6.12 (B) BSEI and elemental X-ray mapping of the cross-section of dissimilar weldment made by AISI 4140 and AISI 304 by keeping burn off length 5 mm, subjected to cyclic oxidation in $\text{Na}_2\text{SO}_4\text{-60\%V}_2\text{O}_5$ at 550°C for 50 cycles, 700 X.

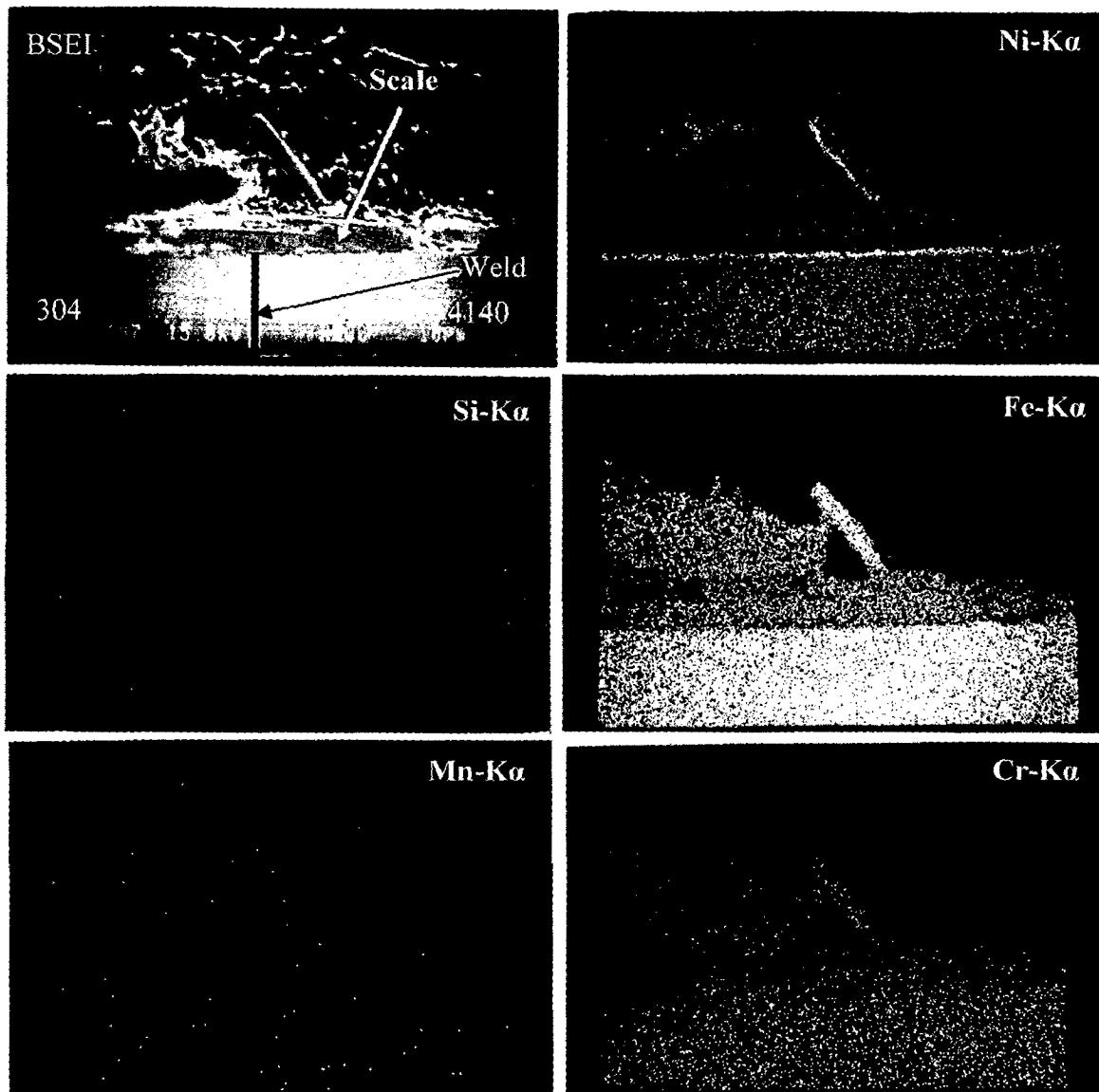


Fig. 6.12 (C) BSEI and elemental X-ray mapping of the cross-section of dissimilar weldment made by AISI 4140 and AISI 304 by keeping burn off length 5 mm, subjected to cyclic oxidation in Na_2SO_4 -60% V_2O_5 at 600°C for 50 cycles, 500 X.

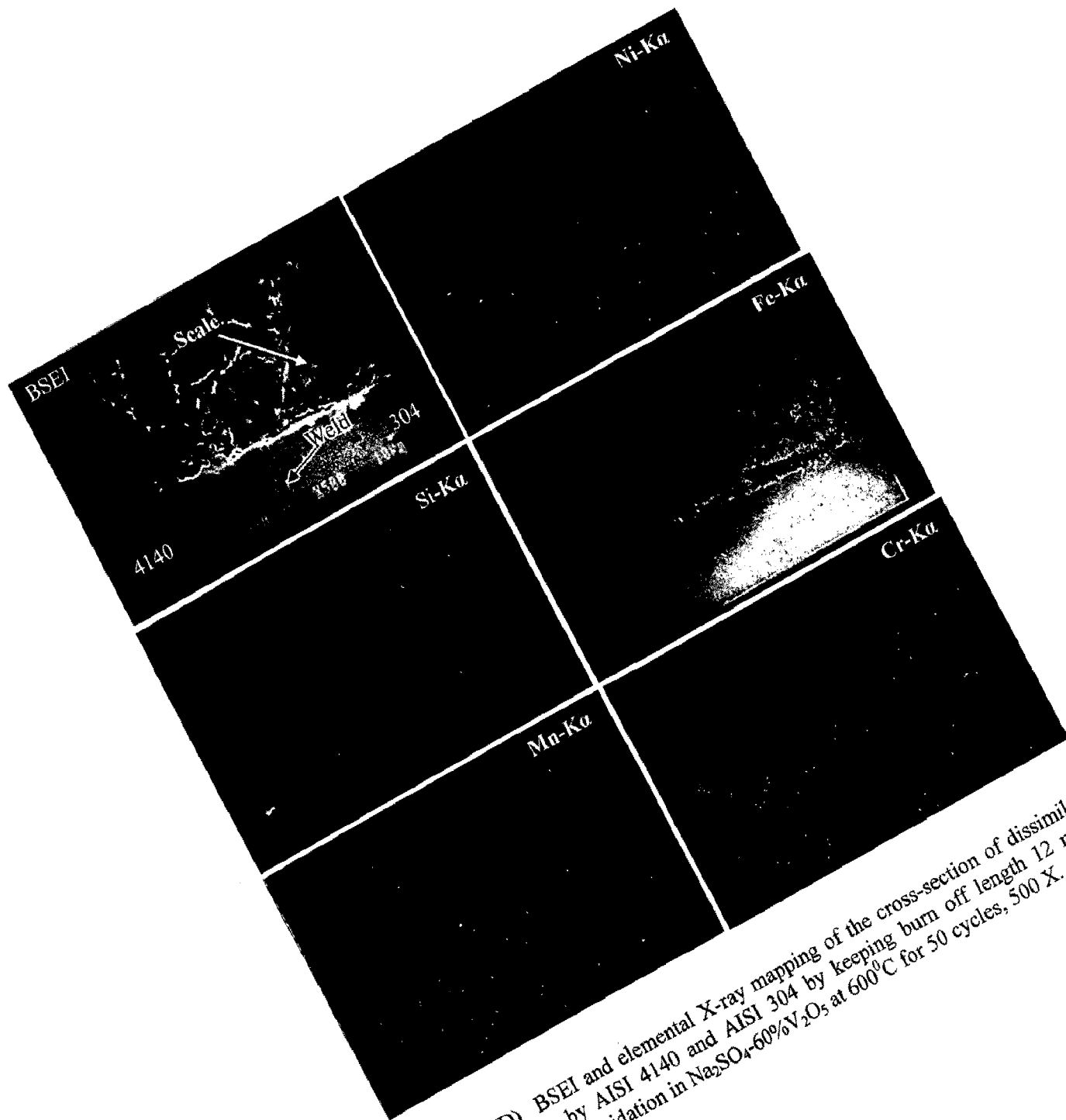


Fig. 6.12 (D) BSEI and elemental X-ray mapping of the cross-section of dissimilar weldment made by AISI 4140 and AISI 304 by keeping burn off length 12 mm, subjected to cyclic oxidation in $\text{Na}_2\text{SO}_4\text{-60\%V}_2\text{O}_5$ at 600°C for 50 cycles, 500 X.

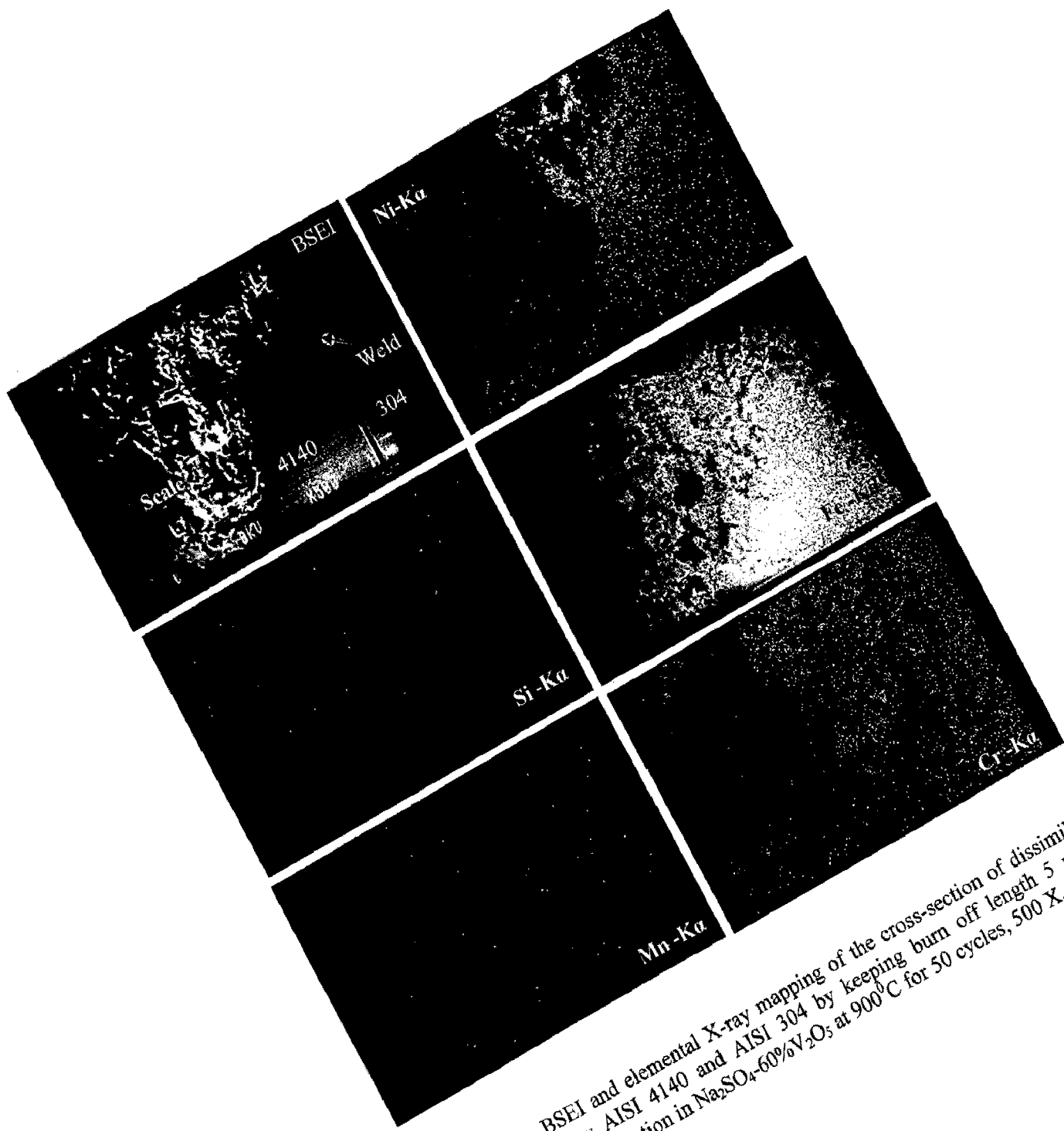


Fig. 6.12 (E) BSEI and elemental X-ray mapping of the cross-section of dissimilar weldment made by AISI 4140 and AISI 304 by keeping burn off length 5 mm, subjected to cyclic oxidation in $\text{Na}_2\text{SO}_4\text{-60\%V}_2\text{O}_5$ at 900°C for 50 cycles, 500 X.

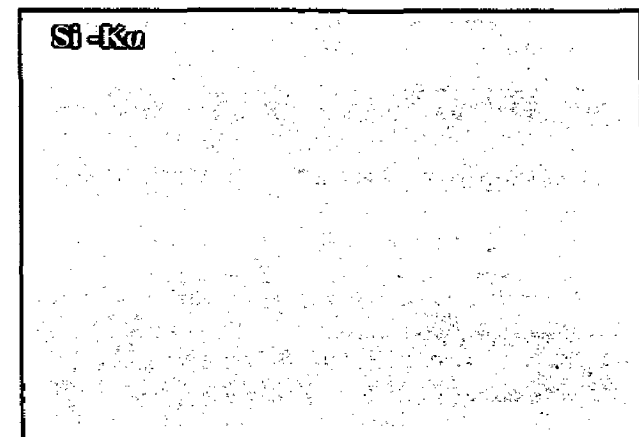
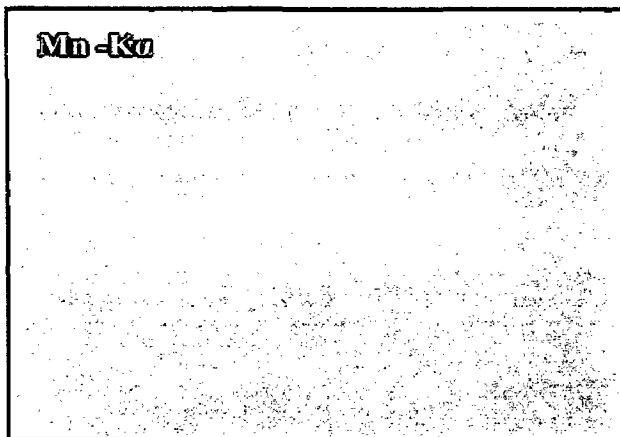
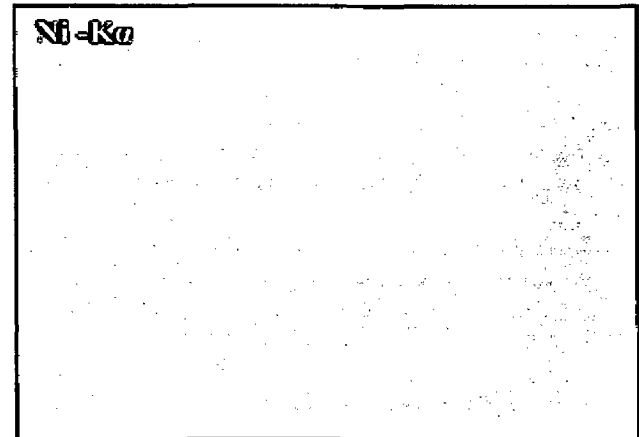
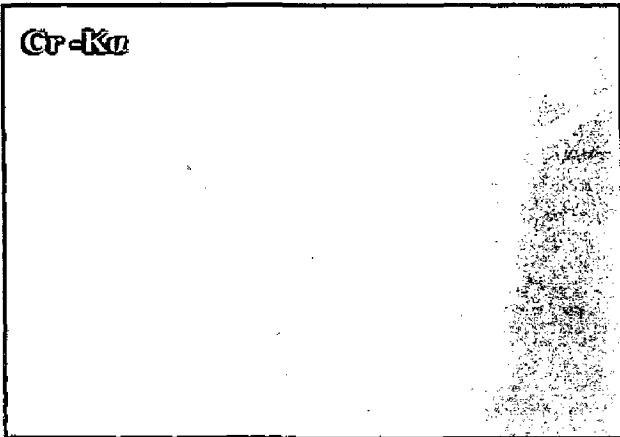
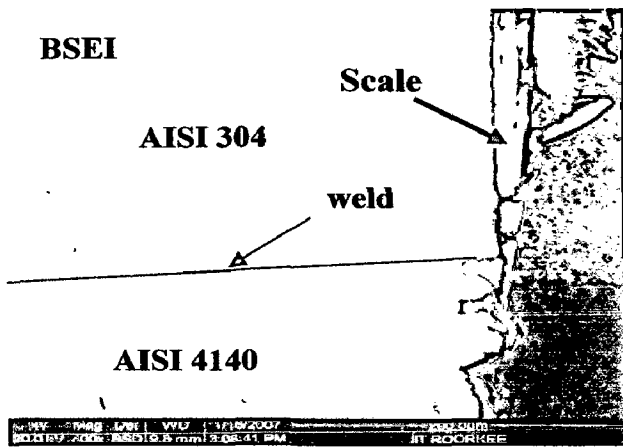


Fig. 6.12 (F) BSEI and X-ray mappings of the cross-section of dissimilar friction welded AISI 304 and AISI 4140 by keeping burn-off length 5mm exposed to Na_2SO_4 -60% V_2O_5 at 600 °C for 50 cycles.

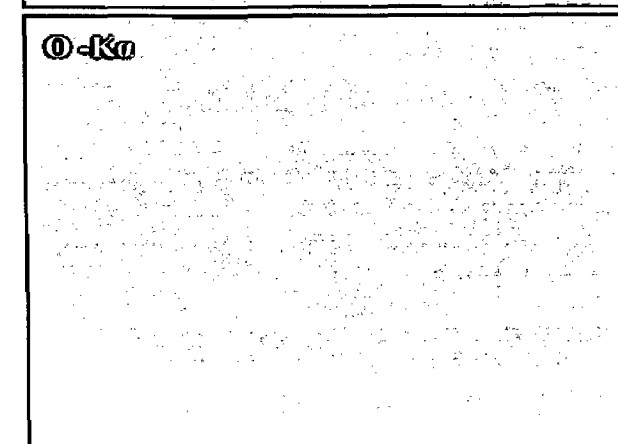
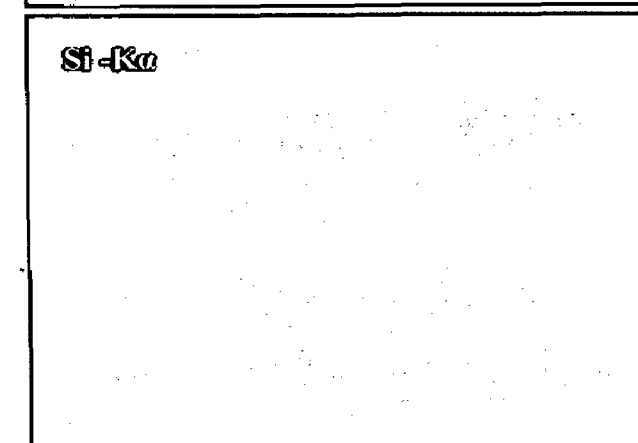
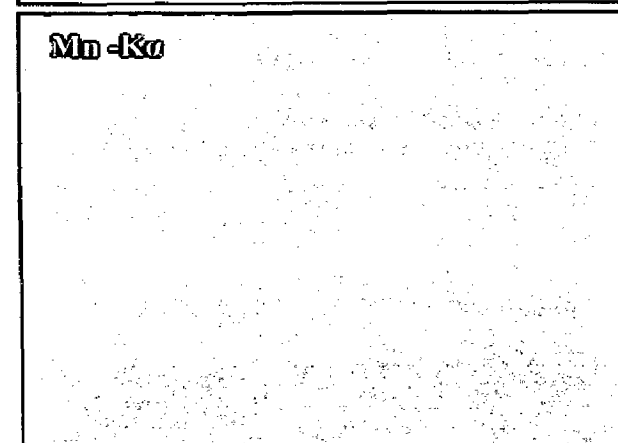
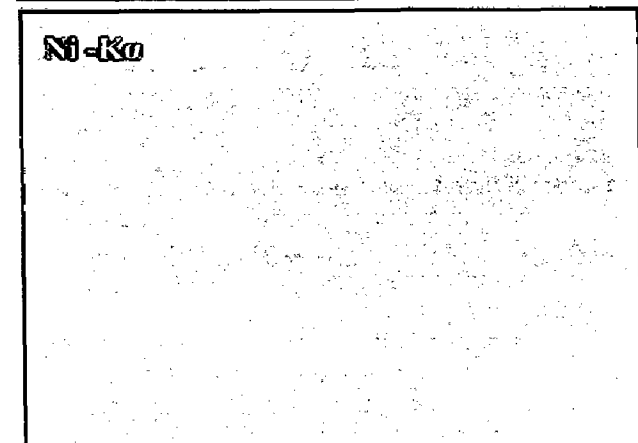
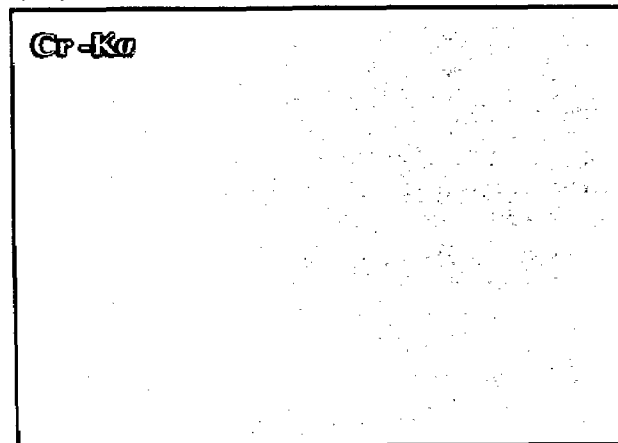
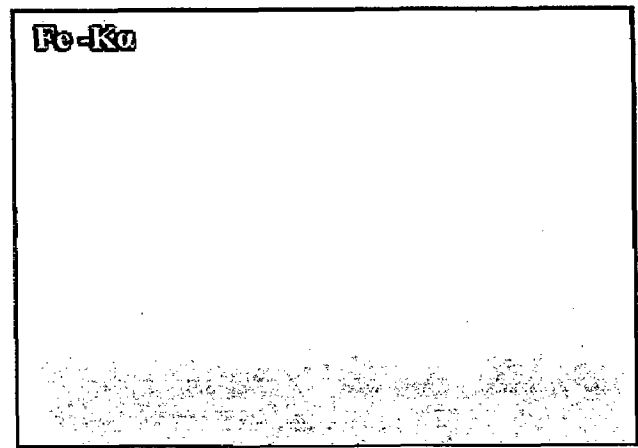
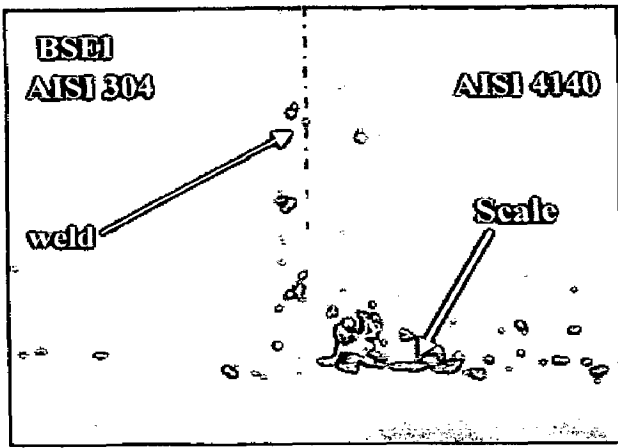


Fig. 6.12 (G) BSEI and X-ray mappings of the cross-section of dissimilar friction welded AISI 304 and AISI 4140 by keeping burn-off length 7mm exposed to $\text{Na}_2\text{SO}_4\text{-60}\%\text{V}_2\text{O}_5$ at $600\text{ }^\circ\text{C}$ for 50 cycles

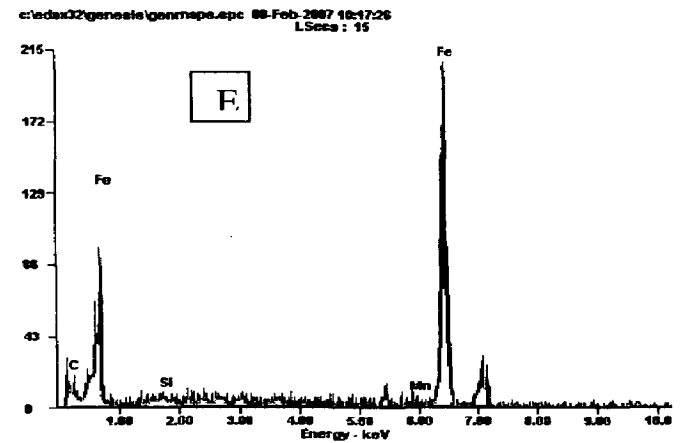
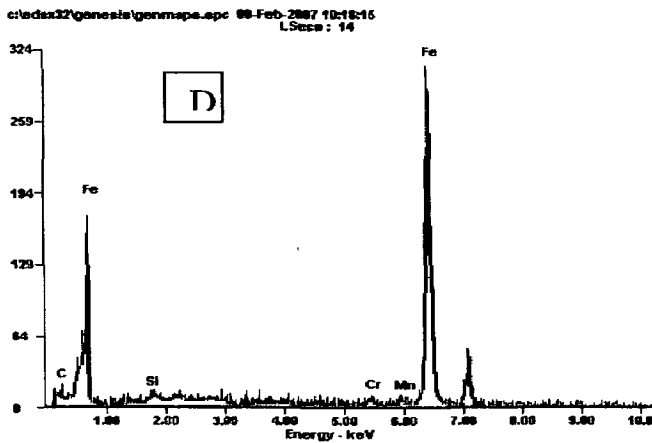
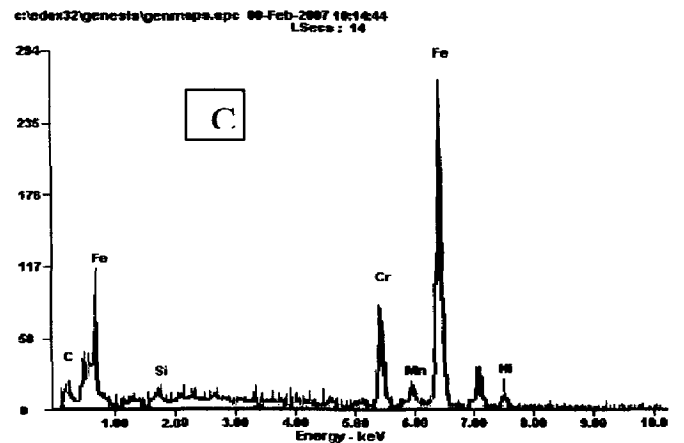
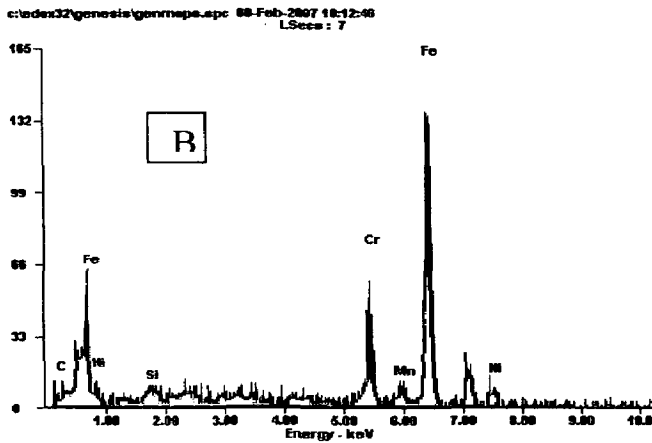
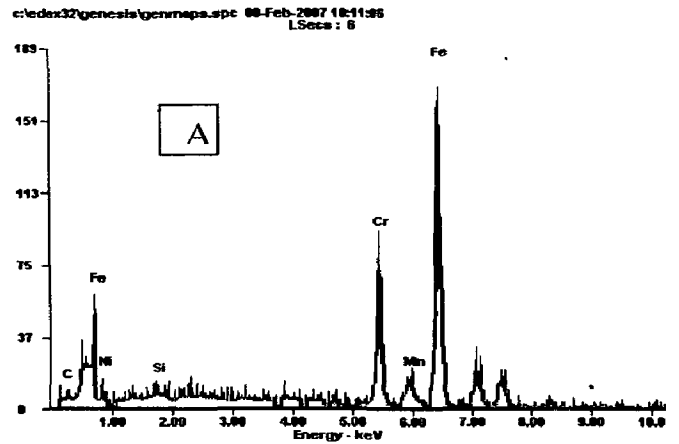
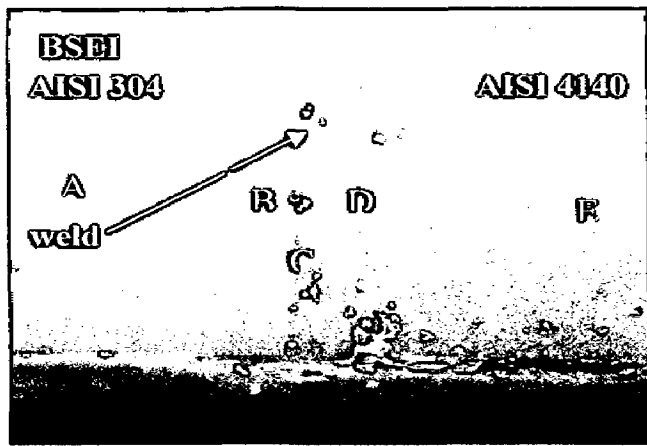


Fig. 6.12(H) BSEI and EDAX of the cross-section of dissimilar friction welded AISI 304 and AISI 4140 by keeping burn-off length 7mm exposed to Na_2SO_4 -60% V_2O_5 at 600 °C for 50 cycles.

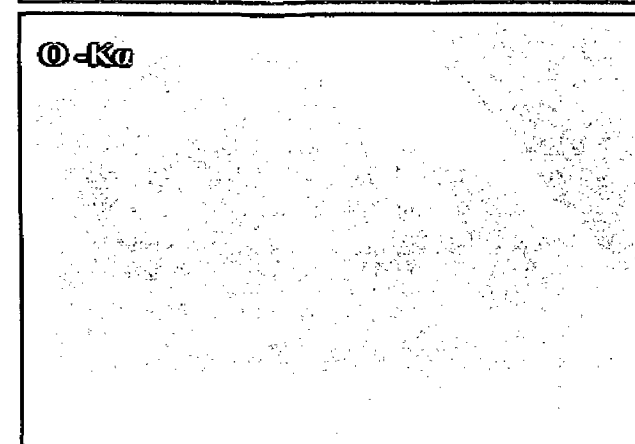
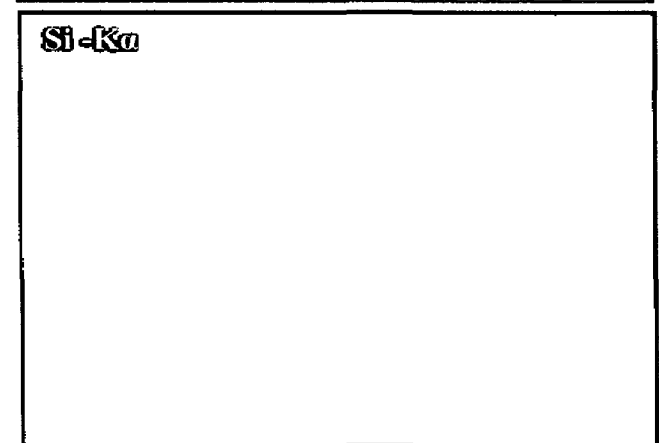
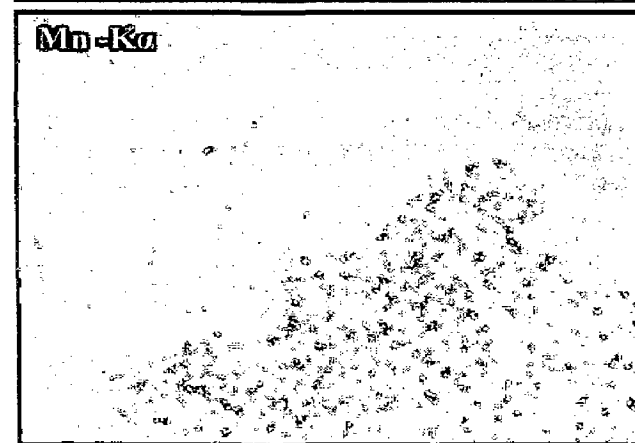
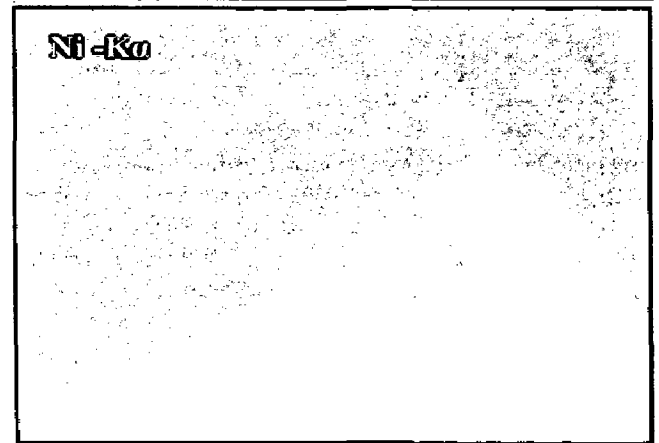
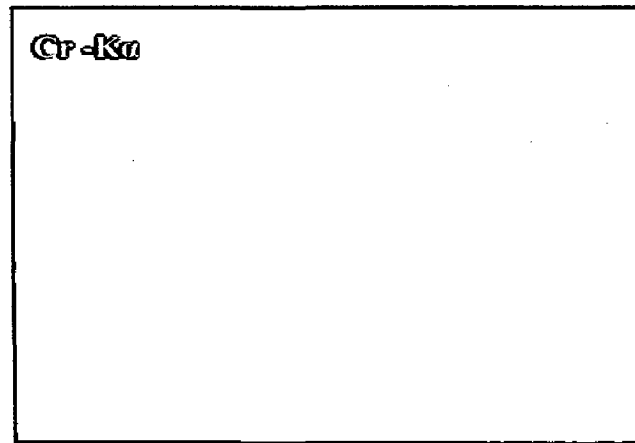
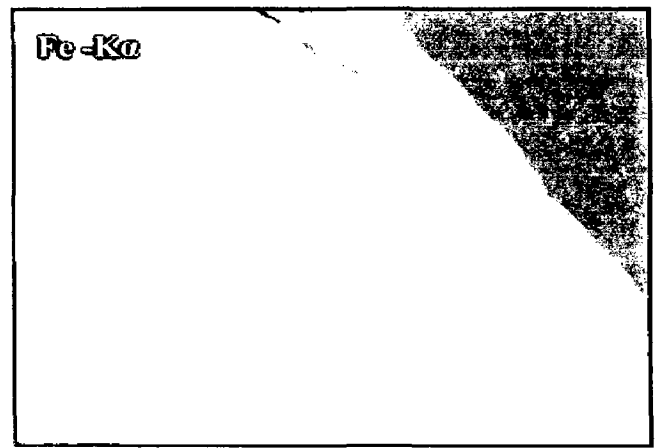
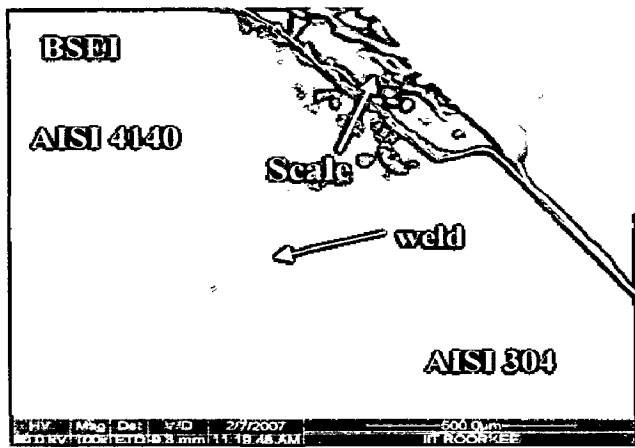


Fig. 6.12(I) BSEI and X-ray mappings of the cross-section of dissimilar friction welded AISI 304 and AISI 4140 by keeping burn-off length 5mm exposed to Na₂SO₄-60%V₂O₅ at 700 °C for 50 cycles

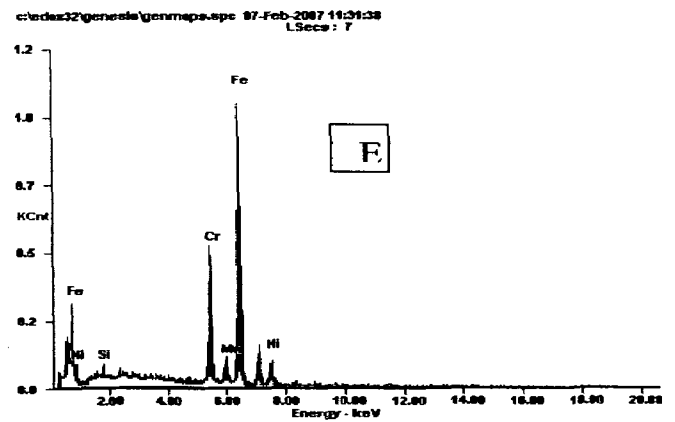
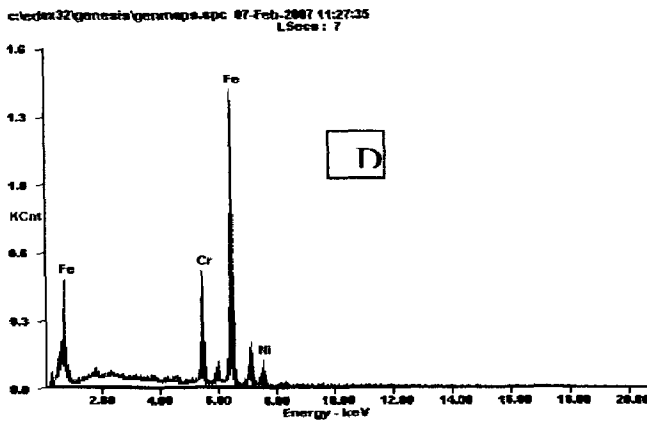
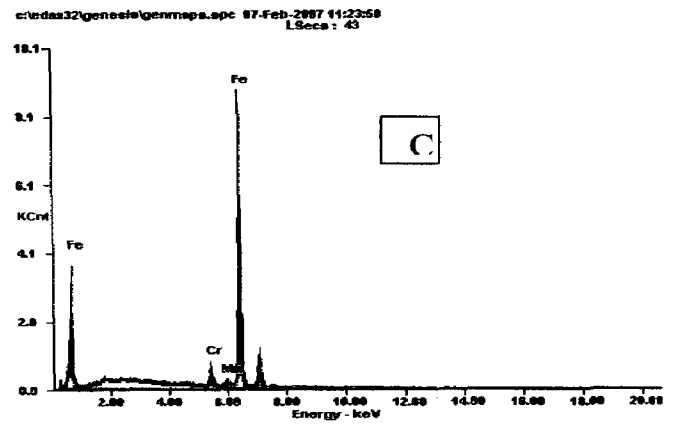
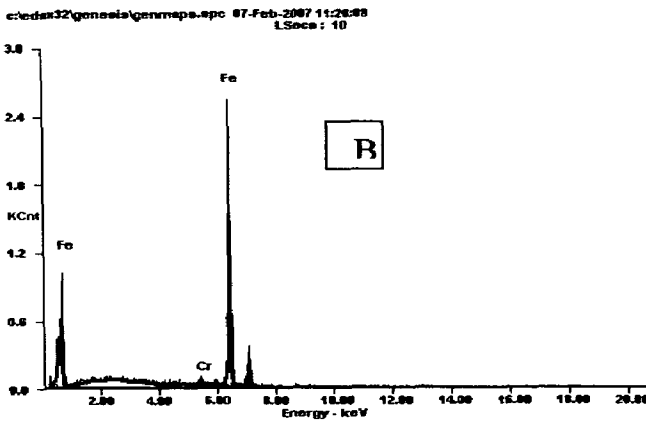
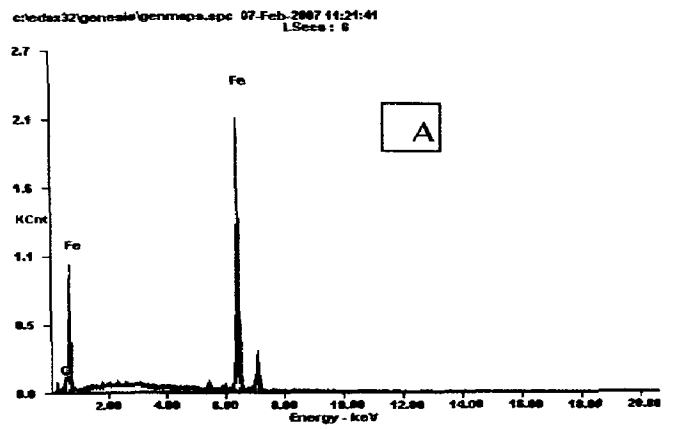
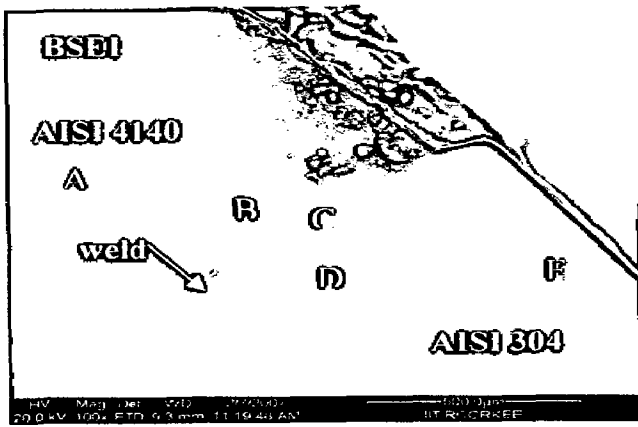


Fig. 6.12(J) BSEI and EDAX of the cross-section of dissimilar friction welded AISI 304 and AISI 4140 by keeping burn-off length 5mm exposed to Na_2SO_4 -60% V_2O_5 at 700 °C for 50 cycles

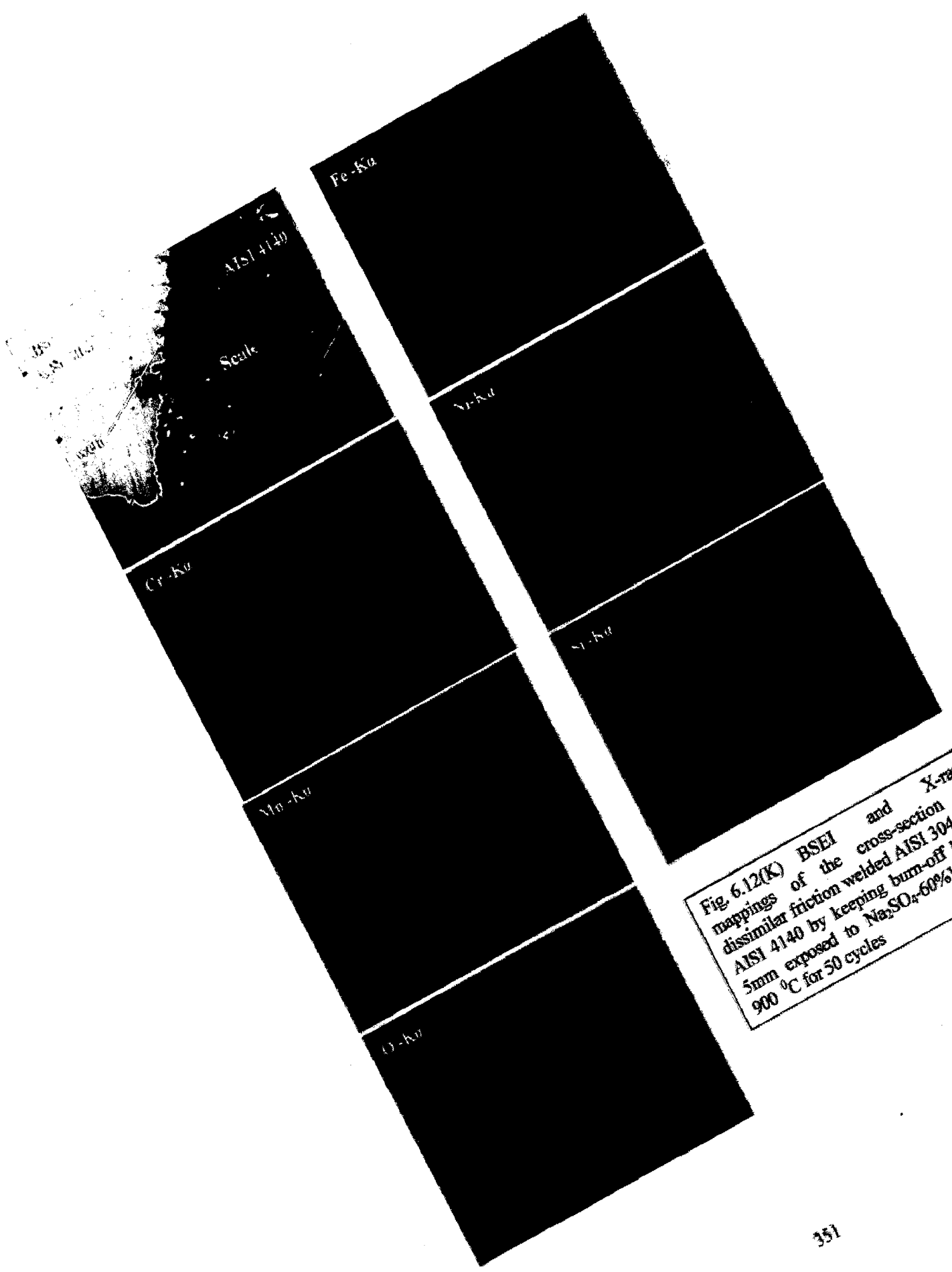


Fig. 6.12(K) BSEI and X-ray mappings of the cross-section of dissimilar friction welded AISI 304 and AISI 4140 by keeping burn-off length 5mm exposed to Na_2SO_4 -60% V_2O_5 at 900 °C for 50 cycles

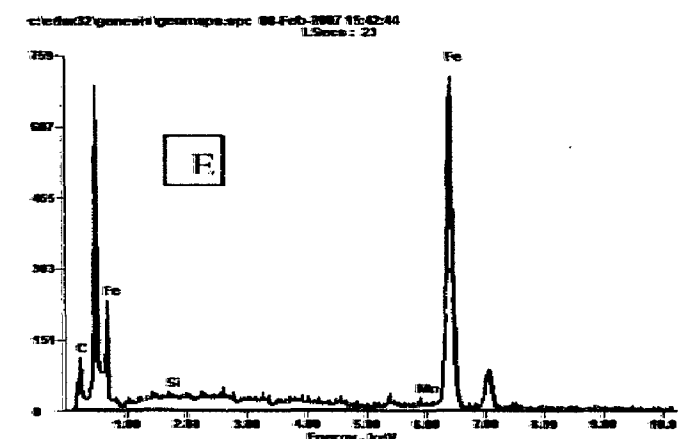
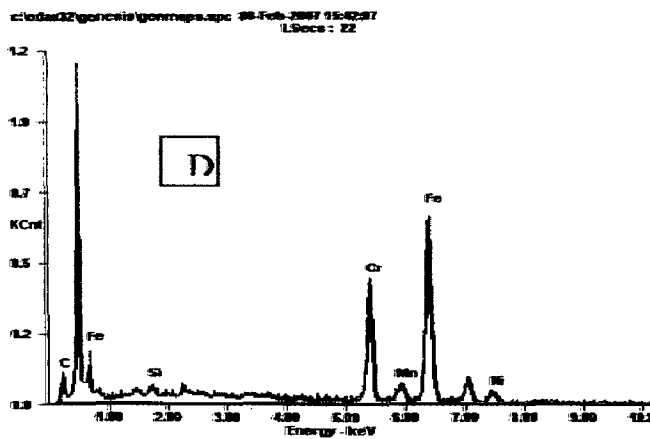
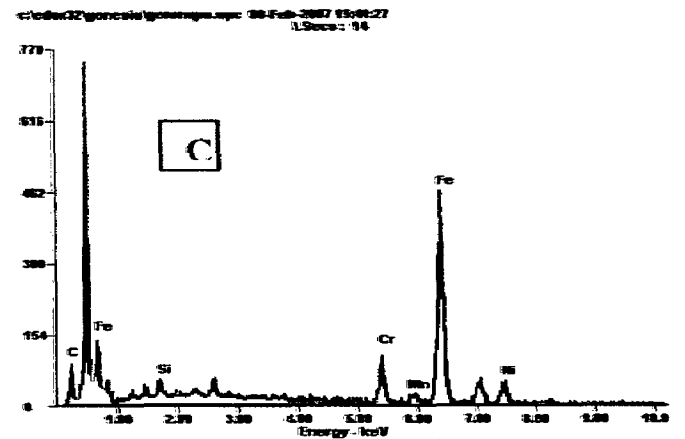
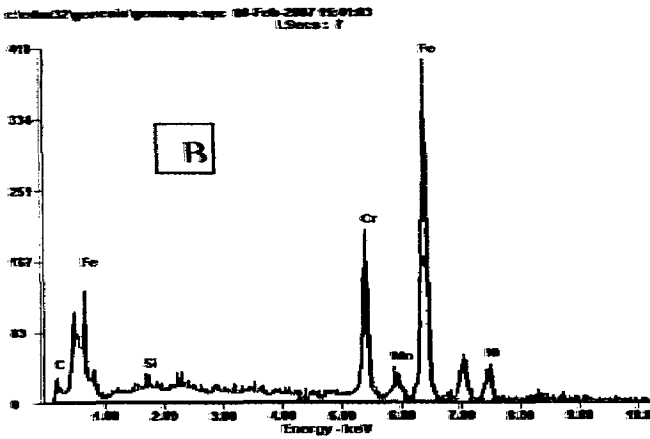
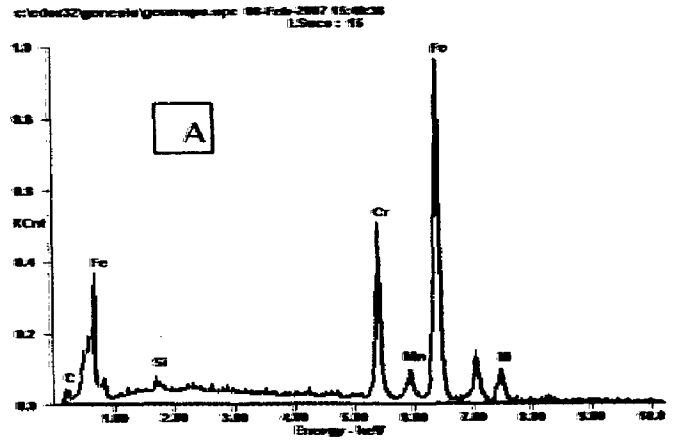
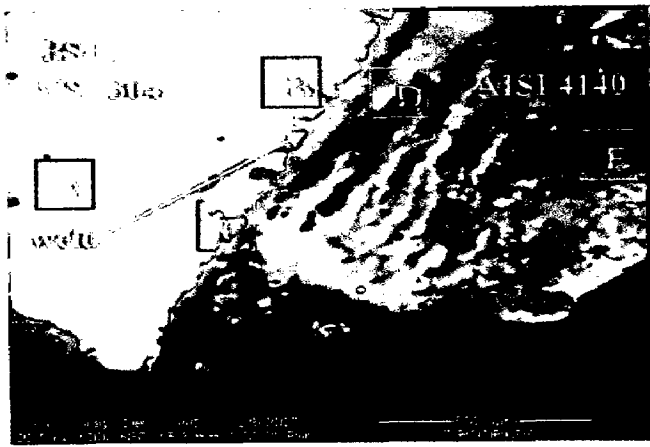


Fig. 6.12(L) BSEI and EDAX of the cross-section of dissimilar friction welded AISI 304 and AISI 4140 by keeping burn-off length 5mm exposed to Na_2SO_4 -60% V_2O_5 at 900 °C for 50 cycles.

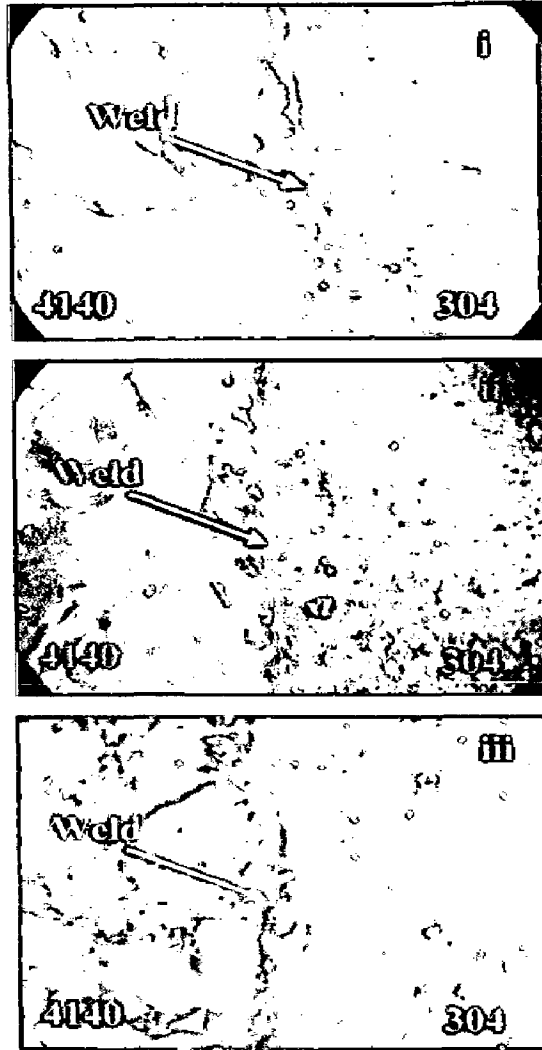


Fig. 6.13 Macrographs dissimilar friction welded AISI 4140 and AISI 304 subjected to cyclic hot corrosion exposed under $K_2SO_4 + NaCl$ (60%) after 50 cycles. (i-iii) Weldment made by keeping 5 mm burn off length and exposed temperature of 500, 550, 600 °C respectively.

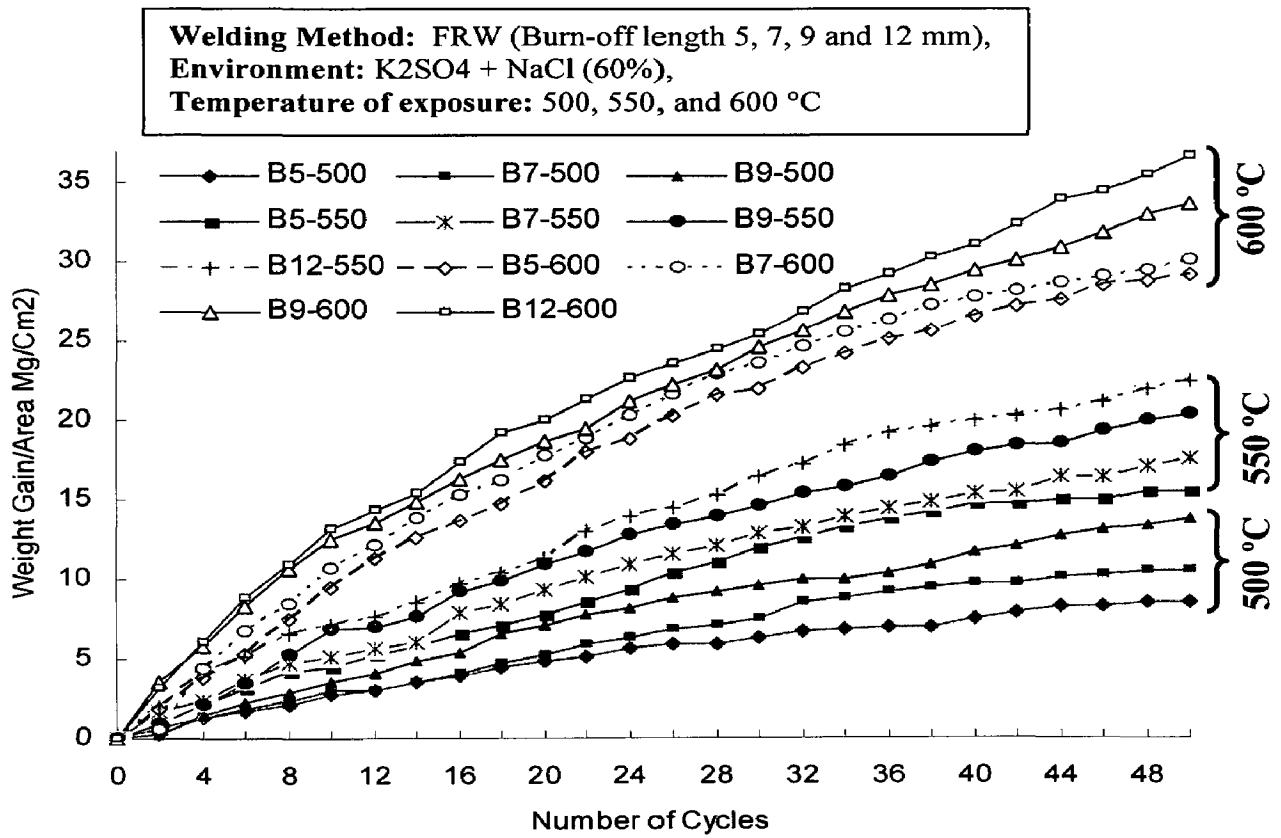


Fig 6.14. Plots of cumulative weight gain (mg/cm^2) as a function of time (number of cycles)

in table 6.2. The parabolic rate constant of dissimilar weldment made by B12 is highest than that of B5 and is around 2.4 times of that for B12 weldment exposure at 500 °C. When increasing the temperature of exposure from 500 to 600 °C, the parabolic rate constant approximately more than 10 times than that of at 500 °C.

Table 6.2 Values of parabolic rate constant Kp

Temperature (°C)	Description		Kp ($10^{-6}(\text{gm}^2\text{Cm}^{-4}\text{S}^{-1})$)
	Temperature (°C)	Burn off length (mm)	
500		5	4.460
		7	7.190
		9	11.120
550		5	15.700
		7	18.310
		9	37.850
		12	30.340
600		5	53.000
		7	56.210
		9	65.380
		12	75.810

6.1.2.3 X-ray Diffraction Analysis

The XRD patterns for the hot corroded surfaces of welded samples by keeping four different burn-off length (B5, B7, B9 and B12 mm) exposed to the K₂SO₄ (40%) and NaCl (60 %) environment at exposure temperature of 500, 550 and 600 °C after 50 cycles are shown in Figs.6.15, 6.16 and 6.17. X-Ray diffraction studies were carried out to analysis the phases existing in the hot corroded product. In the weldment, the scales were found to contain Fe₂O₃ as major oxide with Cr₂O₃, FeS, NiFe₂O₄ and NiCr₂O₄ were present as a minor constituent.

6.1.2.4 Scale Thickness Measurement

The samples were cut across the cross-section after exposure to molten salt at 500, 550 and 600 °C for 50 cycles and mounted. The scale thickness values were measured from SEM

back scattered images shown in Fig. 6.18(i-iii). The exact oxide scale thickness could not be measured for all the weldments due to intense spalling and sputtering. The SEM micrograph shows the fragile and cracked scale for all the weldments.

6.1.2.5 SEM/EDAX Analysis

SEM photographs showing surface morphology of the dissimilar weldment after 50 cycles hot corrosion studies are shown in Fig 6.19 (A-J). EDAX analysis for the weldment shows Fe_2O_3 to be the predominant phase. From the analysis, the scale on the base metals (4140) at 500 °C and 550 °C indicated the presence of small quantities of MnO and K_2O along with higher percentage of Fe_2O_3 (91-99%) whereas at 600 C the 2.58% of Cr_2O_3 is indicated. In the case of base metal stainless steel side, while varying the temperature from 500 to 600 °C the scale has higher percentage of Fe_2O_3 (37-93%) and Cr_2O_3 (2.80 – 21%) along with other minor phases MnO, NiO, SO_3 , etc. EDAX analysis for scale on the weld interface by changing temperatures 500, 550 and 600 C, shows Fe_2O_3 (91-61%) to be the predominant phase with Cr_2O_3 (2 -19%) with other minor phases MnO, NiO, SO_3 , SiO_2 , etc. From the EDAX data, the effect of temperature and burn off length on the formation of oxides in the scale on the weldment shown in Fig 6.19 (K-N).

6.1.2.6 EPMA Analysis

BSEI and X-ray mapping for cross-section of corroded dissimilar weldment exposed to K_2SO_4 (40%) and NaCl (60 %) at 500, 550 and 600 °C for 50 cycles are shown in Fig. 6.20 (A-C). The EPMA of the cross-section of corroded dissimilar weldment made by friction welding by keeping different burn-off length (5, 7, 9 and 12mm) indicates that scale is mainly consisting of Fe, Cr and Ni. Figure 6.21 (A) shows that oxygen penetration in the scale of friction weldment of burn-off length 5 exposed at 500 °C under molten salt environment. The X-Ray mapping elemental distribution on the weldment after exposed at 600 shown in Fig 6.21 (B and C). It was noted that the Cr concentration is more in the weld zone as well as the both side of HAZ.

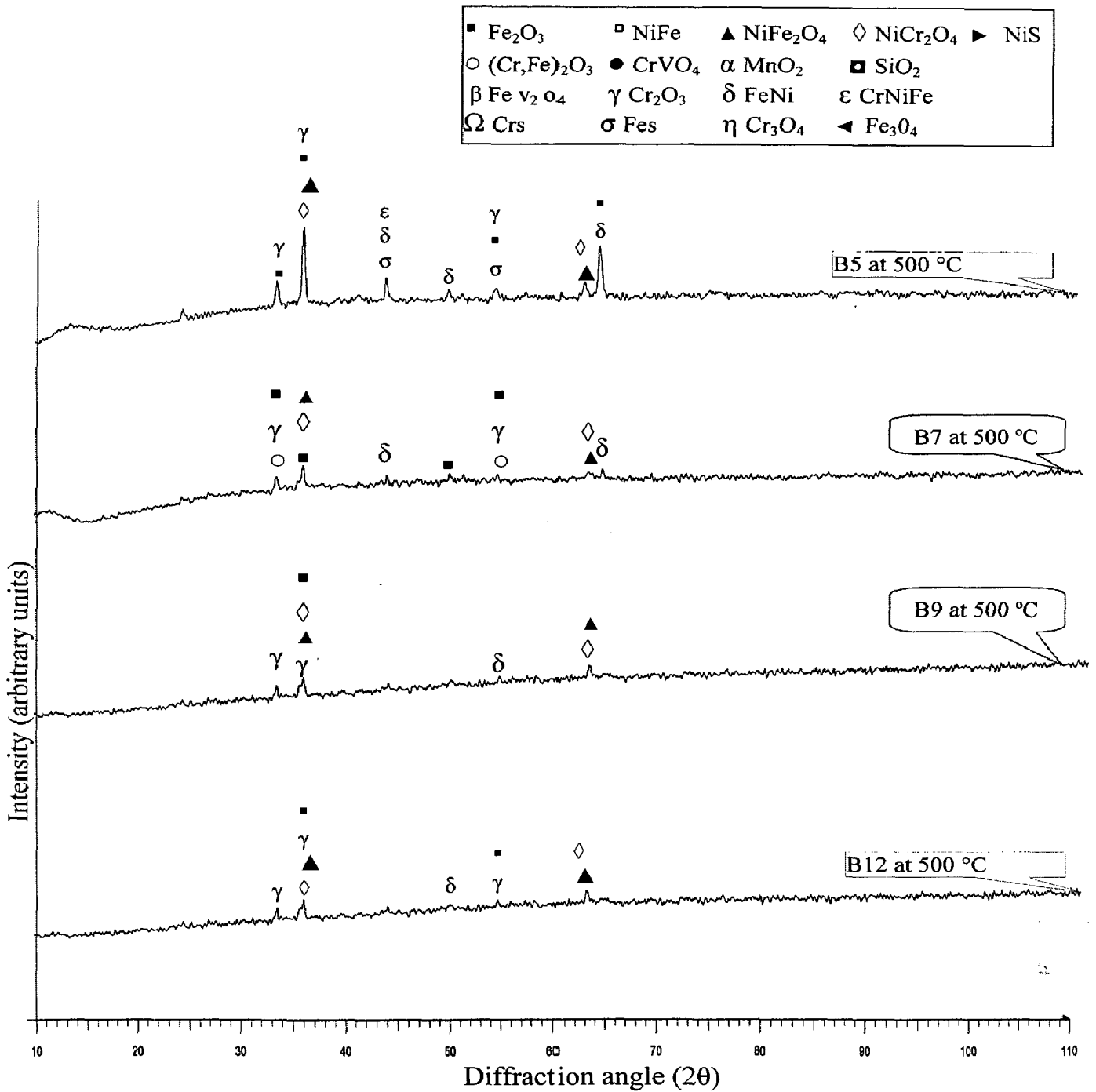


Fig. 6.15 X-ray diffraction patterns for the hot corroded surfaces of friction welded samples by keeping four different burn-off length (B5, B7, B9 and B12 mm) exposed to the K₂SO₄ (40%) and NaCl (60 %) environment at exposure temperature of 500 °C after 50 cycles.

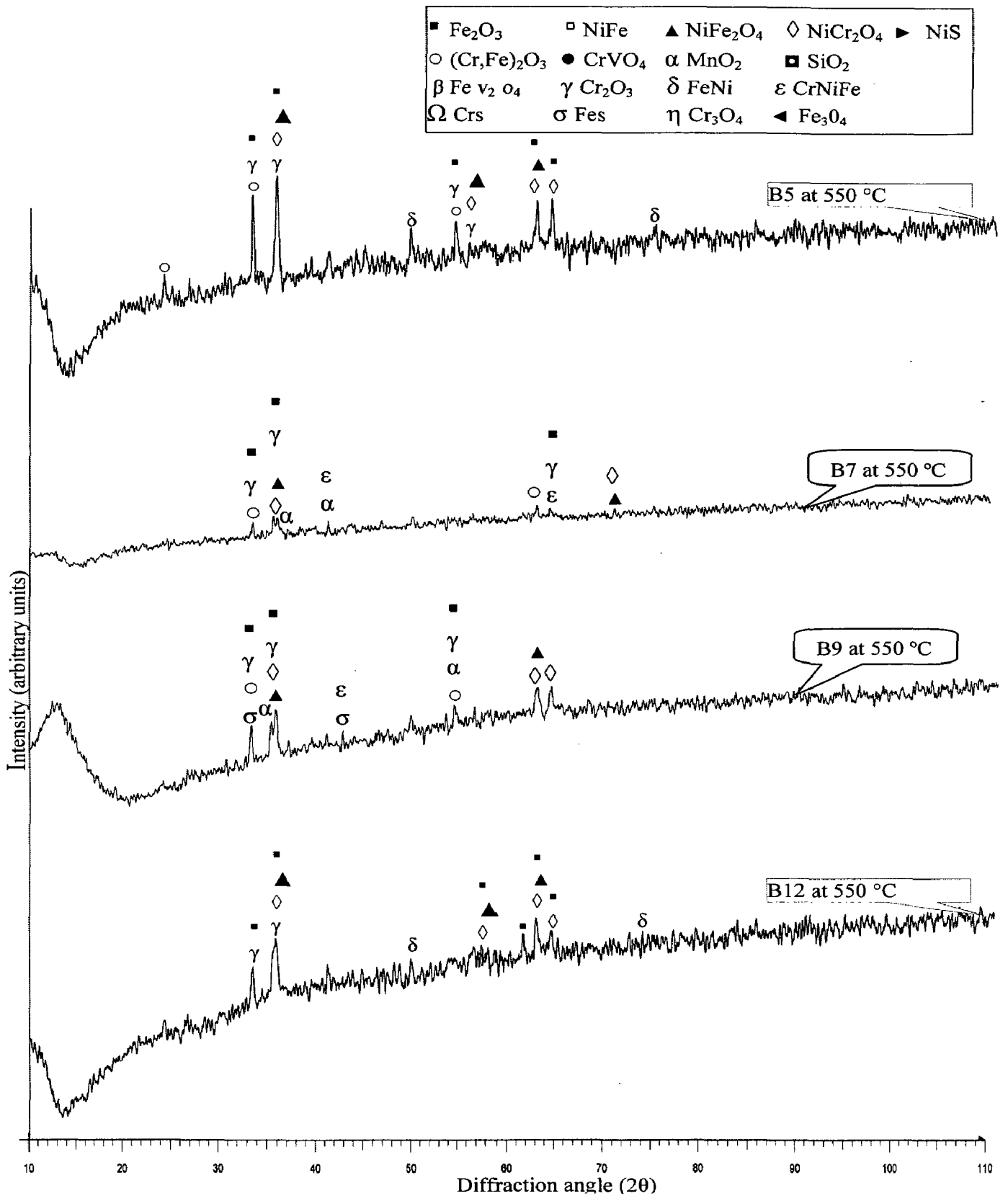


Fig. 6.16 X-ray diffraction patterns for the hot corroded surfaces of friction welded samples by keeping four different burn-off length (B5, B7, B9 and B12 mm) exposed to the K₂SO₄ (40%) and NaCl (60 %) environment at exposure temperature of 550 °C after 50 cycles.

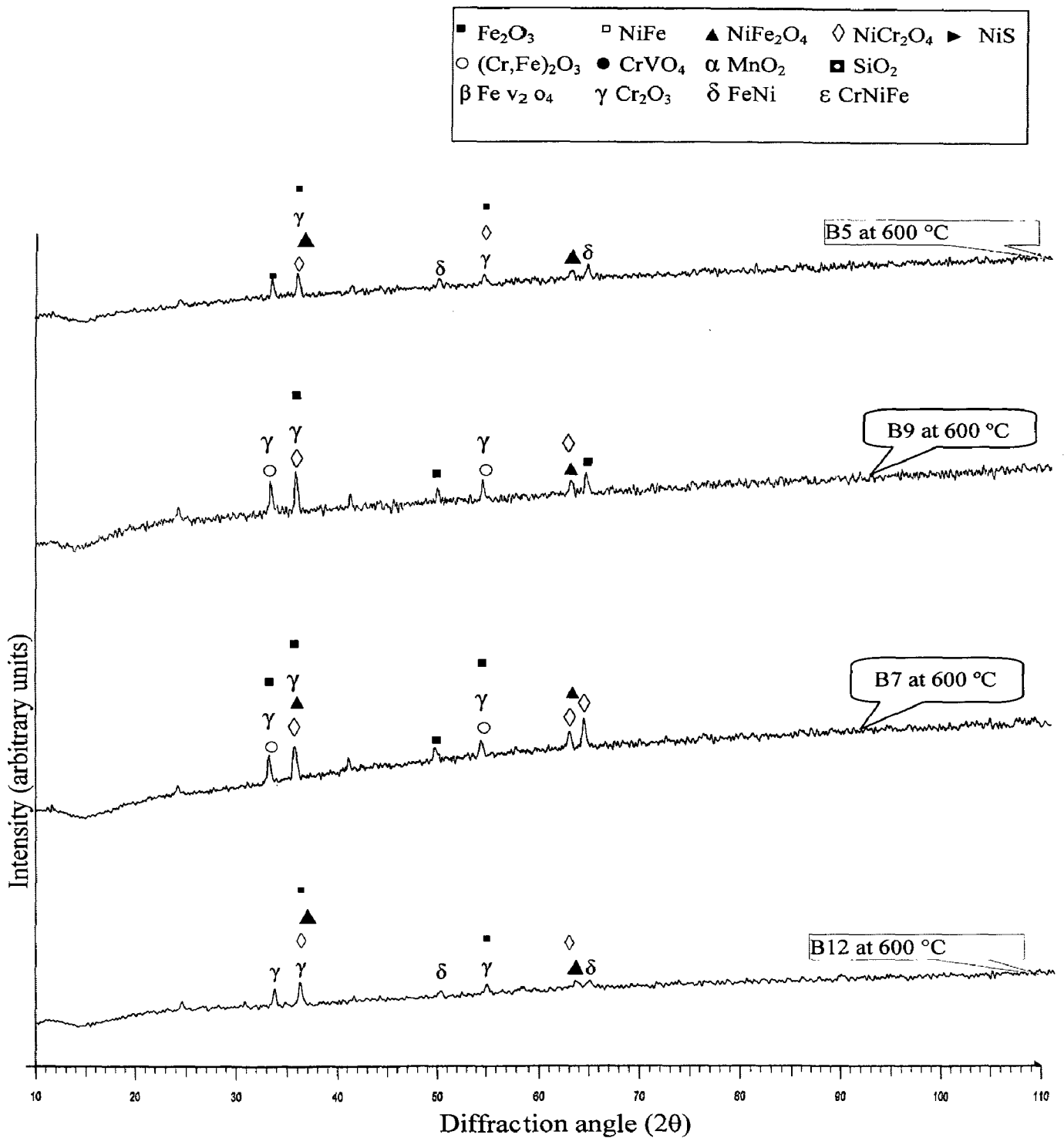


Fig. 6.17 X-ray diffraction patterns for the hot corroded surfaces of friction welded samples by keeping four different burn-off length (B5, B7, B9 and B12 mm) exposed to the K_2SO_4 (40%) and NaCl (60 %) environment at exposure temperature of 600 °C after 50 cycles.

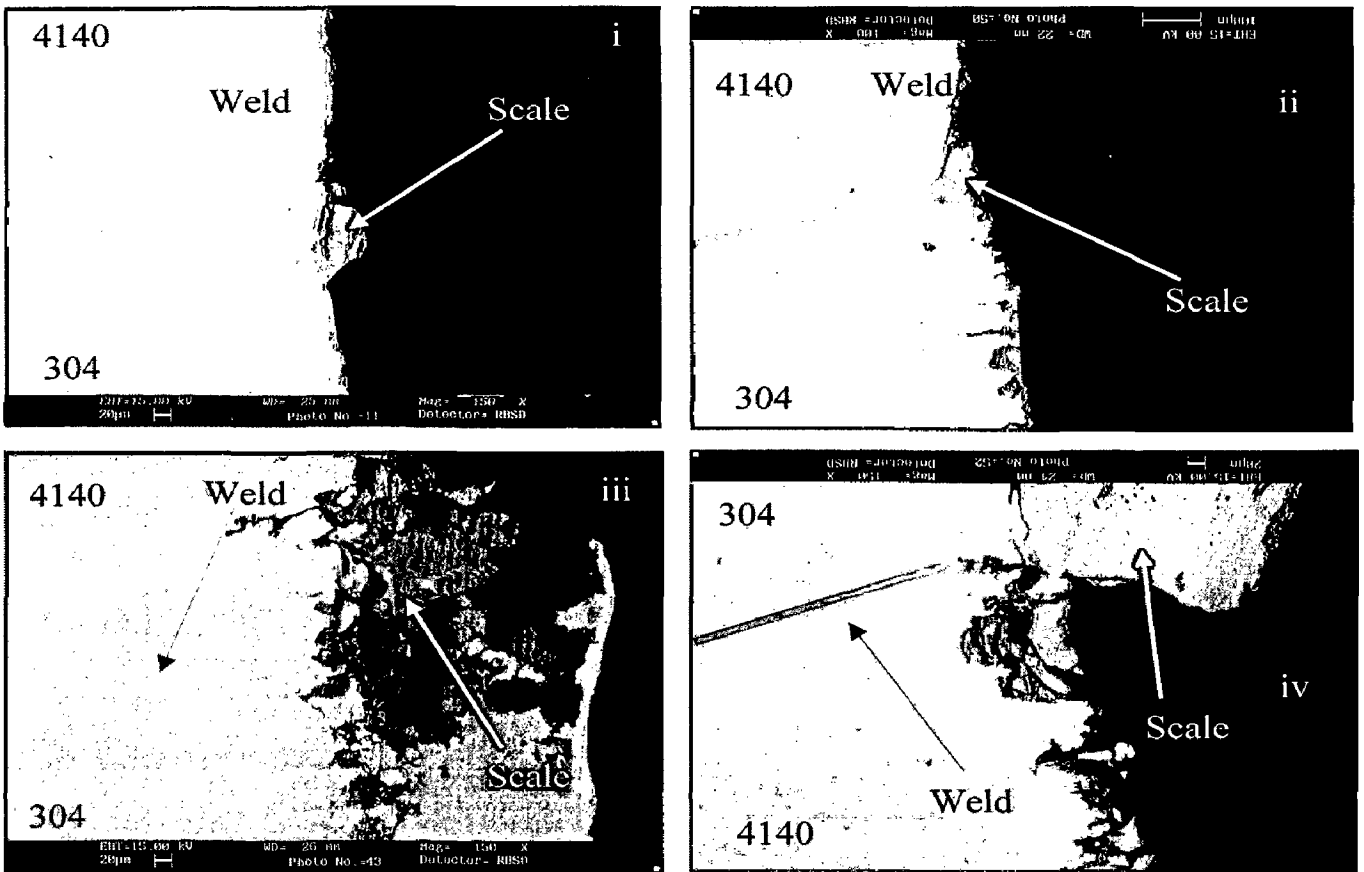


Fig 6.18. BSEI for hot corroded friction weldment under $K_2SO_4 + NaCl$ (60%), exposed temperature of 500, 550, 600. (i) and (ii): Exposed temperature 500 and 600 °C respectively for weldment made by keeping 5 mm Burn off length. (iii) and (iv): Exposed temperature 550 and 600 °C respectively for weldment made by keeping 12 mm Burn off length.

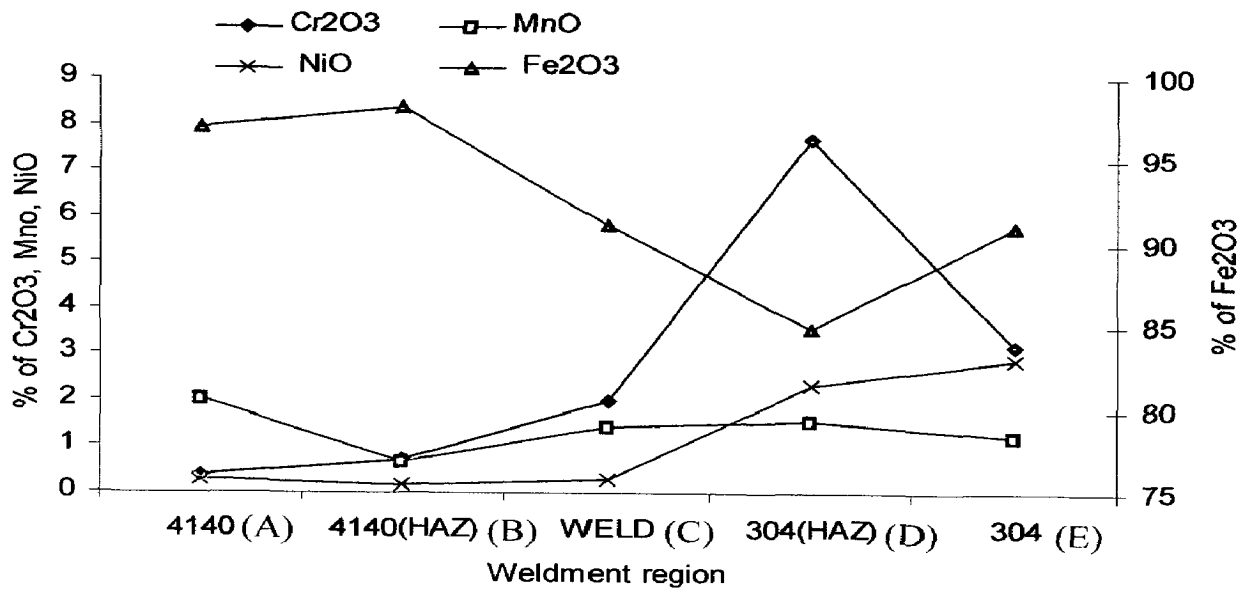
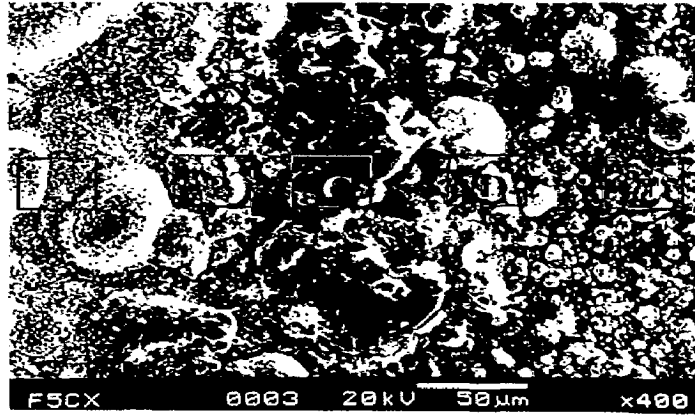


Fig 6.19(A) SEM/EDAX graph shows the friction weldment made by keeping 5 mm burn off length, exposed at 500 °C under K₂SO₄ (40%) and NaCl (60 %) after 50 cycles

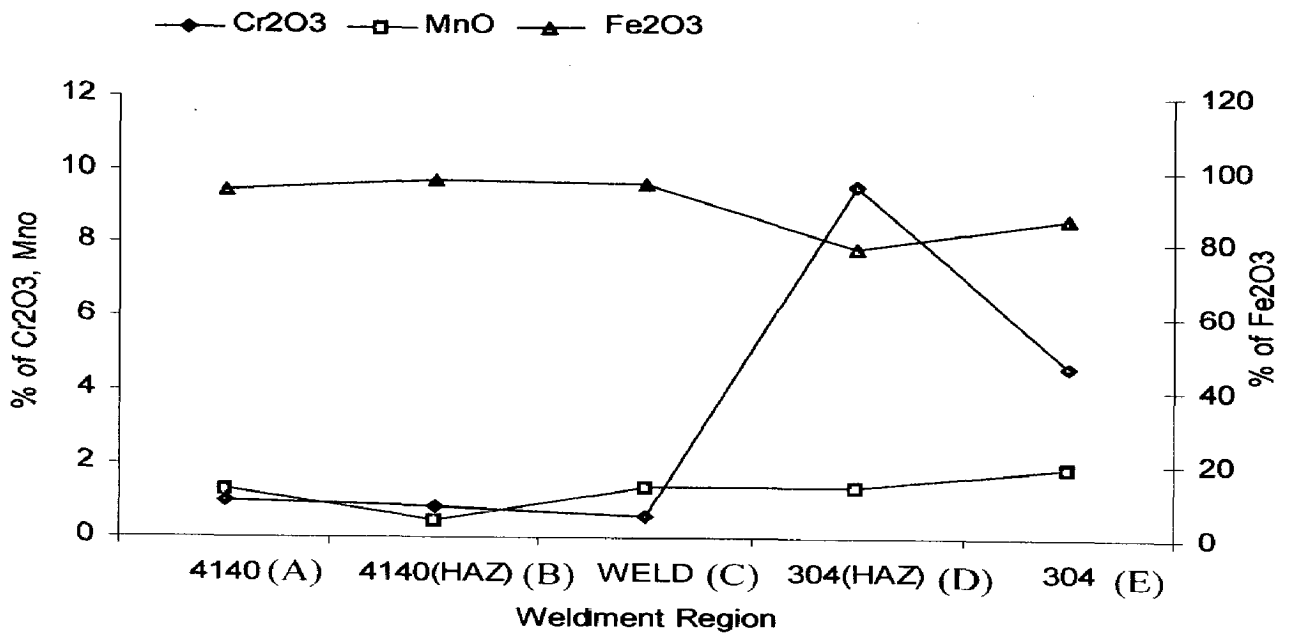


Fig 6.19(B) SEM/EDAX graph shows the friction weldment made by keeping 7 mm burn off length, exposed at 500 °C under K₂SO₄ (40%) and NaCl (60 %) after 50 cycles

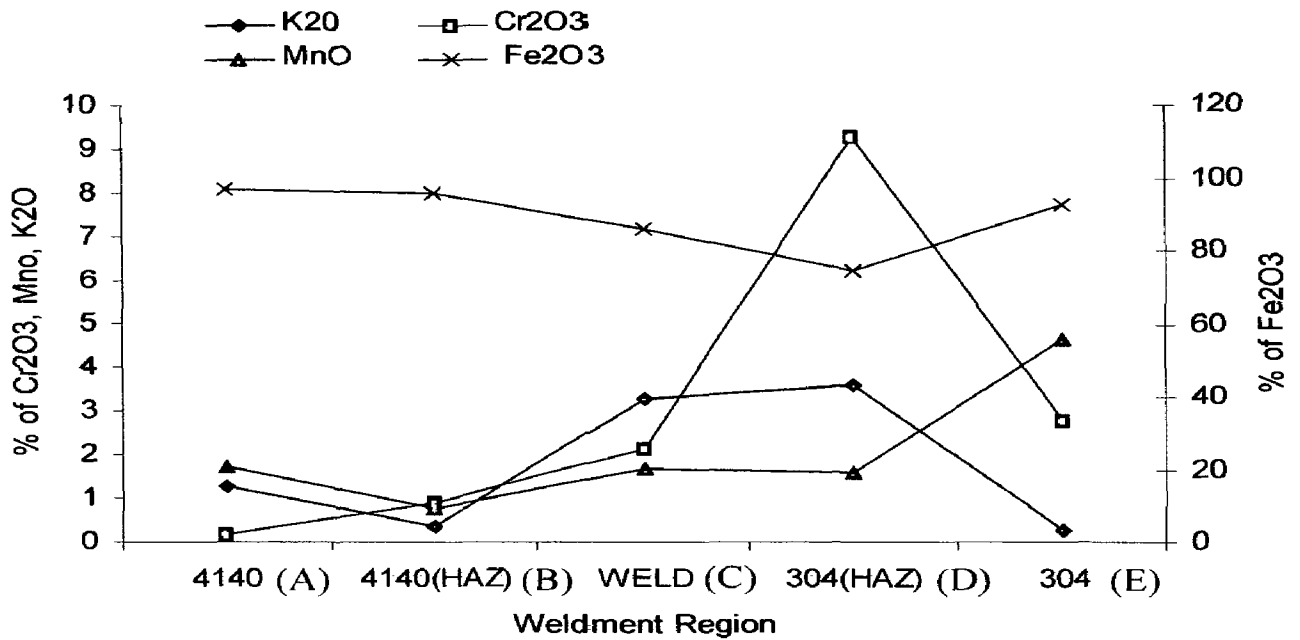
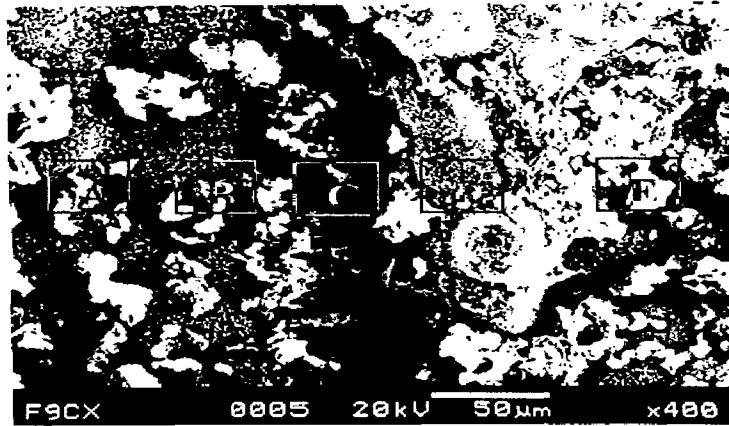


Fig 6.19(C) SEM/EDAX graph shows the friction weldment made by keeping 9 mm burn off length, exposed at 500 °C under K_2SO_4 (40%) and NaCl (60 %) after 50 cycles

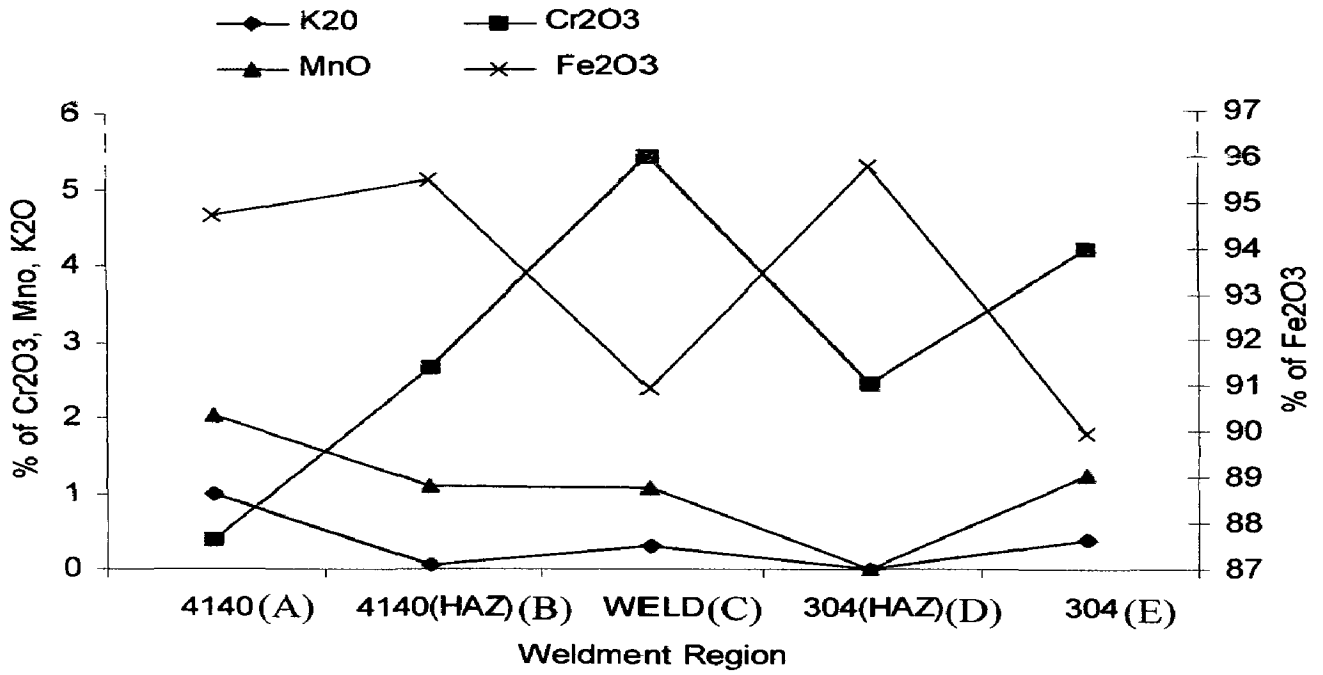


Fig 6.19(D) SEM/EDAX graph shows the friction weldment made by keeping 5 mm burn off length, exposed at 550 °C under K₂SO₄ (40%) and NaCl (60 %) after 50 cycles

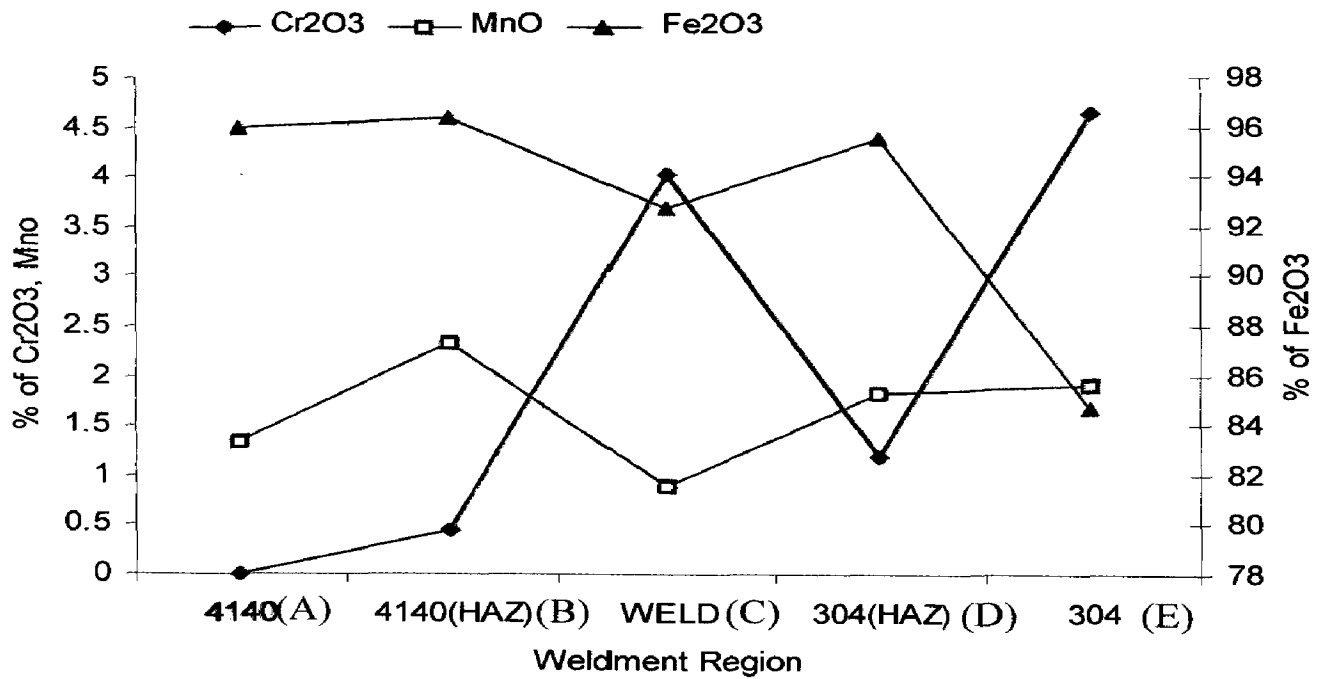


Fig 6.19(E) SEM/EDAX graph shows the friction weldment made by keeping 7 mm burn off length, exposed at 550 °C under K₂SO₄ (40%) and NaCl (60 %) after 50 cycles

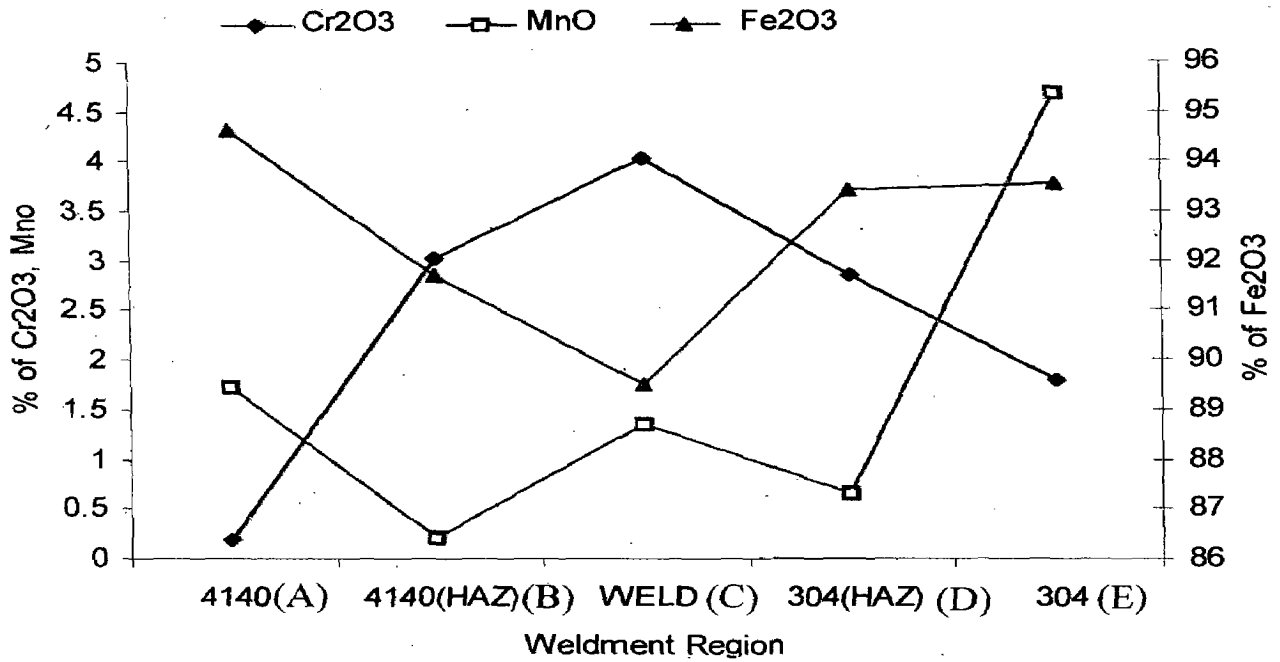
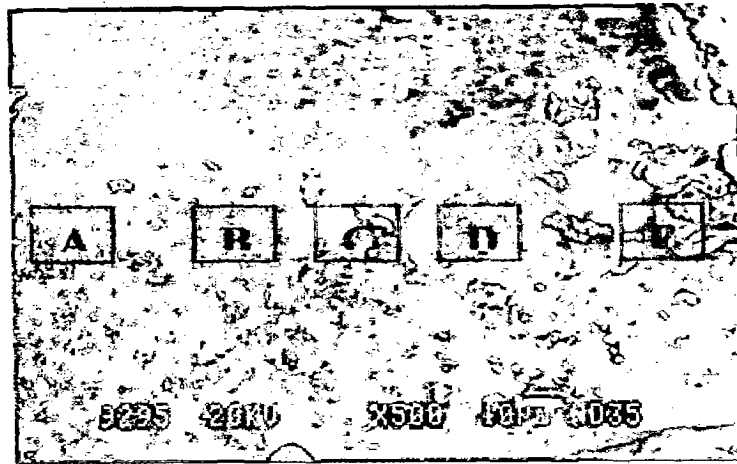


Fig 6.19(F) SEM/EDAX graph shows the friction weldment made by keeping 12 mm burn off length, exposed at 550 °C under K₂SO₄ (40%) and NaCl (60 %) after 50 cycles

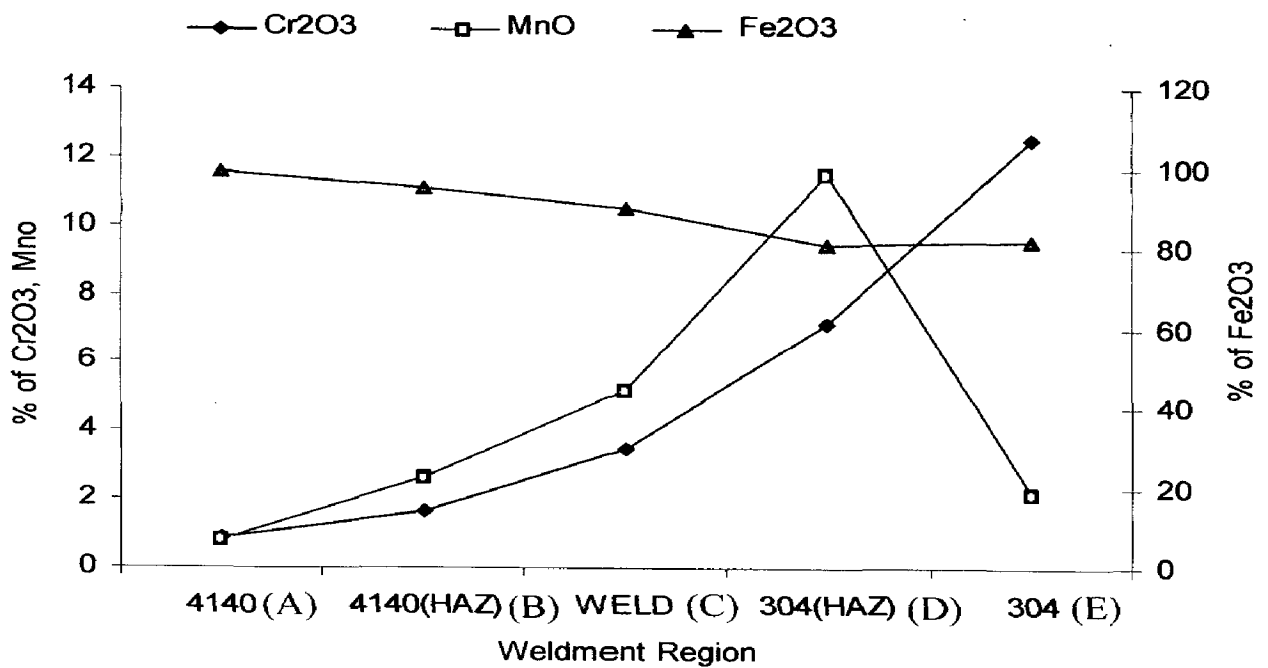
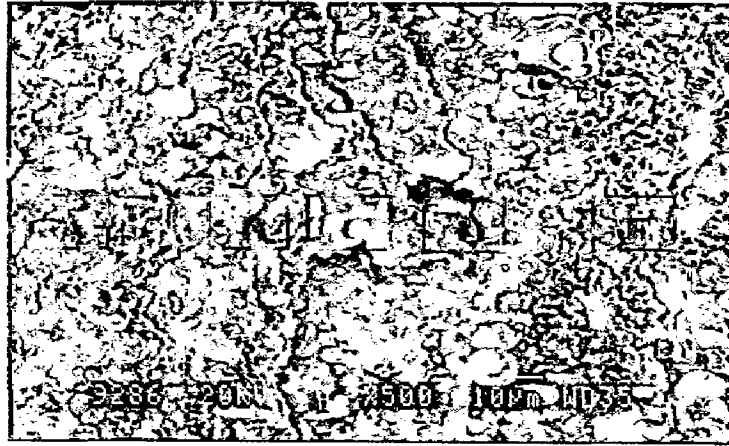


Fig 6.19(G) SEM/EDAX graph shows the friction weldment made by keeping 5 mm burn off length, exposed at 600 °C under K₂SO₄ (40%) and NaCl (60 %) after 50 cycles

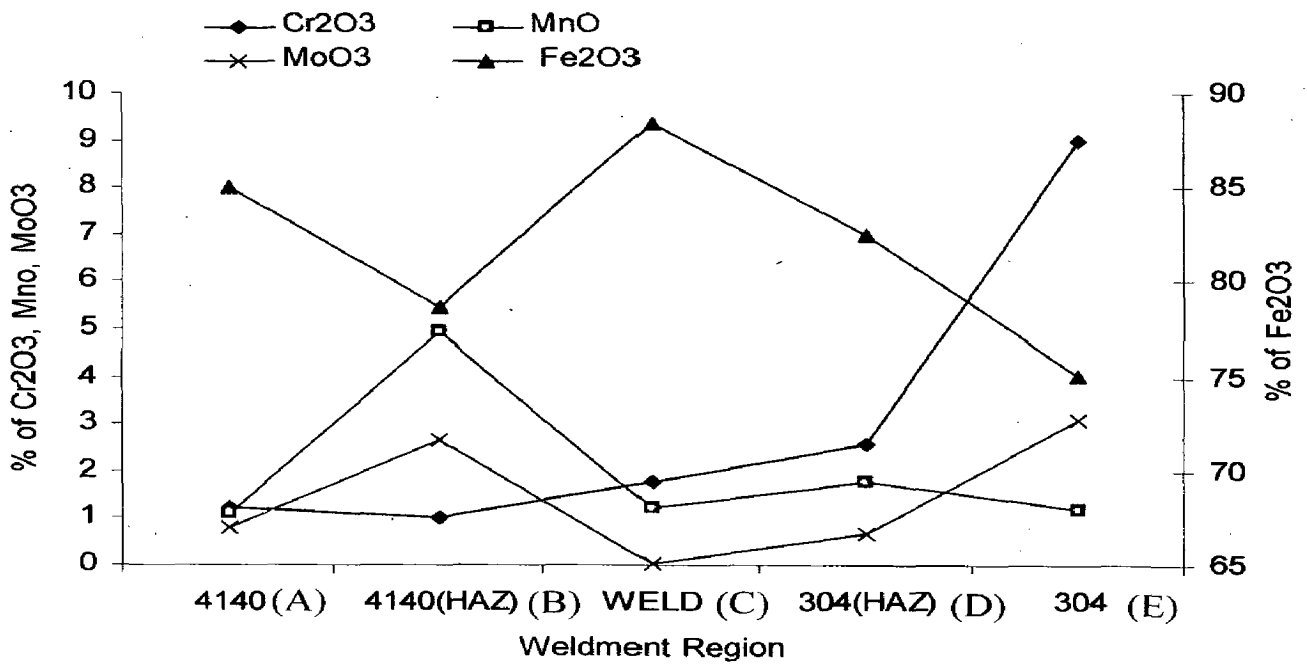
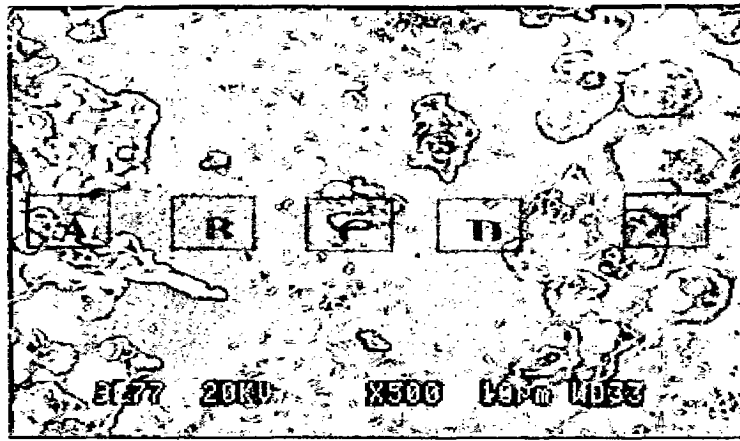


Fig 6.19(H) SEM/EDAX graph shows the friction weldment made by keeping 7 mm burn off length, exposed at 600 °C under K₂SO₄ (40%) and NaCl (60 %) after 50 cycles

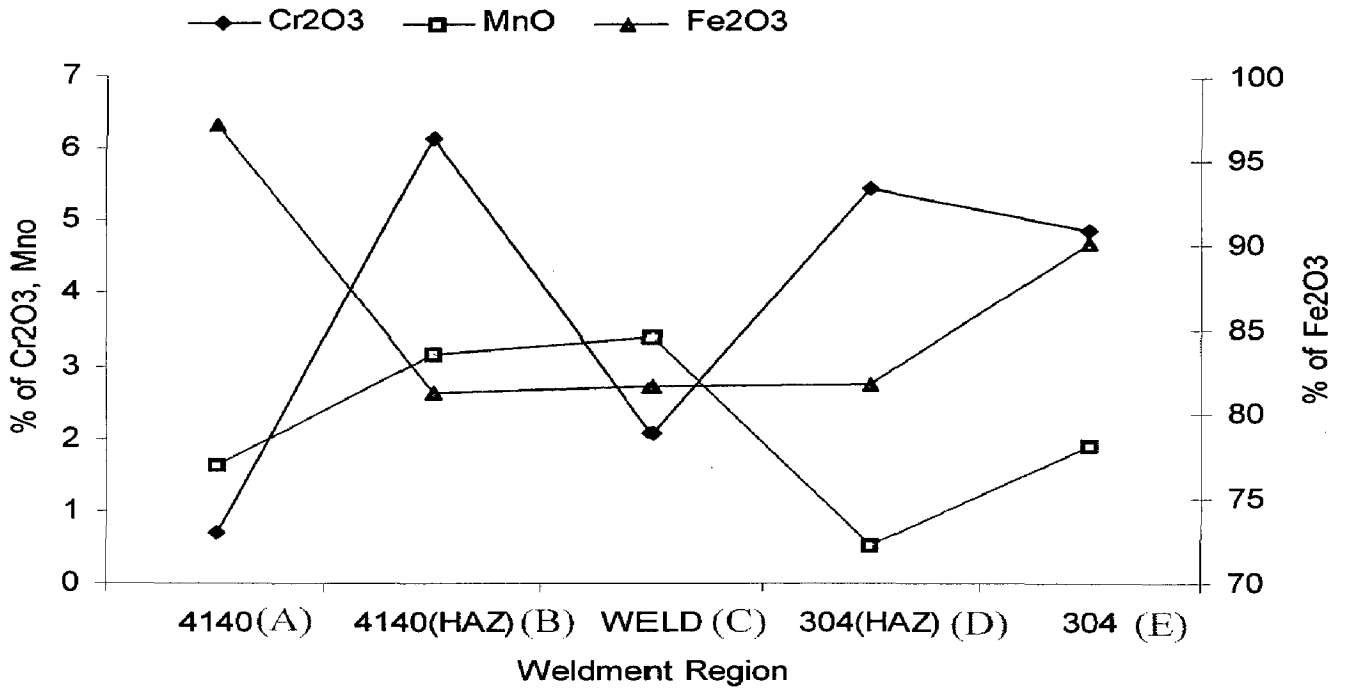
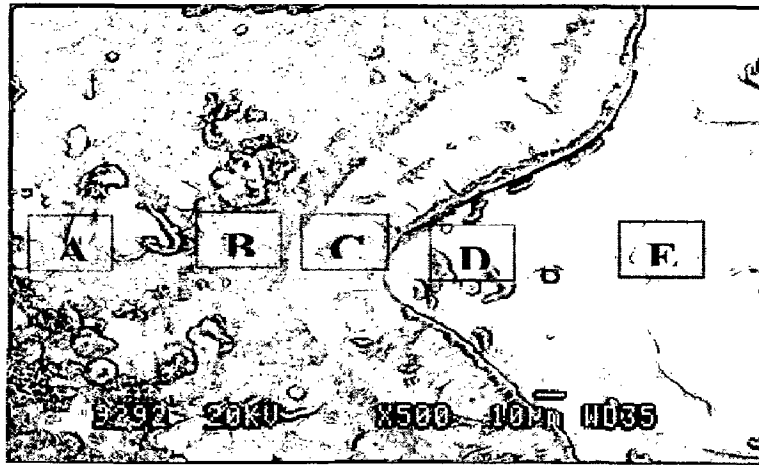


Fig 6.19(I) SEM/EDAX graph shows the friction weldment made by keeping 9 mm burn off length, exposed at 600 °C under K₂SO₄ (40%) and NaCl (60 %) after 50 cycles

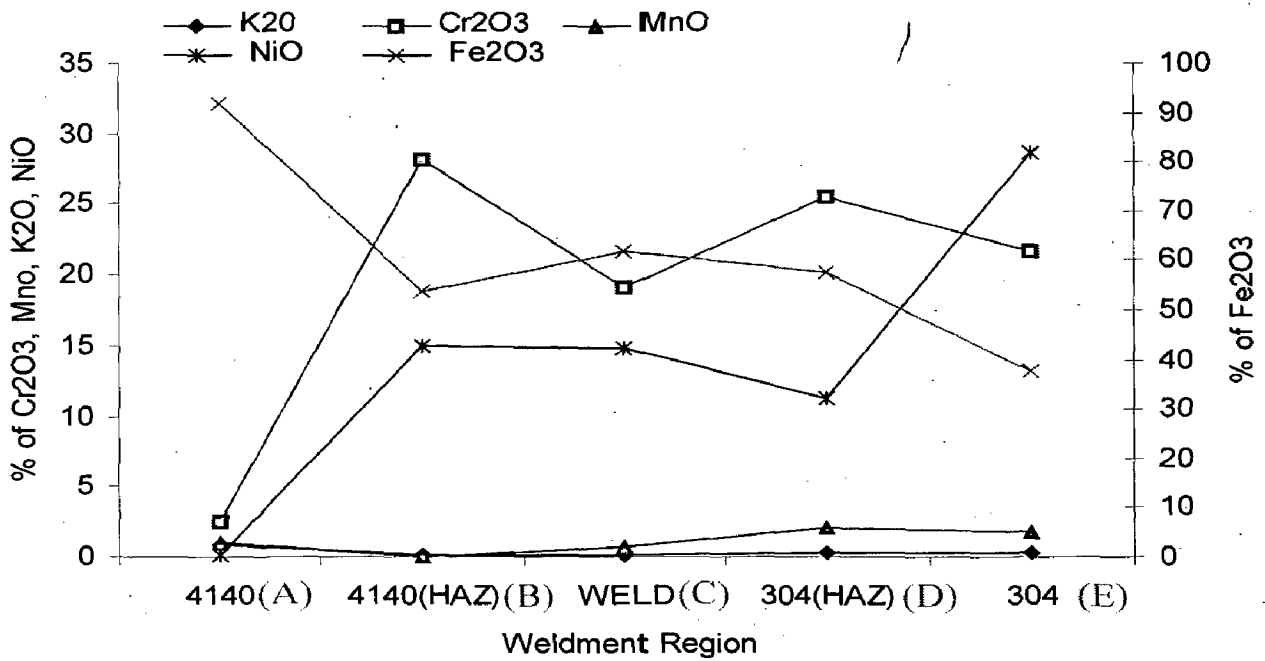
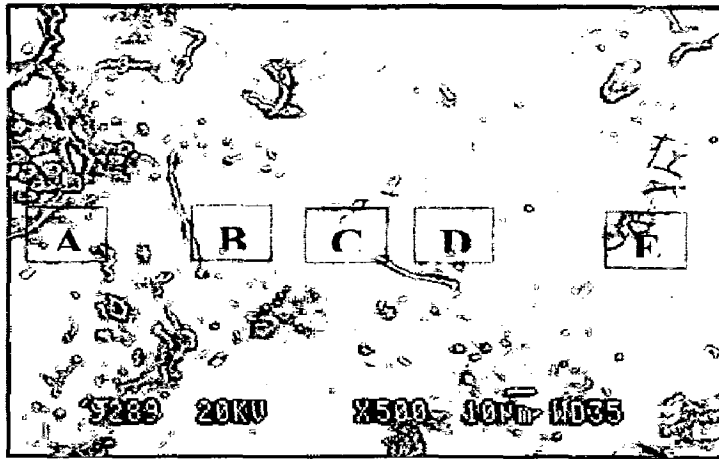


Fig 6.19(J) SEM/EDAX graph shows the friction weldment made by keeping 12 mm burn off length, exposed at 600 °C under K₂SO₄ (40%) and NaCl (60 %) after 50 cycles

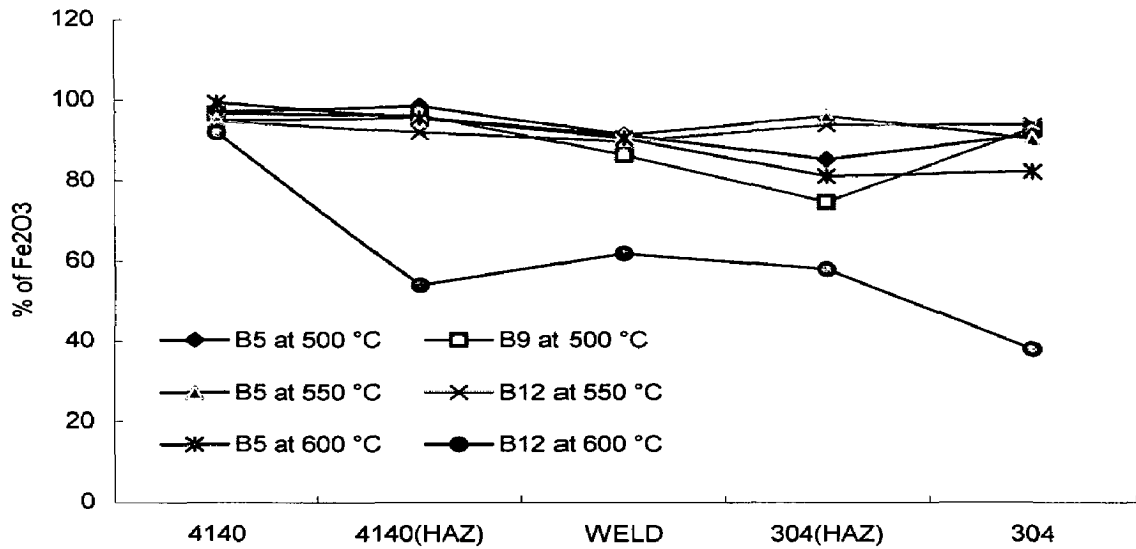


Fig 6.19 (K) EDAX data shows the effect of burn off length and temperature on formation of Fe₂O₃ on the friction weldment under molten salt environment of K₂SO₄-60% NaCl.

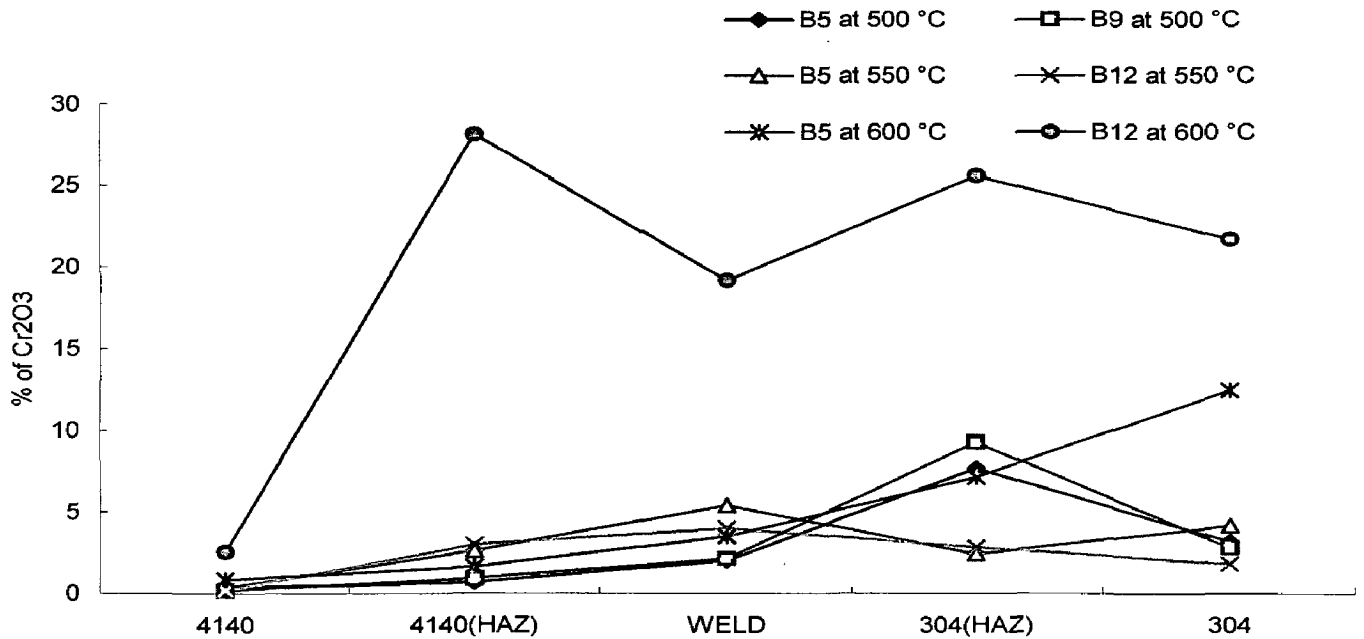


Fig 6.19 (L) EDAX data shows the effect of burn off length and temperature on formation of Cr₂O₃ on the friction weldment under molten salt environment of K₂SO₄-60% NaCl.

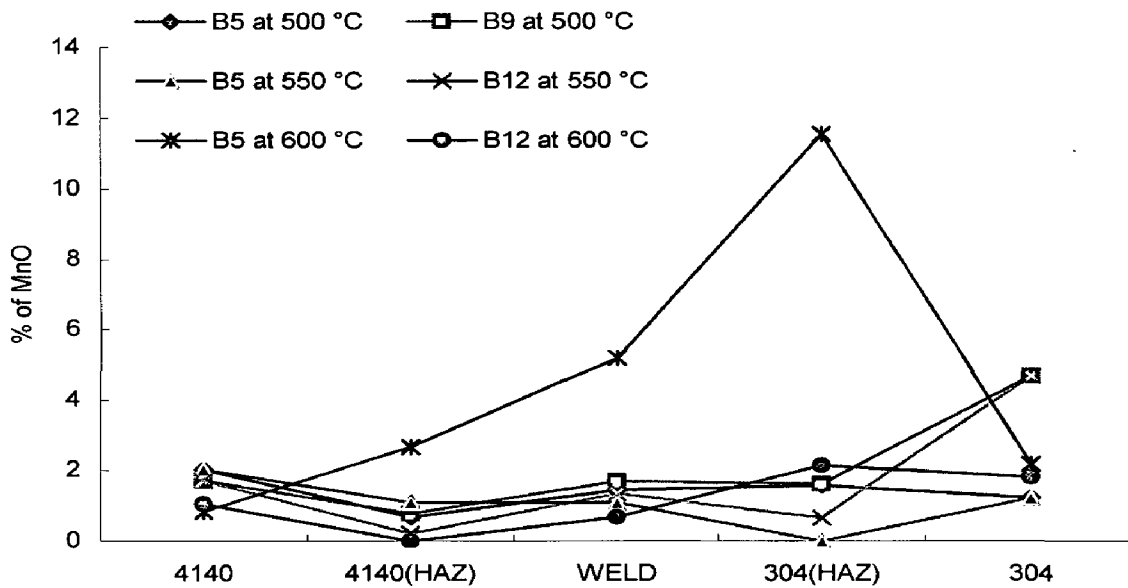


Fig 6.19 (M) EDAX data shows the effect of burn off length and temperature on formation of MnO on the friction weldment under molten salt environment of K_2SO_4 -60% NaCl.

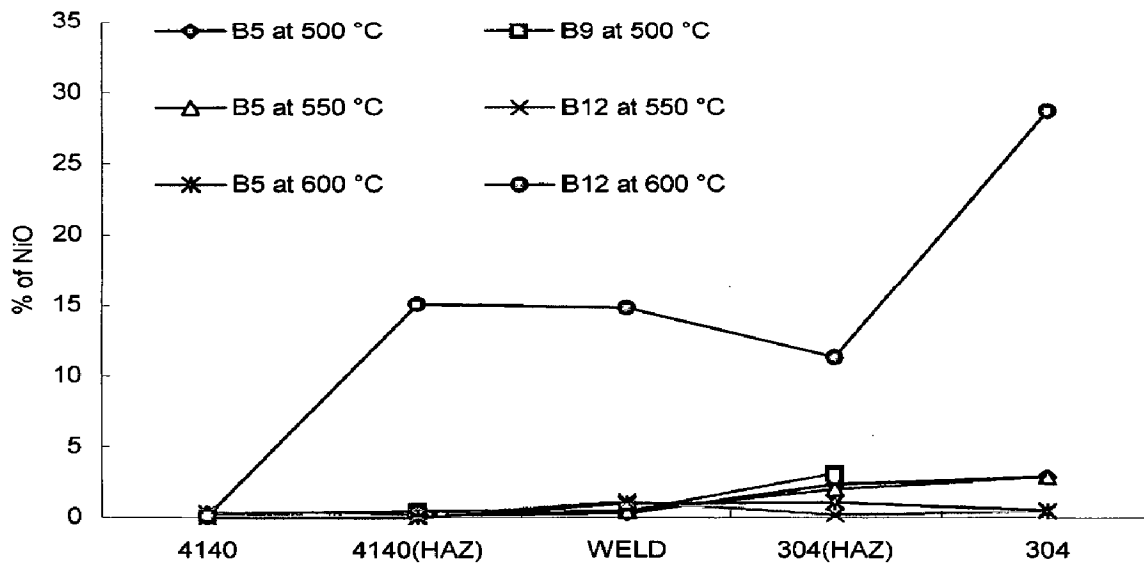


Fig 6.19 (N) EDAX data shows the effect of burn off length and temperature on formation of NiO on the friction weldment under molten salt environment of K_2SO_4 -60% NaCl.

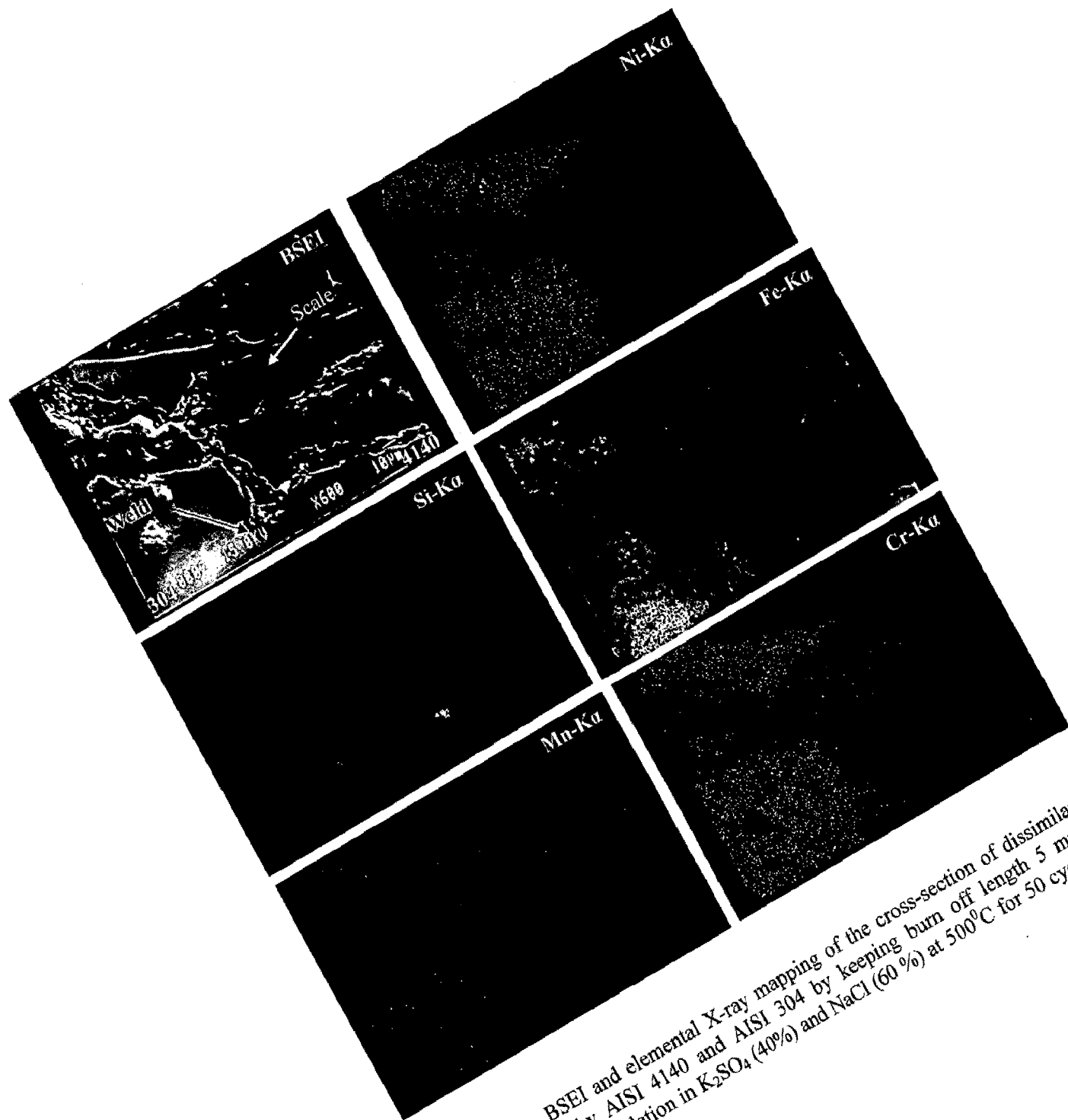


Fig. 6.20(A) BSEI and elemental X-ray mapping of the cross-section of dissimilar weldment made by AISI 4140 and AISI 304 by keeping burn off length 5 mm, subjected to cyclic oxidation in K_2SO_4 (40%) and NaCl (60%) at $500^\circ C$ for 50 cycles, 500 X.

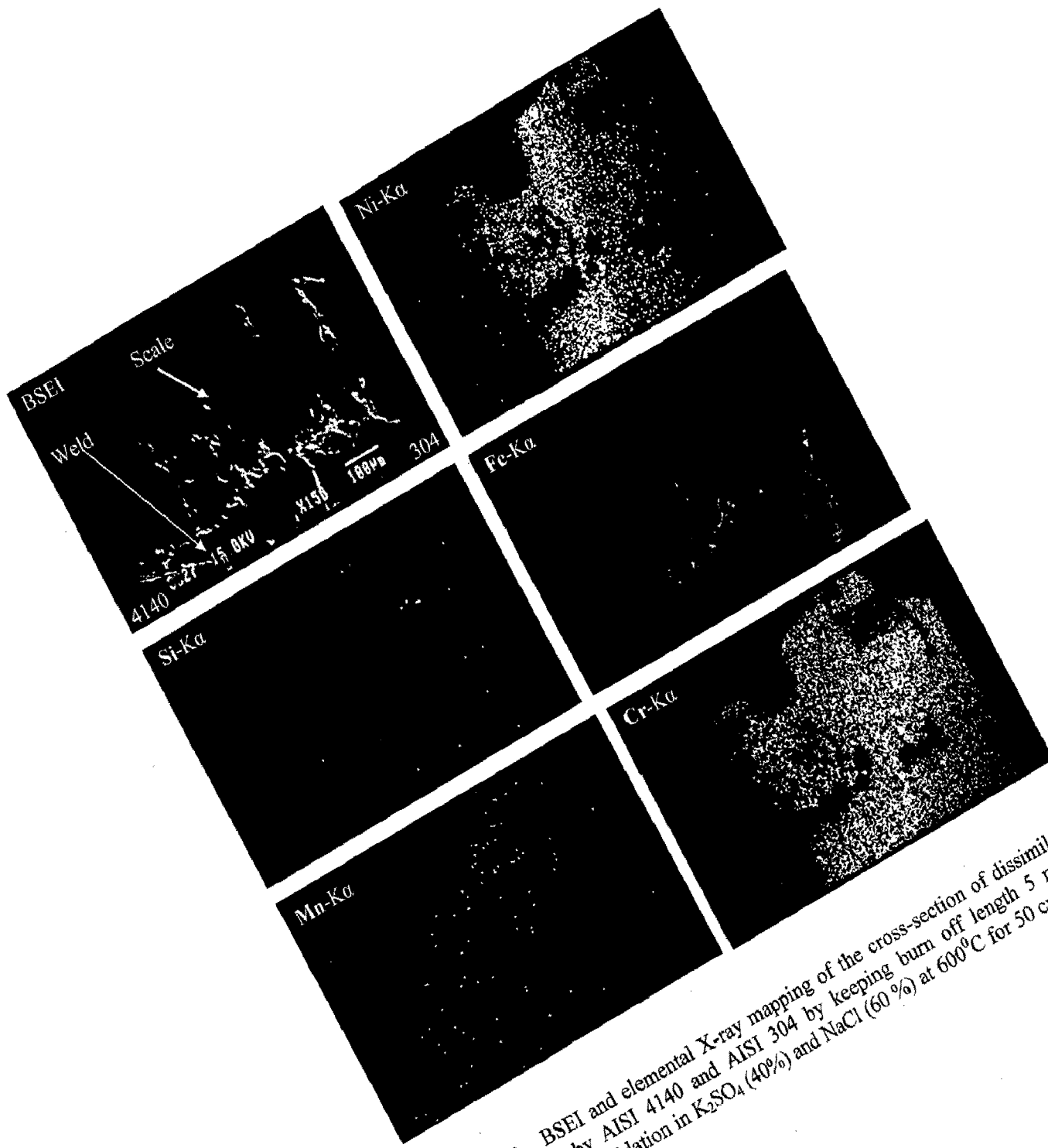


Fig. 6.20(B) BSEI and elemental X-ray mapping of the cross-section of dissimilar weldment made by AISI 4140 and AISI 304 by keeping burn off length 5 mm, subjected to cyclic oxidation in K_2SO_4 (40%) and NaCl (60%) at $600^\circ C$ for 50 cycles, 150 X.

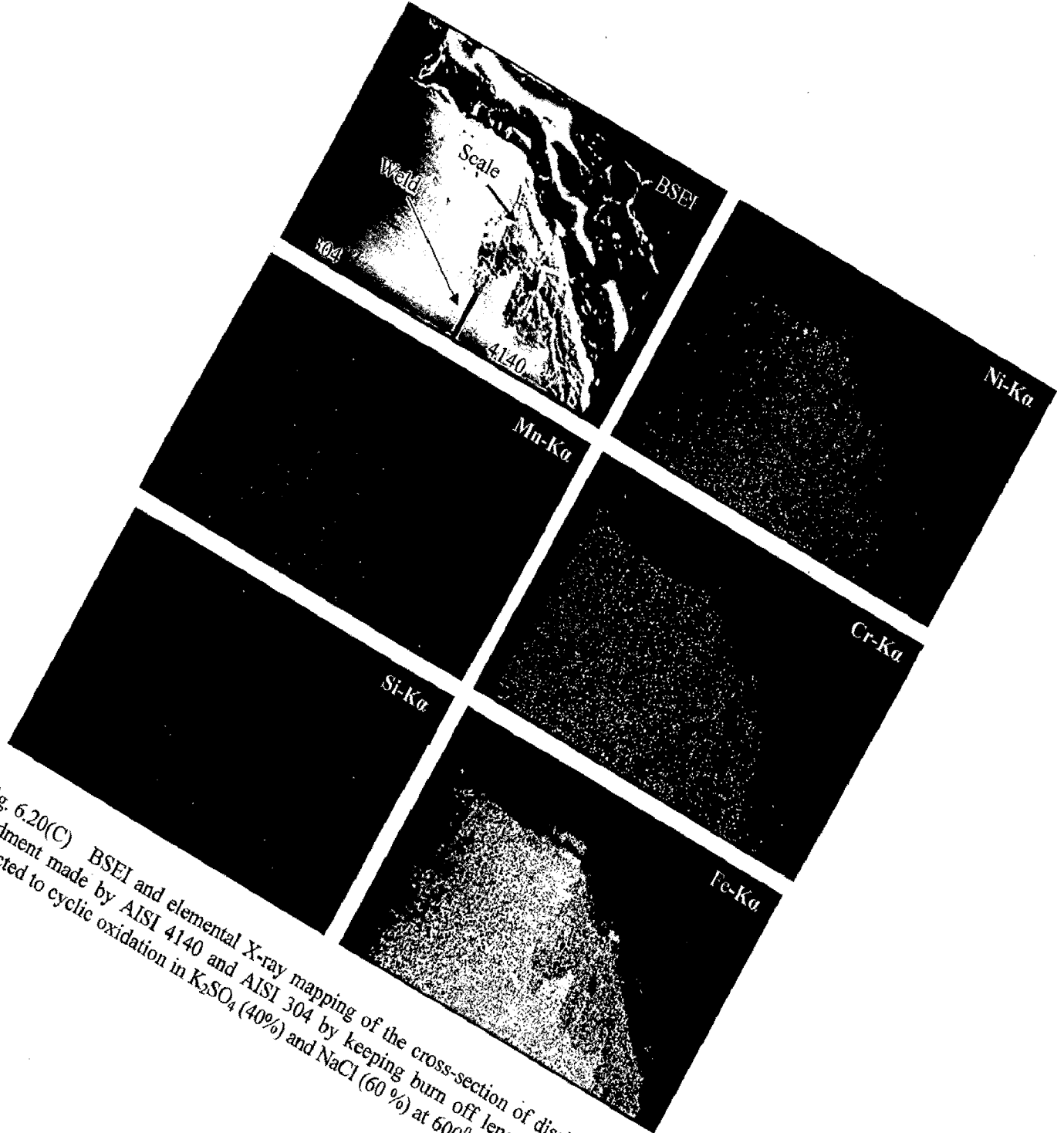


Fig. 6.20(C) BSEI and elemental X-ray mapping of the cross-section of dissimilar weldment made by AISI 4140 and AISI 304 by keeping burn off length 12 mm, subjected to cyclic oxidation in K_2SO_4 (40%) and NaCl (60 %) at $600^\circ C$ for 50 cycles, 150 X.

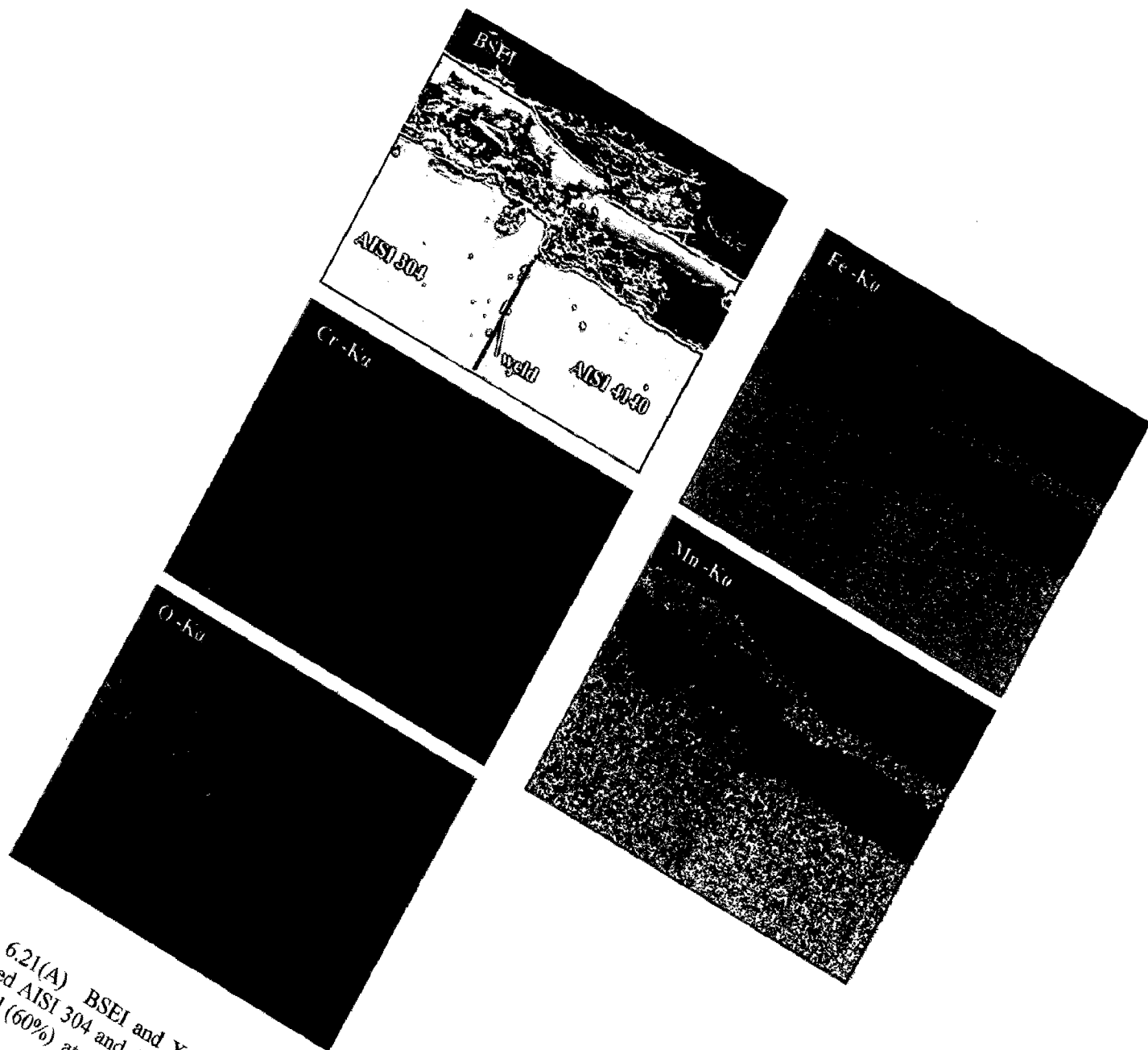


Fig. 6.21(A) BSEI and X-ray mappings of the cross-section of dissimilar friction welded AISI 304 and AISI 4140 by keeping burn-off length 5mm exposed to $K_2SO_4 + NaCl$ (60%) at $500^\circ C$ for 50 cycles.

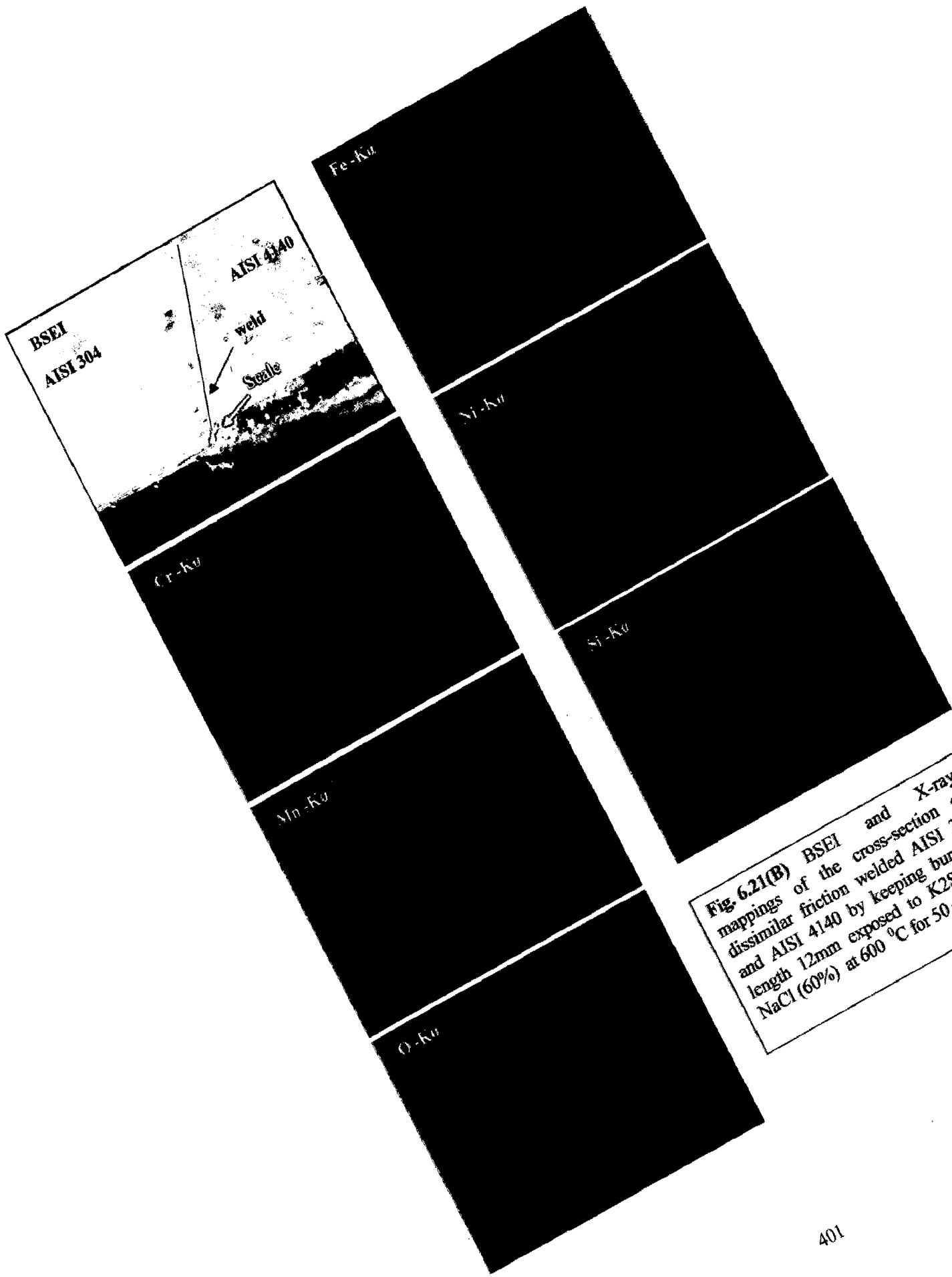


Fig. 6.21(B) BSEI and X-ray mappings of the cross-section of dissimilar friction welded AISI 304 and AISI 4140 by keeping burn-off length 12mm exposed to $K_2SO_4 + NaCl$ (60%) at $600\text{ }^\circ\text{C}$ for 50 cycles.

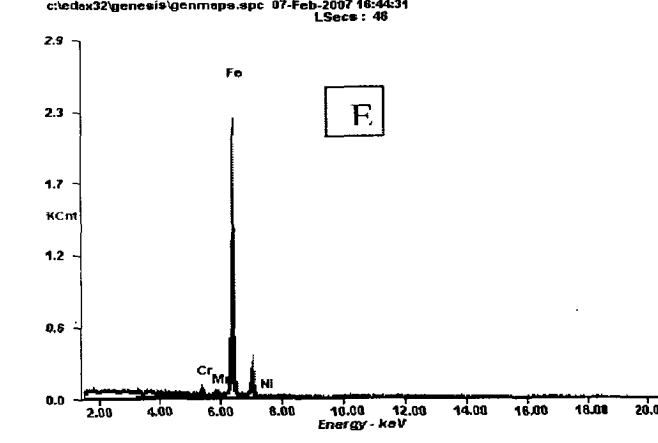
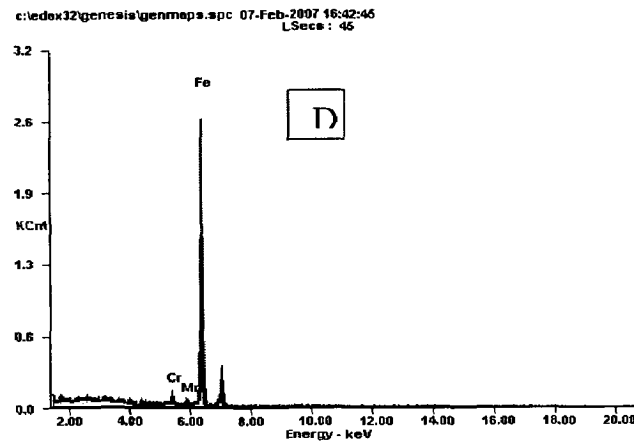
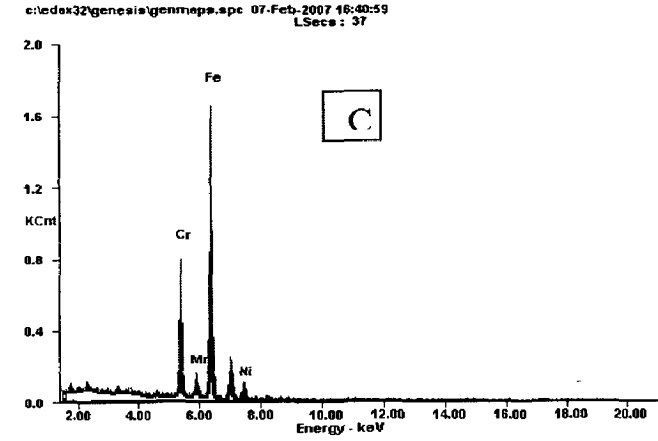
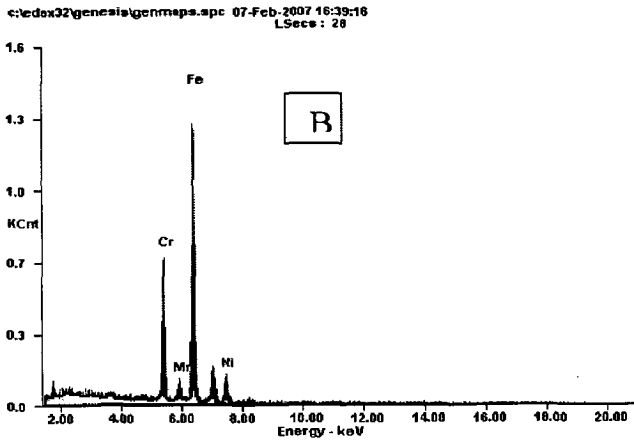
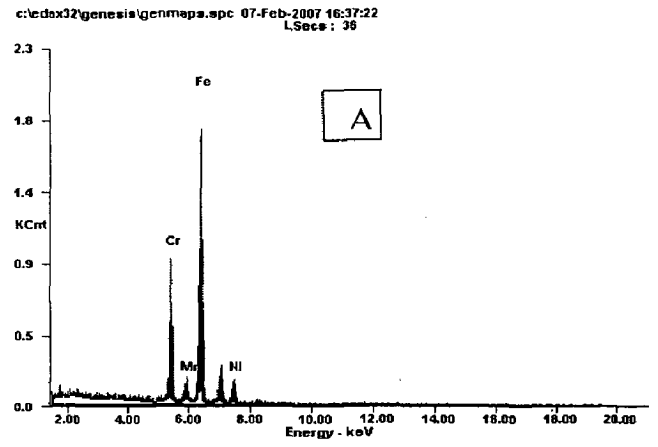
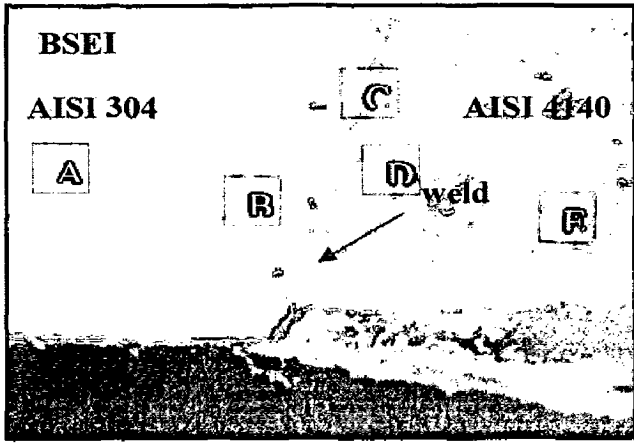


Fig. 6.21(C) BSEI and EDAX of the cross-section of dissimilar friction welded AISI 304 and AISI 4140 by keeping burn-off length 12mm exposed to K₂SO₄ + NaCl (60%) at 600 °C for 50 cycles.

6.1.3 Friction Welded Dissimilar Metals Exposed to Na₂SO₄ (40%) + K₂SO₄ (40%) + NaCl (10%) + KCl (10%)

This subheading deals with the critical examination of corrosion products and the behaviour of friction welded dissimilar weldment made by different burn-off length namely 5, 7, 9, and 12 mm. The hot corrosion studies were performed on the weldments exposed at the temperature from 500, 550 and 600 °C under the Na₂SO₄ (40%) + K₂SO₄ (40%) + NaCl (10%) + KCl (10%) mixture of molten salt for 50 cycles. In view of comparison the thermogravimetric data of each environment along with different exposure of temperature. The parabolic rate constants and scale thicknesses values have been evaluated after 50 cycles of exposure.

6.1.3.1 Visual Examination

In the hot corrosion study of the friction welded 4140 low alloy steel and 304 Stainless steel weldment, after first cycle the white colour salt coating changed in to brown colour with some small black spot appeared on the low alloy steel side. Negligible reaction took place on the stainless steel. After completion of 15 cycles the scale becomes thicker and with dark brown colour on low alloy steel and most of the scale spalled out. Whereas on 304 sides the scale was light brown and adherent and on the weld area the salt attack was not perceptible. With further increase in number of cycles, all the scale spalled out from low alloy steel side, living behind black coloured subscale. The color and texture of scale at weld region was different from that on the base metals. With increase in the temperature from 500 to 550 °C and then 600 °C the thicker scale was observed on the 4140 steel side and extensive spalling took place. At 600 °C of exposure the scale was more fragile and extensive spalling was observed. Fig.6.22 (i-iv), shows the macro structure of hot corroded samples after 50 cycles.

6.1.3.2 Thermogravimetric Data

The weight gain (per unit area) during corrosion test for the dissimilar friction weldment (AISI 304 and AISI 4140) in the presence of a salt layer of (40 wt% K₂SO₄, 40 wt% Na₂SO₄, 10 wt% KCl, and 10 wt% NaCl mixture at different temperature (500, 550 and 600 °C, have been plotted and is shown in Fig.6.23 indicating parabolic behavior. Higher the burn-off length (i.e. B12) shows a highest weight gain for all the temperatures of

exposure. The parabolic rate constants K_p were obtained from the slope of the linear regression fitted line (cumulative weight gain / area)² Vs. number of cycles and is shown in table 6.3. The parabolic rate constant of dissimilar weldment made by burn-off length 'B' 12mm is larger than that of made by burn-off length 5mm for all the temperature of exposure. When increasing the temperature of exposure from 500 to 600 °C, for the weldment of 5 mm burn off length the parabolic rate constant approximately more than 10 times than that of at 500 °C.

Table 6.3 Values of parabolic rate constant K_p

Description		K_p ($10^{-6}(\text{gm}^2\text{Cm}^{-4}\text{S}^{-1})$)
Temperature (°C)	Burn off length (mm)	
500	5	1.670
550	5	3.590
	7	5.260
	9	7.980
	12	11.850
600	5	17.170
	12	23.440

6.1.3.3 X-ray Diffraction Analysis

The XRD patterns for the hot corroded surfaces of welded samples by keeping four different burn-off length (B5, B7, B9 and B12 mm) exposed to the Na_2SO_4 (40%) + K_2SO_4 (40%) + NaCl (10%) + KCl (10%) environment at exposure temperature of 500, 550 and 600 °C after 50 cycles are shown in Fig 6.24(A, B). X-Ray diffraction studies were carried out to analyse the phases formed on hot corrosion product on the dissimilar friction weldment. The surface of the scale has plenty of Fe_2O_3 with minor constituent of Cr_2O_3 , NiFe_2O_4 , NiCr_2O_4 and FeNi were identified. The less intermetallic compound CrNiFe were identified in scales with less intensity for 500 and 550 C exposures.

6.1.3.4 Scale Thickness Measurement

The samples were cut across the cross-section after exposure to molten salt at 500, 550 and 600 °C for 50 cycles and mounted. The scale thickness values were measured from SEM back scattered images shown in Fig. 6.25 (i-vi). The exact oxide scale thickness could not be

measured for all the weldments due to intense spalling and sputtering. The SEM micrograph shows the fragile and cracked scale for all the weldment.

6.1.3.5 SEM/EDAX Analysis

SEM / EDAX analysis showing scale surface morphology and the phases formed after 50 hours cyclic hot corrosion studies on the scale of dissimilar friction weldment as shown in Fig 6.26 (A-F). From the analysis for all the burn-off length and temperature of exposure, Fe_2O_3 is found to be the predominant phase in the scale on the weldment. At 500 C the scale of base metals (4140 and 304) contain plenty of Fe_2O_3 (84-91%) which is very less (52%) in the HAZ of 304 noted in Fig 6.26(A) where as the percentage of Cr_2O_3 and NiO is higher. The maximum amount of Fe_2O_3 (96%) noted on the scale of HAZ of 4140 side where as the % of Cr_2O_3 is negligible. At 600 C hot corrosion the scale on the weldment contains plenty of Fe_2O_3 (88-92 %) and the Cr_2O_3 is not as much as at 500/550 C (Fig 6.26. E, F). EDAX analysis of the scale on the weldment for the three temperatures of exposure shows some unreacted salt as Na_2O , SO_3 and K_2O . From the EDAX data, the effect of temperature and burn off length on the formation of oxides in the scale on the weldment shown in Fig 6.26 (G-N).

6.1.3.6 EPMA Analysis

BSEI and X-ray mapping for cross-section of corroded dissimilar weldment exposed to Na_2SO_4 (40%) + K_2SO_4 (40%) + NaCl (10%) + KCl (10%) at 500, 550 and 600 $^{\circ}\text{C}$ for 50 cycles are shown in Fig. 6.27 (A- F). The EPMA of the cross-section of corroded dissimilar weldment made by friction welding by keeping different burn-off length (5, 7, 9 and 12mm) indicates that scale is mainly consisting of Fe, Cr and Ni. Figure 6.28 (A) shows that oxygen penetration in the scale of friction weldment of burn-off length 7 mm exposed at 550 $^{\circ}\text{C}$ under molten salt environment. The X-Ray mapping elemental distribution on the weldment after exposed at 600 shown in Fig 6.28 (B and C). Higher concentration of Cr_2O_3 is observed on weld zone as well as the both side of HAZ.

6.1.4 Friction Welded Dissimilar Metals Exposed to Na₂SO₄ (50%) + NaCl (50%)

The hot corrosion studies were performed on the weldments made with by different burn off length 5, 7, 9, and 12 mm exposed at the temperature from 500 and 550 °C under the Na₂SO₄ (50%) + NaCl (50%) mixture of molten salt for 50 cycles. The parabolic rate constants have been calculated from the thermogravimetric data for each temperature and scale thicknesses values have been evaluated after 50 cycles of exposure.

6.1.4.1 Visual Examination

In the hot corrosion study of the friction welded 4140 low alloy steel and 304 Stainless steel weldment, in first cycle the white colour salt coating changed in to brown colour with some small black spots observed on the low alloy steel side only where negligible reaction has taken place on the stainless steel side. Thicker scale with dark brown colour could be observed on low alloy steel after 15 cycles. Whereas on 304 side the scale was light brown and adherent and on the weld area the salt coating remain unreacted. With further increase in number of cycles, all the scale spalled out from low alloy steel side, living behind black colour subscales. The color and texture of scale at weld region was different from that on the base metals. With increase in the temperature from 500 to 550 °C, the thicker scale was observed on the 4140 steel side and extensive spalling took place. At 550 °C temperature of exposure the scale becomes fragile and extensive spalling was observed. Fig.6.29 (i, ii) shows the macro structure of hot corroded samples after 50 cycles.

6.1.4.2 Thermogravimetric Data

The corrosion kinetics of specimens under the molten salt deposits (Na₂SO₄ (50%) + NaCl (50%)) is shown Fig 6.30 as parabolic plots of weight gain per unit area versus function of time (number of cycles). The parabolic rate constant K_p were obtained from the slope of the linear regression fitted line (cumulative weight gain / area)² vs. number of cycles and is shown in table 6.4. When increasing the temperature of exposure from 500 to 550 °C, the parabolic rate constant increase to more than 5 times than that at 500 °C.

Table 6.4 Values of parabolic rate constant K_p

Environment	$\text{Na}_2\text{SO}_4 + \text{NaCl (50\%)}$						
Temperature	500 °C			550 °C			
Burn-off length	B5	B7	B9	B5	B7	B9	B12
$K_p \times 10^{-6}$ ($\text{g}^2 \text{cm}^{-4} \text{S}^{-1}$)	1.020	1.740	1.980	2.440	3.190	3.960	5.390

6.1.4.3 X-ray Diffraction Analysis

X-Ray Diffraction studies were carried out to analyse the phases formed in the scale on dissimilar weldment under given molten salt environment. Hot corrosion studies under molten salt environment ($\text{Na}_2\text{SO}_4 + \text{NaCl(50\%)}$) at 500 and 550 °C, Fe_2O_3 and Cr_2O_3 are found to be the predominant phases. Whereas $(\text{Cr, Fe})_2\text{O}_3$, FeNi and FeS observed with low intensity peaks. At 500 °C for 5mm burn-off length NiS, CrNiFe and NiFe_2O have been noted and which is absent for 7 and 9mm burn-off length shown in Fig 6.31(A). Whereas at 550 °C CrNiFe have been observed in the scale on the dissimilar weldment made by 5 and 12 mm burn-off length which is absent for 7 and 9 mm burn off length Fig 6.31(B).

6.1.4.4 Scale Thickness Measurement

The samples were cut across the cross-section after exposure to molten salt at 500 and 550 °C for 50 cycles and mounted. The scale thickness values were measured from SEM back scattered images shown in Fig. 6.32.

6.1.4.5 SEM/EDAX Analysis

SEM photographs show surface morphology the scale formed on dissimilar weldment after cyclic oxidation in given environment at 500 and 550 °C respectively. EDAX analysis of the scales indicates Fe_2O_3 to be the predominant phase as can be seen in Fig 6.33 (A-G). The Fe_2O_3 content is higher on the base metal 4140 side and tend to decrease as one moves towards HAZ(4140) → weld → HAZ(304) → 304 base metal. Whereas Cr_2O_3 content of scale is higher on the heat affected zone of 304 alloy side as compared to 304 base metals as can be seen Fig 6.33 (A-C).

At 550 C under given molten salt environment, the SEM/EDAX analysis shows that Fe_2O_3 and Cr_2O_3 as the predominant phase on the weld interface as well as on the HAZ of

304 side. Where as some minor amount of MoO_3 , MnO and NiO were observed on the remaining part of the Fig 6.33 (D-E). . From the EDAX data, the effect of temperature and burn off length on the formation of oxides in the scale on the weldment shown in Fig 6.33 (J-N).

6.1.4.6 EPMA Analysis

BSEI and X-ray mapping for cross-section of corroded dissimilar weldment exposed to Na_2SO_4 (50%) and NaCl (50 %) at 500 and 550 °C for 50 cycles are shown in Fig. 6.34(A-E). The EPMA of the cross-section of corroded dissimilar weldment made by friction welding by keeping different burn-off length (5, 7, 9 and 12mm) indicates that scale is mainly consisting of Fe, Cr and Ni. Figure 6.35 shows that oxygen penetration in the scale of the friction weldment exposed at 550 °C in the given environment.

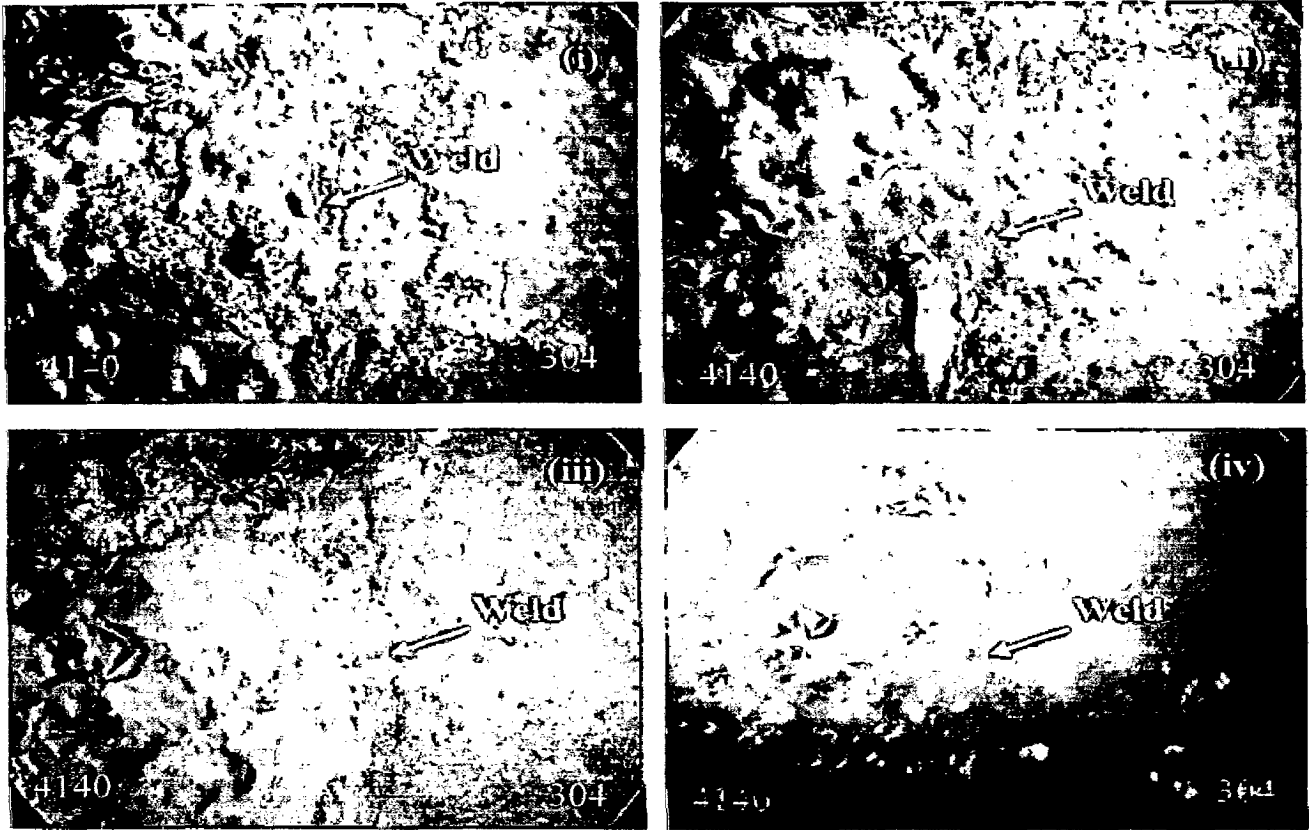


Fig. 6.22 Macrographs dissimilar friction welded AISI 4140 and AISI 304 subjected to cyclic hot corrosion exposed under $K_2SO_4 + NaCl$ (60%) after 50 cycles. (i-iii) Weldment made by keeping 5 mm burn off length and exposed temperature of 500, 550, 600 °C respectively. (iv) Weldment made by keeping 12 mm burn off length and exposed temperature at 600 °C.

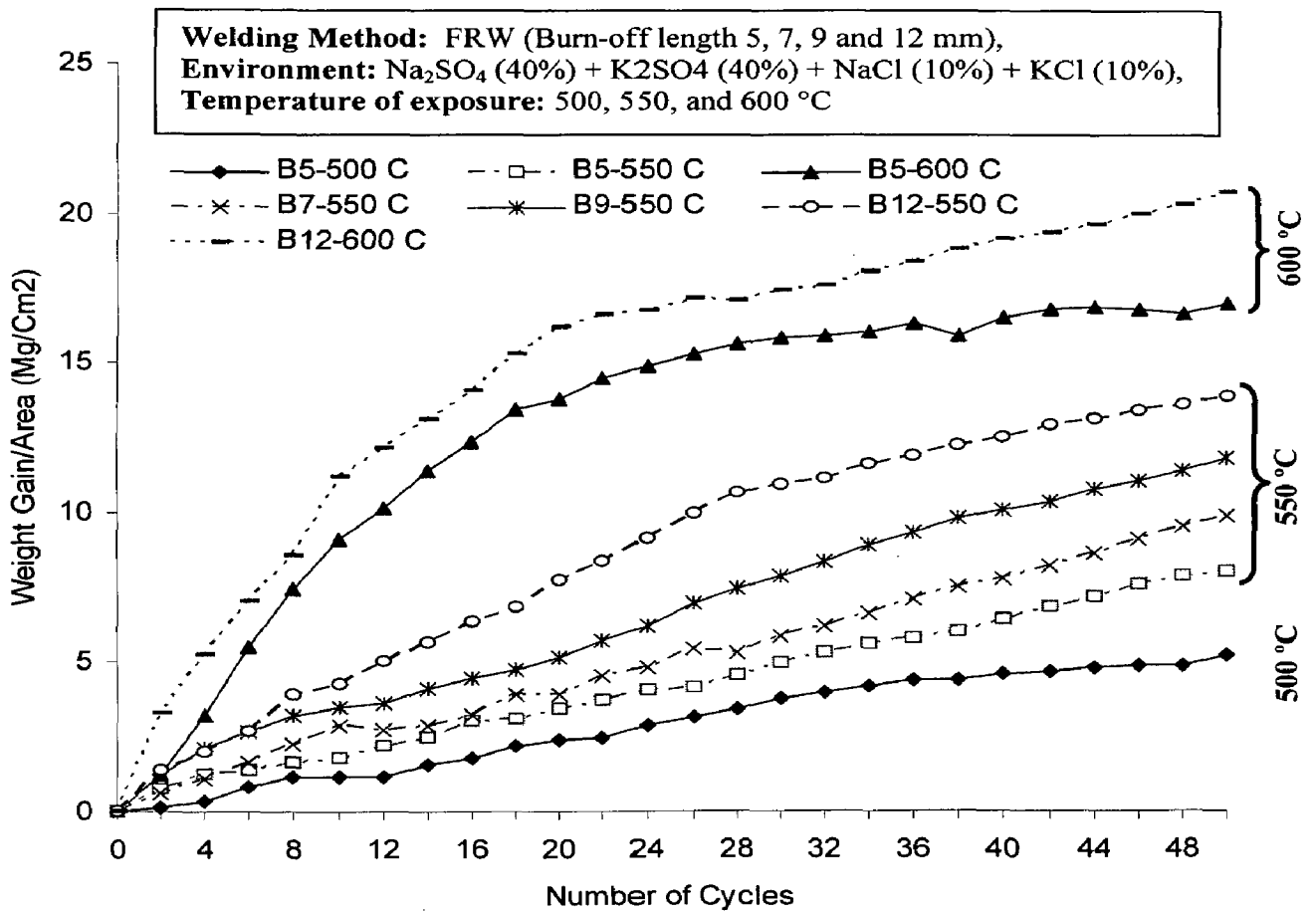


Fig 6.23. Plots of cumulative weight gain (mg/cm^2) as a function of time (number of cycles) for 500, 550 and 600 °C.

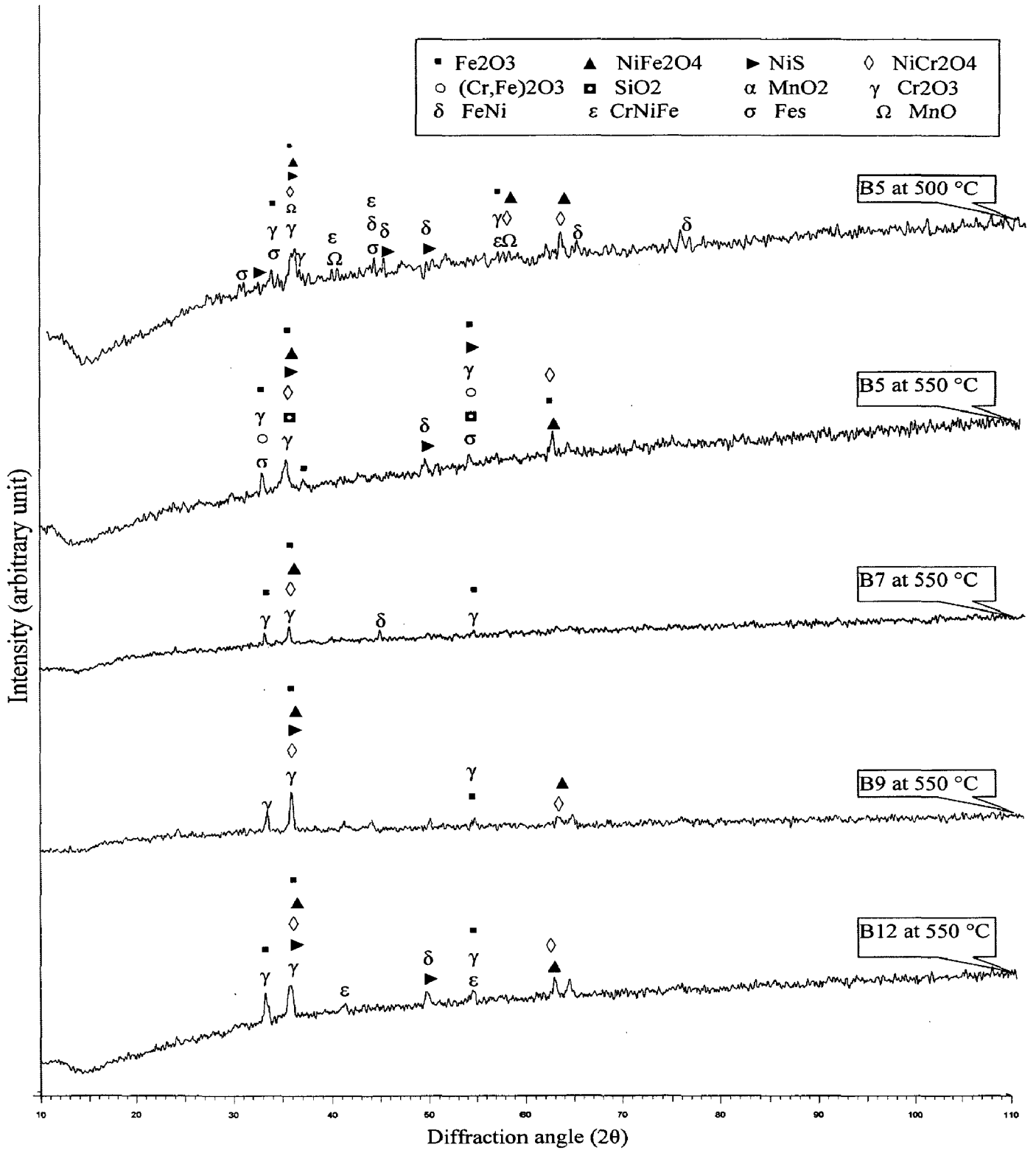


Fig 6.24(A).The XRD patterns for the hot corroded surfaces of welded samples by keeping four different burn-off length (B5, B7, B9 and B12 mm) exposed to the Na₂SO₄ (40%) + K₂SO₄ (40%) + NaCl (10%) + KCl (10%) environment at exposure temperature of 500 and 550 °C after 50 cycles

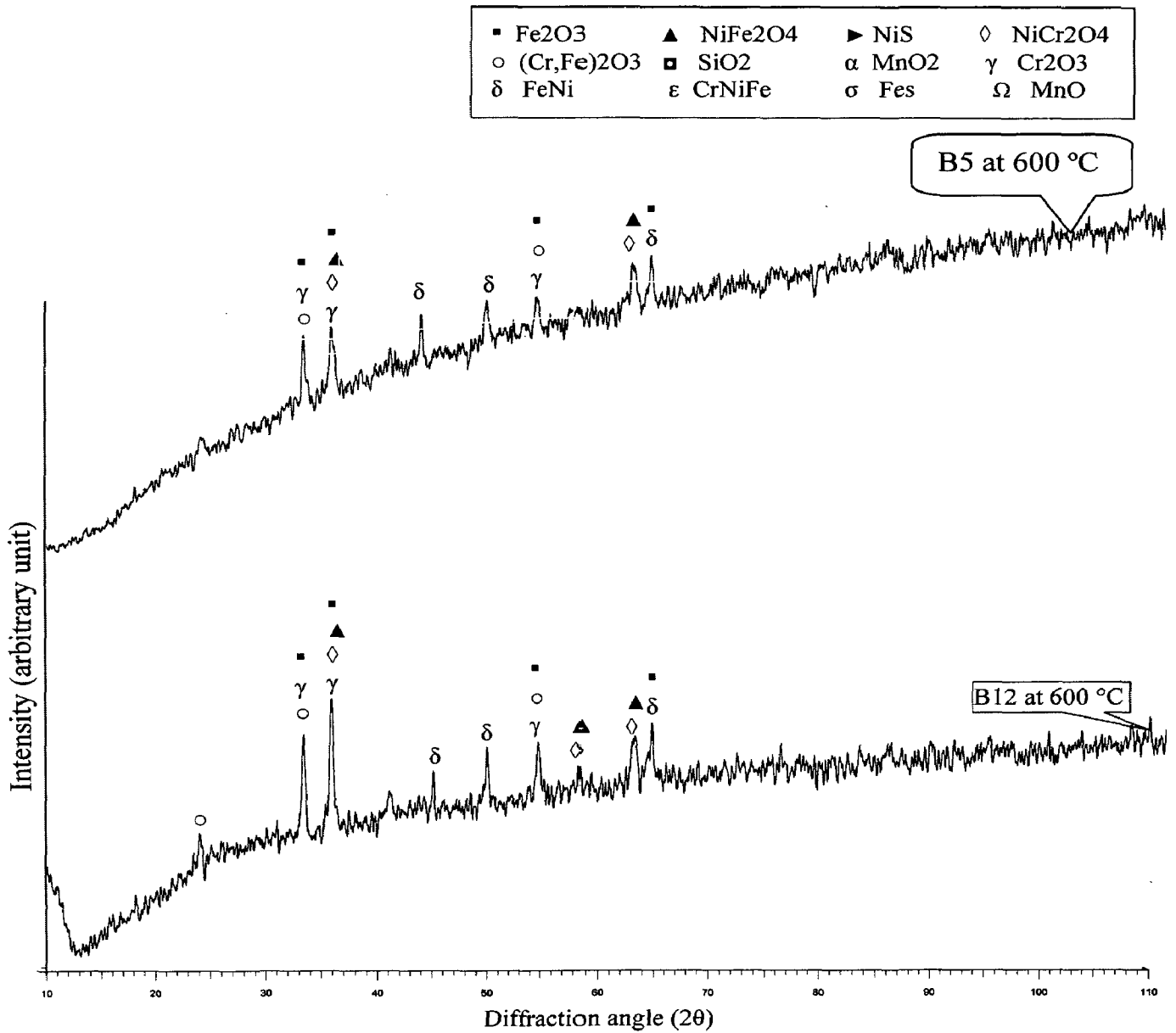


Fig 6.24 (B) The XRD patterns for the hot corroded surfaces of welded samples by keeping four different burn-off length (B5 and B12 mm) exposed to the Na₂SO₄ (40%) + K₂SO₄ (40%) + NaCl (10%) + KCl (10%) environment at exposure temperature of 600 °C after 50 cycles

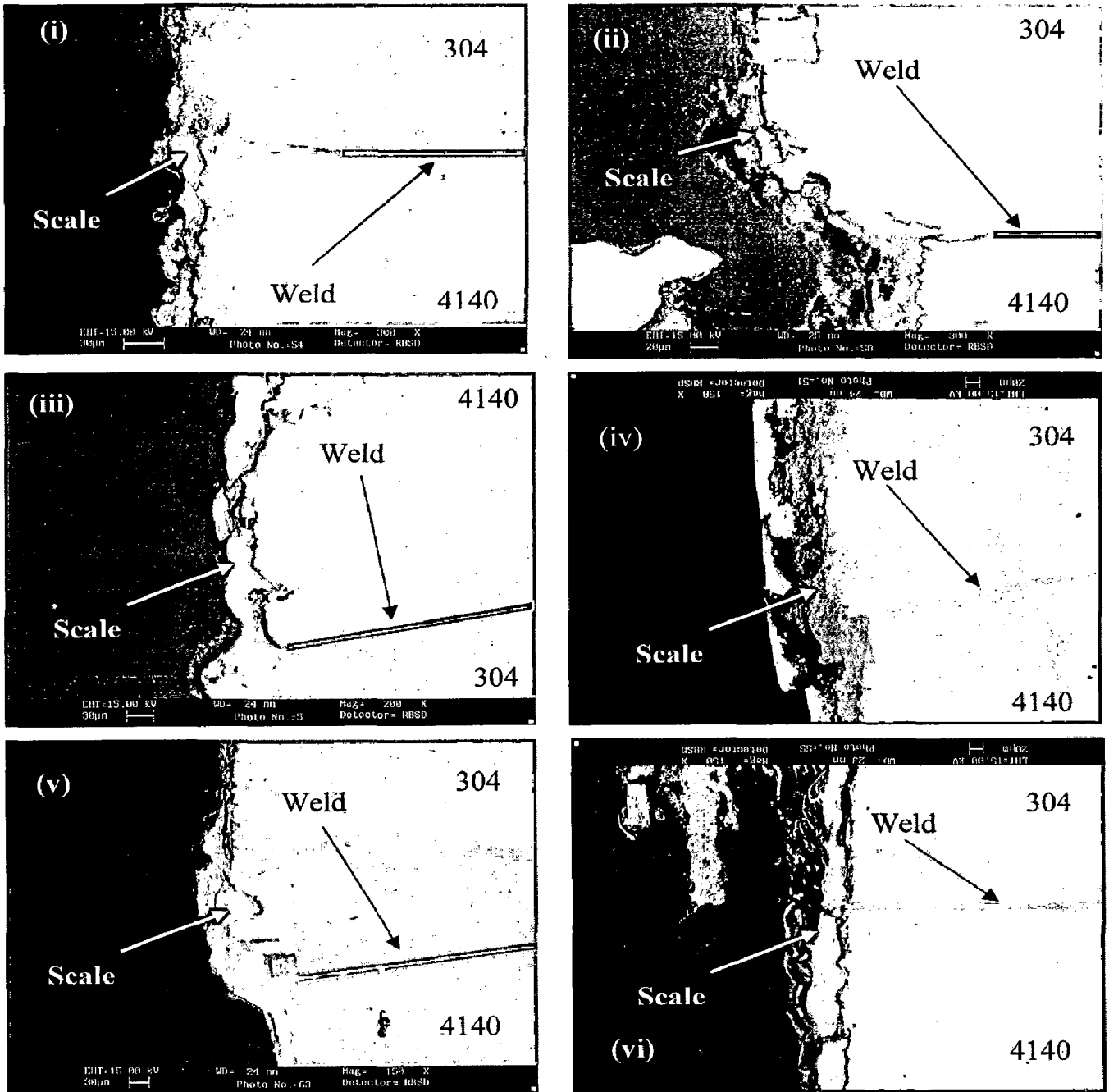


Fig 6.25. BSEI for hot corroded friction weldment under Na_2SO_4 (40%) + K_2SO_4 (40%) + NaCl (10%) + KCl (10%) exposed temperature of 500, 550, 600. (i): Exposed temperature 500 °C for weldment made by keeping 5 mm Burn off length. (ii) and (iv): Exposed temperature 550 °C for weldment made by keeping 5, 7 and 12 mm Burn off length respectively. (v) and (vi): Exposed temperature of 600 °C for weldment made by keeping 5, and 12 mm Burn off length respectively.

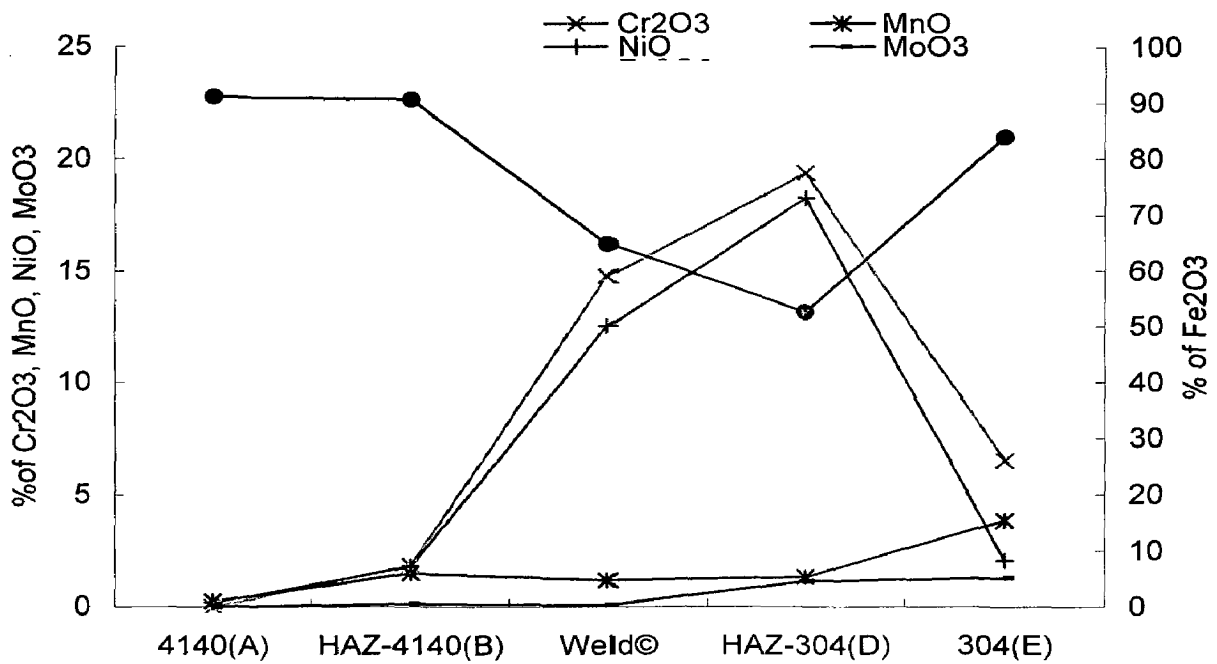
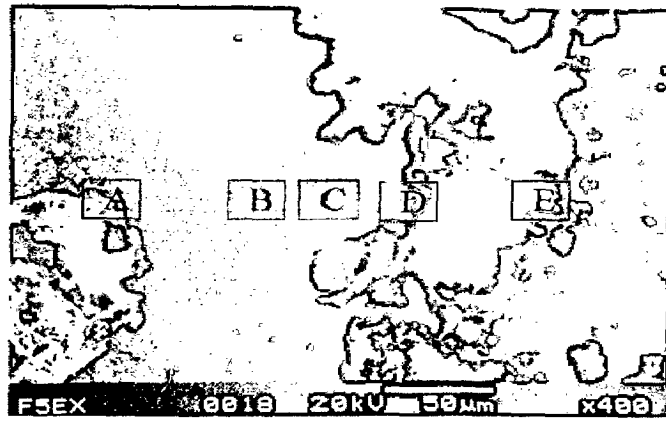


Fig 6.26(A) SEM/EDAX graph shows the friction weldment made by keeping 5 mm burn off length, exposed at 500 °C under Na₂SO₄ (40%) + K₂SO₄ (40%) + NaCl (10%) + KCl (10%) after 50 cycles

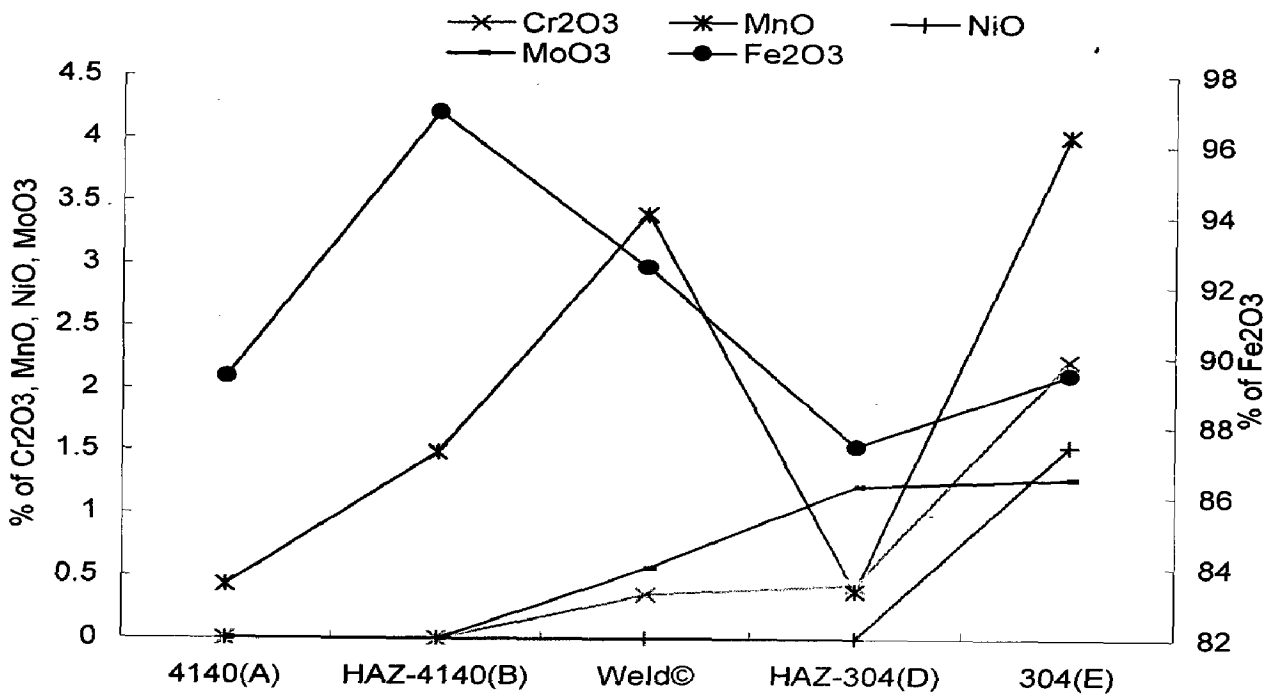
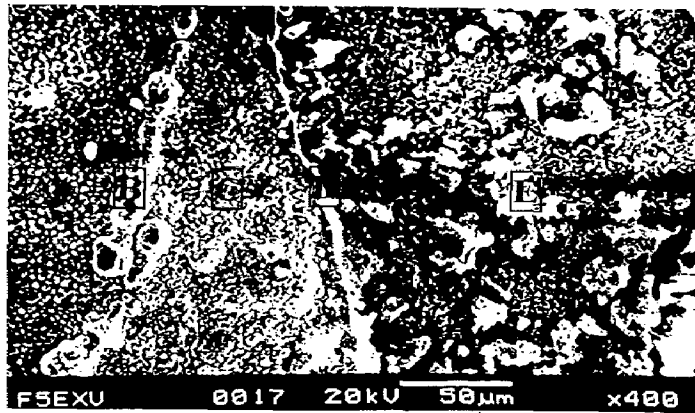


Fig 6.26(B) SEM/EDAX graph shows the friction weldment made by keeping 5 mm burn off length, exposed at 550 °C under Na₂SO₄ (40%) + K₂SO₄ (40%) + NaCl (10%) + KCl (10%) after 50 cycles

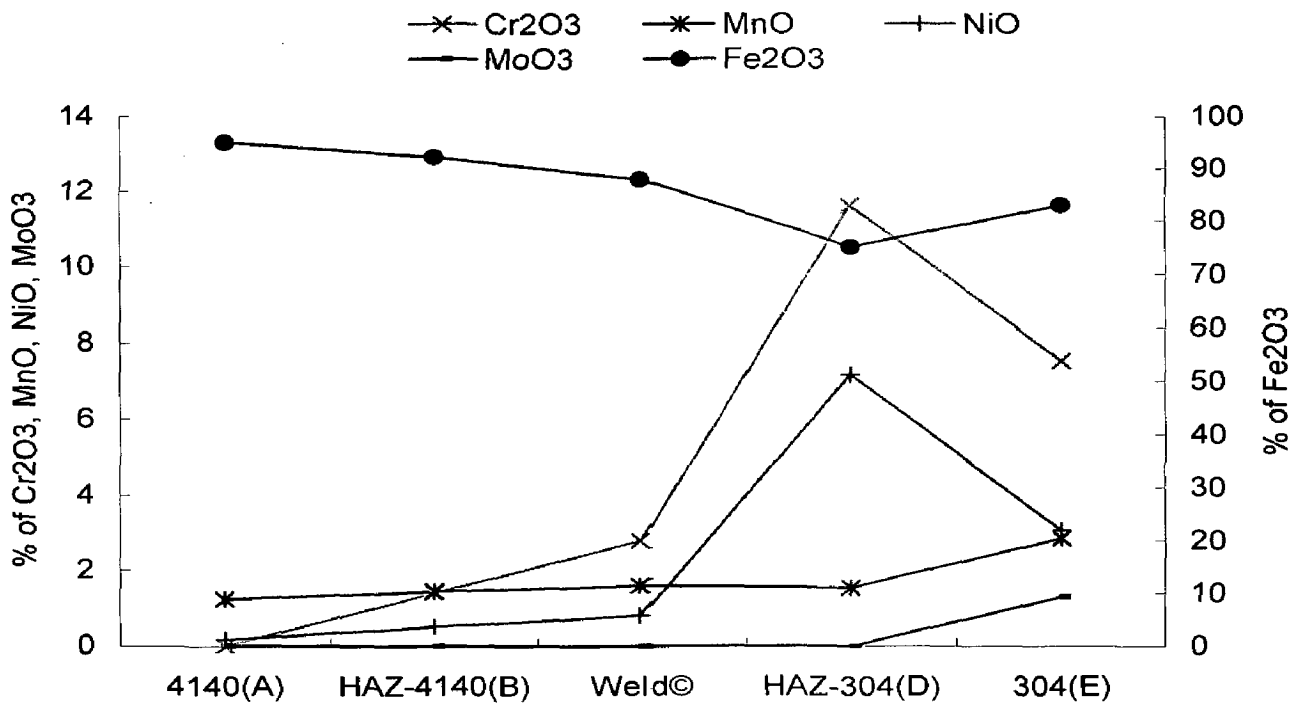
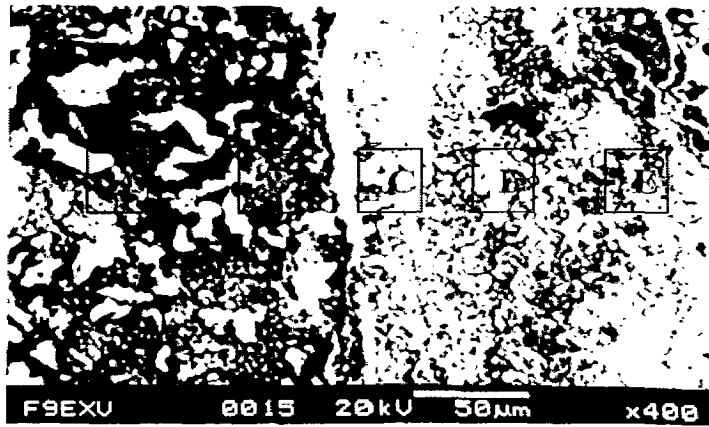


Fig 6.26(C) SEM/EDAX graph shows the friction weldment made by keeping 9 mm burn off length, exposed at 550 °C under Na₂SO₄ (40%) + K₂SO₄ (40%) + NaCl (10%) + KCl (10%) after 50 cycles

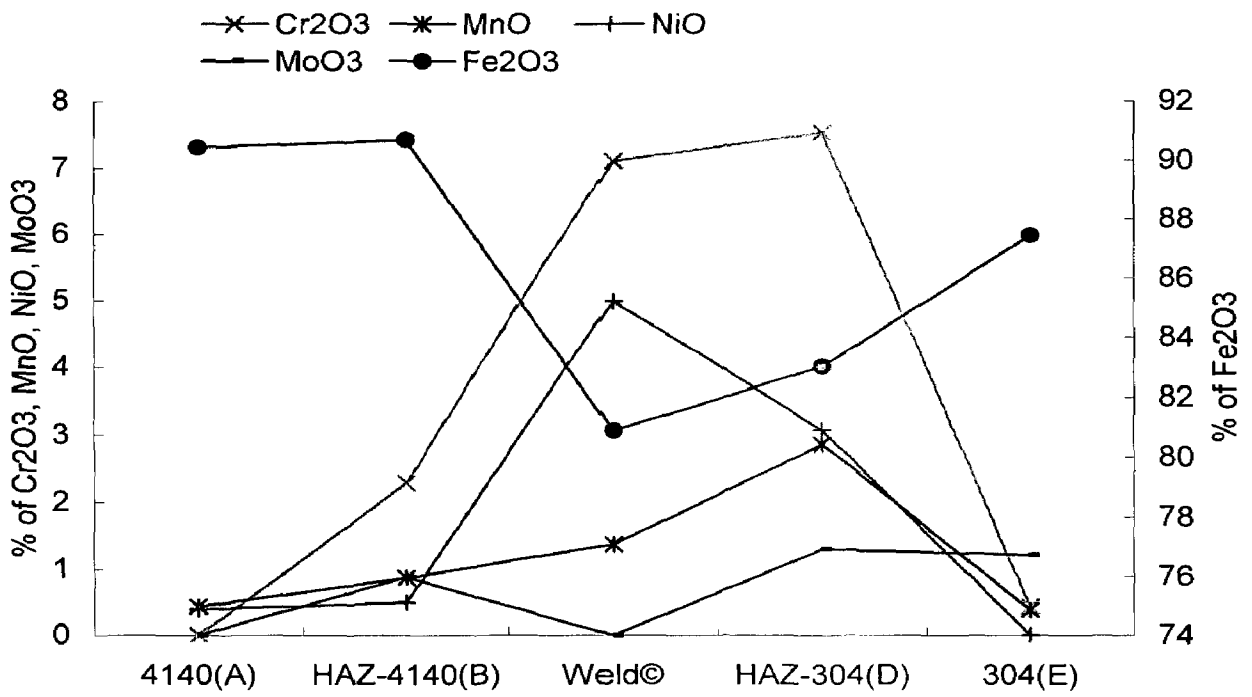
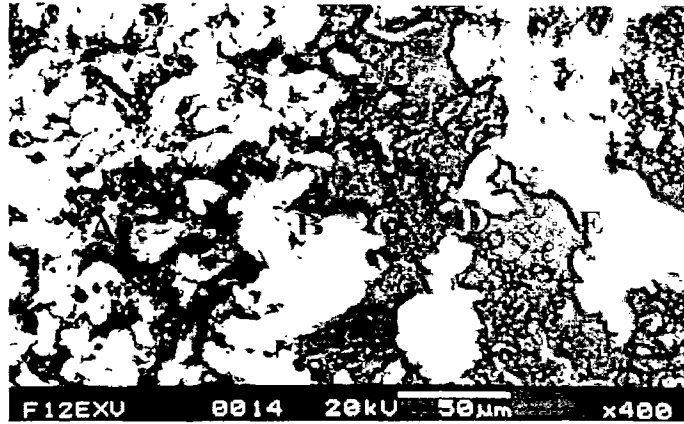


Fig 6.26(D) SEM/EDAX graph shows the friction weldment made by keeping 12 mm burn off length, exposed at 550 °C under Na₂SO₄ (40%) + K₂SO₄ (40%) + NaCl (10%) + KCl (10%) after 50 cycles

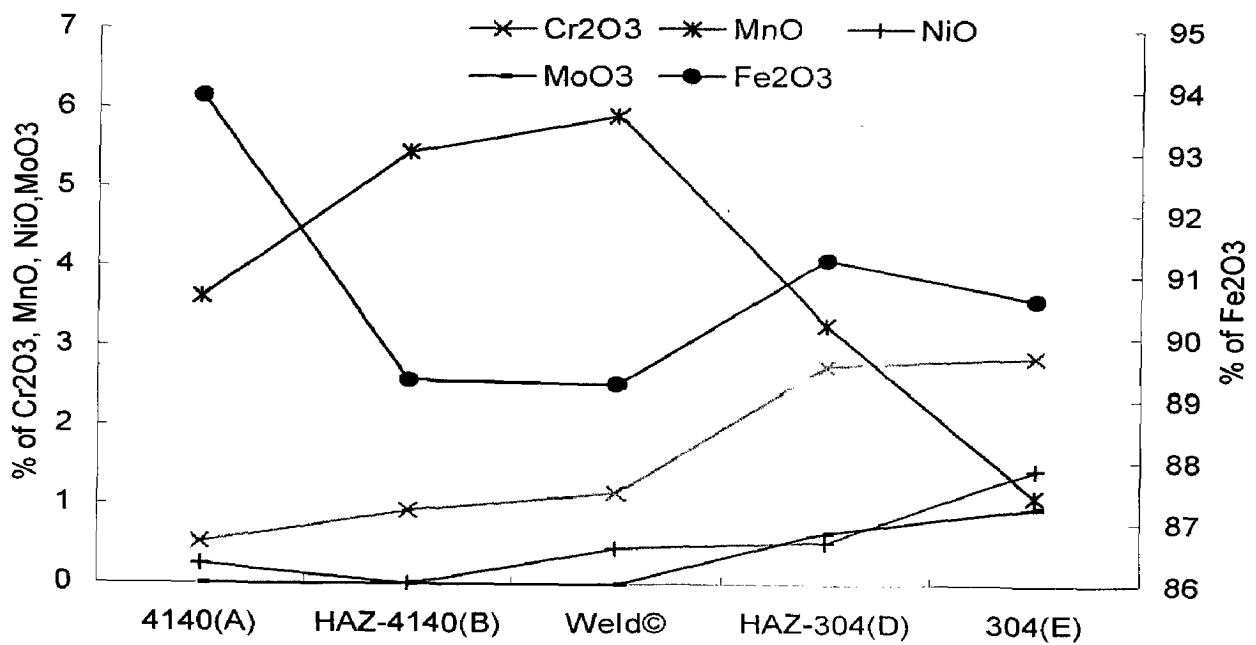
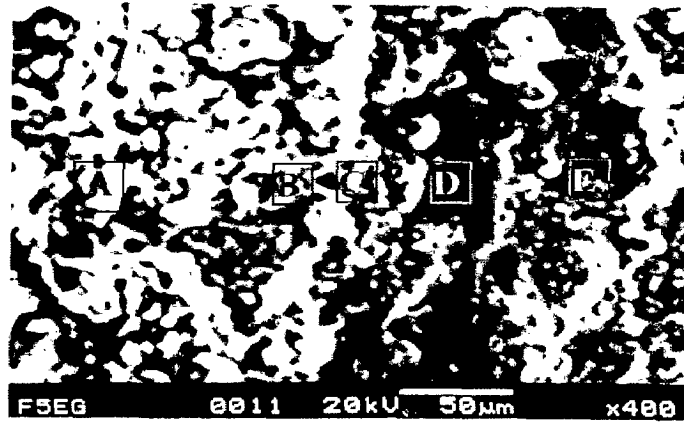


Fig 6.26(E) SEM/EDAX graph shows the friction weldment made by keeping 5 mm burn off length, exposed at 600 °C under Na₂SO₄ (40%) + K₂SO₄ (40%) + NaCl (10%) + KCl (10%) after 50 cycles

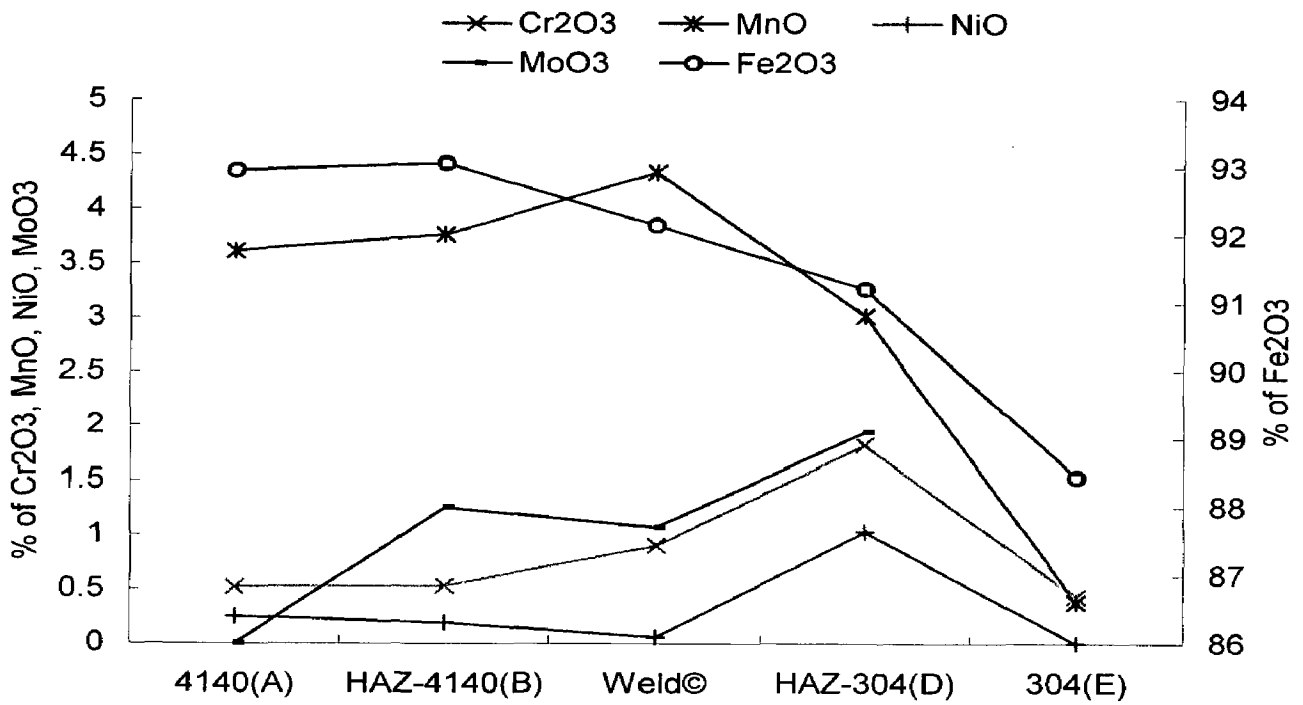
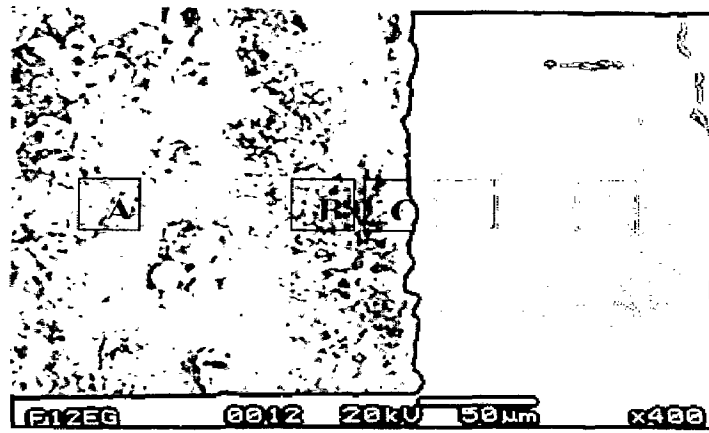


Fig 6.26(F) SEM/EDAX graph shows the friction weldment made by keeping 12 mm burn off length, exposed at 600 °C under Na₂SO₄ (40%) + K₂SO₄ (40%) + NaCl (10%) + KCl (10%) after 50 cycles

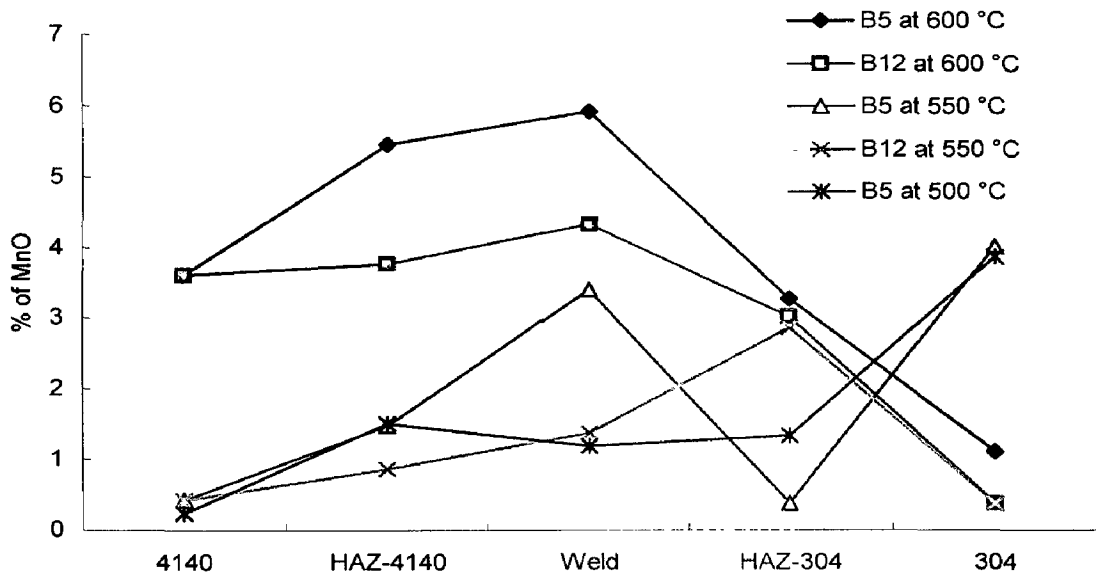


Fig 6.26 (I) EDAX data shows the effect of burn off length and temperature on formation of MnO on the friction weldment under molten salt environment of 40 wt% K_2SO_4 , 40 wt% Na_2SO_4 , 10 wt% KCl, and 10 wt% NaCl.

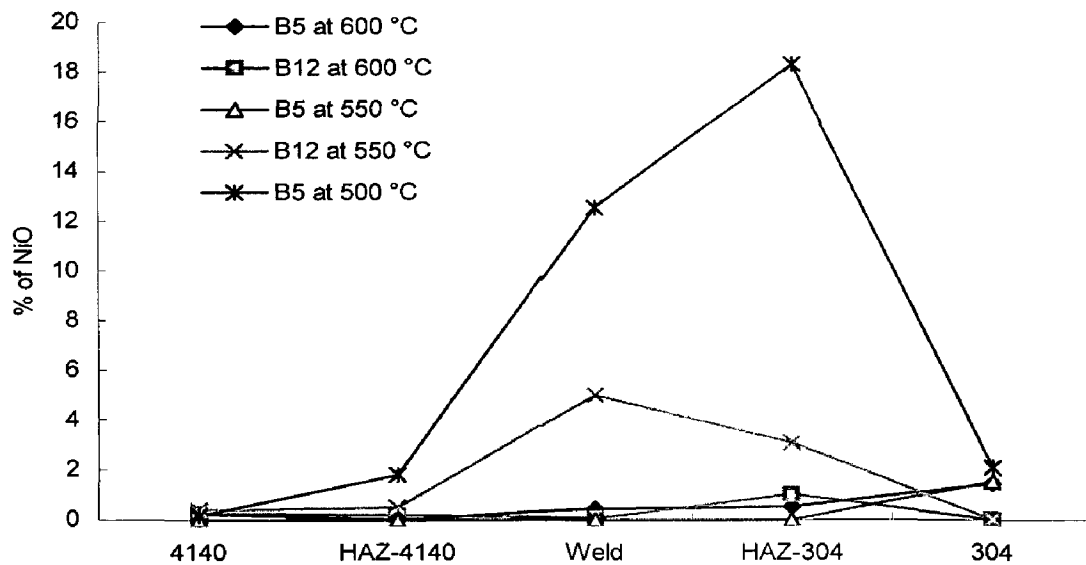


Fig 6.26 (J) EDAX data shows the effect of burn off length and temperature on formation of NiO on the friction weldment under molten salt environment of 40 wt% K_2SO_4 , 40 wt% Na_2SO_4 , 10 wt% KCl, and 10 wt% NaCl.

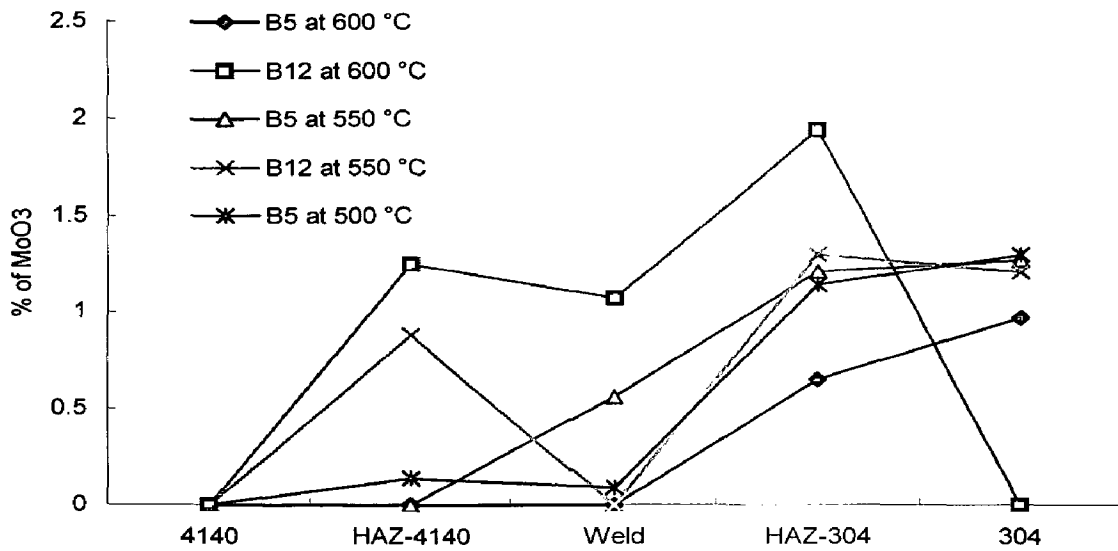


Fig 6.26 (K) EDAX data shows the effect of burn off length and temperature on formation of MoO₃ on the friction weldment under molten salt environment of 40 wt% K₂SO₄, 40 wt% Na₂SO₄, 10 wt% KCl, and 10 wt% NaCl.

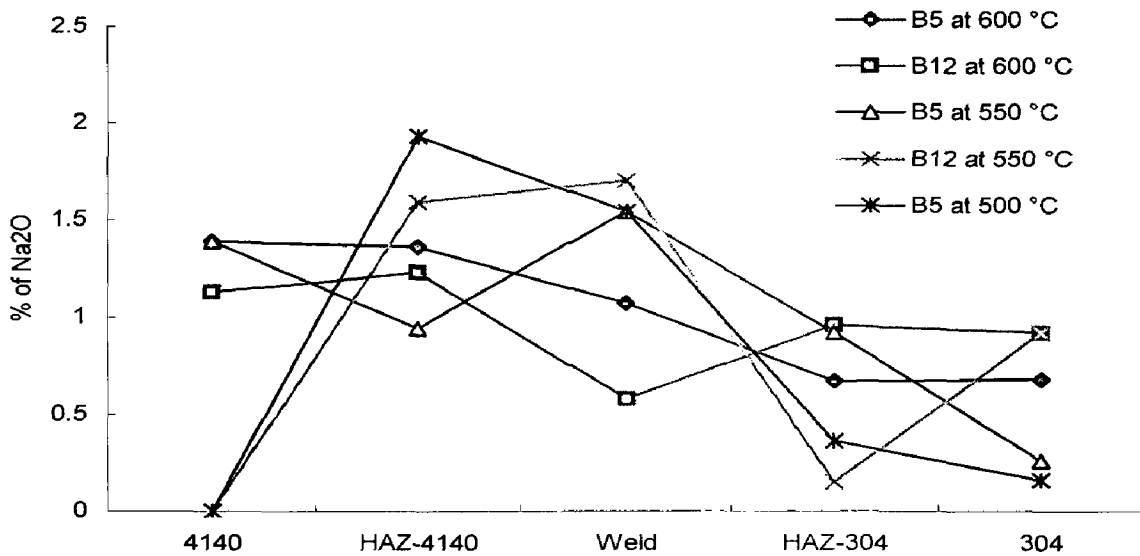


Fig 6.26 (L) EDAX data shows the effect of burn off length and temperature on formation of Na₂O on the friction weldment under molten salt environment of 40 wt% K₂SO₄, 40 wt% Na₂SO₄, 10 wt% KCl, and 10 wt% NaCl.

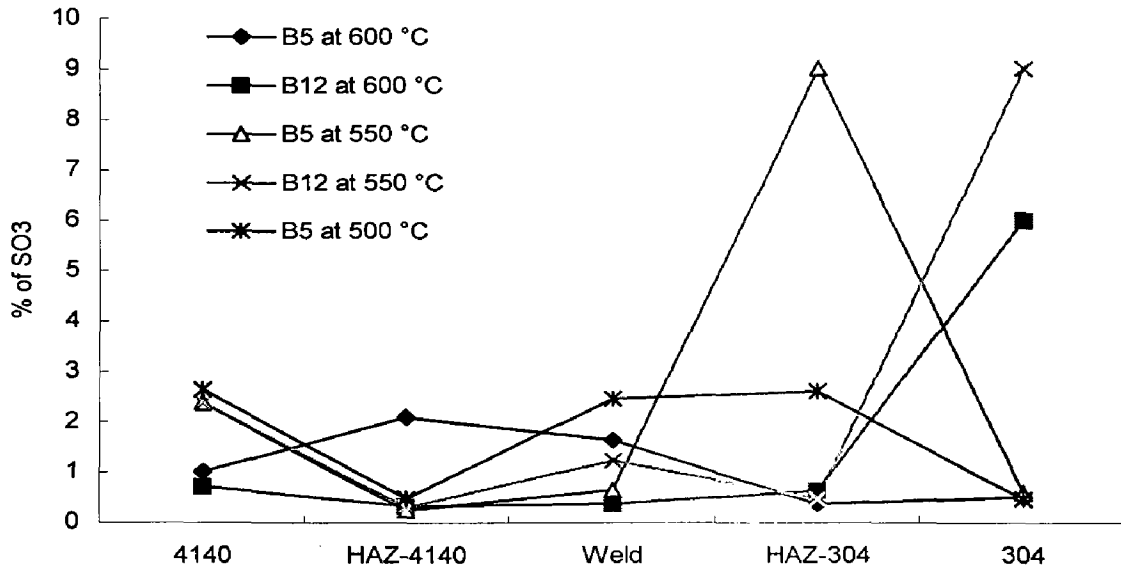


Fig 6.26 (M) EDAX data shows the effect of burn off length and temperature on formation of SO₃ on the friction weldment under molten salt environment of 40 wt% K₂SO₄, 40 wt% Na₂SO₄, 10 wt% KCl, and 10 wt% NaCl.

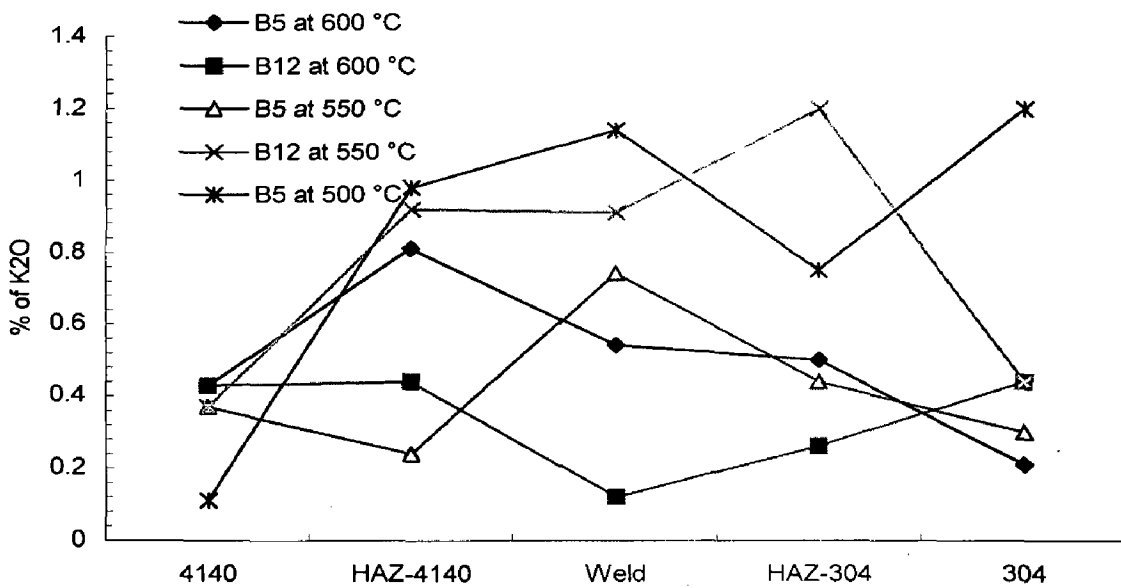


Fig 6.26 (N) EDAX data shows the effect of burn off length and temperature on formation of K₂O on the friction weldment under molten salt environment of 40 wt% K₂SO₄, 40 wt% Na₂SO₄, 10 wt% KCl, and 10 wt% NaCl.

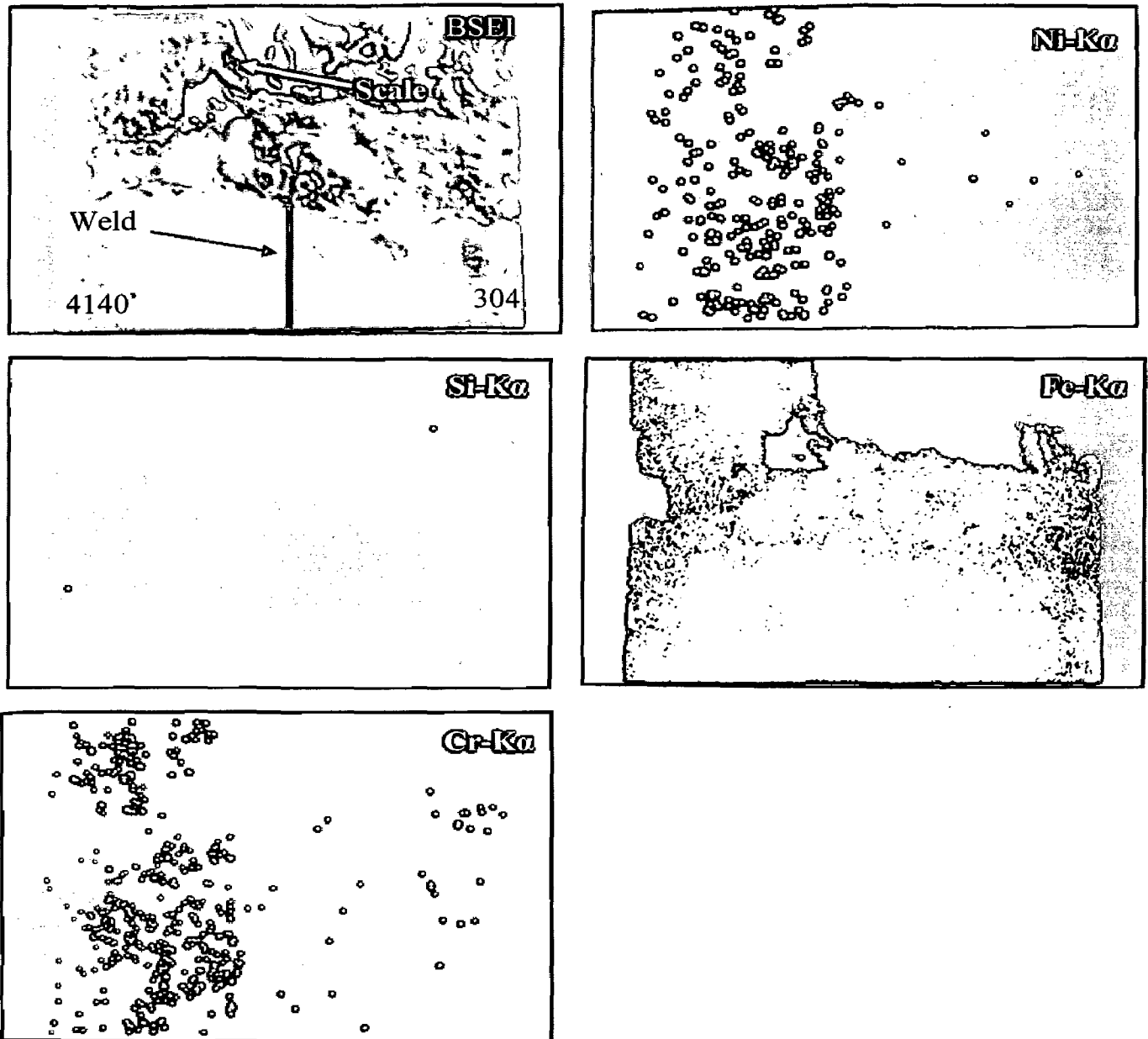


Fig. 6.27(A) BSEI and elemental X-ray mapping of the cross-section of dissimilar weldment made by AISI 4140 and AISI 304 by keeping burn off length 5 mm, subjected to cyclic oxidation in Na_2SO_4 (40%) + K_2SO_4 (40%) + NaCl (10%) + KCl (10%) at 500°C for 50 cycles, 500 X.

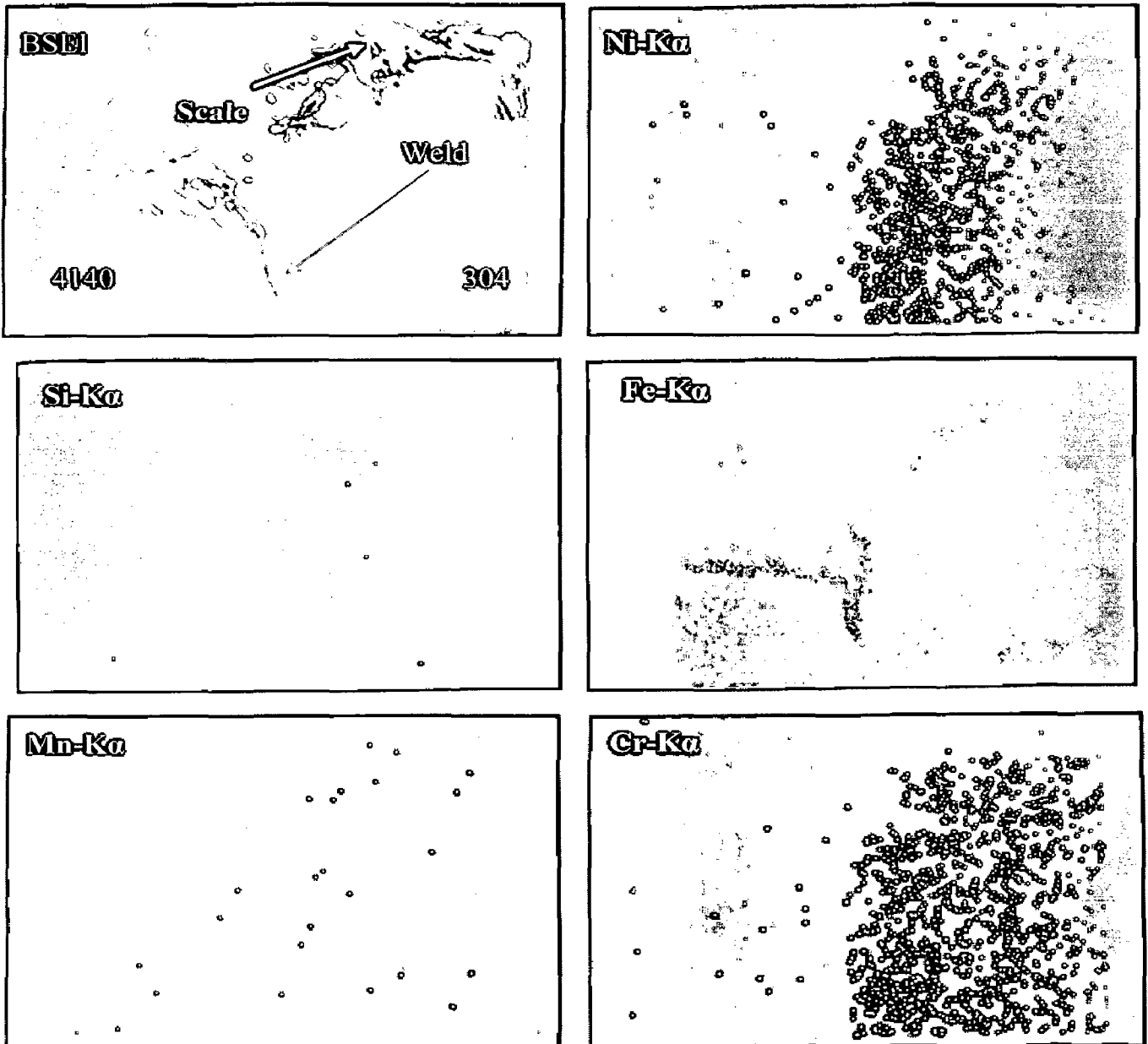


Fig. 6.27(B) BSEI and elemental X-ray mapping of the cross-section of dissimilar weldment made by AISI 4140 and AISI 304 by keeping burn off length 5 mm, subjected to cyclic oxidation in Na_2SO_4 (40%) + K_2SO_4 (40%) + NaCl (10%) + KCl (10%) at 550°C for 50 cycles, 400 X.

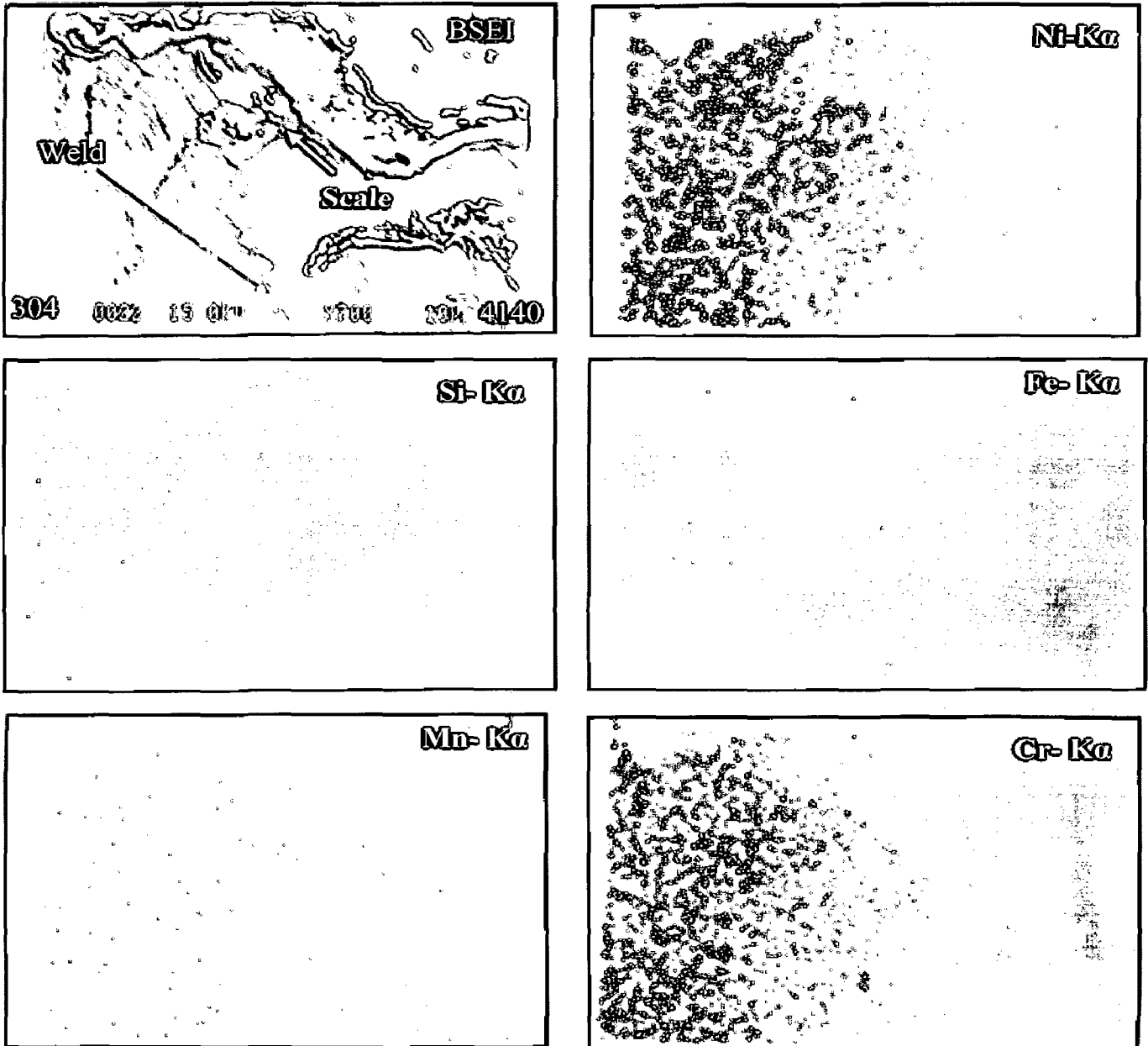


Fig. 6.27(C) BSEI and elemental X-ray mapping of the cross-section of dissimilar weldment made by AISI 4140 and AISI 304 by keeping burn off length 7 mm, subjected to cyclic oxidation in Na_2SO_4 (40%) + K_2SO_4 (40%) + NaCl (10%) + KCl (10%) at 550°C for 50 cycles, 700 X.

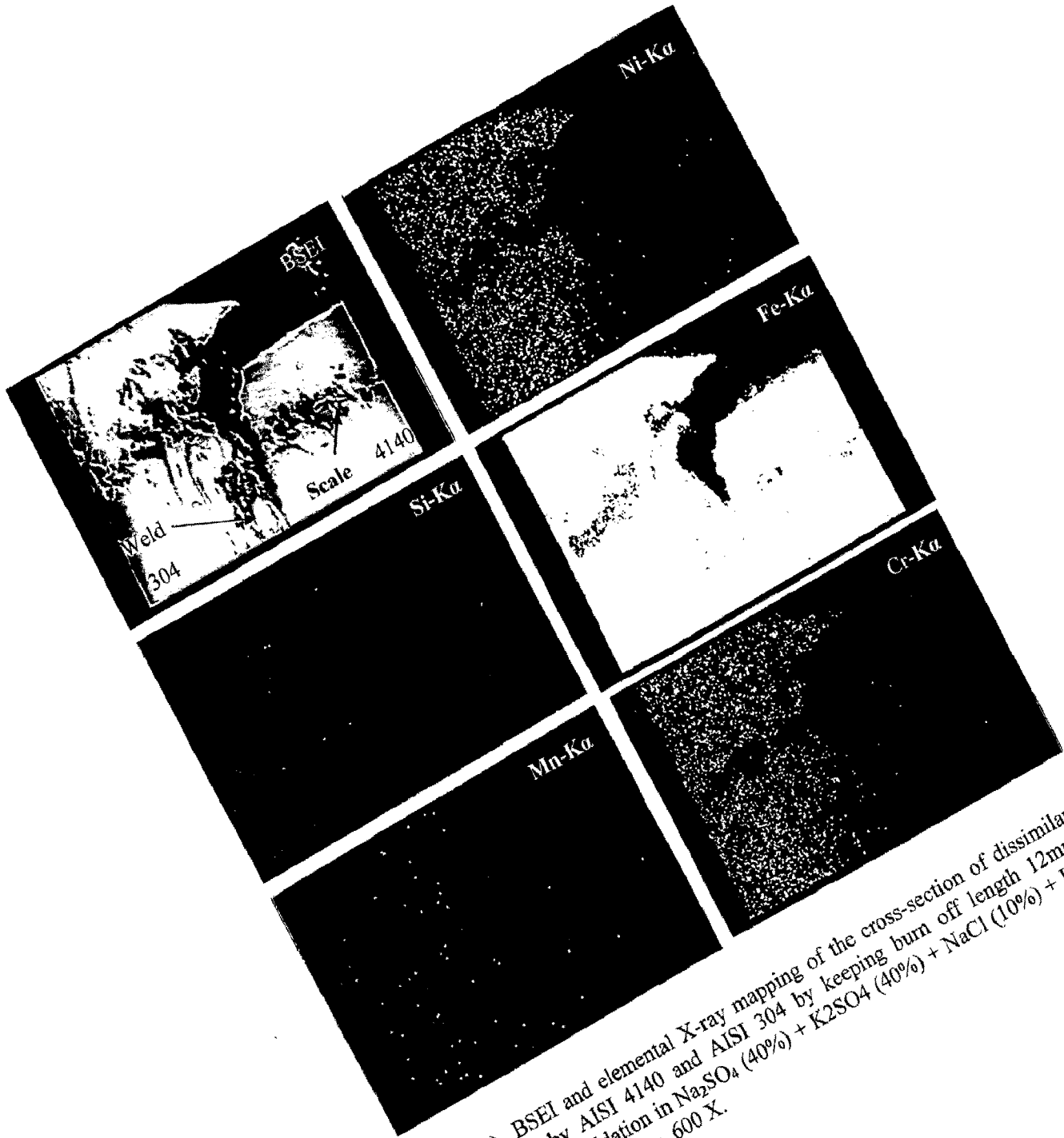


Fig. 6.27(D) BSEI and elemental X-ray mapping of the cross-section of dissimilar weldment made by AISI 4140 and AISI 304 by keeping burn off length 12mm, subjected to cyclic oxidation in Na_2SO_4 (40%) + K_2SO_4 (40%) + NaCl (10%) + KCl (10%) at 550°C for 50 cycles, 600 X.

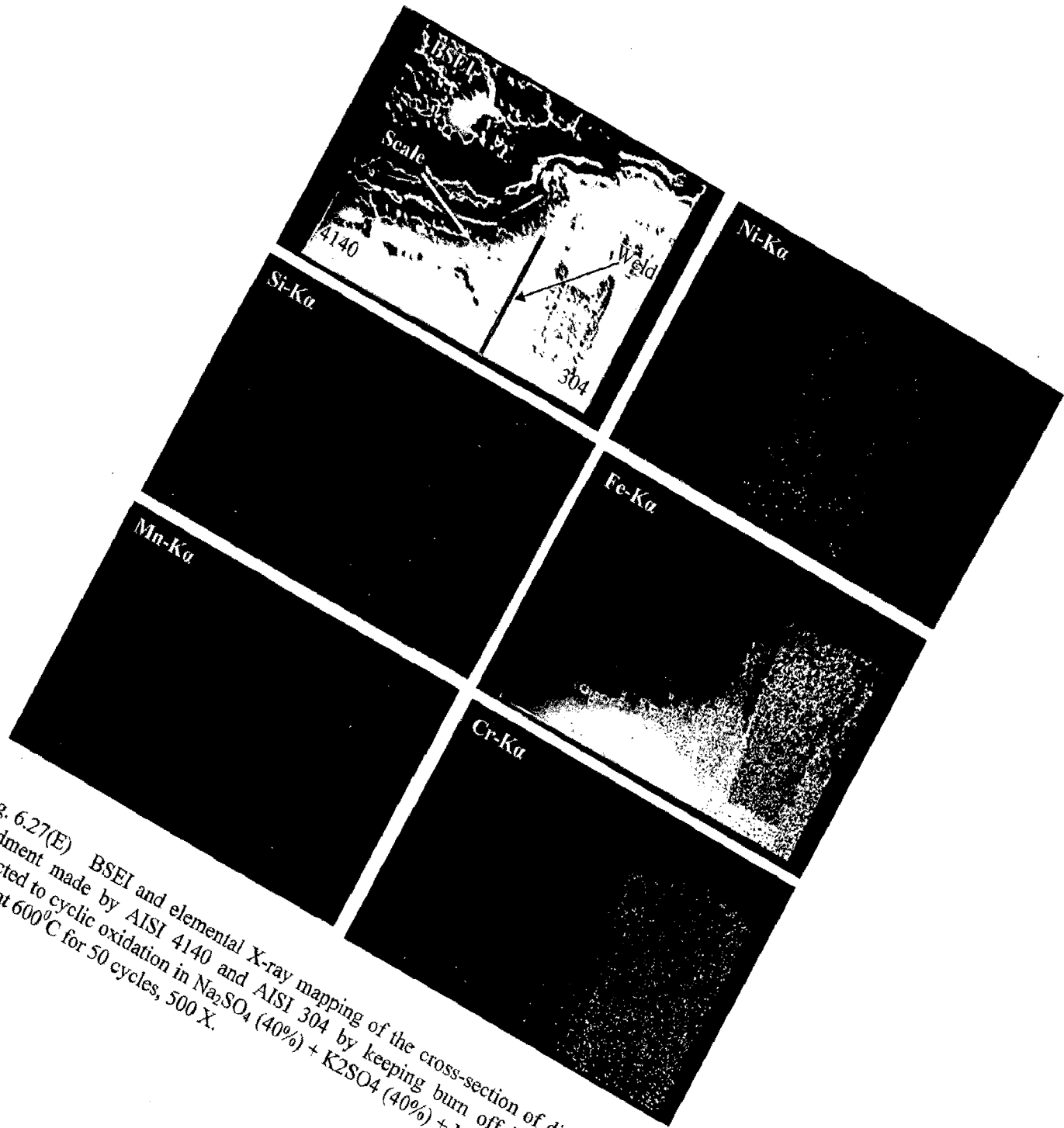


Fig. 6.27(E) BSEI and elemental X-ray mapping of the cross-section of dissimilar weldment made by AISI 4140 and AISI 304 by keeping burn off length 5mm, subjected to cyclic oxidation in Na_2SO_4 (40%) + K_2SO_4 (40%) + NaCl (10%) + KCl (10%) at 600°C for 50 cycles, 500 X.

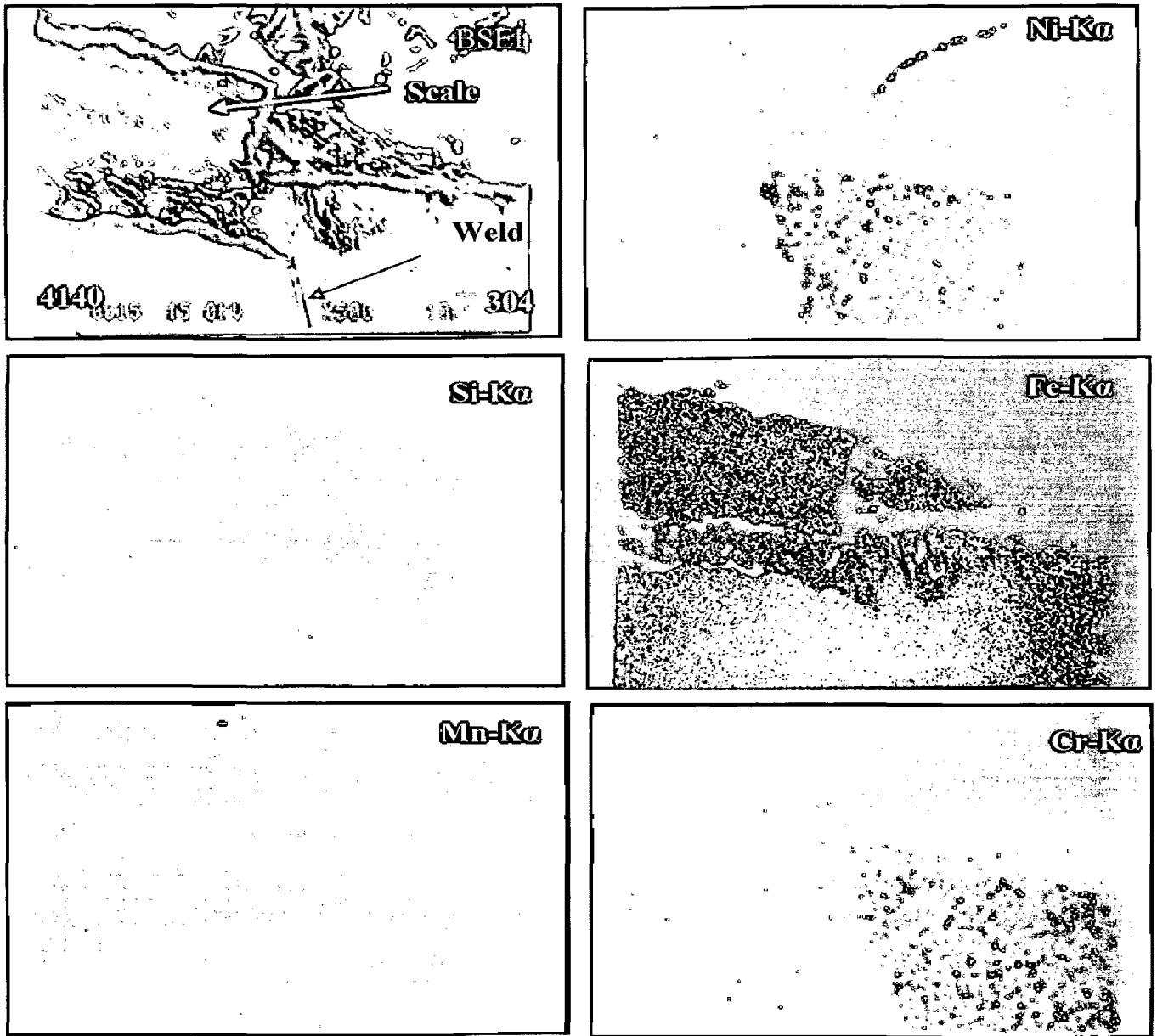


Fig. 6.27(F) BSEI and elemental X-ray mapping of the cross-section of dissimilar weldment made by AISI 4140 and AISI 304 by keeping burn off length 12mm, subjected to cyclic oxidation in Na_2SO_4 (40%) + K_2SO_4 (40%) + NaCl (10%) + KCl (10%) at 600°C for 50 cycles, 500 X.

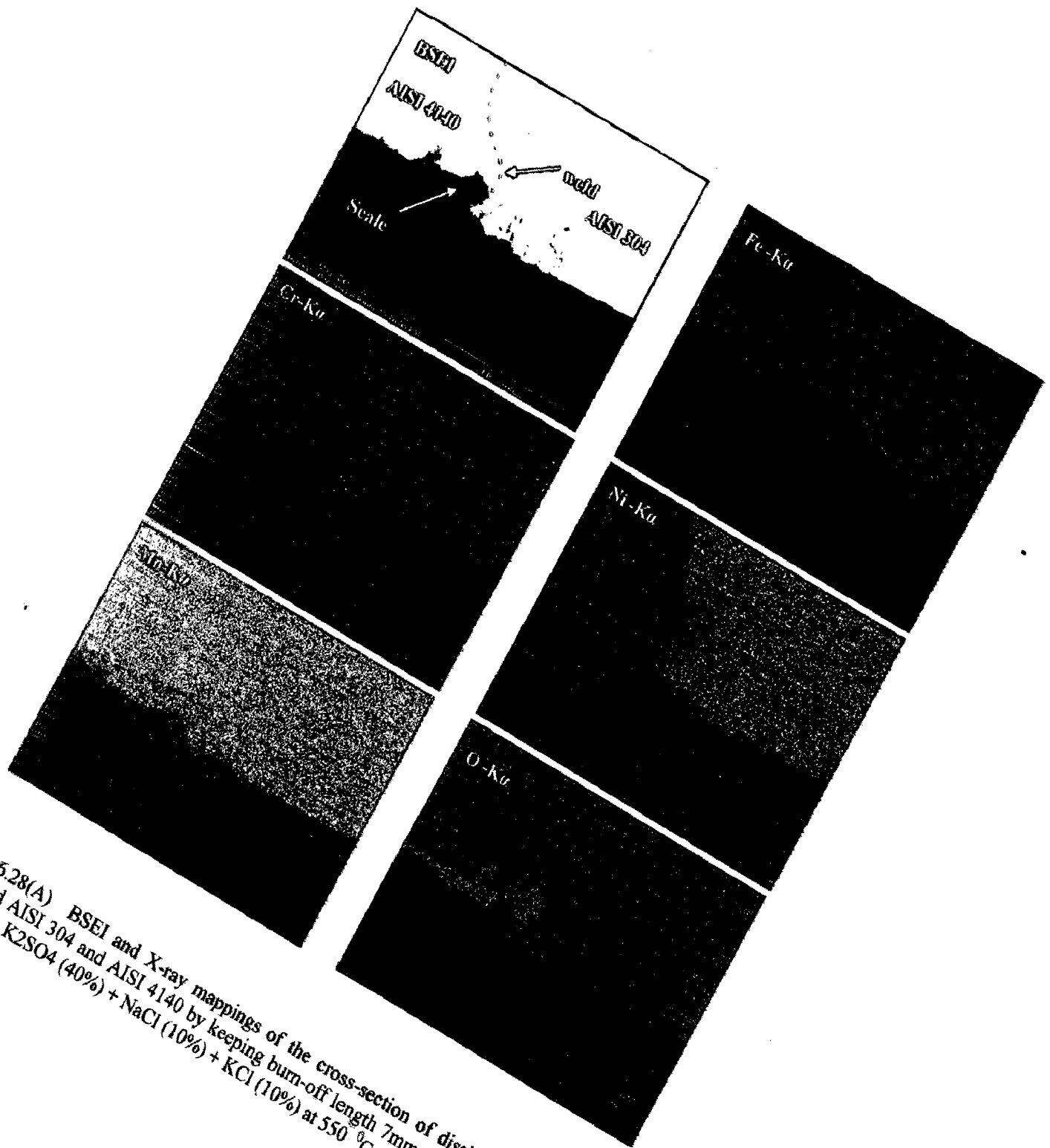
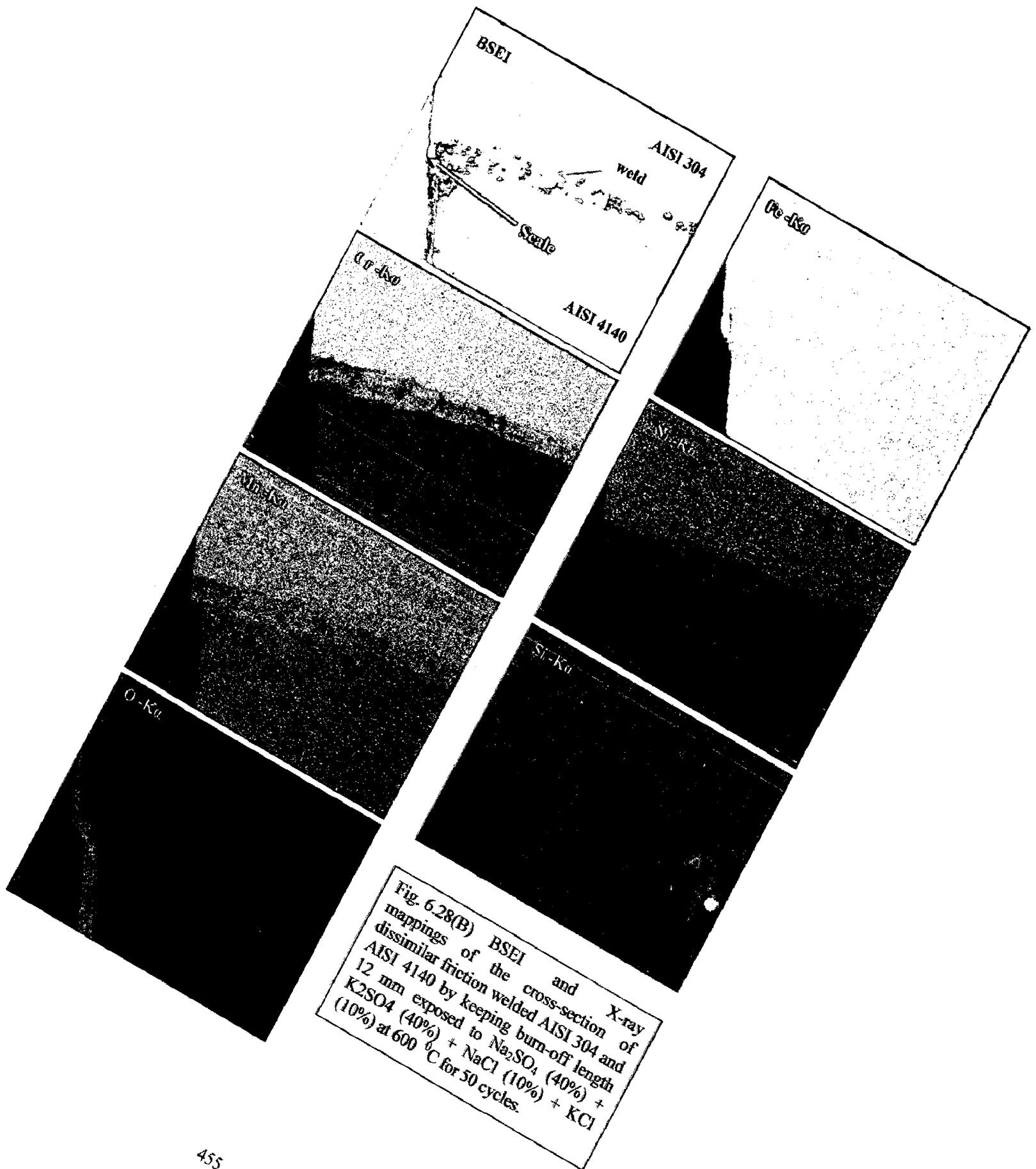


Fig. 6.28(A) BSEI and X-ray mappings of the cross-section of dissimilar friction welded AISI 304 and AISI 4140 by keeping burn-off length 7mm exposed to Na_2SO_4 (40%) + K_2SO_4 (40%) + NaCl (10%) + KCl (10%) at 550 °C for 50 cycles.



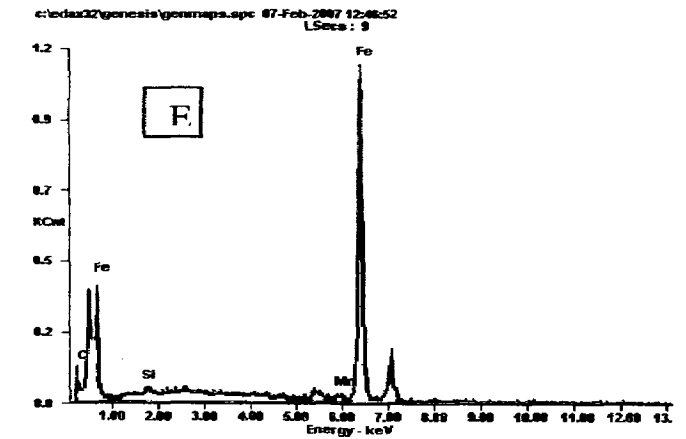
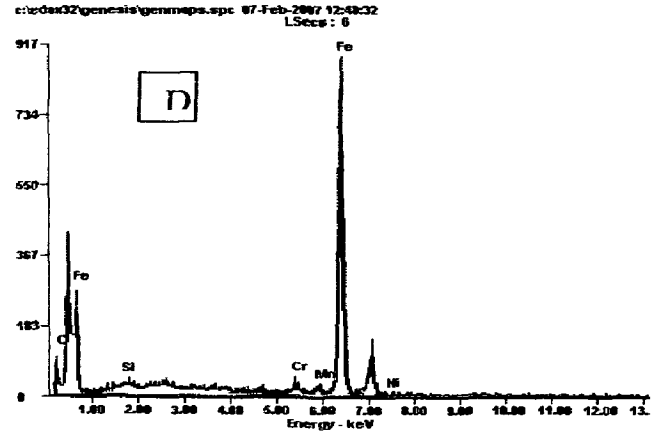
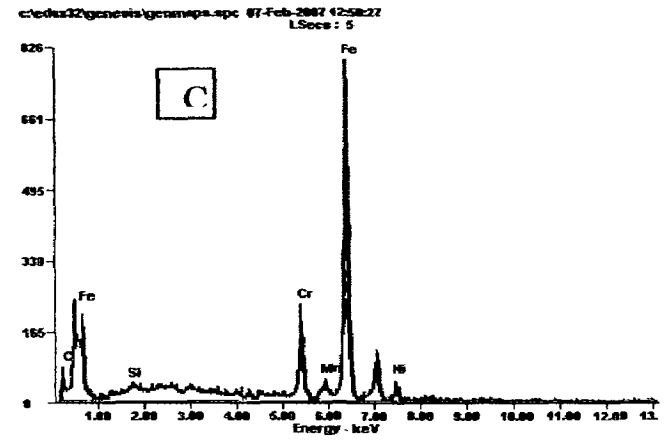
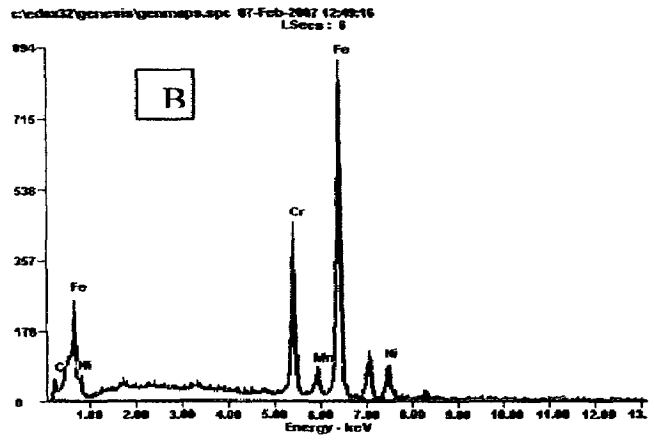
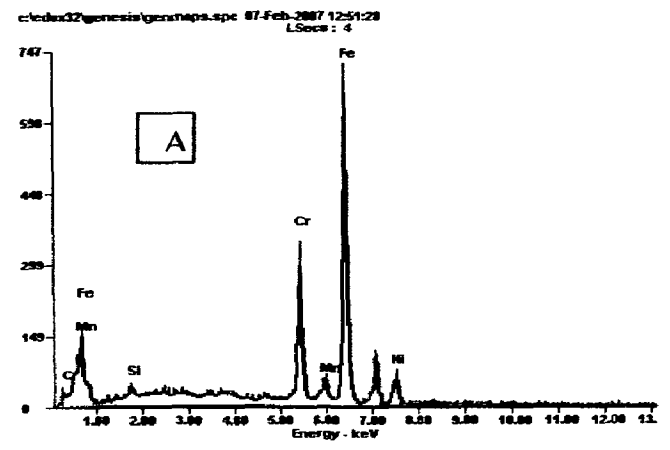
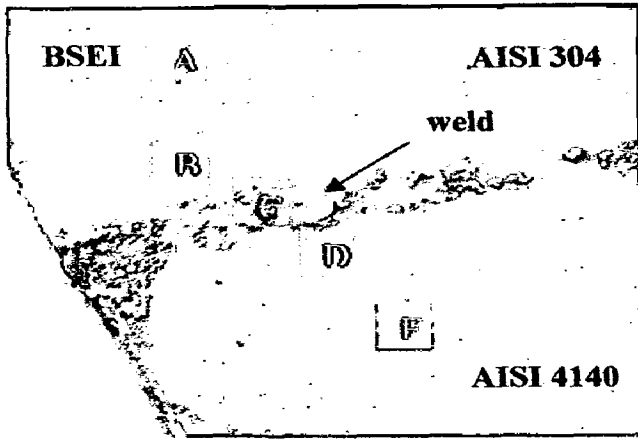


Fig. 6.28(C) BSEI and EDAX of the cross-section of dissimilar friction welded AISI 304 and AISI 4140 by keeping burn-off length 12 mm exposed to Na₂SO₄ (40%) + K₂SO₄ (40%) + NaCl (10%) + KCl (10%) at 600 °C for 50 cycles.

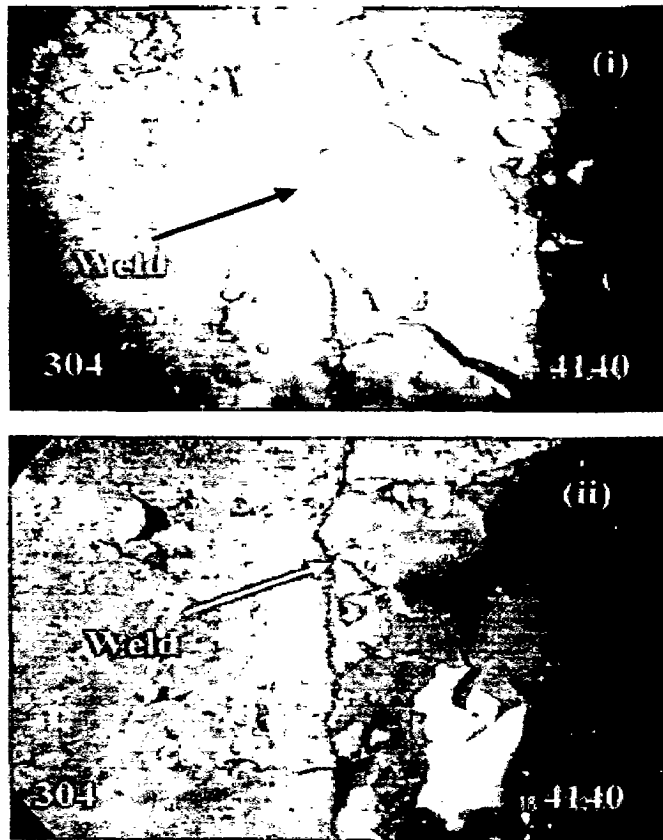


Fig. 6.29 Macrographs dissimilar friction welded AISI 4140 and AISI 304 subjected to cyclic hot corrosion exposed under $\text{Na}_2\text{SO}_4 + \text{NaCl}$ (50%) after 50 cycles. (i) and (ii) Weldment made by keeping 5 mm burn off length and exposed temperature of 500 and 550 °C respectively.

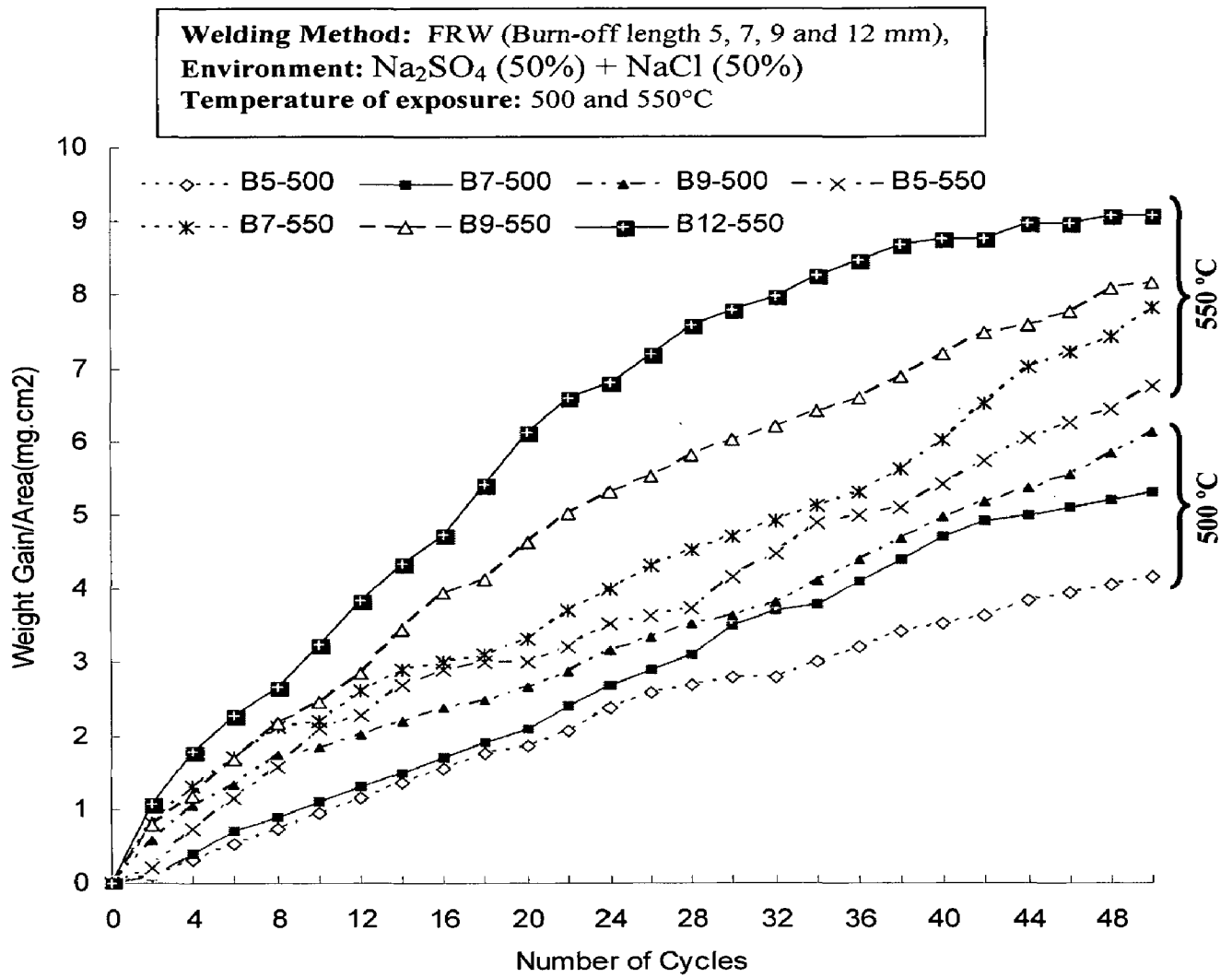


Fig 6.30. Plots of cumulative weight gain (mg/cm²) as a function of time (number of cycles) for the friction weldment in the molten salt environment.

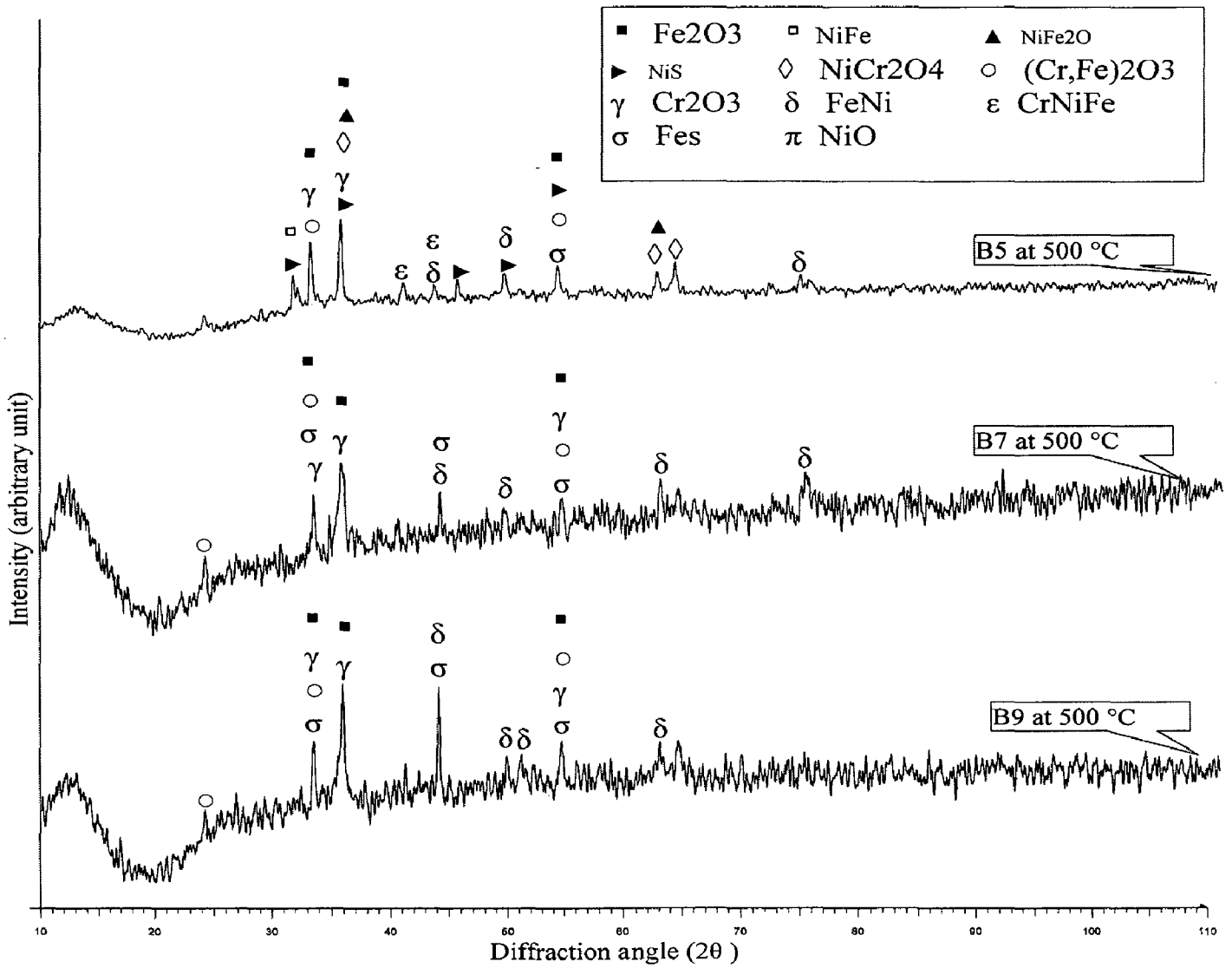


Fig. 6.31(A) X-Ray diffraction patterns for hot corroded dissimilar friction weldment at 500 °C. Burn-off length: B5, B7 and B9, Environment: Na₂SO₄ + NaCl (50%)

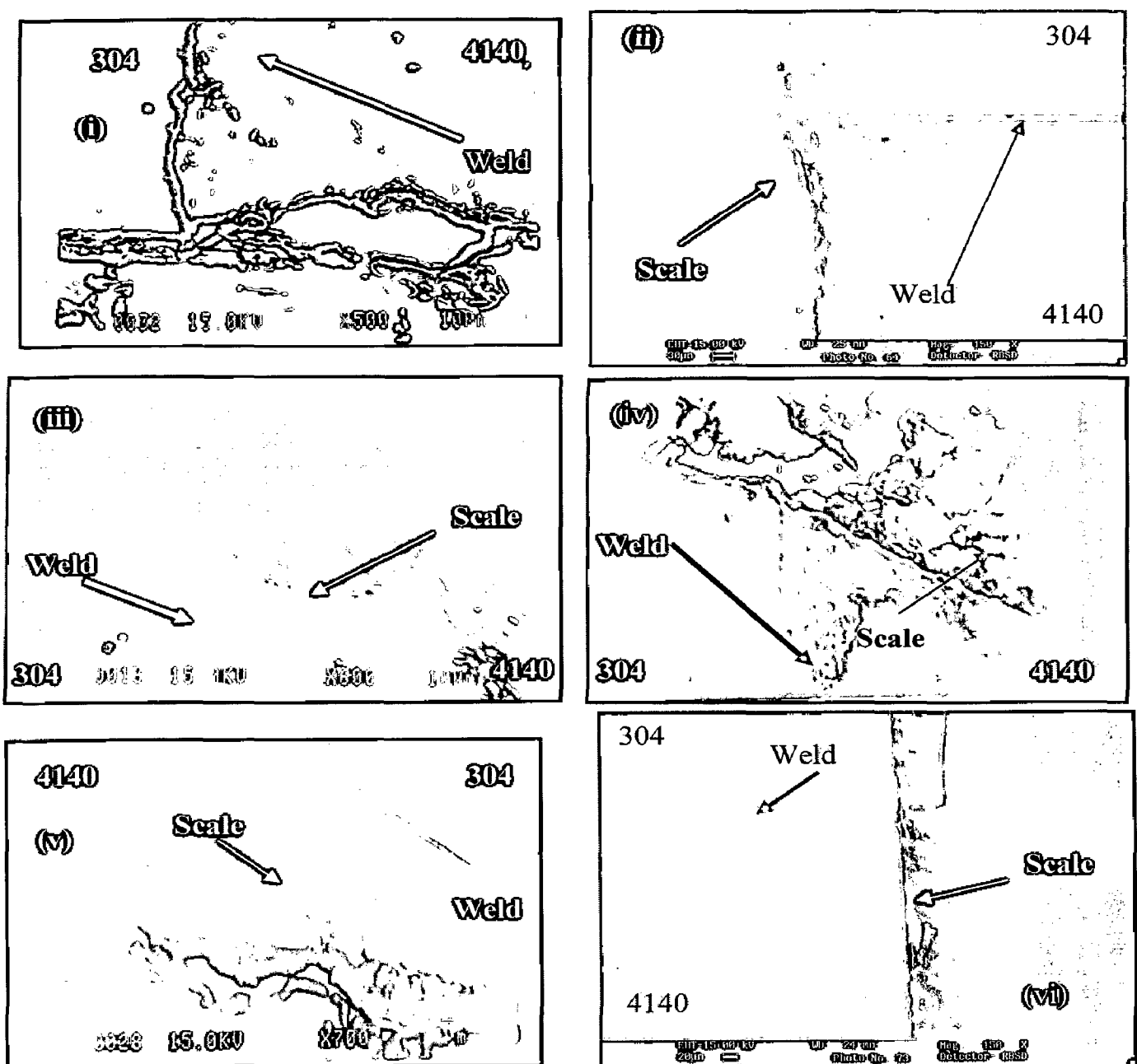


Fig 6.32. BSEI for hot corroded friction weldment under $\text{Na}_2\text{SO}_4 + \text{NaCl}$ (50%) exposed temperature of 500, 550, 600 °C. (i) and (ii): Exposed temperature 500 °C for weldment made by keeping 5 and 7 mm Burn off length respectively. (iii) – (vi): Exposed temperature 550 °C for weldment made by keeping 5, 7, 9 and 12 mm Burn off length respectively.

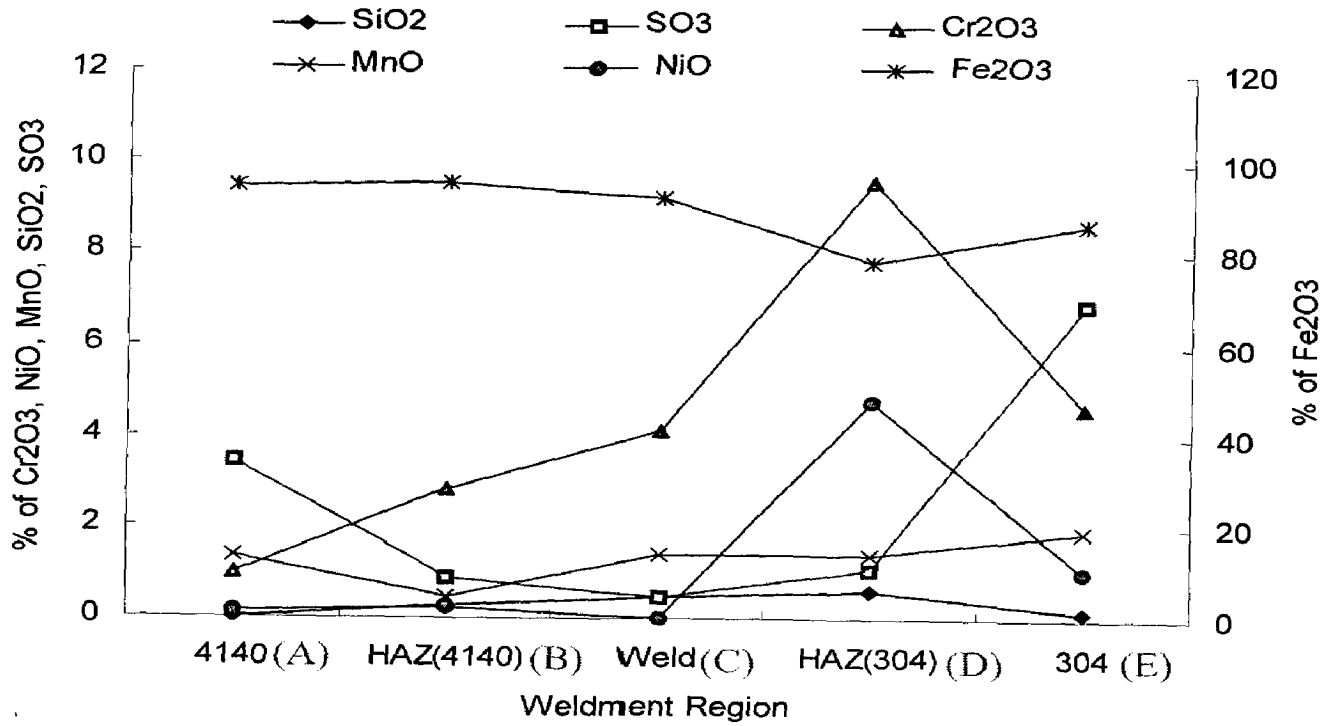
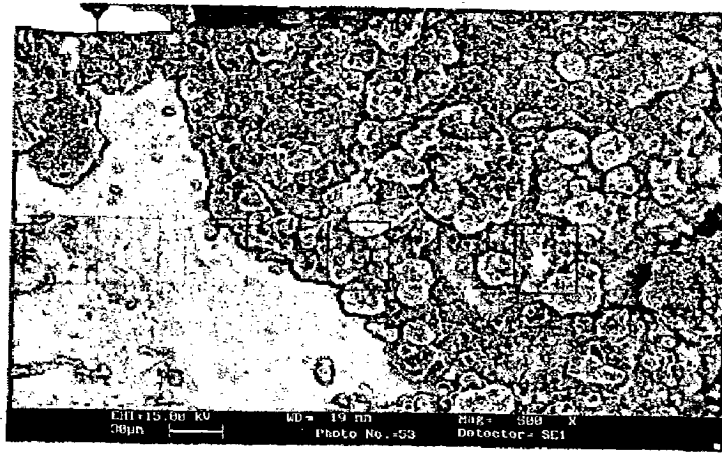


Fig 6.33(A) SEM/EDAX graph shows the friction weldment by keeping 5 mm burn off length, exposed at 500 °C under Na₂SO₄ – NaCl (50%) after 50 cycles.

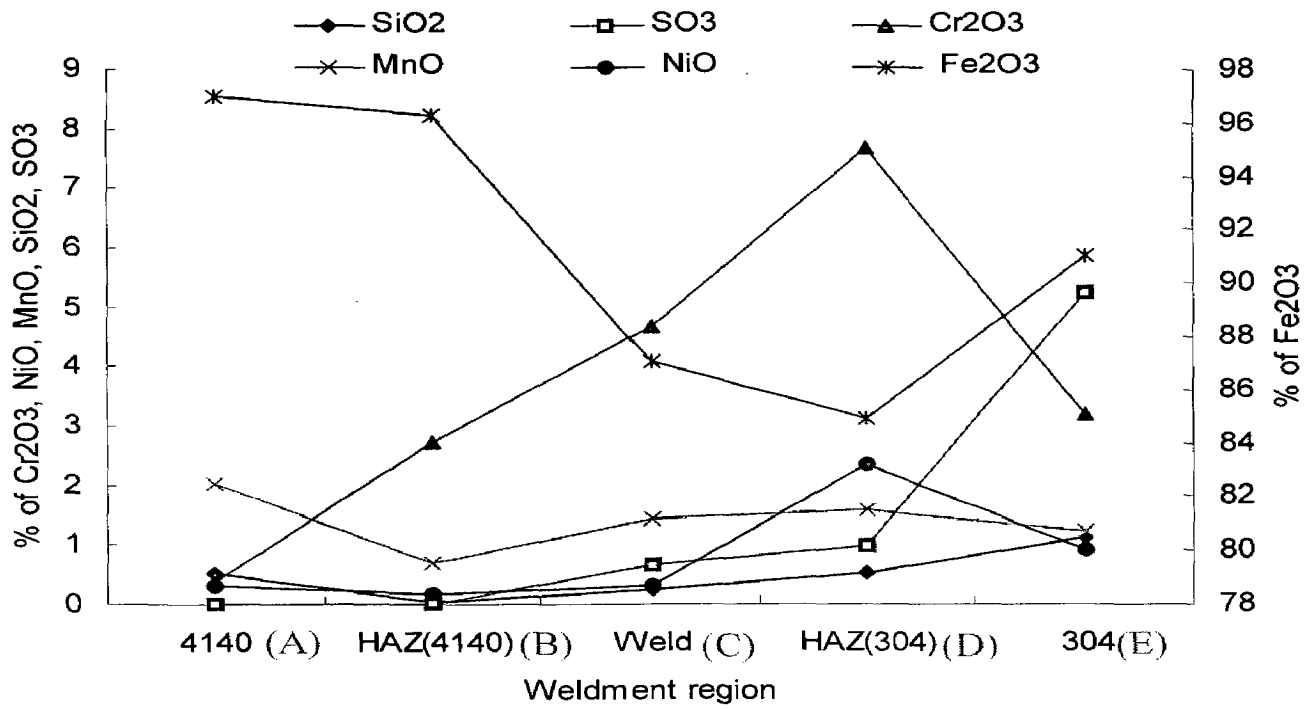
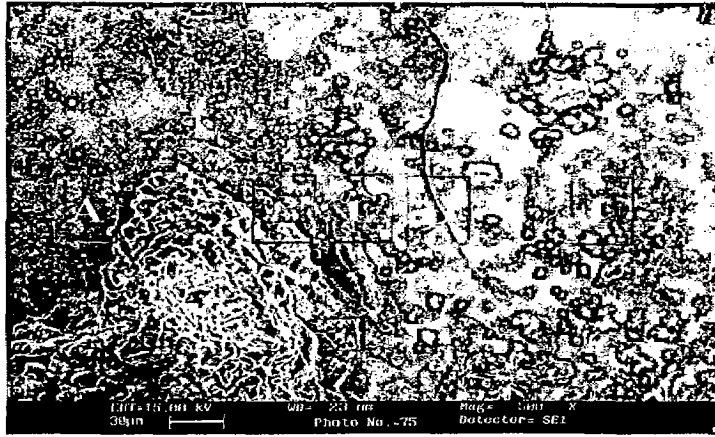


Fig 6.33(B) SEM/EDAX graph shows the friction weldment by keeping 7 mm burn off length, exposed at 500 °C under Na₂SO₄ – NaCl (50%) after 50 cycles.

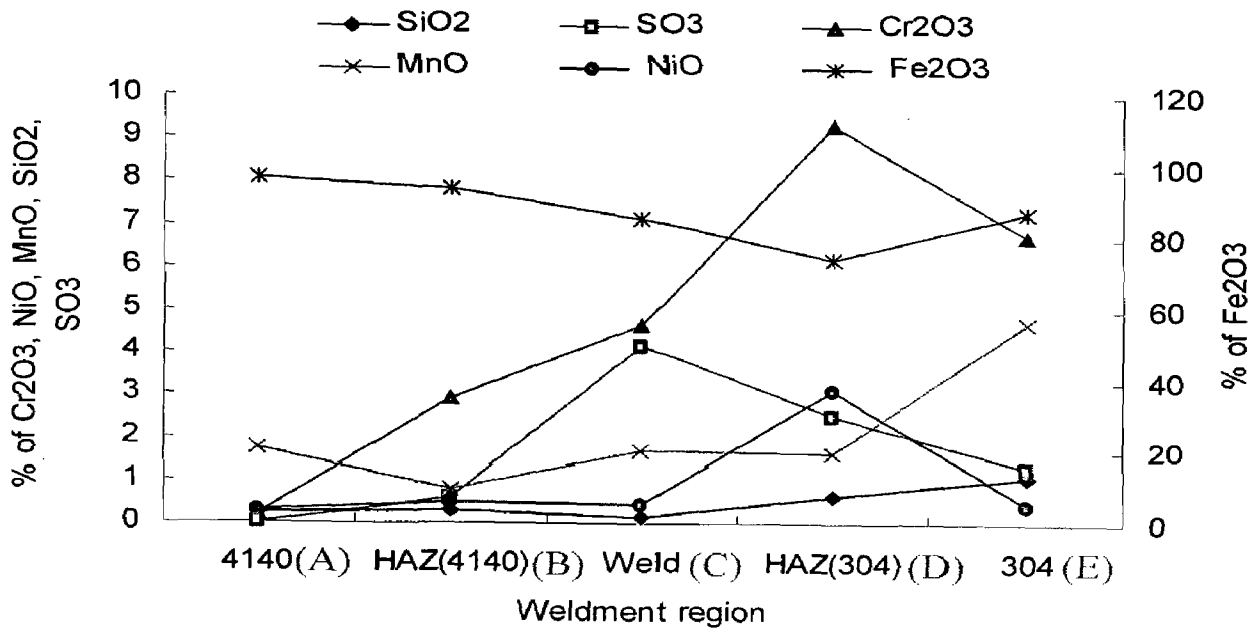
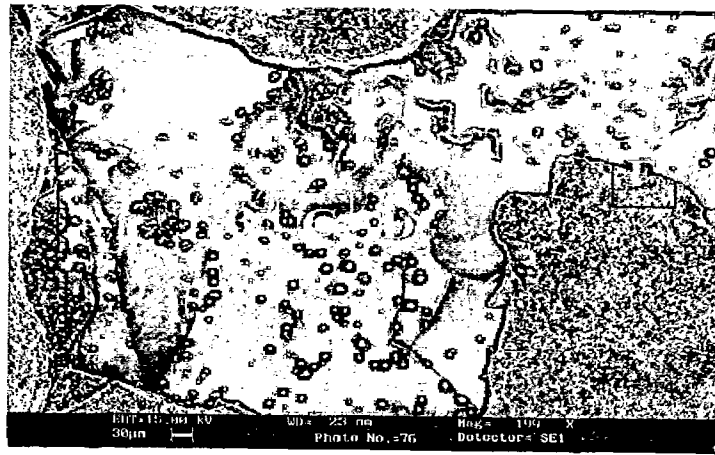


Fig 6.33(C) SEM/EDAX graph shows the friction weldment by keeping 9 mm burn off length, exposed at 500 °C under Na₂SO₄ – NaCl (50%) after 50 cycles.

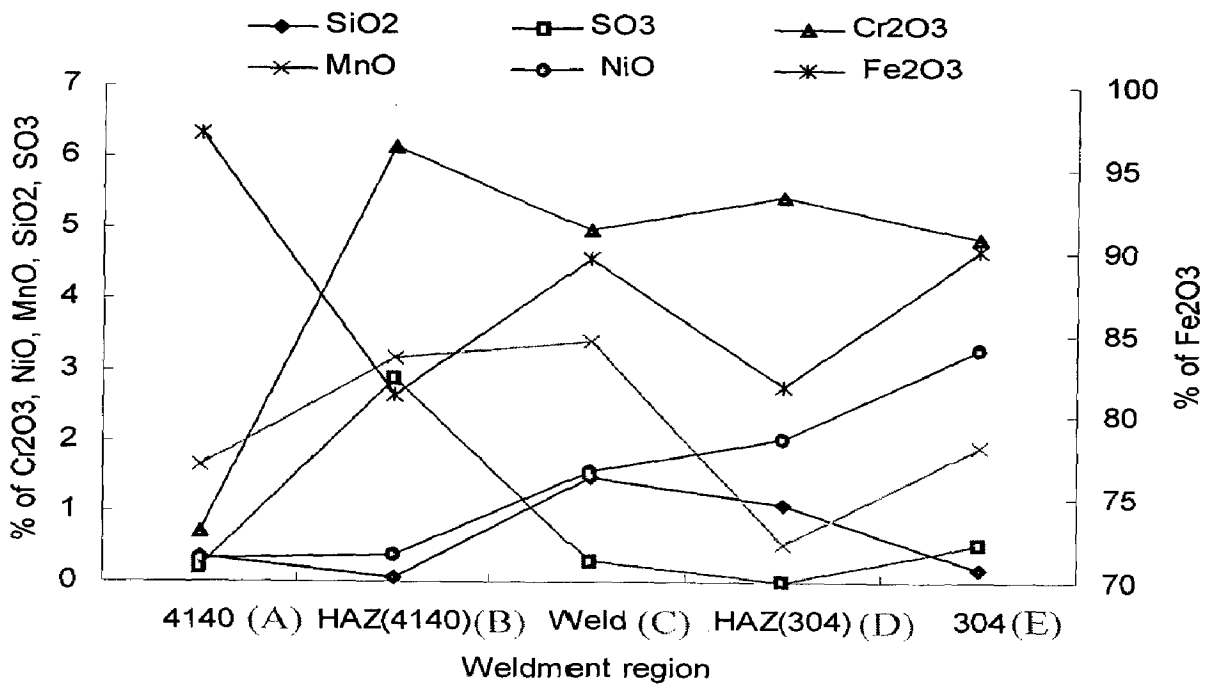


Fig 6.33(D) SEM/EDAX graph shows the friction weldment by keeping 5 mm burn off length, exposed at 550 °C under Na₂SO₄ – NaCl (50%) after 50 cycles.

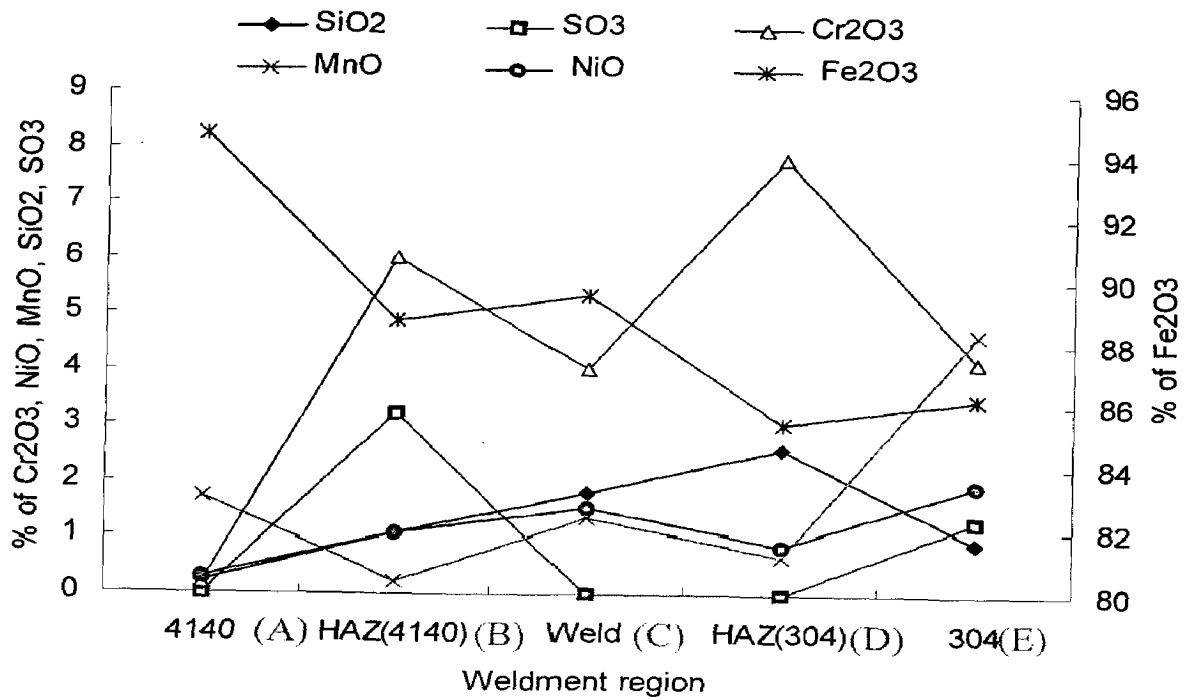
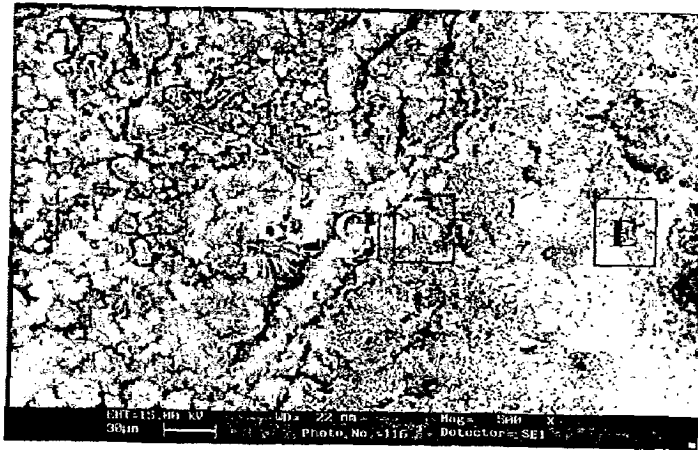


Fig 6.33(E) SEM/EDAX graph shows the friction weldment by keeping 7 mm burn off length, exposed at 550 °C under Na₂SO₄ – NaCl (50%) after 50 cycles.

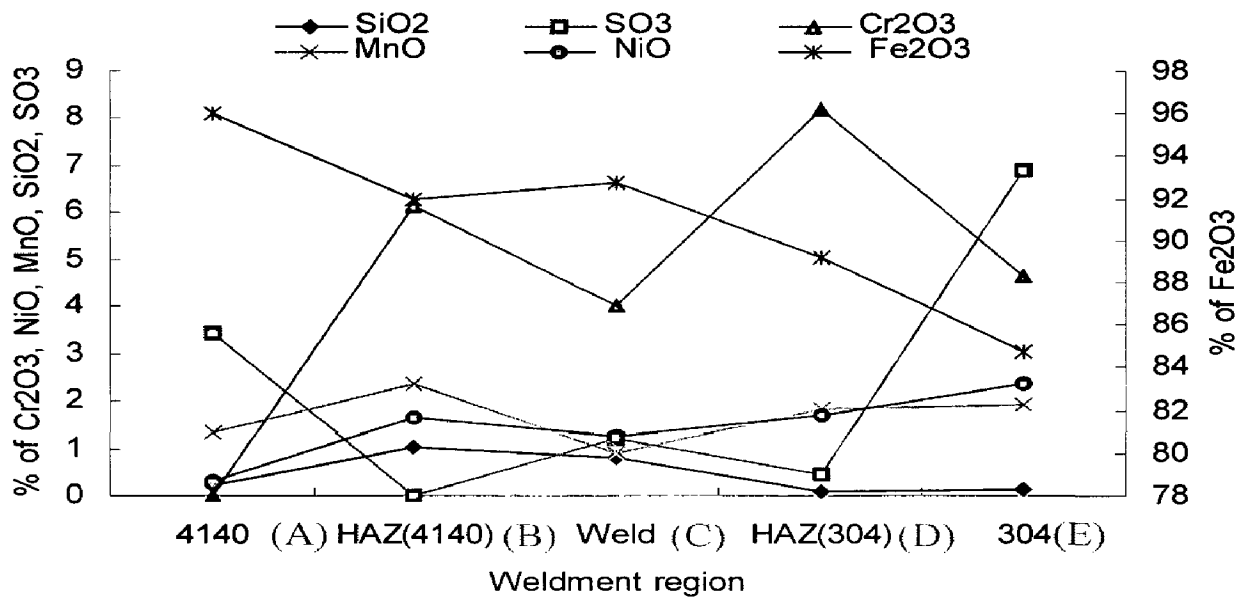
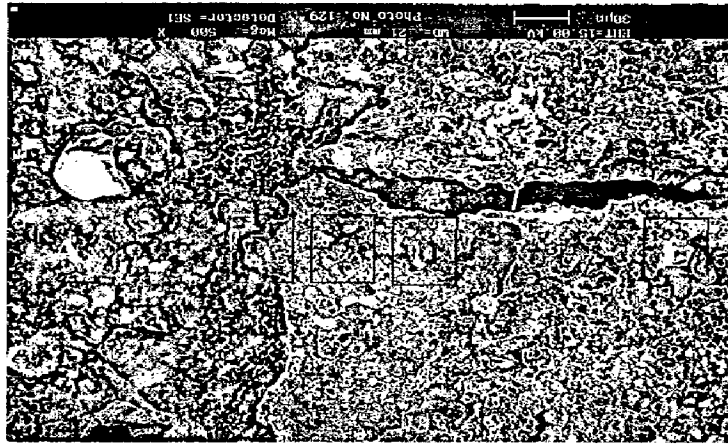


Fig 6.33(F) SEM/EDAX graph shows the friction weldment by keeping 9 mm burn off length, exposed at 550 °C under Na₂SO₄ – NaCl (50%) after 50 cycles.

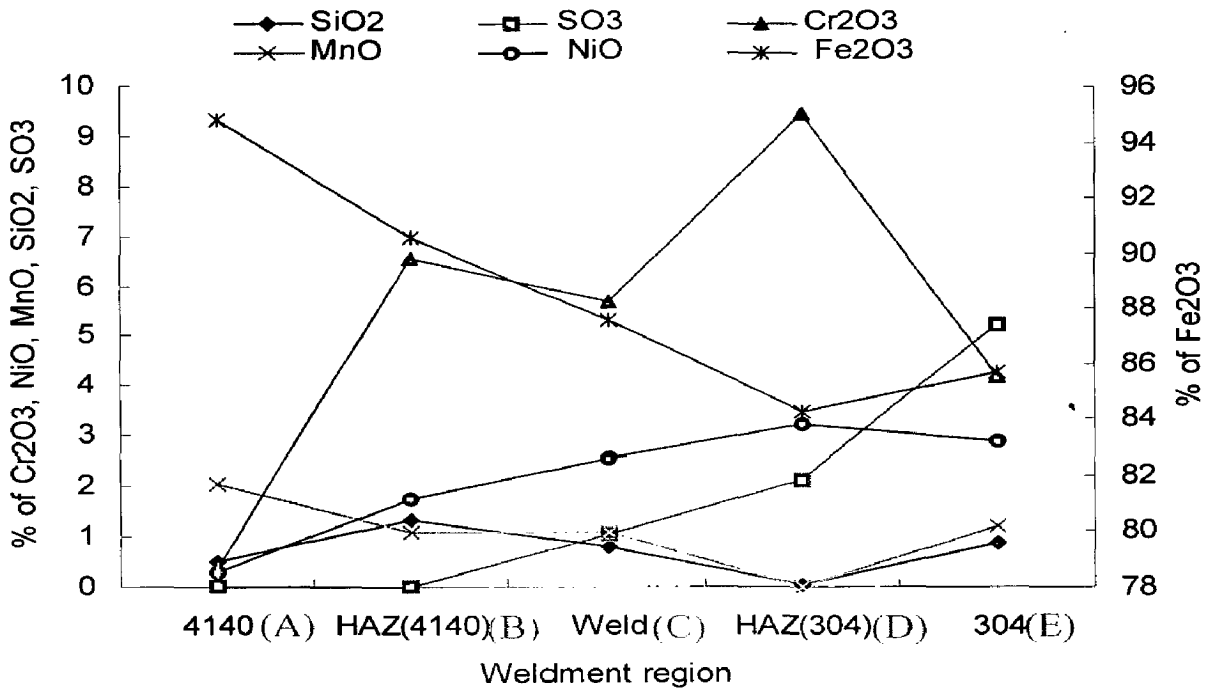
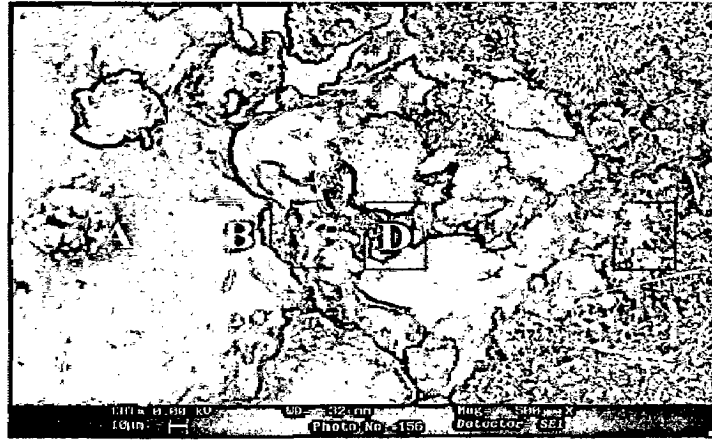


Fig 6.33(G) SEM/EDAX graph shows the friction weldment by keeping 12 mm burn off length, exposed at 550 °C under Na₂SO₄ – NaCl (50%) after 50 cycles.

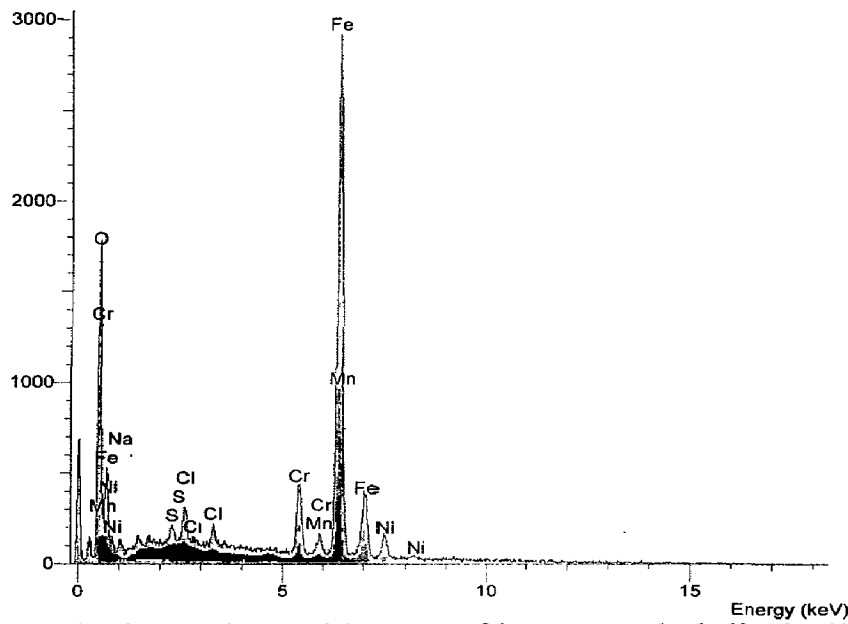


Fig. 6.33(H) EDS analysis on the weld zone of hot corroded dissimilar weldment. Environment: Na₂SO₄ + NaCl (50%), Exposure temp: 550 °C (50 cycles).

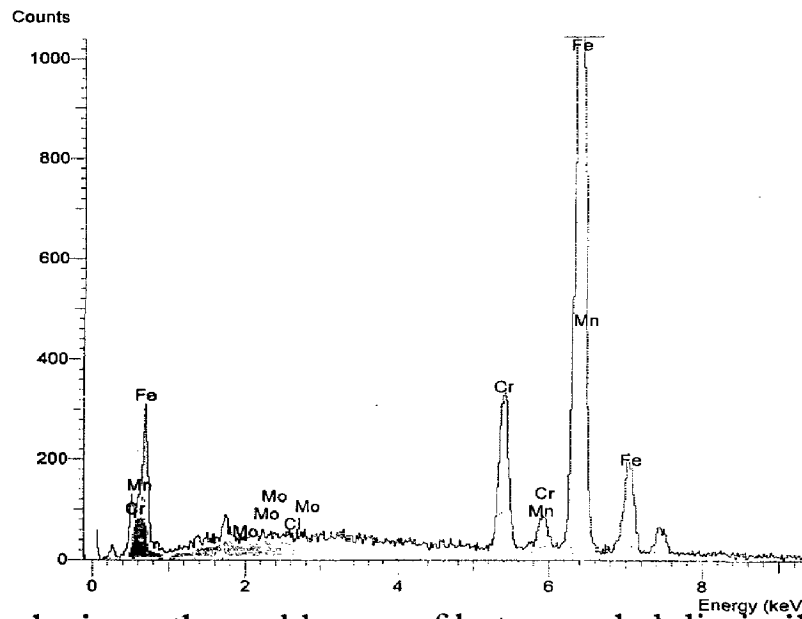


Fig. 6.33(I) EDS analysis on the weld zone of hot corroded dissimilar weldment. Environment: Air Oxidation, Exposure temp: 600 °C (50 cycles).

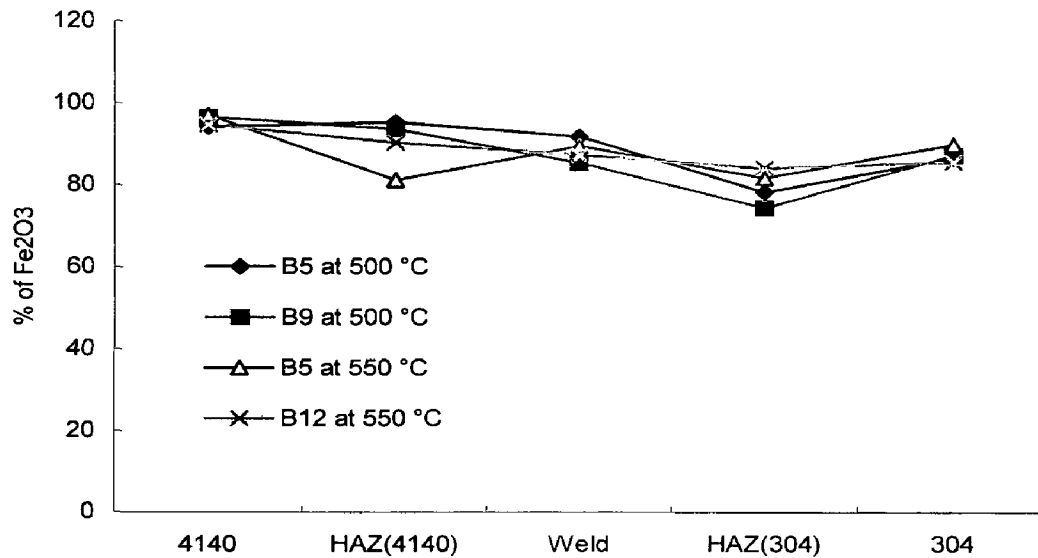


Fig 6.33 (J) EDAX data shows the effect of burn off length and temperature on formation of Fe₂O₃ on the friction weldment under molten salt environment of Na₂SO₄-50% NaCl.

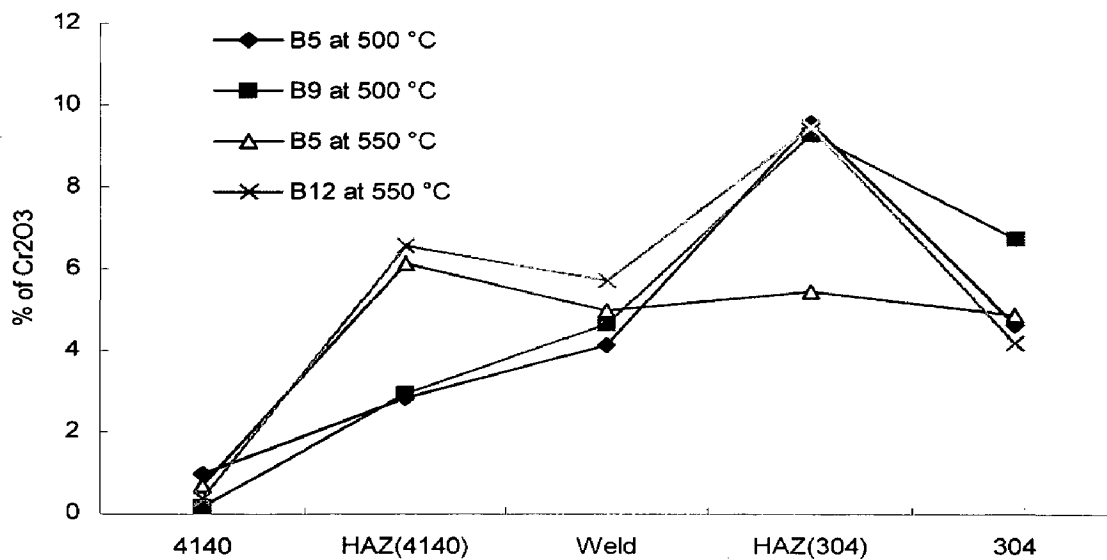


Fig 6.33 (K) EDAX data shows the effect of burn off length and temperature on formation of Cr₂O₃ on the friction weldment under molten salt environment of Na₂SO₄-50% NaCl.

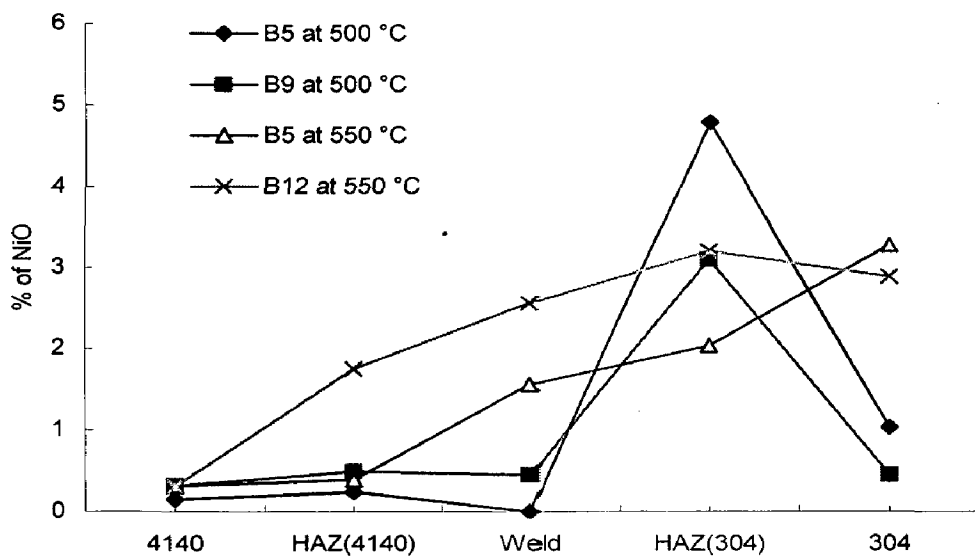


Fig 6.33 (L) EDAX data shows the effect of burn off length and temperature on formation of NiO on the friction weldment under molten salt environment of Na_2SO_4 -50% NaCl.

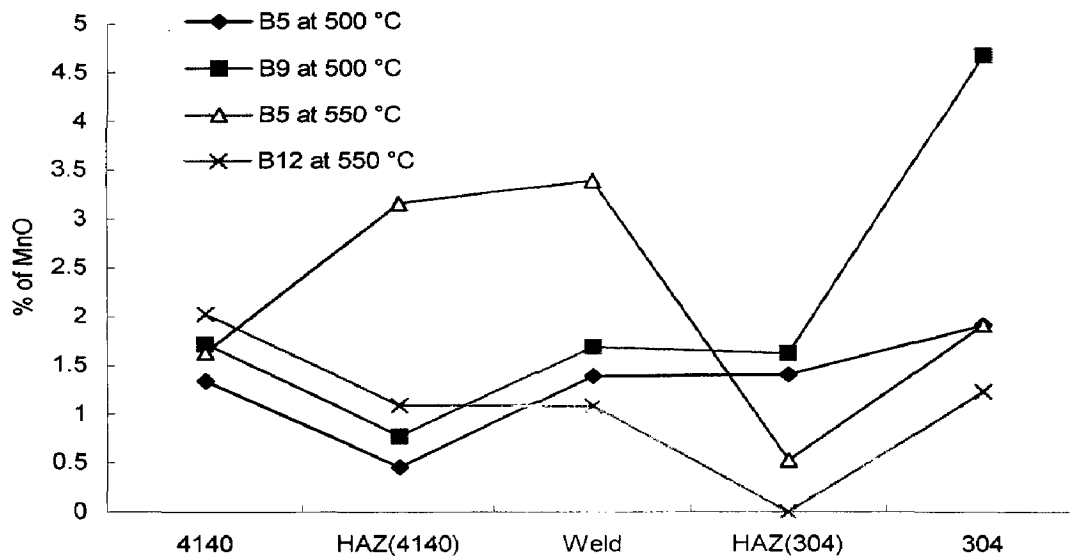


Fig 6.33 (M) EDAX data shows the effect of burn off length and temperature on formation of MnO on the friction weldment under molten salt environment of Na_2SO_4 -50% NaCl.

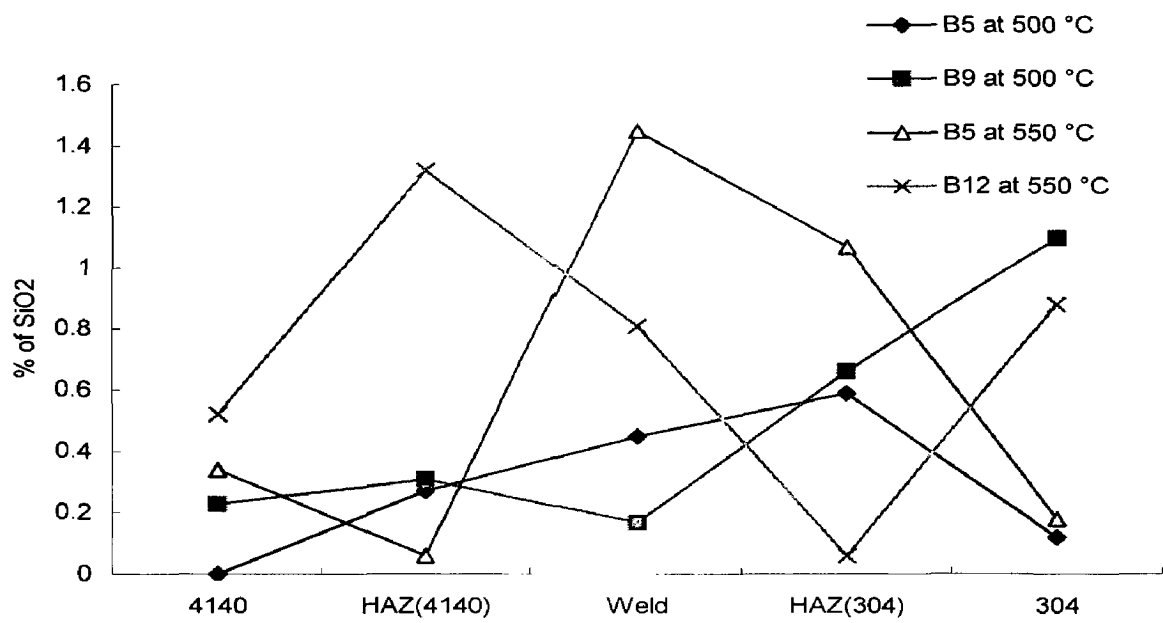


Fig 6.33 (N) EDAX data shows the effect of burn off length and temperature on formation of SiO₂ on the friction weldment under molten salt environment of Na₂SO₄-50% NaCl.

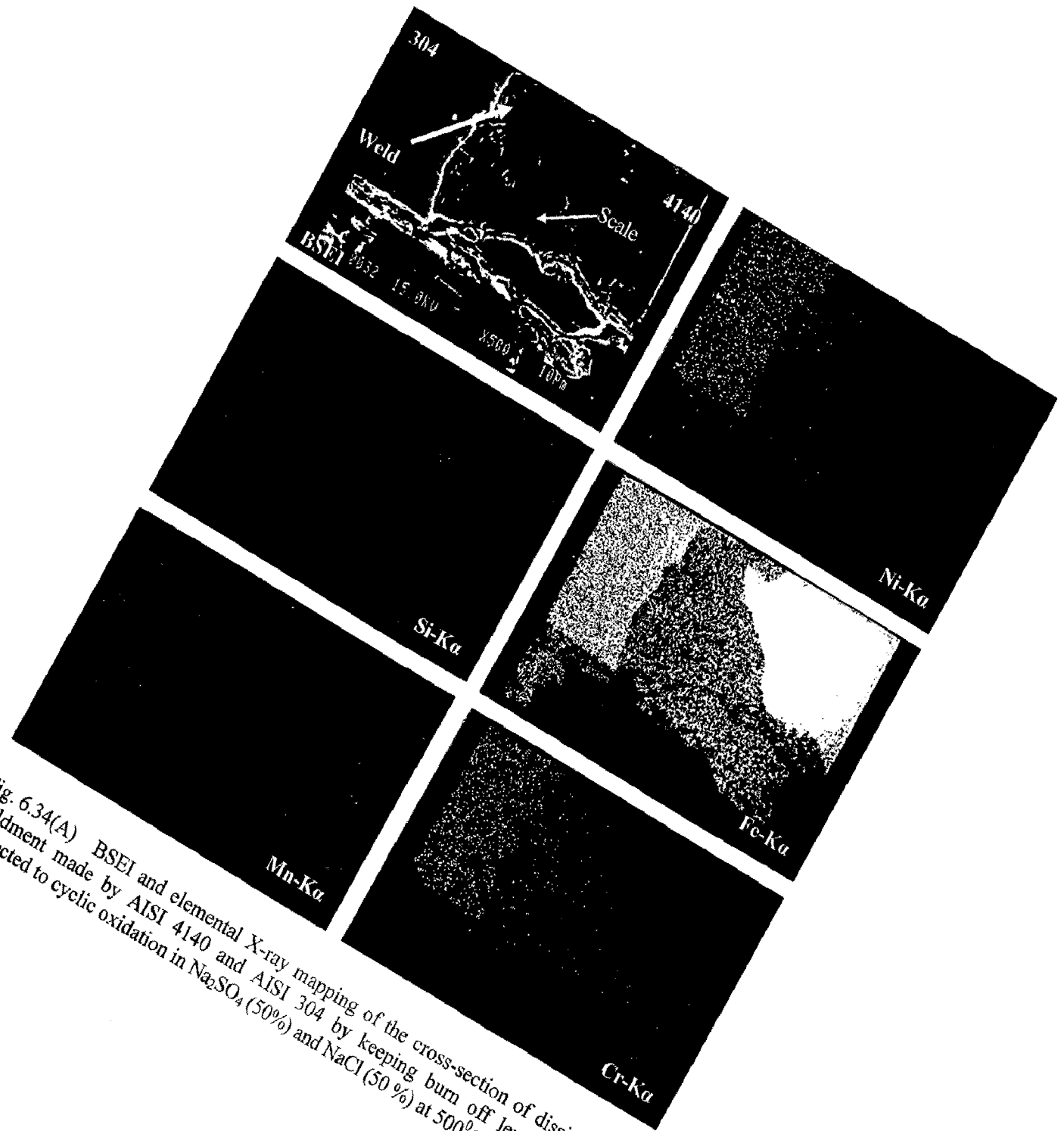


Fig. 6.34(A) BSEI and elemental X-ray mapping of the cross-section of dissimilar weldment made by AISI 4140 and AISI 304 by keeping burn off length 7mm, subjected to cyclic oxidation in Na_2SO_4 (50%) and NaCl (50 %) at 500°C for 50 cycles, 500 X.

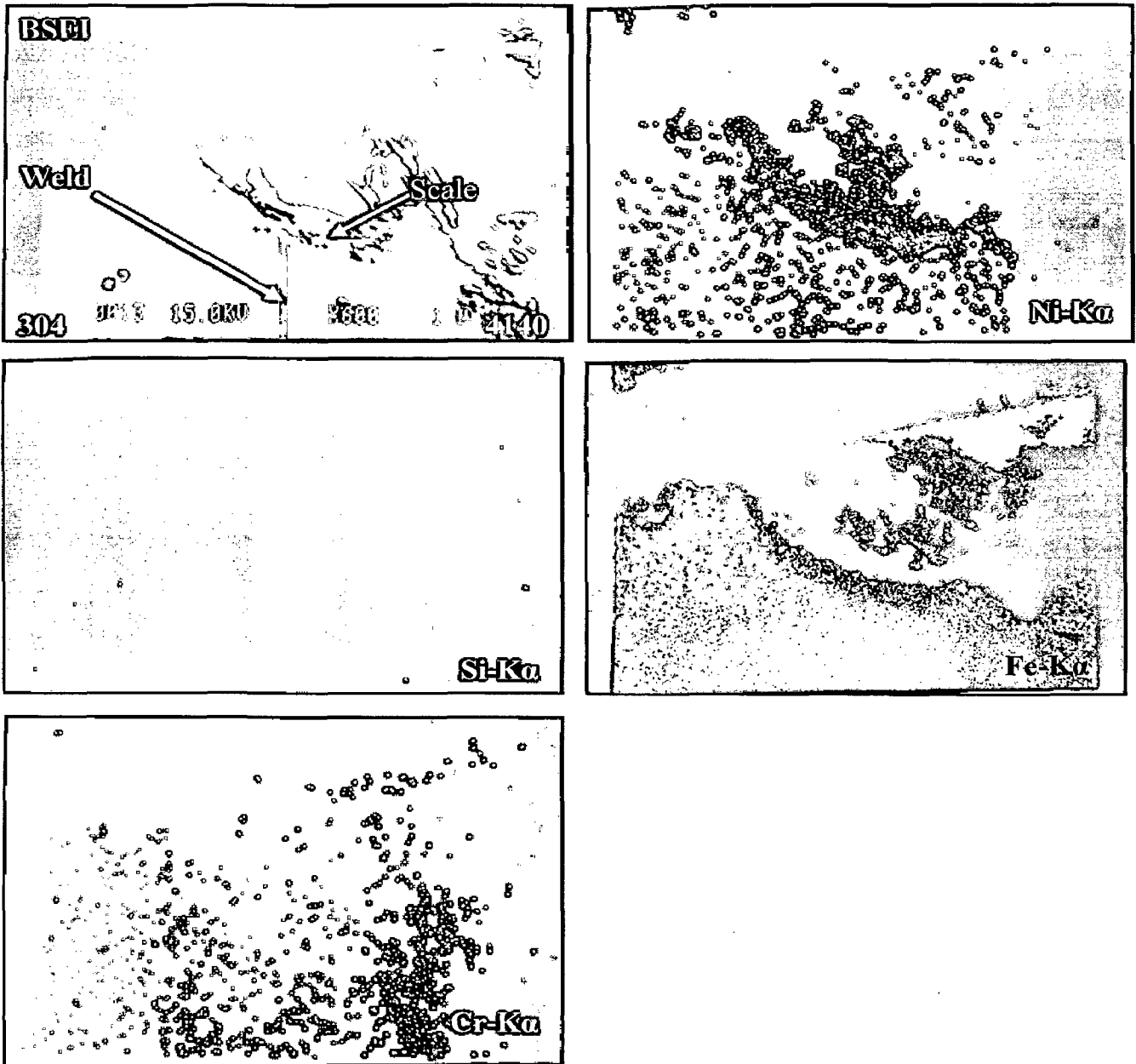


Fig. 6.34(B) BSEI and elemental X-ray mapping of the cross-section of dissimilar weldment made by AISI 4140 and AISI 304 by keeping burn off length 5mm, subjected to cyclic oxidation in Na_2SO_4 (50%) and NaCl (50 %) at 550°C for 50 cycles, 600 X.

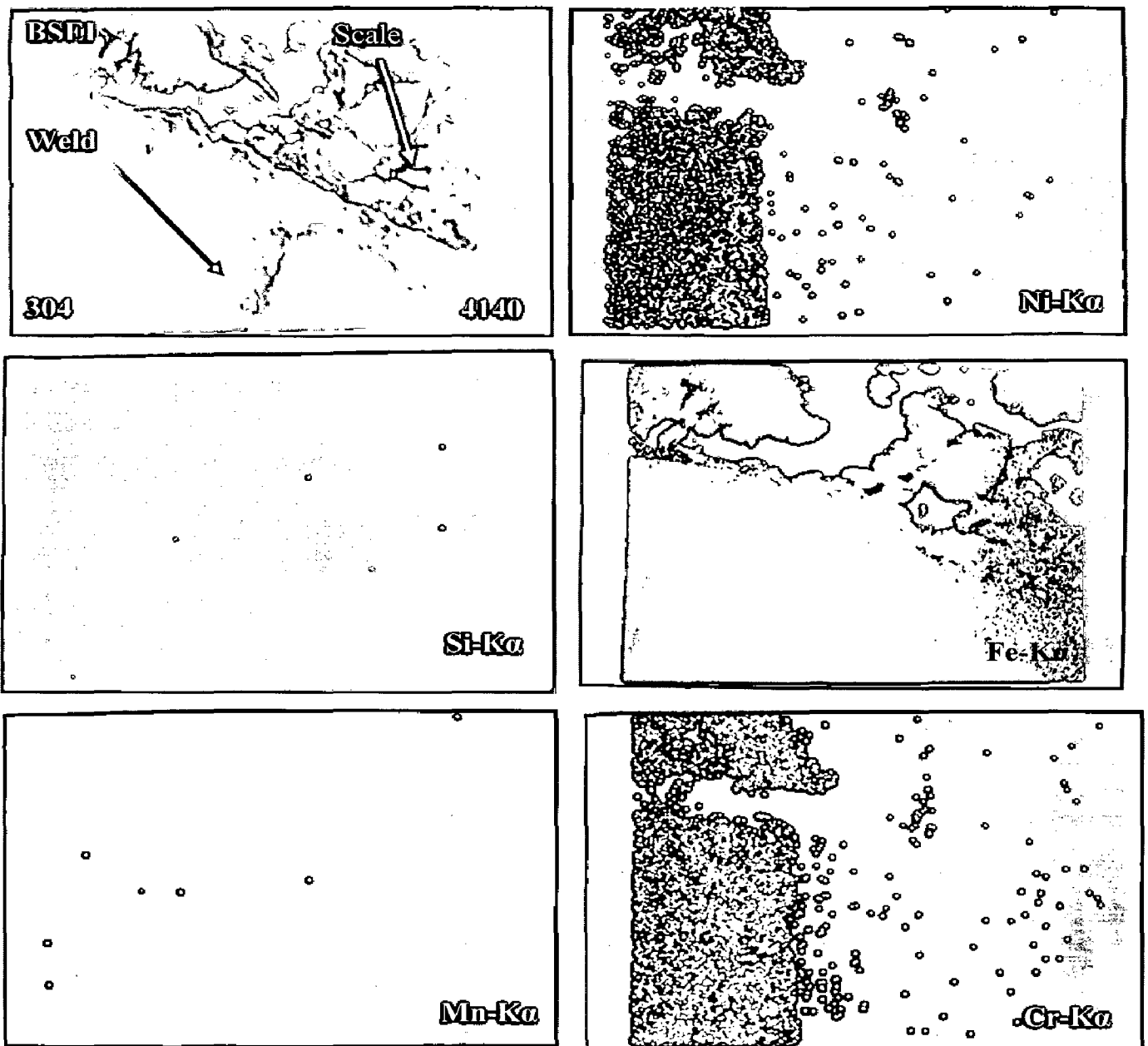


Fig. 6.34(C) BSEI and elemental X-ray mapping of the cross-section of dissimilar weldment made by AISI 4140 and AISI 304 by keeping burn off length 7mm, subjected to cyclic oxidation in Na_2SO_4 (50%) and NaCl (50 %) at 550°C for 50 cycles, 250 X.

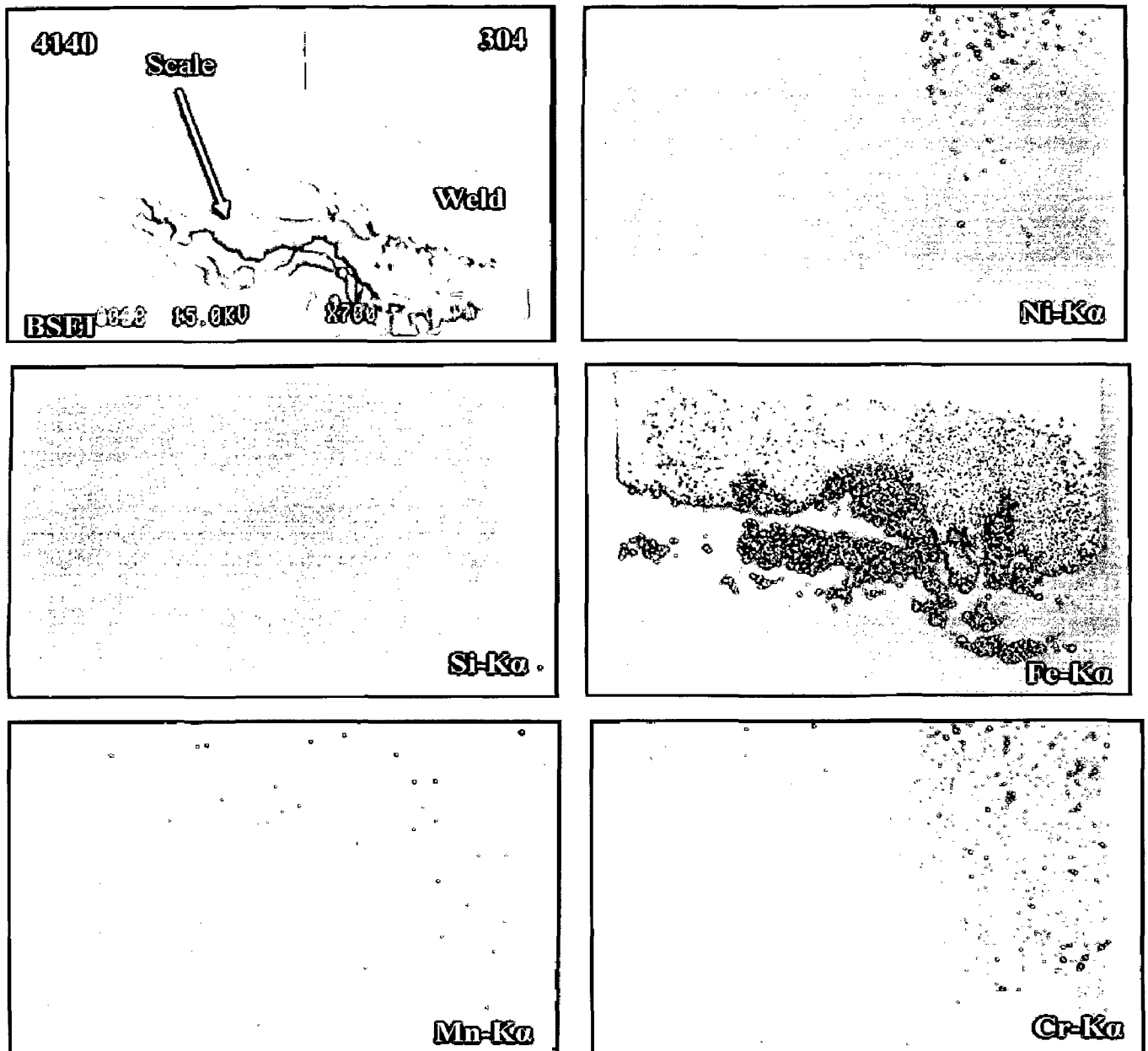


Fig. 6.34(D) BSEI and elemental X-ray mapping of the cross-section of dissimilar weldment made by AISI 4140 and AISI 304 by keeping burn off length 9mm, subjected to cyclic oxidation in Na₂SO₄ (50%) and NaCl (50 %) at 550⁰C for 50 cycles, 700 X.

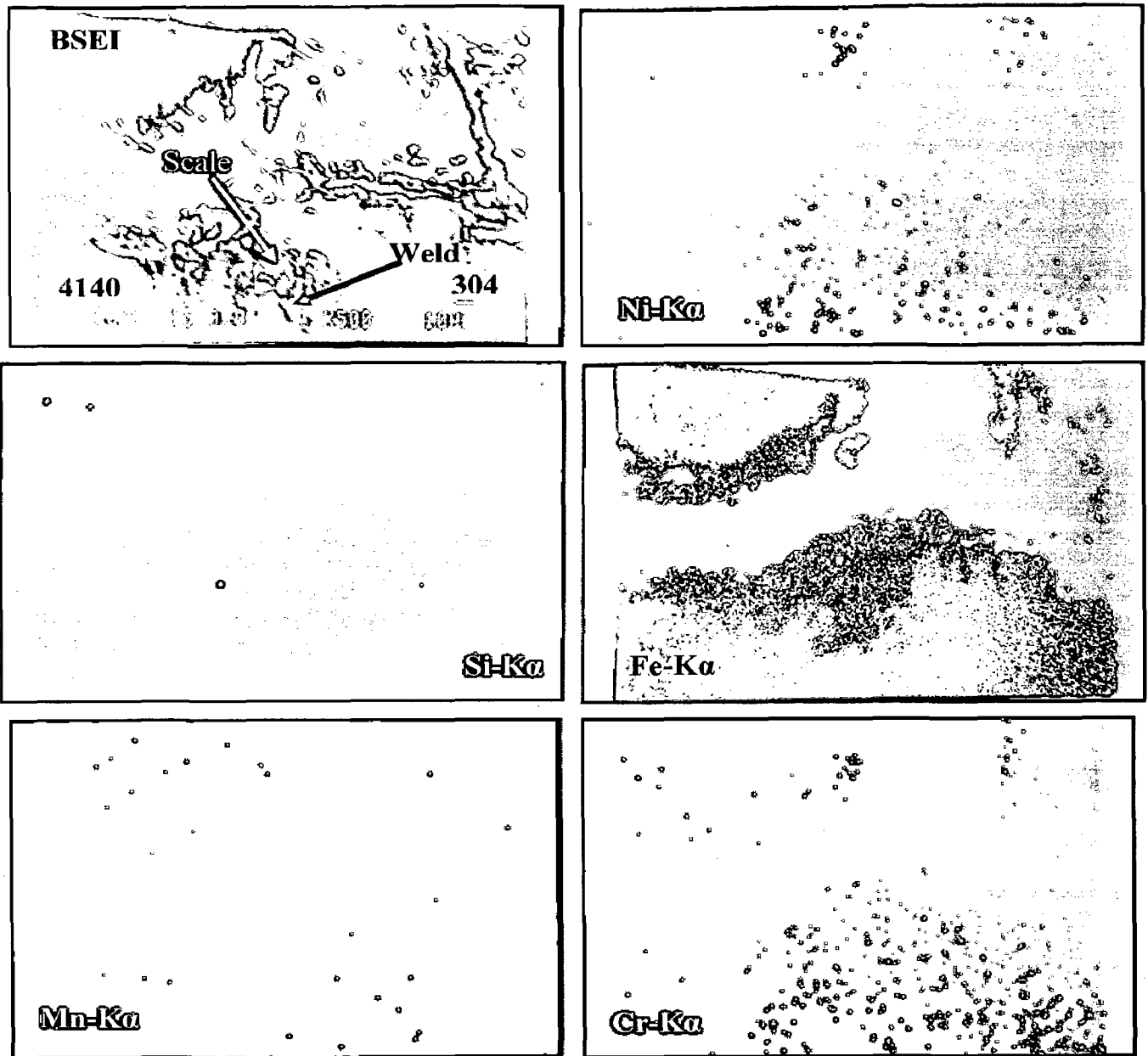


Fig. 6.34(E) BSEI and elemental X-ray mapping of the cross-section of dissimilar weldment made by AISI 4140 and AISI 304 by keeping burn off length 12mm, subjected to cyclic oxidation in Na_2SO_4 (50%) and NaCl (50 %) at 550°C for 50 cycles, 500 X.

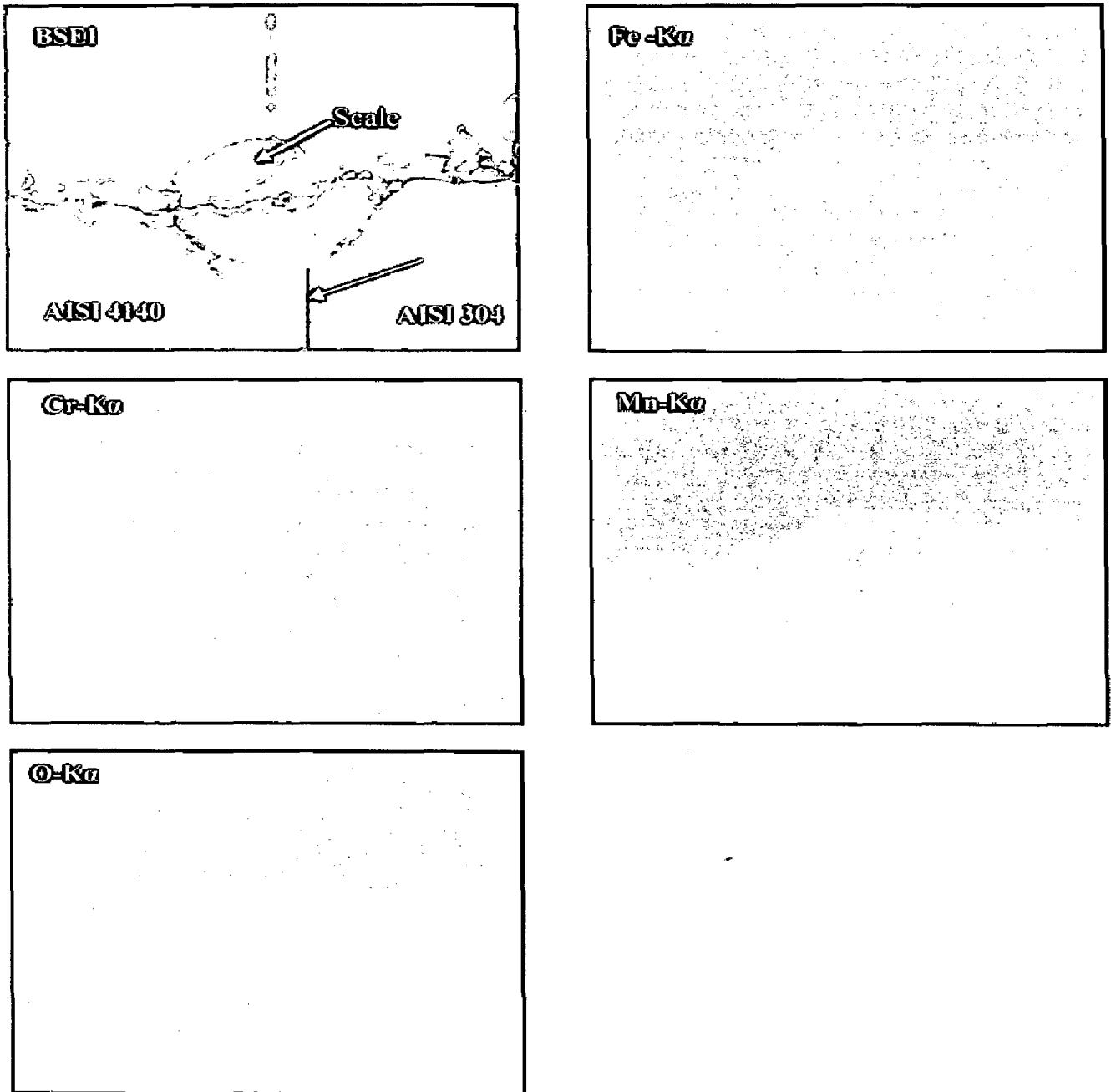


Fig. 6.35 BSEI and X-ray mappings of the cross-section of dissimilar friction welded AISI 304 and AISI 4140 by keeping burn-off length 5mm exposed to Na_2SO_4 - NaCl (50%) at 550°C for 50 cycles.

6.2. Discussion

6.2.1 Friction Welded Dissimilar Metals Exposed to $\text{Na}_2\text{SO}_4 + \text{V}_2\text{O}_5$ (60%)

Thermogravimetric graph shows the weight gain curves, tendency for oscillation type reaction weight gain rate has been observed (Fig.6.2 and 6.3) perhaps due to changes in reaction rate which are associated with the formation of a laminated, inner-oxide layer, made up of bands of fine and coarse grain spinel oxide, as suggested by M.H.Hurdus et al [1990]. The weight gain graph for the dissimilar weldment exposed at 700 and 900 °C shown in Fig. 6.3. The weight gain graph shows that the weight gained by weldment increases continuously, although the rate of increase is relatively high during the initial period of exposure. The Na_2SO_4 -60% V_2O_5 will combine and form NaVO_3 as proposed by Kolta et al [1972]: $\text{Na}_2\text{SO}_4 + \text{V}_2\text{O}_5 = 2\text{NaVO}_3 (1) + \text{SO}_2 + 1/2\text{O}_2$. This NaVO_3 acts as a catalyst and also serves as an oxygen carrier to the base alloy, which will lead to the rapid oxidation of the basic elements and form the protective oxide scales. Studies on the hot corrosion of Ni at lower temperatures in the presence of Na_2SO_4 and SO_3 have shown the formation of nickel sulfide to be the prime mode of degradation which results from initial formation Na_2SO_4 - NiSO_4 molten phase [K.P. Lillerud et al (1984) and A.K. Misra et al (1984)]. The rapid increase in weight gain during the initial period was also reported by Gitanjaly et al and Tiwari et al [Gitanjaly (2003) and Tiwari et al (1997)] in their studies of the hot corrosion behaviour of nickel-based super-alloy. The slower increase in weight gain after an initial rise is probably due to the simultaneous growth and dissolution of oxide scale in the molten salt due to the reaction $\text{Cr}_2\text{O}_3 + 4\text{NaVO}_3 + 3/2 \text{O}_2 \rightarrow 2\text{Na}_2\text{CrO}_4 + 2\text{V}_2\text{O}_5$ [Kofstad P (1988) and Swaminathan J et al (1993)]. Fryburg et al (1984)] have suggested that this Na_2CrO_4 gets evaporated as a gas. The observed intensive spalling/sputtering of the scale on the weldment can be attributed to severe strain developed due to the precipitation of Fe_2O_3 from the liquid phase and inter-diffusion of intermediate layers of iron oxide as has been reported by Sachs (1958).

It is observed that the thickness of scale is more on 4140 side than 304 sides. After completion of 50 cycles hot corrosion treatment, it is indicated that the effect of hot corrosion is more on 4140 side which also can be seen in the degree of scaling and spalling of scale on the 4140 side. Detachment of scale by means the formation of scale with in growing scale as a result of two-way flow of the reactants [A. Atkinson (1982)]. M.J.Graham (1984) demonstrated that oxygen is distributed into the inner region of a growing, adherent Cr_2O_3 scale even though the major transport process during oxidation is outward diffusion chromium. Also in the case of DMW the coefficient of thermal expansion differ for each base metal, weld and the scale, and so further stresses are generated during cooling which may affect adhesion property of the scale.

The XRD graph shows that the scale on (Fig. 6.4 - 6.6) hot corroded weldment has Fe_2O_3 as the main phase which increase with temperature of exposure and burn of length. Relatively weak peaks of Cr_2O_3 are also present. From EDAX data (Fig. 6.10 (A-L)) it can be inferred that, with increase in the burn- off length and hot corrosion temperature, the amount of Fe_2O_3 is higher in the scale on the base 4140 alloy and it keeps on decreasing as we move towards base 304 alloy sides. From the EDAX data it was observed that the scale on the weld zone as well as both HAZ consisting higher percentage of Fe_2O_3 and Cr_2O_3 when the weldment exposed at 700 and 900 C shown in Fig 6.11 (A,B). The cumulative EDAX data shows the effect of burn of length and temperature on oxide formation in the weldment as indicated in Fig 6.11 (C-H). With increase in the temperature of corrosion studies, the higher content of Cr_2O_3 and Fe_2O_3 in scale over the interface is observed which may be due to enrichment of this zone with Fe, Cr and Ni with continuous interdiffusion of elements during hot corrosion cycles. According to L.D.Paul et al (1991), in the molten salt environment, the resistance to corrosion for all the steels is less than that in air. This has been ascribed to presence of vanadium; sodium and sulfur

accelerate the corrosion of steels. Spalling may be one of the reasons for enhanced corrosion. Spalling is due to the oxides of Mo, which cause alloy-induced acidic fluxing [F.S. Pettit et al (1984)]. The formation of Na_2MoO_4 from MoO_3 that accumulates along the oxide scale has been reported by Fryburg et al. (1984). Na_2MoO_4 affects the melting of some discrete areas into a large molten phase and the molten oxide phase migrates across the sample, disrupting and fluxing the scale above it. This is further confirmed by the absence of Mo in the scale. Spalling in medium coal-fired boilers of this type to steel was also observed by Wang (1988), where more than 70% of the scale spalled during testing. The presence of chromium in the scale, along with iron oxide for T22 steel is consistent with the findings of Sadique et al (2000), who reported that Fe-Cr alloys in oxygen at high temperature form spinel (FeCr_2O_4) and Cr_2O_3 on the inner side and Fe_2O_3 on the outside of the scale.

Figure 6.12 (F) shows EPMA results further confirm the formation of Fe_2O_3 , Cr_2O_3 , NiO mainly in the cross section of scale on the weld interface when it exposed at 600°C . Also it was observed that the penetration of oxygen in the scale. Where as at 700 and 900°C the scale on the low alloy steel predominating as compare to stainless steel Fig 6.12 (I, K). EDAX analysis across the cross-section indicates mainly Cr, Fe and Ni in the weld interface Fig 6.12 (H, J and L). This Cr, Fe and Ni rich layer believed to have grown due to the diffusion across the weld interface to form oxides in the upper part of the scale.

6.2.2 Friction Welded Dissimilar Metals Exposed to $\text{K}_2\text{SO}_4 + \text{NaCl}$ (60%)

The corrosion kinetics shows that the hot corrosion weight gain curves, tendency for oscillation type reaction weight gain rate has been observed (Fig.6.14) perhaps due to changes in reaction rate which are associated with the formation of a laminated, inner-

oxide layer, made up of bands of fine and coarse grain spinel oxide, as reported by M.H:Hurdus et al [1990].

Temperature has been found to have pronounced effect on weight gain. Initial rate of weight gain was higher which slowly decreased showing parabolic behaviour. Based on the magnitude of weight gain DSW are found to undergo accelerated oxidation under cyclic conditions in this particular environment of K_2SO_4 and 60 % NaCl. Although the oxidation is accelerated yet not catastrophic as suggested by [Kofstad P [1988]. On comparing our results with that reported by Salisbury et al [1971], hot corrosion of DMW was found to behave in a way similar to corrosion of Fe base alloy with chromium less than 3%, in SO_2 -Ar atmosphere. DMW shows more degradation near the interface with the grains fully degraded as can be seen Fig. 6.13 (i-iii).

After completion of 50 cycles hot corrosion treatment, it is indicated that the effect of hot corrosion is more on 4140 side which also can be seen in the degree of scaling and spalling of scale on the 4140 side was high.

Intensive spalling/sputtering of the scale of the weldment can be attributed by the following reason:

1. Coefficient of thermal expansion differs for each base metal, weld and the scale, which generate the stress.
2. Severe strain developed due to the precipitation of Fe_2O_3 from the liquid phase and inter-diffusion of intermediate layers of iron oxide as reported by Sachs [1958].
3. Formation of scale with in the growing scale as a result of two-way flow of the reactants such as oxygen which is distributed into the inner region of a growing, adherent Cr_2O_3 scale and the outward diffusion of chromium from bar metal to the scale as suggested by A. Atkinson [1982] and M.J.Graham [1984].

From the SEM/EDAX data, the percentage of change in Fe_2O_3 in the scale remain constant from base metal(4140) to 4140-HAZ and tend to decreases from 4140-HAZ to weld zone of the weldment. This trend is almost same for all the burn-off length and temperature of exposure. It further decreases from weld zone to 304-HAZ at 500 °C and increases from 304-HAZ to base 304 (Fig 6.19 (A-C). At 550 °C exposure temperature it increases from weld zone to 304-HAZ and remain constant from 304-HAZ to base metal (304) for B12 and the same decrease from 304-HAZ to base metal (304) for B5 (Fig 6.19 E). At 600 °C the scale on the low alloy steel 4140 side mainly consist of Fe_2O_3 and it decreases as we move towards the 4140-HAZ, weld zone and 304-HAZ and remain constant from 304-HAZ to base metal (304) for B5 and the same decrease from 304-HAZ to base metal (304) for B12 Fig 6.19 (G-J). At 500 °C exposure temperature for B5 and B12, the amount of Cr_2O_3 in the scale of 304-HAZ is maximum and it decreases as we move towards the base metals. At 550 °C, the amount of Cr_2O_3 in the scale on weld interface is maximum and it decreases as we move towards base metal 4140 for both B5 and B12, whereas the same decreases as we move from weld to 304-HAZ. The percentage of variation Fe_2O_3 and Cr_2O_3 on the different zone for different temperature of exposure and burn-off length as can be seen Fig 6.19 (A-J). The cumulative EDAX data shows the effect of burn of length and temperature on oxide formation in the weldment as indicated in Fig 6.19 (K-N).

The galvanic type coupling of the welded joints has accelerated corrosion in the presence of an electrolyte such as molten salt. This is evidenced by the following: The weld metal undergoes little damage due to the presence of considerable amount of chromium which can form a strong protective layer of Cr_2O_3 . This layer may provide a high resistance for the hot corrosion attack to initiate. However, on the base metals (4140 and 304) steel side,

initiation time is negligible and hence a higher attack is noticed on the HAZ on both sides of DMW joints.

EPMA analysis shows that the scale mainly consisting Fe, Cr, Ni (Fig 6.20 (A-C), which may be attributed to diffusion of these element during friction welding as well as hot corrosion cycles. Figure 6.21 (A) shows the EPMA cross section on the weldment when it exposed at 500 °C. It was observed that the formation of continuous layer of chromium Fe, Cr, and oxygen. Depletion of Cr adjacent HAZ of 304 is indicated by the EPMA analysis of hot corroded sample at 600 °C might have been ascribed diffusion of Cr towards the low alloy steel side Fig 6.21 (B) which also proved by cross section EDAX analysis across the weldment Fig 6.21 (C).

6.2.3 Friction Welded Dissimilar Metals Exposed to Na₂SO₄ (40%) + K₂SO₄ (40%) + NaCl (10%) + KCl (10%)

From the hot corrosion weight gain curves tendency for oscillation type reaction weight gain rate has been observed (Fig.6.23) perhaps due to changes in reaction rate which are associated with the formation of a laminated, inner-oxide layer, made up of bands of fine and coarse grain spinel oxide, as suggested by M.H.Hurdus et al [1990].

Temperature has been found to have pronounced effect on weight gain. Initial rate of weight gain was high which slowly decreased resulting parabolic behaviour. Based on the magnitude of weight gain DSW are found to undergo accelerated oxidation under cyclic conditions in this particular environment of 40 wt% K₂SO₄, 40 wt% Na₂SO₄, 10 wt% KCl, and 10 wt% NaCl as also reported by Kofstad P [1988]. DMW shows more degradation near the weld interface with the grains fully degraded as can be seen Fig 6.22 (i-iv).

Intensive spalling/sputtering of the scale of the weldment can be attributed to the following reason: 1. Coefficient of thermal expansion differs for each base metal, weld and the scale, which generate the stress. 2. Severe strain developed due to the precipitation

of Fe_2O_3 from the liquid phase and inter-diffusion of intermediate layers of iron oxide as reported by Sachs [1958]. 3. Formation of scale with in the growing scale as a result of two-way flow of the reactants such as oxygen which is distributed into the inner region of a growing, adherent Cr_2O_3 scale and the outward diffusion of chromium from base metal to the scale as suggested by A. Atkinson [1982] and M.J.Graham [1984].

FeO is not detected in the scale of the weldment exposed to all the three temperatures. This may be due to increase in the Cr_2O_3 content of scale on the weldment. Similar observation has been made by Moretimer et al [1969]. The iron oxidized in preference of Cr in the alloy 4140 where Cr content is only 1.1% and the part of this Cr is present as carbide. This amount of Cr is not sufficient for forming a protective layer of Cr_2O_3 on the surface. The diffusion of Cr from interior to the outer surface is not much as diffusion coefficient of Cr is small. Oxygen diffuses through the outer scale of iron oxides and reacts with chromium to form Cr_2O_3 at the inner layers which exist as particles and not as continuous layers. The amount of Fe_2O_3 is higher in the scale of weldment where as the presence of chromium in the inner scale has been observed for all the temperatures of exposure.

NiFe_2O_4 and NiCr_2O_4 were observed as a minor constituent. In the XRD analysis of the surface, sodium chloride or as chlorides of iron, chromium, molybdenum were not observed. It is well known that chlorides of iron, chromium etc., are volatile. So they might have escaped from the surface or subsurface leaving behind voids, pits, etc.

The dissimilar weldment suffered different corrosion rate over base metals (4140 and 304) and their interface. Heat affected zones were predominantly attacked along weld interface.

Corrosion product was found to be fragile and prone to spalling. Corrosion products contained Fe_2O_3 and Cr_2O_3 with small amount of SO_3 and MoO_3 in many cases

as identified by M.A. Uusitalo et al [2004]. Identification of these elements is possible, but quantitative information on sulfur or molybdenum content of the scales cannot be obtained because of over lapping peaks (S $K\alpha$ and Mo $L\alpha$) in XRD analyses Fig 6.24 (A,B).

From the SEM/EDAX analysis for all the burn-off length and temperature of exposure, Fe_2O_3 is found to be the predominant phase in the scale on the weldment. At 600 °C hot corrosion the scale on the weldment contains plenty of Fe_2O_3 (88-92 %) and the Cr_2O_3 is not as much as at 500/550 C (Fig 6.26. A-F). It was observed that the weld interface consisting higher percentage of Fe_2O_3 and Cr_2O_3 as compared both basen metals mabe be due to diffusion of Fe and Cr across the weldment. EDAX analysis of the scale on the weldment for the three temperatures of exposure shows some unreacted salt as Na_2O , SO_3 and K_2O . The cumulative EDAX data shows the effect of burn of length and temperature on oxide formation in the weldment as indicated in Fig 6.26 (G-N).

The active oxidation process took place in molten salt hot corrosion studies. The formed metal chlorides were oxidized inside the salt layer and part of the released chlorine diffused back to the salt/metal interface. The low allow steel side of the weldment suffered severe corrosion where the Fe_2O_3 is dominating all the cases.

It is observed that the thickness of scale is more on 4140 side than 304 sides. After completion of 50 cycles hot corrosion treatment, it is indicated that the effect of hot corrosion is more on 4140 side which also can be seen in the degree of scaling and spalling of scale on the 4140 side.

EPMA analysis shows that the scale on the weldment consisting mainly Fe, Cr and Ni shown in Fig (6.27 (A-F)). Further EPMA has revealed the penetration of oygen into the inner scale on the weld interface of dissimilar weldment when it exposed at 550 °C as shown in Figs. 6.28 (A,B) leading to internal oxide formation thereby denuding the weld interface of reactive elements. This, in turn, leads to the formation of base-metal oxides at the salt-metal interface.

BSEI and X-ray mappings of the cross-section of dissimilar friction welded AISI 304 and AISI 4140 by keeping burn-off length 12 mm exposed to Na₂SO₄ (40%) + K₂SO₄ (40%) + NaCl (10%) + KCl (10%) at 600 °C for 50 cycles shown in Fig 6.28 (B). It was observed that intergranular / selective oxidation attack is indicated by the EPMA analysis. This may be attributed to the accelerated oxidation under cyclic conditions in this particular environment of 40 wt% K₂SO₄, 40 wt% Na₂SO₄, 10 wt% KCl, and 10 wt% NaCl as also reported by Kofstad P (1988).

6.2.4 Friction Welded Dissimilar Metals Exposed to Na₂SO₄ (50%) + NaCl (50%)

From the oxidation studies weight gain curves tendency for oscillation type reaction weight gain rate has been observed (Fig.6.30) perhaps due to changes in reaction rate which are associated with the formation of a laminated, inner-oxide layer, made up of bands of fine and coarse grain oxide spinel, as suggested by M.H.Hurdus et al [1990]. Temperature has been found to have pronounced effect on weight gain. Initial rate of weight gain was higher which slowly decreased showing parabolic behaviour. Based on the magnitude of weight gain DSW are found to undergo accelerated oxidation under cyclic conditions in this particular environment of Na₂SO₄ + 50 wt% NaCl as also reported by Kofstad P [1988]. DMW shows more degradation near the weld interface with the grains fully degraded as can be seen Fig.6.29 (i,ii). Intensive spalling/sputtering of the scale of the weldment can be attributed by the following reason: 1. Coefficient of thermal expansion differs for each base metal, weld and the scale, which generate the stress. 2. Severe strain developed due to the precipitation of Fe₂O₃ from the liquid phase and inter-diffusion of intermediate layers of iron oxide as reported by Sachs [1958]. 3. Formation of scale within the growing scale as a result of two-way flow of the reactants such as oxygen which is distributed into the inner region of a growing, adherent Cr₂O₃ scale and the

outward diffusion of chromium from bar metal to the scale as suggested by A. Atkinson [1982] and M.J.Graham [1984].

It is widely agreed that the hot corrosion weight gain will be more severe when the temperature is higher than the melting point of salt deposits. Although the testing temperature in this study is lower than the melting point of salt deposit (50 wt % Na₂SO₄ + 50 wt % NaCl (600 °C), the corrosion rate is at least three orders of magnitude higher than that of air oxidation. Corrosion morphology of the weldment shows that the weld interface is more prone to formation of fragile scale than base metals may imply that NaCl coating plays an important role in hot corrosion behavior, even at temperatures lower than 600 °C as also reported by A.U. Seybolt (1970), A.U. Seybolt (1970) and Y. Shinata (1987). Hot corrosion requires a molten salt to be in contact with the specimen. If there are no molten phases, the corrosion rate observed may be low.

The mixtures with salt mixture of 50 wt % Na₂SO₄ + 50 wt % NaCl were partially melted at 500-550 °C, indicating that Na₂SO₄ acidic- and basic-fluxing mechanism which would induce accelerated oxidation of weldment. Whereas at the exposure temperature of more than 600 C, the salt mixtures exist in a completely liquid phase where the fast evaporation characteristics of NaCl led to a residue of solid Na₂SO₄ on the weldment surface as suggested by Charng-Cheng Tsaura et al [2005]. Many researchers have pointed out that the formation of sodium chromate, Na₂CrO₄, could result from oxychloridation in which chromium or chromium oxide reacts with NaCl and oxygen even when the temperature is lower than the melting point of salt deposits [C.J. Wang (2002), M.K. Hossain et al (1978) and N. Hiramatsu et al (1989)]. As the Na₂CrO₄ is formed, the salt will wet the specimen surface due to the low-melting eutectic NaCl-Na₂CrO₄ (500 °C) and lead to a mechanism of hot corrosion dominated by molten salt. Oxychloridation, in which NaCl reacts with metal and the oxygen dissolved in molten

salts to form metal oxides, sodium-containing oxides, and chlorine, is believed to be the initial reaction of NaCl-induced hot corrosion. There are three ways that chlorine may be further reacted in this study [Y. Bourhis et al (1975) and C.J. Wang (2002)]:

(1) Escaped to atmosphere

(2) Dissolved into Cr_2O_3 lattice increasing the content of cation vacancies and accelerating the oxidation of alloy

(3) Reacted with alloy substrate to form metal chlorides.

The metal-chloride generated by the reaction between metal and chlorine produced from the oxychloridation evaporates, diffuses out and oxidizes in a place with appropriate partial pressure of oxygen to form metal-oxide and chlorine which is supported by XRD and EDS shown in Fig 6.33(H,I). From XRD analysis it was observed that Fe_2O_3 in the scale is more predominant which increases with temperature. In molten salt environment, the intensity of Fe_2O_3 , Cr_2O_3 were observed to be higher as compare to air oxidation Fig 6.31(A,B).

The released chlorine is returned back to the process again. Hence, during the cyclic chloridation/oxidation reaction process, the chlorine acts as catalyst to accelerate corrosion [N. Hiramatsu et al (1989)]. SEM/EDAX results shows that the scale on the interface of the weldment is more fragile and spalling in nature. The cumulative EDAX data shows the effect of burn of length and temperature on oxide formation in the weldment as indicated in Fig 6.33 (J-N).

The presence of NaCl in the mixtures of NaCl/ Na_2SO_4 could initiate attack in high chromium content in the interface which is diffuse from austenitic stainless steel to low alloy steel as reported by Johnson et al [D.M. Johnson et al (1975)] as seen in Fig. 6.33 (D) and 6.35. The kinetics of hot corrosion with NaCl/ Na_2SO_4 mixtures shows unstable weight change growth rate and much more severe hot corrosion than is observed with

simple oxidation. In a molten salt environment, sulfur was incorporated into scale and proceeds to a sulfide formation in the alloy substrate. Therefore, as the formation of protective oxide scale was inhibited by the presence of NaCl, chlorides and sulfides tend to form in the alloy substrate as indicated leading to the propagation of hot corrosion as suggested by Charng-Cheng Tsaura et al [2005].

Figure 6.35 shows EPMA results further confirm the formation of Fe₂O₃, Cr₂O₃, MnO mainly in the cross section of scale on the weld interface when it exposed at 550 °C. Further EPMA has revealed the penetration of oxygen into the inner scale on the weld interface of dissimilar weldment. Also it was noted that intergranular / selective oxidation attack is indicated by the EPMA analysis. This may be attributed that the presence of NaCl in the mixtures of NaCl/Na₂SO₄ could initiate attack in high chromium content in the interface which is diffuse from austenitic stainless steel to low alloy steel as reported by Johnson et al [D.M. Johnson et al (1975)].

CHAPTER 7

HOT CORROSION STUDIES OF EBW AND TIG WELDED DISSIMILAR METALS IN MOLTEN SALT ENVIRONMENT

This chapter deals with the critical examination of corrosion products and the behaviour of electron beam welded and tungsten inert gas welded dissimilar weldment (AISI 4140 and AISI 304). The hot corrosion studies were performed on the weldments exposed at the temperature 600 °C under the following mixture of molten salt for 50 cycles.

(i) $\text{Na}_2\text{SO}_4 + \text{V}_2\text{O}_5$ (60%)

(ii) $\text{K}_2\text{SO}_4 + \text{NaCl}$ (60%)

The samples were visually examined at the end of each cycle for any change in the colour, lustre, adherence of scale to the substrate and spalling tendency. The weight change measurements were made at the end of each cycle. Efforts have also been made to understand the mechanism of corrosion wherever possible.

The corrosion products were analysed with the help of XRD, SEM/EDAX and EPMA. The results for different environment of molten salt mixture have been reported under different subheadings. In view of comparison the thermogravimetric data of each environment at 600 °C exposure of temperature were recorded. The parabolic rate constants and scale thickness values have been evaluated after 50 cycles of exposure.

7.1 RESULTS

7.1.1 Electron Beam Weldment exposed to $\text{Na}_2\text{SO}_4 + \text{V}_2\text{O}_5$ (60%) and $\text{K}_2\text{SO}_4 + \text{NaCl}$ (60%) environment at 600 °C

This subheading deals with the critical examination of corrosion products of electron beam welded dissimilar AISI 4140 and AISI 304 metals.

7.1.1.1 Visual Examination

In the hot corrosion study of the EBW welded 4140 low alloy steel and 304 Stainless steel weldment under $\text{Na}_2\text{SO}_4 + \text{V}_2\text{O}_5$ (60%) , after first cycle indicated a light brown scale having dark brown patches. These numbers of dark brown colour patches are more on 4140 side than 304 side. After completion of 10 cycles the scale becomes thicker and with light ash colour on the weld zone. Whereas on 304 side the scale had dark brown patches observed where the scale go spalled out. With further increase in number of cycles, the whole scale turns to darke brown colour. The color and texture of scale at weld region was different from that on the base metals.

In the hot corrosion study of the electron beam welded 4140 low alloy steel and 304 Stainless steel weldment, after first cycle the white colour salt coating changed in to black colour with some small brown spots seen on the low alloy steel side. Negligible reaction has taken place on the stainless steel side. After completion of 15 cycles the scale becomes thicker and is of black colour on low alloy steel and most of it scale spalled out. Whereas on 304 sides the scale was dark ash colour and adherent. With further increase in number of cycles, most of the scale spalled out from low alloy steel side, leaving behind brown colour subscales. The color and texture of scale at weld region was different from that on the base metals. Fig.7.1 (a), (b) shows the typical macrographs of hot corroded samples after 50 cycles.

7.1.1.2 Thermogravimetric Data

The plots of cumulative weight gain (mg/cm^2) as a function of time (number of cycles) for electron beam weldment exposed at the temperature of $600\text{ }^\circ\text{C}$ in Na_2SO_4 (40%) + V_2O_5 (60%) and K_2SO_4 + NaCl (60%) up to 50 cycles are shown Fig 7.2. The weldment showed the high weight gain when it exposed under molten salt mixture of K_2SO_4 + NaCl (60%) as compare to Na_2SO_4 (40%) + V_2O_5 (60%) experiments. The parabolic rate constants, K_p were shown in Table 7.1.

Table 7.1 Values of parabolic rate constant K_p

Welding Technique	Environment	K_p ($10^{-6}(\text{gm}^2\text{Cm}^{-4}\text{S}^{-1})$)
Electron Beam Welding	Na_2SO_4 + V_2O_5 (60%)	7.720
	K_2SO_4 + NaCl (60%)	37.850

7.1.1.3 X-ray Diffraction Analysis

The XRD patterns for the hot corroded surfaces of electron beam welded samples exposed to the Na_2SO_4 - 60% V_2O_5 and K_2SO_4 + NaCl (60%) environment at exposure temperature of $600\text{ }^\circ\text{C}$ after 50 cycles are shown in Fig. 7.3. It is evident from the diffraction patterns that the hot corroded weldment has Fe_2O_3 as the main phase along with relatively weak peaks due of Cr_2O_3 . The peak intensity of these phases under Na_2SO_4 - 60% V_2O_5 is higher as compared to exposed in the molten salt of K_2SO_4 + NaCl (60%).

7.1.1.4 Scale Thickness Measurement

The samples were cut across the cross-section after exposure to Na_2SO_4 - 60% V_2O_5 and K_2SO_4 + NaCl (60%) molten salt at $600\text{ }^\circ\text{C}$ for 50 cycles and mounted. The scale thickness values were measured from SEM back scattered images shown in Fig. 7.4. The exact oxide scale thickness could not be measured for all the weldments due to intense spalling and sputtering. The SEM micrograph shows the fragile and cracked scale for all the weldment.

7.1.1.5 SEM/EDAX Analysis

Surface Morphology

SEM micrographs of the electron beam welded specimens showing surface morphology after cyclic hot corrosion under Na_2SO_4 -60% V_2O_5 for 50 cycles at 600 °C, are shown in Fig.7.5. The micrographs to surfaces of all the corroded weldments clearly indicates a rough scale. The oxide grains of the scale over the weld zone were generally much fine-grained as compared to those over HAZ and base metal region of dissimilar weldment. The EDAX analysis of the scale for the weldment shows Fe_2O_3 to be the predominant phase, with small amounts of Cr_2O_3 , NiO, MnO and SiO_2 . From EDAX analysis across the hot corroded weldment at 600 °C in given molten salt indicate higher concentration of Fe_2O_3 is in the scale over the weld zone as well as HAZ of low alloy steel side, Where as it decreases as one move to the stainless steel side. Also it was observed that the scale on the HAZ of stainless steel mainly consisting of Cr_2O_3 . The same trend was observed when exposed under $\text{K}_2\text{SO}_4 + \text{NaCl}$ (60%) at 600 °C, are shown in Fig 7.6.

7.1.1.6 EPMA Analysis

BSEI and X-ray mapping for cross-section of corroded dissimilar weldment exposed to different molten salt environment of Na_2SO_4 -60% V_2O_5 and $\text{K}_2\text{SO}_4 + \text{NaCl}$ (60%) at 600 °C for 50 cycles. The EPMA of the cross-section of corroded dissimilar weldment made by electron beam welding by exposing different environment indicates that thin scale is mainly consisting of Fe, Cr and O coexisting Fig. 7.7. Cross sectional EDAX analysis indicated that the weld zone contains enrichment of Cr, Ni, Fe and C due to diffusion of Fe and C from 4140 side and Cr and Ni from 304 side Fig 7.8.

7.1.2 TIG Weldment exposed to $\text{Na}_2\text{SO}_4+60\%\text{V}_2\text{O}_5$ and $\text{K}_2\text{SO}_4 + \text{NaCl}$ (60%) environment at 600 °C

This subheading deals with the critical examination of corrosion products of TIG welded dissimilar weldment made by AISI 4140 and AISI 304. The hot corrosion studies were performed on the weldments exposed at the temperature from 600 °C under the $\text{Na}_2\text{SO}_4-60\%\text{V}_2\text{O}_5$ and $\text{K}_2\text{SO}_4 + \text{NaCl}$ (60%) mixture of molten salt for 50 cycles.

7.1.2.1 Visual Examination

In the hot corrosion study of the TIG welded 4140 low alloy steel and 304 Stainless steel weldment under $\text{Na}_2\text{SO}_4 + \text{V}_2\text{O}_5$ (60%) , after first cycle indicated a yellowish brown colour scale. After completion of 5 cycles the scale turns to black colour on the weldment and is prone to spalling. There is not much variation between different zone of the weldment. With further increase in number of cycles, the scale becomes darker in colour. After 50 cycles the color and texture of scale at weld region was different from that on the base metals.

In the case of $\text{K}_2\text{SO}_4 + \text{NaCl}$ (60%) mixture of molten salt the scale formed on the weldment is more fragile and spalled out. The reaction on the HAZ of both sides appeared to be that on more as compare the base metals. After first cycle the scale is of greenish white colour. After 6 cycles the whole surface become reddish brown dots was appeared on the green colour scale. With increase number of cycles the scale becomes red and black patches were observed on the weld zone as well as HAZ. Fig.7.9 (a), (b) shows the typical macrographs of hot corroded samples after 50 cycles.

7.1.2.2 Thermogravimetric Data

The plots of cumulative weight gain (mg/cm^2) as a function of time (number of cycles) for TIG weldment at the temperature of 600 °C in Na_2SO_4 (40%) + V_2O_5 (60%) and $\text{K}_2\text{SO}_4 + \text{NaCl}$ (60%) up to 50 cycles are shown Fig 7.10. The weldment showed the more weight gain when exposed under molten salt mixture of $\text{K}_2\text{SO}_4 +$

NaCl (60%) as compared to Na₂SO₄ (40%) + V₂O₅ (60%). The parabolic rate constants, K_p for TIG weldment are shown in Table 7.2.

Table 7.2 Values of parabolic rate constant K_p

Welding Technique	Environment	K _p (10 ⁻⁶ (gm ² Cm ⁻⁴ S ⁻¹))
Tungsten Inert Gas Welding	Na ₂ SO ₄ + V ₂ O ₅ (60%)	5.92
	K ₂ SO ₄ + NaCl (60%)	35.510

7.1.2.3 X-ray Diffraction Analysis

The XRD patterns for the hot corroded surfaces of TIG welded dissimilar metals exposed to the different environment of Na₂SO₄– 60% V₂O₅ and K₂SO₄ + NaCl (60%) at 600 °C after 50 cycles are shown in Fig. 7.11. It is evident from the diffraction patterns of the hot corroded weldment under both environments consisting Fe₂O₃ as the main phase along with relatively weak peaks of Cr₂O₃, (Cr,Fe)₂O₃, NiFe, NiFe₂O₄ and NiCr₂O₄.

7.1.2.4 Scale Thickness Measurement

The TIG welded samples were cut across the cross-section after exposure to Na₂SO₄– 60% V₂O₅ and K₂SO₄ + NaCl (60%) molten salts at 600 °C for 50 cycles and mounted. The scale thickness values were measured from SEM back scattered images shown in Fig. 7.12. The exact oxide scale thickness could not be measured for all the weldments due to intense spalling and sputtering. The SEM micrograph shows the fragile and cracked scale for all the weldment.

7.1.2.5 SEM/EDAX Analysis

SEM micrographs of the TIG welded specimens showing surface morphology after cyclic hot corrosion under Na₂SO₄ + 60% V₂O₅ for 50 cycles at 600 °C, are shown in Fig.7.13. The micrographs to surfaces of all the corroded weldment clearly indicates the presence of fragile spalling behaviour of the scale. The EDAX analysis of the scale on the weldment shows Fe₂O₃ to be the predominant phase, with small amounts of Cr₂O₃,

NiO, MnO and SiO₂. It was observed that the higher percentage of MoO₃ (11%) in the scale on the weld zone of the dissimilar weldment. Whereas in the case of K₂SO₄ + NaCl (60%) molten salt environment, the percentage of Fe₂O₃ obtained over the scale on the weldment follows the same trend like the above said environment. Also it was noted that MnO of the scale on the weld zone shown is higher as compared to the one on base metals Fig 7.14.

7.1.2.6 EPMA Analysis

BSEI and X-ray mapping for cross-section of corroded dissimilar weldment exposed to different molten salt environment of Na₂SO₄-60%V₂O₅ and K₂SO₄ + NaCl (60%) at 600 °C for 50 cycles. The EPMA of the cross-section of corroded dissimilar weldment made by TIG welding by exposing different environment indicates that scale is mainly consisting of Fe, Cr and Ni. Figure 7.15 (A and B) shows the X- ray mapping and cross sectional EDAX for TIG welded sample of AISI 304 and weld zone respectively and (Fig 7.16 (A and B) shows the weld zone and AISI 4140 side for the same sample.

7.2 DISCUSSION

7.2.1 Electron Beam Welding

Investigation on the effect of hot corrosion on Electron beam Welded AISI 4140 and AISI 304 dissimilar weldment exposed at 600 °C under different molten salt environments are given below.

(i) Na₂SO₄ + V₂O₅ (60%)

(ii) K₂SO₄ + NaCl (60%)

The electron beam welded dissimilar metals after cyclic oxidation in the given salt mixture at 600°C have shown parabolic behaviour Fig 7.2. It intense spalling of scale was observed from the weldment region for molten salt mixture of K₂SO₄ + NaCl (60%). Parabolic rate

constant in this environment is approximately 4.5 times than that of other environment ($\text{Na}_2\text{SO}_4 + \text{V}_2\text{O}_5$ (60%)).

The higher corrosion rate for dissimilar weldment under molten salt mixture of $\text{K}_2\text{SO}_4 + \text{NaCl}$ (60%) which may be due to the more active oxidation process. The metal chlorides must have got oxidized inside the salt layer and part of the released chlorine diffused back to the salt/metal interface. The low alloy steel side of the weldment suffered severe corrosion where the Fe_2O_3 is dominating phase in the scale.

Probably this factor is responsible for the higher weight gain under $\text{K}_2\text{SO}_4 + \text{NaCl}$ (60%) for this dissimilar weldment as compared to $\text{Na}_2\text{SO}_4 + \text{V}_2\text{O}_5$ (60%) environment. Accelerated corrosion observed in the environment of $\text{Na}_2\text{SO}_4 + \text{V}_2\text{O}_5$ (60%) up to the end of exposure may be in accordance with the findings of Misra (1986). During his hot corrosion studies for molybdenum containing nickel base alloy in Na_2SO_4 environment at 750-950°C, the author reported that higher the concentration of Mo, the sooner the melt would attain the MoO_3 activity necessary for the formation of solid NiMoO_4 and this would cause a decrease in the length of the period of accelerated corrosion. Lower percentage of Mo in the low alloy steel side for the present study might have increased the period of accelerating corrosion up to the end of 50 cycles.

The severe spalling of scale identical to the present study for similar type of steel i.e. T22 type of steel during hot corrosion in medium BTU coal gasifier environment has also been reported by D. Wang (1988) where more than 70% of the scale got spalled during their test. M.J.Graham demonstrated that oxygen is distributed into the inner region of a growing, adherent Cr_2O_3 scale even though the major transport process during oxidation is outward diffusion chromium. Also in the case of DMW the coefficient of thermal expansion differ for each base metal, weld and the scale, and so further stresses are generated during cooling which may affect adhesion property of the scale.

The surface XRD indicated the formation of Fe_2O_3 as the main constituent of the scale. The formation of Fe_2O_3 has also been observed by Shi (1993) for the oxidation of iron by Na_2SO_4 at 750°C and by Tiwari and Prakash (1996) during hot corrosion of Iron-base

superalloy in the Na_2SO_4 -60% V_2O_5 environment at 900°C . Weak intensity peaks of Cr_2O_3 in the scale of weld zone may be due to chromium carbide precipitation in the weld zone Fig 7.3. Also it was noted that spinel (FeCr_2O_4) and Cr_2O_3 on the scale. This can also be attributed to depletion of iron due to oxidation to form the upper scale thereby leaving chromium rich pockets those further get oxidised to form iron chromium spinel which is also supported by Sadique et al (2000).

The EDAX data shows the higher percentage of chromium in the weld zone when it exposed under $\text{K}_2\text{SO}_4 + \text{NaCl}$ (60%) as compared to another environment. This may be attributed to chloride + sulfate mixture which supports a higher concentration of dissolved Cr and Fe than sulfate only salts as suggested by David A et al (2004) Fig 7.5 and 7.6. Cross section EPMA and EDAX revealed that the scale on the weld interfaces contained higher amount of Fe, Cr and Ni. Also it was noted that the penetration of oxygen to the weld interface. This may be attributed to diffusion of these elements during welding as well as corrosion cycles.

7.2.2 Tungsten Inert Gas welding

Hot corrosion on TIG Welded AISI 4140 and AISI 304 dissimilar metals exposed at 600°C under different molten salt environments are given below.

(i) $\text{Na}_2\text{SO}_4 + \text{V}_2\text{O}_5$ (60%)

(ii) $\text{K}_2\text{SO}_4 + \text{NaCl}$ (60%)

After cyclic oxidation in the given salt mixture at 600°C have shown parabolic behaviour. Whereas intense spalling and higher corrosion rate was noticed for molten salt mixture of $\text{K}_2\text{SO}_4 + \text{NaCl}$ (60%). Parabolic rate constant of this environment is approximately 5.5 times more than for the other environment ($\text{Na}_2\text{SO}_4 + \text{V}_2\text{O}_5$ (60%)). During the experiment, separation of the oxide layer occurs at the metal-scale interface. Internal oxidation had also occurred in addition to sulphidation. This was possible by the diffusion of oxygen through the cracks in the external oxide layers. The formation of crack

can be attributed to the difference in thermal coefficients of the low alloy steel and stainless steel and weld metal and the higher volume of oxide formed on the weld metal

A less-protective inner scale formed in the case of HAZ and weld zones as compared to the base metal, presumably allowing for a greater inward diffusion of oxygen ions and thus facilitating a greater concentration of oxygen available for reaction with the chromium of the alloy matrix. More rapid diffusion of oxygen ions through the HAZ scale caused extensive internal oxidation and formation of a subscale zone densely populated with internal precipitates due to depletion of Cr.

Higher corrosion rate may be due to the presence of chlorides which allowed a salt phase to exist at the metal/ scale interface. Importantly, this also means that a continuous salt phase pathway exists to deliver oxidant directly to the metallic phase, and in parallel, to move dissolved metal species away from the reaction site which is also supported by S. Ahila et al (1993, 1994).

In the TIG welding the heat affected zone observed wider as compare to EBW. The grain boundary attack of HAZ may be due to sensitization effect. As revealed by XRD, different phases of various reaction products were formed on the weldment. The scale dissimilar welded samples showed an outer layer containing Fe_2O_3 , Cr_2O_3 and FeCr_2O_4 Fig 7.12.

The presence of Fe_2O_3 is maximum on the scale above the weld and HAZ zone, also the constituent of Cr, Ni and Fe in the weld zone as revealed by the cross sectional EDAX and EPMA analysis. It was observed that the penetration of oxygen in weld interface indicate the weld zone and HAZ more prone to corrosion Fig 7.16 (A and B).

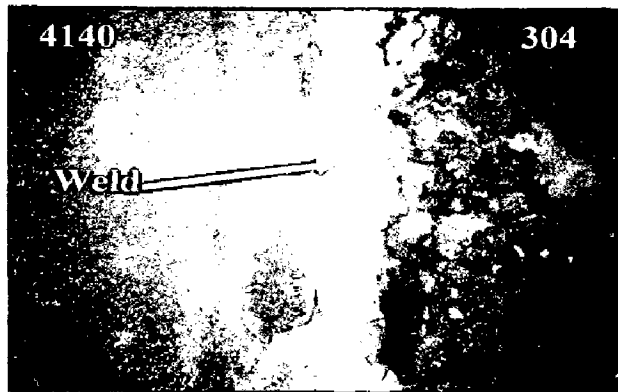


Fig. 7.1(A) Macrographs dissimilar Electron Beam Welded AISI 4140 and AISI 304 subjected to cyclic hot corrosion exposed at temperature of 600 °C under $\text{Na}_2\text{SO}_4 + \text{V}_2\text{O}_5$ (60%) after 50 cycles.

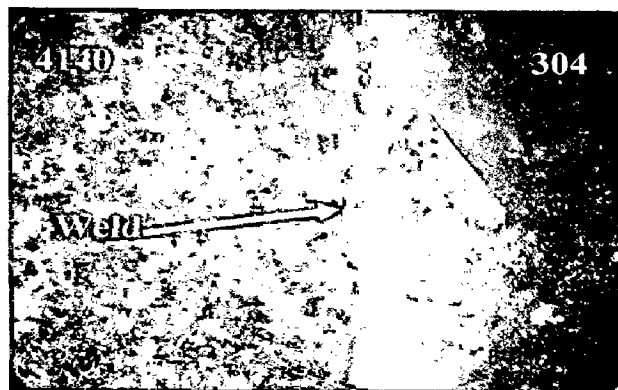


Fig. 7.1(B) Macrographs dissimilar Electron Beam Welded AISI 4140 and AISI 304 subjected to cyclic hot corrosion exposed at temperature of 600 °C under $\text{K}_2\text{SO}_4 + \text{NaCl}$ (60%) after 50 cycles.

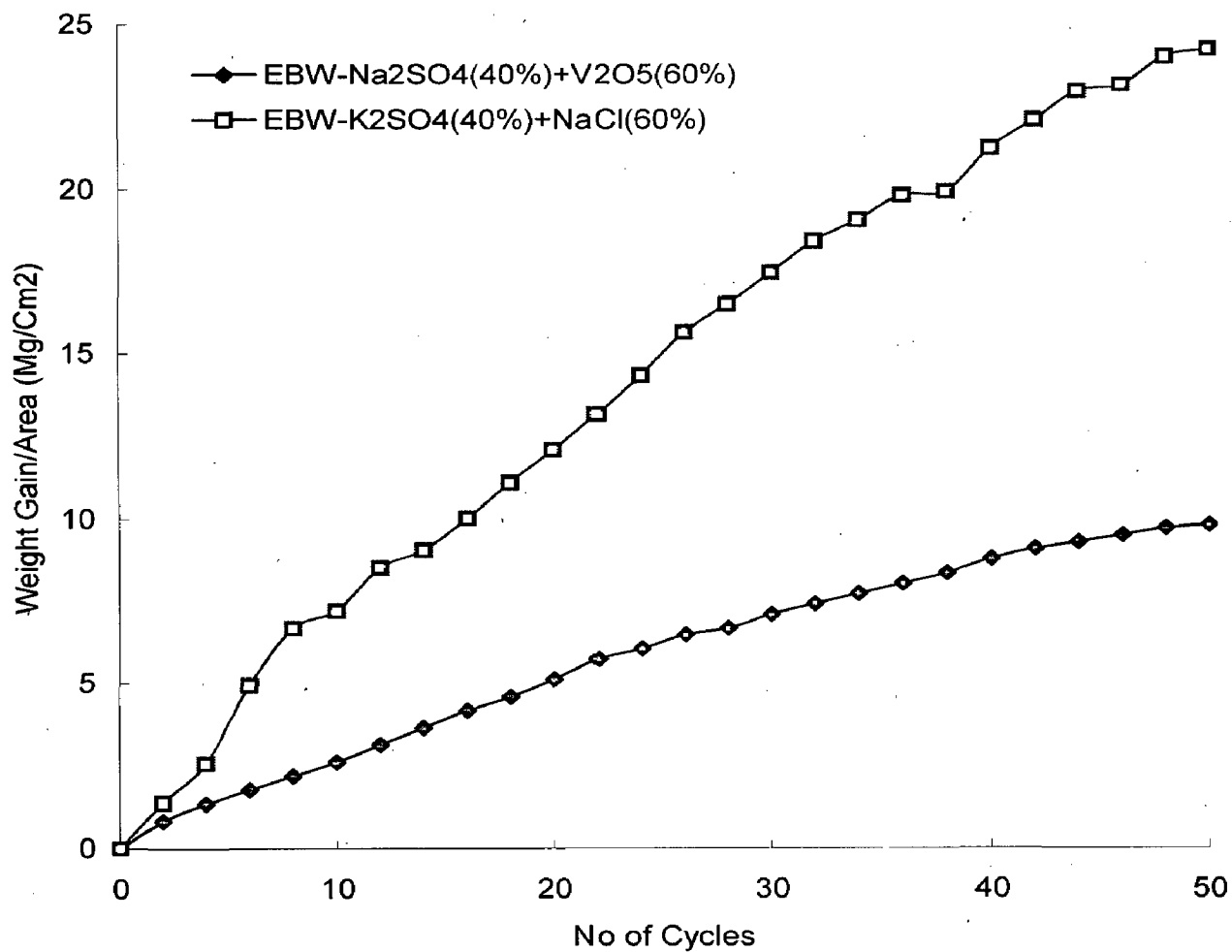


Fig 7.2. Plots of cumulative weight gain (mg/cm^2) as a function of time (number of cycles) for the EBW weldment under cyclic hot corrosion at 600°C , in the molten salt $\text{Na}_2\text{SO}_4 + \text{V}_2\text{O}_5$ (60%) and $\text{K}_2\text{SO}_4 + \text{NaCl}$ (60%).

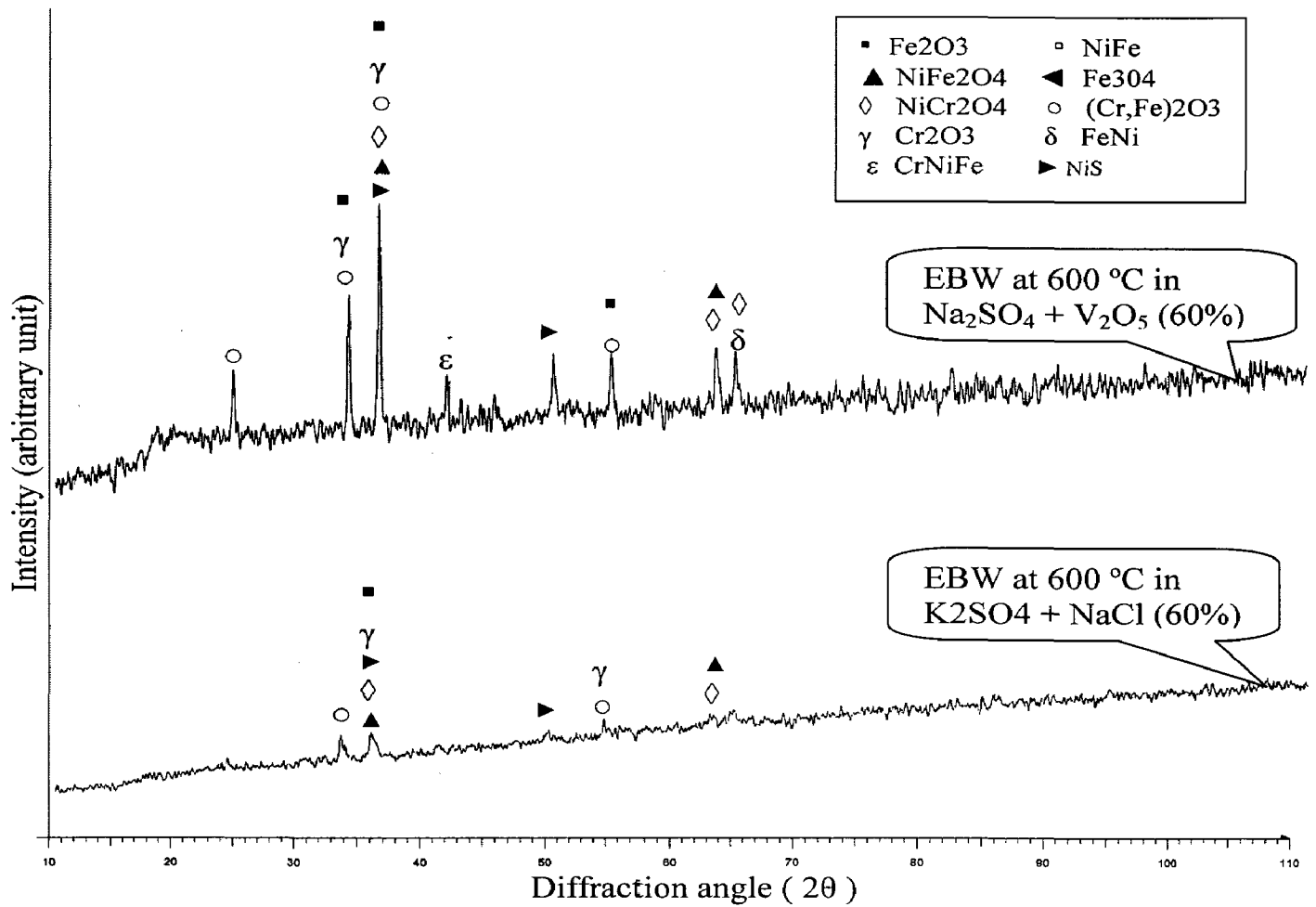


Fig. 7.3 X-Ray diffraction patterns for hot corroded dissimilar EBW weldment of AISI 4140 and AISI 304 exposed at 600 °C in Na₂SO₄ + V₂O₅ (60%) and K₂SO₄ + NaCl (60%) for 50 cycles.

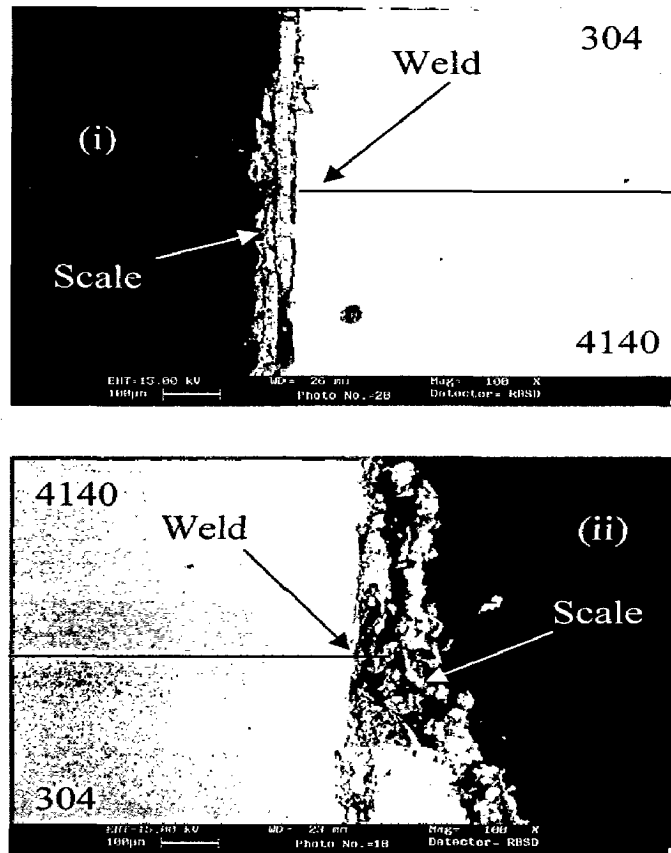


Fig 7.4. BSEI for hot corroded Electron Beam weldment at exposed temperature of 600 °C.

(i) EBW exposed under $\text{Na}_2\text{SO}_4 + \text{V}_2\text{O}_5$ (60%) at 600 °C.

(ii) EBW exposed under $\text{K}_2\text{SO}_4 + \text{NaCl}$ (60%) at 600 °C.

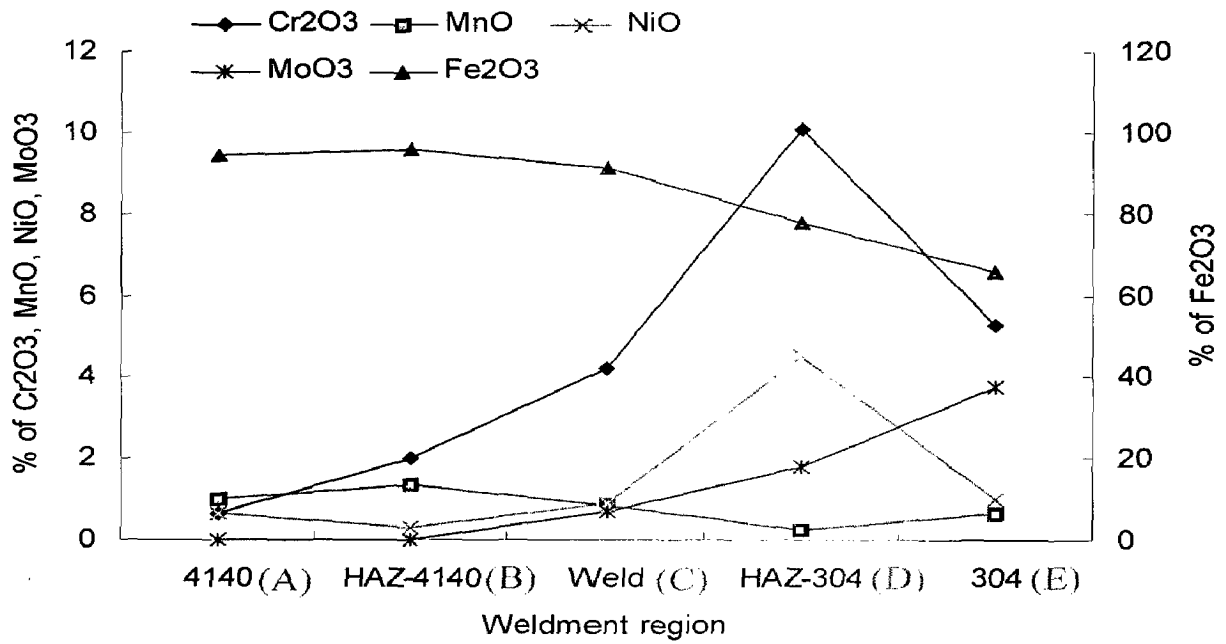
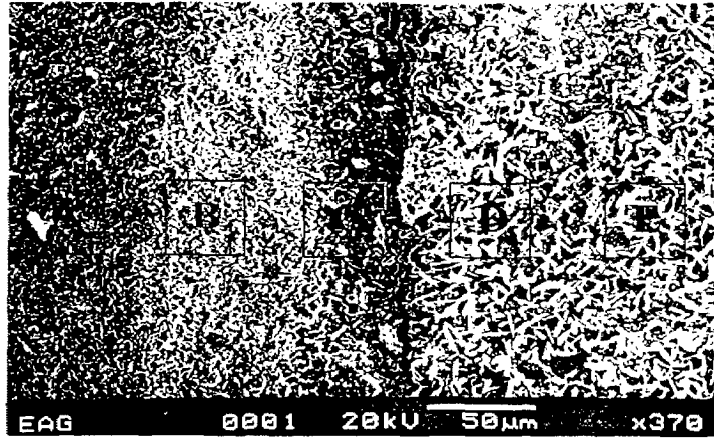


Fig 7.5 SEM/EDAX graph shows the EBW weldment of AISI 4140 and AISI 304 exposed at 600 °C under Na₂SO₄ + V₂O₅ (60%) after 50 cycles.

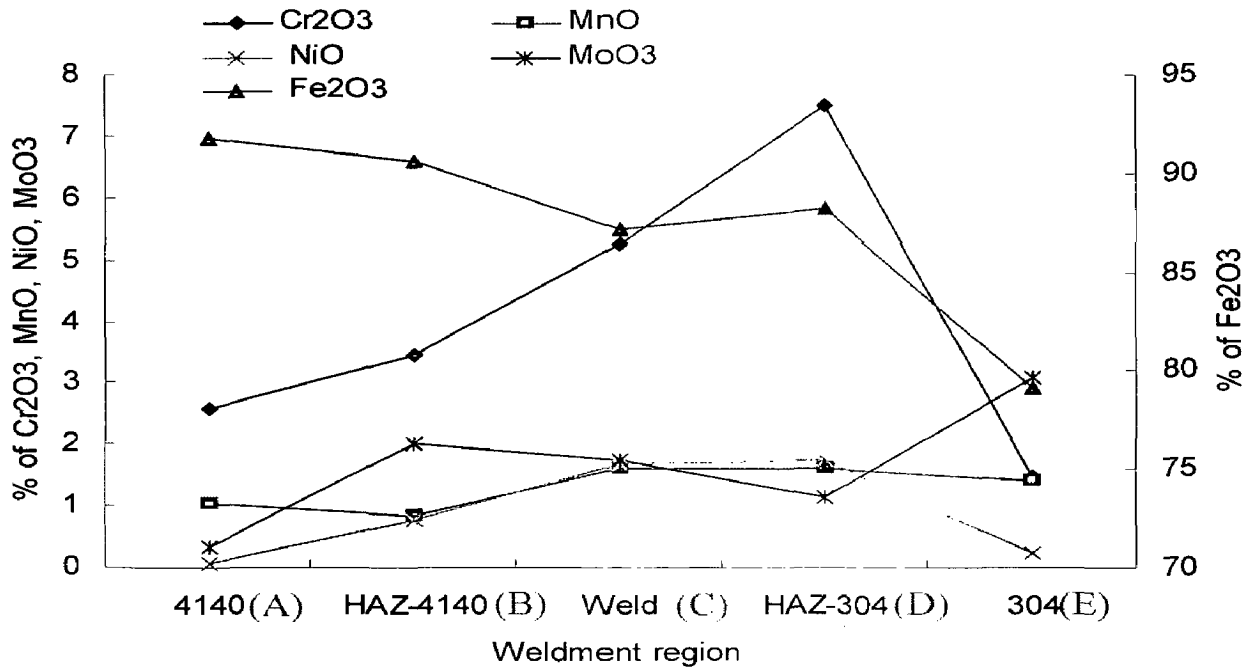
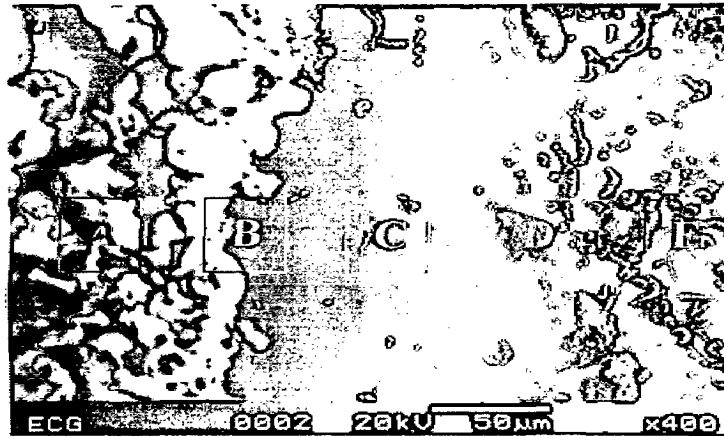


Fig 7.6 SEM/EDAX graph shows the EBW weldment of AISI 4140 and AISI 304 exposed at 600 °C under K₂SO₄ + NaCl (60%) after 50 cycles.

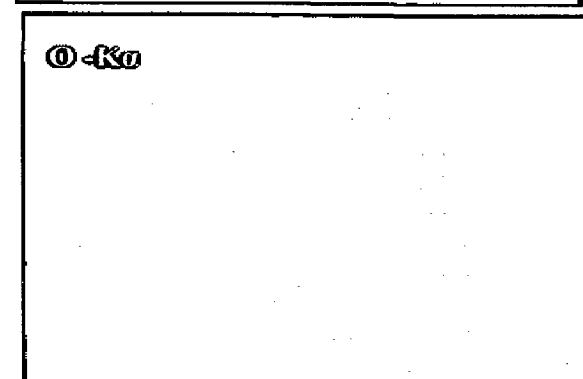
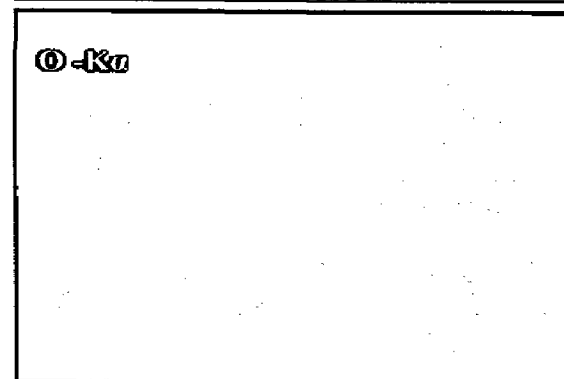
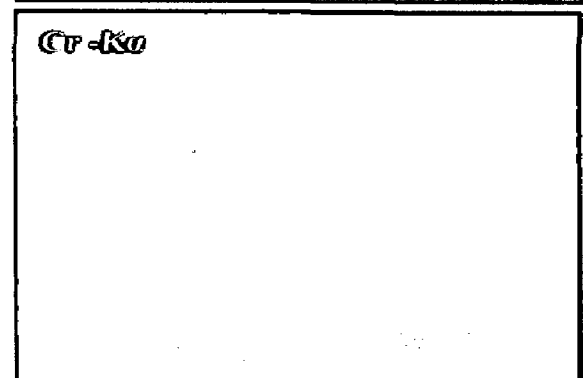
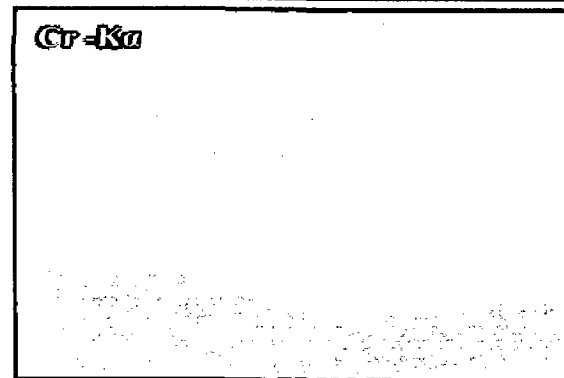
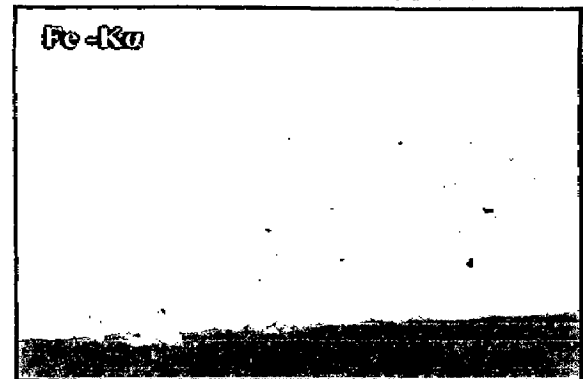
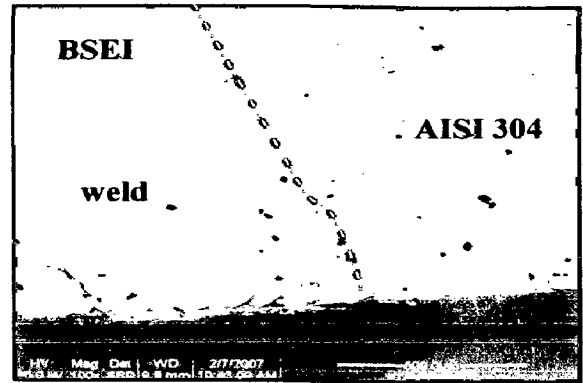
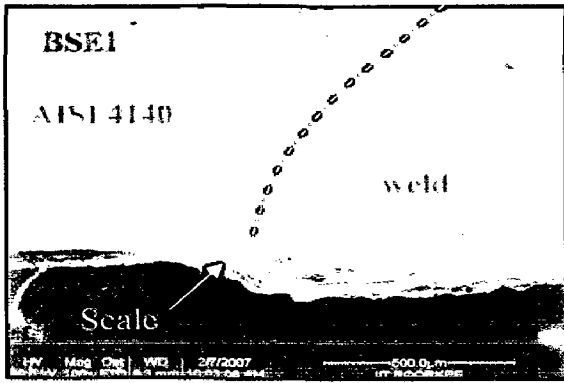


Fig. 7.7 BSEI and elemental X-ray mapping of the cross-section of dissimilar EBW weldment of AISI 4140 and AISI 304, subjected to cyclic hot corrosion in K₂SO₄ + NaCl (60%) at 600^oC for 50 cycles, 100 X.

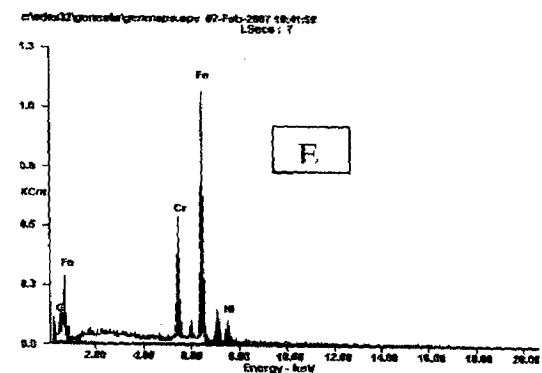
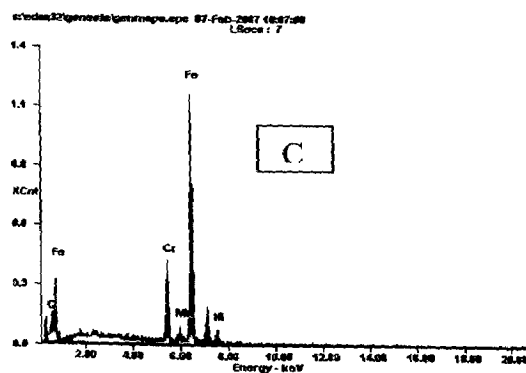
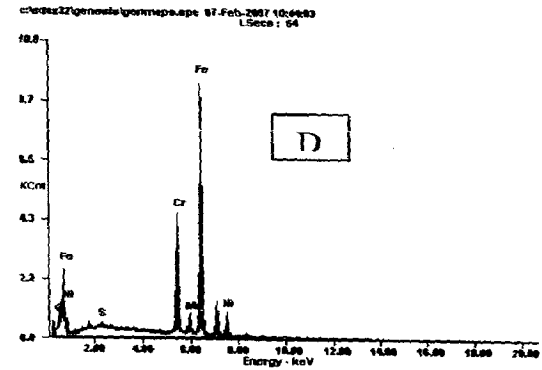
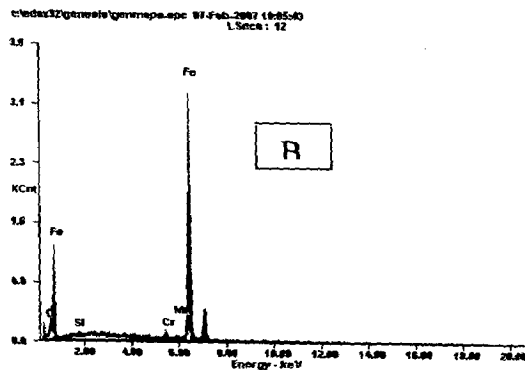
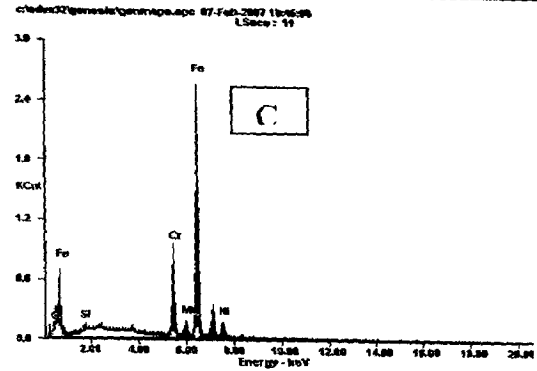
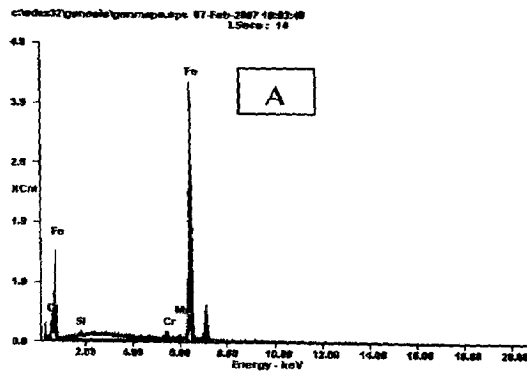
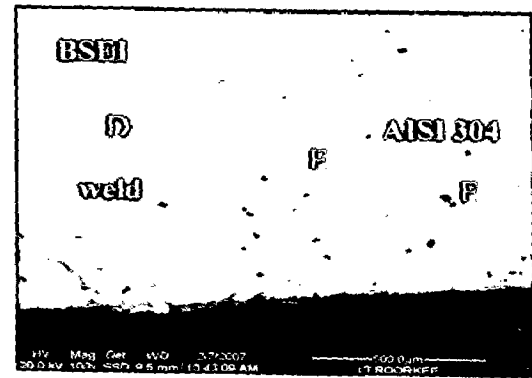
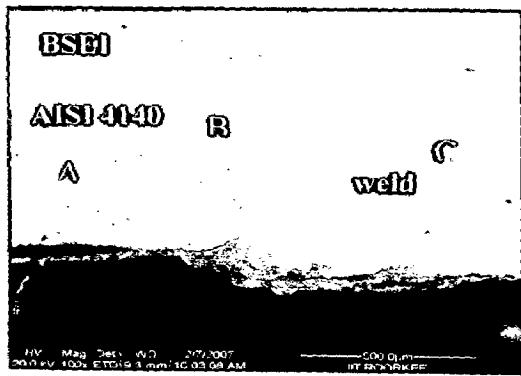


Fig. 7.8 BSEI and EDAX of the cross-section of EBW dissimilar metals of AISI 304 and AISI 4140 exposed to K_2SO_4 -60%NaCl at 600 °C for 50 cycles.



Fig. 7.9(A) Macrographs dissimilar TIG Welded AISI 4140 and AISI 304 subjected to cyclic hot corrosion exposed at temperature of 600 °C under $\text{Na}_2\text{SO}_4 + \text{V}_2\text{O}_5$ (60%) after 50 cycles.

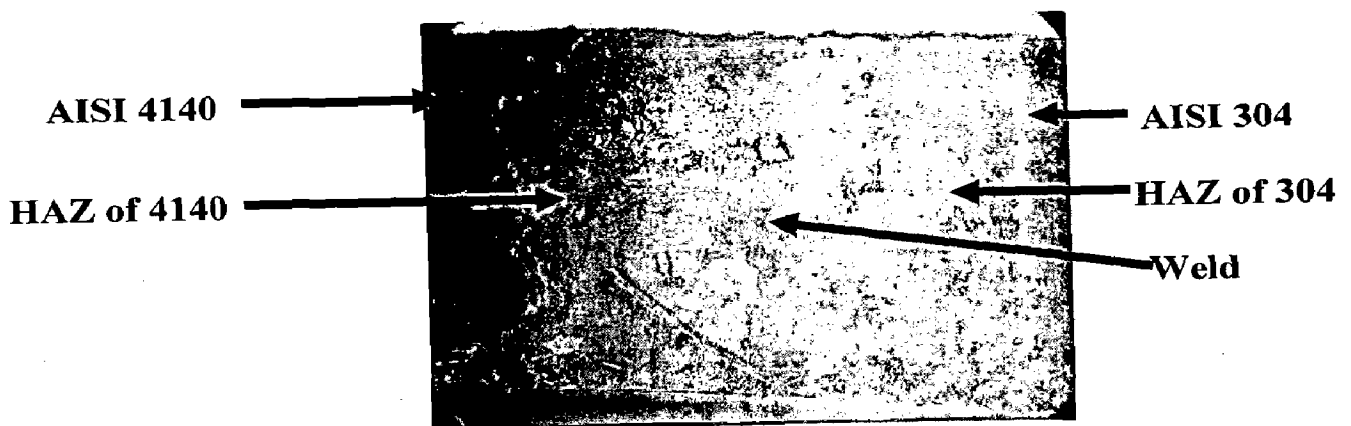


Fig. 7.9(B) Macrographs dissimilar TIG Welded AISI 4140 and AISI 304 subjected to cyclic hot corrosion exposed at temperature of 600 °C under $\text{K}_2\text{SO}_4 + \text{NaCl}$ (60%) after 50 cycles.

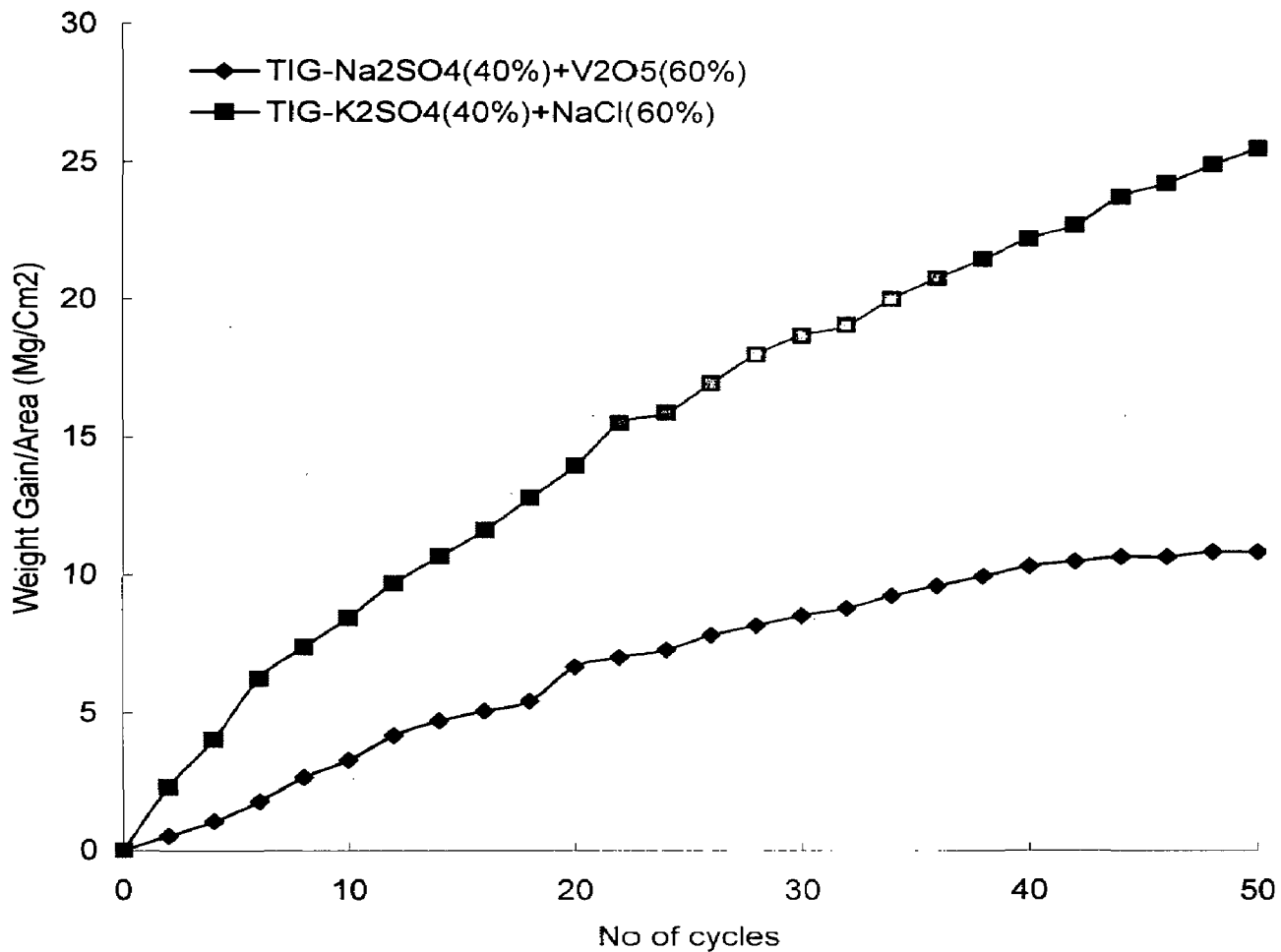


Fig 7.10. Plots of cumulative weight gain (mg/cm^2) as a function of time (number of cycles) for the TIG weldment under cyclic hot corrosion, at $600\text{ }^\circ\text{C}$ in the molten salt $\text{Na}_2\text{SO}_4 + \text{V}_2\text{O}_5$ (60%) and $\text{K}_2\text{SO}_4 + \text{NaCl}$ (60%).

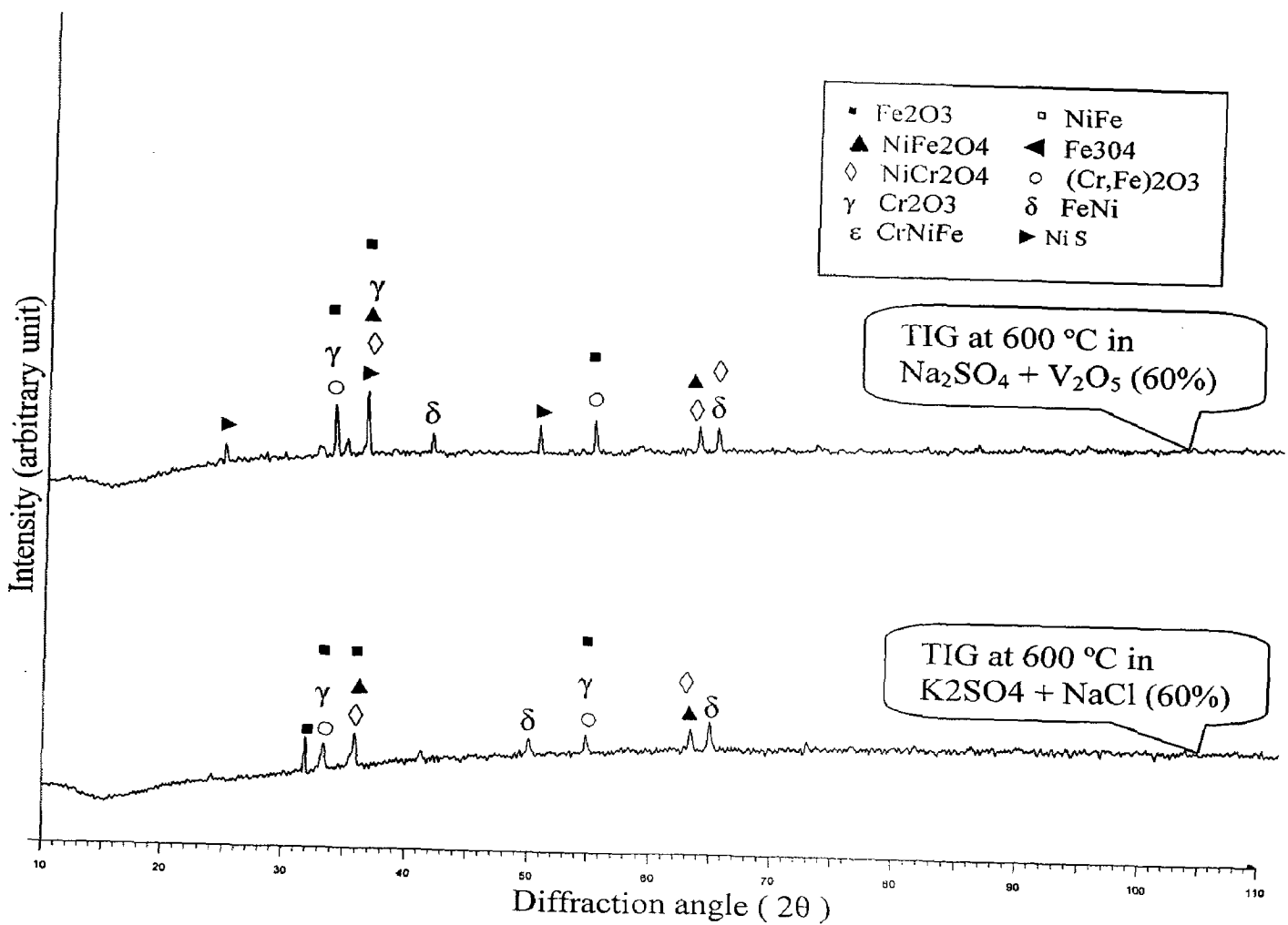


Fig. 7.11 X-Ray diffraction patterns for hot corroded dissimilar TIG weldment of AISI 4140 and AISI 304 exposed at 600 °C in Na₂SO₄ + V₂O₅ (60%) and K₂SO₄ + NaCl (60%) for 50 cycles.

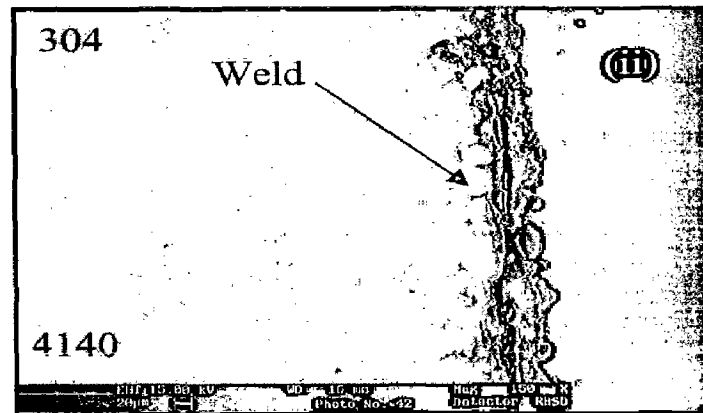
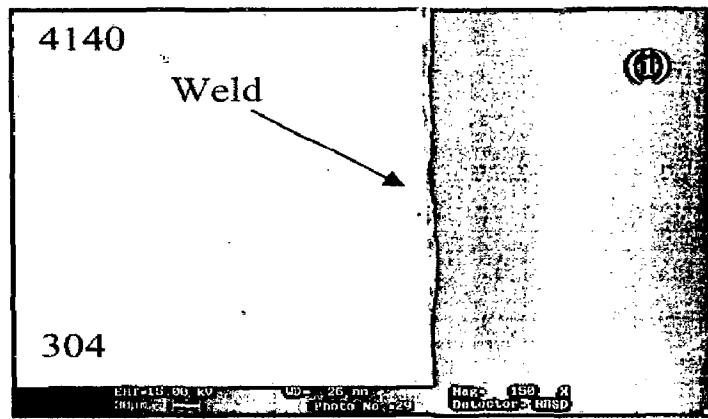


Fig 7.12. BSEI for hot corroded TIG weldment at exposed temperature of 600 °C.

(i) TIG exposed under $\text{Na}_2\text{SO}_4 + \text{V}_2\text{O}_5$ (60%) at 600 °C.

(ii) TIG exposed under $\text{K}_2\text{SO}_4 + \text{NaCl}$ (60%) at 600 °C.

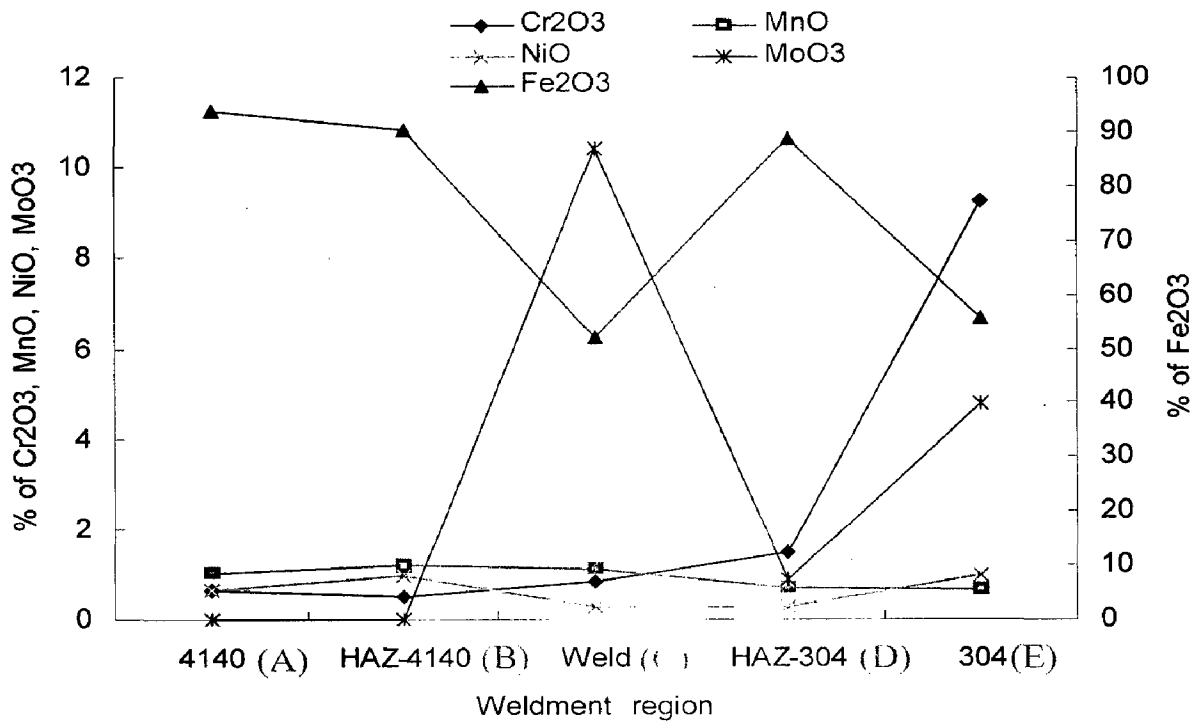
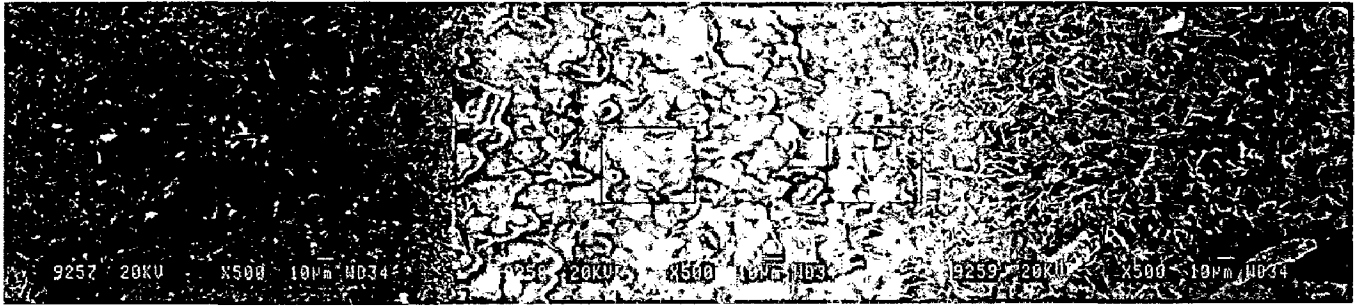


Fig 7.13 SEM/EDAX graph shows the TIG weldment of AISI 4140 and AISI 304 exposed at 600 °C under $\text{Na}_2\text{SO}_4 + \text{V}_2\text{O}_5$ (60%) after 50 cycles.

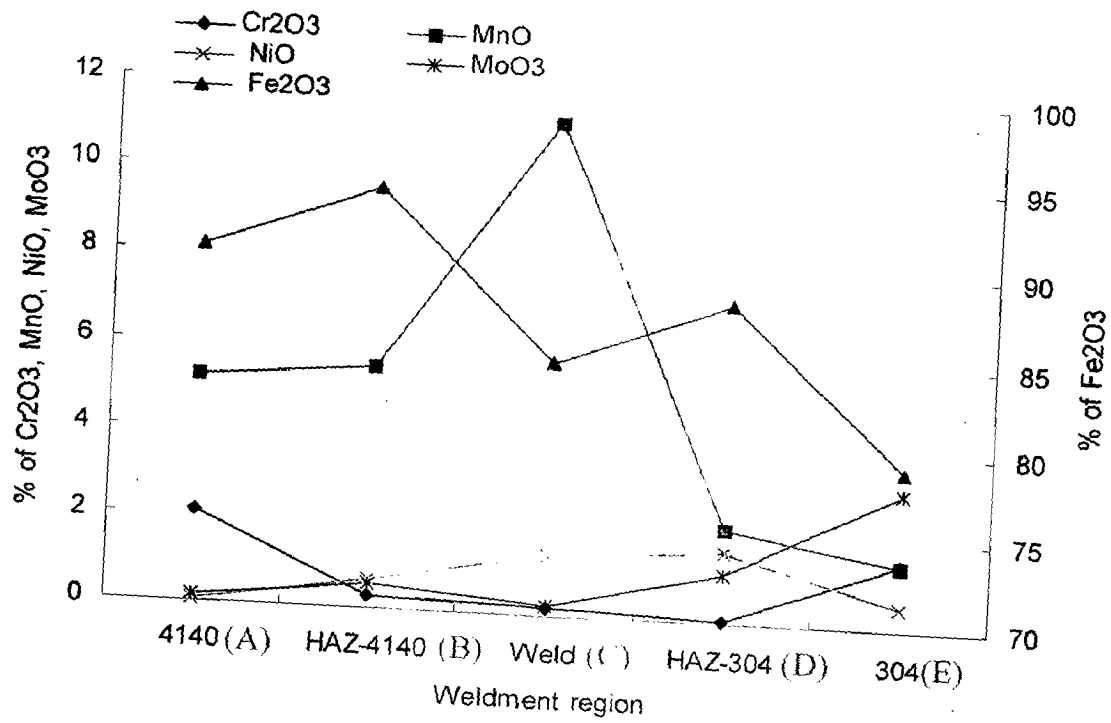
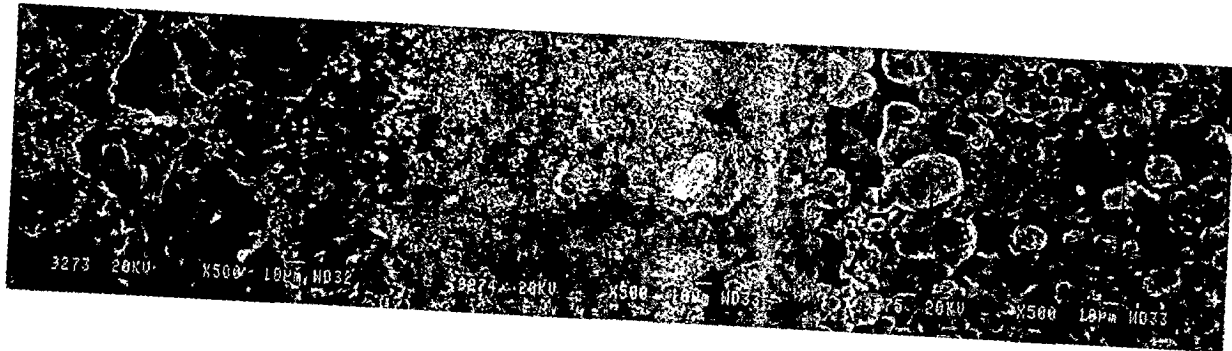


Fig 7.14 SEM/EDAX graph shows the TIG weldment of AISI 4140 and AISI 304 exposed at 600 °C under K2SO4 + NaCl (60%) after 50 cycles.

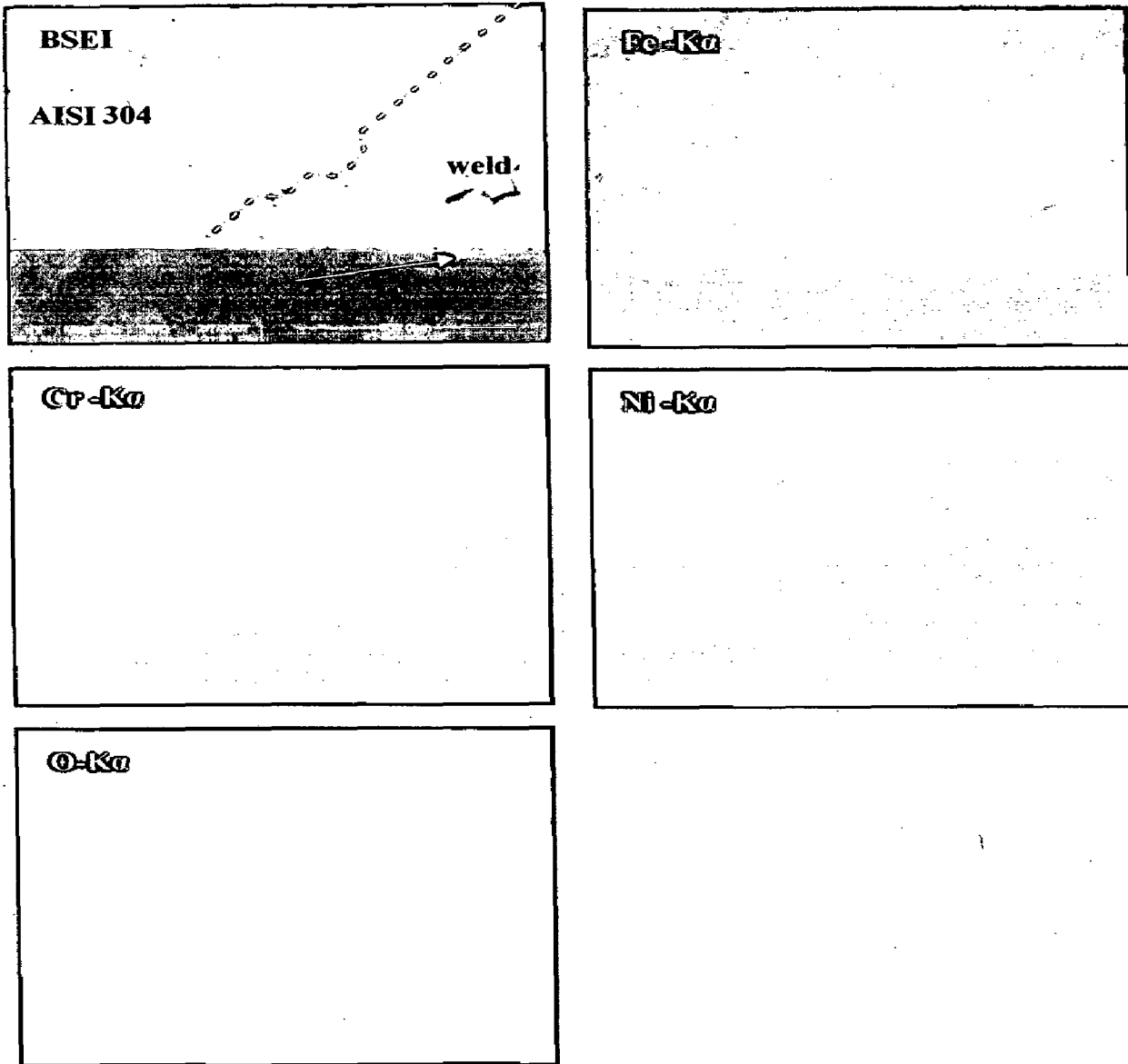


Fig. 7.15 (A) BSEI and elemental X-ray mapping of the cross-section of dissimilar TIG weldment of AISI 304 and weld zone, subjected to cyclic hot corrosion in K_2SO_4 - 60%NaCl at $600^\circ C$ for 50 cycles, 120 X.

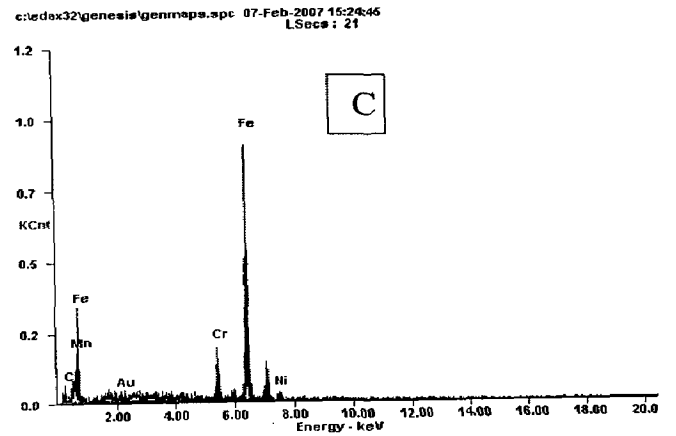
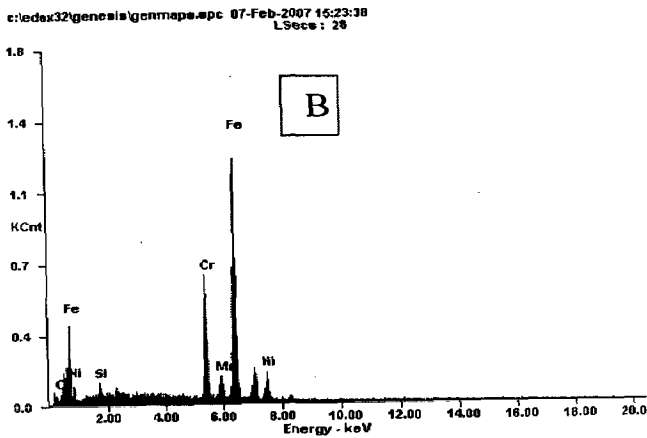
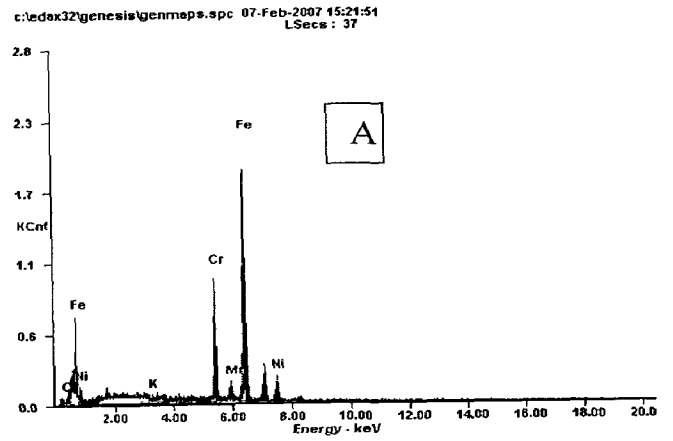
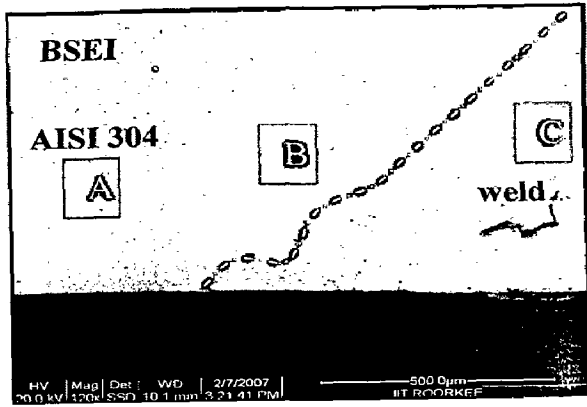


Fig. 7.15 (B) BSEI and EDAX form cross section of dissimilar TIG weldment of AISI 304 and weld zone, subjected to cyclic hot corrosion in K_2SO_4 - 60%NaCl at $600^{\circ}C$ for 50 cycles, 120 X.

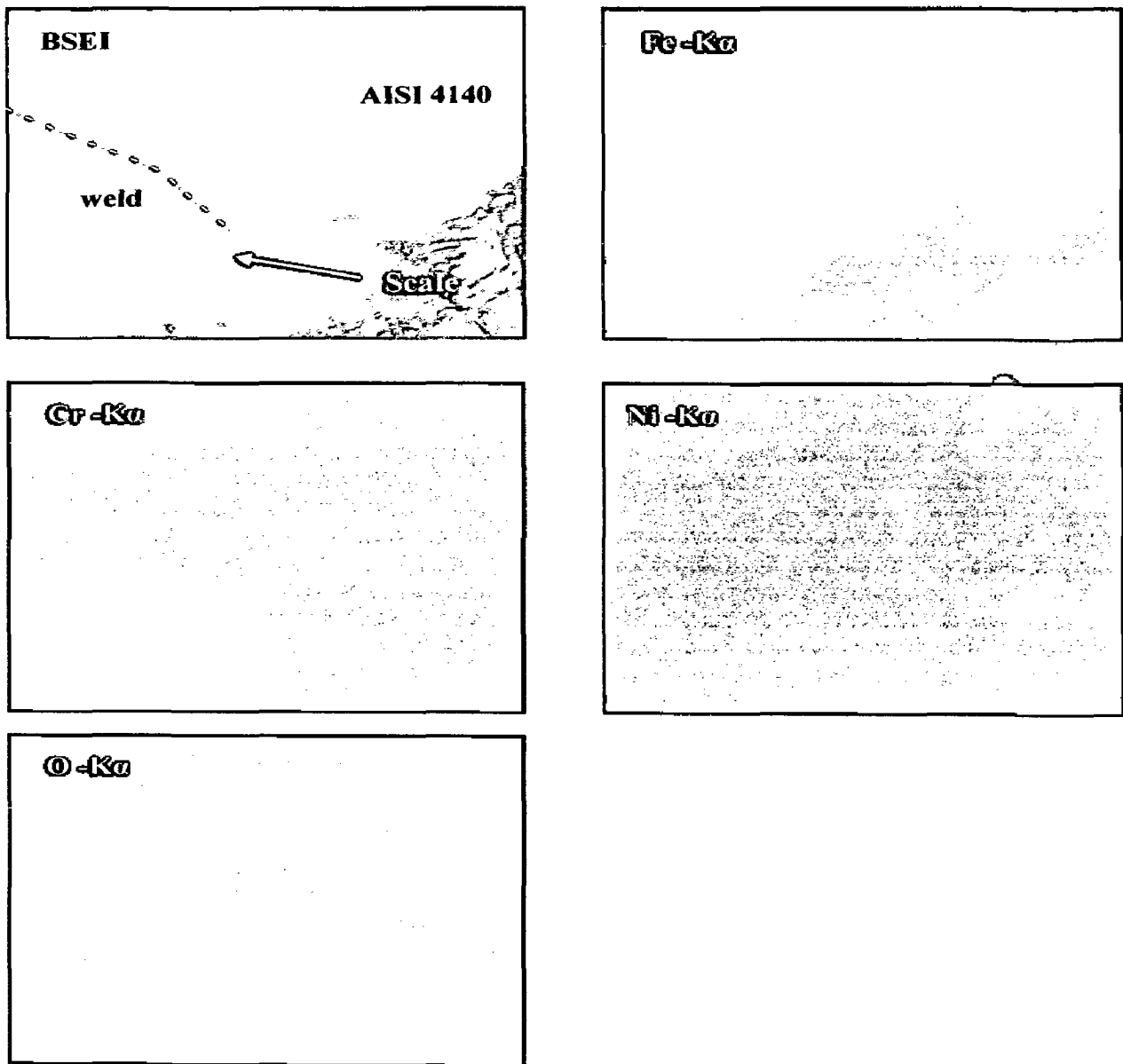


Fig. 7.16 (A) BSEI and elemental X-ray mapping of the cross-section of dissimilar TIG weldment of weld zone and AISI 4140, subjected to cyclic hot corrosion in $K_2SO_4 - 60\%NaCl$ at $600^\circ C$ for 50 cycles.

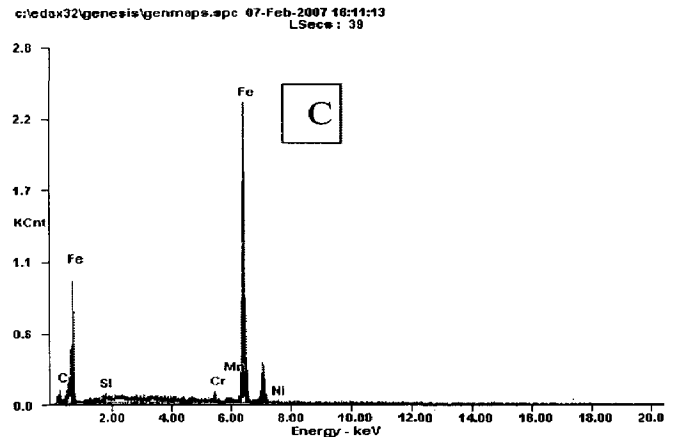
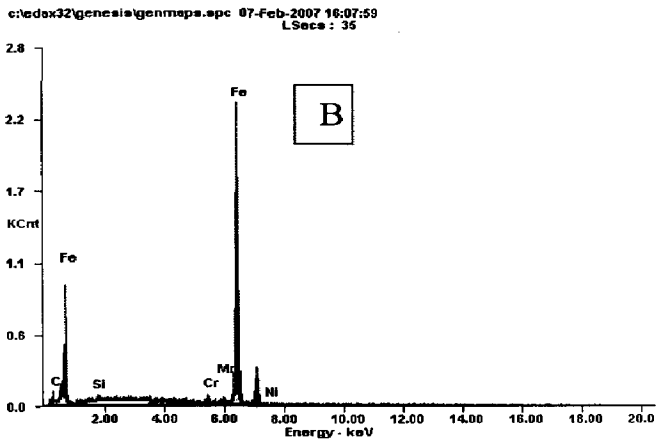
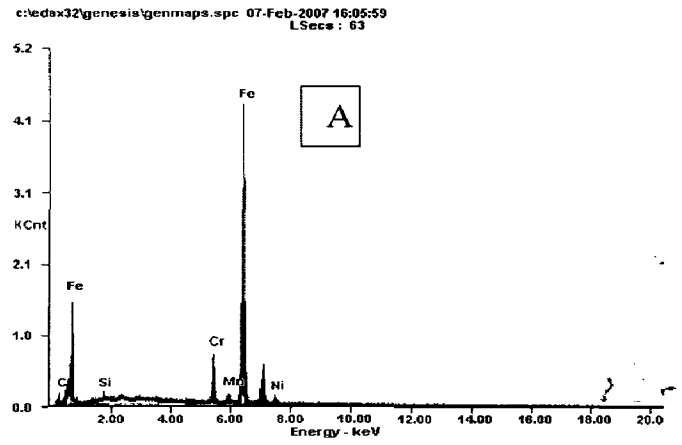
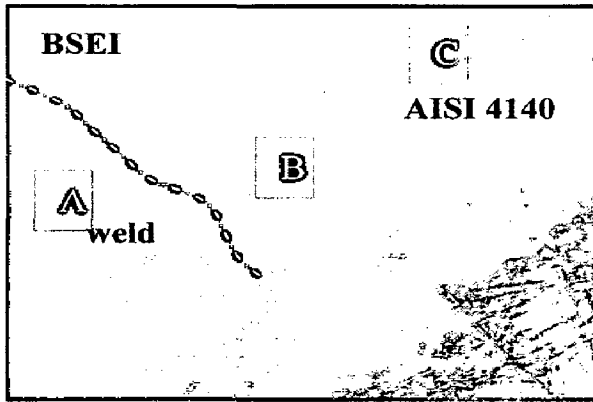


Fig. 7.16 (B) BSEI and EDAX form cross section of dissimilar TIG weldment of weld zone and AISI 4140, subjected to cyclic hot corrosion in $K_2SO_4 - 60\%NaCl$ at $600^{\circ}C$ for 50 cycles.

CHAPTER 8

COMPARATIVE DISCUSSION

In this chapter, an attempt has been made to present the results of the current investigation giving comparative mechanical properties of AISI 4140 and AISI 304 dissimilar weldment with friction welding, electron beam welding and tungsten inert gas welding process. The hot corrosion behaviour of these weldments under different environment as has also been discussed below.

The mechanical properties of AISI 4140 and AISI 304 dissimilar weldment made by friction welding, electron beam welding and tungsten inert gas welding are reported in Table 8.1. The bar charts showing the overall mechanical properties for the dissimilar weldment made by FRW, EBW and TIG are presented in Figs. 8.1.

Sound welds could be obtained with all the three welding processes. The mechanical properties of the welds are similar to ones reported by N.O. Zdemir et al (2007), J. Tusek et al (2001), A. Celik (1999) and V.V. Satyanarayana et al (2005).

The tensile strength value of the dissimilar alloy joints made by the three welding processes is more than the individual parent metals. Moreover from the investigation it was observed that the yield strength of weldment made by EBW (681 MPa) was higher than the one made by TIG (634 MPa) or FRW (485 MPa). The ductility of the EBW and TIG weldment were higher with an elongation of 24 % and 31 % respectively when compared with friction weldment, where elongation was around 18%. The sequence for the overall yield strength of dissimilar weldment made by three welding process has been observed as given below:

$$\text{EBW} > \text{TIG} > \text{FRW}$$

Micro hardness tests were taken along a line in the middle of the thickness and included both base metals, the heat-affected zones (HAZ), and the weld area for all types of dissimilar welds. The hardness data for weldment made by friction welding process shows that the higher hardness values were generally obtained in the weld regions of the friction weldment. The effect of burn off length on hardness shows that the higher

hardness (386 HV) is observed when the burn off length 12 mm. where as it is 305 HV for burn off length of 5 mm. The sequence for the hardness at weld zone of friction welded dissimilar metals for different burn off length has been observed to follows.

$B_{12} > B_9 > B_7 > B_5$

In case of the dissimilar alloy weldment made by EBW and TIG weldment, the maximum hardness values has been recorded in the weld zone adjacent to AISI 304 side. It is higher (738 HV) in the weldment made by EBW as compared to the value recorded in the weldment made by TIG welding process (548 HV). The sequence for the overall maximum hardness recorded in the weldment made by three welding process has been observed as given below:

$EBW > TIG > FRW$

The impact strength of friction welded dissimilar metals by keeping burn off length 5 mm is 26 J, where as it is 11 J for 12 mm burn off length. It was also observed that the impact strength of weldment made by TIG and EBW welding process is 25.5 J and 21 J respectively.

Investigation on the effect of burn-off length on friction welded AISI 4140-AISI 304 dissimilar metals revealed that in general the impact toughness of these welds is very low with increase the burn off length. The inverse relation between hardness and toughness is as per the established trends. The sequence for the impact strength of friction welded dissimilar metals has been observed as given below:

$B_5 > B_7 > B_9 > B_{12}$

The reduction in toughness and increase in hardness with increase in burn-off length is related to increased carbon and iron migration from the low alloy steel side towards stainless steel whereas Cr and Ni diffuse from stainless steel side towards low alloy steel side due to higher temperatures that prevail around the weld interface with increase in burn-off length. Diffusion of these elements leads to formation of intermetallic and precipitation of carbide at the weld interface, which is also supported by XRD, EDS and EPMA analysis. The sequence for the overall impact strength in the weldment made by three welding process has been observed as given below:

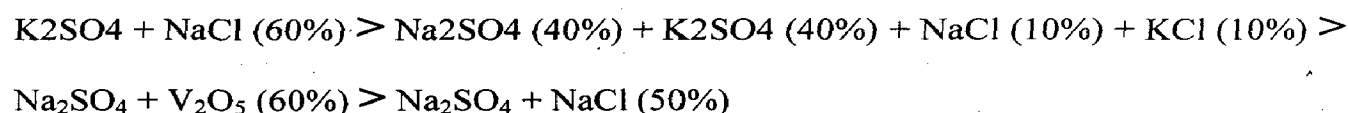
$TIG > EBW > FRW$

Results as obtained after hot corrosion of AISI 4140 and AISI 304 dissimilar weldment made by FRW, EBW and TIG under different environments as well as temperatures are given below and the results are summarized in Table 8.2 to 8.6. These tabulated results are ready reference to compare the hot corrosion behaviour of the dissimilar weldments.

The bar charts showing the overall weight gains in air and molten salt environments after 50 cycles for the dissimilar weldment made by FRW, EBW and TIG are presented in Figs. 8.2 (a). It further reported by Kp values as referred in bar chart Fig 8.2 (b).

From the bar charts, it can be inferred that the friction welded dissimilar metals under study have shown low oxidation resistance against the given molten salt environments as compared to that against the air under cyclic conditions. The maximum weight gain at 600 °C exposed to Na₂SO₄ + V₂O₅ (60%) is 50 times than that of exposed under air under cyclic condition. Where as it is 190 times in the environment of K₂SO₄ + NaCl (60%). In the case of Na₂SO₄ (40%) + K₂SO₄ (40%) + NaCl (10%) + KCl (10%) the weight gain is around 100 times as compared to the weldment exposed to air, whereas the weight gain is around 50 times in the environment of Na₂SO₄ + NaCl (50%).

The hot corrosion rates for the investigated friction welded dissimilar metals based on the overall weight gains after 50 cycles of oxidation at all temperature and environments could be arranged in the following order:



In general friction welded dissimilar metals made by keeping burn off length 5 mm has indicated a maximum resistance to molten salt environment amongst the weldment made by keeping burn off length 7, 9 and 12 mm. The weight gain of the weldment made by keeping 12 mm burn off length, exposed to any given molten salt environment is around 1.4 times as compared to weight gain for weldment by keeping 5 mm burn off length. The sequence for the overall protective behaviour of dissimilar

weldment in all the molten salt environments used in this study has been observed as given below:

$$B5 > B7 > B9 > B12$$

From the bar charts, it can be inferred that friction welded dissimilar metals has provided minimum resistance to oxidation in the molten salt environment at 600 C as compared to the weldment exposed at 500 C. In general the weight gain of weldment for the given environments at 600 C is around 3.5 times than that of the weldment exposed at 500 C.

From the investigation it can be concluded that of $K_2SO_4 + NaCl$ (60%) is most aggressive environment. The maximum weight gain recorded for the weldment made by keeping 12 mm burn off length exposed to $K_2SO_4 + NaCl$ (60%) at 600 C, is 3.86 times higher than that exposed to $Na_2SO_4 + V_2O_5$ (60%). Also it is 1.8 times higher as compared to the environment of Na_2SO_4 (40%) + K_2SO_4 (40%) + $NaCl$ (10%) + KCl (10%). The portion of $NaCl$ in salt mixtures makes the mixture more aggressive as it leads to highest weight gains through out the 50 cycles which has been already explained in Chapter 6 and 7.

From bar chart for the weight gain by weldment made by three welding process exposed to $Na_2SO_4 + V_2O_5$ (60%) and $K_2SO_4 + NaCl$ (60%) at 600 C. It can be inferred that the weight gain of weldment made by EBW and TIG exposed to $Na_2SO_4 + V_2O_5$ (60%) is around 1.5 times higher than that of the weight gain of weldment made by FRW. The weight gain of weldment made by FRW exposed to $K_2SO_4 + NaCl$ (60%) is around 1.2 times lower than that of the weight gain of the weldment made by EBW and TIG. It shows that the environment of $K_2SO_4 + NaCl$ (60%) is more aggressive for the weldment made by FRW as compared to one made by EBW and TIG. It was observed that the weight gain for the weldment made by EBW and TIG, exposed to $K_2SO_4 + NaCl$ (60%) is around 2 times than that of the weldment exposed to $Na_2SO_4 + V_2O_5$ (60%). The sequence for the overall protective behaviour of dissimilar weldment in molten salt environment has been observed as given below:

At 600 C exposed to $Na_2SO_4 + V_2O_5$ (60%):

FRW-B5 > FRW-B7 > FRW-B9 > FRW-B12 > EBW > TIG

At 600 °C exposed to $K_2SO_4 + NaCl$ (60%):

EBW > TIG > FRW-B5 > FRW-B7 > FRW-B9 > FRW-B12

EDAX data represents the constituent of oxide in the scale on the friction welded AISI 4140 and AISI 304 dissimilar metals with different environments given in Fig 8.3 (A to L). It was observed that at 600 °C temperature of exposure under air oxidation, Fe_2O_3 , Cr_2O_3 and NiO dominating in the scale on the weld zone as well as 304 side. In the molten salt environment of $K_2SO_4 + NaCl$ (60%), the constituent of Cr_2O_3 in the scale on the weld zone is very less 5 to 7 % as compared to air oxidation where it is 10 to 20 %. Attack on weld zone as well as HAZ of both base metals was due to the formation of a liquid phase which could flow along the grain boundaries and weaken them. This led to accelerated corrosion and intensive spalling/sputtering of the scale of the weldment. This might be responsible for high corrosion rate to in $K_2SO_4 + NaCl$ (60%) environment.

In the molten salt environment of $Na_2SO_4 + V_2O_5$ (60%), the scale on the weld zone as well as HAZ of both side consisted of Cr_2O_3 (7 to 10 %) and NiO (2 to 4.5 %), where as other environment incorporated with $NaCl$, the percentage of these phases decreased. It can be inferred that the presence of alkali chlorides in the deposit causes much more aggressive hot corrosion attack than a salt deposit containing only alkali sulfates. Active oxidation, involving transport of metal chlorides in the liquid salt phase, destroys the normally protective Cr_2O_3 scale as suggested by Bani P et al (2004). Also Y.S. Li et al (2005) reported that Cr is not an effective element for corrosion resistance improvement of Fe-base and Ni-based alloys due to chloride salt attack. M.A. Uusitalo et al (2004) found that active oxidation caused accelerated corrosion when the low alloy steel and austenitic stainless steel were exposed to molten salt containing 40 wt% K_2SO_4 , 40 wt% Na_2SO_4 , 10 wt% KCl , and 10 wt% $NaCl$ at 550 °C for 50 hours.

From the EDAX data, the scale on the weld zone of EBW and TIG weldment contains higher amount of Cr_2O_3 and NiO . Which is higher as compared to Friction weldment when exposing under $K_2SO_4 + NaCl$ (60%) at 600 °C Fig 8.4 (A - J). It can be inferred for this that EBW and TIG weldment has provided maximum resistance to corrosion in this environment as compared to friction welded weldment. Fast formation of a continuous chromia scale on the weld zone has been attributed to the easy diffusion of Cr, and Ni towards the weld zone from alloy 304 side as suggested by C. Zhang et al (2005). Also it was observed that the concentration of MoO_3 in scale on the weld zone of

TIG and EBW weldment, which may have led for improvement the corrosion resistance under this environment as suggested by Tetsuo Ishitsuka et al (2002).

The corrosion rate is less when the weldment exposing in molten salt environment at 500 and 550 °C temperature. It can be inferred that corrosion rate decreases significantly, if the deposit temperature is below the first melting temperature. Chemical reactions are generally faster in liquid phase than as solid-solid reactions. The liquid phase also provides an electrolyte for ionic transport or electrochemical attack as suggested by K. Salmenoja et al (2000), N. Hiramatsu et al (1989), M.J. McNallan et al (1981), H.J. Grabke et al (1998), O.H. Larsen et al (1996), J. Klower et al (1995), Y. Kawahara (1997)].

At 700 and 900 °C rapid corrosion rate was observed due to rapid reaction of molten salt when the friction welded dissimilar metals were exposed to $\text{Na}_2\text{SO}_4 + \text{V}_2\text{O}_5$ (60%) environment.

Table 8.1 The cumulative mechanical properties of AISI 4140 and AISI 304 dissimilar welment made by FRW, EBW and TIG.

Welding	B.L (mm)	XRD	Max. Hard. At weld (HV)	Yield strength (MPa)	% of Elangation	Tensile Fractography	Impact Toughness (Joule)	Impact Fractography	Remark
Friction Welding	5	FeNi, Ni ₃ C	305	485.2	18.15	Failure at low alloy steel side. micro void ductile fracture	26	Low burn-off length indicates ductile fracture and higher burn off length shows brittle fracture.	Diffusion of Fe, Cr Ni, C high at higher burn-off length. At lower burn good mechanical property noted.
	7	(Cr,Fe) ₇ C ₃ , Cr-Ni-Mo, Cr-Si-C, FeNi, Cr-Ni-Fe	322	493.7	18.89		22		
	9	Cr-Ni-Fe, (Cr,Fe) ₇ C ₃ , Cr-Ni-Mo, Ni,Fe, Ni ₃ C, FeNi	351	474.35	17.15		16		
	12	Cr-Ni-Mo, Cr-Ni-Fe, Ni ₃ C, FeNi	386	476.4	18.30		11		
Electron Beam welding	---	(Cr,Fe) ₇ C ₃ , Ni,Fe, Cr-Ni-Mo, Ni ₃ C, Cr-Ni-Fe	400	681	31.97	Failure at HAZ of 4140 side. micro void ductile fracture	21	Ductile fracture	excellent mechanical property
Tungsten Inert Gas Welding	---	(Cr,Fe) ₇ C ₃ , Cr-Ni-Fe, Ni ₃ C, FeNi, Ni,Fe, Cr-Ni-Mo	400	634.5	24.96	Failure at HAZ of 4140 side. micro void ductile fracture	25.5	Cleavage fracture	excellent mechanical property also micro cracks noted at weld

Table 8.2 Oxidation data of friction weldment of dissimilar metals of AISI 4140 and AISI 304 in Air environment

Oxidation	Temp (°C)	Weight gain 10mg/cm ²	Kp (10 ⁻⁶ (gm ² Cm ⁻⁴ S ⁻¹))	XRD	SEM/EDAX
Cyclic Oxidation	500	0.022	0.297	Fe ₂ O ₃ , NiO	Fe ₂ O ₃ , Cr ₂ O ₃ higher at weld
	600	0.027	0.383	Fe ₂ O ₃ , Cr ₂ O ₃ , NiFe ₂ O ₄ , NiFe ₃ O ₄	Fe ₂ O ₃ , Cr ₂ O ₃ and NiO higher at weld
Isothermal Oxidation (50 hours)	500	0.001	--	Fe ₂ O ₃ , NiFe ₂ O ₄ , NiCr ₂ O ₄ , NiO	Fe ₂ O ₃ , Cr ₂ O ₃ higher at 304 (HAZ)
	700	0.150	--	Fe ₂ O ₃ , Cr ₂ O ₃ , NiFe ₂ O ₄ , NiCr ₂ O ₄	Fe ₂ O ₃ , Cr ₂ O ₃ higher at 304 (HAZ)
	900	0.446	--	Fe ₂ O ₃ , Cr ₂ O ₃ , NiFe ₂ O ₄ , NiCr ₂ O ₄	Fe ₂ O ₃ , Cr ₂ O ₃ higher at 304 (HAZ)

Table 8.3 Friction weldment of dissimilar metals of AISI 4140 and AISI 304 in Na₂SO₄ + V₂O₅ (60%) environment in cyclic condition

Welding	Temp (°C)	B.L (mm)	Weight gain mg/cm ²	Kp 10 ⁻⁶ (gm ² Cm ⁻⁴ S ⁻¹)	XRD	SEM/EDAX
FRW	500	5	0.287402	0.229	Fe ₂ O ₃ , Cr ₂ O ₃ , Fe ₃ O ₄ , NiS	Fe ₂ O ₃ , Cr ₂ O ₃ and NiO higher at weld interface. Also increase while increase burn-off length.
		7	0.347851	0.336	MnO ₂ , Fe ₂ O ₃ , NiS, Cr ₂ O ₃ , NiFe ₂ O ₄ , NiCr ₂ O ₄	
		9	0.414729	0.477	Fe ₂ O ₃ , Cr ₂ O ₃	
		12	0.454973	0.575	NiS, Fe ₂ O ₃ , Cr ₂ O ₃ , Fe ₃ O ₄	
	550	5	0.500999	0.697	Fe ₂ O ₃ , Cr ₂ O ₃ , NiS	Fe ₂ O ₃ , Cr ₂ O ₃ and NiO higher at weld interface. Also increase while increase burn-off length and temperature
		7	0.61563	0.858	MnO ₂ , Fe ₂ O ₃ , NiS, Cr ₂ O ₃ , NiFe ₂ O ₄ , NiCr ₂ O ₄	
		9	0.574456	0.916	Fe V ₂ O ₄ , Fe ₂ O ₃ , Cr ₂ O ₃ , MnO ₂ , NiFe ₂ O ₄ , NiCr ₂ O ₄	
		12	0.634823	1.100	Fe ₂ O ₃ , Cr ₂ O ₃ , Fe ₃ O ₄ , MnO ₂	
	600	5	0.914877	2.32	Fe ₂ O ₃ , Cr ₂ O ₃ , Cr ₃ O ₄ , NiS,	Fe ₂ O ₃ , Cr ₂ O ₃ and NiO higher at weld interface. Also increase while increase burn-off length and temperature
		7	1.032473	2.96	Fe ₂ O ₃ , Cr ₂ O ₃ , NiFe ₂ O ₄ , NiCr ₂ O ₄	
		9	1.194571	3.96	Fe ₂ O ₃ , Cr ₂ O ₃ , NiFe ₂ O ₄ , NiCr ₂ O ₄ , NiS, (Cr,Fe) ₂ O ₃	
		12	1.354622	5.09	Fe ₂ O ₃ , Cr ₂ O ₃ , NiS, SiO ₂ , (Cr,Fe) ₂ O ₃	
700	5	9.492102	250.000	Fe ₂ O ₃ , NiS, Cr ₂ O ₃ , NiCr ₂ O ₄ , (Cr,Fe) ₂ O ₃	Fe ₂ O ₃ , Cr ₂ O ₃ and NiO higher at 304 (HAZ)	
900	5	27.48982	2099.000	Fe ₂ O ₃ , NiS, Cr ₂ O ₃ , NiCr ₂ O ₄ , (Cr,Fe) ₂ O ₃ , Fe V ₂ O ₄	Cr ₂ O ₃ higher than Fe ₂ O ₃ at 304 (HAZ)	
EBW	600	---	1.459452	5.92	Fe ₂ O ₃ , NiS, Cr ₂ O ₃ , NiFe ₂ O ₄ , NiCr ₂ O ₄ , (Cr,Fe) ₂ O ₃ ,	Fe ₂ O ₃ , Cr ₂ O ₃ and NiO higher at 304 (HAZ)
TIG	600	---	1.666733	7.720	Fe ₂ O ₃ , Cr ₂ O ₃ , NiS, NiFe ₂ O ₄ , NiCr ₂ O ₄ , (Cr,Fe) ₂ O ₃	Fe ₂ O ₃ and MoO ₃ high at weld zone

Table 8.4 Friction weldment of dissimilar metals of AISI 4140 and AISI 304 in K₂SO₄ + NaCl (60%) environment in cyclic condition

Welding	Temp (°C)	B.L (mm)	Weight gain mg/cm ²	Kp 10 ⁻⁶ (gm ² Cm ⁻⁴ S ⁻¹)	XRD	SEM/EDAX	
Friction Welding	500	5	1.267281	4.460	Fe ₂ O ₃ , Cr ₂ O ₃ , NiFe ₂ O ₄ , NiCr ₂ O ₄ , FeS	Fe ₂ O ₃ , Cr ₂ O ₃ and NiO higher at 304(HAZ)	
		7	1.609037	7.190	Fe ₂ O ₃ , Cr ₂ O ₃ , NiFe ₂ O ₄ , NiCr ₂ O ₄ , (Cr,Fe) ₂ O ₃	Fe ₂ O ₃ , Cr ₂ O ₃ and NiO higher at 304(HAZ)	
		9	2.00075	11.120	Fe ₂ O ₃ , Cr ₂ O ₃ , NiFe ₂ O ₄ , NiCr ₂ O ₄	Fe ₂ O ₃ , Cr ₂ O ₃ and K ₂ O higher at 304(HAZ)	
		12	--	--			
	550	5	2.382436	15.700	Fe ₂ O ₃ , Cr ₂ O ₃ , NiFe ₂ O ₄ , NiCr ₂ O ₄ , (Cr,Fe) ₂ O ₃	Fe ₂ O ₃ , Cr ₂ O ₃ higher at weld as well as HAZ of 304 and 4140	
		7	2.568073	18.310	Fe ₂ O ₃ , Cr ₂ O ₃ , (Cr,Fe) ₂ O ₃ , MnO ₂	Fe ₂ O ₃ , Cr ₂ O ₃ higher at weld as well as HAZ of 304 and 4140	
		9	2.98379	24.730	Fe ₂ O ₃ , Cr ₂ O ₃ , (Cr,Fe) ₂ O ₃ , MnO ₂	-----	
		12	3.304694	30.340	Fe ₂ O ₃ , Cr ₂ O ₃ , NiFe ₂ O ₄ , NiCr ₂ O ₄ , (Cr,Fe) ₂ O ₃	Fe ₂ O ₃ , Cr ₂ O ₃ higher at weld	
	EBW	600	5	4.369897	53.000	Fe ₂ O ₃ , Cr ₂ O ₃ , NiFe ₂ O ₄ , NiCr ₂ O ₄	Fe ₂ O ₃ , Cr ₂ O ₃ and MnO higher at 304(HAZ)
			7	4.498333	56.210	Fe ₂ O ₃ , Cr ₂ O ₃ , NiFe ₂ O ₄ , NiCr ₂ O ₄ , (Cr,Fe) ₂ O ₃	Fe ₂ O ₃ and MnO higher at 4140(HAZ)
			9	4.851598	65.380	Fe ₂ O ₃ , Cr ₂ O ₃ , NiFe ₂ O ₄ , NiCr ₂ O ₄ , (Cr,Fe) ₂ O ₃	Fe ₂ O ₃ , Cr ₂ O ₃ and MnO higher at 4140(HAZ)
			12	5.224079	75.810	Fe ₂ O ₃ , Cr ₂ O ₃ , NiFe ₂ O ₄ , NiCr ₂ O ₄	Fe ₂ O ₃ , Cr ₂ O ₃ and MnO higher at weld as well as HAZ of 304 and 4140
TIG	600	--	3.691206	37.850	Fe ₂ O ₃ , Cr ₂ O ₃ , NiS, NiFe ₂ O ₄ , NiCr ₂ O ₄ , (Cr,Fe) ₂ O ₃	Fe ₂ O ₃ , Cr ₂ O ₃ and NiO higher at 304 (HAZ)	
TIG	600	--	3.691206	37.850	Fe ₂ O ₃ , Cr ₂ O ₃ , NiS, NiFe ₂ O ₄ , NiCr ₂ O ₄ , (Cr,Fe) ₂ O ₃	Fe ₂ O ₃ and MnO high at weld zone	

Table 8.5 Friction weldment of dissimilar metals of AISI 4140 and AISI 304 in Na₂SO₄ (40%) + K₂SO₄ (40%) + NaCl (10%) + KCl (10%) environment in cyclic condition

Welding	Temp (°C)	B.L (mm)	Weight gain mg/cm ²	Kp (10 ⁻⁶ (gm ² Cm ⁻⁴ S ⁻¹))	XRD	SEM/EDAX
Friction Welding	500	5	0.773951	1.670	Fe ₂ O ₃ , Cr ₂ O ₃ , NiFe ₂ O ₄ , NiCr ₂ O ₄ , NIS, FeS	Fe ₂ O ₃ , Cr ₂ O ₃ and NiO higher at weld and 304 (HAZ)
		5	1.136662	3.590	Fe ₂ O ₃ , Cr ₂ O ₃ , NiFe ₂ O ₄ , NiCr ₂ O ₄ , NIS, (Cr,Fe) ₂ O ₃ , SiO ₂	Fe ₂ O ₃ , MnO higher at weld
	550	7	1.375863	5.260	Fe ₂ O ₃ , Cr ₂ O ₃ , NiFe ₂ O ₄ , NiCr ₂ O ₄	-----
		9	1.694993	7.980	Fe ₂ O ₃ , Cr ₂ O ₃ , NiFe ₂ O ₄ , NiCr ₂ O ₄	Fe ₂ O ₃ , Cr ₂ O ₃ and NiO higher at 304 (HAZ)
		12	2.065188	11.850	Fe ₂ O ₃ , Cr ₂ O ₃ , NiFe ₂ O ₄ , NiCr ₂ O ₄	Fe ₂ O ₃ , Cr ₂ O ₃ and NiO higher at weld and 304 (HAZ)
		5	2.486162	17.170	Fe ₂ O ₃ , Cr ₂ O ₃ , NiFe ₂ O ₄ , NiCr ₂ O ₄ , (Cr,Fe) ₂ O ₃	Fe ₂ O ₃ and MnO hogher at weld as well as both HAZ. Cr ₂ O ₃ higher at 304 (HAZ)
	600	12	2.904824	23.440	Fe ₂ O ₃ , Cr ₂ O ₃ , NiFe ₂ O ₄ , NiCr ₂ O ₄ , (Cr,Fe) ₂ O ₃	Fe ₂ O ₃ and MnO hogher at weld as well as both HAZ. Cr ₂ O ₃ higher at 304 (HAZ)

Table 8.6 Friction weldment of dissimilar metals of AISI 4140 and AISI 304 in Na₂SO₄ + NaCl (50%) environment in cyclic condition

Welding	Temp (°C)	B.L (mm)	Weight gain mg/cm ²	Kp 10 ⁻⁶ (gm ² Cm ⁻⁴ S ⁻¹)	XRD	SEM/EDAX
Friction Welding	500	5	0.605805	1.020	Fe ₂ O ₃ , Cr ₂ O ₃ , NiFe ₂ O ₄ , NiCr ₂ O ₄ , NiS, FeS, (Cr,Fe) ₂ O ₃	Fe ₂ O ₃ , Cr ₂ O ₃ NiO hogher at 304 (HAZ)
		7	0.792465	1.740	Fe ₂ O ₃ , Cr ₂ O ₃ , FeS, (Cr,Fe) ₂ O ₃	Fe ₂ O ₃ , Cr ₂ O ₃ hogher at weld and 304 (HAZ)
		9	0.845577	1.980	Fe ₂ O ₃ , Cr ₂ O ₃ , FeS, (Cr,Fe) ₂ O ₃	Fe ₂ O ₃ , Cr ₂ O ₃ hogher at weld and 304 (HAZ)
		12	--	--		
	550	5	0.938083	2.440	Fe ₂ O ₃ , Cr ₂ O ₃ , NiFe ₂ O ₄ , NiCr ₂ O ₄ , NiS, NiO	Fe ₂ O ₃ , Cr ₂ O ₃ and MnO hogher at weld
		7	1.072381	3.190	Fe ₂ O ₃ , Cr ₂ O ₃ , NiCr ₂ O ₄ , NiS, NiO, (Cr,Fe) ₂ O ₃	Fe ₂ O ₃ , Cr ₂ O ₃ hogher at weld
		9	1.194152	3.960	Fe ₂ O ₃ , Cr ₂ O ₃ , (Cr,Fe) ₂ O ₃	Fe ₂ O ₃ , Cr ₂ O ₃ hogher at weld
		12	1.393557	5.390	Fe ₂ O ₃ , Cr ₂ O ₃ , NiFe ₂ O ₄ , NiCr ₂ O ₄	Fe ₂ O ₃ , Cr ₂ O ₃ hogher at weld

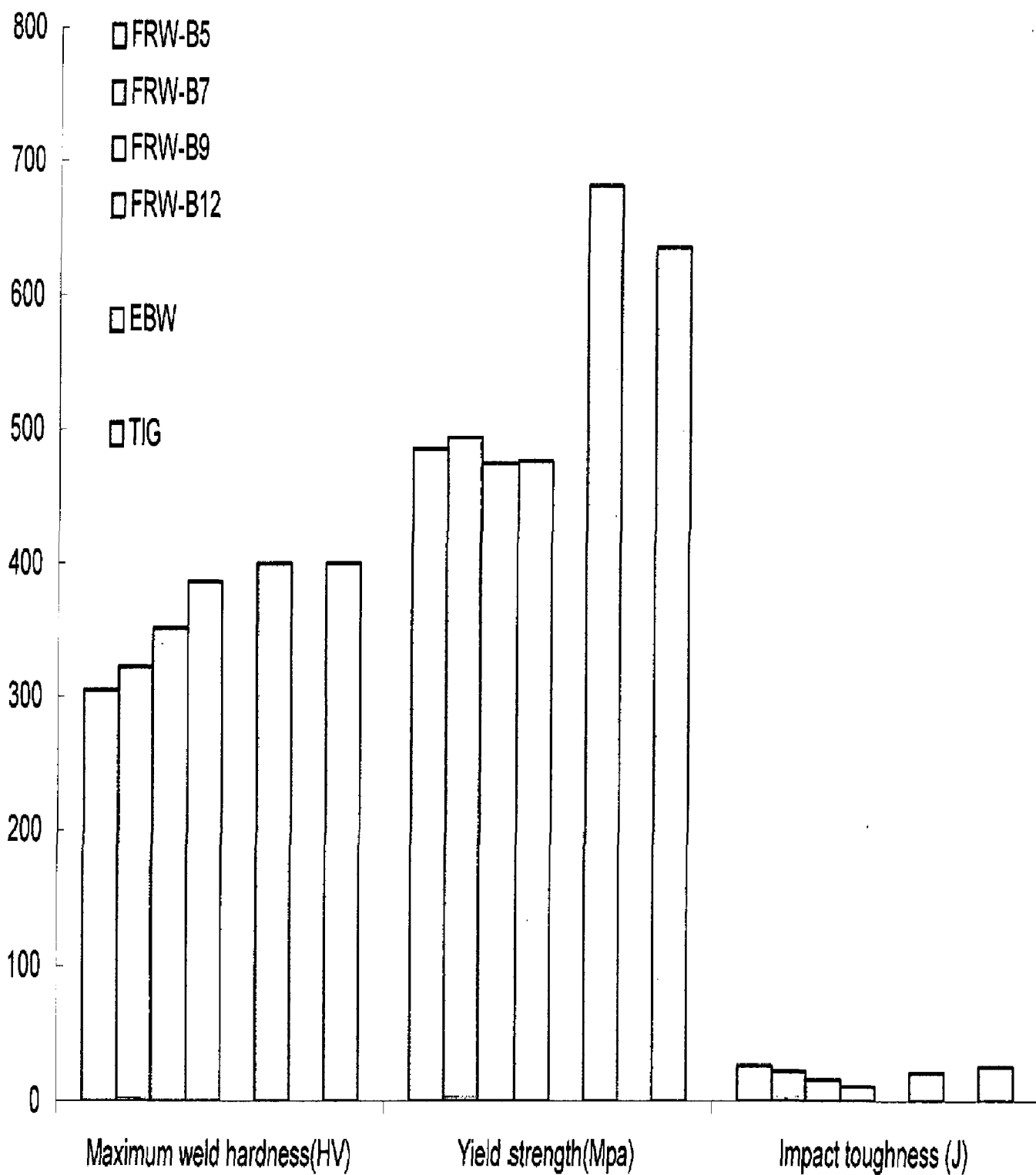


Fig. 8.1 Bar charts showing cumulative mechanical properties of AISI 4140 and AISI 304 dissimilar metals made by FRW, EBW and TIG.

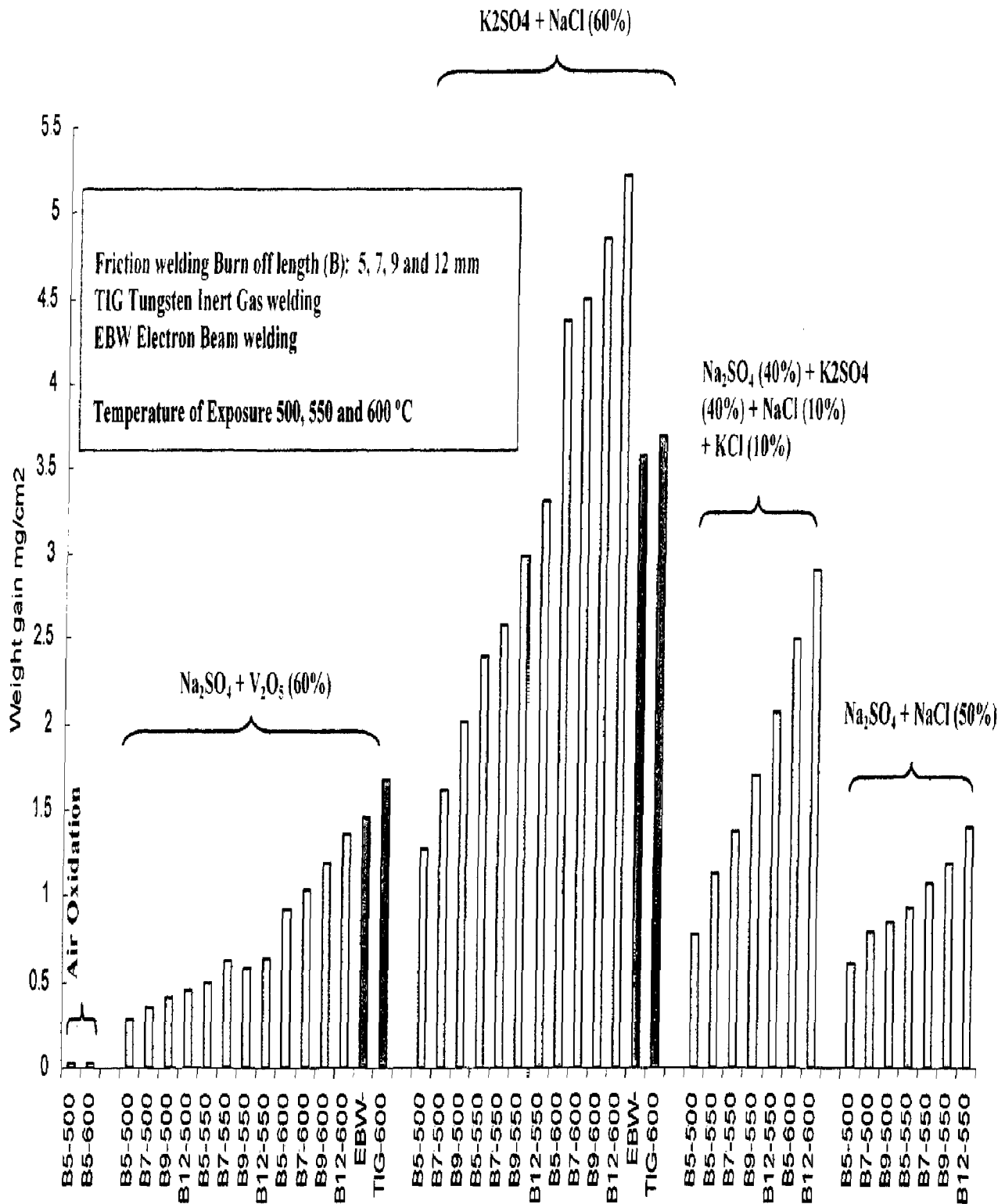


Fig. 8.2 (a) Bar charts showing cumulative weight gain (mg/cm²) for dissimilar weldment subjected to cyclic oxidation in air and molten salt environment for 50 cycles

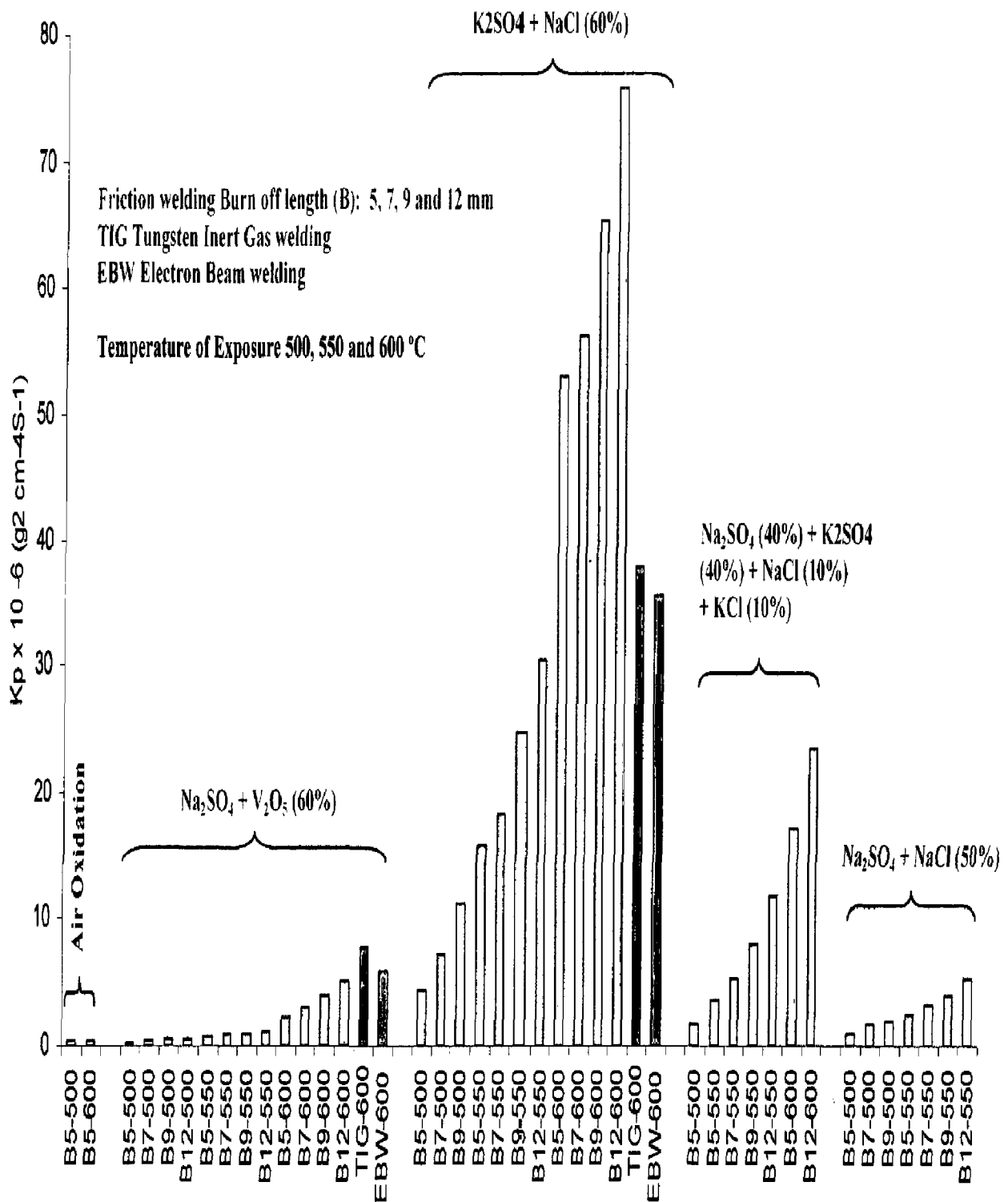


Fig. 8.2 (b) Bar charts showing parabolic rate constant K_p ($10^{-6}(\text{gm}^2\text{Cm}^{-4}\text{S}^{-1})$) for dissimilar weldment subjected to cyclic oxidation in air at and molten salt environment for 50 cycles

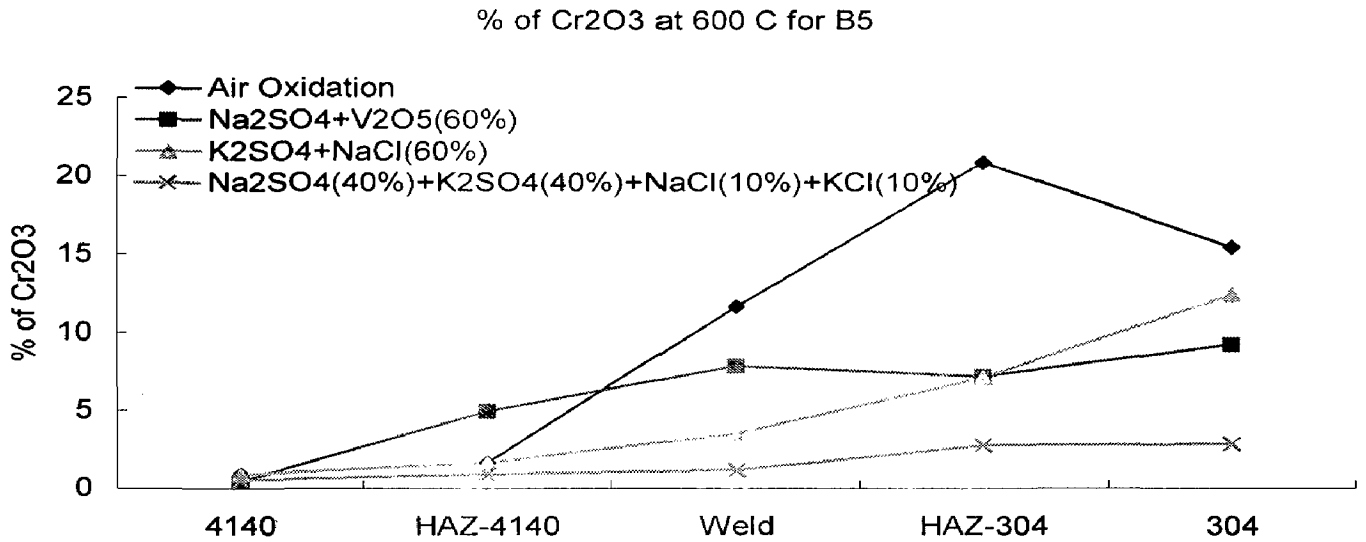


Fig 8.3(A) The constituent of Cr₂O₃ in the scale on friction weldment exposing in different environments at 600 °C.

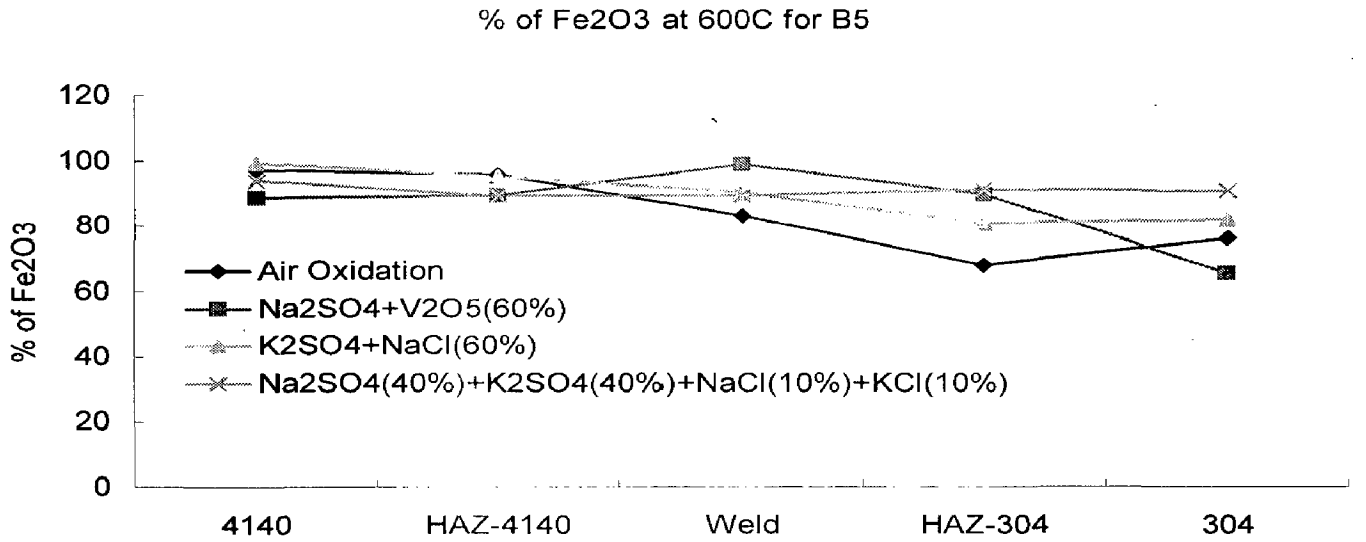


Fig 8.3(B) The constituent of Fe₂O₃ in the scale on friction weldment exposing in different environments at 600 °C.

% of MnO at 600 C for B5

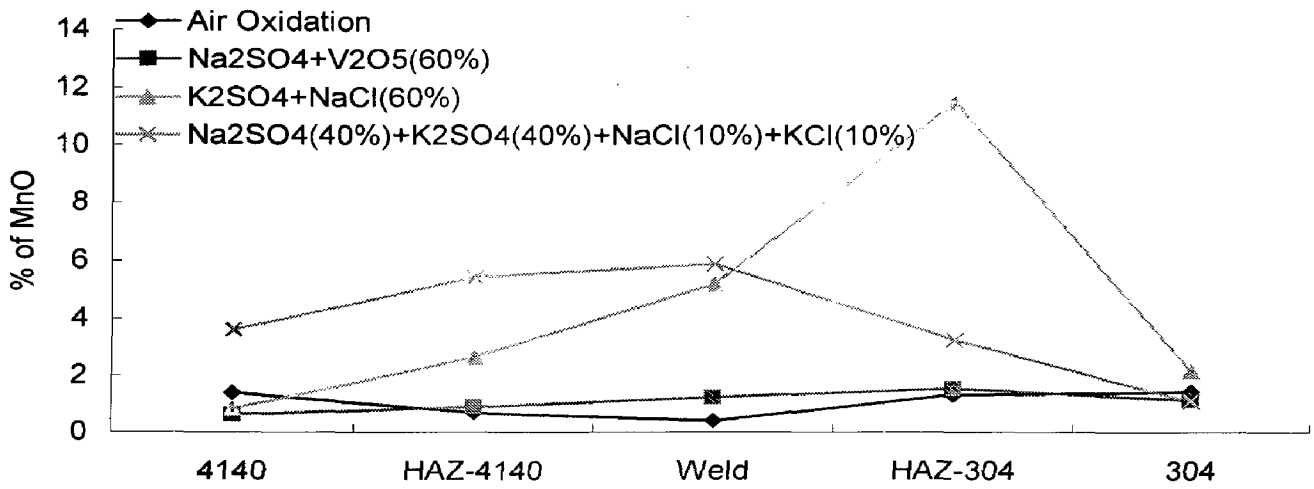


Fig 8.3(C) The constituent of MnO in the scale on friction weldment exposing in different environments at 600 °C.

% of NiO at 600 C for B5

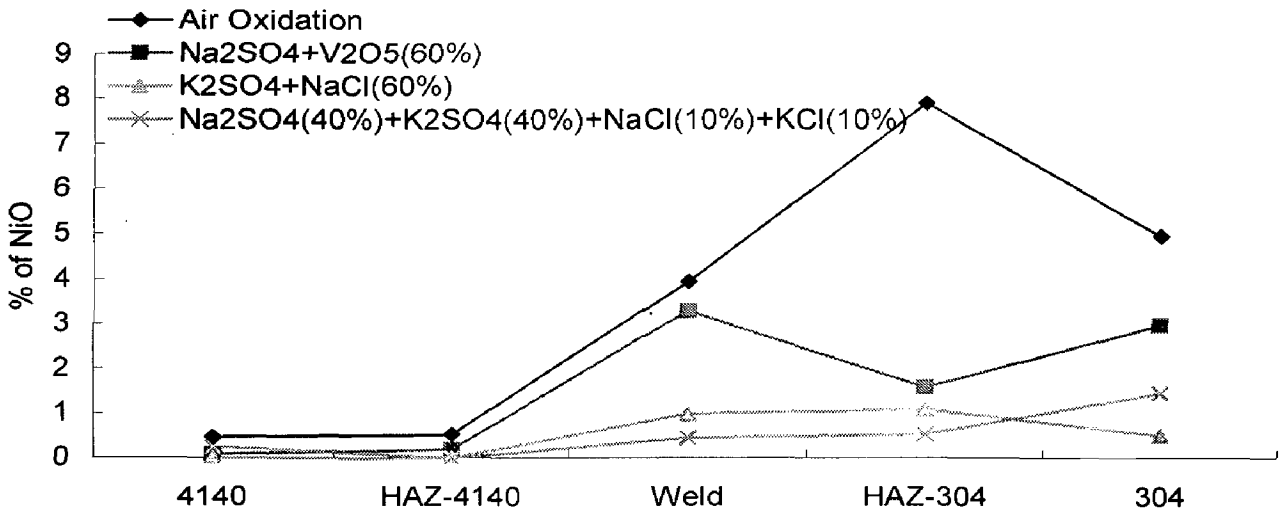


Fig 8.3(D) The constituent of NiO in the scale on friction weldment exposing in different environments at 600 °C.

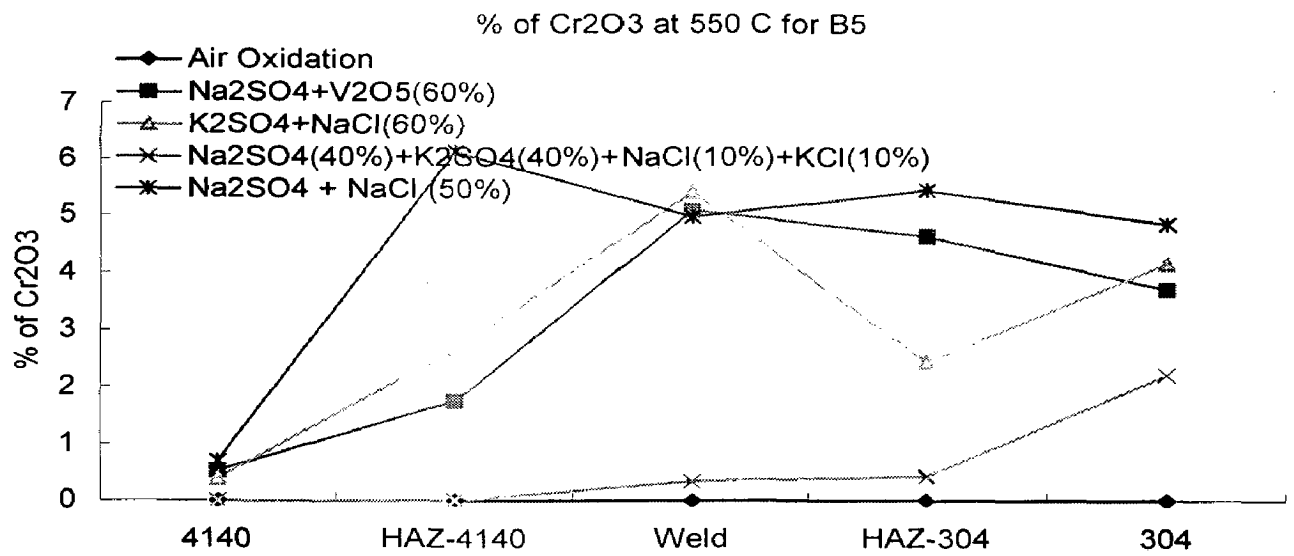


Fig 8.3(E) The constituent of Cr₂O₃ in the scale on friction weldment exposing in different environments at 550 °C.

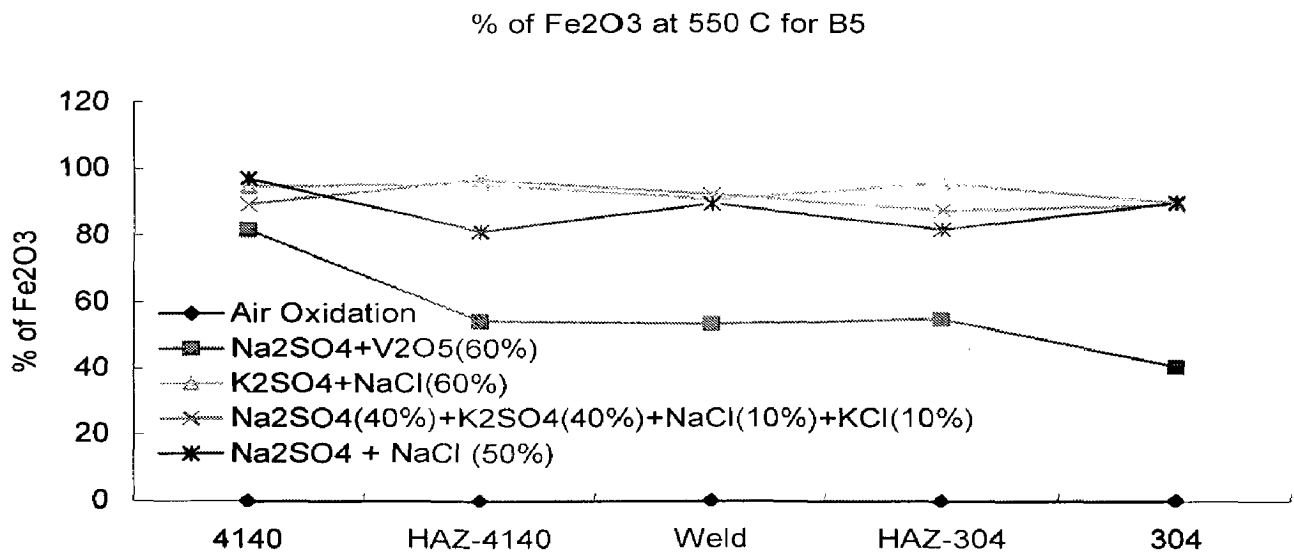


Fig 8.3(F) The constituent of Fe₂O₃ in the scale on friction weldment exposing in different environments at 550 °C.

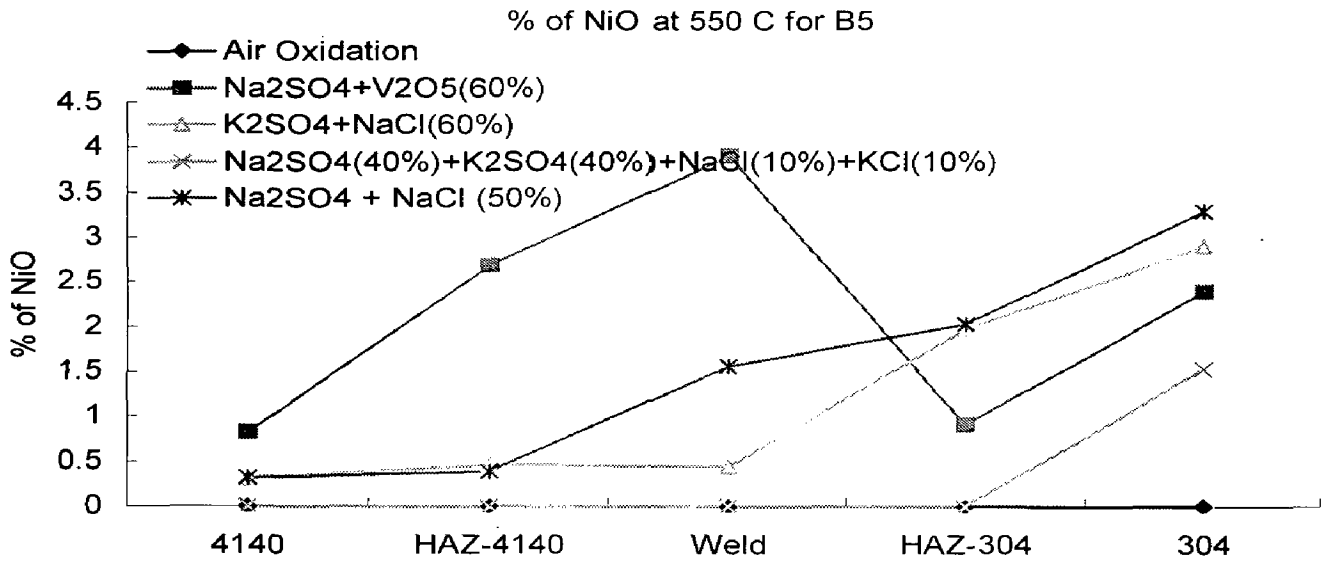


Fig 8.3(G) The constituent of NiO in the scale on friction weldment exposing in different environments at 550 °C.

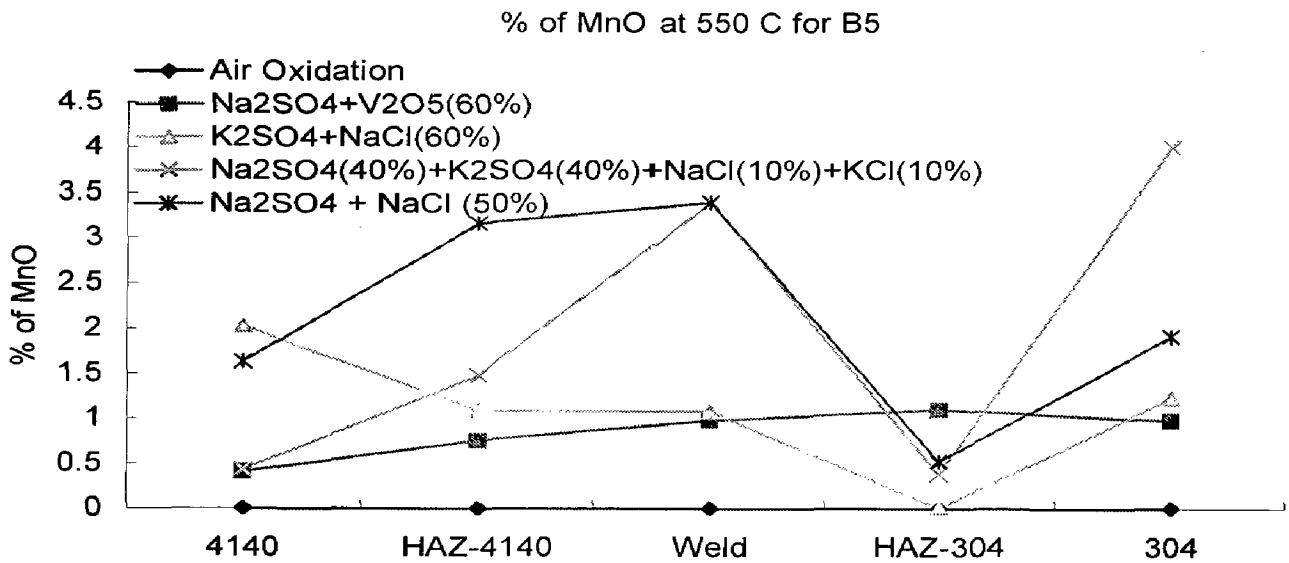


Fig 8.3(H) The constituent of MnO in the scale on friction weldment exposing in different environments at 550 °C.

% of Cr₂O₃ at 500 C for B5

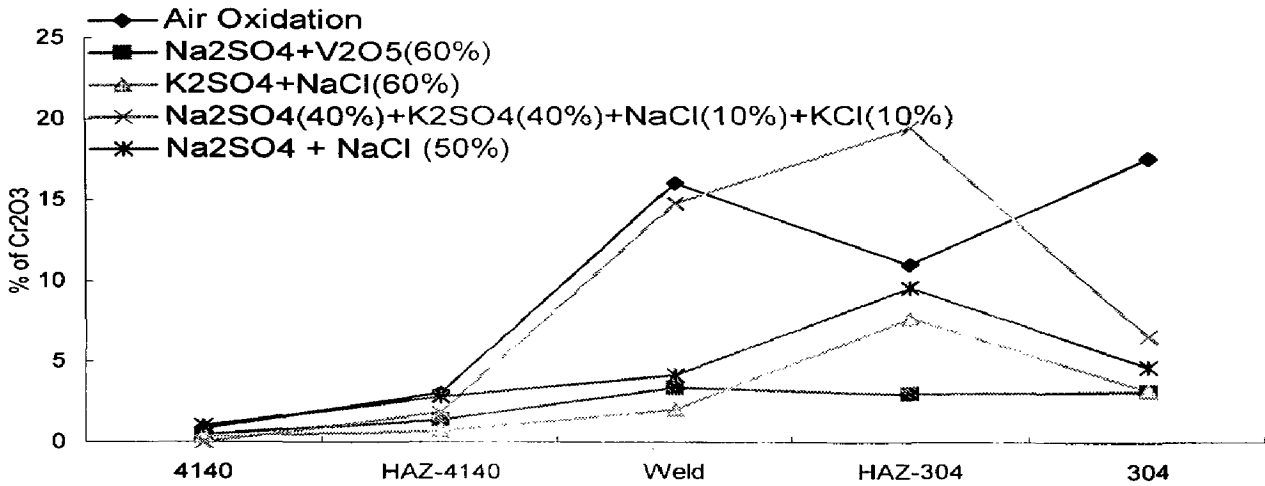


Fig 8.3(I) The constituent of Cr₂O₃ in the scale on friction weldment exposing in different environments at 500 °C.

% of Fe₂O₃ at 500 C for B5

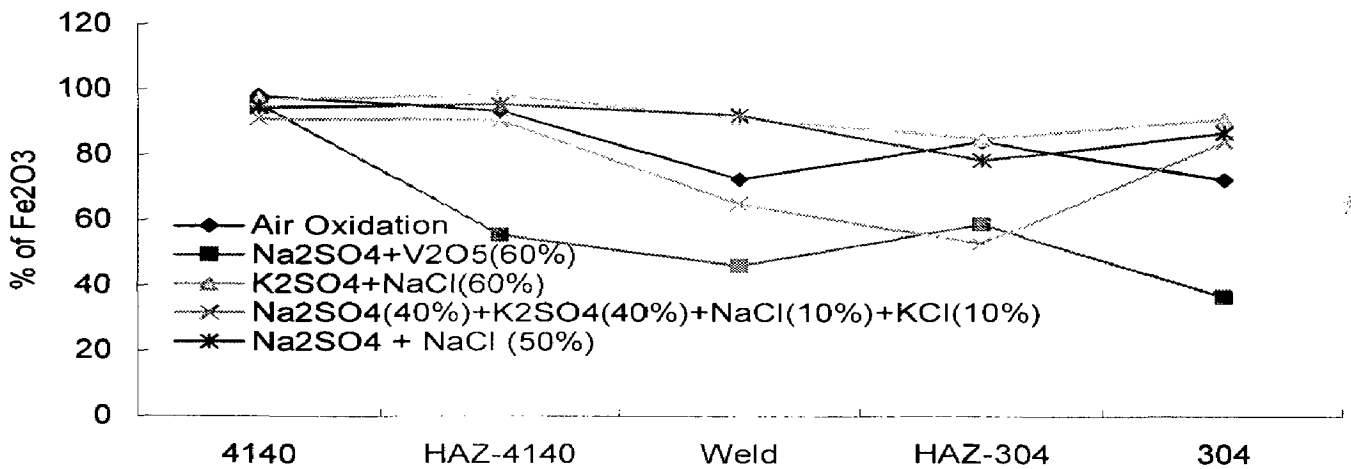


Fig 8.3(J) The constituent of Fe₂O₃ in the scale on friction weldment exposing in different environments at 500 °C.

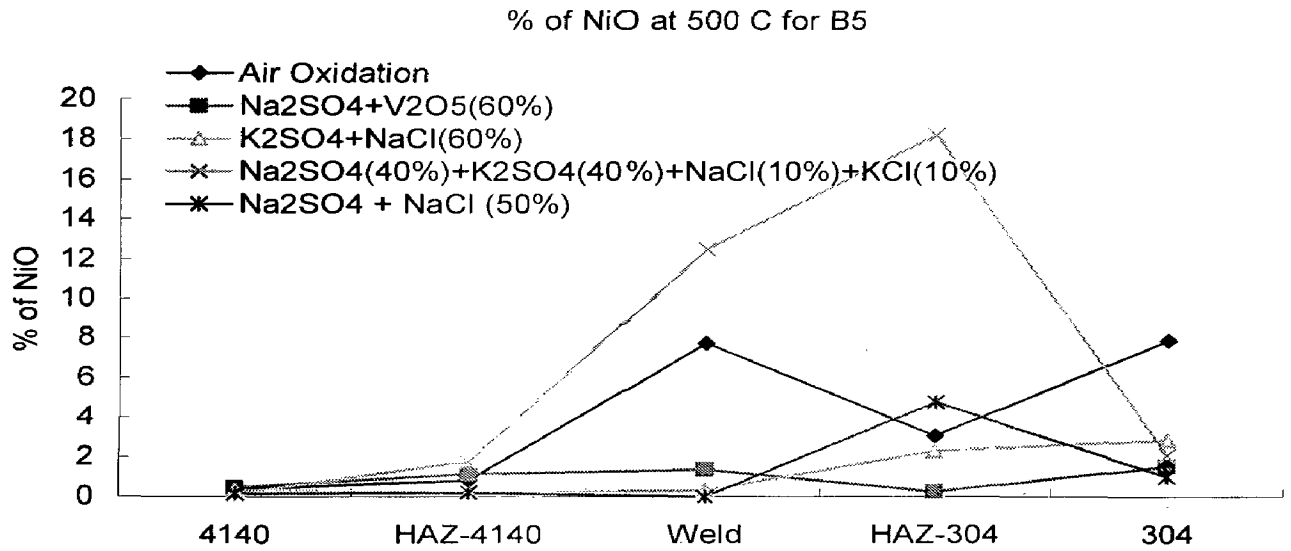


Fig 8.3(K) The constituent of NiO in the scale on friction weldment exposing in different environments at 500 °C.

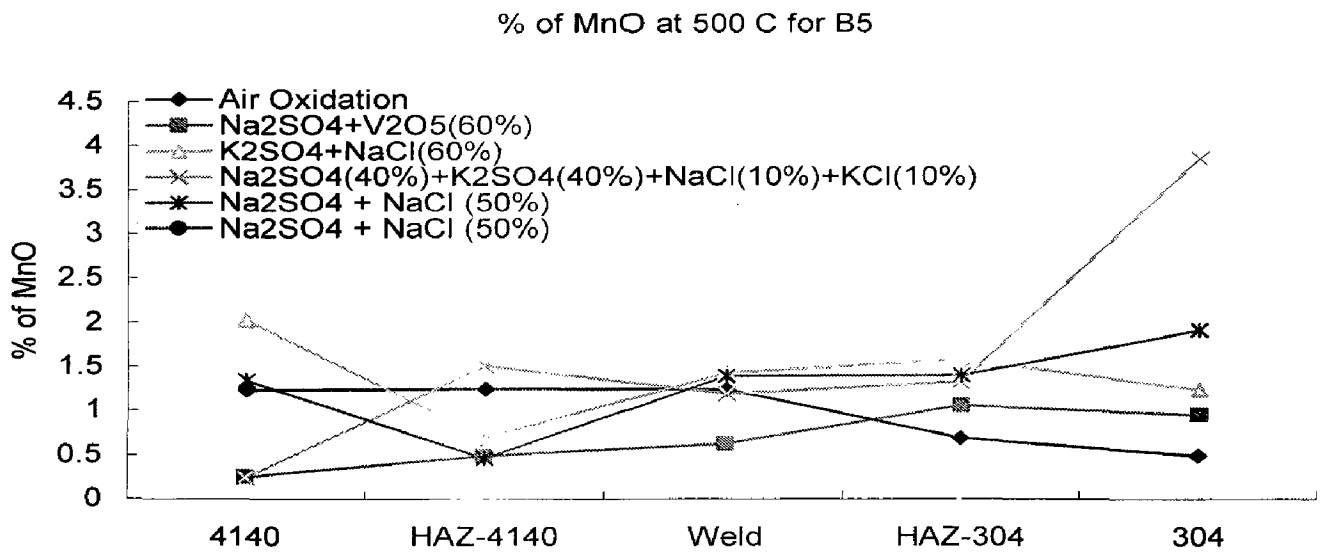


Fig 8.3(L) The constituent of MnO in the scale on friction weldment exposing in different environments at 500 °C.

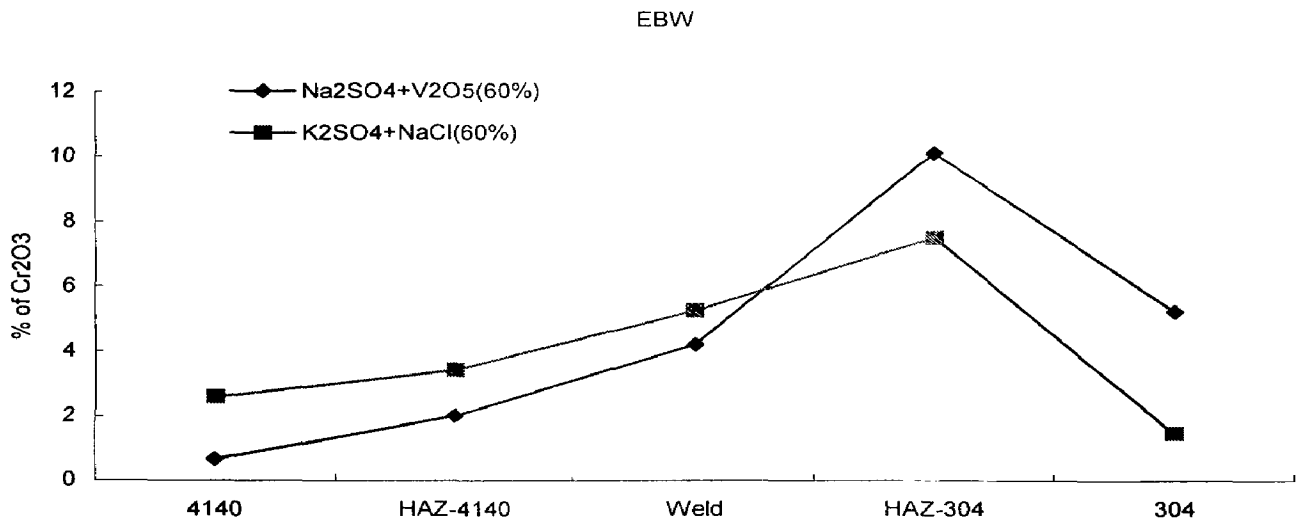


Fig 8.4(A) The constituent of Cr₂O₃ in the scale on EBW weldment exposing in different environments at 600 °C.

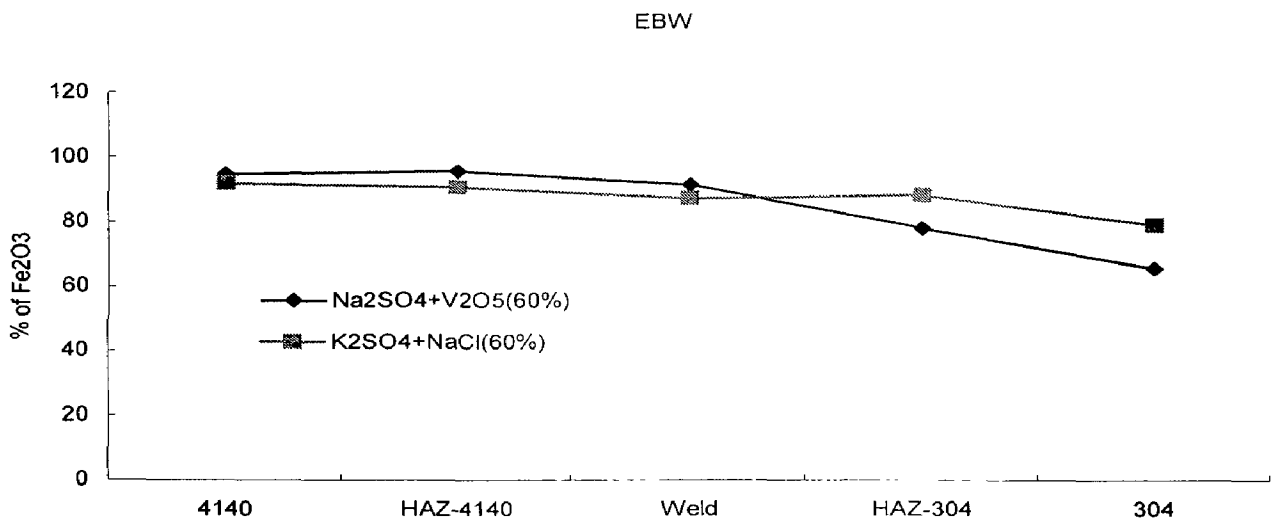


Fig 8.4(B) The constituent of Fe₂O₃ in the scale on EBW weldment exposing in different environments at 600 °C.

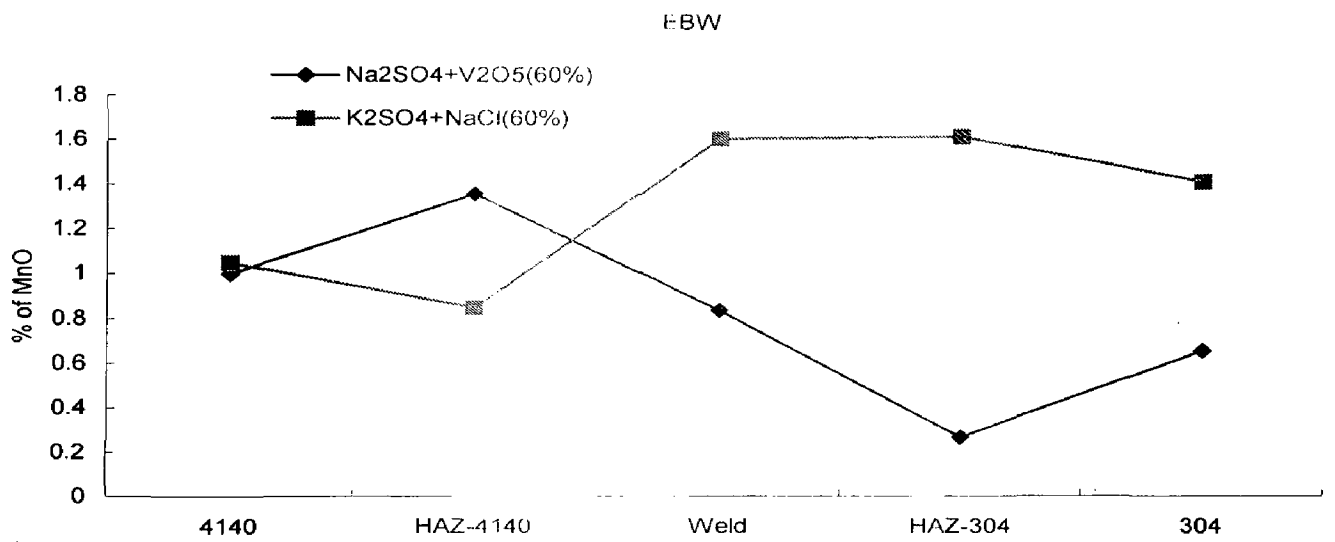


Fig 8.4(C) The constituent of MnO in the scale on EBW weldment exposing in different environments at 600 °C.

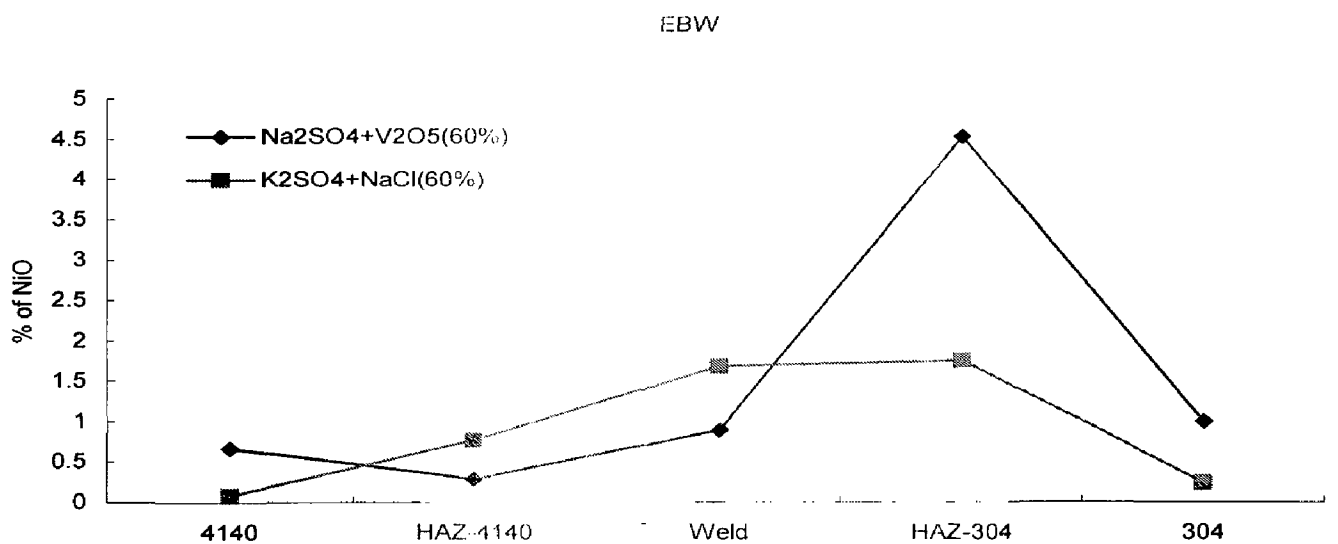


Fig 8.4(D) The constituent of NiO in the scale on EBW weldment exposing in different environments at 600 °C.

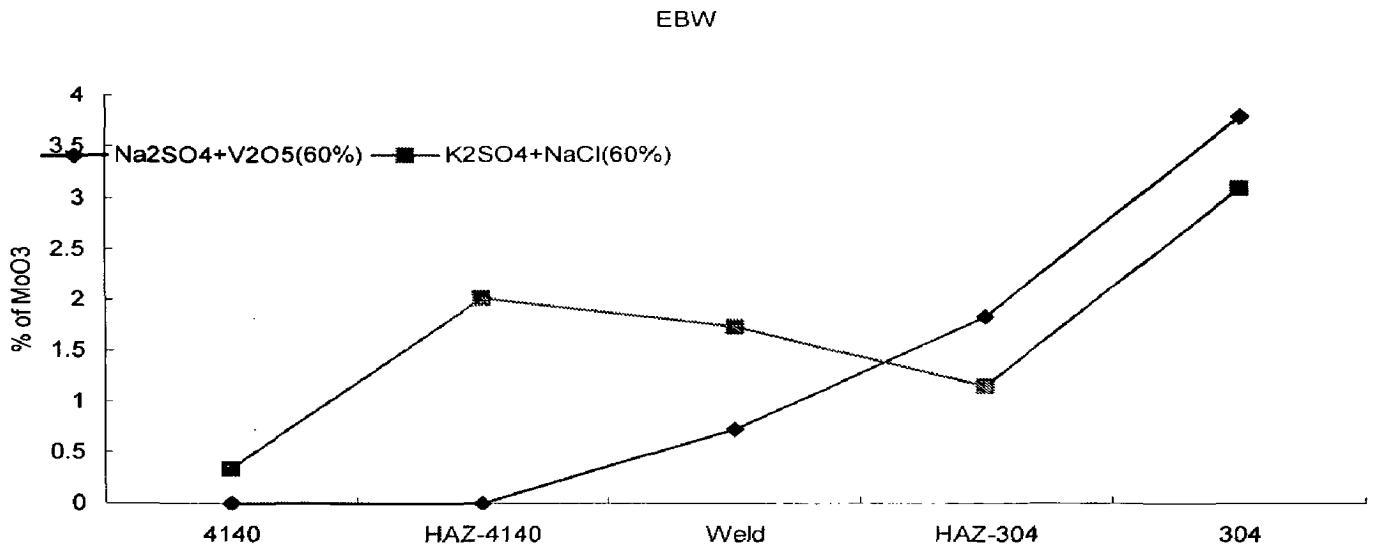


Fig 8.4(E) The constituent of MoO₃ in the scale on EBW weldment exposing in different environments at 600 °C.

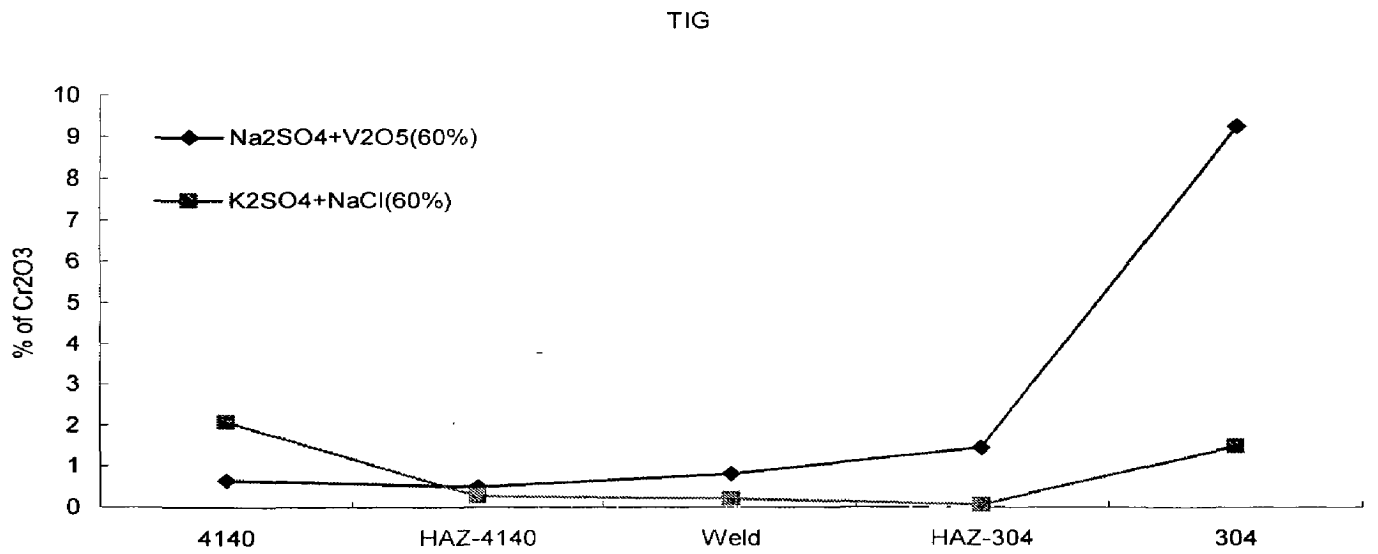


Fig 8.4(F) The constituent of Cr₂O₃ in the scale on TIG weldment exposing in different environments at 600 °C.

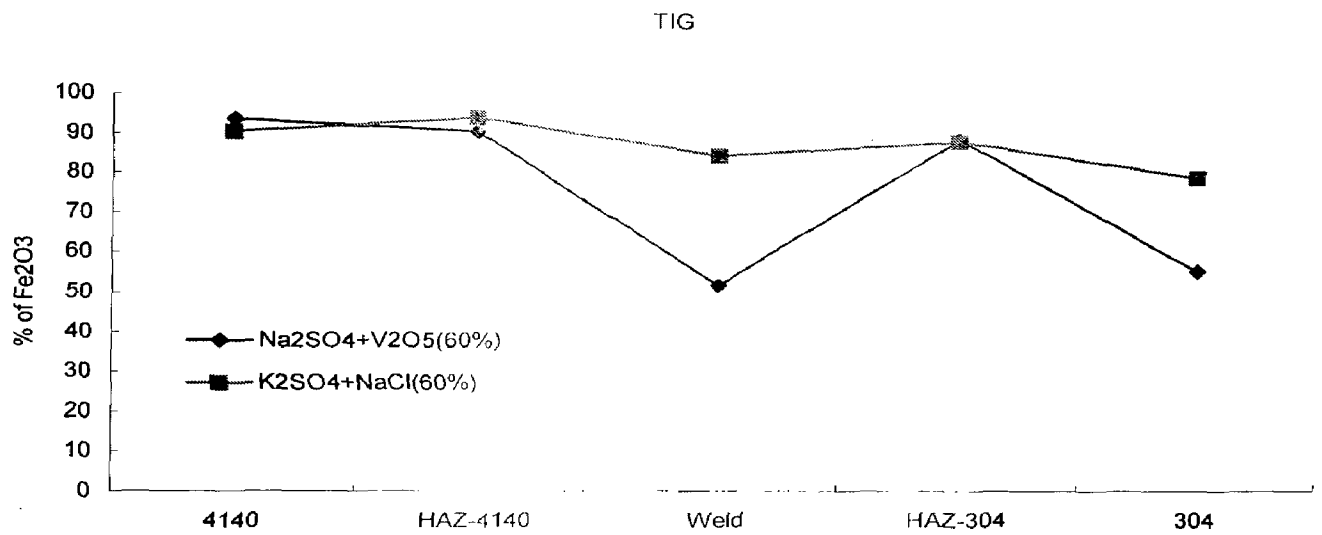


Fig 8.4(G) The constituent of Fe₂O₃ in the scale on TIG weldment exposing in different environments at 600 °C.

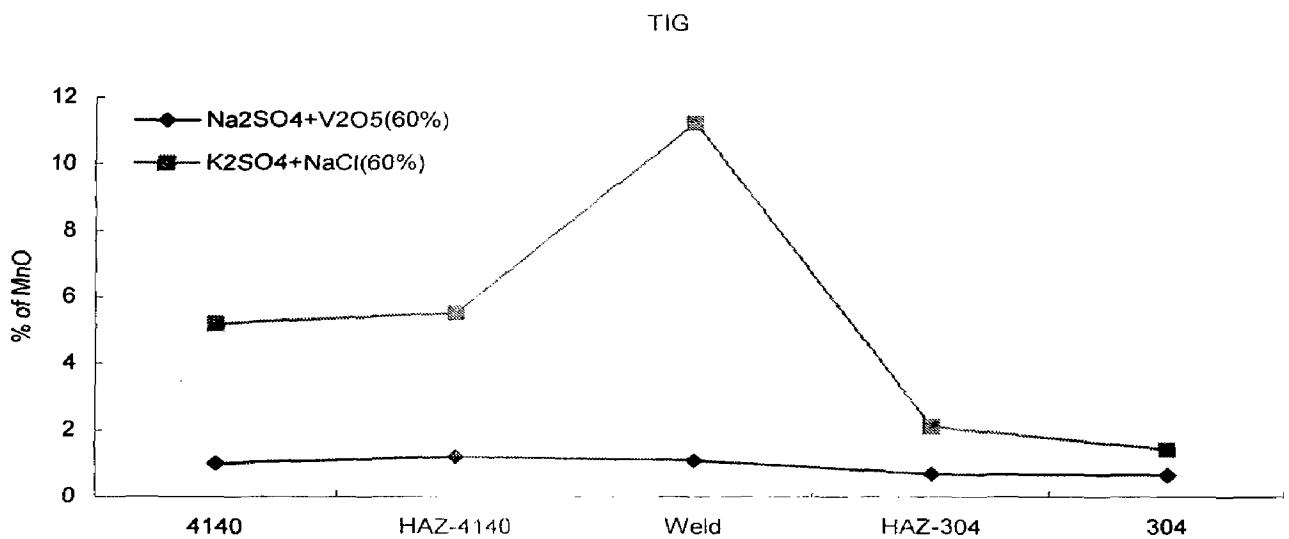


Fig 8.4(H) The constituent of MnO in the scale on TIG weldment exposing in different environments at 600 °C.

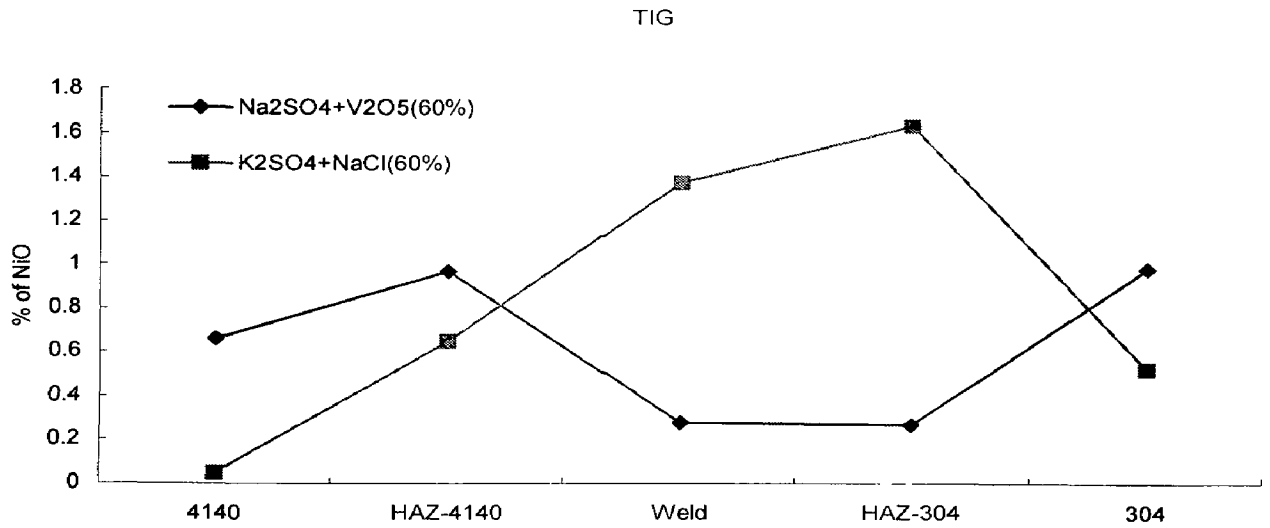


Fig 8.4(I) The constituent of NiO in the scale on TIG weldment exposing in different environments at 600 °C.

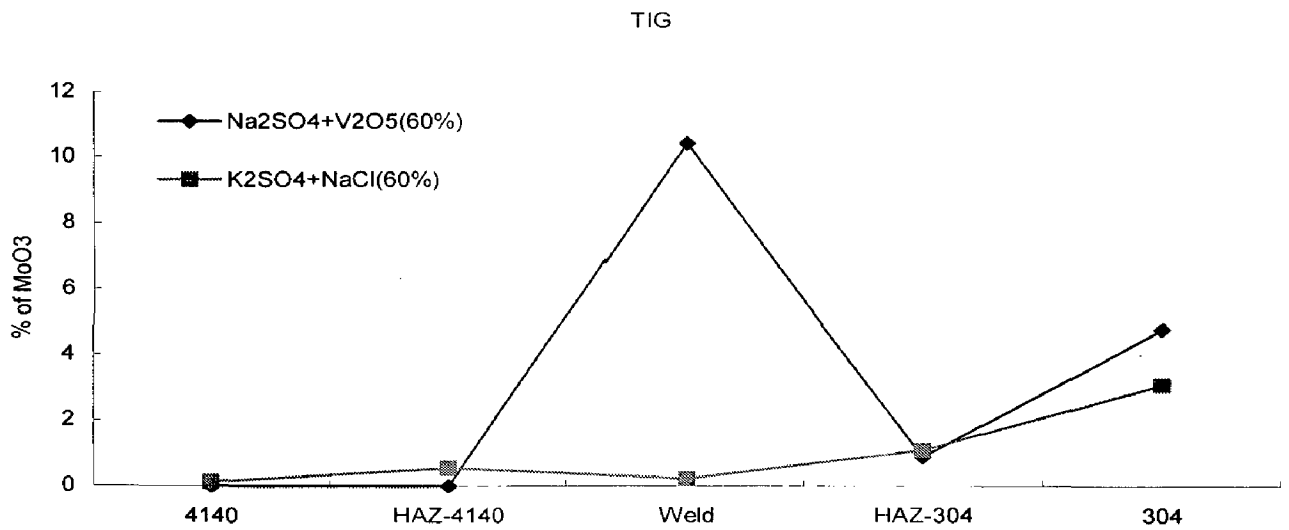


Fig 8.4(J) The constituent of MoO₃ in the scale on TIG weldment exposing in different environments at 600 °C.

CHAPTER 9

CONCLUSIONS

The conclusions from the present study containing weldment of AISI 304 and AISI 4140 dissimilar metals obtained by three types welding process namely Friction Welding (FRW), Electron Beam Welding (EBW) and Tungsten Inert Gas welding (TIG). All the weldments was critically examined the mechanical properties namely micro-hardness across the weldment, impact toughness and tensile strength. The cyclic oxidation studies were conducted on the weldment in air as well as the different molten salt environment of

(i) $\text{Na}_2\text{SO}_4 + \text{V}_2\text{O}_5$ (60%); (ii) $\text{K}_2\text{SO}_4 + \text{NaCl}$ (60%); (iii) Na_2SO_4 (40%)+ K_2SO_4 (40%)+ NaCl (10%) + KCl (10%); (iv) $\text{Na}_2\text{SO}_4 + \text{NaCl}$ (50%).

Salient conclusions from the present study are enumerated below:

1. The results of this investigation have shown that AISI 304 austenitic stainless steel can be welded to AISI 4140 low alloy steel by above mentioned welding process.
2. Sound welds could be obtained between AISI 304 austenitic stainless steel and AISI 4140 low alloy steel by all the three welding techniques.
3. Heat affected zone of dissimilar weldment made by TIG is wider as compared to EBW and FRW.
4. Formation of carbide and intermetallic compound in the friction weld zone is less as compared to EBW and TIG welding.

5. All the three welding processes the soft zone is observed on the heat affected zone of low alloy steel AISI 4140 side may be due to carbon depletion as it is migrating to AISI 304 side.

6. In friction welding process it was noted that the peak hardness increases with increase in burn-off length. Whereas the hardness values in adjacent low alloy steel further falls with an increase in burn-off length. This behavior can be attributed to carbon migration from the low alloy steel side to stainless steel side.

7. The peak hardness on the weld zone made by FRW is less as compared to TIG and EBW. This can be attributed to formation of carbides and intermetallic compounds in the weld zone with TIG and EBW which is also supported by XRD analysis. The sequence for the peak hardness in the weld zone has been observed is in following order.

TIG > EBW > FRW

8. In friction welded AISI 304 and AISI 4140 dissimilar metals, the reduction in toughness and increase in hardness across the weld with increase in burn-off length is related to increased carbon migration from the low alloy steel side towards stainless steel due to higher temperatures that prevail around the interface region with increase in burn-off length.

9. In friction weldment that brittle fracture was observed as we increase the burn off length which further supporting the formation of carbides and intermetallic compounds. From the SEM fractographic of impact tested dissimilar weldment made by EBW and TIG shows cleavage fracture. The sequence for the impact toughness of dissimilar weldment has been observed as given below.

FRW (B5) > TIG > EBW

10. The yield strength of dissimilar weldment made by EBW is higher as compared to TIG and FRW. The failure was observed on AISI 4140 side for friction weldment.

Where as in the case of weldment made by EBW and TIG, the failure occurred on HAZ of AISI 4140. The sequence for the yield strength has been observed to be as follows.

EBW > TIG > FRW

11. From EPMA analysis on the dissimilar weldment it is observed that chromium and nickel diffuse towards AISI 4140 from the AISI 304 and diffusion of iron from AISI 4140 side towards AISI 304. The extent of diffusion is more in case of EBW welded dissimilar metals as compared to the weldment made by TIG and FRW. Also from the micro-hardness data it was noted that the diffusion of carbon from AISI 4140 side towards AISI 304 side.

12. A distinct weld region with enrichment of chromium, nickel, iron and carbon is prominent the weldment made by EBW as compared to TIG and FRW. The sequence for the enrichment of above mentioned elements in the weld zone has been observed as given below.

EBW > TIG > FRW

13. The oxidation rates for the investigated friction welded dissimilar metals based on the overall weight gains after 50 cycles of oxidation in all the environments could be arranged in the following order:

$K_2SO_4 + NaCl (60\%) > Na_2SO_4 (40\%) + K_2SO_4 (40\%) + NaCl (10\%) + KCl (10\%)$
 $> Na_2SO_4 + V_2O_5 (60\%) > Na_2SO_4 + NaCl (50\%) > Air$

14. The oxidation rates for the investigated dissimilar weldment made by EBW and TIG based on the overall weight gains after 50 cycles of oxidation in all the environments could be arranged in the following order:

$K_2SO_4 + NaCl (60\%) > Na_2SO_4 + V_2O_5 (60\%)$

15. The effect of burn off length (B) on oxidation rates for the investigated friction welded dissimilar metals based on the overall weight gains after 50 cycles of oxidation in all the environments could be arranged in the following order:

$B_{12} > B_9 > B_7 > B_5$

16. The oxidation rates for the investigated dissimilar weldments made by FRW, EBW and TIG based on the overall weight gains after 50 cycles of oxidation in the $K_2SO_4 + NaCl$ (60%) environment at 600 °C could be arranged in the following order:

$TIG > EBW > FRW$

17. The oxidation rates for the investigated dissimilar weldment made by FRW, EBW and TIG based on the overall weight gains after 50 cycles of oxidation in the $Na_2SO_4 + V_2O_5$ (60%) environment 600 °C could be arranged in the following order:

$FRW > TIG > EBW$

18. There is noticeable weight gain in the in dissimilar weldment. This may be attributed to the galvanic type of attack arising out of heterogeneity in composition – weld interface material, HAZ and the base materials.

19. Rate of oxidation was observed to be high in the early cycles of the study in all the investigated environments for all the exposed temperatures, which may be attributed to the fact that during transient period of oxidation, the scales formed may be providing protection to the underneath metals.

20. Dissimilar weldment suffered accelerated hot corrosion in the chloride + sulfate mixed molten salt environment in the form of intense spalling and sputtering of its scale.

21. The cracking of oxide scale on the weldment as observed in the present study in air and molten salt for all the temperatures of exposure might be attributed to different composition of base metals, weld metals and oxide formed. Their thermal expansion coefficients are not exactly equal, which inevitably results in thermal-stresses as suggested by Rapp et al (1981) and Liu et al (2001).

22. The scale on HAZ of 4140 thicker and prone to spalling which may be attributed to the iron oxidized in preference of Cr in the alloy 4140 where Cr content is less and the part of this Cr is present as carbide. This amount of Cr is not sufficient for forming a protective layer of Cr_2O_3 on the surface. The diffusion of Cr from interior to the outer surface is not much as diffusion coefficient of Cr is small. Oxygen diffuses through the outer scale of iron oxides and reacts with chromium to form Cr_2O_3 at the inner layers which exist as particles and not as continuous layers.

23. The higher content of Fe_2O_3 and Cr_2O_3 on scale over weld zone may be due to enrichment of this zone with Fe and Cr as indicated by EPMA.

24. The weld zone of dissimilar weldment made by TIG and EBW is more prone to corrosion due to heterogeneous microstructure as compared to FRW. This phenomenon is the result of the continuous spalling of scale from the weld zone due to the damage occurring in the protective oxide layer provides paths by which corrosive gases can reach the base material and will thus allow significant grain boundary corrosion attack (Danyluk and Park, 1979; Wang, 1988 and Sadique et al, 2000).

25. Only minor spalling of the scales was observed in AISI 304 base metals during the molten salt corrosion for all the environments. The scales in general showed no tendency towards spalling/cracking and were found intact.

26. All the dissimilar weldments after exposure to air as well as molten salt induced oxidation have shown the presence of mainly oxides as has been indicated by surface XRD and EDAX analysis. The phases revealed are Fe_2O_3 , Cr_2O_3 , NiO , MnO , NiFe_2O_4 , NiCr_2O_4 , $(\text{Cr,Fe})_2\text{O}_3$. These oxides especially Cr_2O_3 offer a better protection against oxidation/hot corrosion due to their low growth rate, strongly bounded compositions and ability to act as effective barriers against ionic migration (Stott, 1989).

27. For better hot corrosion resistance, the heat-generating phase has to be kept to a minimum by keeping optimum burn-off length for friction welding process as it will decrease the amount of intermetallics and maintain better uniformity of microstructure.

SUGGESTIONS FOR FUTURE WORK

1. The use of friction welding with buttering material like nickel may reduce the problem of carbon migration.
2. The studies can be made in the effect of friction force and forging force on mechanical and corrosion properties.
3. Studies can be made for the exposure of these weldments for different lengths of time so that progressive development of the scale can be studied and mechanism of transport of species and gradual development of the scale can be understood.
4. Hot stage microscopy can also be used to follow the development of the scale throughout the oxidation and hot corrosion runs.
5. Studies can be made to evaluate the detailed mechanism of hot corrosion in the dissimilar weldment.
6. To have better insight into the behaviour of weldments in aggressive environment, reactions between oxides and molten salt should be studied in more detail.
7. The weldment behaviour can be studied in the actual running boiler for longer duration may be for few years.

Reference	Look in	Reference	Look in
Kosecek A.M.	A	Voronov N.P.	N
Lopatko A.P.	A	Braun O.	O
Price A.T.	A	Larsen O.H.	O
Phaniraj C.	C	Vartia P.	P
Wang C.J.	C	Haas P.E.	P
Powers D.E.	D	Daniel P.L.	P
Johnson D.M.	D	Nicholson R.D.	R
Brandes E.A.	E	Sinko R.J.	R
Latham E.P.	E	Singh Raman R.K.	R
Franchini F.	F	Kleuh R.L.	R
Becket F.J.	F	Parmar R.S.	R
Israel G.	G	Ahila S.	S
Sayegh G.	G	Elliott S.	S
Nikiforov G.D.	G	Lin S.	S
Linnert G.E.	G	Matsui S.	S
Theus G.J.	G	Yin S.	S
Grigorenko G.M.	G	Meshram S.D.	S
Grabke H. J.	H	Bhole S.D.	S
Tran H.N.	H	Sunderesan S.	S
Klower J.	J	Nelson T. W.	T
Ruge J.	J	Siewert T.A.	T
Tusek J.	J	Dragunov V.K.	V
Oakey J.E.	J	Nesterenkov V.M.	V
Ruge J.L.	J	Satyanarayana V.V.	V
Salmenoja K.	K	Johnson W.R.	W
Murti K.G.K.	K	Akutsu Y.	Y
Lee K.N.	K	Arata Y.	Y
Wang K. K.	K	Hiraoka Y.	Y
Beres L.	L	Itoh Y.	Y
Okazaki M.	M	Kawahara Y.	Y
Uusitalo M.A.	M	Liu Y.	Y
Hollander M.B.	M	Shinata Y.	Y
Mayoral M.C.	M	Li Y.S.	Y
Hurdus M.H.	M	Sun Z.	Z
McNallan M.J.	M		
Hossain M.K.	M		
Schwartz M.M.	M		
Birks N.	N		
Trafford N. H.	N		
Hiramatsu N.	N		
Zdemir N. O	N		
Electron N.N.	N		

REFERENCES

1. A.M. Kosecek, J. Bobcik and J. Andrlík, (1986), Electron beam welding of hobbing cutters, Conf. Electron and Laser Beam Welding, Tokyo, Japan, July 12-19, Pergamon, Oxford, UK, 1986, pp. 101-107.
2. A.P. Lopatko and N.I. Nikitin, (1985), Effect of beam oscillations in electron beam welding on the structure of the fusion zone of pearlitic and austenitic steels, *Weld. Prod. (USSR)*, 32(11), 37-39.
3. A.T. Price, (1982), in: Proceedings of the AWS/EPRI Conference on joining dissimilar Metals, Pittsburg, PA, pp. 48-79.
4. Agarwal, A., Katipelli, L. R. and Dahotre, N. B., (2000), "Elevated Temperature Oxidation of Laser Surface Engineered Composite Boride Coating on Steel," *Metall., Mater. Trans. A*, Vol. 31A, No. 2, pp. 461-73.
5. Ahila .S, Ramakrishna Iyer and V M Radhakrishnan, (1994), Hot corrosion of 2.25 Cr-1Mo boiler tube steel and its weldments Part I: Thermo Gravimetric And Metallurgical Study, *Trans Indian Inst Met*, Vol 47, nos 2-3 , pp 169-182.
6. Ahmet Durgutlu, (2004), Experimental investigation of the effect of hydrogen in argon as a shielding gas on TIG welding of austenitic stainless steel *Materials and Design*, 25 19–23.
7. Almeraya, C. F., Martinez, V. A. and Gonzalez, R. J. G., (1998), "Electrochemical Studies of Hot Corrosion of Type 347H Stainless Steel," *British Corros. J.*, Vol. 33, No. 4, pp. 288-91.
8. Arivazhagan N, Surendra Singh, SatyaPrakash and Reddy G.M, (2006), "High Temperature corrosion studies on friction welded dissimilar metals", *Materials Science & Engineering: B journal*, Vol 132, 222-227.
9. ASME. (1986), ASME Boiler and Pressure Vessel Code, Code Case N-47. New York: ASME.
10. ASME, (1986), ASME Boiler and Pressure Vessel Code, Code Case N-47. New York: ASME.
11. Avery R.E. (1991), *Chemical Engineering Progress*, p.70.
12. Bani P. Mohanty, David A. Shores, (2004), Role of chlorides in hot corrosion of a cast Fe–Cr–Ni alloy. Part I: Experimental studies, *Corrosion Science* 46 2893–2907

13. Barbooti, M. M., Al-Madfai, S. H. and Nassouri, H. J., (1988), "Thermochemical Studies on Hot Ash Corrosion of Stainless Steel 304 and Inhibition by Magnesium Sulphate," *Thermochimica Acta*, Vol. 126, pp. 43-49.
14. Barnhouse EJ, Lippold JC. (1988), Microstructure/property relationship in dissimilar welds between duplex stainless steel and carbon steels. *Welding J*; (December):477–87.
15. Birks, N. and Meier, G. H., (1983), "Introduction to High Temperature Oxid. Met.," Edward Arnold (Publ.) Ltd, 41 Bedford Square, London WC1B 3DQ.
16. Bland J. (1956), *Welding J—Res Suppl*; 35:181s.
17. Bornstein, N. S. and Decrescente, M. A., (1970), "The Role of Sodium and Sulfur in the Accelerated Oxidation Phenomena-Sulfidation," *Corrosion*, Vol. 26, No. 7, pp. 209-214.
18. Bornstein, N. S., Decrescente, M. A. and Roth, H. A., (1975), "Effect of Vanadium and Sodium Compounds on the Accelerated Oxidation of Nickel Base Alloys," *Proc. of Conf. on Gas Turbine Mater. in the Marine Environment*, MMIC-75-27, Columbus, Ohio, USA, pp. 115-60.
19. Byeong Geun Seonga, Soon Young Hwanga, Kyoo Young Kimb,U, (2000), High-temperature corrosion of recuperators used in steel Mills, *Surface and Coatings Technology* Vol. 126, 256-265.
20. C. Phaniraj, M. Valson, S.L. Mannan, and P. Rodriquez, (1984), *Proc. Workshop-on Oxidation of Metals and Alloys*, Kalpakkam, Indian Inst. of Metals, Kalpakkam Branch, pp. 171-95.
21. C.J. Wang , J.W. Lee , T.H. a b, Twua, (2003), Corrosion behaviors of low carbon steel, SUS310 and Fe–Mn–Al alloy with hot-dipped aluminum coatings in NaCl-induced hot corrosion *Surface and Coatings Technology* 163 –164 37–43.
22. C.J.Cheng, (1963), Transient Temperature Distribution During Friction Welding of Two Dissimilar Materials in Tabular Form, *Welding Journal*, Vol. 54(5): 233s-240s, May,
23. Celik and A. Alsarhan, (1999), Mechanical and Structural Properties of Similar and Dissimilar Steel Joints, *MATERIALS CHARACTERIZATION* 43:311–318

24. Charng-Cheng Tsaura, James C. Rocka, Chaur-Jeng Wangb, Yung-Hua Sub, (2005), The hot corrosion of 310 stainless steel with pre-coated NaCl/Na₂SO₄ mixtures at 750 °C *Materials Chemistry and Physics* 89 445–453.
25. Chatterjee, U. K., Bose, S. K. and Roy, S. K., (2001), “Environmental Degradation of Metals,” Pub., Marcel Dekker, 270 Madison Avenue, New York.
26. Chaur-Jeng Wang and Tien-Tsuo He, (2002), Morphological Development of Subscale Formation in Fe–Cr–(Ni) Alloys with Chloride and Sulfates Coating, *Oxidation of Metals*, Vol. 58, Nos. 3/4.
27. Chew B, Harris P. (1979), *Met Construction*; 11(5):11.
28. Colebeck EW, Rait JR. (1952), High temperature steel and alloys for gas turbines. *Ist special rep*; 43:107.
29. D.E. Powers and B.W. Schumacher, (1989), Using the electron beam in air to weld conventionally produced sheet metal parts, *Weld, J.*, 68(2), 48-53.
30. D.E. Powers, (1988), Electron beam welding—an overview, in E.A. Metzbower and D. Hauser (eds.), *Proc. Conf. Power Beam Processing*, ASM International, Ohio, , pp. 25-33.
31. D.E. Powers, (1988), Electron beam welding—an overview, in E.A. Metzbower and D. Hauser (eds.), *Proc. Conf. Power Beam Processing*, ASM International, Ohio, , pp. 25-33.
32. D.M. Johnson, D.P. Whittle, (1975), *J. Stringer, Corros. Sci.* 15 649.
33. Danyluk, S. and Park, J. Y., (1979), “Technical Note: Corrosion and Grain Boundary Penetration in Type 316 Stainless Steel Exposed to a Coal Gasification Environment,” *Corrosion*, Vol. 35, No. 12, pp. 575-76.
34. Deb, D, Iyer, S. R. and Radhakrishnan, V. M., (1996), “A Comparative Study of Oxidation and Hot Corrosion of a Cast Nickel Base Superalloy in Different Corrosive Environments,” *Mater. Letters*, Vol. 29, pp. 19-23.
35. Decker, C. Oestmann and J. Ruge, (1986), Metallurgical properties of electron beam welded dissimilar metal joints, *Conf. Welding in Nuclear Engineering*, Nuremberg, Germany, November 26-28, Deutschen Verband fur Schweisstechnik e.V., Dusseldorf, Germany, 1986, pp. 147-152.
36. Detka, (1989), Electron beam welding of tantalum and niobium, *Przegl. Spawalnictwa*, 41(2) 14-16.

37. Dooley, R. B. and Wilson, J. R., (1975), "The Corrosion of 50Cr-50Ni Alloy in Liquid Vanadate Systems in the Temperature Range 750-950⁰C," Trans. ASME, July, pp. 422-28.
38. E.A. Brandes (ed.), 1983, Smithwells Metals Reference Book, Butter-worth, London, 6th ed.
39. E.P. Latham, D.B. Meadowcroft, L. Pinder, Materials Science and Technology 5 (1989), 813.
40. EPRI. (1993), EPRI report TR-102433-V2, boiler tube failure metallurgical guide. Palo Alto, EPRI;
41. F. Franchini and P. Pierantozzi, (1992), Electron beam welding of different materials: Niobium-base alloy C-103 with titanium-base alloy Ti-6Al-4V ELI, Weld. Int. 6(10) 792-797.
42. F. Franchini, (1993), Electron beam welding of heterogeneous materials for steam turbine blades, Weld. Int., 7(3) 206-210.
43. F.J. Becket, (1987), Electron beam welding in product design and manufacture, Conf. Power Beam Technoi.. Brighton, UK, 10-12 Sept. 1986, The Welding Institute, Cambridge, UK, , pp. 97-112.
44. Ferrous Alloys: High Temperature Property Data, ASM International.
45. Fryburg, G. C., Kohl, F. J. and Stearns, C. A., (1984), "Chemical Reactions Involved in the Initiation of Hot Corrosion of IN-738," J. Electrochem. Soc., Vol. 131, No. 12, pp. 2985-96.
46. G. Israel, (1986), Experiences with transition welds between a copper-chromium-zirconium alloy and NiCr15Fe on nickel limiters, Schweissen Schneiden, 38(10) 495-501.
47. G. Sayegh and R. Cazes, (1985), Where does laser beam compete with electron beam in industrial welding applications?, Conf. the Laser versus the Electron Beam in Welding, Cutting and Surface Treatment: State of the Art, Reno, Nevada, USA, Nov. 6-8., Vol. I, Bakish Materials Corp., Englewood, New Jersey, USA, pp. 273-288.
48. G. Sayegh, (1985), Application of electron beams in welding metals, Conf. 6th General Assembly CENIM (6th Asamblea General del CENIM) II, Madrid, Spain, Oct. 8-11, Paper No. 43, CEN'M, Avda. Madrid, Spain, p. 10.

49. G. Sayegh, (1985), Application of electron beams in welding metals, Conf. 6th General Assembly CENIM (6th Asamblea General del CENIM) II, Madrid, Spain, Oct. 8-11, Paper No. 43, CENIM, Avda. Madrid, Spain, p. 10.
50. G.D. Nikiforov, E.N. Sivov, N.P. Krutogolovov and N.E. Si-bova, (1986), Corrosion resistance of weld joints of niobium with steel in boiling nitric acid, Svar. Proizvod, (1) 22-24.
51. G.E. Linnert, (1994), Welding Metallurgy, Carbon and Alloy Steels, vol. 1, 4th ed., AWS, Miami, FL, USA.
52. G.J. Theus and P.L. Daniel, (1983), "Corrosion in Power Generating Equipment". Proc. 8 The International Brown Boveri Symposium, Baden, Switzerland, p.185.
53. G.M. Grigorenko and A.A. Gordonnaya, (1991), Effect of the number of passes on the structure, phase composition and properties of electron-beam welded joints between joints between alitised 12Kh18N10T steel and ADI aluminium, Paton Weld. J., 3(11) 861-864.
54. Gardiner, C. P. and Melchers, R. E., (2002), "Corrosion of Mild Steel by Coal and Iron Ore," Corros. Sci., Vol. 44, No. 12, pp. 2665-73.
55. Gatlinburg, Tenn., May 18-22, (1986), (Ed. S. A. David), ASM International, Metals Park, Ohio, 509-513.
56. Goebel, J. A. and Pettit, F. S., (1970), "Na₂SO₄ - Induced Accelerated Oxidation (Hot Corrosion) of Nickel," Met. Trans., Vol. 1, pp. 1943-54.
57. Goebel, J. A. and Pettit, F. S., (1970), "Na₂SO₄ - Induced Accelerated Oxidation (Hot Corrosion) of Nickel," Met. Trans., Vol. 1, pp. 1943-54.
58. Goebel, J. A., Pettit, F. S. and Goward, G. W., (1973), "Mechanisms for the Hot Corrosion of Nickel-Base Alloys," Metall. Trans., Vol. 4, pp. 261-75.
59. Gurrappa, (1999), Hot Corrosion Behavior of CM 247 LC Alloy in Na₂SO₄ and NaCl Environments Oxidation of Metals, Vol. 51, Nos. 5/6.
60. H. J. Grabke, (1991), Incinerating Municipal and Industrial Waste (ed. R. W. Bryers), pp. 161-177. Hemisphere Publ. Corp.
61. H. J. Grabke, E. Reese and M. Spiegel, (1995), The Effects Of Chlorides, Hydrogen Chloride, And Sulfur Dioxide In The Oxidation Of Steels Below Deposits, Corrosion Science, Vol. 37, No. 7, pp. 1023-1043.
62. H.J. Grabke, (1995), E. Reese, M. Spiegel, Corrosion Science 37 1023.
63. H.J. Grabke, E. Reese, M. Spiegel, (1998), Molten Salt Forum 5-6 405.

64. H.J. Grabke, (1991), Fundamental mechanisms of the attack of chlorine, HCl and chlorides on steels and high temperature alloys in the temperature range 400 to 900 °C, in: R.W. Bryers (Ed.), Inc incrating Municipal and Industrial Wastes, Hemisphere, New York, pp. 161–176.
65. H.N. Tran, D. Barham, M. Hupa, (1988), Materials Performance 27 40.
66. H.P. Nielsen, K. Dam-Johansen, L.L. Baxter, (2000), Progress in Energy and Combustion Science 26 283.
67. Hancock, P., (1987), “Vanadic and Chloride Attack of Superalloys,” Mater.Sci. Technol., Vol. 3, pp. 536-44.
68. Hancock, P., (1987), “Vanadic and Chloride Attack of Superalloys,” Mater. Sci. Technol., Vol. 3, pp. 536-44.
69. Haugsrud, R., (2003), “On the High-Temperature Oxidation of Nickel,” Corros. Sci., Vol. 45, No. 1, pp. 211-35.
70. He, J. L., Chen, K. C., Chen, C. C., Leyland, A. and Matthews, A., (2001), “Cyclic Oxidation Resistance of Ni-Al Alloy Coatings Deposited on Steel by a Cathodic Arc Plasma Process,” Surf. Coat. Technol., Vol. 135, pp. 158-65.
71. Heath, G. R., Heimgartner, P., Irons, G., Miller, R. and Gustafsson, S., (1997), “An Assessment of Thermal Spray Coating Technologies for High Temperature Corrosion Protection,” Mater. Sci. Forum, Vol. 251-54, pp. 809-16.
72. Hiramatsu, N. and Stott, F. H., (2000), “The Effects of Molybdenum on the High-Temperature Oxidation Resistance of Thin Foils of Fe-20Cr-5Al at very High Temperatures,” Oxid. Met., Vol. 53, No. 5-6, pp. 561-75.
73. Hwang, Y. S. and Rapp, R. A., (1989), “Thermochemistry and Solubilities of Oxides in Sodium Sulfate-Vanadate Solutions,” Corrosion, Vol. 45, No. 11, pp. 933-37.
74. Hwang, Y. S. and Rapp, R. A., (1989), “Thermochemistry and Solubilities of Oxides in Sodium Sulfate-Vanadate Solutions,” Corrosion, Vol. 45, No. 11, pp. 933-37.
75. Iyer, S. R., Iyer, K. J. L. and Radhakrishnan, V. M., (1987), “High Temperature Corrosion of a Ni-Base Superalloy by Vanadium,” Proc. of 10th ICMC, Madras, India, Vol. IV, pp. 3665-70.
76. J. Klower, F.E. White, (1995), High temperature corrosion of commercial heat-resistant alloys under deposits of alkali salts: recent laboratory data,

- Proceedings of the 8th International Symposium on Corrosion in the Pulp & Paper industry, Tappi Press, Atlanta, USA, pp. 179–188.
77. J. Klower, F.E. White, (1995), High temperature corrosion of commercial heat-resistant alloys under deposits of alkali salts: recent laboratory data, in: Proceedings of the 8th International Symposium on Corrosion in the Pulp & Paper industry, Tappi Press, Atlanta, USA, pp. 179-188.
 78. J. Ruge, C. Oestmann, I. Decker and K. Iversen, (1986), Welding of dissimilar metals by using the method of electron beam welding with filler wire, Proc. Conf. Electron and Laser Beam Welding, Tokyo, Japan, July 12-19, Pergamon, Oxford, UK, pp. 193-203.
 79. J. Ruge, C. Oestmann, I. Decker and K. Iversen, (1986), Welding of dissimilar metals by using the method of electron beam welding with filler wire, Proc. Conf. Electron and Laser Beam Welding, Tokyo, Japan, July 12-19, Pergamon, Oxford, UK, pp. 193-203.
 80. J. Tusek, Z. Kampus, M. Suban, (2001), “Welding of tailored blanks of different materials”, Journal of Materials Processing Technology 119 180-184.
 81. J.E. Oakey, A.J. Minchener, N.J. Hodges, (1991), Journal of the Institute of Energy Vol 64, 3.
 82. J.L. Ruge, C.M. Oestmann and I.A. Decker, (1986), Joint quality of EB welds using filler wire (EBW-FW), Conf. Power Beam Technol., Brighton, UK, 10-12 Sept., The Welding Institute, Cambridge, UK, pp. 351-359.
 83. J.L. Ruge, C.M. Oestmann and I.A. Decker, (1987), Joint quality of EB welds using filler wire (EBW-FW), Conf. Power Beam Technol., Brighton, UK, Sept. 10-12 The Welding Institute, Cambridge, UK, pp. 351-359.
 84. Joh.F.Fickel, (1964), Diffusion across Dissimilar metal joints, Welding Journal, Vol. 43(4): 170s-178s.
 85. K. Salmenoja, (2000), Field and Laboratory Studies on Chlorine-induced Corrosion in Boilers Fired with Biofuels, Academic dissertation, Abo Academi, Turku, Finland,
 86. K. Salmenoja, (2000), Field and Laboratory Studies on Chlorine-induced Corrosion in Boilers Fired with Biofuels, Academic dissertation, Abo Academi, Turku, Finland.

87. K. Salmenoja, K. Makela, M. Hupa, R. Backman, (1996), J. Institute of Energy 69 155.
88. K. Salmenoja, K. Makela, Tappi, (1999), Journal 82 161.
89. K. Salmenoja, K. Makela, Tappi, (1999), Journal 82 161.
90. K.G.K.Murti and S.Sundarsean, (1985), Thermal Behavior of Austenitic-Ferritic Transition Joints Made by Friction Welding, Welding Journal 64(12): 327s-334s.
91. K.N. Lee, D.A. Shores, (1990), Transport considerations in the hot corrosion of Ni by Molten alkali carbonates, J. Electrochem. Soc. 137, 859–871.
92. Kane, R. H., (1980), “Characterization of High Temperature Gaseous Environments,” Corrosion, Vol. 36, No. 3, pp. 112-18.
93. Kenneth Easterling: Introduction to the Physical Metallurgy of Welding, 2nd edition, Butterworth-Heinmann Publishers.
94. Kerby, R. C. and Wilson J. R., (1973), “Corrosion of Metals by Liquid Vanadium Pentoxide and the Sodium Vanadates,” Trans. ASME, January, pp. 36-44.
95. Khanna, A. S. and Jha, S. K., (1998), “Degradation of Materials Under Hot Corrosion Conditions,” Trans. Indian Inst. Met., Vol. 51, No. 5, pp. 279-90.
96. Khanna, A. S. and Jha, S. K., (1998), “Degradation of Materials Under Hot Corrosion Conditions,” Trans. Indian Inst. Met., Vol. 51, No. 5, pp. 279-90.
97. Khare A.K., (1981), Ferritic steels for high temperature applications. ASM International conference, Warrendale, PA.
98. K. K.Wang, (1975), Friction Welding, WRC Bulletin 204.
99. Klueh R.L. and King J.F, (1982), 61:9.
100. Kofstad, P., (1990), “High Temperature Corrosion of Metals,” Proc. of Conf. on Microscopy of Oxidation, London, pp. 1-9.
101. Kolta, G. A., Hewaidy, L. F. and Felix, N. S., (1972), “Reactions Between Sodium Sulphate and Vanadium Pentoxide,” Thermochem. Acta, Vol. 4, pp. 151-64.
102. Krishna, B. V. and Sidhu, R. K., (2001), “High Temperature Corrosion of INCONEL 600 Tube– A Case Study,” Met. Mater. Procs., Vol. 14, No.1, pp. 21-26.

103. Krishna, B. V. and Sidhu, R. K., (2002), "Pitting Corrosion of Steel Tubes in an Air Preheater, Practical Failure Analysis," ASM Int., Vol. 2, No. 5, pp. 61-66.
104. Kuiry, C., Seal, S., Bose, S. K. and Roy, S. K., (1994), "Effect of Surface Preparation on the High-Temperature Oxidation Behaviour of AISI 316 Stainless Steel," ISIJ Int., Vol. 34, No. 7, pp. 599-606.
105. L. Beres, A. Balogh, W. Irmer, and C. S. Kirk, (2003), Welding Research, November 330.
106. Laha K, Rao KBS, Mannan SL. Mater Sci Engng, (1990), 129:183.
107. Lai, G. Y., (1990), "High temperature corrosion of engineering alloys," ASM International Book.
108. Lai, G. Y., (1990), "High temperature corrosion of engineering alloys," ASM International Book.
109. Lambert.P, Champagne.B, Arseneault.B, (1991), Canadian Metallurgical Quarterly 30 (2), pp125-130.
110. Lee, W. H., and Lin, R. Y., (1999), "Oxidation, Sulphidation and Hot Corrosion of Intermetallic Compound Fe₃Al at 605⁰C to 800⁰C," Mater. Chem. Phy., Vol. 58, No. 3, pp. 231-42.
111. Levy, M., Huie, R. and Pettit, F., (1989), "Oxidation and Hot Corrosion of Some Advanced Superalloys at 1300 to 2000⁰F (704 to 1093⁰C)," Corrosion, Vol. 45, No. 8, pp. 661-74.
112. Liu, P. S., Liang, K. M., Zhou, H. Y., Gu, S. R., Sun, X. F., Guan, H. R., Jin, T. and Yang, K. N., (2001), "Cyclic Oxidation Behavior of Aluminide Coatings on the Co-Base Superalloy DZ40M," Surf. Coat. Technol., Vol. 145, pp. 75-79.
113. Luthra, K. L., (1985), "Kinetics of the Low Temperature Hot Corrosion of Co-Cr-Al Alloys," J. Electrochem. Soc., Vol. 132, No. 6, pp. 1293-98.
114. M. Okazaki, Y. Mutoh and Y. Ikeda, (1989), Creep-fatigue strength and its prediction of dissimilar metal electron beam welded joint, J. Soc. Mater. Sci. Jpn., 38(425) 168-174.
115. M. Okazaki, Y. Mutoh and Y. Ikeda, (1989), Creep-fatigue strength and its prediction of dissimilar metal electron beam welded joint, J. Soc. Mater. Sci. Jpn., 38(425) 168-174.

116. M.A. Uusitalo, P.M.J. Vuoristo, T.A. Mantyla, (2002), Chlorine corrosion of thermally sprayed coatings at elevated temperatures, in: E. Lugsheider (Ed.), International Thermal Spray Conference, Essen, Germany, March 4-6, DVS, pp. 429–434.
117. M.A. Uusitalo, P.M.J. Vuoristo, T.A. Maantyla, (2004), High Temperature Corrosion of Coatings and Boiler Steels Below Chlorine-Containing Salt Deposits, *Corrosion Science* 46 1311–1331
118. M.A. Uusitalo, P.M.J. Vuoristo, T.A. Mantyla, (2004), High temperature corrosion of coatings and boiler steels below chlorine-containing salt deposits, *Corrosion Science* 46, 1311–1331.
119. M.B.Hollander, C.J.Cheng and J.C.Wyman., (1963), Friction Welding Parameters Analysis, *Welding Journal*, Vol. 54(11):495s-501s.
120. M.C. Mayoral, J.M. Andre's, J. Belzunce, V. Higuera, (2006), Study of sulphidation and chlorination on oxidized SS310 and plasma-sprayed Ni–Cr coatings as simulation of hot corrosion in fouling and slagging in combustion, *Corrosion Science* 48 1319–1336.
121. M.H. Hurdus, L.Tomlinson, J.M. Tichmarsh, (1990), *Oxidation of Metals.*; 34:5.
122. M.J. McNallan, W.W. Liang, S.H. Kim, G.T. Kang, (1981), Acceleration of the high temperature oxidation of metals by chlorine, R.A. Rapp (Ed.), *High Temperature Corrosion*, San Diego California, March 2–6, Nace, pp. 316–321.
123. M.K. Hossain, S.R.J. Saunders, (1978), *Oxid. Met.* 12 1.
124. M.M. Schwartz, (1969), *Modern Metal Joining Techniques*, Wiley, New York,.
125. Malik, A. U. and Mobin, M., (1987), “Studies on Some Solid State Reactions Relevant to Hot Corrosion,” *Proc. of 10th ICMC*, Madras, India, Vol. IV, pp. 3345-65.
126. Mandich LS, Fogelmen EL, Gulya JA., (1956), *Symposium heat treated steel for elevated temperature services*. New Orleans, LA: ASME.
127. *Metals Handbook*, (1975), "Failure analysis and Prevention," Vol.10, ASM Publication, Metals Park Ohio.
128. Meuronen, (1994), private communication with Valmet Lentokonete-ollisuus Oy, Linnavuori, Finland,.

129. Misra, A. K., (1986), "Mechanism of Na₂SO₄-Induced Corrosion of Molybdenum Containing Nickel-Base Superalloys at High Temperatures," J. Electrochem. Soc., Vol. 133, No. 5, pp. 1029-37.
130. Mobin, M., Malik, A. U., Ahmad, S., Hasan, S. K. and Ajmal, M., (1996), "Studies on the Interactions of Metal Oxides and Na₂SO₄ at 1100 and 1200 K in Oxygen," Bull. Mater. Sci., Vol. 19, No. 5, pp. 807-21.
131. Moujahid, S. E., (1987), "High Temperature Corrosion of Cast Iron Chains by Coal Ash," Proc. of 10th ICMC, Madras, India, Vol. I, pp. 857-60.
132. N. Birks and G.M. Meyer, (1982), Introduction to High Temperature Oxidation of Metals, Edward Arnold, London.
133. N. H. Trafford and D. P. Whittle, (1980), The Salt-Induced Corrosion Behaviour of Fe-Cr Alloys at Elevated Temperatures. II. Alloys Rich in Chromium, Corrosion Science, Vol. 20, Pp. 509 to 530.
134. N. Hiramatsu, Y. Uematsu, T. Tanaka, M. Kinugasa, (1989), Materials Science and Engineering, A Vol 120, 319.
135. N. Ozdemir, F. Sarsilmaz, A. Hascalik, (2007), Effect of rotational speed on the interface properties of friction-welded AISI 304L to 4340 steel, Materials and Design 28 301–307
136. N.N. Electron, (1993), beam process improves weld quality, Shiprepair. 45-55.
137. N.P. Voronov, (1991), Electron beam welding EP-288 steel and VZhL-14 alloy, Paton Weld. J, 3(4) 317-318.
138. NACE, (1982), "Corrosion Estimating of Chemical Cleaning Solvents", NACE publication, Material Performance,; 3M: 182
139. Nanni, P., Buscaglia, V., Asmundis, C. D. and Roy, S. K., (1987), "Sodium Sulphate Induced Hot Corrosion of Pure Fe, Mn and Cr in Combustion Gas," Proc. of 10th ICMC, Madras, India, Vol. IV, pp. 3413-22.
140. Natesan, K., (1976), "Corrosion-Erosion Behavior of Materials in a Coal-Gasification Environment," Corrosion, Vol. 32, No. 9, pp. 364-70.
141. Natesan, K., (1985), "High-Temperature Corrosion in Coal Gasification Systems," Corrosion, Vol. 41, No. 11, pp. 646-55.
142. O. Braun, J.J. Chene and G. Schmelzer, (1991), Towards a full exploitation of the electron beam welding process, Proc. Int. Conf. Joining/ Welding 2000, The Hague, The Netherlands, July 1-2, Pergamon, Oxford, pp. 107-118.

143. O.H. Larsen, N. Henriksen, (1996), Ash deposition and high temperature corrosion at combustion of aggressive fuels, in: Power Plant Chemical Technology, Kolding, Denmark, September 4-6, Elsam, pp. 7.1-7.18.
144. Omar A., (1991), Conference proceedings on Welded dissimilar metals in wet sour service National Association of corrosion engineers (NACE), Arabian Gulf Section, p. 453.
145. Otero, E., Merino, M. C., Pardo, A., Biezma, M. V. and Buitrago, G., (1987), "Study on Corrosion Products of IN657 Alloy in Molten Salts," Proc. of 10th ICMC, Madras, India, Vol. IV, pp. 3583-91.
146. Otero, E., Pardo, A., Hernaez, J. and Perez, F. J., (1990), "The Hot Corrosion of IN-657 Superalloy in Na₂SO₄-V₂O₅ Melt Eutectic," Corros. Sci., Vol. 30, pp. 677-83.
147. Otero, E., Pardo, A., Hernaez, J. and Perez, F. J., (1992), "The Corrosion of Some Superalloys (At 1000 K) in Molten Eutectic Mixture 60% V₂O₅-40% Na₂SO₄. The Influence of the Oxygen and Carbon Residues," Corros. Sci., Vol. 34, pp. 1747-57.
148. P. Vartia, (1993), private communication with the Technical Research Centre of Finland, Espoo, Finland.
149. P.E. Haas, (1982), in: Proceedings of the AWS/EPRI Conference on joining dissimilar Metals, Pittsburgh, PA, pp. 37-47.
150. P.L. Daniel, L.D. Paul, J.M. Tanzosh, R. Hubinger, (1989), Materials Performance Vol 27, 41.
151. Pantony, D. A. and Vasu, K. L., (1968), "Studies in the Corrosion of Metals Under Melts-1. Theoretical Survey of Fire-Side Corrosion of Boilers and Gas-Turbines in the Presence of Vanadium Pentoxide," J. Inorg. Nucl. Chem., Vol. 30, pp. 423-32.
152. Peters, K. R., Whittle, D. P. and Stringer, J., (1976), "Oxidation and Hot Corrosion of Nickel-Based Alloys Containing Molybdenum," Corros. Sci., Vol. 16, pp. 791-804.
153. Pettit, F. S. and Giggins, C. S., (1987), "Hot Corrosion, Ch. 12," Superalloys II, Sims, C. T., Stoloff, N. S. and Hagel, W. C. (Eds.), Wiley Pub., N. Y.
154. Pettit, F. S. and Meier, G. H., (1984), "Oxidation and Hot corrosion of Superalloys," Superalloys , M. Gell, C. S. Kartovich, R. H. Bricknel, W. B.

- Kent, J. F. Radovich (Eds.), The Met. Soc. of AIME, Warrendale, Pennsylvania, pp. 651-687.
155. Prakash, S., Singh, S., Sidhu, B. S. and Madeshia, A., (2001), "Tube Failures in Coal Fired Boilers," Proc. National Seminar on Advances in Material and Processing, 9-10th Nov., IIT, Roorkee, India, pp. 245-53.
 156. R.D. Nicholson, (1984), Met. Technol. 11 115.
 157. R.J. Russell, (1980), Electron beam welding for dual metal strip, Weld. J. 61(1) 21-24.
 158. R.J. Sinko in S.A. David and J.M. Vitek, (eds.), (1993), Niobium to copper electron beam weldability study, Proc. Int. Conf. on Trends in Welding Research, Gatlinburg, TN, June 1992, ASM Int., pp. 787-791.
 159. R.J. Sinko in S.A. David and J.M. Vitek, (eds.), (1993), Niobium to copper electron beam weldability study, Proc. Int. Conf. on Trends in Welding Research, Gatlinburg, TN, June 1992, ASM Int., pp. 787-791.
 160. R.K. Singh Raman and J.B. Gnanamborthy, (1992), J. Mater. Sci., vol. 27, pp. 3435-41.
 161. R.K. Singh Raman and J.B. Gnanamoorthy, (1993), Corr. Sci., vol. 34, pp. 1275-88.
 162. R.K. Singh Raman, B.C. Muddle, (2002), High temperature oxidation in the context of life assessment and microstructural degradation of weldments of 2.25Cr-1Mo steel International Journal of Pressure Vessels and Piping 79 585-590.
 163. R.K. Singh Raman, J.B. Gnanamoorthy, S.K. Roy S.K, (1994), Oxidation of metals, 42:5.
 164. R.K. Singh Raman, (1998), Metall. Mater. Trans., vol. 29A, pp. 577-86.
 165. R.L.Kleuh and J.F.King, (1982), Austenitic Stainless Steel-FerriticSteel Weld Joint Failures, Welding Journal 61(9): 302s-31 Is.
 166. R.S.Parmar, Welding Processes and Technology, Khanna Publishers.
 167. Rapp, R. A. and K. S. Goto, (1981), "The Hot Corrosion of Metals by Molten Salts," Symposium on Fused Salts, J. Braunstein and J. R. Selman (Eds.), The Electrochemical Society, Pennington, N. J., pp.159.
 168. Rapp, R. A. and Zhang, Y. S., (1994), "Hot Corrosion of Materials: Fundamental Studies," JOM, Vol. 46, No. 12, pp. 47-55.

169. Rapp, R. A., (1986), "Chemistry and Electrochemistry of the Hot Corrosion of Metals," *Corrosion*, Vol. 42, No. 10, pp. 568-77.
170. Rapp, R. A., (2002), "Hot Corrosion of Materials: A Fluxing Mechanism," *Corros. Sci*, Vol. 44, No. 2, pp. 209-21.
171. Roine, (1999), *HSC Chemistry4.0*, Outokumpu Research Oy, Pori, Finland,.
172. Roy, K., Bottino, C., Rakesh, V. R., Kuiry, S. C. and Bose, S. K., (1995), "Improved High Temperature Oxidation Behaviour of AISI 347 Grade Stainless Steel by Superficial Coating of CeO₂," *ISIJ Int.*, Vol. 35, No. 4, pp. 433-42.
173. S. Ahila, S. Ramaktishna Iyer, V.M. Radlmkrishnan and P.B.S.N.V.Prasad, (1993), A comparative study of hot corrosion of welded and unwelded 2.25 Cr- 1 MO steel, *Mater&Letters* 16 130-133.
174. S. Elliott, (1986), *New fusion joining processes for dissimilar metals*, *Welding Dissimilar Metals*, The Welding Institute, Cambridge, UK, pp. 16-19.
175. S. Lin, B. Fan and Z. Guan, (1986), Electron beam welding of dissimilar metals (niobium-molybdenum, porous tungsten-molybdenum), *Conf. Electron and Laser Beam Welding*, Tokyo, Japan, 12-19 July 1986, Pergamon, Oxford, UK, pp. 227-235.
176. S. Lin, B. Fan and Z. Guan, (1986), Electron beam welding of dissimilar metals (niobium-molybdenum, porous tungsten-molybdenum), *Conf. Electron and Laser Beam Welding*, Tokyo, Japan, July 12-19, Pergamon, Oxford, UK, pp. 227-235.
177. S. Matsui, H. Matsummura and K. Yasuda, (1987), The application of laser cutting and electron beam welding to the manufacturing of turbine nozzle diaphragms, *Weld. World*, 25 (1-2) 1)841-845.
178. S. Yin and P. Hakonen, (1991), Electron-beam welded copper-to-silver joints for thermal contact at low temperatures, *Rev. Sci. lustrum.*, 62(5) 1370-1371.
179. S.D. Meshram, T. Mohandas, G. Madhusudhan Reddy, (2007), Friction welding of dissimilar pure metals, *Journal of Materials Processing Technology* 184 330–337.
180. S.D.Bhole, (1991), Interface properties in Friction Welding- A Technical Note, *Welding Journal*, Vol. 82(7): 168s- 172s.
181. S.Sunderesan, (1976), *Joining of Dissimilar Materials*, IIW report,.

182. Sadique, S. E., Mollah, A. H., Islam, M. S., Ali, M. M., Megat, M. H. H. and Basri, S., (2000), "High-Temperature Oxidation Behavior of Iron-Chromium-Aluminum Alloys," *Oxid. Met.*, Vol. 54, Nos. 5-6, pp. 385-400.
183. Sakai T., Asami K., Katsumata M., Takada H., and Tanaka O, (1982), ASM International, Materials Park, Ohio.; p. 340.
184. Sanderson , C.S. Punshon, J.D. Russell, (2000), Advanced welding processes for fusion reactor fabrication, *Fusion Engineering and Design* 49–50, 77–87.
185. Saxena A, Han J and Banerji K, (1987), creep crack growth behaviour in power plant Boiler and Steam Pipe Steels, EPRI Report on Project 225-10, Electric power Research institute, palo Atlo, CA
186. Seal, S., Bose, S. K. and Roy, S. K., (1994), "Improvement in the Oxidation Behaviour of Austenitic Stainless Steels by Superficially Applied, Cerium Oxide Coatings," *Oxid Met.*, Vol. 41, No. 1-2, pp. 139-78.
187. Seiersten, M. and Kofstad, P., (1987), "The Effect of SO₃ on Vanadate-Induced Hot Corrosion," *High Temp. Technol.*, Vol. 5, No. 3, pp. 115-22.
188. Shi, L., (1993), "Accelerated Oxidation of Iron Induced by Na₂SO₄ Deposits in Oxygen at 750⁰C- A New Type Low-Temperature Hot Corrosion," *Oxid. Met.*, Vol. 40, Nos. 1-2, pp. 197-211.
189. Shi, L., (1995), "On the Possibility of a Na₂SO₄-Na₂O Eutectic Melt Developing on Metals Coated with Na₂SO₄ Deposit in Oxygen/Air at Intermediate Temperatures," *Corros. Sci.*, Vol. 37, No. 8, pp. 1281-87.
190. Shih, S., Zhang, Y. and Li, X., (1989), "Sub-Melting Point Hot Corrosion of Alloys and Coatings," *Mater. Sci. Engg. A*, Vol. A120, pp. 277-82.
191. Shores, D. A., (1983), "New Perspectives on Hot Corrosion Mechanisms", *High Temperature Corrosion*, R.A. Rapp (Ed.), NACE, Houston, Texas.
192. Shushan S.M, Charles E. A and Congleton J., (1996), The Environment Assisted Cracking Of Diffusion Bonded Stainless Steel To Carbon Steel Joints In An Aqueous Chloride Solution, *corrosion science*, vol. 38, No 5, pp 673.
193. Stott, F. H., (1998), "The Role of Oxidation in the Wear of Alloys," *Trib. Int.*, Vol. 31, No. 1-3, pp. 61-71.
194. Suito, H. and Gaskell, D. R., (1971), "The Thermodynamics of Melts in the System VO₂-V₂O₅," *Metall. Trans.*, Vol. 2, pp. 3299-303.

195. Swaminathan, J., Raghavan, S. and Iyer, S. R., (1993), "Studies on the Hot Corrosion of Some Nickel-Base Superalloys by Vanadium Pentoxide," *Trans. IIM*, Vol. 46, No. 3, pp. 175-81.
196. T. W. Nelson, J. C. Lippold And M. J. Mills, (2000) Nature and Evolution of the Fusion Boundary in Ferritic-Austenitic Dissimilar Metal Welds — Part 2: On-Cooling Transformations *Welding Journal*, 267-277.
197. T.A. Siewert and D.P. Vigliotti, (1989), Mechanical properties of electron beam welds in thick copper, *Conf. Advances in Cryogenic Engineering: Materials*, Los Angeles, California, USA, July 24-28, Plenum, New York, Vol. 36B, pp. 1185-1192.
198. Tetsuo Ishitsuka, Koichi Nose, (2002), Stability of protective oxide films in waste incineration environment solubility measurement of oxides in molten chlorides, *Corrosion Science* Vol 44 247-263.
199. Tiwari, S. N. and Prakash, S., (1996), "Hot Corrosion Behaviour of an Iron-Base Superalloy in Salt Environment at Elevated Temperatures," *Proc. of Symp. on Metals and Materials Research*, IIT, Madras, 4-5th July, pp. 107-17.
200. Tiwari, S. N. and Prakash, S., (1997), "Studies on The Hot Corrosion Behaviour of Some Superalloys in Na₂SO₄-V₂O₅," *Proc. of SOLCEC*, Kalpakkam, India, 22-24th Jan., Paper C33.
201. Tiwari, S. N. and Prakash, S., (1998), "Literature Review-Magnesium Oxide as Inhibitor of Hot Oil Ash Corrosion", *Materials Science and Technology*, Vol. 14, pp. 467-72.
202. V.K. Dragunov, T.P. Muraveva and Yu.P. Rodionov, (1991), Electron beam welding dissimilar alloys used in electromagnetic devices, *Weld. Int.*, Vol 5(9) 723-725.
203. V.M. Nesterenkov, D.Yu. Novikov and I.P. Kirpach, (1991), Structure of electron beam welded joints in dissimilar steels, *Paton Welding J.*, 3(10) 841-845.
204. V.V. Satyanarayana , G. Madhusudhan Reddyb, T. Mohandasb, (2005), Dissimilar metal friction welding of austenitic–ferritic stainless steels, *Journal of Materials Processing Technology* Vol 160 128–137.
205. VILL.V.I, *Friction Welding of Metals*, American Welding Society Inc., New York.

206. W.R. Johnson, C.R. Barrett, and W.D. Nix, (1972), Metall. Trans., vol. 3, pp. 695-98.
207. Wang K.K, (1975), Friction Welding, WRC Bulletin, 204.
208. Wang, D., (1988), "Corrosion Behavior of Chromized and/or Aluminized 2¹/₄Cr-1Mo Steel in Medium-BTU Coal Gasifier Environments," Surf. Coat. Technol., Vol. 36, pp. 49-60.
209. Welding Handbook, (1982), 7th ed, American Welding Society, Miami, Florida.; Vol. 4,p. 524 .
210. Welding Handbook, (1991), American Welding Society, Miami, Florida, 8th edn., Vol. 2.
211. Welding Handbook, Metals and Their Weldability, 7th edition, Volume 4.
212. West, J. M., (1986), "Basic Corrosion and Oxidation," ELLIS Horwood Ltd., Chichester.
213. Wu, Y. and Hwang, S. K., (2002), "Microstructural Refinement and Improvement of Mechanical Properties and Oxidation Resistance in EPM TiAl-Based Intermetallics with Yttrium Addition," Acta Materialia, Vol. 50, pp. 1479-93.
214. Wyatt L.M, (1982), Materials of construction for steam power plants, ISBN 085334 661 5, London
215. Wyatt L.M, (1982), Materials of construction for steam power plants, ISBN 085334 661 5, London,.
216. Wyatt, (1978), "The Performance of Cr-Mo Steels In the Boilers of CEGB Power Stations". Proc. International Conference on Ferritic Steels for Fast Reactor Steam Generators, Ed SF Pugh and E A Little, Vol 2, p.27.
217. Xu, H., Hocking, M. G. and Sidky, P. S., (1994), "Sulfidation-Oxidation Behavior of Alloy 800H in SO₂-O₂ and H₂-H₂S-CO-CO₂ Atmospheres," Oxid. Met., Vol. 41, No. 1-2, pp. 81-101.
218. Y. Akutsu, (1980), Application of electron beam welding to steam turbine diaphragms, Beam technol. Lectures of the Int. Beam Technol. Conf, Essen, Germany, May 7-8, pp. 63-69.
219. Y. Arata, (1985), Development of ultra high energy density heat source and its application to heat processing, Okada Memorial Jpn. Soc, Tokyo.
220. Y. Hiraoka and R. Fukuda, (1992), Electron-beam welding of dissimilar refractory metals, J. High Temperature Soc Jpn., 18(1) 45-55.

221. Y. Itoh, K. Tomoda and Y. Yuasa, (1987), Fracture properties of electron beam welded dissimilar metal joints with incomplete penetration, *J. Soc. Mater. Sci. Jpn.*, 36(405) 549-555.
222. Y. Kawahara, (1997), *Materials at High Temperatures* 14 261.
223. Y. Liu, C. Sun and X. Chen, (1987), Investigation on the equipment and technology of partial vacuum electron beam welding in the continuous manufacture of bimetallic saw blade, *Trans. China Weld. Inst.*, 8(1) 31-37.
224. Y. Shinata and Y. Nishi, *Oxid. (1986), Met.*, Vol 26, 201.
225. Y. Shinata, M. Hara, T. Nakagawa, (1991), *Mater. Trans. JIM* 32, 969.
226. Y. Shinata, (1987), *Oxid. Met.* 27 315.
227. Y.S. Li, M. Spiegel, S. Shimada, (2005), Corrosion behaviour of various model alloys with NaCl–KCl coating *Materials Chemistry and Physics* 93 217–223
228. Yutaka Shinata, Fujio Takahashi, Kokichi Hashiura, (1987), NaCl-induced Hot Corrosion of Stainless Steels, *Materials Science and Engineering*, 87 399-405 399.
229. Yuuzou Kawahara, (2002), High temperature corrosion mechanisms and effect of alloying elements for materials used in waste incineration environment, *Corrosion Science* 44 223-245.
230. Z. Sun, (1996), Feasibility of producing ferritic/austenitic dissimilar metal joints by high energy density laser beam process, *Int. J. Pres. Ves. & Piping* Vol 68, 153-160.
231. Zahs, M. Spiegel, H.J. Grabke, (2000), *Corrosion Science* Vol 42 1093.
232. Zhang, X. Peng, z J. Zhao, and F. Wang, (2005), Hot Corrosion of an Electrodeposited Ni-11 wt % Cr, Nanocomposite under Molten Na₂SO₄–K₂SO₄–NaCl, *Journal of The Electrochemical Society*, 152 (9), B321-B326.